A Mechanistic Basis for the Mechanical Regulation of Skeletal Development

Claire A. Shea, B.A. (Honors), M.Sc.

A thesis submitted to the University of Dublin in partial fulfilment of the requirements for the degree of

Doctor of Philosophy

2018

Supervisor

Prof. Paula Murphy

Declaration

I declare that this thesis has not been submitted as an exercise for a degree at this or any other university and it is entirely my own work.

I agree to deposit this thesis in the University's open access institutional repository or allow the library to do so on my behalf, subject to Irish Copyright Legislation and Trinity College Library conditions of use and acknowledgement.

Claire A. Shea

May 2018

Summary

Movement is essential to the formation of a functional skeleton during embryonic development. In humans, Foetal Akinesia Deformation Syndrome (FADS) manifests clinically when a lack of foetal movement causes joint contractures (arthrogryposis), and weakened bones (hypomineralisation) (Punnett et al., 1974, Pena and Shokeir, 1976, Moessinger, 1983, Hall, 2009). During skeletogenesis, bone, cartilage, and associated tissues form from mesenchymal progenitors, and this differentiation requires precise localisation and timing of both molecular and mechanical signals. Using mouse and chick models, the host lab previously showed that mechanical forces influence gene regulation and tissue patterning during skeletal development (Nowlan et al., 2008b, Roddy et al., 2011b, Rolfe et al., 2014); however, there remains a lack of knowledge concerning the molecular mechanisms that underpin the influence of mechanical signals, which this work sought to address.

This thesis explored the activity of key signalling pathways, Wnt and BMP, under normal and reduced mechanical stimulation. Both pathways are crucial to skeletal development and are affected under reduced mechanical stimulation in the mouse forelimb (Rolfe et al., 2014). Here, canonical Wnt pathway activity is shown to be restricted to the normal developing joint, and this activity is reduced under immobilisation. Contrastingly, BMP pathway activity is restricted to transient cartilage; under immobilisation, activity expands to the joint territory. Concomitant increase in BMP pathway activity and loss of canonical Wnt activity at the joint indicates reciprocal co-ordinated regulation of the pathways under mechanical influence. This occurs simultaneously with increased expression of several pathway components in a peripheral joint territory, identifying a possible region of progenitor cells.

The work also explored two mechanisms for the transduction of mechanical signals, the Hippo-YAP pathway and the primary cilium. The Hippo pathway is known to influence cellular differentiation and is mechanosensitive (reviewed in Yu et al., 2015), but its activity in the developing skeleton is unknown. Here, spatial localisation of the pathway effector YAP is shown in regions of morphological expansion in the developing bones, with notable reduction in the chondrogenous layers of the joints. This localisation was increased and expanded in the muscle-less mutant, demonstrating that YAP localisation is mechanosensitive. Expression of YAP target genes *Ctgf* and

Cyr61 also increased, particularly at the joints. To test the role of YAP in skeletal development, high-density chondrogenic cultures (micromass) were treated with the inhibitory molecule verteporfin, which reduced chondrogenic differentiation, suggesting that YAP is pro-chondrogenic. To identify upstream control of YAP activity, *Fat4* expression was characterised, revealing expression in numerous developing tissues, including the developing limbs. However, the lack of detectable *Fat4* expression in the core of the rudiments suggests that YAP protein localisation is controlled by a *Fat4*-independent mechanism.

The primary cilium is responsive to mechanical cues and is implicated in Hedgehog and Wnt signalling. Here, features of the primary cilium in developing skeletal tissues were characterised, showing that cilia occurrence varies across the developing rudiment but is consistent between wildtype and muscle-less mutant. Cilia were also generally shorter in the mutant. Cilia were observed to be positioned and oriented away from the joint line, which was maintained in the mutant. These data characterise cilia during normal and impaired skeletal development, and could explain some observed differences in chondrocyte behaviour under immobilisation.

Finally, two methods for assaying the spatial control of chondrogenesis *in vitro* were established. First, high-density micromass culture was used to explore the self-organising formation of chondrogenic condensations (nodules) under a Turing-like mechanism. An optimised, automated approach for nodule characterisation quantified changes in nodule number, size, shape, spacing, and proximity over time and under signalling molecule treatment. Treatment with BMP-2 increased nodule number and spacing, but not nodule proximity, demonstrating the robust spatial organisation of nodule patterns. Second, a custom-designed bending bioreactor was used to explore the relationship between patterns of mechanical stimulation and chondrogenic differentiation and hypertrophy in 3-dimensional constructs. This showed that dynamic bending increased mineralisation in a spatially localised manner, supporting a role for spatial variation of mechanical forces in cellular differentiation.

The work presented here elucidates multiple mechanistic aspects of the relationship between mechanical signals and skeletal development. These data offer a means to further explore the mechanoregulation of skeletal development, and highlight several possible avenues for further exploration.

Acknowledgements

First, I thank my thesis supervisor Prof. Paula Murphy, for her guidance and support throughout my PhD. From taking me on as a student, to poring over data, to editing my chapters, she has consistently been enthusiastic, thoughtful, and rigorous. Without her support, I would not have been able to complete this thesis.

To the other members of the Developmental Biology group, I am grateful for having worked with you all over the past four years. Rebecca, Danielle, Anurati, Aisha, Hanan, and Georgia — thank you for your companionship and for all the trips to Hansel & Gretel.

To everyone in the Zoology department, who have made the it such a lively place to work. Thank you to the technical staff: Alison, who never met a problem or piece of equipment she couldn't fix, Sarah-Louise, Peter, and Martyn. To Fiona, who always had an ear to listen, I will truly miss our chats.

To the Kelly Lab in TBSI, especially Simon, Gráinne, and Paola, thank you for all the discussion and help. Thank you particularly to Dr. Danny Kelly for his support and for serving on my Steering Committee. Thank you to Prof. Amitabha Bandyopadhyay and Dr. Pratik Singh, for their collaboration and for hosting me so warmly in Kanpur.

To my friends in Dublin for reminding me there's a life outside the lab, and to those elsewhere who have given me support from all over the world. Especially Meaghan, who has been there since long before I started my "slicin' and dicin' and micin'."

To Oliver and Simon, thank you both for supporting your nerdy older sister. To the McCoys, thank you for your generosity and cheerleading all these years.

To Eamon, for the constant love and encouragement, and for listening to me complain (a lot). Thank you for helping me reach the finish line – I couldn't have gotten my doctorate (or my driver's license) without you.

Finally, to Mom and Dad, for encouraging me academically since Day One and for making sacrifices to enable me to go to college and choose whatever path I wanted. You probably didn't think I'd be in school for 25 years, but thank you for being there through it all, and for letting me move thousands of miles away to do it. This is for you.

This work was supported by a Postgraduate Studentship from the Irish Research Council and partially supported by an EMBO short-term fellowship.

Publications resulting from this work

Shea CA, Rolfe RA, Murphy P. "The importance of foetal movement for co-ordinated cartilage and bone development in utero: clinical consequences and potential for therapy." Bone Joint Res. 2015 Jul;4(7):105-16. Review.

Singh PNP, **Shea CA**, Sonker SK, Rolfe RA, Ray A, Kumar S, Gupta P, Murphy P, Bandyopadhyay A. Precise spatial restriction of BMP signalling in developing joints is perturbed upon loss of embryo movement. *Development*. 2018 Mar 12;145(5). pii: dev153460. doi: 10.1242/dev.153460

Presentations resulting from this work

Shea CA, Rolfe RA, Murphy P. "Interaction between BMP and Wnt signalling controls the spatial pattern of cartilage differentiation in embryonic limb bud micromass culture." **14th International Conference on Limb Development and Regeneration**. 23-26 July 2017. Poster presentation.

Shea CA, Rolfe RA, Murphy P. "Spatial localisation of YAP during skeletal development implicates the Hippo pathway in skeletal mechanotransduction and morphogenesis." **17th meeting of the International Society for Developmental Biology**. 18-22 June, 2017. Poster presentation.

Rolfe RA, **Shea CA**, Murphy P. "Spatial control of chondrogenesis assessed through micromass cultures of embryonic limb bud cells." **17th meeting of the International Society for Developmental Biology**. 18-22 June, 2017. Poster presentation.

Shea CA, Nash A, Carroll S, Kelly DJ, Murphy P. "Spatially organised differentiation of bone and cartilage in mechanically-stimulated MSC-seeded constructs: a paradigm for skeletal development." **Cell Therapy Today: Achievements, hopes, and hype; the European Molecular Biology Organization (EMBO).** 9-12 September, 2015. Poster presentation. **Awarded conference prize for best poster.**

Shea CA, Nash A, Carroll S, Kelly DJ, Murphy P. "Spatial organisation of bone and cartilage differentiation in mechanically-stimulated MSC-seeded constructs: a paradigm for co-ordinated skeletal development." In Proceedings of the **21st Annual Conference of the Section of Bioengineering of the Royal Academy of Medicine in Ireland**, Maynooth, Ireland.17 January, 2015. Oral presentation.

Rolfe RA, **Shea CA**, Kelly DJ, Murphy P. "The impact of mechanical stimulation from muscle contractions on ossification and joint formation during mouse development: exploring developmental mechanisms disturbed in the absence of contractions." **1st joint meeting of the British Society for Matrix Biology (BSMB) and the British Society for Developmental Biology (BSDB): The Musculoskeletal System, from Development to Disease**. University of East Anglia, Norwich UK. 1-3 September, 2014. Poster presentation.

Table of Contents

Declaration ..... **i**
Summary ..... **ii**
Acknowledgements ..... **iv**
Publications resulting from this work ..... **v**
Presentations resulting from this work ..... **vi**
Table of Contents ..... **vii**
List of Figures ..... **xi**
List of Tables ..... **xiv**
Abbreviations ..... **xv**
Gene and pathway name abbreviations xv
Chapter 1. Introduction **1**
1.1 The importance of movement to skeletal development 1
1.2 Overview of limb skeletal development 3
1.2.1 Endochondral ossification 5
1.2.2 Synovial joint formation 9
1.3 The role of signalling pathways in skeletal development 12
1.4 Movement and mechanical stimulation during skeletal development 18
1.4.1 Clinical implications of reduced foetal movement for skeletal development 18
1.4.2 Animal models of immobilisation *in utero/in ovo* 20
1.4.3 The effects of reduced movement on skeletal development: phenotypic differences and changes in gene expression 22
1.4.4 Mechanical forces present during skeletal development 28
1.5 Mechanotransduction during skeletal development 28
1.5.1 The Hippo cell signalling pathway 31
1.5.2 The role of cilia in cell signalling, development, and mechanotransduction 35
1.6 Differentiation of skeletal tissues *in vitro* and the impact of mechanical stimulation 40
1.7 Objective and aims of this thesis 46
Chapter 2. Materials and Methods **49**
2.1. Animal lines 49
2.1.1. Embryo Collection 49

2.1.2. Embryo genotyping 50
2.1.3. Preparation of cryo samples and sections 50
2.1.4. Preparation of paraffin samples and sections 51
2.2. Histological Staining 51
2.2.1. Safranin-O 51
2.2.2. Mallory's Trichrome 52
2.2.3. Alcian Blue 52
2.2.4. Alizarin Red 52
2.3. *In situ* hybridisation 52
2.3.1. Generation of RNA probes 52
2.3.2. *In situ* hybridisation on wholemount specimens (WISH) and vibratome sections 53
2.3.3. *In situ* hybridisation on cryosections 56
2.3.4. OPT sample preparation, scanning, and reconstruction 57
2.4. Immunostaining 58
2.5. Image collection 61
2.6. Quantitative Real Time RT-PCR 61
2.6.1. RNA purification and cDNA synthesis 61
2.6.2. Quantitative real time RT-PCR 62
2.7. *Ex ovo* embryo culture and electroporation 63
2.7.1. Ex ovo chick embryo culture 63
2.7.2. Limb bud electroporation 64
2.8. Micromass culture manipulation 66
2.8.1. Micromass Culture 66
2.9. Methods described elsewhere 68
Chapter 3. A spatial description of expression of Wnt and BMP signalling pathway component and disturbances in pathway activity under altered mechanical and molecular environments 69
3.1 Introduction 69
3.1.1 Aims of this chapter 74
3.2 Results 76
3.2.1 The Wnt pathway in normal and immobilised skeletogenesis 76

3.2.2 Identification of gene regulatory disturbances at the joint in mouse and chick immobilisation models 92
3.2.3 Characterization of BMP signalling pathway activity during altered embryonic movement....96
3.3 Discussion 98
Chapter 4. Investigation of a candidate mechanism of mechanotransduction in the developing skeleton 107
4.1 Introduction 107
4.1.1 Aims of this chapter 111
4.2 Results 113
4.2.1 Major components of the Hippo pathway are expressed in the developing skeletal rudiments. 113
4.2.2 YAP protein localisation in the developing forelimb skeleton 121
4.2.3 Manipulation of YAP activity *in vitro* 131
4.2.4 Expression of the canonical Hippo pathway receptor *Fat4* during limb development 133
4.3 Discussion 144
Chapter 5. Investigation of a candidate mechanism of mechanotransduction in the developing skeleton: The primary cilium 151
5.1 Introduction 151
5.1.1 Aims of this chapter 154
5.2 Methods 155
5.2.1 Immunolocalisation of cilia and image collection 155
5.2.2 Image processing....156
5.2.3 Quantification of cilia properties 161
5.3 Results 165
5.3.1 Characterisation of primary cilia in the wildtype developing skeletal rudiments....165
5.3.2 Characterisation of primary cilia in the mutant developing skeletal rudiments....175
5.4 Discussion 184
Chapter 6. Establishment of *in vitro* methods to test chondrogenesis. 191
6.1 Introduction 191

6.1.1 Aims of this chapter 195
6.2 Methods 197
6.2.1 Micromass Image Analysis 197
6.2.2 Mechanical Stimulation of Cell-Seeded 3-D Agarose Constructs 202
6.3 Results 205
6.3.1 Analysis and manipulation of chondrogenic differentiation patterns in limb bud micromass culture 205
6.3.2 Timing of chondrogenesis in micromass culture is altered on addition of BMP and Wnt pathway signalling molecules 213
6.3.3 Mechanical stimulation (3-point bending) of seeded 3D-hydrogel constructs 217
6.4 Discussion 222
Chapter 7. Discussion 229
7.1 Significance of key findings 229
7.1.1 Localised, complimentary Wnt and BMP signalling activity and mechanosensitive gene expression at the developing joint 229
7.1.2 The Hippo-YAP pathway as a mechanotransductor during skeletal development 232
7.1.3 Characteristic cilium properties in the developing rudiments: the potential of the primary cilium as a mechanotransductor 235
7.1.4 Contributory regulatory signals to pattern formation during *in vitro* chondrogenesis 237
7.2 Future directions and implications of this work 239
7.2.1 Integration of signalling pathways 239
7.2.2 Localised alteration of signalling activity 240
7.2.3 The cytoskeleton and other mechanisms of mechanotransduction 241
7.2.4 Application of mechanical and molecular stimuli *in vitro* 242
7.2.5 Potential therapeutic applications for *in utero* skeletal developmental defects 243
References 247
Appendix A. Supplementary gene expression data and plasmid maps. 289
Appendix B. Procedure for analysis of micromasses in ImageJ. 297
Appendix C. Nearest Neighbour Distance Calculations. 301

List of Figures

Fig. 1.1. The major stages of limb skeletal development. 4
Fig. 1.2. Overview of endochondral ossification. 6
Fig. 1.3. Progressive differentiation of chondrocytes during endochondral ossification. 8
Fig. 1.4. Overview of synovial joint formation. 10
Fig. 1.5. Features of Foetal Akinesia Deformation Sequence (FADS). 20
Fig. 1.6. Summary of phenotypic and gene expression changes in the skeleton resulting from reduced embryonic mechanical stimulation. 23
Fig. 1.7. The Hippo pathway is mostly conserved between *Drosophila* and mammals. 33
Fig. 2.1. Schematic of fluorescent labelling methods used. 60
Fig. 2.2. Structure of proteins encoded by electroporated constructs. 65
Fig. 2.3. Schematic of limb bud micromass culture method. 67
Fig. 3.1. Tissue sources of transcriptomic studies analysed here. 73
Fig. 3.2. Graph of transcriptomic reads of Wnt ligand and Fzd receptor-encoding genes as detected by RNAseq. 77
Fig. 3.3. Wnt ligands are expressed at the shoulder, elbow, and digit joints of the developing forelimb skeleton, with limited expression within the rudiments. 80
Fig. 3.4. Fzd3 and Fzd6 are expressed peripheral to the shoulder and elbow joints. 82
Fig. 3.5. Expression of the Wnt pathway genes *Wnt4* and *Sfrp2* is upregulated in the peripheral joint cells in the muscle-less mutant. 84
Fig. 3.6. Canonical Wnt pathway activity in the perichondrium, elbow joint, and hypertrophic zone in the developing forelimb revealed through a TCF/LEF:H2B-GFP reporter. 85
Fig. 3.7. Immunolocalisation of β-catenin in wildtype and Spd muscle-less tissue. 87
Fig. 3.8. Establishment of an e*x ovo* electroporation technique. 89
Fig. 3.9. Electroporation of chick forelimbs with constructs to alter Wnt pathway activity affected skeletogenesis. 91
Fig. 3.10. Gene expression of articular cartilage specific genes is similarly altered in immobilised mouse and chick joints. 96
Fig. 3.11. Immunolocalisation of pSMAD1/5/8 and Noggin protein at the wildtype and muscle-less mutant elbow joint. 97
Fig. 3.12. Model for signalling pathway activity and regulation at the joint in normal and immobilised embryos. 100
Fig. 3.13. Smurf expression and activity at the chick knee. 104
Fig. 4.1. Schematic representation of the canonical Hippo pathway, with alternative upstream regulatory mechanisms. 108
Fig. 4.2. Multiple components of the Hippo pathway are expressed in the E14.5 developing humerus and joints. 118
Fig. 4.3. Schematic representation of Hippo pathway components and their relative expression in the E14.5 humerus. 119
Fig. 4.4. Hippo pathway genes are relatively highly expressed in the E14.5 humerus. 120
Fig. 4.5. Regions of elevated YAP protein are localised in the forelimb skeletal rudiments. 121
Fig. 4.6. Phosphorylated YAP protein is detected throughout the rudiment with slightly elevated levels in the hypertrophic zone. 123
Fig. 4.7. YAP protein is localised to the nucleus in the developing skeleton. 124
Fig. 4.8. YAP levels are elevated and more evenly distributed in the muscle-less mutant. 125

Fig. 4.9. Phosphorylated YAP is not visibly altered in the muscle-less mutant.....126
Fig. 4.10. YAP protein is more strongly detected in the muscle-less mutant, while being similarly localised to the nucleus. 127
Fig. 4.11. YAP target genes *Ctgf* and *Cyr61* have localised expression in the skeletal rudiments which is altered in the muscle-less ($Spd^{-/-}$) mutant.....131
Fig. 4.12. Nodule formation is altered in the presence of Verteporfin.....132
Fig. 4.13. *Fat4* is expressed in multiple tissue over key stages of limb development. 134
Fig. 4.14. Virtual sections of wholemount embryos *in situ* hybridised with *Fat4*. 136
Fig. 4.15. *Fat4* is expressed in the forelimb ectoderm, perichondrium, and digit joints at E14.5.....141
Fig. 4.16. Expression of *Col2aI* (to visualise the forming skeleton) in *Fat4* and *Spd* wildtype and mutant mouse forelimb skeleton.....143
Fig. 5.1. Methodology for visualisation and imaging of primary cilia.....155
Fig. 5.2. Processing of colour images for cilia analysis. 156
Fig. 5.3. Processing of greyscale images for cilia analysis. 159
Fig. 5.4. Aspects of cilia captured in this analysis. 163
Fig. 5.5. Cilia are present on chondrocytes throughout the humerus and its associated joints. 166
Fig. 5.6. Regions of the developing rudiment have differing proportions of ciliated cells.....168
Fig. 5.7. Cilia are significantly shorter at the elbow joint than at the shoulder joint and proliferative zone.....169
Fig. 5.8. Cilium distance from the cell centre varies between regions.....170
Fig. 5.9. The position of cilia on individual cells differs between regions of the developing skeleton. 172
Fig. 5.10. Preferred cilium orientation by region in the wildtype forelimb rudiments and joints. 174
Fig. 5.11. Cilia in mutant rudiments display a similar trend to cilia in wildtype rudiments. 176
Fig. 5.12. Cilium length is shorter in the mutant forelimb skeleton.....178
Fig. 5.13. Cilium distance from the cell centre varies between regions in mutant rudiments and joints, and between wildtype and mutant at the shoulder joint and elbow resting zone.....179
Fig. 5.14. The position of cilia on individual cells differs between regions of the developing skeleton in mutant forelimbs. 182
Fig. 5.15. Cilium orientation is most distinct at the elbow joint, and varies between regions in the mutant forelimb rudiments and joints.....183
Fig. 5.16. Summary of cilia characteristics measured in this work.....185
Fig. 6.1. Mechanical forces influence differentiation of MSCs. 194
Fig. 6.2. Quantification of nodule characteristics and pattern.....196
Fig. 6.3. Methodology for micromass image processing using ImageJ. 199
Fig. 6.4. Schematic explanation of the shape descriptors circularity and solidity. 200
Fig. 6.5. Quantification of nodule pattern: spacing and proximity. 201
Fig. 6.6. Experimental setup of a bending bioreactor.....203
Fig. 6.7. Cartilage nodules forming in micromass culture change in number, size, and shape over time.....207
Fig. 6.8. Nodule spacing changes over time.....208
Fig. 6.9. More nodules form in BMP-2 treated cultures, while Noggin and WNT-3A treatment severely impact nodule formation. 210

Fig. 6.10. Nodules in BMP treated micromasses are spaced closer together than in control micromasses, but the distance between nodule edges does not change significantly. 212
Fig. 6.11. BMP-2 treatment increases amount and onset of chondrogenesis and hypertrophy, while Noggin and WNT-3A suppress these processes. 215
Fig. 6.12. Dynamic bending resulted in increased visible mineralisation in constructs. 217
Fig. 6.13. Bending constructs show greater cartilage formation and mineralisation in a spatially localised manner. 219
Fig. 6.14. Bending constructs expressed higher levels of chondrogenic genes, and bending constructs were more heterogenous. 221
Fig. A.1. Articular cartilage-specific, mechanosensitive genes have altered expression at the immobilised chick knee. 292
Fig. A.2. Smurf1 electroporation construct. 293
Fig. A.3. Map of GFP-encoding construct. 294
Fig. A.4. Maps of Wnt pathway constructs for chick limb bud electroporation. 295

List of Tables

Table 1.1. Summary of phenotypic and gene expression changes in the skeleton occurring under altered embryonic mechanical stimulation.....25
Table 1.2. Primary cilia mutations in mouse with relevance to appendicular skeletal development. 39
Table 2.1. Sequences of primers used for *Pax3*^{Spd} genotyping. 50
Table 2.2. Details of RNA probes used for in situ hybridisation. 54
Table 2.3. List of antibodies used in this work.....59
Table 2.4. Details of primers used in qRT-PCR.....62
Table 3.1. RNAseq read counts of other Wnt pathway component genes in TS23 *Pax3*$^{Spd/Spd}$ mutant vs. wildtype humeri and associated joints. 78
Table 3.2. Overlap in genes differentially expressed in muscle-less mouse humeri and enriched in chick articular cartilage (as indicated). 93
Table 4.1. Transcription of Hippo pathway component genes in E14.5 humeri as detected by RNAseq. 114
Table 4.2. Expression level fold changes of selected YAP target genes in mutant vs. wildtype *Spd* humeri. 128
Table 4.3. *Fat4* expression in developing structures and tissues, outside the limbs at E10.5-E13.5. 138
Table 5.1. Proportion of ciliated cells (cilia occurrence) in regions of the developing humerus. 167
Table 5.2. Cilium length in regions of the developing wildtype humerus. 168
Table 5.3. Proportion of ciliated cells (cilia occurrence) in regions of the developing wildtype and mutant humerus. 175
Table 5.4. Cilium length in regions of the developing wildtype and mutant humerus.177
Table 6.1. Number of micromass cultures analysed.....202
Appendix Table A.1. RNA-Seq and microarray readout of Wnt ligands in TS23 wildtype vs. Spd mutant humeri and associated joints. 289
Appendix Table A.2. Table 3.3. RNA-Seq and microarray readout of Fzd receptors in TS23 wildtype vs. Spd mutant humeri and associated joints. 290
Appendix Table A.3. Differentially regulated Wnt target genes.....291

Abbreviations

Apical ectodermal ridge	AER
Articular cartilage	AC
Alkaline phosphatase	AP
5-bromo-4-chloro-3-indolyl-phosphate	BCIP
Bone marrow	BM
3-[3-Cholamidopropyl) dimethyl-ammonio]-2hydroxy-1-propanesulfonate	CHAPS
Cycle threshold	Ct
Day zero	D0
Diethylpyrocarbonate	DEPC
Digoxigenin	DIG
Deoxyribonucleic acid	DNA
Embryonic day	E
Ethanol	EtOH
Extracellular matrix	ECM
Elbow joint	EJ
Foetal Akinesia Deformation Syndrome	FADS
Finite element	FE
Forelimb	FL
Green fluorescent protein	GFP
Hamburger and Hamilton (Stage)	HH
Hindlimb	HL
Horseradish peroxidase	HRP
Hour(s)	hr
Hypertrophic zone	HZ
In situ hybridisation	ISH
Low melting point	LMP
Methanol	MeOH
Mesenchymal stem cell	MSC
Microgram	µg
Microlitre	µl
Micron	µm
Milligram	mg
Millilitre	ml
Millimeter	mm
Minute(s)	min
Mutant	MUT
4-nitro blue tetrazolium chloride	NBT
Nanometer	nm
Osteogenesis imperfecta	OI
Optical Projection Tomography	OPT
Osteoarthritis	OA
Osteoporosis	OP
Phosphate-buffered solution	PBS
PBS with Tween	PBST
Polymerase chain reaction	PCR
Paraformaldehyde	PFA
Prehypertrophic zone	PHZ
Proliferative zone	PZ
Quantitative real-time reverse transcriptase polymerase chain reaction	qRT-PCR
Ribonucleic acid	RNA
Region of interest	ROI
Room temperature	RT
Sodium dodecyl sulfate	SDS
Shoulder joint	SJ
Splotch delayed	Spd
Saline-sodium citrate buffer	SSC
Temporary Brittle Bone Disease	TBBD
Tris-buffered saline solution	TBS
TBS with Tween	TBST
Transforming growth factor beta	TGF-β
Theiler Stage	TS
Wholemount *in situ* hybridisation	WISH
Wildtype	WT

Gene and pathway name abbreviations

Aggrecan	*Acan*
Ankyrin repeat domain 1	*Ankrd1*
Baculoviral IAP Repeat Containing 5	*Birc5*
Bone morphogenetic protein	BMP
Cell and tissue growth factor	*Ctgf*
Cysteine rich angiogenic inducer 61	*Cyr61*
Collagen type 2aI	*Col2aI*,
Collagen type 8aI	*Col8aI*
Collagen type 10aI	*Col10aI*
Fibroblast growth factor	Fgf
Growth differentiation factor 5	*Gdf5*
Hedgehog	Hh
Indian hedgehog	*Ihh*
Parathyroid hormone-related protein	*Pthrp*
TEA-domain family member	*Tead*
Transforming growth factor beta	TGF-β
Wingless	Wnt

Chapter 1

Introduction[1]

1.1 The importance of movement to skeletal development

The vertebrate skeleton gives structure and support, while allowing for and facilitating movement. This is most apparent in the appendicular skeleton of the limbs, which have a large range of motion relative to the central axis of the body, and which enable movement of the entire organism through its environment. Movement is dependent on both the precise articulation of bones at joints, and on the rigidity and support offered by the bones themselves. Dysfunction of these skeletal features, such as inflexible joints or brittle bones, impede movement, leading to pain and degeneration of tissues and adversely affecting the health of the individual.

While facilitating movement of the organism, the skeleton is, in turn, itself shaped by the organism's movement. Physical forces are now well-recognised as having the capacity to influence the adult skeleton; this was first proposed in Wolff's law of 1888 which stated that bone strength is proportional to the physical loads that the structure endures (described in Frost, 1994, Chen et al., 2010). The two sides of this law are apparent in examples of extreme load which humans experience: the increased bone mass in the dominant arms of athletes (McClanahan et al., 2002) and the reduction of bone mass in microgravity during spaceflight (Orwoll et al., 2013). The responsivity of bone to mechanical forces depends on input from a biological mechanism, which was

[1] Elements of this chapter have been published in Shea CA, Rolfe RA, Murphy P. "The importance of foetal movement for co-ordinated cartilage and bone development in utero: clinical consequences and potential for therapy." Bone Joint Res. 2015 Jul;4(7):105-16. Review.

suggested in Frost's mechanostat theory (Frost, 2001). This postulated that mechanical forces, as transmitted to the skeleton by attached muscles, trigger a biochemical response which builds or deconstructs bone and results in adaptive bone remodelling. Essential to this theory is the concept of mechanotransduction, or the capacity for mechanical forces to be transduced to a biochemical signal. Multiple mechanotransductive mechanisms have been implicated in adult bone remodelling, including different signalling pathways (Spyropoulou et al., 2015), but there is still a lack of understanding concerning how mechanical forces regulate bone development.

While the adult skeleton has long been accepted as a mechanosensitive tissue, until recently little attention had been paid to the role of movement in embryonic skeletal formation, which is the subject of the work presented in this thesis. This introductory chapter will present an overview of limb skeletal development (Section 1.2) and the signalling pathways involved (Section 1.3). It then reviews the clinical evidence for the importance of movement during foetal development, and will examine experimental evidence from animal models (Section 1.4). Clinical observations reveal that movement of the human foetus impacts formation of the skeleton, in addition to its later growth and remodelling (Section 1.4.1), while conclusive evidence of the importance of movement to embryonic skeletal development comes from animal models, where experimental manipulation was used to identify the specific changes which occur when movement is inhibited (Section 1.4.2). Identification of how these changes in mechanical stimulation are transmitted to cells, or mechanotransduction, remains a significant question, with multiple mechanisms of mechanotransduction open to investigation (Section 1.5). Two potential mechanotransductive mechanisms – the Hippo-YAP pathway and the primary cilium – are reviewed here. Finally, *in vitro* differentiation of skeletal tissues will be presented (Section 1.6). A better understanding of the role of movement during development of the embryonic skeleton will elucidate fundamental mechanisms for the role of mechanical stimuli in cellular differentiation and tissue patterning. This has therapeutic relevance for foetal health, as well as potential applications for regenerative tissue engineering.

1.2 Overview of limb skeletal development

Development of a functional skeleton relies on the integration of bone and joint formation. The long bones of the appendicular skeleton form via endochondral ossification, in which a cartilage template prefigures ossification (described in detail in Section 1.2.1). Concurrently, joint tissues differentiate into opposing articular cartilages, encapsulated by a fluid-filled membrane, which allows for the articulation of bones (described in detail in Section 1.2.2). Coordination of these processes, along with the development of associated structures such as tendons, ligaments, and menisci, ensures maximum functionality of the skeleton. Limb development is largely similar across vertebrate species, with mouse (*Mus musculus*) and chick (*Gallus gallus*) models widely used to elucidate the process of human skeletal development. The zebrafish model (*Danio rerio*) has more recently been used in studies of jaw development and movement, and is also reviewed here.

The cells of the limb buds derive from the lateral plate mesoderm, where fibroblast growth factor (FGF)10 signalling in the mesoderm and FGF8 in the overlying ectoderm establish a positive feedback loop which promotes localised cellular proliferation (Ohuchi et al., 1997, Xu et al., 1998, Nishimoto and Logan, 2016). The resultant outward bulging of mesenchymal cells overlaid by ectoderm are the first appearance of limbs, and begins approximately at embryonic day (E) 8-8.5 (Theiler Stage (TS) 13), in mouse, at E2.5 (Hamburger and Hamilton (HH) stage 16) in chick, and at gestational day 30 (Carnegie Stage 12) in humans (Hamburger and Hamilton, 1951, Theiler, 1989, O'Rahilly and Muller, 2010, Tickle, 2015) (Fig. 1.1a). The fore- and hindlimb buds emerge at species-specific positions along the anteroposterior axis of the organism which are indicated by expression of the transcription factors *Tbx5* in the forelimb and *Tbx4*, *Pitx1*, and *Islet1* in the hindlimb (Isaac et al., 1998, Logan et al., 1998, Logan and Tabin, 1999, Itou et al., 2012).

Development of the limb skeleton commences when mesenchymal cells at the core of the limb bud condense in the location of the future skeletal elements (approximately E10.5-11.5 in the mouse) (Hall and Miyake, 2000) (Fig. 1.1b). Condensation requires the presence of the extra-cellular molecule hyaluronan as well as membrane-bound cadherins, which allow for cell-cell and cell-environment interactions and subsequent cellular aggregation (Oberlender and Tuan, 1994, Maleski and Knudson, 1996). In

addition, the regression of blood vessels to create avascular cell populations is required for condensation and subsequent cartilage differentiation; the skeletal elements will remain avascular until blood vessels penetrate

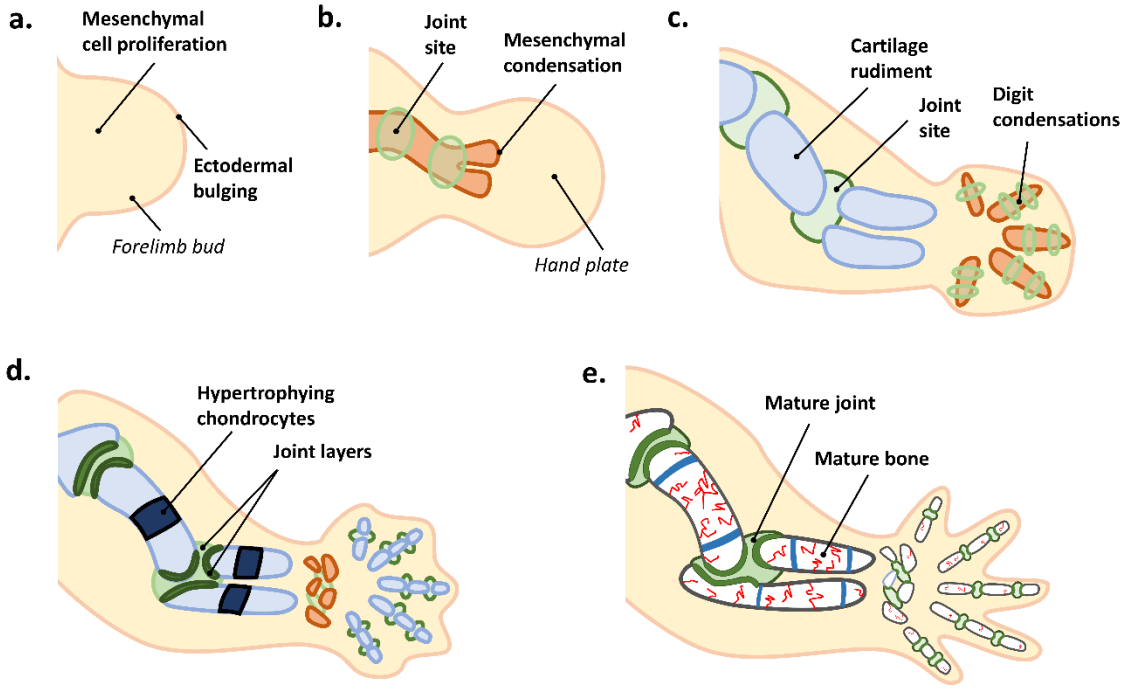

Fig. 1.1. The major stages of limb skeletal development. Limbs first appear as mesenchymal buds overlaid with ectoderm (shown here, Theiler Stage (TS) 17-18/ embryonic day (E) 10.5) (a). Cells at the core of the limb bud condense (orange); joint sites are specified (green circles), and the digital (hand) plate is distinguishable (TS19/E11.5) (b). Condensations differentiate to cartilage rudiments (light blue); digit and wrist condensations are progressively added (TS20-21/E12.5) (c). Chondrocytes begin to hypertrophy at the centre of each rudiment (dark blue); chondrogenous and interzone layers of the joints are distinguishable (dark and light green) (TS22/E13.5) (d). Cartilage undergoes ossification, becoming mature vascularised bone (white; red blood vessels); joints consist of articular cartilage, a synovial cavity and synovial membrane (green); digits are fully separated (post-natal) (e).

the long bones during ossification (Yin and Pacifici, 2001). Molecularly, mesenchymal condensations are distinguished by expression of the Sry-related transcription factor *Sox9*, which is expressed throughout the condensation and which directly regulates the expression of collagen type 2aI (*Col2aI*) and aggrecan, major components of cartilage that characterise the differentiation of mesenchymal cells to cartilage cells (chondrocytes) (Bell et al., 1997, Lefebvre et al., 1997, Bi et al., 1999, Sekiya et al., 2000). While these condensations express *Sox9* homogenously, cells within this

population will contribute to both the future joints, as well as the future long bones (Soeda et al., 2010, Shwartz et al., 2016) (Fig. 1.1b, c). For example, a y-shaped condensation in the forelimb represents the future humerus, radius, and ulna, as well as the humero-ulnar and humero-radial aspects of the future elbow joint (Fig. 1.1b, c). As the limb buds elongate, the hand- and foot- plates become distinguishable, followed by indentations between the emerging digits (Theiler, 1989) (Fig. 1.1b-e). More distal condensations, prefiguring the bones of the wrist, ankle, and digits, emerge and differentiate at the hand- and foot-plates (Fig. 1.1c, d). The cartilage rudiments undergo endochondral ossification and synovial joints are formed beginning at E13.5-14.5 in mouse and E4.5-5 in chick (Fig. 1.1d-e); these processes are described in detail in the following sections (Fig. 1.2, Fig. 1.4).

1.2.1 Endochondral ossification

Where the future long bones will form, the *Sox9*-positive cellular condensations differentiate to *Col2aI*-rich cartilage, thereby forming a template for later ossification. Cartilage in the long bones is transient, and progressively undergoes endochondral ("within cartilage") ossification to form bone (Fig. 1.2, Fig. 1.3) (reviewed in Mackie et al., 2008). Cartilage maturation, cellular hypertrophy, and ossification commences at the longitudinal mid-point of the shaft (diaphysis), and spreads proximally and distally to the ends (epiphyses) of the long bones (Fig. 1.2c-e, Fig. 1.3b, c). This progressive ossification stratifies chondrocytes into different populations, with characteristic cell morphologies and expressing unique genetic markers (reviewed in Adams et al., 2007, Kerkhofs et al., 2012) (Fig. 1.3).

As cartilage differentiation progresses, cells pass through well-defined stages of maturation before forming bone (Fig. 1.3). Immature resting chondrocytes express *Sox9*, *Col2aI*, and other markers characteristic of immature cartilage (Fig. 1.3a', b'). Rounded, resting chondrocytes respond to signals to differentiate to proliferative chondrocytes (Fig. 1.3b'). These chondrocytes are characteristically flattened and arranged in columns; additionally, this zone of chondrocytes serves as a cell source, increasing the size of the bones during development. Indian hedgehog (*Ihh*) secreted by adjacent pre-hypertrophic chondrocytes promotes proliferation within this zone, ensuring a steady supply of cells to recruit towards further differentiation (Fig. 1.3b')

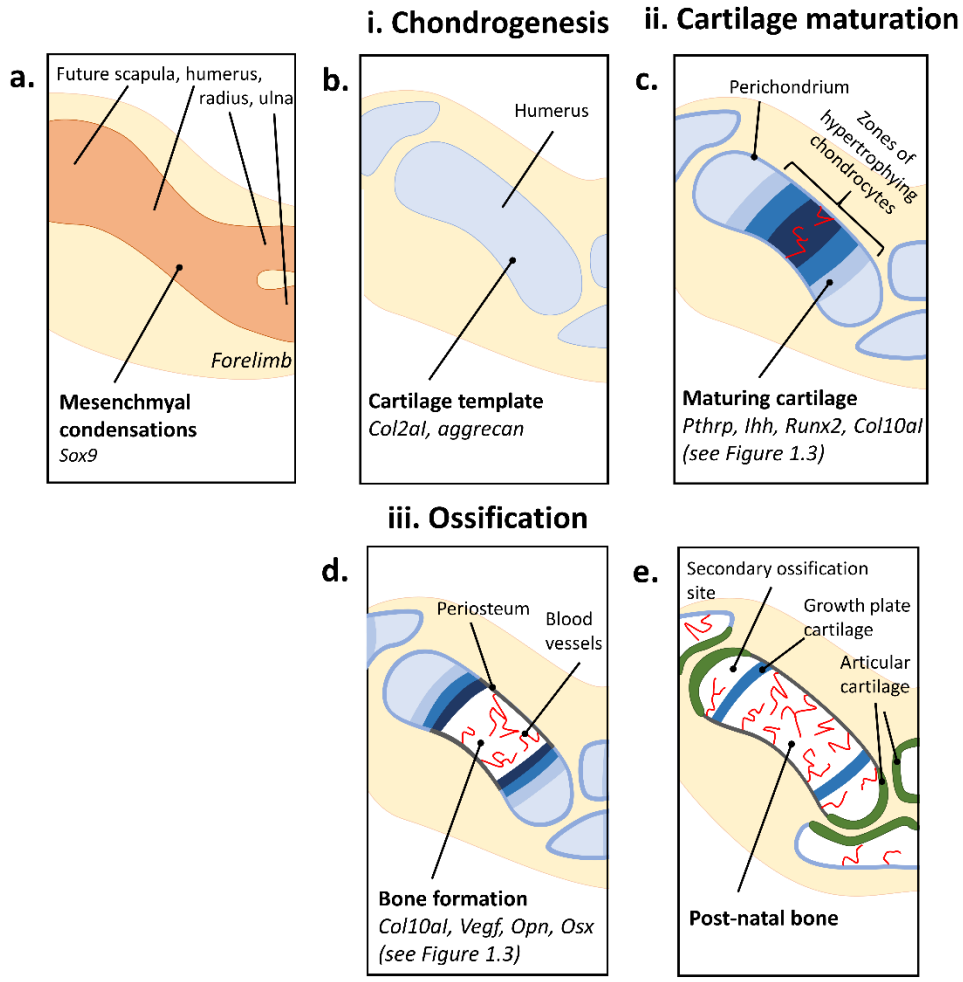

Fig. 1.2. Overview of endochondral ossification. The major events in endochondral ossification – chondrogenesis (i), cartilage maturation (ii), and ossification (iii) – are outlined in the humerus of the developing forelimb. Mesenchymal condensations and expression of *Sox9* are the earliest signs of skeletal development (a). Cartilage cells (chondrocytes) subsequently secrete collagen type 2aI (*Col2aI*) and other structural proteoglycans during chondrogenesis (b). Chondrocytes undergo stereotypic stages of maturation, expressing characteristic gene markers (Fig. 1.3) (c). Chondrocyte hypertrophy leaves behind a rigid matrix to be invaded by blood vessels and osteoblasts (d). The perichondrium simultaneously ossifies to form the bone collar (periosteum). Mature bone is fully ossified, with the exception of growth plate cartilage (e). Mature bones are also capped by permanent articular cartilage at their termini.

(St-Jacques et al., 1999, Karp et al., 2000). *Ihh* operates in a negative feedback loop with Parathyroid hormone-related protein (*Pthrp*), which is expressed by chondrocytes at the termini of the rudiment and which inhibits chondrocyte hypertrophy (Vortkamp et al., 1996) (Fig. 1.3b). Pre-hypertrophic chondrocytes also express bone morphogenetic proteins (*Bmp*) 2 and 6, and the transcription factor *Runx2*, which is

required for hypertrophy; morphologically, they lose the columnar orientation of proliferative chondrocytes and increase in size (Yoshida et al., 2004, Kobayashi et al., 2005) (Fig. 1.3b'). Finally, chondrocytes undergo hypertrophy by swelling and bursting, undergoing apoptosis and leaving behind a matrix to be invaded and populated by bone-forming cells (osteoblasts) (Fig. 1.3b', c'). Osteoblastic precursors are carried into the hypertrophic zone by blood vessels which invade the cartilage template at the site of hypertrophy; they are also responsible for secreting vascular endothelial growth factor (*Vegf*) which promotes blood vessel formation in the developing bone, facilitating exchange of nutrients and secreted factors (Kusumbe et al., 2014, Hu and Olsen, 2017) (Fig. 1.3b', c'). Further, osteoblastic differentiation requires the transcription factors *Runx2* and osterix (*Osx*) (Nakashima et al., 2002).

Another structural feature of the developing bones is the perichondrium, a bi-layer fibroblastic-chondrogenous structure which encapsulates the rudiment and regulates maturation and hypertrophy of adjacent chondrocytes (Long and Linsenmayer, 1998) (Fig. 1.3b'). Cells of the perichondrium undergo differentiation to osteoblasts, and form a bone collar (periosteum) (Fig. 1.3c'). The periosteum contributes to ossification of the underlying cartilage by mediating transforming growth factor beta (Tgfβ) signalling and by generating osteoblasts which travel to the hypertrophic zone via invading blood vessels (Alvarez et al., 2001, Minina et al., 2002, Colnot et al., 2004).

The extra-cellular matrix, the network of structural molecules which surrounds and supports cells, is also remodelled as chondrocytes mature and hypertrophy (reviewed in Melrose et al., 2016). During cartilage differentiation, chondrocytes secrete matrix components, including collagens and structural proteoglycans such as aggrecan and perlecan, to build an extracellular matrix (ECM) (Kosher et al., 1986, Handler et al., 1997, Watanabe et al., 1998). Matrix metalloproteinases, including MMP-9 and MMP-13 secreted by mature chondrocytes degrade the collagen II- and proteoglycan-rich cartilage structure and replace it with collagen type 10aI (*Col10aI*), and other structural components such as osteopontin (*Opn*, or secreted phosphoprotein (*Spp*) 1) (Schmid and Linsenmayer, 1985, Vu et al., 1998, reviewed in Ortega et al., 2004, Paiva and Granjeiro, 2014) (Fig. 1.3b', c').

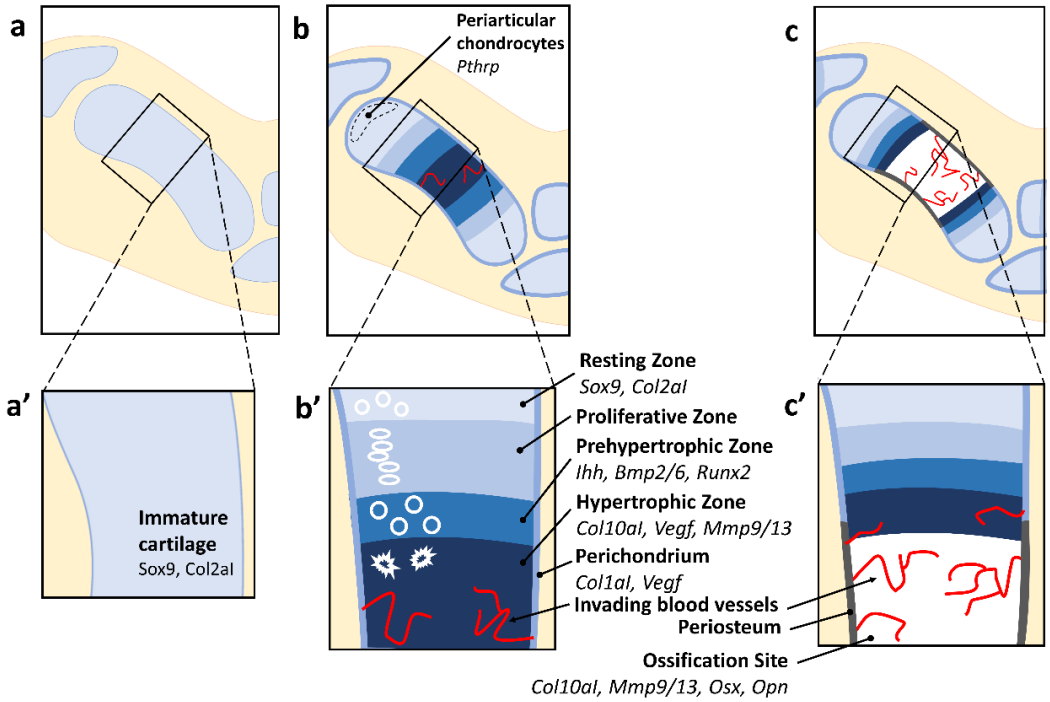

Fig. 1.3. Progressive differentiation of chondrocytes during endochondral ossification. Chondrocytes of the developing skeletal rudiments undergo a regulated process of differentiation towards bone. Immature cartilage expresses *Sox9* and collagen 2aI (*Col2aI*) (a, a'); maturation spreads towards the termini (epiphyses) of the bone (b, b'), thereby stratifying chondrocytes into distinct stages of maturation (b') which express characteristic genetic markers, as indicated. Characteristic chondrocyte shapes are indicated by white outlines in each zone. Osteoblasts carried into the hypertrophic zone via blood vessels (red lines) commence ossification (c, c').

The majority of cartilage within the appendicular skeleton will undergo ossification before birth, with two exceptions. First, bands of cartilage at either end of the diaphysis, called growth plates, will temporarily persist as sites of chondrocyte proliferation, allowing for primarily longitudinal bone growth during post-natal development (Fig. 1.2e). These growth plates are fully ossified at the onset of adulthood, when the organism has reached its adult size (reviewed in Mackie et al., 2011). Second, permanent, stable cartilage capping the epiphyses of the bones will persist throughout the lifetime of the organism as articular cartilage and will contribute to the mature joint structure (Fig. 1.2e). This cartilage facilitates movement by cushioning the bones as they move against one another during joint articulation, and is developmentally distinct from underlying sub-chondral cartilage/bone (Fig. 1.2e, Fig. 1.4) (Section 1.2.2). Degradation of this articular cartilage, and the resulting inhibition of joint movement, is a feature of osteoarthritic disease (reviewed in Poulet, 2017).

1.2.2 Synovial joint formation

Mature joints of the appendicular skeleton allow for a wide range of motion by articulation of the long bones. The long bones and joints form concurrently, via closely related processes. Synovial joint formation can be described with three distinct stages: specification of the joint site, differentiation of joint tissues, and joint cavitation (Pacifici et al., 2006) (Fig. 1.4). Synovial joints arise from the *Sox9*-positive mesenchymal condensations which also give rise to the skeletal rudiments (Fig. 1.4a). Within the mesenchymal condensations, future joint sites (interzones) are specified at precise locations and become visibly apparent as regions of increased cell density (Holder, 1977, Mitrovic, 1978) (Fig. 1.4b). Early joint sites can be molecularly identified by expression of *Gdf5*, a member of the bone morphogenetic protein (BMP) family of secreted ligands (Storm and Kingsley, 1999). However, *Gdf5* itself is not sufficient for joint specification, a process which remains poorly understood (Tsumaki et al., 2002). Another early marker of synovial joints, the ligand *Wnt9a*, can induce *Gdf5* expression but is not necessary for joint formation (Spater et al., 2006). The transcription factor *c-Jun*, part of the JNK/non-canonical transforming growth factor (TGF)-β signalling pathway, has emerged as a joint site determiner upstream of both *Wnt9a* and *Gdf5*, and could serve to specify joint sites in the early limb skeleton (Kan et al., 2013, reviewed in Salva and Merrill, 2017). During joint patterning, cells within the interzone organise into layers which are genetically and morphologically distinct: a central intermediate layer is sandwiched by chondrogenous layers (Fig. 1.4c). These territories correspond to the structure of the mature joint, which consists of a central fluid-filled cavity and opposing articular cartilages (Pacifici et al., 2006) (Fig. 1.4d).

The simultaneous differentiation of divergent tissue types in adjacent territories has required the use of multiple mouse reporter lines to attempt to elucidate the origins of subchondral and articular cartilages and of associated joint structures such as tendons, ligaments, and the synovial capsules. Use of an inducible *Sox9-Cre/LacZ* reporter mouse demonstrated that cells of the chondrogenous layers at the joint, as well as the cruciate ligament of the knee and the Achilles and patellar tendons of the hindlimb, derive from the initial *Sox9*-positive population which emerges early in skeletal development (Soeda et al., 2010). Despite a common progenitor population, from an early stage of joint

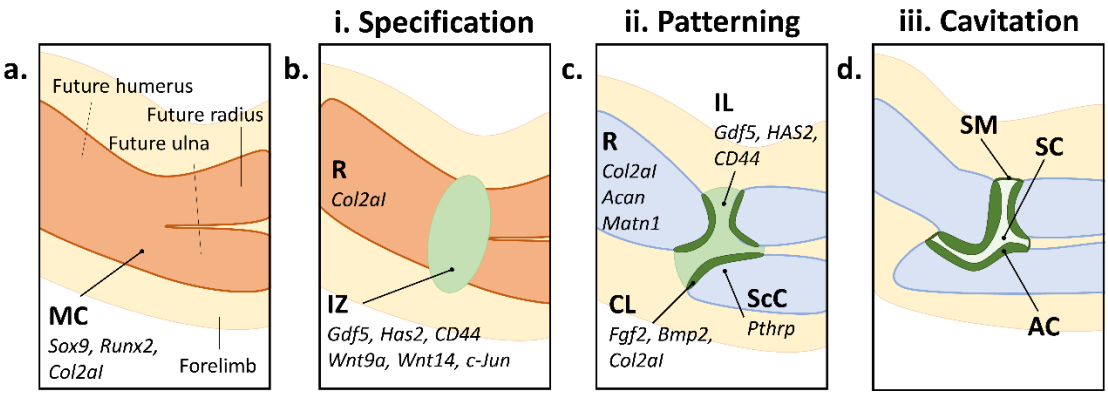

Fig. 1.4. Overview of synovial joint formation. The major stages of joint formation are represented here, using the elbow joint as an example. Synovial joints form from initially homogenous mesenchymal condensations (MC) which also give rise to the future skeletal rudiments (a). Future joint sites (interzones (IZ) are first specified (b); patterning then occurs when cells differentiate into layers: an intermediate layer (IL) is sandwiched between opposing chondrogenous layers (CL), which are distinct from periarticular/subchondral cartilage (ScC) (c). During cavitation, the chondrogenous layers have differentiated to articular cartilages (AC), while the interzone becomes a fluid-filled, cell-free space, the synovial cavity (SC), encapsulated by the synovial membrane (SM) (d). At each stage, characteristic gene markers are indicated. Abbreviations: articular cartilage (AC), chondrogenous layers (CL), intermediate layer (IL), interzone (IZ), rudiment (R), subchondral cartilage (ScC), synovial cavity (SC), synovial membrane (SM).

development cells that are incorporated into the joint interzone are distinct from those which form the underlying bone. This distinction is clear using a LacZ reporter under the control of a *Col2aI* or matrilin-1 promoter: *Col2aI* activity appears continuous across the joint territory, while staining in the matrilin-1 reporter is restricted to cells of the underlying epiphyses which do not contribute to any joint structures, even in postnatal mice (Hyde et al., 2007). Intriguingly, comparison of the *Col2aI/LacZ* reporter with *Col2aI* expression as assessed by *in situ* hybridisation at E13.5 reveals that the knee joint structures are derived from *Col2aI*-positive populations which later lose *Col2aI* expression as joint differentiation progresses (Hyde et al., 2008). Other knee joint structures, such as the menisci, develop from a mix of *Col2aI*-positive cells with migrating *Col2aI*-negative cells (Hyde et al., 2008). *Gdf5* is a well-characterised marker of joint specification, and is expressed early during joint development (Storm and Kingsley, 1999). Use of a *Gdf5-Cre/LacZ* reporter demonstrated that *Gdf5*-positive cells eventually contribute to the articular cartilage,

synovial lining, and certain ligaments, demonstrating a common *Col2aI*- and *Gdf5*-positive identity for joint cells (Koyama et al., 2008).

Despite these details which have answered questions concerning the origin of joint tissues, it is not fully understood how the distinct chondrogenous populations which contribute specifically to transient or articular cartilage are specified or differentiate. Crucially, little is known about why articular cartilage fails to undergo hypertrophy as transient cartilage does during endochondral ossification. For example, while it has been shown that articular cartilage does not express hypertrophy markers such as *Ihh* or *Bmp*6 (Eames et al., 2003), it is unknown why these cells do not express those markers. At the patterning stage of joint development, as the tissue territories of the joint are being defined, morphogenesis of the rudiment ends is also occurring (Roddy et al., 2009). Morphogenesis is driven partially by differential cellular proliferation (Roddy et al., 2011a) and has an impact on later joint functionality, as it determines the articulation of opposing bones. Proliferating cells at the rudiment ends have been shown to contribute to both transient and articular cartilage in the phalangeal joints, reinforcing the idea that joint patterning and rudiment morphogenesis are closely linked processes (Ray et al., 2015).

Joint cavitation occurs when a cell-free space at the joint mid-line emerges. The mature cavity is fully encapsulated by a double-layered membrane which is continuous with articular cartilage of the long bones and which encases the synovial fluid (Pitsillides and Ashhurst, 2008). The synovial fluid serves as a lubricant and is rich in hyaluronan and lubricin, molecules which contribute to the fluid's viscosity (Toole et al., 1972). The timing of joint cavitation corresponds to increased localised production of hyaluronan, which may contribute to cell dissociation and cavitation (Edwards et al., 1994, Dowthwaite et al., 2003).

Around the time of joint cavitation, cells migrate into the intermediate layer of the joint from nearby *Col2aI*-negative tissues (Pacifici et al., 2006, Hyde et al., 2008). At even later stages, *Tgfbr2*-positive cells at the peripheral joint migrate and contribute to the synovial lining, ligaments, and menisci (Li et al., 2013). The potential of these migrating cells for joint regeneration was demonstrated by the surgical removal of the elbow joint territory, which was followed by migration of cells posterior to this territory and recovery of joint formation (Ozpolat et al., 2012). Further evidence of peripheral joint contributions to the joint comes from Shwartz et al. (2016) who demonstrated that

Gdf5-positive cells continuously migrate into the forming joint from adjacent regions over the course of joint development. Peripheral joint cells could serve as progenitor or stem cell populations, contributing to joint development during skeletogenesis, and to postnatal repair and regeneration. Stem cells have also been isolated from mature articular cartilage, although it is not known how these cells relate to developmental populations (Archer et al., 2012).

1.3 The role of signalling pathways in skeletal development

Multiple signalling pathways and networks contribute to skeletal development. Initial skeletal patterning is established by molecular signals which originate in the adjacent ectoderm and flank mesoderm (reviewed in Zeller et al., 2009, Tickle, 2015). Morphogen gradients, originating from the apical ectodermal ridge (AER) and the zone of polarizing activity (ZPA), are well-established mechanisms for establishing, respectively, proximo-distal and antero-posterior axes in the limb bud (Delgado and Torres, 2016). Recently, more complex models incorporating Turing reaction-diffusion mechanisms have been proposed to explain the robust formation of skeletal elements in the limb skeleton (Delgado and Torres, 2016). Turing reaction-diffusion models are based on mathematical equations which explain how a system containing soluble molecules, which diffuse at differential rates and which interact biologically with one another, generate repetitive spatial patterns (Turing, 1990, Ball, 2015). For example, a Turing mechanism integrating Wnt and BMP signalling with *Sox9* expression has been shown to be capable of generating the pattern of multiple digits in the limb autopod (Raspopovic et al., 2014). Early patterning mechanisms can serve to establish crude spatial territories which become further refined by local cell-cell interactions and signalling.

Cell signalling pathways which are known to be active during skeletal development include the Wnt, transforming growth factor beta (TGF-β)/bone morphogenetic protein (BMP), Hedgehog (Hh), fibroblast growth factor (FGF), Notch, and retinoic acid (RA) signalling pathways. These pathways coordinate cartilage differentiation and maturation, as well as joint formation, and contribute to giving each region of the skeleton distinct cellular characteristics. Aspects of these pathways which contribute to

limb skeletal patterning, and which are relevant to the work presented in this thesis, are described here.

Wnt. Wnt signalling is necessary to both bone and joint development, but despite its demonstrably crucial role, its precise involvement has remained difficult to elucidate. Both canonical and non-canonical signalling are involved in differentiation of bone and joint tissues at specific stages. Canonical Wnt signalling, which involves stabilisation of the intracellular effector molecule β-catenin, is suppressed during initial chondrogenic differentiation (leading to degradation of β-catenin by the Dishevelled destruction complex), but is simultaneously active at joint interzone sites, where cartilage formation is inhibited (Ryu, 2002, Guo et al., 2004, Day et al., 2005, Spater et al., 2006). Contrarily, non-canonical Wnt signalling, by the planar cell polarity (PCP) and calcium (Ca^{2+}) pathways, promotes chondrogenesis (Hartmann and Tabin, 2000, Li and Dudley, 2009). PCP signalling is most relevant in the zone of proliferative chondrocytes, where it is involved in the process of convergent extension to lengthen the long bones. Canonical Wnt is later active during chondrocyte hypertrophy and osteoblastogenesis, inhibiting *Pthrp* to promote chondrocyte maturation (Rudnicki and Brown, 1997, Hartmann and Tabin, 2000, Enomoto-Iwamoto et al., 2002, Guo et al., 2009).

Wnt signalling is activated by binding of a Wnt ligand to a Frizzled (*Fzd*) co-receptor (reviewed in Widelitz, 2005). Among ligands, *Wnt4*, *Wnt9a*, and *Wnt16* are active at the developing joint. *Wnt4* is detected within the developing digit joints of both chick and mouse at these stages (Hartmann and Tabin, 2000, Guo et al., 2004). Retroviral misexpression of *Wnt4* in posterior chick limb buds can accelerate chondrocyte hypertrophy, resulting in longer bones with more mineralisation (Hartmann and Tabin, 2000).

Wnt9a (previously known as *Wnt14*) is expressed in both mouse and chick within the developing phalangeal and metatarsophalangeal joints and in tissue surrounding the elbow joints (Hartmann and Tabin, 2000, Guo et al., 2004). Retroviral misexpression of *Wnt9a* in chick resulted in gaps in cartilaginous rudiments, absent rudiments, and chondrocytes within rudiments appearing morphologically similar to interzone cells and upregulated expression of joint-specific genes (*Gdf5*, Autotaxin, Chordin) suggesting the formation of ectopic joint tissue in infected chicks (Hartmann and Tabin, 2001). Similarly, loss of *Wnt9a* in mouse results in ectopic cartilage formation and partial joint

fusion, while retroviral infection with *Wnt9a* transforms sternal chondrocytes to more fibroblast-like cells (Spater et al., 2006).

Wnt16 is expressed in the metatarsophalangeal and digit joints in mouse at E13.5-14.5 (Guo et al., 2004). *Wnt4*, along with *Wnt9a* and *Wnt16*, are active in canonical Wnt/β-catenin signalling at the joint, and constitutively-active β-catenin under a *Col2aI* promoter generated mice with shortened bones and ectopic formation of joint-like tissues (Guo et al., 2004).

*Wnt5a***,** *Wnt5b*, and *Wnt11* are the only ligands definitively detected within the rudiments (not including the perichondrium). At E12.5, *Wnt5a* is expressed in the perichondrium of the developing forelimb rudiments in mouse (Yamaguchi et al., 1999). At E13.5, *Wnt5a* was detected at the boundary of prehypertrophic and proliferative chondrocytes in the humeri, overlapping *Ihh* expression in the prehypertrophic zone and adjacent to *Col10aI* expression in the hypertrophic zone (Yang et al., 2003). By E15.5, expression in the long bones of the forelimb is limited to the perichondrium and very faint expression in the pre-hypertrophic chondrocytes (Witte et al., 2009). In the chick, *Wnt5a* detection was limited to the perichondrium of the ulna at HH32 (E7.5) (Hartmann and Tabin, 2000).

Wnt5a null mice display a dramatic reduction in skeletal size, with loss of distal skeletal elements such as the phalanges; further, they show reduced chondrocyte proliferation, delayed ossification, and drastically reduced expression of markers of chondrocyte maturation and hypertrophy (Yamaguchi et al., 1999, Yang et al., 2003). Surprisingly, ectopic expression of *Wnt5a* in mouse, under a *Col2aI* promoter/enhancer similarly resulted in reduced chondrocyte proliferation and hypertrophy (Hartmann and Tabin, 2001, Yang et al., 2003). However, examination of *Col2aI* revealed an increase in expression in the null mutant, and a decrease in the ectopic *Wnt5a* model, suggesting that *Wnt5a* promotes hypertrophy by repressing *Sox9*-mediated expression of *Col2aI*, a marker of immature cartilage (Yang et al., 2003). Similarly, retro-viral ectopic *Wnt5a* in chick forelimbs appeared to delay chondrocyte maturation: expression patterns of the maturation markers *Col10aI*, *Ihh*, and *Pthrp* in infected limbs were reduced and resembled that of earlier-stage limbs, while gene expression in the perichondrium was unaffected (Hartmann and Tabin, 2000).While canonical Wnt/β-catenin signalling has been implicated in chondrocyte hypertrophy (Guo et al., 2009), *Wnt5a* has been shown

to act via both canonical and non-canonical pathways, and it is not clear which pathway *Wnt5a* acts through during cartilage maturation (van Amerongen et al., 2012).

Wnt5b, like *Wnt5a*, is detected in the pre-hypertrophic chondrocytes and in the perichondrium of E15.5 mouse humeri, (Yang et al., 2003, Witte et al., 2009). However, expression of *Wnt5a* extends into the hypertrophic zone, overlapping slightly with *Col10aI*-expression (Yang et al., 2003, Witte et al., 2009). In the chick, *Wnt5b* was also observed in the perichondrium of the ulna, but with expression extending further towards the core of the diaphysis than that of *Wnt5a* (Hartmann and Tabin, 2000). Similar to *Wnt5a* misexpression, ectopic *Wnt5b* under a *Col2aI*-promoter/enhancer dramatically delayed chondrocyte hypertrophy. In contrast to ectopic *Wnt5a*, however, ectopic *Wnt5b* resulted in increased *Col2aI* expression, suggesting that *Wnt5b* promotes chondrocyte proliferation at the expense of chondrocyte maturation (Yang et al., 2003).

Wnt11 is detected in HH30 chick in prehypertrophic chondrocytes, with strongest detection in cells adjacent to the perichondrium (Church et al., 2002), as well as in metacarpal and phalangeal joints of mouse at E13.5 and E15.5 (Witte et al., 2009). Retroviral infection of *Wnt11* in chick limbs resulted in slightly shorter limbs with some joint fusion, suggesting a role for *Wnt11* in the regulation of chondrocyte differentiation (Church et al., 2002).

Although expression data for *Fzd* genes during skeletogenesis is limited, Fzd transmembrane receptors, which bind Wnt ligands, are essential to the transduction of both canonical and non-canonical Wnt signals (Wang et al., 1996) and certain receptors potentially have a role in skeletal development. Expression of several *Fzd* genes has been detected within skeletal tissues, as early as TS19 when limited expression of several genes is detectable in the mouse forelimb (Summerhurst et al., 2008). In the HH32 (E7.5) chick ulna, *Fzd1* was detected throughout the perichondrium; human mutations in Fzd1 are associated with reduced bone mineral density, and *Fzd1* is required for osteoblast differentiation *in vitro*, implicating this gene in later skeletal development (Hartmann and Tabin, 2000, Yu et al., 2013b). *Fzd2* expression was reported in mesenchymal or developing muscle tissues of the chick forelimb, but there was no observable expression within the skeletal elements (Nohno et al., 1999). However, a human mutation in *Fzd2* has been linked to severe limb shortening (omodysplasia), and *Fzd2* mutants have a mild reduction in skeleton size, as well as

craniofacial defects (Yu et al., 2010, Saal et al., 2015). *Fzd3* was detected within the rudiments of E18.5 mouse tibia, with widespread expression; deletion of SoxC genes (*Sox4*, *Sox11*, and *Sox12*) decreased *Fzd3* expression and resulted in disorganised proliferative chondrocytes, suggesting that *Fzd3* is involved in non-canonical Wnt/PCP here (Kato et al., 2015). *Fzd7* has reported expression in terminal chondrocytes in the articular region, and was also faintly detected in the perichondrium; ectopic *Fzd7* resulted in shortened bones and decreased mineralisation, potentially antagonizing cartilage maturation (Hartmann and Tabin, 2000). *Fzd9* was detected in the precartilaginous condensations of mouse limbs at TS19 (Wang et al., 1999), but there is no description of later expression. Notably, *Fzd9* null mice have slightly decreased bone formation post-natally, suggesting a role for *Fzd9* in the ossification of bone (Albers et al., 2011, reviewed in Maupin et al., 2013). *Fzd4* was reported to have a similar expression pattern to *Fzd2*, while *Fzd6* and *Fzd8* were undetectable within the developing skeleton (Nohno et al., 1999); none of these have known roles in skeletal development. No relevant limb developmental expression data for *Fzd5* or *Fzd10*, or reported roles for these genes during appendicular skeletal development, is reported in the literature, although increased expression of *Fzd5* in osteoarthritic synovial tissue and during *in vitro* differentiation of embryonic calvarial osteoblasts suggests that this gene may have a role in later skeletal development or maintenance (Sen et al., 2000, Guo et al., 2008).

TGF-β/BMP. TGF-β signalling is involved in many developmental processes, and acts through phosphorylation-mediated activation of SMAD transcription factors (Wu and Hill, 2009). TGF-β signalling is active from the early stages of skeletal development, promoting mesenchymal cell proliferation and priming these cells to respond to BMP signals to undergo chondrogenesis (Karamboulas et al., 2010, Keller et al., 2011). Later, the pathway promotes chondrocyte cell proliferation, while inhibiting chondrocyte maturation and further differentiation (Pelton et al., 1991, Serra et al., 1997, Yang et al., 2001). The pathway is also responsible for a potential progenitor cell population at the joint, as *Tgfbr2*-positive cells migrate into the joint to contribute to synovial structures (Li et al., 2013).

Bone morphogenetic proteins (BMPs) are a subfamily of secreted TGF ligands which are required for the formation of mesenchymal condensations, as well as chondrogenic differentiation through activation of Sox-family members (Pizette and Niswander,

2000, Chimal-Monroy et al., 2003, Yoon and Lyons, 2004). *Bmp2* is expressed in mesenchyme surrounding early cartilage condensations, while *Bmp4* and *Bmp7* are expressed in the rudiment perichondrium in mouse (Lyons et al., 1995, Duprez et al., 1996). After ossification commences, *Bmp5* mRNA was detected at high levels in hypertrophic chondrocytes compared to proliferative chondrocytes, and is involved in matrix accumulation during ossification (Mailhot et al., 2008). Overexpression of the pathway ligands *Bmp2* or *Bmp4*, resulted in increased size of cartilage rudiments, potentially through increased recruitment of chondrocyte progenitors or increased cellular proliferation; joint fusion also occurred (Duprez et al., 1996, Minina et al., 2001). Overexpression of *Bmp2* or *Bmp4* results in delayed hypertrophy, while treatment with the BMP antagonist Noggin accelerated chondrocyte hypertrophy, suggesting that one role of BMP signalling is to regress hypertrophy (Duprez et al., 1996, Minina et al., 2001). Contrastingly, overexpression of a constitutively active form of the pathway receptor *Bmpr1a* had the opposite effect to ligand overexpression, causing accelerated hypertrophy and rudiment shortening; this receptor was shown to regulate downstream *Ihh* activity, further demonstrating multiple roles for BMP signalling during skeletal development (Zou et al., 1997, Kobayashi et al., 2005).

The BMP ligand *Gdf5* is the earliest molecular signal of joint development, and is widely used as an indicator of joint specification (Storm and Kingsley, 1999). Other BMP ligands, as well as antagonists, are also involved in joint development: ectopic expression of BMP ligands resulted in joint fusion, as does knocking out the BMP antagonist Noggin (*Nog*) (Duprez et al., 1996, Brunet et al., 1998). Ray et al. (2015) report that *Nog*-expressing cells adjacent to the articular cartilage serve to insulate joint and articular cartilage from BMP signals during joint differentiation, offering a model for simultaneous requirement of *Nog* and BMP activity.

Hedgehog. Hedgehog signalling is crucial to many aspects of vertebrate morphogenesis, and relies on the binding of hedgehog ligands to cells surface receptors (Lee et al., 2016). Within the cartilage, parathyroid hormone-related protein (*Pthrp*) and Indian hedgehog (*Ihh*) signals are important for proliferating and pre-hypertrophic chondrocytes, respectively, and participate in a signalling feedback loop. *Pthrp* expressed by resting chondrocytes toward the rudiment termini induces neighbouring proliferating chondrocytes to divide, thereby ensuring sufficient numbers of cells for bone growth, while *Ihh* promotes chondrocyte maturation and positively feeds back

onto *Pthrp* to promote further proliferation and maintain a progenitor pool (Karaplis et al., 1994, Lanske et al., 1996, Vortkamp et al., 1996). These signals are also exchanged between the perichondrium and its underlying cartilage (St-Jacques et al., 1999, Chung et al., 2001). Hedgehog signalling is also involved in several processes during phalangeal joint development: *Ihh*-null mutants fail to develop digit joints and exhibit populations of *Gdf5*-positive cells at the periphery of the joint territory, rather than within (Koyama et al., 2007). *Shh* is also required for digit joint formation; null mutants have longitudinal, rather than transverse, phalangeal joints and reduced production of hyaluronic acid (Koyama et al., 2007, Liu et al., 2013). The involvement of Hedgehog signalling in both bone and joint formation suggests co-ordination of these processes.

1.4 Movement and mechanical stimulation during skeletal development

1.4.1 Clinical implications of reduced foetal movement for skeletal development

Autonomous movement of the embryo, driven by muscle contractions, commences during early limb development and persists throughout gestation. Foetal movement in humans typically begins at 9 weeks postmenstrual age (approximately Carnegie stage 18), which occurs shortly after the forelimbs are innervated (Shinohara et al., 1990, de Vries and Fong, 2006); this coincides with key steps in early ossification and joint patterning during early formation of the skeletal rudiments.

In the 1970s a series of clinical case studies appeared, describing neonates presenting with a syndrome of ankylosis (stiffening of the joints due to bone fusion), pulmonary hypoplasia, and facial abnormalities. Several cases noted underlying neuromuscular dysfunction and suggested this as the cause of the observed syndrome (Mease et al., 1976), while others argued that it was caused by autosomal-recessive mutations, distinct but related genetic disorders, or environmental teratogens (Punnett et al., 1974, Pena and Shokeir, 1976, Lazjuk et al., 1978). The prevalence of such deformities in consanguineous families and sibling pairs also suggested a genetic cause (Say et al., 1979). However, despite existing experimental evidence that reduced embryonic movement could lead to skeletal abnormalities, particularly of the joints (Drachman and Sokoloff, 1966), the correspondence between this clinical syndrome and reduced

movement *in utero* was not highlighted until 1983, when Moessinger presented a rat model for Foetal Akinesia Deformation Sequence (FADS) (Fig. 1.5). In this model, pregnant rats were injected with the muscle relaxant curare to induce foetal immobility; this reproducibly generated neonates with joint and other abnormalities comparable to the human syndrome described above, confirming that prolonged reduced foetal movement can give rise to a characteristic set of developmental malformations. Clinically, this set of traits was re-named to Pena-Shokeir phenotype (after the early patient descriptions), indicating that it is a set of features caused by a range of underlying conditions via the mechanism of foetal akinesia (Hall, 1986). Numerous causes of FADS exist, both genetic and environmental; these include congenital neurological, muscular, or connective tissue diseases, maternal drug use or illness, and reduced amniotic fluid (oligohydramnios) (Hall 2009). Causes that had previously been presumed to be genetic in nature (increased prevalence in twins) (Hall et al., 1983) were re-examined as potentially environmental (crowding caused by multiple foetuses) (Hall et al., 2014). However, despite the diversity of causes, FADS is the result of reduced foetal movement, and repeatedly gives rise to a similar spectrum of skeletal defects. This includes hypomineralised, brittle bones which are prone to fracture, and contracture or other dysplasias of the joints (Rodriguez et al., 1988a, Rodriguez et al., 1988b, Aronsson et al., 1994, Miller and Hangartner, 1999).

FADS is associated with a transient condition called Temporary Brittle Bone Disease (TBBD) (Paterson et al., 1993, Miller, 2003, Paterson and Monk, 2011). In this condition, bone is hypomineralised during development and leaves affected babies prone to broken bones and injury during their first year (Marini and Blissett, 2013). It regresses after the first year, as the mechanical stimulation received by the baby's normal environment is enough to strengthen the bone. This contrasts with other diseases such as osteogenesis imperfecta (OI) (or brittle bone disease (BBD)), where a mutated structural collagen forms permanently weakened bones (Forlino et al., 2011).

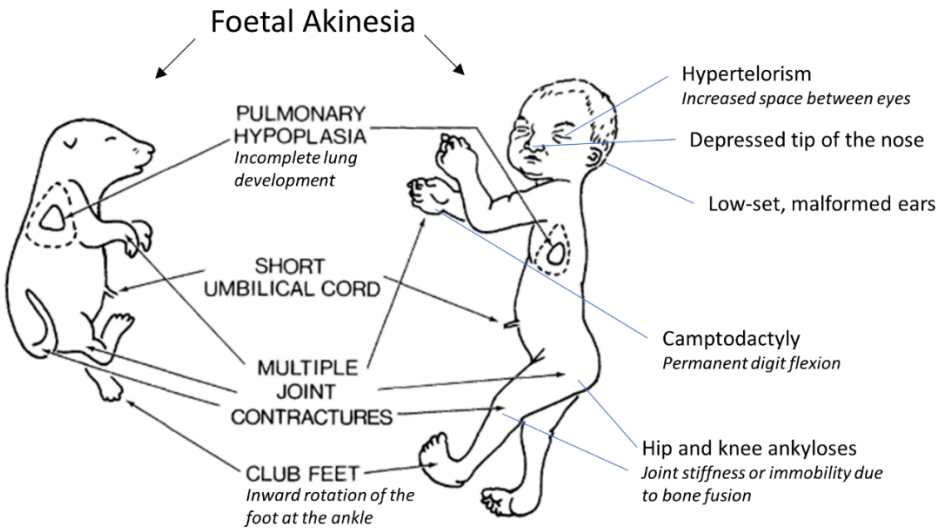

Fig. 1.5. Features of Foetal Akinesia Deformation Sequence (FADS). Reduced or absent movement during development (foetal akinesia) gives rise to a set of malformations, collectively called Foetal Akinesia Deformation Sequence (FADS), as indicated in both the rat model (left) and a typical affected human neonate (right). Adapted from Moessinger (1983) and Hall (2009).

1.4.2 Animal models of immobilisation *in utero/in ovo*

Moessinger's rat model of FADS demonstrated the effects of embryonic immobilisation on skeletal development (Moessinger, 1983). Mouse and chick models have been used to better characterise the morphological and genetic effects of reduced mechanical stimulation on the development of bones and joints. Musculoskeletal development has been well-conserved during vertebrate evolution, allowing for extensive use of mouse and chick models in the study of skeletal development. As in human, regular muscular movement commences early in the mouse and chick, and corresponds to the elongation and innervation of the limb buds. In mouse, movement starts at embryonic day (E) 12.5 (Theiler Stage (TS) 20), and in chick at E3.5 (Hamburger and Hamilton (HH) stage 21) (Hamburger and Balaban, 1963, Suzue and Shinoda, 1999). At these stages, muscles and tendons are gradually forming alongside the skeletal elements (Marturano et al., 2013, Huang, 2017), so it is not yet known at which point effective mechanical loads begin to be transmitted to cells within the developing skeleton. However, because movement (including whole-body swaying) occurs from the early stages of limb skeletal development, and due to its necessary role in this process, it is safe to assume that cells within the developing skeleton experience movement-induced mechanical loading at early stages.

Genetic mutations and pharmacological treatments can be used to manipulate embryonic movement in mouse and chick systems, and to observe the resulting effects on skeletal development. In chick, embryonic immobilisation can be affected by the direct addition of neuromuscular blocking agents to chick embryos, inducing either flaccid or rigid paralysis (Hall and Herring, 1990, Drachman and Sokoloff, 1966, Osborne et al., 2002, Nowlan et al., 2008b, Roddy et al., 2011b). The effects of physical stimulation on skeletal development have also been assessed by *in vitro* culture of skeletal rudiments, with physical manipulation such as ultrasound stimulation, application of hydrostatic pressure, or manual movement (Lelkes, 1958, Mitrovic, 1982, Nolte et al., 2001, Henstock et al., 2013).

Pharmacological treatments can also be used to reduce embryonic movement in mouse; for example, the neurotransmitter-blocker curare (used in the rat model of FADS) can be injected into pregnant mice (Rodriguez et al., 1992). However, pharmacological agents must be administered by skilled individuals, and the effective amount transmitted to the animal can vary between users or experiments. Therefore, mutations of genes required for muscle development or contraction offer a more reproducible means for reduction of mechanical stimulation during embryonic development (reviewed in Rolfe et al., 2013). The muscular dysgenesis (mdg) model is useful for observing the effects of inactive muscle, as muscle fibres in this mouse lack excitation-contraction coupling, resulting in total paralysis (Pai, 1965, Kahn et al., 2009). *Dock1*-null mutants have reduced muscle due to defects in myoblast fusion during muscle development (Laurin et al., 2008), while *Myf5/MyoD* double mutants lack differentiated muscle (Rudnicki et al., 1993). The Splotch mutant line, which has a mutation in *Pax3*, has normal axial muscle development but this mutation specifically impairs muscle progenitor migration into the limbs (Franz et al., 1993). A number of different Splotch mutations and alleles have been characterised with slightly different phenotypes. The Splotch delayed mutation used in this work ($Pax3^{Spd/Spd}$) has the important advantage of a slightly milder phenotype and lethality is delayed, which allows for examination of limb skeletogenesis (Vogan et al., 1993). Immobilisation models have also been generated in the zebrafish, where the ease of generating mutant screens makes this an inexpensive and relatively rapid option for genetic exploration. Zebrafish mutants lacking skeletal muscle or with inactive skeletal muscle have been used to examine the effects of immobilisation on the craniofacial and pectoral skeletons

(van der Meulen et al., 2005, Hinits et al., 2011, Shwartz et al., 2012, Brunt et al., 2015, Brunt et al., 2017).

1.4.3 The effects of reduced movement on skeletal development: phenotypic differences and changes in gene expression

As noted above, human infants with reduced foetal movement *in utero* were observed to have thin, hypomineralised bones at birth (Rodriguez et al., 1988b). In animal models of immobilisation, reduced endochondral ossification was observed, as was altered rudiment morphology and synovial joint formation (reviewed in Rolfe et al., 2013) (Fig. 1.6, Table 1.1). Importantly, these observations are consistent across models, with genetically-modified mouse and pharmacologically-immobilised chick exhibiting similar defects in skeletal development under reduced mechanical stimulation.

Reduced ossification and reduced bone thickness, such as that exhibited in the skeletons of immobilised embryos, makes bones mechanically weaker with a reduced load-bearing capacity (Nowlan et al., 2008b, Nowlan et al., 2010b, Sharir et al., 2011). Related to reduced ossification, there is altered expression of prehypertrophic and hypertrophic marker genes such as *Ihh*, *Col10a1* and *Spp1* in immobilised chick and muscle-less mouse embryos (Nowlan et al., 2008b, Rolfe et al., 2014) (Fig. 1.6a, summarised in Table 1.1). These data suggested misregulation of chondrocyte maturation and hypertrophy, resulting in the production of abnormal bone. Notably, ossification of forelimbs and proximal rudiments in muscle-less mice was more affected than that of hindlimbs and distal rudiments, and reduced mechanical stimulation had a greater effect on the expression of skeletal markers such as *Ihh* and *Col10aI* in the humerus (forelimb), compared to the femur (hindlimb) (Nowlan et al., 2010a, Nowlan et al., 2012). It is known that different molecular cues, such as the transcription factors *Tbx5*, *Tbx4*, *Pitx1*, and *Islet1*, are present in the fore- and hindlimbs and contribute to the limbs' unique identity (Logan et al., 1998, Logan and Tabin, 1999, Rodriguez-Esteban et al., 1999, Minguillon et al., 2005, Itou et al., 2012). Additionally, the fore- and hindlimbs could be subject to different mechanical stimuli and indeed computational modelling predicted that hindlimbs experience greater stimulation via passive movement than do forelimbs (Nowlan et al., 2012). Passive

movement is another source of mechanical stimulation, distinct from movement generated by muscle contractions; it is the displacement of limbs caused by maternal or littermate movement, and could potentially compensate for reduced embryonic movement in the hindlimbs. Computational modelling predicted that displacement of the zeugopod (distal limb) generates higher mechanical stimuli in the hindlimbs, compared to the forelimbs; contrastingly, predicted mechanical stimuli resulting from muscle contractions were comparable between fore- and hindlimbs (Nowlan et al., 2012). Therefore, in the muscle-less mouse, the loss of muscle-generated mechanical forces would be compensated by forces generated by passive movement in the hindlimbs, but not the forelimbs. This is supported by there being no such difference between fore- and hindlimbs in the immobilised chick embryo, which develops within a closed environment and is therefore not exposed to this type of passive movement.

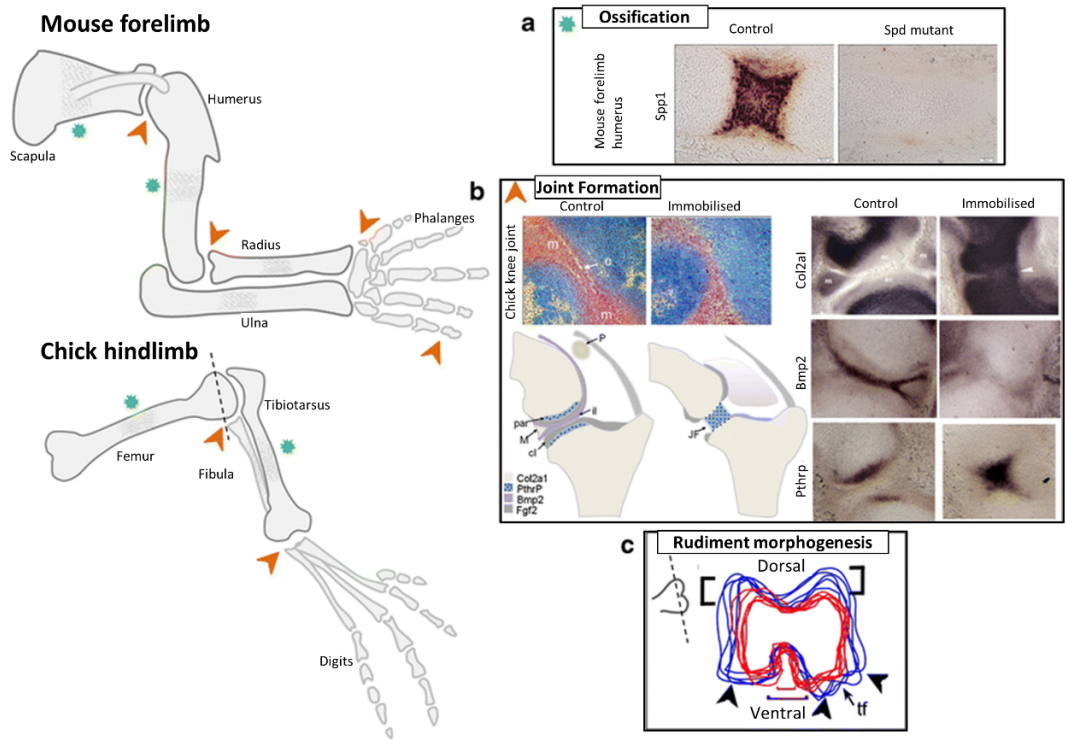

Fig. 1.6. Summary of phenotypic and gene expression changes in the skeleton resulting from reduced embryonic mechanical stimulation. Embryonic immobilisation results in weakened bones as a result of reduced ossification (green asterisks; box a), failure of joint formation (orange arrowheads; box b), and altered rudiment morphogenesis (dark grey outlines; box c), as demonstrated by observed changes in the expression of marker genes (here, *Spp1* at the hypertrophic zone and *Col2aI*, *Bmp2*, and *Pthrp* at the joint). Evidence comes from both mouse and chick models of immobilisation (schematics on left). Adapted from Rolfe et al. (2013).

As noted previously, signalling during skeletal development regulates the relationship between cellular proliferation and differentiation. The balance of these processes is linked and determines size and shape of the eventual bones. During development, rudiments expand asymmetrically and develop features such as condyles and tuberosities, which are outgrowths from the main shape of the rudiment that facilitate joint articulation and muscle attachment. In immobilised mouse and chick, cartilage rudiments are shorter, with reduced definition of morphological features at the rudiment termini, and at the tuberosities which serve as tendon attachment points (Hall and Herring, 1990, Hosseini and Hogg, 1991a, Rot-Nikcevic et al., 2006, Gomez et al., 2007, Nowlan et al., 2008b, Nowlan et al., 2010a, Roddy et al., 2011b) (Fig. 1.6b, summarised in Table 1.1). This corresponds to observations of reduced chondrocyte proliferation in the growth plate (which contributes to overall length), the terminal condyles, and the bony eminence of the humeral tuberosity (Germiller and Goldstein, 1997, Blitz et al., 2009, Roddy et al., 2011a) under reduced mechanical stimulation. Chondrocyte proliferation *in vitro* has been shown to be stimulated by dynamic mechanical stress (Wu et al., 2007, Ryan et al., 2009, Liang et al., 2017), which suggests that embryonic movement could regulate chondrocyte proliferation and that this process is inhibited under immobilisation. This would affect the ultimate size and shape of rudiments, explaining observed differences in morphology in immobilised rudiments, and would have a knock-on effect for skeletal functionality (Roddy et al., 2011a). Another cellular process that contributes to rudiment size and shape is chondrocyte intercalation, where daughter cells of proliferating chondrocytes divide along a plane perpendicular to the long axis of the bone, and subsequently reposition themselves in columns parallel to the long axis, thereby lengthening the bone during chondrocyte proliferation. This process is disrupted in the jaws of immobilised zebrafish and mildly affected in muscle-less mouse (Shwartz et al., 2012, Brunt et al., 2015). Orientation of cells adjacent to the jaw joints in the zebrafish is also affected by immobilisation (Brunt et al., 2015). Misregulation of cell proliferation and organisation is further suggested by observations of misshapen jaw joints in immobilised fish, which inhibits jaw function (Brunt et al., 2015).

Table 1.1. Summary of phenotypic and gene expression changes in the skeleton occurring under altered embryonic mechanical stimulation.

Changes in phenotype or gene expression	Reference
Endochondral ossification/bone size	
Thin, hypomineralised bones*	Rodriguez et al. (1988a), Rodriguez et al. (1988b)
Lower bone mass, reduced mechanical strength	Gomez et al. (2007), Sharir et al. (2011)
Reduced radial & longitudinal growth, reduced chondrocyte proliferation at the growth plate	Hall and Herring (1999), Hosseini and Hogg (1991b), Hogg and Hosseini (1992), Osborne et al. (2002), Lamb et al. (2003), Nowlan et al. (2008b), Rot-Nikcevic et al. (2006), Gomez et al. (2007), Drachman and Sokoloff (1966)
Reduced bone collar and ossification, expression of *Col10aI* (down) and *Ihh* (up)	Nowlan et al. (2008b), Nowlan et al. (2010a)
HYPERMOBILITY: Increased length, increased chondrocyte proliferation	Heywood et al. (2005)
Rudiment morphology/bone shape	
Misshapen condyles, reduced chondrocyte proliferation at condyle sites	Germiller and Goldstein (1997), Rot-Nikcevic et al. (2006), Nowlan et al. (2008), Nowlan et al. (2010a), Roddy et al. (2011b), Drachman and Sokoloff (1966)
Regressed tuberosities, reduced chondrocyte proliferation at humeral tuberosity	Blitz et al. (2009), Nowlan et al. (2010a)
Synovial joint formation	
Joint contractures, hip dysplasia*	Pena and Shokeir (1976), Aronsson et al. (1994)
Reduction/absence of synovial cavity; fusion of rudiments	Fell and Canti (1934), Hamburger and Waugh (1940), Lelkes (1958), Drachman and Sokoloff (1966), Murray and Drachman (1969), Ruano-Gil et al. (1978), Mitrovic (1982), Hosseini and Hogg (1991a), Mikic et al. (2000), Osborne et al. (2002), Rot-Nikcevic et al. (2006), Kahn et al. (2009), Nowlan et al. (2010a), Roddy et al. (2011b), Persson (1983)
HYPERMOBILITY: Enlarged synovial cavities	Ruano-Gil et al. (1985)
Absence of inter-articular ligaments, chondrogenous layer & menisci	Roddy et al. (2011b), Ruano-Gil et al. (1978), Hosseini and Hogg (1991b), Hamburger and Waugh (1940), Drachman and Sokoloff (1966), Mikic et al. (2000)
Disorganisation of tissue patterning; altered expression patterns of *Fgf2*, *Bmp2*, *Pthrp*	Nowlan et al. (2010a), (Roddy et al., 2011b)

*Human/clinical observation.

Joint malformation in humans, especially at the hip, ankles, and digits, has been documented in infants following reduced movement (Aronsson et al., 1994). In animal

models, including mouse, chick, and zebrafish, joint reduction or contraction has also been demonstrated in limb joints as well as in the vertebral and jaw joints (Fell and Canti, 1934, Hamburger and Waugh, 1940, Lelkes, 1958, Drachman and Sokoloff, 1966, Murray and Drachman, 1969, Ruano-Gil et al., 1978, Mitrovic, 1982, Hosseini and Hogg, 1991a, Mikic et al., 2000, Rot-Nikcevic et al., 2006, Kahn et al., 2009, Nowlan et al., 2010a, Roddy et al., 2011a, Brunt et al., 2015, Rolfe et al., 2017). Most studies have made use of neuromuscular blockers which induce rigid paralysis, although studies of flaccid paralysis where muscles are permanently relaxed, also causes joint reduction (Osborne et al., 2002). This suggests that the dynamic nature of mechanical stimulation during embryonic movement is essential to skeletal development. This is further supported by observations that hypermobilisation has been shown to induce joint enlargement (Ruano-Gil et al., 1985).

As described earlier, joint development can be described as three distinct stages (Fig. 1.4). In human infants, observed cases show that immobilisation ultimately affects the morphology and function of mature joints, and the use of animal immobilisation models has allowed for the identification of the specific processes of joint development which are altered under reduced mechanical stimulation. The first stage of joint formation, specification, is not affected: joint sites, as indicated by *Gdf5* expression, emerge at the correct locations in the developing embryo. The second stage, patterning, is profoundly affected: joint tissues, especially the chondrogenous layers, fail to differentiate correctly at the joint site (Kavanagh et al., 2006, Kahn et al., 2009, Nowlan et al., 2010a, Roddy et al., 2011b). In chick, immobilisation alters the expression of tissue-specific markers at the joint: *Fgf2* and *Bmp2* expression in the chondrogenous and intermediate layers, respectively, is lost, and expression of *Col2aI* and *Pthrp* is increased, extending across the joint territory instead of being restricted to the rudiments (Roddy et al., 2011b). These findings are similar to misexpression of markers in the muscle-less mouse (Nowlan et al., 2010a). Gene misexpression demonstrates that signalling events at the joint which specify the chondrogenous and intermediate tissues are misregulated under reduced mechanical stimulation. Because joint specification is not altered, it suggests that cells earlier specified as belonging to the joint do not proceed towards joint differentiation under reduced mechanical stimulation, and potentially take the chondrogenic identity of nearby cells within the rudiments. The third stage of joint formation, cavitation, is preceded by joint

morphogenesis and therefore relies on correct differentiation of tissues at the joint and the underlying bone during the second stage of joint formation (Nowlan and Sharpe, 2014). As immobilisation causes changes in the shape of the condyles, this stage of joint formation is impacted by immobilisation (Roddy et al., 2011b). Altogether, movement is crucial to the regulation of gene expression during tissue differentiation and joint cavitation, which ultimately affects functionality of the mature joint.

Initial analyses of gene expression changes under reduced mechanical stimulation involved a candidate gene approach, focusing on well-characterised gene markers of chondrogenesis and ossification (e.g. *Col2aI*, *Ihh*, *Bmp2*) (Nowlan et al., 2008b, Roddy et al., 2011b). However, a transcriptomic approach, such as microarray or RNA-Seq, allows for unbiased examination of all genes which are differentially regulated as a result of immobilisation. This approach was subsequently used to compare the transcriptomes of muscle-less ($Pax3^{Spd/Spd}$) (Vogan et al., 1993) and control mouse humeri and associated joints at TS23, when the effects of immobilisation on ossification and joint formation are apparent (Rolfe et al., 2014). Within the set of differentially regulated genes that was generated by this transcriptomic study, Gene Ontology analysis demonstrated an enrichment for genes associated with cytoskeletal architecture, cell signalling, and development and differentiation, suggesting widespread disturbance of these biological processes under immobilisation (Rolfe et al., 2014). Among major signalling pathways, including TGF-β/BMP, FGF, and Notch, whose components had differential expression under reduced mechanical stimulation, the Wnt pathway had the most affected components (34 genes), identifying Wnt as the cell signalling pathway most affected by reduced mechanical stimulation in this context. This correlated with observed differences in the spatial expression of key Wnt pathway components in muscle-less mouse forelimb suggesting that misregulation of Wnt signalling could be a key contributor to the phenotypic differences seen in the skeleton upon immobilisation (Rolfe et al., 2014). A role for Wnt signalling in chondrogenesis and ossification during *in vitro* mechanical stimulation has been suggested by numerous studies (Hens et al., 2005, Robinson et al., 2006, Caverzasio and Manen, 2007, Bikkavilli et al., 2008, Case et al., 2008), but there are few studies which have examined this relationship *in vivo* (Kahn et al., 2009, Brunt et al., 2017), making an examination of Wnt signalling in the developing immobilised skeleton an area of interest.

1.4.4 Mechanical forces present during skeletal development

Taking the data together it can be concluded that during skeletal development, mechanical forces influence cellular differentiation by providing cells with temporal and spatial physical cues which impact cell behaviour, promoting the proliferation and differentiation of cells in the appropriate location within the skeletal rudiment and at the appropriate stage of development. Limb movement would expose cells of the developing skeleton to several types of physical stimuli, including stress, strain, hydrostatic pressure, and fluid flow (Nowlan et al., 2008a, Roddy et al., 2011a). Finite Element (FE) modelling allows for prediction of the patterns of forces generated in the developing skeleton during limb flexion/extension. Physical stimuli occurring in developing tissues cannot currently be measured directly, but this predictive modelling, based on emerging rudiment morphology and measurements of the mechanical properties of tissues is useful for examination of stress and strain patterns. This modelling work showed strikingly that the predicted patterns of dynamic stimuli correspond both spatially and temporally to the tissues most dramatically affected by immobilisation (Nowlan et al., 2008a, Roddy et al., 2009, Roddy et al., 2011a, Nowlan et al., 2012). For example, at the knee joint, the patella, condyles, and the joint interzone are all impacted by reduced movement; FE modelling at the joint predicts physical stimuli peaks at the future patella and in the condyles of the distal femur, and dynamic levels of hydrostatic pressure at the joint interzone (Roddy et al., 2011a). Within the avian tibiotarsus, peak physical stimuli were predicted at the diaphyseal mid-point, and at later stages predicted to radiate outwards towards the end of the long bone; this pattern mimics that of ossification and, crucially, shortly precedes it (Nowlan et al., 2008a). Altogether, this demonstrates several important characteristics of mechanical stimulation in the developing skeleton: that it is dynamic, and that it corresponds to known patterns of tissue differentiation and maturation, and that it co-localises to tissues which are severely impacted by reduced mechanical stimulation.

1.5 Mechanotransduction during skeletal development

Movement during skeletal development is demonstrably important to tissue differentiation and the formation of functional skeletal elements, and reduced

mechanical stimulation alters gene expression during tissue differentiation. Despite the clear relationship between movement and gene expression, the mechanisms by which mechanical stimuli influence gene regulation are not clear. However, there is clear evidence that physical properties of the extra-cellular environment are capable of influencing cell behaviour, and specifically evidence from this and other research groups that signalling pathways which are important to skeletal development are capable of being regulated by mechanical stimuli.

Studies of gene regulation and expression in developing tissues under reduced mechanical stimulation have demonstrated that changes in gene expression following immobilisation is characteristic of corresponding phenotypic abnormalities (Nowlan et al., 2008b, Kahn et al., 2009, Roddy et al., 2011b, Rolfe et al., 2014, Havis et al., 2016). However, despite a demonstrable relationship between mechanical environment and embryonic development, to date there has been no clearly defined mechanism for transduction of mechanical stimuli to gene regulation identified in the embryonic skeleton. This presents a clear gap in understanding how, and to what extent, mechanical stimulation plays a role in the patterning of skeletal tissues. Identification of the required mechanoregulatory mechanism, or potentially multiple mechanisms acting simultaneously, is essential to understanding this level of gene regulation during skeletal development.

Suggestions for various mechanotransduction mechanisms have emerged following the seminal work of Engler et al. (2006) which showed that i*n vitro* differentiation of mesenchymal stem cells can be mechanically influenced by controlling substrate stiffness. Cells on softer substrates differentiate towards neurons or fat cells (adipocytes), while those on stiffer substrates differentiate to muscle cells (myocytes), and those on even more rigid substrates differentiate to osteoblasts (Engler et al., 2006). Cells can sense substrate stiffness via integrin receptors coupled to the cytoskeleton, whose tension is regulated by RhoA/ROCK signalling (Provenzano and Keely, 2011, reviewed in Ross et al., 2013, Yu et al., 2013a). This pathway is implicated in both chondrogenesis and osteogenesis and therefore offers a way for cytoskeletal tension to directly influence cellular differentiation; indeed, integrins have been shown to influence myogenic and osteogenic differentiation of mesenchymal stem cells (Woods et al., 2005, Arnsdorf et al., 2009, Shih et al., 2011, Yu et al., 2013a). Cell shape and spread, which can be linked to substrate stiffness, are also capable of influencing

cellular differentiation: flattened, spread mesenchymal stem cells (MSCs) undergo osteogenesis while round, restricted MSCs undergo adipogenesis (McBeath et al., 2004). This was also shown in mesenchymal progenitors in the branchial arches, where round, unspread cells switched on the transcription factors Pax9 and Msx1 and underwent odontogenesis while flattened, spread cells did not (Mammoto et al., 2011). Intriguingly, odontogenic progenitor shape was determined by cell density, which in turn was based on the presence of the signalling molecules Fgf8 and semaphorin (Sema) 3f in the overlying ectoderm. While Fgf8 acted as a cell attractant, Sema3f repulsed cells, thereby controlling cell spread and shape. Cell shape change was shown to be sufficient to induce odontogenic differentiation, highlighting an elegant example of mechanical control of cellular differentiation *in vivo*. In this and other examples, cell differentiation was shown to be regulated by RhoA/ROCK signalling, which further suggests a role for cytoskeletal tension in sensation of physical cellular properties and control of differentiation (McBeath et al., 2004, Mammoto et al., 2011).

The cytoskeleton is a dynamic system which is linked to cell signalling processes and could serve to integrate mechanical cues from the cellular environment with intracellular signalling responses during skeletal development (reviewed in Ohashi et al., 2017). The Wnt, TGF-β, and BMP signalling pathways have been demonstrated to regulate the actin cytoskeleton and also to be regulated by cytoskeletal dynamics (Edlund et al., 2002, Akiyama and Kawasaki, 2006, Matsumoto et al., 2010, Wang et al., 2012). Numerous cytoskeletal genes are differentially regulated in the humeri and associated joints of muscle-less mouse (Rolfe et al., 2014), which suggests that changes in cytoskeletal architecture under reduced mechanical stimulation could potentially affect intracellular signalling and impact the differentiation of skeletal tissues.

The extra-cellular matrix (ECM) of tissues is an important component by which the mechanosensation of cells in developing tissues can be manipulated. Cartilage ECM is composed of collagen fibres and glycoproteins, which provides structure and protects the tissue from physical stress, and which can also regulate the dispersal and binding of diffusible signalling molecules (Gao et al., 2014). During cartilage maturation and endochondral ossification, the ECM is remodelled by the activity of matrix metalloproteases and other factors, and this could regulate or promote skeletal development (reviewed in Ortega et al., 2004, Paiva and Granjeiro, 2014). The actin cytoskeleton is linked to ECM components by focal adhesions, which are protein

complexes composed of integrins as well as signalling molecules. Regulation of focal adhesions, which can experience high turnover during processes such as cell migration, is another means by which mechanical factors could influence intracellular signalling (reviewed in Ross et al., 2013). Formation of cell-matrix junctions such as these impacts cell signalling and cellular differentiation, including chondrogenesis and hypertrophy (Koshimizu et al., 2012, Zhang et al., 2015, Du et al., 2016). Ion channels are also mechanosensitive and localised to focal adhesions in cartilage, representing another mode by which the ECM could regulate cellular differentiation (reviewed in Mitsou et al., 2017). Inhibition of integrins and stretch-activated ion channels (SACs) has been shown to negatively regulate downstream signalling and chondrocyte proliferation (Wu and Chen, 2000, Chowdhury et al., 2004, McMahon et al., 2008).

While numerous mechanisms of mechanotransduction have been investigated during the differentiation of skeletal cells *in vitro*, few have been explored during embryonic skeletogenesis. The work included in this thesis focused on two potential mechanotransduction mechanisms; the Hippo cell signalling pathway and primary cilia. These mechanisms have been previously demonstrated to have mechanotransductive potential in adult skeletal tissues or *in vitro* systems of skeletal tissue differentiation, but have not been adequately examined in the context of mechanotransduction during embryonic skeletal development.

1.5.1 The Hippo cell signalling pathway

The Hippo pathway is one candidate mechanism of mechanotransduction. First identified and characterised in *Drosophila* as a regulator of cellular proliferation and organ growth, it has since been well-characterised in mammalian cells *in vitro* as a pathway capable of responding to external environmental cues (reviewed in Yu et al., 2015). There is now growing evidence of Hippo pathway activity in developing mammalian tissues, including organogenesis of the lungs, heart, kidneys, dentition, and craniofacial skeleton (Reginensi et al., 2013, Zhou et al., 2015, Fu et al., 2017, Posfai et al., 2017, Wang et al., 2017, Wang and Martin, 2017). In the early embryo, Hippo signalling has been demonstrated as crucial to the process of lineage determination, where cells of the trophectoderm segregate from the inner cell mass, and to early angiogenesis in conjunction with vascular endothelial growth factor (*Vegf*) (Nishioka et

al., 2009, Posfai et al., 2017, Wang et al., 2017). While Hippo signalling during lineage determination and angiogenesis has been reported to be modulated by contact inhibition and actin cytoskeletal dynamics, the mechanism of pathway activity in more developmentally advanced tissues, and the relationship between mechanotransduction and Hippo signalling during organogenesis, remains unclear.

Components of the Hippo pathway were initially discovered through genetic screens in *Drosophila* where a number of mutations in independent genes gave similar phenotypes involving excessive tissue growth, leading to names for mutated loci such as "*Hippo*" and "*Warts*" (reviewed in Yu et al., 2015). Several of the genes discovered in this screen encoded kinases (Salvador, Hippo, Mats, Warts) that operate in a co-ordinated pathway (the Hippo pathway) through an effector molecule, the co-transcriptional activator Yorkie (*Yki*), linking Hippo signalling to cellular proliferation (Huang et al., 2005). The pathway functions via activation of the Hippo kinase (*Hpo*), which phosphorylates and activates the kinase Warts (*Wts*), which then phosphorylates the Ser127 residue of Yorkie (*Yki*) to sequester it to the cytoplasm, silencing transduction to the nucleus and target gene activation (Fig. 1.7). Subsequent phosphorylation of additional serine residues leads to ubiquitination and degradation (Oh and Irvine, 2008). When Hpo is inactive, unphosphorylated Yki translocates to the nucleus, binds Scalloped (*Sd*) transcription factors, and regulates expression of target genes involved in proliferation, apoptosis, and differentiation (Wu et al., 2008).

The pathway functions similarly in mammals: MST1/2 (the mammalian orthologue of *Drosophila* Hpo) phosphorylates LATS1/2 (*Drosophila Wts*), which phosphorylates and inactivates YAP/TAZ (*Drosophila Yki*) (Zhao et al., 2007, Hao et al., 2008, Zhou et al., 2009) (Fig. 1.7). When YAP/TAZ are unphosphorylated, they can translocate to the nucleus to bind TEA-domain family member (TEAD) (*Drosophila Sd*) transcription factors 1-4 (Zhao et al., 2008b). In addition to the core kinase cascade of Hpo/ MST1/2 and Wts/ LATS1/2, a number of proteins which regulate the activity of these kinases, and of Yki or YAP/TAZ, have been identified (reviewed in Zhao et al., 2010, Yu et al., 2015) (Fig. 1.7). Many of these regulatory relationships are conserved between *Drosophila* and mammals (reviewed in Zhao et al., 2010) (Fig. 1.7). In the mammalian system, MST1/2 directly phosphorylates and activates LATS1/2, but also promotes its phosphorylation indirectly through MOB1 and SAV1, the first of which inactivates the autoinhibitory domain of LATS1/2 (Praskova et al., 2008, Callus et al., 2006).

LATS1/2 is also recruited for MST1/2 activation by Neurofibromin2 (NF2) and Kibra proteins (Zhang et al., 2010b, Xiao et al., 2011). Pathway regulation in *Drosophila* occurs similarly via homologous fly proteins.

Models of the Hippo pathway in Drosophila and mammals.

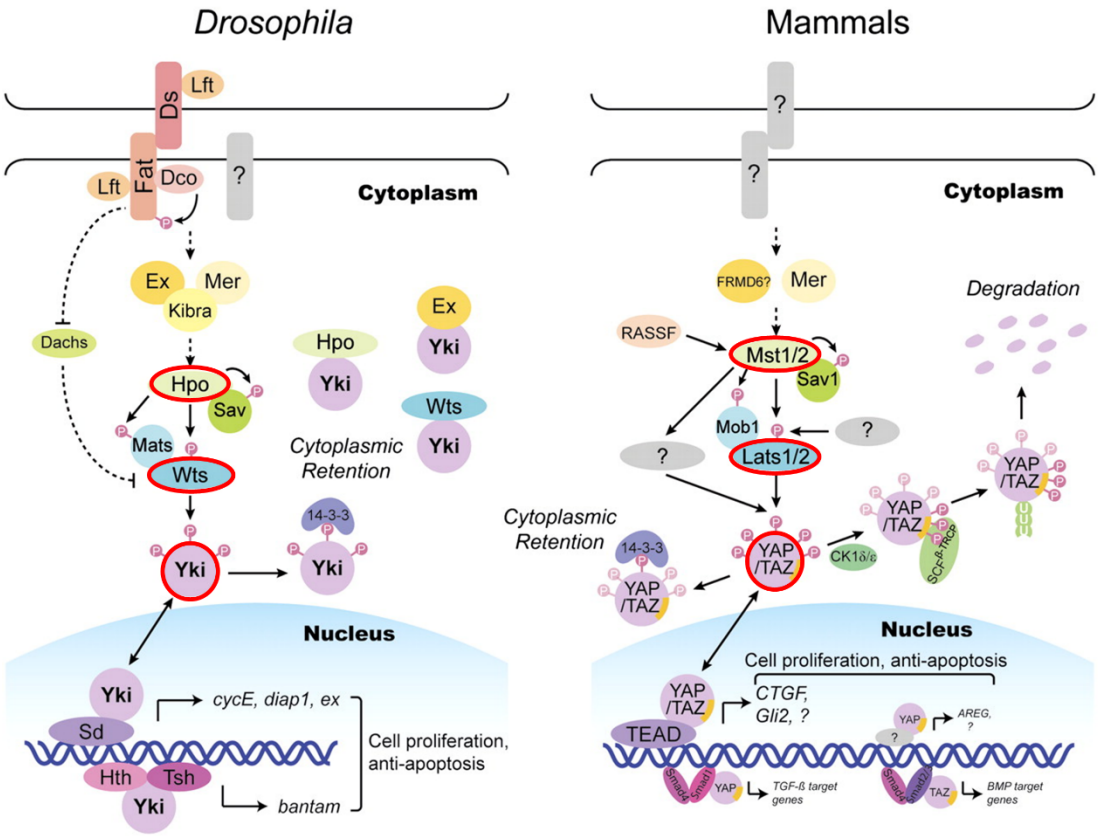

Fig. 1.7. The Hippo pathway is mostly conserved between *Drosophila* and mammals. The major components of the Hippo cell signalling pathway are shown, in *Drosophila* (left) and mammals (right); equivalent components in the two systems are similarly colour-coded. The core of the pathway is a kinase cascade consisting of Hippo (Hpo; Mst1/2) and Warts (Wts; Lats1/2), which phosphorylate and sequester Yorkie (Yki; YAP/TAZ) to the cytoplasm (components outlined in red). Inactivation of the kinase cascade allows Yki or YAP/TAZ to translocate to the nucleus, and bind Scalloped (Sd; TEAD) transcription factors to regulate expression of downstream target genes. From Zhao et al. (2010).

In *Drosophila*, the kinase cascade of Hpo and Wts is modulated by binding of the atypical cadherin Fat (*Ft*) to the cadherin Dachsous (*Ds*) on neighbouring cells (Cho and Irvine, 2004, Willecke et al., 2006). This serves as a mechanism for cells to sense

neighbours and to accordingly regulate growth and proliferation. In the mammal, there are four Fat family members (*Fat1*-4); however, *Fat4* is considered to be orthologous to *Drosophila* Ft, while Fat1-3 have a different intracellular domain to *Fat4* and are considered orthologous to *Drosophila* Fat-like (Tanoue and Takeichi, 2005). Despite structural similarities, it is not clear if *Fat4* is capable of regulating YAP/TAZ in a manner similar to Fat regulation of Yki, nor if it is dependent on binding to Dchs, the mammalian ortholog of Ds (Mao et al., 2011). Additionally, LATS1/2 phosphorylation independent of MST1/2, and YAP/TAZ phosphorylation independent of LATS1/2 by MAP4K kinases have been demonstrated in the mammalian system (Zhao et al., 2012, Meng et al., 2015).

Other mechanisms of YAP/TAZ control include Hippo-independent sequestration of YAP/TAZ at cell junctions by Angiomotin (AMOT), α-catenin, and the protein tyrosine phosphatase PTPN14 (reviewed in Yu and Guan, 2013). Notably, YAP/TAZ nuclear localisation and activity can be regulated in response to mechanical cues, such as cell size, shape, and substrate stiffness, which are transmitted by the actin cytoskeleton (Dupont et al., 2011, Halder et al., 2012, Piccolo et al., 2014, Yu et al., 2015). Dupont et al. (2011) demonstrated that YAP/TAZ are localised to the nucleus and have higher target gene expression in spread cells on stiff matrices, but are localised to the cytoplasm in cells confined to fibronectin islands or on soft matrices. Crucially, YAP/TAZ were required for cells to respond to cues of spreading or matrix rigidity, and to differentiate accordingly, and that this response was mediated independently of the canonical Hippo cascade, potentially through the actin cytoskeleton (Dupont et al., 2011). The ability of YAP/TAZ to respond rapidly and robustly to the cellular mechanical environment makes it a potent candidate mechanotransductive mechanism. Two studies have explored the Hippo pathway in the developing skeleton (Karystinou et al., 2015, Deng et al., 2016), but none so far have related pathway activity to possible mechanoregulation of gene expression during development of these tissues, raising the possibility that the Hippo pathway could be involved in this process.

Hippo pathway activity, via its YAP/TAZ effector proteins, has previously been demonstrated by binding of TEAD transcription factors and expression of widely-accepted reporter genes. However, YAP/TAZ have been shown to interact with other transcription factors in addition to TEADs, such as SMADs, RUNX2, Vgll1-4, β-catenin, TBX5, and numerous others (reviewed in Varelas, 2014). Binding can

positively regulate the expression of target genes, or, as in the case of the vestigial-like (Vgll) family member 4 (homologs of *Drosophila* Vestigial, or Vg), can supplant TEAD binding and repress YAP/TAZ activity (Zhang et al., 2014). Several target genes of YAP/TAZ and TEADs have been identified by transcriptomic screens of mammalian cells, including *Anrkd1*, *CTGF*, *Cyr61*, *Birc5*, *Inha*, and *Col8aI*, and are widely-used indicators of YAP/TAZ activity (Zhao et al., 2008b, Zhang et al., 2009, Zanconato et al., 2015). Likewise, transcriptional targets of Yki in *Drosophila* have also been identified (*Bantam*, *Diap1*, *Cyclin E*, *Expanded*), which play a role in cellular proliferation (Thompson and Cohen, 2006, Shu and Deng, 2017). Although many regulatory mechanisms of Hippo signalling are evolutionarily well-conserved between *Drosophila* and mammals, there appears to be little overlap between Yki and YAP/TAZ target genes (Yu et al., 2015). YAP and TAZ are capable of differential gene regulation (Reginensi et al., 2013, Kaan et al., 2017, Sun et al., 2017), and several genes which are widely-used as indicators of YAP/TAZ transcriptional activity can be regulated by other mechanisms or signalling pathways such as Wnt/β-catenin and TGF-β (Kim and Jho, 2014, Luo, 2017), suggesting that care should be taken in the definitive identification of genes as YAP/TAZ transcriptional targets. Further, the diversity of tissues and cells in which Hippo and YAP/TAZ activity have been examined suggests that target genes could be tissue- or cell type-specific.

1.5.2 The role of cilia in cell signalling, development, and mechanotransduction

The primary cilium is another attractive candidate mechanotransduction mechanism in the developing skeleton. This non-motile, microtubule-supported organelle projects outward from the cell surface, allowing the cilium to sense mechanical forces such as fluid flow which occur in the cellular environment (Singla and Reiter, 2006, Malone et al., 2007, Spasic and Jacobs, 2017b). The membrane encapsulating the cilium axoneme, or microtubule core, is distinct from the adjacent cellular membrane, with localised membrane-bound receptors and other cilium-specific proteins (reviewed in Jensen and Leroux, 2017). Notably, components of the Hedgehog, Wnt, and TGF-β signalling pathways have been shown to be localised at or near the ciliary membrane, suggesting that the primary cilium can function as a centre for cell signalling activity (He, 2008, Wong and Reiter, 2008, Christensen et al., 2012, Clement et al., 2013). Primary cilia on MSCs have been shown to promote osteoblastic differentiation and

bone formation by sensing fluid flow (Hoey et al., 2012b); contrastingly, cilia appear to be less important to chondrocyte differentiation, and reduction in their length or number may be necessary for this process, as well as for proliferation (Tummala et al., 2010, reviewed in Yuan et al., 2015, Thompson et al., 2017). In established tissues, chondrocyte cilia have been reported to act as mechanosensors and to be crucial for the maintenance of healthy articular cartilage (Ruhlen and Marberry, 2014), and cilia are suggested to act as osteocyte mechanosensors in bone maintenance (Nguyen and Jacobs, 2013). These data suggest a potential role for the primary cilium in mechanosensation and differentiation of tissues during skeletal development.

The ciliary membrane is biochemically distinct from the cellular membrane, with a unique lipid and protein composition (Vieira et al., 2006). Receptors of multiple signalling pathways are localised to the ciliary membrane, and shuttling of receptors to the cilium, as well as localisation to the cilium base or tip, may be required for the function of certain receptors, including components of the Hedgehog (Hh) pathway and polycystic kidney disease proteins (Pazour et al., 2000, Rohatgi et al., 2007, Rohatgi and Snell, 2010). In the absence of Hedgehog ligands, Patched (Ptc) receptors, which are localised near cilia, bind and inhibit the vesicular Smoothened (Smo) receptor (reviewed in Bangs and Anderson, 2017). This results in the processing of Gli transcription factors to their repressor forms, thereby inactivating Hedgehog target genes. When Hh signalling is active, Ptc releases Smo, which is transported to the ciliary membrane; Gli proteins are processed to their active form, and Hedgehog transcriptional activity is permitted. Inhibition of Smo trafficking to the cilium and subsequent activation of Smo inhibits Hh signalling (Rohatgi et al., 2009), suggesting that co-localisation of Smo and Gli processing proteins in the primary cilium is essential to Hh signal transduction. While most studies of Hh signalling at the cilium have focused on the Sonic hedgehog (Shh) ligand, Indian hedgehog (*Ihh*), which is crucial to skeletal development, has also been related to ciliary function (Ruiz-Perez et al., 2007).

Wnt/β-catenin signalling occurs as described in Section 1.3. In addition to the canonical/β-catenin pathway, there are also two non-canonical pathways: calcium (Ca^{2+}) signalling and planar cell polarity (PCP). In the developing kidney, both canonical and non-canonical Wnt components are localised to the primary cilium, including Frizzled (Fz) receptors, Inversin (Inv), Dishevelled (Dvl), Vangl, and β-

catenin (reviewed in Gerdes et al., 2009, Goggolidou, 2014). Mutations in primary cilia genes result in disrupted PCP signalling and disorganised cell polarity (reviewed in Goetz and Anderson, 2010a). However, the role of cilia in modulating canonical Wnt signalling is not as clear as for PCP or Hh signalling. For example, Corbit et al. (2008) and Jiang et al. (2016) report that ablation of embryonic primary cilia represses canonical Wnt activity and while Ocbina et al. (2009) report that in multiple ciliary mutants, canonical Wnt signalling remains unaffected. Cilia have also been linked to Wnt/calcium (Ca^{2+}) signalling, via the PC1 and PC2 transmembrane protein channels (Lancaster and Gleeson, 2010), although this has recently been disputed (Delling et al., 2016).

During development, the primary cilium has been identified as a mechanotransductive mechanism during the establishment of embryonic asymmetry at the node, where motile cilia generate a directional fluid flow that is sensed by neighbouring primary cilia, directing cellular signalling and driving organismal symmetry-breaking events (Nonaka et al., 1998, 2002). Later, during organogenesis, it is essential to the development of the kidneys, nervous system, heart, and craniofacial and appendicular skeletons; conditional ablation of cilia in these structures leads to malformations of varying severity (reviewed in Fry et al., 2014). Cilia have previously been ablated in cartilage by conditional excision of numerous genes required for cilium construction or for protein shuttling along the cilium axoneme, termed intra-flagellar transport (IFT) (summarised in Table 1.2). Cre-mediated ablation of cilia under the control of the *Prx1* enhancer, which targets all cells in the early limb bud, revealed the importance of cilia to normal hedgehog (Hh) signalling (Haycraft et al., 2007b). During normal limb development, Sonic hedgehog (Shh) signalling is active at the Zone of Polarising Activity (ZPA) in the distal, posterior limb bud; cilia absence under the *Prx1* enhancer resulted in aberrant Shh signalling here and led to misspecification of digits and polydactyly (Haycraft et al., 2007b). Early ablation of cilia had a knock-on effect for later gene expression: in E18.5 long bones, Indian hedgehog (*Ihh*) expression was reduced in pre-hypertrophic chondrocytes, while expression of the Hh signalling components Gli1 and Ptch1 in the proliferating and pre-hypertrophic chondrocytes and in the perichondrium was absent (Haycraft et al., 2007b). This effectively links ciliary function to differentiation of skeletal tissues.

Interestingly, ablation of cilia under a sub-element of the Msx2 enhancer (which targets the AER during early limb development (Sun et al., 2000)), did not result in any gross malformations (Haycraft et al., 2007b). Later, the absence of cilia from mesenchymal condensations (under Dermo1-Cre) or cartilage (*Col2aI*-Cre), or global mutations of genes required for cilia formation or function, result in limb shortening, disorganised chondrocytes, craniofacial abnormalities, hypomineralisation, and dwarfism, suggesting alterations in cell signalling impacting skeletal differentiation (summarised in Table 1.2).

The gross defects observed as a result of cilia ablation point to an important role for cilia, and cilia-mediated signalling, during skeletogenesis. However, there is little description of typical cilium structure or distribution in developing skeletal tissues, aside from the sternal cartilage (Poole et al., 2001, Jensen et al., 2004). Descriptions of cilia in post-natal growth plate cartilage or adult articular cartilage have examined cilia orientation and length (McGlashan et al., 2007, Ascenzi et al., 2011), but it is unclear how these properties of adult cilia relate to those found in immature tissues. Moreover, while numerous studies have examined the effects of removing cilia from different tissues during skeletal development (Table 1.2), few have examined the impact of ciliary ablation on the specific aspects of skeletogenesis which are impacted by reduced mechanical stimulation, although several studies have explored changes in gene expression and cell signalling. In addition to the observed changes in Shh and *Ihh* signalling reported by Haycraft et al. (2007b), Yuan and Yang (2015) showed that primary chondrocytes derived from postnatal cilia-deficient mice had deficient Hh signalling and enhanced responsiveness to canonical Wnt signals. Components of both the Hh and Wnt pathways are altered under reduced mechanical stimulation, and the suggestion that cilia act as mediators of these signalling pathways in the context of skeletal development, as they do in other tissues, raises the question of cilia as signalling mechanotransductors in these tissues. Additionally, cilia may have a role in Hippo signalling, as the possible Hippo pathway receptor *Fat4* is localised to renal cilia (Saburi et al., 2008). Cilia have been linked directly to the YAP/TAZ effectors of Hippo signalling, as the actin cytoskeleton was shown to modulate YAP/TAZ subcellular trafficking, as well as ciliogenesis, via ciliary vesicle trafficking (Kim et al., 2015). Cilia could therefore link together mechanical signals, intracellular signalling, and cytoskeletal architecture during skeletal development.

Table 1.2. Primary cilia mutations in mouse with relevance to appendicular skeletal development. References indicate identification of specific cilia-related genes (in grey boxes) or examination of specific cilia-gene knockouts (in white boxes). Abbreviations: embryonic day (E), intraflagellar transport (IFT), post-natal day (P).

Gene altered/ Strain Name (Reference)	Observed phenotypes (at specified stages)
Evc Ellis-van Creveld syndrome (EVC) is caused by mutations in 2 Evc genes which have an unclear function but are localised to primary cilia basal bodies and necessary for cilia-mediated signalling (Ruiz-Perez and Goodship, 2009)	
Evc$^{-/-}$ Ruiz-Perez et al. (2007)	E16.5 tibia: decreased *Ptch1* and *Gli1* expression E17.5 tibia: reduced mineralisation, disorganized growth plates P6: shortened appendicular long bones, ulnar modelling defect
Ftm/Rpgrip1l Encodes a protein, RPGRIP1L, which is localised to the ciliary basal body and regulates protein degradation and processing (Gerhardt et al., 2015)	
Ftm $^{-/-}$ Vierkotten et al. (2007)	E11.5: reduced *Ptc1* expression in limb bud E18.5: preaxial polydactyly, craniofacial reduction/fusion
Ift80 Encodes a component of IFT complex B, which regulates ciliary anterograde transport; mutated in Jeune asphyxiating syndrome (Beales et al. (2007)	
Ift80$^{gt/gt}$ (hypomorphic) Rix et al. (2011)	P21: Shortened long bones, disorganized growth plate chondrocytes, short rib polydactyly
Col2Cre;Ift80$^{fl/fl}$ Yuan and Yang (2015)	Neonate tibia: chondrodysplasia, shortened long bones, reduced ossification
Ift88/Tg737/Polaris Encodes a component of IFT; required for cilium assembly (Pazour et al., 2000)	
Ift88^{orpk} (hypomorphic) Zhang et al. (2003)	P4: Cranial malformation, polydactyly
Ift88^{orpk} (hypomorphic) McGlashan et al. (2007)	P4 tibiae: Disorganised growth plate chondrocytes
Prx1Cre;Ift88$^{LoxP/LoxP}$ Haycraft et al. (2007b)	E11.5 limb buds: gene misexpression E18.5 tibia: polydactyly, reduced *Ptch1* and *Gli* expression, reduced tibial growth plate, ectopic mineralization in perichondrium P11 limbs: shortening of long bones
Col2aCre;Ift88$^{LoxP/LoxP}$ Song et al. (2007a)	E15.5 forelimb: no major defects P7, P10, P15: dwarfism
Ift172 Encodes a protein involved in anterograde IFT (Huangfu and Anderson, 2005)	
Ift172^{avc}/Ift172^{wim} (hypomorphic/null) Friedland-Little et al. (2011)	Neonate: Shortened long bones of fore- and hindlimbs; preaxial polydactyly
Prx1Cre; Ift172$^{fl/\Delta}$ Howard et al. (2010)	Neonate: Shortened long bones; polydactyly
Ift144 (Wdr19) Encodes a protein involved in retrograde IFT (Liem et al., 2012)	
Ift144^{twt} Ashe et al. (2012) (hypomorphic missense)	E10.5 limb bud: expanded *Ptch1* expression E18.5 limb: Polydactyly, short limb outgrowth

Gene altered/ Strain Name (Reference)	Observed phenotypes (at specified stages)
Kif3a Encodes a protein involved in anterograde IFT; necessary for Hh signalling (Huangfu and Anderson, 2005)	
Prx1Cre;Kif3a$^{LoxP/LoxP}$ Haycraft et al. (2007b)	E11.5 limb buds: polydactyly; reduced size E14.5 radii: no obvious defect E18.5: reduced tibial growth plate
Prx1Cre;Kif3a$^{LoxP/LoxP}$ Hart et al. (2007)	Neonate: Severely shortened limbs, polydactyly
Col2aCre;Kif3a$^{LoxP/LoxP}$ Song et al. (2007a)	E15.5 forelimb: reduced *Ptc1* expression P7, P10, P15: Postnatal dwarfism, disorganized chondrocytes
Dermo1-Cre;Kif3a$^{LoxP/LoxP}$ Hart et al. (2007)	E18.5 ulnae and tibiae: long bones: disorganised growth plate and ectopic cartilage Neonates: shortened limbs, short ribs, polydactyly
Pkd1 Mutations in 2 Pkd genes cause polycystic kidney disease (PKD); proteins encoded by these genes are localised to primary cilia and are involved in calcium signalling (Ma et al., 2017)	
Pkd1^{null} Lu et al. (2001)	E14.5: delayed ossification in humerus P0: shorter and thinner long bones
Pkd1^{m1Bei} (strong hypomorphic/null) Xiao et al. (2006)	E15.5: reduced ossification in femur Adult (12-week): overall reduced skeletal size
Pkd1$^{\Delta 17-21\beta geo}$ (truncation) Boulter et al. (2001)	E13.5: Shorter and smaller long bones with delayed cartilage differentiation

1.6 Differentiation of skeletal tissues *in vitro* and the impact of mechanical stimulation

Evidence from *in vivo* animal models has established that mechanical stimulation has an important role in skeletal development (described in Section 1.4.3). To further examine the role of mechanical stimulation in cellular differentiation, *in vitro* systems have been used to manipulate physical stimuli, thereby isolating the effects of physical forces in a controlled environment. These systems have also introduced the possibility of engineering tissues *ex vivo*, for later implantation to replace or repair damaged tissues. In the context of the skeletal system, this approach is particularly relevant for engineering articular cartilage and bone tissues to treat osteoarthritis and osteoporosis, respectively (Kim et al., 2017, reviewed in Rai et al., 2017). Biologically accurate *in vitro* models of skeletal tissues also have the potential to be used in the study of skeletal-damaging conditions such as obesity and cancer, and to design and test

treatments for these conditions (reviewed in Bhattacharjee et al., 2015, Kwakwa et al., 2017).

Efforts to differentiate skeletal tissues *in vitro* have frequently made use of mesenchymal stem cells (MSCs), which are capable of forming cartilage and bone, as well as fat, muscle, and other tissues under appropriate conditions (Pittenger et al., 1999). As movement is essential to the correct differentiation of skeletal tissues *in vivo*, so is mechanical stimulation integral to the *in vitro* differentiation of cartilage and mineralised tissues from MSCs. Differentiation of MSCs toward osteogenic, chondrogenic, neurogenic, adipogenic, or myogenic lineages has been shown to be a mechano-sensitive process that was dependent on matrix elasticity, cell shape, and cytoskeletal tension (McBeath et al., 2004, Engler et al., 2006, Gao et al., 2010, Huebsch et al., 2015, reviewed in Steward and Kelly, 2015). In these studies, cells which were flattened and spread, with high cytoskeletal tension, or which were adhered to stiff, rigid matrices (34-60 kPa), tended towards osteogenesis or chondrogenesis. Conversely, rounded cells, with low cytoskeletal tension, or which were adhered to soft matrices (circa 10 kPa) tended towards adipogenesis, (McBeath et al., 2004, Engler et al., 2006, Gao et al., 2010). These data suggest that differentiation of durable skeletal tissues requires cells to experience mechanical tension.

Use of bioreactors to apply external physical forces – tension, compression, and hydrostatic pressure – to MSCs, often in conjunction with treatment of appropriate biochemical factors, has revealed the importance of mechanical stimulation to osteogenic and chondrogenic differentiation (reviewed in Delaine-Smith and Reilly, 2012, Steward and Kelly, 2015, Fahy et al., 2017). A variety regimes have been published, incorporating a range of magnitudes, frequencies, and study lengths, and using cells from multiple sources (including bovine, equine, and human), seeded in varying biomaterials (such as agarose, alginate, fibrin and collagen scaffolds) (reviewed in Steward and Kelly, 2015). Nevertheless, several trends have emerged that underline key features of the mechanoregulation of chondrogenic and osteogenic differentiation. A common feature of these studies is the importance of dynamic mechanical stimulation to chondrogenesis, with application of cyclic, rather than static, forces thought to mimic the dynamic environment experienced by chondrocytes at the joint (Adams, 2006). Notably, mechanical stimuli have been shown to be capable of

increasing chondrogenesis and simultaneously reducing osteogenic differentiation, offering a way to attenuate hypertrophy *in vitro* (reviewed in Steward and Kelly, 2015).

Cyclic compression ranging from 2.5-10% strain increases expression of chondrogenic markers, proteoglycan synthesis, and stiffness of hydrogel constructs seeded with MSCs (Huang et al., 2004, Kisiday et al., 2009, Huang et al., 2010a). Numerous studies have noted that treatment of MSC cultures with TGF-β increases chondrogenesis, and it has also been shown that dynamic compression can increase TGF-β1/3 production in constructs, suggesting that mechanical stimulation could promote chondrogenesis by regulating the synthesis of necessary signalling molecules (Huang et al., 2004, Li et al., 2010a). Interestingly, the timing of mechanical stimulation appears to be crucial to chondrogenic differentiation, as dynamic compression during early culture appears to negatively impact chondrogenesis, while free-swelling followed by mechanical stimulation increases chondrogenesis (Mouw et al., 2007, Thorpe et al., 2008, Huang et al., 2010a). While 10% strain is the typically applied compressive force in the literature, magnitudes up to 30% were found to be more effective in inducing chondrogenesis, suggesting that further adjustment of loading regimes could additionally increase chondrogenesis in culture (Li et al., 2010b). Additionally, treatment of articular chondrocytes with dynamic compression has been shown to increase synthesis of chondrogenic matrix components, which indicates a role for mechanical force in the maintenance of a cartilage phenotype in differentiated tissues (Mauck et al., 2000, Stoddart et al., 2006).

Several studies have shown that bone marrow-derived MSCs subjected to cyclic hydrostatic pressure (10 MPa/10% strain) and treated with TGF-β undergo chondrogenic differentiation and subsequently have reduced calcification compared to free-swelling controls (Bian et al., 2012, Carroll et al., 2014). The chondrogenic effect of hydrostatic pressure has been demonstrated in other progenitor cell types, including those derived from the infrapatellar fat pad and the synovial membrane, which have also been explored as potential sources of skeletal stem cells (Vinardell et al., 2012). However, hydrostatic pressure has also frequently been examined in conjunction with TGF-β application, and pressure alone was determined to be insufficient to suppress calcification once a chondrogenic TGF-β-rich medium was supplanted with factors promoting hypertrophy, suggesting that exposure to signalling molecules is crucial to maintenance of a cartilage phenotype (Carroll et al., 2014). Another interesting finding

was that dynamic hydrostatic pressure increases chondrogenesis more in cells on stiff matrices compared to soft ones, corroborating earlier findings regarding the importance of matrix stiffness to cellular differentiation (Steward et al., 2014).

Tension and fluid flow have also been implicated in differentiation of MSCs (reviewed in Steward and Kelly, 2015). Tension (2-10% strain) has been shown to induce an osteogenic response in MSCs (Sumanasinghe et al., 2006, Ward et al., 2007). Contrastingly, tensile force has also been reported to promote chondrogenesis and proteoglycan synthesis, although this could be partially due to application of TGF-β (McMahon et al., 2008). Indeed, comparison of hydrostatic pressure with tension suggested that tension promotes osteogenesis and fibrogenesis while hydrostatic pressure is a stronger promoter of chondrogenesis, suggesting that different mechanical forces induce distinct cellular responses (Haudenschild et al., 2009). Oscillatory fluid flow (5-20 dyn/cm^2 on 2-D cultures; perfusion of 0.3-3 mL/min in 3-D cultures) has similarly been linked to osteogenic differentiation of adipose- and bone marrow-derived MSCs, via intracellular calcium signalling pathways (Bancroft et al., 2002, Li et al., 2004, Datta et al., 2006, Riddle et al., 2006, Stavenschi et al., 2017). The osteogenic response of MSCs to fluid flow has been shown to be regulated by the primary cilium, further highlighting a role for the primary cilium in differentiation of skeletal tissues (Hoey et al., 2012b).

The accessibility and plasticity of MSCs, which are typically harvested and isolated from adult stromal bone marrow, makes them a prime candidate for engineering of cartilage or bone tissues *in vitro*. However, when these cells are differentiated to cartilage under currently used *in vitro* regimes, they tend to spontaneously progress towards hypertrophy, forming only transient cartilage (Pelttari et al., 2006). Therefore, to date they have not been suitable for the generation of stable articular cartilage or multi-layered cartilage and subchondral bone tissues for implantation. Use of progenitor cell populations such as the embryonic limb buds for *in vitro* chondrogenic and osteogenic differentiation has been limited relative to the widespread use of MSCs. However, use of embryonic cells to investigate the role of mechanical stimulation in tissue differentiation will allow for a better understanding of the capacity of different populations of cells to form regenerative tissues *in vitro*, and for identification of the limitations of adult-derived cells for this purpose. Embryonic cells are more robust progenitors of skeletal tissues and require fewer exogenous signals such as signalling

molecules, making them simpler models of *in vitro* differentiation, well-suited to examination of the relationship between mechanical signals and cellular differentiation.

Mouse and chick embryonic limb buds are a multipotent source of mesenchymal progenitor cells, capable of differentiation to chondrogenic, osteogenic, and other tissue types. While the use of embryonic-derived cells to examine the role of mechanical stimulation in differentiation has been limited, several key similarities and differences to adult-derived cells have emerged. Notably, cyclic compression and hydrostatic pressure act similarly in cultures of embryonic cells as in adult MSCs, increasing expression of chondrogenic markers and matrix synthesis compared to free-swelling groups. Treatment of chick limb bud cells with cyclic compression (20% strain) was demonstrated to increase the number of chondrogenic condensations occurring within constructs, as well as production of a cartilaginous matrix (Elder et al., 2000). Although Elder et al. (2000) found that static compressive forces did not significantly increase chondrogenesis compared to free-swelling controls, Takahashi et al. (1998) found that a similar magnitude of constant compression (20-30% strain) increased expression of *Sox9*, *Col2aI*, and other chondrogenic markers in cultures of mouse limb bud cells. These contrasting observations could be explained by differing cell sources (chick vs. mouse), scaffold (agarose vs. collagen), or choice of chondrogenic assays (sulfate incorporation and density of chondrogenic condensations vs. gene expression and histological staining) (Takahashi et al., 1998, Elder et al., 2000).

Hydrostatic pressure has been observed to increase chondrogenesis and to suppress hypertrophy in embryonic limb bud cultures, similar to its effect on MSCs. Juhasz et al. (2014) applied dynamic hydrostatic pressure (600 Pa) to chick cultures and observed increases in expression of *Col2aI*, aggrecan, and other cartilage markers, as well as increased cartilage matrix synthesis. Saha et al. (2016) applied a much higher force (1 MPa) of hydrostatic pressure, comparable to that applied to MSCs, and similarly observed increases in chondrogenic marker gene expression in mouse limb bud cultures. In addition to increasing chondrogenesis, hydrostatic pressure reduced mineralisation and expression of hypertrophic markers (Saha et al., 2016).

Several other similarities between adult and embryonic-derived progenitor cells have also been reported: for example, oscillatory fluid flow has been shown to influence osteogenic differentiation of murine C3H10T1/2 cells (an embryonically-derived cell line) (Arnsdorf et al., 2009), and rigid matrices support osteogenic differentiation of

pluripotent early embryonic stem cells (Evans et al., 2009). These commonalities suggest that progenitor cells are capable of responding similarly to mechanical environmental factors. However, the use of signalling molecules has been required for the robust induction of chondrogenesis or osteogenesis in MSC culture, but not in cultures of embryonic cells. These molecules reinforce known signalling activities during embryonic skeletogenesis: BMP-2 and TGF-β1 are highly chondrogenic, FGF-2 promotes proliferation but reduces differentiation, and canonical Wnt signals enhance osteogenesis (reviewed in Augello and De Bari, 2010). A notable aspect of embryonic cultures is their capacity to undergo chondrogenesis or osteogenesis without need for these signals, which suggests that although adult and embryonic cells appear to respond similarly to physical stimuli, there are key differences in their responses that are as yet unexplained. This could be a difference in gene regulation in response to mechanical loading, or the involvement of different mechanotransductive mechanisms.

Studies which have been conducted using limb bud-derived cells have highlighted another key difference between embryonic and adult cultures: the tendency of high-density embryonic cultures to form chondrogenic cellular condensations (nodules) (Elder et al., 2000, Juhasz et al., 2014, Saha et al., 2016). This chondrogenic pattern of nodules occurs spontaneously, with no signalling molecule treatment required, and suggests that embryonic cells can self-organise into heterogenous cultures. This is intriguing, as elucidation of the mechanisms involved in the generation of patterns by a population of progenitor cells will contribute towards a better understanding of tissue differentiation *in vivo*, as well as offer potential solutions for the controlled differentiation of complex tissues. A challenge facing current therapeutic strategies is the co-differentiation of cartilage and bone for osteochondral implants, which are superior to pure cartilage in terms of joint repair (Scotti et al., 2010, Huey et al., 2012). An additional feature of *in vivo* articular cartilage is the zonal stratification of chondrocytes into distinct layers, which make articular cartilage a biomechanically heterogenous tissue, and which has not been successfully replicated *in vitro* (Schuurman et al., 2015). New technologies to 3-D print precise, heterogenous scaffolds for differentiation of multiple complex tissues in a single culture are promising (reviewed in Daly et al., 2017), but require an understanding of cellular responses to patterns of mechanical forces experienced by cells *in vivo*. Therefore,

examination of self-organising patterns, as well assessing the potential of spatially organised mechanical stimuli to generate patterns could address these concerns.

1.7 Objective and aims of this thesis

Mechanical stimulation generated by embryonic movement has been shown to be important to the differentiation of tissues within the developing skeleton. There is a large gap however in knowledge concerning the mechanisms by which molecular processes are affected by movement, and how this change in physical stimuli is transmitted to cells. Further, there is a need for *in vitro* assays to assess chondrogenesis and the role of molecular and mechanical signals in cellular differentiation.

The work presented here is comprised of three main aims that address these gaps in knowledge, outlined as follows:

Aim 1: To elucidate the response of Wnt and BMP signalling pathways to mechanical stimuli during embryonic joint and bone development.

Many components of the Wnt and BMP signalling pathways have been implicated in skeletal development, but the activity of these pathways in the differentiation of skeletal tissues, particularly at the joint, and under an altered mechanical environment, has not been clearly defined. Therefore, the expression of pathway components and activity of the pathways at a key stage of skeletal development (TS23), when the developing skeletal rudiments are known to be responsive to mechanical cues, were assessed by *in situ* hybridisation of ligands and other pathway components and by immunolocalisation of pathway effectors. Further, the alteration of pathway activity under immobilisation was assessed, with a particular focus on the joint tissues which are profoundly affected in the absence of mechanical stimulation.

Aim 2: To investigate potential mechanisms of mechanotransduction in the developing skeleton. Two specific mechanisms have been investigated.

A) *To describe Hippo-YAP pathway activity in the developing skeleton, and to characterize changes in pathway activity in the muscle-less mutant.*

The first potential mechanotransduction mechanism examined was the Hippo-YAP pathway, which has been shown to be mechanosensitive and to be involved in the differentiation of cells in the embryo and in culture. Evidence indiating a role Hippo-

YAP signalling in the developing skeleton of the mouse forelimb was uncovered, by examining which components are expressed in the skeletal rudiment and developing joints from a transcriptomic screen. Further evidence of Hippo pathway involvement was revealed by specific characterisation of the immunolocalisation patterns of its main effector, YAP, and *in situ* gene expression patterns of its target genes in normal and immobilised developing forelimbs. A role for YAP in chondrogenesis was functionally tested by pharmacological manipulation of YAP in embryonic cells in micromass culture, to examine the role of YAP in this context.

B) *To characterize primary cilia in the developing skeleton, examining both wildtype and muscle-less rudiments.*

The second potential mechanotransduction mechanism examined was the primary cilium, an organelle which has been demonstrated to sense mechanical stimuli and to regulate intracellular signalling pathways which are developmentally relevant. Primary cilia have been shown to be necessary for digit number and for the correct formation of the mature skeleton, but few experiments specifically investigate cilia during the formation and patterning of developing skeletal rudiments. Therefore, primary cilia were identified by double immunostaining, and were first characterised in the developing rudiments, comparing their prevalence and other characteristics between regions at differing stages of maturity, utilising automated image processing for quantification of cilia properties. This was then compared to rudiments of the muscle-less mutant, to examine if changes in cilia properties in this environment could explain some of the observed skeletal defects present in this model.

Aim 3: To establish *in vitro* chondrogenesis systems where contributory regulatory signals can be analysed.

Examination of the role of molecular and mechanical cues in developing tissues is complex and can be complicated by secondary effects and ineffective treatment regimes. Therefore, to more reliably assess the role of molecular and mechanical cues in chondrogenic differentiation, systems of chondrogenesis which could be easily manipulated and assessed are required. Chapter 6 presents the establishment of two distinct culture systems, designed ultimately to ask distinct questions. First, the use of micromass cultures of embryonic limb bud-derived cells was used to investigate spontaneous chondrogenic patterns, establishing a methodology that can be used in the

future to assess the contributions of signalling molecules and mechanical cues on the generation of spatial patterns. Second, the development of a custom-designed bending bioreactor, designed to mimic the effect of limb flexion was used in order to examine the effect of patterns of mechanical stimuli on local differentiation of progenitor cells.

Chapter 2

Materials and Methods[1]

2.1. Animal lines

Outbred CD-1 and heterozygous *Splotch delayed* (*Pax3*$^{Spd/+}$) (Vogan et al., 1993) (acquired from Jackson Laboratories) mouse lines were bred and euthanized by carbon dioxide inhalation followed by cervical dislocation, under the supervision and approval of the Trinity College Bioresources Unit and the Bioethics committee and under licence from the Irish Medicines Board/Health Products Regulatory Authority. *Splotch delayed* mutant embryos were generated by crossing heterozygous males and females.

TCF/LEF:H2B-GFP reporter mice (Ferrer-Vaquer et al., 2010) were housed and bred at the MRC Human Genetics Unit, Institute of Genetics and Molecular Medicine, Edinburgh, UK. Pregnant mothers were euthanized at E11.5-14.5 according to UK ethical guidelines. Embryos were harvested, fixed, genotyped, and transported to Trinity College Dublin. I embedded, sectioned, and stained the embryos for analysis. Embryos were cryo-embedded, sectioned, and immunostained with anti-GFP as detailed below (Section 2.4, Table 2.3).

2.1.1. Embryo Collection

After overnight matings, females were checked the following morning and the presence of a vaginal plug was taken to indicate mating and designated to be embryonic day (E) 0.5. Embryos were harvested at E10.5-14.5 of gestation by sacrificing the mother and dissecting out the uterine horns into cold phosphate buffered solution (PBS). Embryos

[1] Additional methodology specific to approaches in Chapters 5 and 6 only are described within those chapters.

were further dissected out of the uterine muscle and the embryonic membranes. Embryos from the *Splotch delayed* (Pax3^{Spd}) line were assigned a precise Theiler Stage (TS) according to morphological criteria (Theiler, 1989). The homozygous *Pax3*$^{Spd/Spd}$ phenotype could also be scored using the typical visible signs of spina bifida, exencephaly, curly tail, and thin arms, as indicators of homozygous (muscle-less) mutants. Embryo heads were dissected off and taken for genotyping, while bodies were fixed in 4% paraformaldehyde in PBS overnight. Following fixation, embryos were washed in PBS (2 x 5 minute (min)) dehydrated (10 min each in 25% methanol (MeOH)/PBS, 50% MeOH/PBS, 75% MeOH/PBS, and absolute MeOH) and stored in absolute MeOH at -20°C for later tissue analysis.

2.1.2. Embryo genotyping

During tissue collection, heads of *Pax3*^{Spd} embryos were dissected off and placed in DNA extraction buffer (100 mM Tris-HCl, pH 7.5; 1mM EDTA; 250mM NaCl; 0.2% SDS; 100 µg/mL Proteinase K) overnight, shaking, at 37°C. DNA was purified using chloroform-phenol purification, precipitated with ice-cold absolute EtOH, and resuspended in 10 mM Tris-EDTA. Genotype was confirmed by PCR amplification of the wildtype and mutant *Spd* alleles, using primers designed after Keller-Peck and Mullen (1997) (Table 2.1). Wildtype and mutant alleles are differentiated based on amplicon size (210 and 230 bp for the wildtype and mutant alleles, respectively), which could be distinguished by separating PCR products on a 2% agarose gel.

Table 2.1. Sequences of primers used for *Pax3*^{Spd} genotyping.

Primer	Sequence (5'-3')
Forward (wildtype)	AGGGCCGAGTCAACCAGCAC
Forward (mutant)	AGTGTCCACCCCTCTTGGCCTCGGCCGAGTCAACCAGGTC
Reverse	CACGCGAAGCTGGCGAGAAATG

2.1.3. Preparation of cryo samples and sections

Limbs from storage in absolute MeOH at -20°C were rehydrated in a reverse order series of MeOH washes and either prepared for cryo or wax sectioning. Cryo samples were prepared by equilibrating limbs in 30% sucrose in PBS (2 x 60 min), rapidly freezing them over a dry ice-ethanol slurry, and storing at -80°C until use. Samples were mounted on a chuck with Tissue-Tek OCT Compound (VWR, Radnor PA), and sections were generated using a freezing microtome (cryostat) (Leica CM1850). Sections (5-10µm) were collected on SuperFrost Plus slides (VWR, Radnor PA) which

were stored at -20°C. For staining, cryosections were equilibrated to room temperature for at least 20 min, then rehydrated with 2 x 10 min washes in PBST or TBST. PBST solution was made from PBS tablets (Invitrogen, Waltham MA) and added detergent; this solution contained 10 mM Na_3PO_4, 2.68 mM KCl, 140 mM NaCl and 0.1% Tween-20 detergent. TBST solution contained 137 mM NaCl, 2.68 mM KCl, 16.5 mM Tris HCl and 0.1% Tween-20 detergent.

2.1.4. Preparation of paraffin samples and sections

Wax samples were prepared by dehydrating limbs into absolute ethanol (EtOH) (2 x 15 min in 50% EtOH/PBS, 30 min in 70% EtOH/PBS, 1 hour (hr) in 90% EtOH/H_2O, and 2 x 1 hr in absolute EtOH), clearing overnight with Histo-Clear II (National Diagnostics), infiltrating with paraffin wax (1 hr in 50% Histo-Clear/wax, 2 x 1 hr in wax at 60°C), and finally embedding in paraffin wax, taking care to precisely orient the limb or construct for sectioning. Dehydration and embedding of agarose constructs (Section 6.2.2) was performed similarly, with reduced wash lengths (e.g. 2 x 5 min in alcohol washes and 2 x 30 min washes in wax). Sections (8-10 μm) were generated using a microtome, collected on SuperFrost Plus slides (VWR, Radnor PA) and stored at room temperature until use. For staining, wax sections were de-waxed by treating with Histo-Clear II (2 x 5 min), and rehydrated via a graded EtOH series (2 x 5 min in absolute EtOH, 2 x 5 min in 90% EtOH/H_2O, 5 min in 70% EtOH/PBS, 5 min in 50% EtOH/PBS, and 2 x 5 min in PBS or TBS).

2.2. Histological Staining

2.2.1. Safranin-O

Paraffin sections were dewaxed and rehydrated (Section 2.1.4). Nuclei were stained with Weigerts iron haematoxylin solution in 95% EtOH (1 min), and rinsed with running tap water. Slides were stained with Fast Green solution (0.001% in H_2O) for 5 min, rinsed quickly with 1% acetic acid, and counterstained with Safranin-O (0.1% in H_2O) for 5 min. Slides were dehydrated through the same EtOH series as above, to absolute EtOH, and washed in Histo-Clear for 5 min before mounting in DPX mounting medium (Sigma-Aldrich, St. Louis MO).

2.2.2. Mallory's Trichrome

Paraffin sections were dewaxed and rehydrated as above. Following rehydration, sections were stained in Weigerts iron haematoxylin solution in 95% EtOH (2 min), stained in acid fuchsin (0.1% in H_2O, 5 min), rinsed in running tap water, stained in phosphotungstic acid (1% in H_2O, 10 min), rinsed, stained in Aniline Blue (0.5% Aniline Blue, 2% Orange G, and 2% oxalic acid in H_2O, 30 seconds). Slides were rapidly dehydrated through the same EtOH series (<30 seconds per wash) and Histo-Clear, and mounted with DPX mounting medium.

2.2.3. Alcian Blue

Alcian Blue staining of fixed micromasses was done in 1% Alcian Blue 8X (Sigma-Aldrich, St. Louis MO) in HCl for 30 min. Excess stain was removed with three rinses of PBS, and micromasses were imaged in PBS or mounted with Aqua-Poly/Mount.

2.2.4. Alizarin Red

Paraffin sections were dewaxed and rehydrated as above. Alizarin Red (0.1 %, Sigma-Aldrich A5533 in ddH_2O; St. Louis MO) was applied for 5 min at room temperature. Slides were rinsed, dehydrated, and mounted in DPX mounting medium (Sigma-Aldrich, St. Louis MO).

2.3. *In situ* hybridisation

2.3.1. Generation of RNA probes

RNA probes were produced using linearised DNA templates which were generated by restriction enzyme fragmentation of either cDNA clones belonging to a mouse expressed sequence tag (EST) library (IMAGE, Source Biosciences) or of custom-designed clones obtained from other sources (details in Table 2.2). Templates were amplified using transformed *E. coli* bacteria: bacterial inoculates were streaked on Luria-Bertani[1] (LB) agar plates (Sigma-Aldrich 2897, St. Louis MO) with 100µg/mL

[1] LB is widely taken to represent the names of its developers, Salvador Luria and Guiseppe Bertani. It is interesting, however, that Bertani himself stated: "The acronym has been variously interpreted, perhaps flatteringly, but incorrectly, as Luria broth, Lennox broth, or Luria-Bertani medium. For the historical record, the abbreviation LB was intended to stand for 'lysogeny broth'". Bertani, G., Lysogeny at Mid-Twentieth Century: P1, P2, and Other Experimental Systems. Journal of Bacteriology, 2004. 186(3): p. 595-600.

ampicillin (Sigma-Aldrich, St. Louis MO) and plates were incubated overnight at 37°C. Single colonies were selected and incubated in small cultures of 3 mL LB broth (Sigma-Aldrich 3022, St. Louis MO) with ampicillin for 6-8 hr, shaking, at 37°C. Large cultures using 0.5 mL of small culture added to 100 mL of LB broth with ampicillin were incubated overnight (no more than 16 hr), shaking, at 37°C. Plasmids were purified from bacteria with a PureYield plasmid midi prep kit (Promega).

Antisense digoxigenin-labelled RNA probes were generated by *in vitro* transcription using 1 μg of linearised template DNA with adjacent promoter sites for T7, T3, or SP6 RNA polymerases. Reactions included 20 mM dithiothreitol (DTT), 1X transcription buffer (Roche, Germany), 0.5 mM DIG-labelled nucleotides (Roche, Germany), 40 U Protector RNase inhibitor (Roche, Germany), and 20 U T7, T3, or SP6 polymerase (Roche, Germany). A small amount of the reaction was run on a 1% agarose gel to visualise the probe and verify transcription. The template was digested with DNase for 15 min at 37°C. Probes were purified in 50 μl of nuclease-free H_2O with Illustra MicroSpin G-25 columns (GE/Amersham Biosciences, Chicago IL), quantified with a Nanodrop ND-1000 or a Qubit 2.0 Fluorometer (Thermo Fisher, Waltham MA), and stored at -20°C.

2.3.2. *In situ* hybridisation on wholemount specimens (WISH) and vibratome sections

The same hybridisation protocol was used to detect gene expression in vibratome (vibrating microtome) sections and in wholemount specimens. Vibratome sections were generated by rehydrating embryos as detailed above, dissecting limbs off the main body trunk, and embedding the limbs in 4% low melting point agarose (Invitrogen, Waltham MA) in PBS. The agarose was trimmed with a razor blade so that blocks contained a single limb, which were then mounted on a vibratome chuck with superglue. A vibratome (Leica VT1000 S) was used to cut thick (60 μm) sections which were picked up with a paintbrush and floated in diethylpyrocarbonate (DEPC)-treated PBS in a 12-well dish. For wholemount *in situ*, whole embryos were rehydrated from storage into DEPC PBS and any remaining extra-embryonic membranes were dissected off. The hindbrain, eyes, and other cavities were pierced with a sterile needle to prevent reagent trapping during processing.

Whole embryos or vibratome sections were treated with Proteinase K (10 µg/mL in DEPC PBS). Treatment length was 5 min for vibratome sections, and variable for whole embryos depending on age (9 min for E10.5, 20 min for E11.5, 25 min for E12.5, 30 min for E13.5). Embryos or sections were washed (all washes were 3 x 5 min in DEPC PBS), post-fixed for 20 min in ice-cold 4% PFA, and washed again. Prehybridisation was done by a 5 min wash and then an overnight incubation in hybridisation buffer (50% deionised formamide, 5X SSC, 2% blocking powder (Boehringer 1096176), 0.1% TritonX-100, 0.5% CHAPS, 100 µg/ml yeast RNA, 5 mM EDTA, and 50 µg/mL heparin) at 55°C. The following day, hybridisation buffer (Hyb) was removed and embryos or sections were incubated with 0.5-1 µg/mL RNA probes diluted in Hyb, overnight at 55-60°C. Concentrated probe in Hyb had been denatured at 80°C for 3min immediately previously. RNA probes used in this study are detailed in Table 2.2.

Table 2.2. Details of RNA probes used for in situ hybridisation. Correspondence between probe and mRNA nucelotide sequences are indicated (reference sequence numbers as according to Nucleotide database, National Institutes of Health, Bethesda, MD).

Gene Symbol	Extent of insert on reference sequence	Source
Ankrd1	Nucleotides 12-1765 on NM_013468.3	I.M.A.G.E EST Library
Birc5	Nucleotides 1424-3416 on NM_001012273.1	I.M.A.G.E EST Library
BOC	Nucleotides 53-4418 on NM_172506.2	I.M.A.G.E EST Library
Col2aI	Nucleotides 4,678-5,083 on NM_031163.3	Cliff Tabin, Cambridge, USA
Col2aI	Nucleotides 68-5,149 on NM_03163.3	I.M.A.G.E EST Library
chick Col2aI	Nucleotides 3887-4689 on NM_204426.1	BBSRC Chick EST Library
Col26aI (Emid2)	Nucleotides 1,069-2,705 on NM_024474.2	I.M.A.G.E EST Library
CTGF	Nucleotides 80-2418 on NM_010217.2	I.M.A.G.E EST Library
Cyr61	Nucleotides 15-2028 on NM_010516.2	I.M.A.G.E EST Library
Dkk2	Nucleotides on NM_020265.4	Christof Niehrs, Mainz, Germany
Dkk3	Nucleotides 102-3354 on NM_015814.2	I.M.A.G.E EST Library
Fat4	Nucleotides 13,940-14,924 on NM_183221.3	Dr. Helen McNeill
Fzd1	Nucleotides 2774-3663 on NM021457.2	Gareth Brady and Kristen Summerhurst, TCD
Fzd2	Nucleotides 3289-3628 on NM_020510.2	I.M.A.G.E EST Library
Fzd3	Nucleotides 1-1321 on NM_021458.1	Ugo Borelo/Giulio Cossu
Fzd4	Nucleotides 832-1834 on NM_008055.3	Ugo Borelo/Giulio Cossu
Fzd5	Nucleotides 1513-1742 on NM_022721.3	Ugo Borelo/Giulio Cossu
Fzd6	Nucleotides 1794-2642 on NM_008056.2	Ugo Borelo/Giulio Cossu
Fzd7	Nucleotides 468-1290 on NM_008057.3	Ugo Borelo/Giulio Cossu
Fzd8	Nucleotides 968-1965 on NM_008058.1	Ugo Borelo/Giulio Cossu
Fzd9	Nucleotides 823-1323 on XM_284144.5	Ugo Borelo/Giulio Cossu
Fzd10	Nucleotides 1829-2988 on NM_175284.3	I.M.A.G.E EST Library

Gene Symbol	Extent of insert on reference sequence	Source
Gata2	Nucleotides 322-1043 on NM_008090.5	Jeannette Nardelli, Paris, France
Gata3	Nucleotides 388-2440 on NM_008091.3	Jeannette Nardelli, Paris, France
Grem1	Nucleotides 31-1594 on NM_011824.4	I.M.A.G.E EST Library
Lrp5	Nucleotides 19-5169 on NM_008513.3	I.M.A.G.E EST Library
Kremen1	Nucleotides 86-1507 on NM_032396.3	Christof Niehrs, Mainz, Germany
Kremen2	Nucleotides 165-1555 on NM_028416.2	Christof Niehrs, Mainz, Germany
Rspo2	Nucleotides 652-903 on NM_172815.3	Thomas Theil, Edinburgh, UK
Rspo3	Nucleotides 395-1850 on NM_028351.3	Thomas Theil, Edinburgh, UK
Sfrp2	Nucleotide 82 to 852 on U88567.1	Amir Rattner, MD, USA
Sfrp3 (Frzb1)	Nucleotides2059-2522 on NM_011356.4	Patrick Frankel, TCD
Sostdc1	Nucleotides 81-1038 on NM_025312.3	I.M.A.G.E EST Library
Smurf1	Nucleotides 1-2708 on NM_001038627.1	I.M.A.G.E EST Library
Tead1	Nucleotides 712-2133 on NM_001166585.1	IMAGE Mouse EST bank
Tead2	Nucleotides 707-1452 on NM_001285498.1	PCR amplification
Tead3	Nucleotides 884-1596 on NM_001098226.3	PCR amplification
Tead4	Nucleotides 1928-2448 on NM_011567.2	PCR amplification
Tppp3	Nucleotides 56-2550 on NM_02648.3	I.M.A.G.E EST Library
Wnt2	Nucleotides 35-1510 on NM_023653.4	Andy McMahon, NJ, USA
Wnt2b	Nucleotides 1010-1215 on NM_009520.3	Lise Zakin
Wnt4	Nucleotides 639-1101 on NM_009523.1	Andy McMahon, NJ, USA
Wnt5a	Nucleotides 576-2714 on NM_009524.2	Andy McMahon, NJ, USA
Wnt5b	Nucleotides 111-1429 on NM_009525.2	Andy McMahon, NJ, USA
Wnt9a	Nucleotides 1698-2247 on NM_139298.2	John Kealy, Karen Roddy, TCD
Wnt11	Nucleotides 169-1821 on NM_009519.1	Andy McMahon, NJ, USA
Wnt16	Nucleotide 537 to 1531 on NM_053116.3	RT-PCR generated (Summerhurst et al., 2008)

Post-hybridisation washes were applied to remove unbound, non-specific probe. Embryos or sections underwent a series of washes of increasing stringency, composed of Post-hybridisation solution (PH) (50% formamide, 5X SSC, 0.5% CHAPS), Wash Solution 1 (W1) (2X SSC, 0.1% CHAPS), and Wash Solution 2 (W2) (0.2X SSC, 0.1% CHAPS). Washes were applied as follows, all at 65°C, and all for 30 min (except the first wash, which was 5 min): 100% PH, 75% PH/25% W1, 50% PH/50% W1, 25% PH/75% W1, W1 (twice), W2 (twice). Embryos or sections were then washed in TNT (100 mM Tris-HCl pH 7.5, 150 mM NaCl, and 0.1% Triton X-100), 2 x 10 min at room temperature, and blocked in maleic acid blocking buffer (MABB) (100 mM malic acid, 150 mM NaCl, 3% blocking powder, pH 7.5) for 1-2 hr at room temperature. Antibody

(anti-Digoxigenin-AP, Fab fragments (Roche 11 093 274 910, Germany), 1:3000 in MABB), was applied overnight at 4°C, rocking.

Post-antibody washes were done as follows: 2 x 5 min and 4 x 1 hr in TNT at room temperature, rocking, then overnight in TNT at 4°C. Embryos or sections were then equilibrated to pH 9.5 with 3 x 15 min washes in NMT (100 mM Tris-HCl pH 9.5, 50 mM $MgCl_2$, 100 mM NaCl). Embryos or sections were stained with a solution of NBT (nitro-blue tetrazolium chloride) and BCIP (5-bromo-4-chloro-3'-indolyphosphate) at a final concentration of 0.525 mg/mL each in NMT. Tissue was carefully monitored for colour development, and stain changed as necessary for up to several days. Once staining was deemed to be optimal, embryos or sections were rinsed in PBS and fixed in 4% PFA for 1 hr-overnight. Whole embryos were imaged and embedded for OPT scanning (as detailed below). Vibratome sections were carefully transferred to glass slides and mounted with Aqua-Poly/Mount (VWR, Radnor PA).

2.3.3. *In situ* hybridisation on cryosections

In situ hybridisation was conducted on thin (10 µm) cryosections, prepared as described in Section 2.1.4. Stored slides were equilibrated to room temperature for at least 20 min and rehydrated in DEPC PBS (2 x 10 min) in a humidified chamber. Slides were pre-fixed with ice-cold 4% PFA for 15 min, washed (all washes were 3 x 5 min DEPC PBS), permeabilised with Proteinase K (10 µg/mL in DEPC PBS for 10 min), washed, post-fixed with ice-cold 4% PFA for 10 min, and washed again. To de-charge the slides and encourage RNA hybridisation, slides were treated with 26.4 mM acetic anhydride in 0.1 M triethanolamine (TEA) for 10 min, and washed again. Slides were air-dried for 10-30 min and treated with RNA probes diluted in hybridisation buffer as described in Section 2.3.2. Hybridisation was carried out overnight, at 55-60°C, in a humidified chamber.

The next day, unbound probe was washed off through a series of sodium citrate buffer (SSC) (Sigma-Aldrich, St. Louis MO) and deionized formamide (Sigma-Aldrich, St. Louis MO) washes of increasing stringency. Slides were taken through the following washes: 50% 5X SSC/50% formamide (10 min at 65°C), 50% 2X SSC/50% formamide (2 x 30 min at 65°C), 2X SSC (3 x 10 min at 65°C), 0.2X SSC (3 x 10 min at room temperature), and TNT (2 x 10 min at room temperature). Slides were blocked in MABB solution for 1 hr at room temperature in a humidified chamber, and incubated

with 1:3000 anti-Digoxigenin-AP, Fab fragments (Roche 11 093 274 910, Germany) in MABB block at 4°C, overnight.

The following day, antibody was recovered and slides were washed in TBST (3 x 10 min), then equilibrated to pH 9.5 with NMT solution (as above, 3 x 5 min). Slides were developed using the NBT/BCIP staining solution in NMT (as above), and monitored for colour development. When colour was deemed to be sufficient, slides were rinsed in PBS, then H_2O, and mounted with Aqua-Poly/Mount.

2.3.4. OPT sample preparation, scanning, and reconstruction

Once stained, whole embryos were fixed in 4% paraformaldehyde in PBS overnight at 4°C and embedded in 1-1.5% (w/v) low melting point agarose in H_2O. Embedded specimens in agarose were trimmed to the correct orientation and mounted on metal chucks with superglue in the correct orientation for scanning (long axis vertical). Mounted specimens were then dehydrated in absolute MeOH and cleared in 1:2 benzyl-alcohol:benzyl-benzoate for at least 6 hr. OPT scanning was performed on a custom built OPT Scanner (prototype; built at the MRC Human Genetics Unit, Edinburgh (Sharpe et al., 2002)), using a QImaging Retiga Exi camera and a Leica MZ FLIII microscope. Scans were captured using visible light from a 20 W halogen lamp with a 700 nm longpass filter, and using UV light with a GFP1 filter (425/60 nm excitation, 480 nm emission). Visible light scans generated images of the WISH staining patterns, while UV scans were used to capture tissue autofluorescence in order to show morphology of the entire specimen. Each scan was collected as a series of 400 raw projected images which were loaded onto a Linux workstation and reconstructed using Edinburgh Mouse Atlas Project (EMAP)-designed programmes. Reconstructions were visualised with EMAP-designed software, MA3DView and MAPaint (Baldock et al., 2001, Sarma et al., 2005), which were used to generate volume-renders of gene expression patterns. Volume renders or virtual sections were the exported as .jpeg or .tif images.

2.4. Immunostaining

Wax or cryo sections were prepared from storage and rehydrated as described above. At this stage, antigen retrieval was performed for YAP and cilia immunolabelling. Heat-mediated antigen retrieval was performed for both colourimetric and fluorescent YAP immunolabelling, by immersing slides in boiling 0.01 M sodium citrate (pH 6), and incubating at 90°C for 20 min. Sections were then cooled to room temperature, washed (2 x 15 min) in TBST, and proceeded to blocking. Enzyme-mediated antigen retrieval was performed for cilia immunolabelling by incubating slides with 20 µg/mL Proteinase K in 0.1M Tris-HCl for 10 min at 37°C. Sections were then washed twice with TBST and continued to the blocking step. All sections were blocked in 5% goat serum in TBST for 1-2 hr at room temperature. Primary antibody was then applied at the appropriate dilution in blocking solution (Table 2.3) and slides were incubated in a humid chamber overnight at 4°C. The following day, slides were washed 3 x 15 min in TBST, incubated in the appropriate secondary antibody (Table 2.3) diluted in blocking solution for 2 hr at room temperature and washed 3 x 15 min in TBST. Fluorescent samples were then mounted with ProLong Gold Antifade Reagent with DAPI (Life Technologies) or counterstained (2-5 min in DAPI (Santa Cruz, 1.5 µg/ml) in H2O) and mounted in Mowiol mounting medium (10% Mowiol 4-88 (Millipore) with 2.5% DABCO (Sigma-Aldrich, St. Louis MO), in 25% glycerol and 0.1 M Tris-HCl (pH 8.0)). For colourimetric samples, slides were equilibrated to pH 9.5 in NMT buffer (0.1 M Tris pH 9.5, 0.05 M MgCl2, 0.1% Tween), then developed with NBT/BCIP diluted in NMT, as for *in situ* hybridisation.

Table 2.3. List of antibodies used in this work.

	Antibody	Supplier and product number	Species and clonal characteristics	Dilution used	Secondary antibody used
	Primary antibodies				
	anti-GFP	Invitrogen A11122	Mouse monoclonal	1:200	6
	anti-YAP (63.7)	Santa Cruz sc-101199	Mouse monoclonal	1:100	1, 2, 3, 7
	anti-phospho-YAP (Ser127)	Cell Signalling #4911	Rabbit polyclonal	1:200	6, 7
	anti-phospho-SMAD1/5/8	Cell Signaling, 9511	Rabbit polyclonal	1:200	6, 7
	anti-β-catenin	BD Transduction Laboratories C19220-050	Mouse monoclonal	1:200	1, 2
	anti-noggin	R&D Systems AF719	Goat polyclonal	1:200	8
	anti-acetylated-α tubulin	Sigma T7451	Mouse monoclonal	1:200	1
	anti-γ-tubulin	Sigma T5192	Rabbit polyclonal	1:200	6
	anti-FLAG	Sigma F4042	Mouse monoclonal	1:200	1
	anti-HA.11	BioLegend MMS-101p	Mouse monoclonal	1:200	1, 2
	Secondary antibodies				
1	anti-mouse AlexaFluor 568	Invitrogen A11031	Goat	1:200	
2	anti-mouse Alkaline Phosphatase	Santa Cruz sc-2008	Goat	1:300	
3	biotinylated anti-mouse	Santa Cruz sc-2039	Goat	1:250	
4	AlexaFluor 568 conjugated tyramide	Invitrogen T20934	-		
5	streptavidin-conjugated horseradish peroxidase	Invitrogen T20934	-	1:800	
6	anti-rabbit AlexaFluor 488	Invitrogen A21206	Donkey	1:250	
7	anti-rabbit Alkaline Phosphatase	Invitrogen G21079	Goat	1:300	
8	anti-goat horseradish peroxidase	Vector Labs, PI-9500	Donkey	1:100	

For fluorescent detection of YAP, customary treatment with a fluorescently-labelled secondary antibody was not sufficient to detect a clear fluorescent signal. To resolve this, tyramide signal amplification was used (van Gijlswijk et al., 1997, Faget and Hnasko, 2015). Although this resulted in signal detection in some areas of the rudiment, it was not sensitive enough to detect a signal in areas of presumably lower protein expression. To further amplify the signal, an additional amplification step using

a biotinylated secondary antibody was added. These methods are summarised in Fig. 2.1; details of specific antibodies are given in Table 2.3. Following treatment with primary antibody and washes, endogenous peroxidases were blocked by treating slides with 3% H_2O_2 in MeOH for 30 min, followed by washes in TBST. Subsequently, a biotinylated anti-mouse secondary antibody (Santa Cruz sc-2039) was applied for 2 hr at room temperature. Subsequent tyramide amplification was performed using a Tyramide Signal Amplification (TSA) kit (Invitrogen T20934, Waltham MA). Following secondary antibody incubation and washes, slides were incubated with streptavidin-HRP (1:400 in blocking solution) for 1 hr, then washed. Slides were then treated with a tyramide substrate labelled with AlexaFluor 568 (1:100 in kit-supplied amplification buffer, with 0.0015% H_2O_2) for 10 min and washed. DAPI staining and mounting was performed as described above.

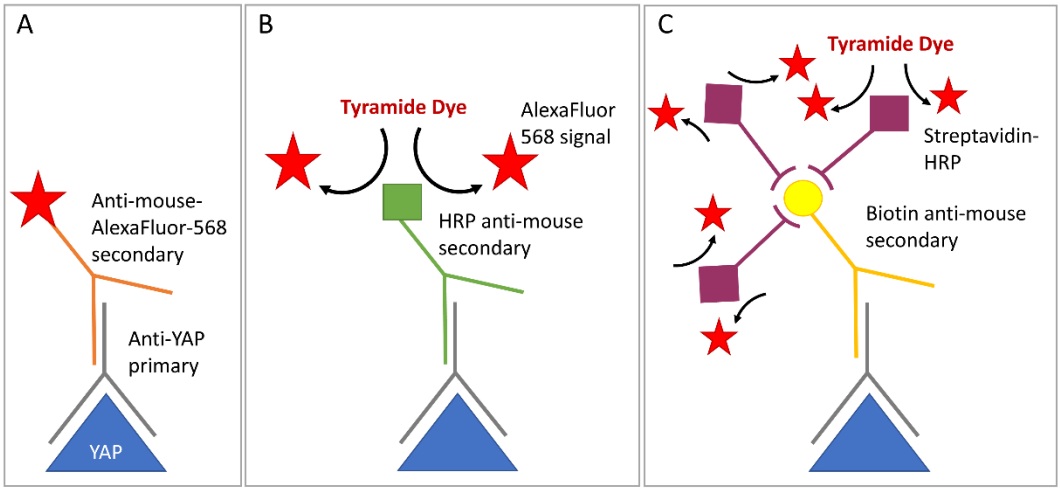

Fig. 2.1. Schematic of fluorescent labelling methods used. Customary fluorescent immunolabelling involves treatment with a primary antibody recognising a protein of interest (in this case, YAP), followed by a secondary antibody raised against the species used to produce the primary antibody which is labelled with a fluorescent marker (e.g. an anti-mouse AlexaFluor 568 if it is a monoclonal antibody) (A). Tyramide amplification increases the sensitivity of the fluorescent detection by using an enzyme-conjugated secondary antibody (here, an anti-mouse antibody conjugated to horseradish peroxidase (HRP)) which results in conversion of the tyramide dye to an activated, form with an AlexaFluor 568 fluorophore (B). For greater sensitivity, an additional amplification step was performed by using a biotinylated secondary antibody, followed by a streptavidin-conjugated HRP which allows for greater levels of the fluorescent substrate, due to multiple streptavidin binding sites per biotin molecule (C). Adapted from TSA kit product manual (Thermo Fisher, Waltham MA; https://tools.Thermo Fisher.com/ content/sfs/manuals/mp20911.pdf).

2.5. Image collection

Colourimetric (antibody staining and *in situ* hybridisation) and fluorescent images were collected using an Olympus DP72 camera and CellSens software (v1.6). Low-magnification whole embryo and cell culture images were taken on an Olympus SZX12 dissecting microscope with either a QImaging camera and IP Lab software or an Olympus camera and CellSens software as above. Confocal images were taken using a Leica TCS SP8 scanning confocal microscope (Leica-Microsystems, Germany) with Leica Application Suite software (LAS v5.1). Images were analysed using ImageJ software (version 1.8.0, National Institutes of Health, Bethesda, MD).

2.6. Quantitative Real Time RT-PCR

2.6.1. RNA purification and cDNA synthesis

For gene expression analysis of the TS23 forelimb skeleton, micro-dissected humeri and associated joints had previously been mechanically homogenised and total RNA extracted using an SV Total RNA Isolation System (Promega). For RNA extraction from micromass cultures (Section 2.8.1), cells were harvested by removing culture medium, rinsing with PBS, and incubating each well with 100 µl of TRIzol reagent for 2 min. The liquid was then taken up with a P100 pipette tip and the well bottom rinsed and scraped several times to fully detach cells. Several wells (2-4 per sample) were pooled together to ensure sufficient RNA quantity, and samples were stored at -80°C until further processing. For RNA extraction from cells in agarose constructs (Section 6.2.2), whole or half constructs were finely chopped with a razor blade and stored in TRIzol reagent at -80°C.

Frozen, stored samples were thawed from -80°C and incubated for 5 min at room temperature. RNA was separated into an aqueous phase by the addition of chloroform. RNA was then precipitated with an equal volume of 70% RNase-free EtOH, and purified with a PureLink RNA Mini kit (Invitrogen 12183018A) or a GenElute Mammalian Total RNA Miniprep Kit (Sigma-Aldrich RTN70, St. Louis MO). Purified RNA was eluted in 30 µl of RNase-free water and quantified using a Qubit 2.0 fluorometer with the Qubit RNA High Sensitivity kit (Q32852). Synthesis of cDNA was carried out using a High-Capacity cDNA Reverse Transcription kit (Thermo

Fisher, Waltham MA), according to manufacturer's instructions, using 100 ng of RNA per 20 µl reaction.

2.6.2. Quantitative real time RT-PCR

Detection of chondrogenic genes and other markers was conducted using SYBR Green master mix (Invitrogen, Waltham MA), and custom- or pre-designed primers (Sigma-Aldrich, St. Louis MO) (Table 2.4). Reactions were set up in 96-well plates (Invitrogen, Waltham MA), with genes assessed for each sample in triplicate. Each well was set up with 1 µl of cDNA, 10 µl SYBR Green Master Mix (2x), 1 µl each of 10 mM forward and reverse primers, and 7 ul of dH2O. For qRT-PCR of bioreactor samples, porcine TaqMan primers (Table 2.4) and Universal Master Mix II (Applied Biosystems) were used instead of SybrGreen.

Table 2.4. Details of primers used in qRT-PCR.

MOUSE			
Gene	**RefSeq**	**Dye**	**Primer Sequence**
GAPDH	NM_008084	SYBR	Fwd: TGGCCTCCAAGGAGTAAGAAAC Rev: GGGATAGGGCCTCTCTTGCT
YAP related genes			
Ankrd1	NM_013468.3	SYBR	Fwd: GTCTGCGATGAGTATAAACG Rev: CTGTGGATTCAAGCATATCTC
Birc5	NM_001012273.1	SYBR	Fwd: TAGAGGAGCATAGAAAGCAC Rev: CTCTTTTTGCTTGTTGTTGG
Ctgf	NM_010217.2	SYBR	Fwd: GAGGAAAACATTAAGAAGGGC Rev: AGAAAGCTCAAACTTGACAG
Cyr61	NM_010516.2	SYBR	Fwd: AGAGGCTTCCTGTCTTTG Rev: GTTGTCATTGGTAACTCGTG
YAP	NM_001171147.1	SYBR	Fwd: GATGTCTCAGGAATTGAGAAC Rev: CTGTATCCATTTCATCCACAC
Chondrogenesis Marker Genes			
Col2aI	NM_01163.3	SYBR	Fwd: AAGTCACTGAACAACCAGATTGAGA Rev: AAGTGCGAGCAGGGTTCTTG
Sox9	NM_011448.4	SYBR	Fwd: CGGCTCCAGCAAGAACAAG Rev: TGCGCCCACACCATGA
Ihh	NM_010544.2	SYBR	Fwd: CCACCTTCAGTGATGTGCTTATTT Rev: CAGAGGAGTAGAGGCCGTTTGA
Col10aI	NM_009925.4	SYBR	Fwd: TGCAATCATGGAGCTCACAGA Rev: CAGAGGAGTAGAGGCCGTTTGA
PORCINE			
Gene	**RefSeq**	**Dye**	**Assay ID**
GAPDH	NM_001206359.1	FAM	Ss03374854_g1
Acan	NM_001164652.1	FAM	Ss03373380_m1
Col2aI	AF201724.1	FAM	Ss03373344_g1
Col10aI	NM_001005153.1	FAM	Ss03391766_m1
Ihh	NM_001244470.1	FAM	Ss03373541_m1

Plates were run on an Applied Biosystems 7500 Real-Time PCR system. Following each qPCR run, triplicate wells were averaged and outliers were removed as appropriate. ΔCt values were calculated by normalising the cycle threshold values for each gene to the endogenous control gene, GAPDH. Gene expression was then calculated as the fold change relative to a reference sample (-2^ΔΔCt) . For gene expression in whole humeri, wildtype humeri samples were used as the reference sample. For signalling molecule-treated micromasses, the reference sample was unplated cells collected at the time of plating (called Day 0 (D0) cells). For Verteporfin treatment, the reference samples were DMSO-treated samples.

2.7. *Ex ovo* embryo culture and electroporation

2.7.1. Ex ovo chick embryo culture

Fertilised chick eggs were obtained from a commercial supplier (Enfield Broiler breeders Ltd, breed Ross 503) and incubated in a humidified incubator (Natureform Hatchery UT350N) at 37°C. Eggs were incubated for 72 hr (3 days) before embryos were transferred to an *ex ovo* culture set up, modelled after Schomann et al. (2013). Autoclaved glasses (IKEA GODIS, 800.921.09; 7.75 oz./23 cl. volume) were filled with 160 ml ddH_2O, and a layer of cling film was loosely placed on top, so that it was in contact with the underlying water. The cling film was then secured in place with an elastic band around the outer rim of the glass. Embryos and associated yolks and membranes were transferred *ex ovo* by cracking the bottom of the egg shell against the rim of the glass and swiftly pulling apart the halves of the egg shell to release the entire contents into the cling film support. Five mL of DMEM culture medium, 50 µl of 100X Antibiotic-Antimycotic (Gibco 15240096) were added directly to the embryo. A small amount of ground eggshell, which had been previously prepared by grinding EtOH-sterilised eggshells with a mortar and pestle, was also added to each culture, being careful not to touch the embryo directly. Either the lid or dish of a sterile 9 cm petri dish was placed on top of the glass to create a covered humidified environment for the embryo. The entire *ex ovo* set-up was then placed in the incubator until electroporation on day 5 of culture.

2.7.2. Limb bud electroporation

Chick forelimb buds were electroporated at day 5 of embryo culture. With the embryo remaining in the *ex ovo* set-up as described above, the embryonic membranes were carefully dissected away to allow access to the forelimb bud. Throughout the experimental procedure, embryos were kept from drying out by the addition of small volumes of sterile PBS. Experimental forelimb buds were micro-injected with a mixture of fast-green dye (0.5 µl of a 0.05% solution), a GFP-encoding construct (1 µl of a 1 µg/µl solution) (Fig. A.3), and a construct encoding either a β-catenin-Tcf fusion protein or a modified Frzb protein (1 µl of a 1 µg/µl solution) (Fig. A.4). Control (sham) forelimb buds were micro-injected with the same mixture of fast-green and the GFP-encoding construct, as well as 1 µl of PBS. Structure of the proteins encoded by the experimental constructs are given in Fig. 2.2; details of all three constructs are given in Fig. A.4 and Fig. A.3. All constructs were generated using cultures of transformed bacteria, as described in Section 2.3.1, and plasmids were purified using a Qiagen plasmid extraction kit. The final concentration of purified plasmids was at least 1 µg/µl. Microinjection was done using a mouth-pipette coupled with a sterile, pulled capillary. The capillary was inserted in the presumptive region of the developing elbow joint, approximately in the centre of the limb bud, taking care not to completely pierce the limb bud. Use of fast-green dye allowed for visualisation of micro-injection into the limb bud; the location and amount of injected solution were noted. Immediately following microinjection, an electric current was delivered by electrodes which had been placed longitudinally on either side of the limb bud but not touching the tissue. Optimised electroporation parameters were six 60 ms pulses of 25 volts, at an interval of 100 ms.

After electroporation, DMEM culture medium, Antibiotic-Antimycotic, and ground eggshell were added in the proportions detailed above, the petri dish lid was replaced on top of the glass, and the *ex ovo* culture was replaced in the incubator. Embryos were incubated a further 24 hr after electroporation and harvested the next day (day 6) by dissection out of the membranes. Embryo viability (alive or dead; coloration and overall appearance of embryo and vasculature) was assessed. Hamburger and Hamilton stage for each embryo was noted at the time of electroporation, as well as at harvest. Electroporation efficiency was immediately assessed by visualising GFP in the electroporated limb, on a dissecting microscope with a GFP filter and fluorescent

illumination. Specimens were then fixed overnight in 4% PFA, washed, dehydrated, and stored in MeOH as described in Section 2.1.1.

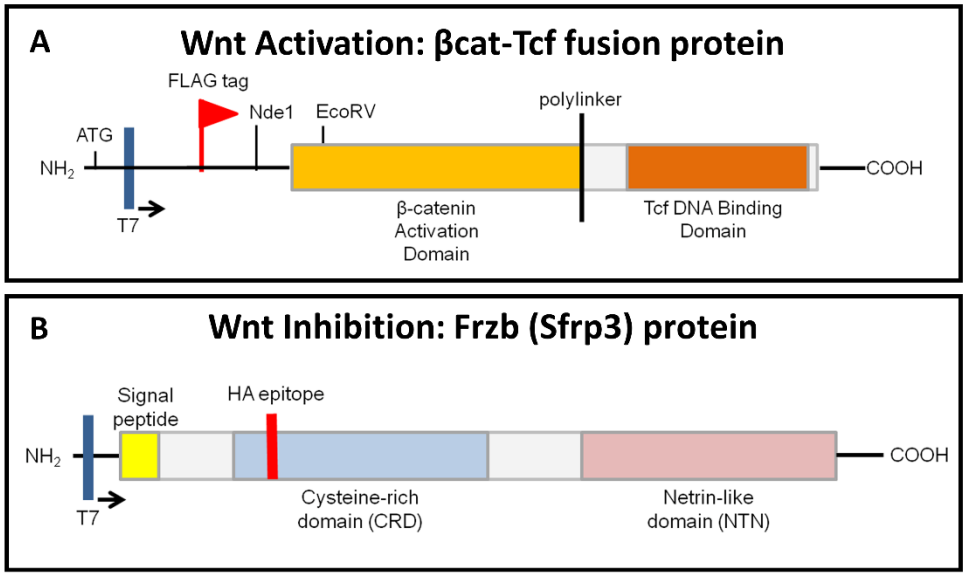

Fig. 2.2. Structure of proteins encoded by electroporated constructs. Constructs encoding a β-catenin-Tcf fusion protein to activate canonical Wnt signalling (A) or a Frzb (Sfrp3) protein to inhibit canonical Wnt signalling (B) were electroporated into chick forelimb buds. The β-catenin and Sfrp3 proteins contained FLAG and HA tag sequences, respectively, to enable protein detection. Adapted figures from Rebecca Rolfe (unpublished).

To assess construct uptake and expression, protein tags encoded in the experimental constructs were utilised. The β-catenin-Tcf fusion protein contains a FLAG tag sequence (Hopp et al., 1988), and the Frzb protein contains a haemagglutin (HA) HA epitope (Field et al., 1988) (Fig. 2.2). Both FLAG and HA proteins are detectable via antibody staining, as an indication of construct expression in tissue. Forelimb buds were cryo embedded and sectioned, as described in Section 2.1.3. Sections were stained with anti-FLAG or anti-HA.11 antibodies and corresponding fluorescent or colourimetric secondary antibodies (Section 2.4 and Table 2.3). Immunostaining revealed that detectable HA or FLAG protein co-localised with GFP expression, indicating that GFP is a reliable indicator of construct uptake and expression.

2.8. Micromass culture manipulation

2.8.1. Micromass Culture

Outbred CD1 embryos were harvested at E11.5 (c.f. Section 2.1.1) and immediately placed in sterile, warm (37°C) Base Medium (DMEM F12 (Sigma-Aldrich D8437, St. Louis MO) with Penicillin-Streptomycin (100 U/mL, Sigma P4333), and L-Glutamine (2 mM, Sigma-Aldrich G7513, St. Louis MO). Embryos were individually dissected out of the uterine horns in warm base medium under a sterile flow hood. Limb buds were dissected off by positioning a pair of forceps behind the attachment of the limb buds to the body trunk, and pinching off the limb buds (Fig. 2.3a). Forelimbs and hindlimbs were pooled together in Base Medium, and the liquid was aspirated off and replaced with 1-2 mL of 1x Trypsin-EDTA buffer (Sigma-Aldrich, St. Louis MO) (Fig. 2.3b). The limb buds in trypsin were incubated for 15 min at 37°C, before adding 1-2 mL of foetal bovine serum (FBS) (Sigma-Aldrich, St. Louis MO) to stop trypsin activity. A flame-polished glass pipette was used to create a single-cell suspension by triturating 15-18 times, before passing the cell suspension through a 70 µm cell strainer (Fig. 2.3c). Cells were pelleted at 1000 RPM (625 G) for 5 min, supernatant removed, resuspended in a small amount (typically 1 mL) of Growth Medium (Base Medium (as above) supplemented with 10% FBS and Ascorbic Acid (50 µg/mL, Sigma-Aldrich A8960, St. Louis MO) and counted on a haemocytometer. The volume was adjusted to yield a final cell density of 1-2 x 10^7 cells/mL. 10-30 µl of this suspension was stored in 200 µl TRIzol at -80°C for later qRT-PCR analysis, as described in Section 2.6. Cells were plated as 10 or 15 µl drops, either directly on tissue-culture grade treated plastic dishes (Thermo Fisher/Nunc 176740 or 142485), or on poly-ornithine treated glass coverslips (Fig. 2.3d). To prepare the coverslips, 50 µl of a 0.015 M solution of poly-D-ornithine (Sigma-Aldrich, St. Louis MO) was pipetted on top of a 10-mm glass coverslip (Invitrogen, Waltham MA), which was incubated for 30 min at room temperature, rinsed twice with sterile dH_2O, air-dried in a sterile flow hood, and used immediately or stored for up to 2 weeks at room temperature. After plating, micromass cultures were allowed to adhere for at least one hr in incubation conditions (37°C and 5% CO_2), then gently flooded with 400 µl of growth medium per well.

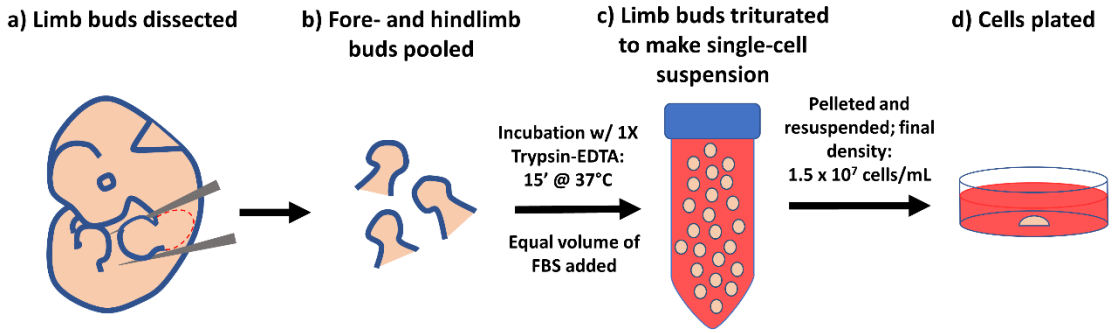

Fig. 2.3. Schematic of limb bud micromass culture method. Forceps (in grey) are placed behind and underneath the protruding limb bud and pinched to separate the entire limb bud (outlined by red dashed line) from the embryo (a). Limb buds are pooled together (b), processed to a single-cell suspension (c), and plated at high density (d).

2.8.1.1. Signalling molecule treatment

For comparison of signalling molecules, growth medium was supplemented to a final concentration of 100 ng/mL with human BMP-2 (R&D Systems 355-BM), human Noggin (R&D Systems 719-NG), 50 ng/mL mouse WNT-3A (R&D Systems 1324-WN), or 200 ng/mL human WNT-3A (R&D Systems 5036-WN) recombinant protein. Control groups were treated with un-supplemented growth medium. Medium was changed every other day, for the duration of the experiments, by removing half the well volume (200 µl) and replacing it with an equal volume of fresh medium. This was done to ensure the cells experienced a more consistent environment over the course of the experiment. Micromasses were harvested on days 2, 4, and 6 of culture.

2.8.1.2. Verteporfin treatment

For Verteporfin experiments, experimental cultures were treated for the entire culture period with Verteporfin (Sigma-Aldrich SML0534, St. Louis MO; 200 nM in DMSO) in growth medium, while control cultures were in growth medium supplemented with an equivalent volume of DMSO. A stock solution (2 mM) of verteporfin was prepared by solubilising the powder fully in DMSO, and passing through a 0.2 µm filter to remove insoluble powder. The stock solution of verteporfin was titrated to test a range of concentrations (2 mM – 50 nM) on micromasses. The optimal concentration of verteporfin for the micromass experiments was determined to be 200 nM: higher concentrations killed cells, while lower concentrations produced no visible effect on

nodule formation. Medium was fully changed every other day starting on day 2, and micromasses were harvested at Day 6 for Alcian Blue or qRT-PCR analysis.

2.8.1.3. Micromass Processing

For Alcian Blue staining, cells were harvested by removing the medium, rinsing with PBS, then fixing for 30 min at room temperature in cold 4% PFA. Cells were washed twice with PBS and stored in PBS at 4°C until staining, as described in Section 2.2.3. Images of stained micromasses were taken on a dissecting microscope (Olympus).

2.9. Methods described elsewhere

Immunolocalisation of cilia and image collection (Section 5.2.1)

Cilia Image processing (Section 5.2.2)

Quantification of cilia properties (Section 5.2.3)

Micromass image analysis (Section 6.2.1)

Mechanical stimulation of cell-seeded 3-D agarose constructs (Section 6.2.2)

Chapter 3

A spatial description of expression of Wnt and BMP signalling pathway components and disturbances in pathway activity under altered mechanical and molecular environments[1]

3.1 Introduction

Reduced movement during development in both chick and mouse results in skeletal malformation, where bones are thin and hypomineralised, and joints are reduced or fused. These gross abnormalities are accompanied by observed changes in the expression patterns of key patterning and marker genes including collagens (types 2aI and 10aI), and signalling ligands such as Indian hedgehog (*Ihh*), bone morphogenetic protein (BMP) 2, and fibroblast growth factor (FGF) 2 (Nowlan et al., 2008b, Roddy et al., 2011b). More recent work showed that the expression of thousands of genes is affected under reduced mechanical stimulation (Rolfe et al., 2014) but little is known about how these regulatory changes are realised, or the role of signalling networks in coordinating changes in gene expression in this environment. This is a major gap in

[1] Some work presented in this chapter was conducted in collaboration with Prof. Amitabha Bandyopadhyay and Dr. Pratik Singh at the Indian Institute of Technology, Kanpur, as well as in collaboration with Dr. Rebecca Rolfe. Part of the data is presented in: Singh PNP, **Shea CA**, Sonker SK, Rolfe RA, Ray A, Kumar S, Gupta PMurphy P, Bandyopadhyay A. Precise spatial restriction of BMP signaling in developing joints is perturbed upon loss of embryo movement. *Development*. 2018 Mar 12;145(5). pii: dev153460. doi: 10.1242/dev.153460

This work was partially supported by an EMBO Short-Term Fellowship.

our understanding of how mechanical stimulation from movement can be transduced to influence molecular mechanisms.

The Wnt and BMP signalling pathways have a demonstrated role in skeletogenesis (as reviewed in Section 1.3 and summarised below), and they were also noted to be impacted by reduced mechanical stimulation, suggesting that they may have a regulatory role in this context (Rolfe et al., 2014). To further understand the roles of Wnt and BMP pathways in mechanoregulation, examination of the expression and activity of specific pathway components in normal and immobilised contexts is required.

A number of the 19 Wnt ligand-encoding genes are known to be expressed during appendicular skeletal development at the stage of joint formation and long bone ossification (reviewed in Section 1.3). *Wnt4*, *Wnt9a*, and Wnt16 have been implicated in canonical Wnt/β-catenin signalling at the joint, while *Wnt5a* and *Wnt5b* are involved in chondrocyte maturation and differentiation within the long bones, and *Wnt11* has an unspecified role in prehypertrophic chondrocytes. A small number of the 10 Fzd receptor encoding genes have been detected during skeletal development, including Fzd1 and Fzd7 in the perichondrium and Fzd3 in the long bones (Hartmann and Tabin, 2000, Kato et al., 2015). The expression of all Wnt and Fzd genes was assessed up to TS19 (E11.5) (Summerhurst et al 2008) yet there is no comprehensive examination of Fzd receptor expression in the skeleton at later stages.

BMP signalling is active during skeletal development: several ligands are expressed in the cartilage rudiments, and are involved in cartilage differentiation from mesenchymal progenitors, as well as chondrocyte proliferation and maturation (Duprez et al., 1996, Minina et al., 2001). Different ligands either stimulate or inhibit chondrocyte hypertrophy, which has been demonstrated both *in vivo* and *in vitro* (Yoon and Lyons, 2004, Lorda-Diez et al., 2014). Several BMP ligands have also been detected at the joints, most notably the BMP-related ligand *Gdf5*. Despite the expression of ligands at some developing joints, the pathway effector pSMAD1/5/8 has been shown to be restricted at a distance away from the joint site, indicating a complex regulation of the pathway during bone and joint formation (Ray et al., 2015). Further, while expression of BMP2 and *Gdf5* have been shown to be mechanically influenced (Kahn et al., 2009, Roddy et al., 2011b), there is no study of other pathway components under reduced mechanical stimulation.

Wnt and BMP signalling activities are demonstrably important to limb skeletal development, although most studies have focused on the contributions of one or a few genes. However, there is no suitably comprehensive description of component genes of these pathways at the stage of limb development where the key events of joint morphogenesis and mineralisation are commencing. As both events require appropriate mechanical stimulation to progress normally (reviewed in Shea et al. (2015)), this highlighted a need for a thorough evaluation of gene expression patterns as well as an examination of the stabilisation and localisation of key protein effectors in each of these pathways.

To functionally test the role of Wnt signalling in skeletal tissue patterning, knockouts or mis-expression of Wnt ligands and other functional components have been used (Hartmann and Tabin, 2000, Hartmann and Tabin, 2001, Day et al., 2005). Alteration of Wnt signalling *in vivo* has previously been generalised (in the case of retroviral injection) or under the control of tissue-wide promoters (e.g. *Col2aI*) (Hartmann and Tabin, 2001, Yang et al., 2003, Guo et al., 2004). By contrast, e*x ovo* electroporation offers the potential to transiently activate or inhibit the Wnt pathway in a spatially localised manner without the need for tissue-specific transgenics. Targeted co-injection of GFP- and Wnt pathway-encoding constructs designed to alter pathway activity allows for direct identification of electroporated cells where the balance of Wnt signalling may have been shifted, in order to examine the effects on these and nearby cells and tissues.

Both mouse and chick have been used as immobilisation models, as described in detail in Section 1.4.2. Transgenic mice can be produced either lacking limb muscle (in the case of $Pax3^{Spd/Spd}$ and others) or with non-contractile muscle. Both fore- and hindlimb skeletons are affected by reduced movement in these transgenic mouse models, but the forelimbs are more severely affected, possibly due to greater passive movement that hindlimbs experience *in utero* (Nowlan et al., 2012). Neuromuscular blockers, such as decamethonium bromide, offer a means of inducing immobilisation in chick, where transgenic lines are difficult to establish. Again, as in mouse, different modes of paralysis (e.g., flaccid vs. rigid immobilisation) result in similar skeletal deformations (Osborne et al., 2002). Both fore- and hindlimb are affected in chick, but at the stages where the immobilisation phenotype becomes apparent, the hindlimb is greater in size and more easily accessible *in ovo* (Hamburger and Hamilton, 1951). Phenotypic

similarities between immobilisation models of mouse and chick (i.e. reduced mineralisation and fused joints) suggest that the observed phenotypic changes occurring as a result of immobilisation are the result of reduced mechanical stimulation itself, rather than non-specific genetic or environmental effects. This allows for confidence when comparing mouse forelimb to chick hindlimb, as was done in the work presented here.

Previously-published work from this group indicated that Wnt and BMP signalling components were differentially expressed under altered mechanical stimulation (Rolfe et al., 2014). Transcriptomic analyses (both RNAseq and microarray) were performed comparing *Splotch delayed* (*Pax3*$^{Spd/Spd}$) muscle-less to wildtype tissue, using dissected humeri and associated shoulder and elbow joints (Rolfe et al., 2014) (Fig. 3.1A). Theiler Stage (TS) 23 (E14.5) was chosen for the tissue harvest, as this stage marks the commencement of ossification at the midpoint of the humeral diaphysis, and emergence of shape and form in the shoulder and elbow joints; most importantly, it is also the stage where the muscle-less skeletal phenotype becomes apparent (Nowlan et al., 2010a, Nowlan et al., 2012). Gene Ontology (GO) analysis established that many differentially-regulated genes (more than 2-fold difference between mutant and wildtype, with significance <0.05), both up- and down-regulated were associated with cell-signalling. Genes that encode signalling components such as signalling molecules, receptors, and transcription factors were enriched in the differentially regulated gene set. This indicated that gene regulatory changes resulting from reduced mechanical stimulation could be implicated in altered cellular signalling.

Differentially regulated genes from these screens were therefore sorted by their association with major signalling pathways to determine which were the most affected in the muscle-less mutant. Wnt was the signalling pathway with the highest number of differentially-expressed component genes. The 34 differentially-regulated genes associated with the Wnt pathway encode pathway agonists, antagonists, ligands, receptors, and target genes. Although only five differentially expressed genes were associated with the BMP pathway, these related to multiple levels of the pathway and included a co-receptor, a ligand, and three target genes.

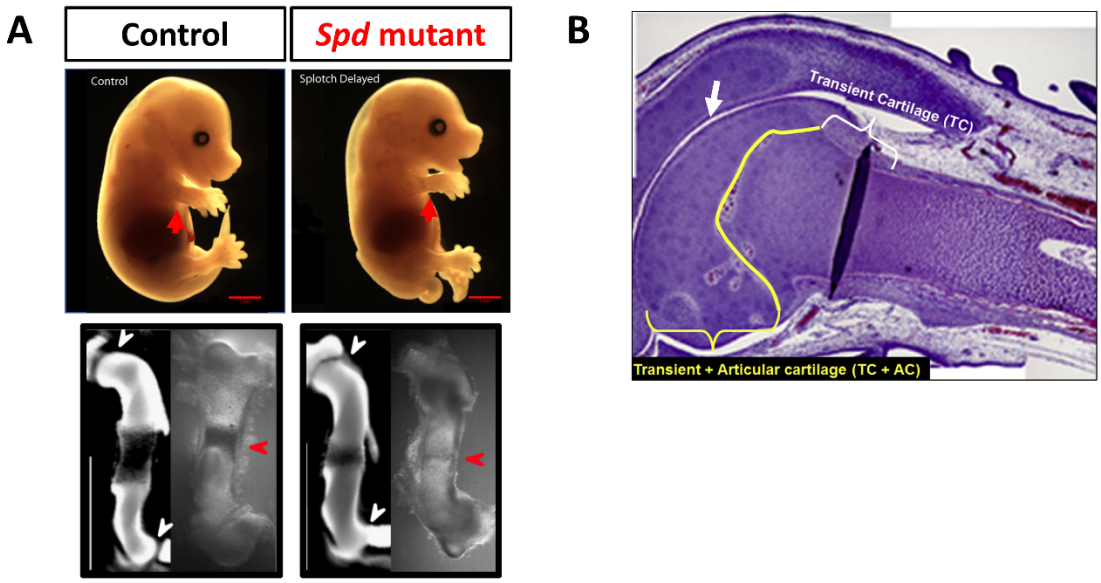

Fig. 3.1. Tissue sources of transcriptomic studies analysed here. Adapted from Rolfe et al. (2014) and Singh et al. (2016).

A) RNAseq and microarray transcriptomic analyses were previously performed on tissue from control and *Spd* homozygote mutant tissue at TS23 (E14.5) (Rolfe et al., 2014). Whole embryos show clear differences in the mutatnt, namely visibly thinner limbs (red arrows). Humeri were dissected, along with associated joints (shoulder and elbow), shown here. Clear fusion between elements is seen in the mutant humerus compared to the wildtype (white arrowheads), as is reduced mineralisation in the hypertrophic zone at the diaphysis midpoint (red arrowhead).

B) A microarray assay had also previously been performed on chick knee tissue (Singh et al., 2016). Chicks at HH38 and HH40 were dissected; a combination of transient and articular cartilage (TC + AC, yellow bracket) was compared to solely transient cartilage (TC, white bracket). Genes detected in TC + AC which were not detected in just TC were deemed enriched in AC.

The developing joint is of particular interest as it is profoundly affected under reduced mechanical stimulation. In the mutant *Pax3*$^{Spd/Spd}$ forelimb, the cartilage and synovial tissues at the shoulder and elbow joints fail to form, resulting in full or partial rudiment fusion (Nowlan et al., 2010a). Absence of chondrogenous layers and knee and elbow joint fusion is also described in immobilised chick (Roddy et al., 2011b). The mature synovial joint is comprised of two or more layers of articular cartilage separated by a fluid-filled cavity, encapsulated by a synovial membrane. Histological staining of *Spd* mutant specimens shows that, relative to wildtype tissue, the articular cartilage layers are reduced and the synovial cavity is reduced or absent. Despite the importance of articular cartilage to joint function, there are few genetic markers of articular cartilage.

Further, little is known about the genes which contribute directly to the articular cartilage lineage, which is distinct from that of the transient cartilage that composes the rest of the skeletal rudiments. To address this, a transcriptomic analysis was previously carried out using HH38 and HH40 chick knee tissue (Fig. 3.1B) (Singh et al., 2016). A microarray profile of genes expressed in transient and articular cartilage was compared to genes expressed in solely transient cartilage (the boundary between transient and articular cartilage is not distinct, making it unfeasible to directly dissect out the articular cartilage for analysis). Comparison of the two data sets returned a set of 172 genes which were enriched in the articular cartilage. This set of articular-cartilage enriched genes offered a straight-forward way to screen for articular cartilage-specific genes that are mechanosensitive. The molecular and genetic characterisation of normal articular cartilage is necessary to define how this tissue is specified and patterned during normal development. Further, documenting the changes that occur as a result of immobilisation gives an understanding of how these processes are mis-regulated under reduced mechanical stimulation.

3.1.1 Aims of this chapter

Previous transcriptomic studies suggested that the Wnt and BMP signalling pathways could have a role as mechanosensitive regulators during skeletogenesis, yet left open the question of how pathway activity is changed in the muscle-less environment. To that end, the objective of this part of the work was to elucidate the involvement of specific signalling pathways in interpreting or responding to mechanical stimuli during skeletogenesis, with a particular focus on joint morphogenesis. This chapter specifically investigated the process of skeletogenesis in mouse forelimbs at TS23 (E14.5). The specific aims were:

A) *To carry out a spatial description of Wnt pathway component gene expression during an early stage of skeletal development which is senstitive to mechanical stimulation.* To identify tissues where Wnt pathway components are present, the gene expression patterns of Wnt ligands, Fzd receptors, and other pathway components were assessed by *in situ* hybridisation, which allows for visualisation of spatially restricted patterns of gene expression and for comparison of gene expression levels between tissues.

B) *To identify regions of Wnt pathway activity under normal and reduced mechanical stimulation.* To identify tissues where the Wnt pathway is active, the localisation of β-catenin protein, the effector molecule of the canonical Wnt pathway, and reporter expression in a canonical Wnt readout mouse were characterised. β-catenin protein localisation was compared between wildtype and muscle-less tissue.

C) *To alter signalling during skeletal development: preliminary functional analysis.* To attempt direct assessment of the role of transiently activating or inhibiting the Wnt pathway in a localised manner, electroporation of chick embryos was used to examine *in vivo* skeletal development.

D) *To expand knowledge on gene regulatory disturbances at the joint.* Transcriptomic studies were compared to identify articular cartilage-specific genes which are also mechanosensitive. These candidate genes were assessed in normal and immobilised mouse and chick models.

E) *To compare BMP pathway activity in normal and immobilised skeletogenesis.* Tissues with detectable BMP pathway activity, as indicated by localisation of the effector pSMAD1/5/8, were identified and compared between normal and muscle-less mouse.

3.2 Results

3.2.1 The Wnt pathway in normal and immobilised skeletogenesis

3.2.1.1. Wnt pathway ligands, receptors, and other components expressed in the developing skeleton at E14.5

Transcriptomic data were previously generated for wildtype and muscle-less ($Pax3^{Spd/Spd}$) humeri and associated joints at Theiler Stage (TS) 23 by RNAseq and microarray (Rolfe et al., 2014). Analysis of the RNAseq data revealed the transcript levels for all Wnt ligand and Frizzled receptor encoding genes (Fig. 3.2). Transcripts for 11 out of the total 19 Wnt ligand encoding genes were detected (read count > 5) in wildtype TS23 humeri and joints at various levels (Fig. 3.2a). The highest transcript levels by far were detected for *Wnt5a* at 1,873 reads, while *Wnt4*, *Wnt5b*, *Wnt9a*, and *Wnt11* were detected at moderate levels, greater than 100 reads. *Wnt2*, *Wnt2b*, *Wnt6*, *Wnt7b*, *Wnt10b*, and *Wnt16* were detected at lower levels (5-100 reads), and the remaining Wnt family members were undetected or detected at <5 reads (Appendix Table A.1). In contrast to the Wnt ligands, all 10 Frizzled receptor genes (Fzd1-10) were expressed in the humerus and associated joints at TS23 (Fig. 3.2b). More than 1000 reads were detected for Fzd1-4 and 7-9 in control tissue; 400-800 reads were detected for Fzd5 and Fzd6 (Appendix Table A.2).

Examination of read counts from mutant humeri revealed that nearly all Wnt ligands detected in the wildtype showed higher average levels in the mutant. In particular, *Wnt2*, *Wnt2b*, *Wnt4* and *Wnt16* showed levels significantly increased by more than 2 fold ($p \leq 0.05$) (Fig. 3.2a and Appendix Table A.1). Analysis of the muscle-less mutant transcriptome data revealed that expression of the Fzd-encoding genes was broadly similar in mutant humeri, with, in most instances, average read counts slightly elevated (Fig. 3.2b and Appendix Table A.2).

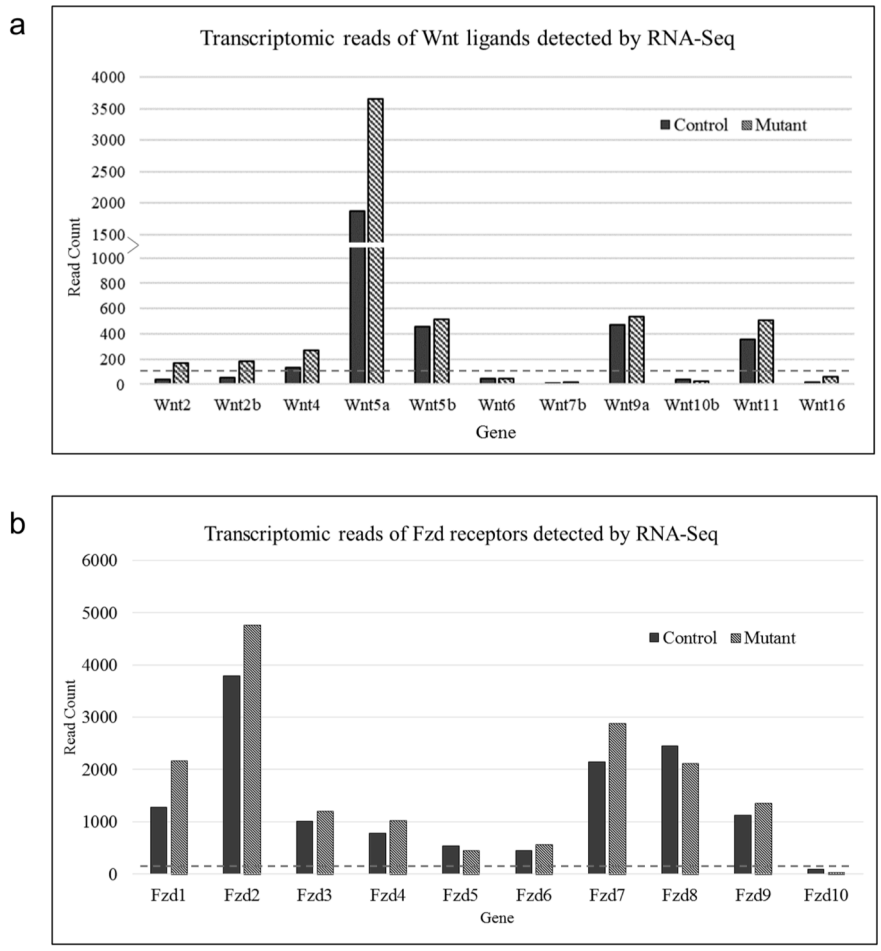

Fig. 3.2. Graph of transcriptomic reads of Wnt ligand and Fzd receptor-encoding genes as detected by RNAseq. Whole genome RNA-seq analysis was previously carried out on E14.5 humeri and associated joints in wildtype and *Spd* mutant mouse (Rolfe et al., 2014), and average read counts (n=3) for genes encoding Wnt ligands (a) and Fzd receptors (b) were assembled and are represented here. Genes with control or mutant read counts less than 5 are excluded from the graphs. Dashed grey lines indicate 100 reads. Note the broken y-axis in (a).

Expression of other families of genes that influence ligand-receptor interaction at the cell surface and which modulate Wnt signalling activity were examined. These included the Dickkopf protein family (*Dkk1-3*), the co-receptors Lipoprotein receptor related protein (*Lrp5* and *6*), the Kremen regulatory receptors (*Krm1* and *2*), the Sclerostin domain-containing protein 1 (*Sostdc1*) inhibitor, the alternative co-receptors Ryk and Ror, the antagonist secreted frizzled-related protein family (*Sfrp1-5*), and the antagonist inhibitors R-spondin (*Rspo*) 2 and 3 (Table 3.1). Among these genes, several were significantly differentially regulated in the mutant: *Krm2* (down-regulated), *Rspo2* and *Rspo3* (upregulated), and *Sfrp2* (upregulated). Analysis of Wnt pathway target genes revealed that many were differentially regulated in the mutant, mostly down-regulated; these are listed in Appendix Table A.3.

Table 3.1. RNAseq read counts of other Wnt pathway component genes in TS23 *Pax3*$^{Spd/Spd}$ mutant vs. wildtype humeri and associated joints. Genes more than 2-fold up- or down-regulated in the mutant, with p<0.05 are indicated in bold. Abbreviations: antagonist (Ant), antagonist receptor (Ant Rec), co-receptor (Co-Rec); co-transcriptional activator (Co-Tr); regulator (Reg).

Gene symbol	Role in Wnt Pathway	RNAseq			
		Read number		Fold Change	Adjusted P-value
		Wildtype	Mutant		
Dkk1	Ant	60	56	1.07 down	1
Dkk2	Ant	1984	4833	2.43 up	1.57E-06
Dkk3	Ant	3441	4370	1.27 up	0.4727
Krm1	Ant Rec	1743	1125	1.55 down	0.0433
Krm2	Ant Rec	230	6	37.59 down	4.83E-05
Lrp5	Co-Rec	3310	3735	1.13 up	0.8055
Lrp6	Co-Rec	4727	7682	1.63 up	0.0628
Rspo1	Reg	24	9	2.67 down	0.8107
Rspo2	Reg	331	802	2.43 up	4.65E-05
Rspo3	Reg	784	1585	2.03 up	8.62E-06
Ryk	Co-Rec	3199	3510	1.09 up	0.9502
Ror2	Co-Rec	1072	1037	1.03 up	1
Sostdc1	Ant	231	240	1.04 up	0.9485
*Sfrp*1	Ant	1958	3513	1.79 up	0.0015
***Sfrp*2**	Ant	2888	6041	2.08 up	1.13E-06
*Sfrp*3 (Frzb1)	Ant	2105	3349	1.59 up	0.4684
*Sfrp*4	Ant	106	197	1.86 up	0.1952
*Sfrp*5	Ant	199	339	1.70 up	0.1777

3.2.1.2. Wnt component genes have spatially localised expression patterns

The assessment of transcriptomic data identified which Wnt ligand and Fzd receptor genes, as well as other Wnt pathway component genes, are expressed in the developing skeleton at TS23. The level of expression (read count), also indicated the genes most likely to be detectable by *in situ* hybridisation, to allow for an analysis of the spatial localisation of transcripts within the developing rudiments and joints. Based on the transcriptomic data analysis, *Wnt2*, *Wnt2b*, *Wnt4*, *Wnt5a*, *Wnt5b*, *Wnt9a*, *Wnt11*, and Wnt16 were selected for expression analysis by *in situ* hybridisation as they had read counts of more than 100 in either wildtype or mutant tissue at TS23. From this analysis, several remarkable expression patterns emerged at the forelimb joints (Fig. 3.3A) and within the forelimb rudiments (Fig. 3.3B).

Wnt4 expression was detected only in joint regions, adjacent to the elbow joint (Fig. 3.3a) and more extensively through the metacarpal and phalangeal joint lines (Fig. 3.3b). Otherwise it was also detected in the ectoderm of the limb, most highly in the interdigital region. *Wnt5a*, the most abundantly expressed Wnt gene, was also detected at the periphery of the developing shoulder joint (Fig. 3.3c) and most strongly in the digits, in the tissue adjacent to the digit joints and the developing phalanges where *Wnt5b* shows a similar pattern (Fig. 3.3d, e). *Wnt9a*, like *Wnt4*, is also expressed adjacent to the shoulder and elbow joints (Fig. 3.3f, black arrow); however, unlike *Wnt4* at this stage it is also expressed through the joint line, in the chondrogenous layers of the humerus and scapula at the shoulder joint (Fig. 3.3f, red arrow). The peripheral expression, adjacent to the joint also extends more distally from the humeral head, in tissue adjacent to the humeral rudiment (Fig. 3.3f, arrowhead). Similar to *Wnt4*, *Wnt9a* is detected within the digit joints (Fig. 3.3g). *Wnt11* shows similar expression to *Wnt9a*, outlining the humeral head at the shoulder joint (Fig. 3.3h, red arrow), and extending past the joint territory distally (Fig. 3.3h, black arrow). There is also distinct expression in the digits, outlining the distal cartilage anlage and at phalangeal joints (Fig. 3.3i, black arrows).

Several Wnt ligands were observed to be expressed within the rudiments (Fig. 3.3B). *Wnt5a* had faint expression in the pre-hypertrophic chondrocytes of the humerus which extends into the territory of the proliferative chondrocytes(Fig. 3.3j, red arrows), while

Wnt5b had stronger expression which was limited to the pre-hypertrophic chondrocytes (Fig. 3.3k, red arrows). For *Wnt2*, *Wnt2b*, *Wnt5a*, and *Wnt9a*, staining was detected in the perichondrium of the rudiments, near the hypertrophic zone (Fig. 3.3j-n, black arrows) (note also perichondrial expression near the joint regions for *Wnt9a* (above)). *Wnt11*, which was detected at the joints (Fig. 3.3h, i) was not detected in the hypertrophic zone or in other cell types within the rudiment (not shown). Despite expression being detected by RNAseq in the skeleton at this stage (Fig. 3.2A), although with a very low read count (19 reads in the wildtype), Wnt16 expression was not detectable by *in situ* hybridisation in either the developing joints or rudiments (not shown); this could be due to dispersed, low level expression.

To further survey Wnt ligand expression, the EurExpress database was consulted (Fig. 3.3C). This is a database consisting of high-throughput, high-resolution *in situ* hybridisation data for whole mouse cryosections at E14.5 (Diez-Roux et al., 2011). Because there is no previous description of *Wnt2* or *Wnt2b* in the developing skeleton, to corroborate the present findings, expression data for these genes were examined, also revealing weak staining for *Wnt2* (Fig. 3.3p', black arrows) and, more strongly, *Wnt2b* in the perichondrium of the scapula and humerus, as well as in tissue in the proximity of the shoulder joint (Fig. 3.3p', black arrows). *Wnt9a* data in EurExpress was also examined (Fig. 3.3C) since novel *Wnt9a* staining in the perichondrium of the rudiment diaphysis was also noted (Fig. 3.3n). EurExpress data analysis indeed showed detectable *Wnt9a* expression in the perichondrium of the scapula and humerus, as well as in chondrocytes at the core of the humerus (Fig. 3.3q', black arrows).

Fig. 3.3 (next page). Wnt ligands are expressed at the shoulder, elbow, and digit joints of the developing forelimb skeleton, with limited expression within the rudiments. Vibratome sections (60 μm) of TS23 forelimbs were *in situ* hybridised for expression of Wnt ligands, revealing expression patterns in the joints (A) and rudiments (B). Expression was observed for *Wnt4* (a, b), *Wnt5a* (c, d, j), *Wnt5b* (e, k), *Wnt9a* (f, g), *Wnt11* (h, i), *Wnt2* (l), *Wnt2b* (m), *Wnt9a* (n). (C) shows data retrieved from the EurExpress database (http://www.eurexpress.org) of *in situ* hybridisation on E14.5 whole embryo cryosections. Skeletal expression of *Wnt2* (o-o'), *Wnt2b* (p-p'), and *Wnt9a* (q-q'). (o'-q') are enlarged images of the boxed regions in (o-q), respectively. Scale bars are equal to 200 μm. Black and red arrows indicate observable expression patterns. Abbreviations: humerus (H), scapula (S).

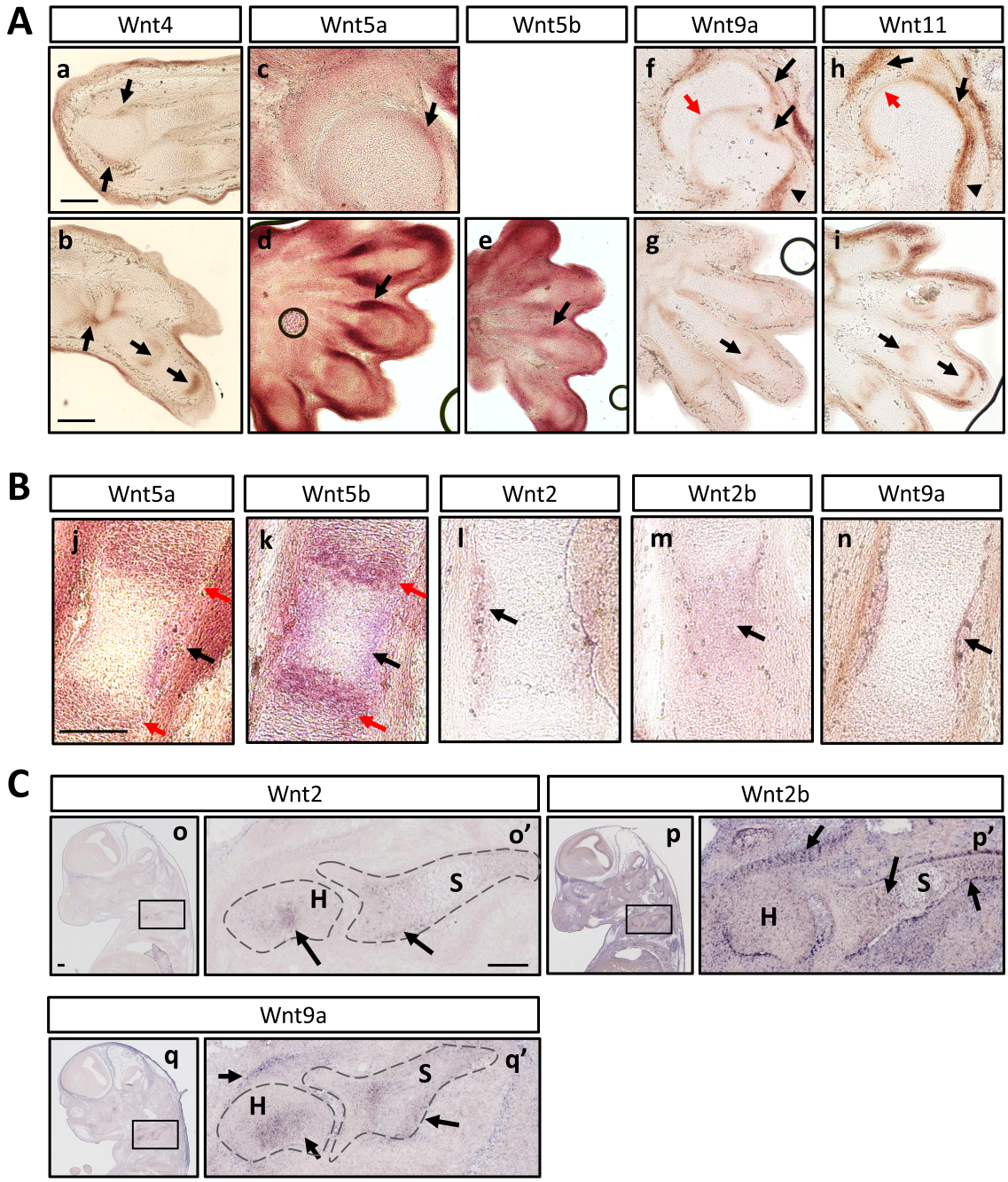

Based on transcriptomic data indicating that all Fzd genes are expressed at higher levels in the E14.5 mouse forelimb skeleton (Fig. 3.2B), all ten Fzd receptor genes were assessed for expression via *in situ* hybridisation. However only two Fzd receptor encoding genes, Fzd3 and Fzd6, showed localised expression patterns (Fig. 3.4). Expression of Fzd3 was observed peripheral to the elbow joint and, to a lesser extent, the shoulder joint (Fig. 3.4a, c; black arrows); it was also observed in the perichondrium (Fig. 3.4a, red arrowhead) and in the developing muscles and ectoderm (Fig. 3.4a black arrowheads). Fzd6 was also seen to be expressed peripheral to the elbow and shoulder joints (Fig. 3.4b, d; black arrows). Further, expression of Fzd6 was

observed within the shoulder joint (Fig. 3.4b, red arrow), and in the ectoderm (Fig. 3.4d, black arrowhead). There was no detectable pattern of expression of any of the Fzd genes in the rudiments, including at the hypertrophic zone, which may be due to low level expression throughout the tissue giving an elevated read count overall yet no detectable spatial pattern. All probes were tested and showed expected expression patterns as described at other stages or in other tissues (Summerhurst et al., 2008). Eurexpress data for Fzd3 shows light perichondrial staining of the long bones, and strong staining of muscle fibres; data for Fzd6 shows strong staining adjacent to the joint territory which corroborates data presented in this study.

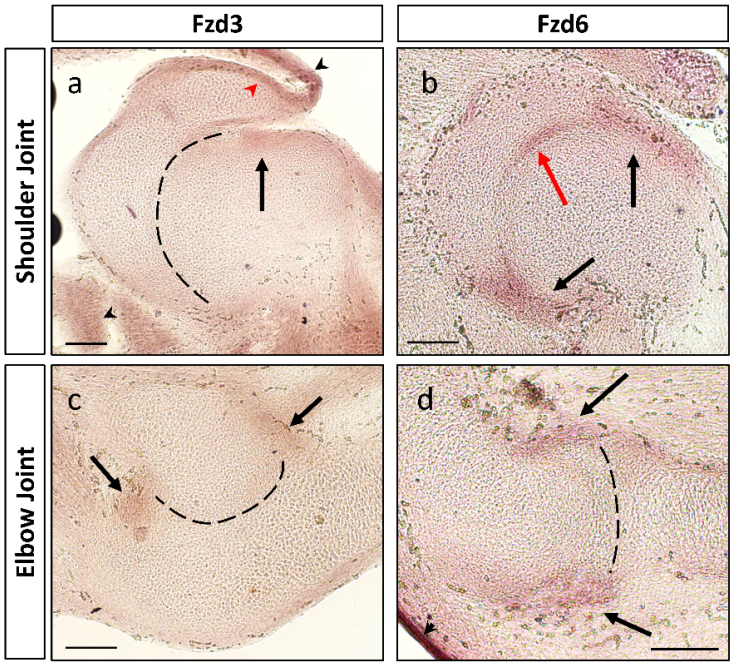

Fig. 3.4. Fzd3 and Fzd6 are expressed peripheral to the shoulder and elbow joints. Fzd3 and Fzd6 expression in the region of the shoulder (a, b) and elbow joints (c, d) is indicated. Black arrows indicate expression peripheral to the joint; the red arrow indicates expression at the joint line. Black arrowheads in (a) and (d) indicate expression in ectoderm and muscle; the red arrowhead in (a) indicates perichondrial expression. Dashed black lines indicate joint lines. Scale bars are 100 µm.

3.2.1.3. Expression of Wnt component gene expression under altered mechanical stimulation

Transcriptomic data had indicated that several genes in the Wnt pathway were significantly differentially expressed (fold change ≥2 and $p \leq 0.05$) in the TS23

Pax3$^{Spd/Spd}$ muscle-less humerus and associated joints, compared to wildtype tissue. Of genes assessed by *in situ* hybridisation (8 Wnt ligands, 10 Fzd receptors, and 4 other Wnt pathway components – Kremen2, *Rspo2* and *3*, and *Sfrp2*), *Wnt4* and *Sfrp2*, a pathway antagonist, were the only components to show localised increases in expression (Fig. 3.5). At TS23, the wildtype shoulder and elbow joints are distinct, as is apparent from the gap between the collagen type 2aI (*Col2aI*)-expressing rudiments (Fig. 3.5a, b; black arrows). In comparison, the mutant shoulder and elbow have reduced separation, and partial fusion of the *Col2aI*-positive, cartilaginous territories (Fig. 3.5a', b'; red arrows). These differences are visible across serial sections through the forelimb (n>10), and have also been demonstrated previously in wholemount specimens (Kahn et al., 2009). In the wildtype shoulder, *Wnt4* was not detected at the joint line, yet was lightly detected in tissue adjacent to the elbow joint (Fig. 3.5c, d; black arrows). In the mutant, expression adjacent to the shoulder joint was observed, and peripheral expression in the elbow joint was increased relative to the wildtype (Fig. 3.5c', d'; black arrows). *Sfrp2* expression was faint or absent at the shoulder or elbow (Fig. 3.5e, f). In the mutant, an increase in expression was seen in tissue adjacent to the shoulder and elbow joints (Fig. 3.5e', f'; black arrows).and expression was also detected within both of these joints (Fig. 3.5e'; red arrow).

The increased expression of *Wnt4* and *Sfrp2* in cells adjacent to the shoulder and elbow joints following immobilisation highlighted a region of interest within the forelimb: the peripheral cells of the joints (Fig. 3.5B). To better visualise these cells, Mallory's Trichrome stain was used (Fig. 3.5g-h'). This stain differentiates cartilaginous collagen (which stains with aniline blue) from connective tissues (which stains with acid fuchsin); in particular, muscle tissue is stained bright red. In this study, it was found to better visualise cells than the conventional histological stain haematoxylin and eoisin (H&E) and to better differentiate the cartilage rudiments from surrounding tissue. Longitudinal forelimb sections revealed that the territory of peripheral cells, as characterised by diffuse acid fuchsin staining, was enlarged in the muscle-less mutant (Fig. 3.5h, h'; dashed area) compared to the wildtype (Fig. 3.5g, g'; dashed area). In the wildtype section, muscle cells strongly stained with acid fuchsin (Fig. 3.5g', white arrow) are clearly visible, and delineate the border of the peripheral territory. This observed increase in peripheral cell territory in the mutant corresponds to increases in expression of the Wnt pathway components *Wnt4* and *Sfrp2* in this region.

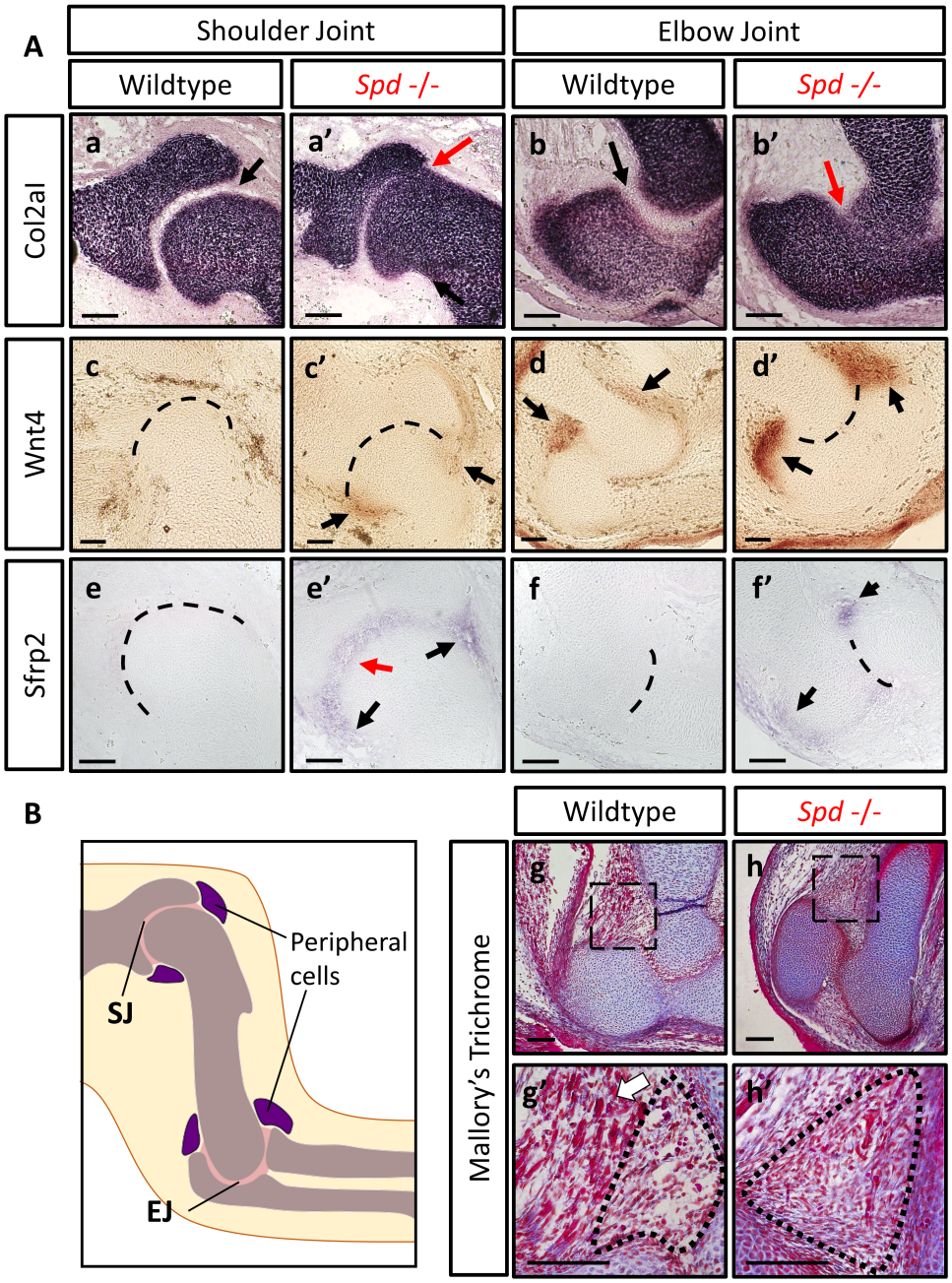

Fig. 3.5. Expression of the Wnt pathway genes *Wnt4* and *Sfrp2* is upregulated in the peripheral joint cells in the muscle-less mutant. TS23 forelimb sections of wildtype and muscle-less (*Spd*) mutant tissue, *in situ* hybridised for *Col2aI* and *Sfrp2* (cryosections) or *Wnt4* (vibratome) (A), or stained with Mallory's trichrome (paraffin sections) (B). Rudiment separation (a, b) or fusion (a', b') is indicated by black and red arrows, respectively. Expression of *Wnt4* and *Sfrp2* peripheral to shoulder (c, c', e, e') and elbow joints (d, d', f, f') and at the joint line (e') is indicated by black and red arrows, respectively. (B) Schematic representation of peripheral joint cells (dark purple) and peripheral elbow territory in wildtype and mutant forelimbs (g-h', outlined areas). Dashed lines in (A) indicate joints. Dashed lines in (g', h') indicate the peripheral cell territory. The white arrow in (g') indicates muscle cells. Scale bars are 100 µm.

3.2.1.4. Canonical Wnt pathway activity is restricted to the joint line in the E14.5 developing skeleton and is lost in the muscle-less mutant.

To directly assess canonical Wnt pathway activity in the developing skeleton on a cellular level, the TCF/Lef:H2B-GFP reporter mouse (Ferrer-Vaquer et al., 2010) was utilised (Fig. 3.6). Although GFP is typically directly detectable, fixation and storage of specimens may have reduced fluorescence and detection via immunofluorescent staining was clearer. Additionally, the signal of GFP in the muscle was much stronger relative to the signal within the developing rudiments (Fig. 3.6a, b, f; red arrows); this may be impacted by cartilage proteins which render immunodetection difficult (Ahrens and Dudley, 2011). Nevertheless, GFP was detected in several regions in the normal developing skeleton at E14.5. GFP-positive cells were observed within the elbow joint (Fig. 3.6c, red arrow). Within the rudiments, the cells of the perichondrium showed low level GFP positivity (Fig. 3.6d, red brackets), and numerous positive cells were noted in the hypertrophic zone (Fig. 3.6e, red arrows) (controls show that this is not autofluoresence or non-specific binding of antibody). As noted above, the signal in the developing muscles was very strong, and multi-nucleated muscle cells were easily observed (Fig. 3.6f, red arrow). The muscle GFP positivity extends into the muscle attachment point (future tendon) at the elbow, but is not elevated or more extensive here (Fig. 3.6g, red brackets). In summary, observed canonical pathway activity is very limited in the developing forelimb skeleton at E14.5, restricted largely to joint line and hypertrophic cells, with low levels of activity in the rudiment perichondrium.

Fig. 3.6 (next page). Canonical Wnt pathway activity in the perichondrium, elbow joint, and hypertrophic zone in the developing forelimb revealed through a TCF/LEF:H2B-GFP reporter. Longitudinal cryo sections (10 μm) of E14.5 forelimbs were immunostained for GFP expression and counter-stained with DAPI (a). GFP expression is noted in the developing muscle tissue (a, f) extending up to the tendon/muscle attachment point (g), elbow joint (c), perichondrium (d, brackets), and hypertrophic zone (e) (shown in the humerus). The images in (b) are higher-magnification images of the box indicated in (a). The images in (c-g) are higher-magnification images of regions corresponding to the boxes indicated in (a) and (b). Red arrows and brackets indicate GFP-positive cells. Abbreviations: humerus (H), radius (R), ulna (U). Scale bars are 100 μm.

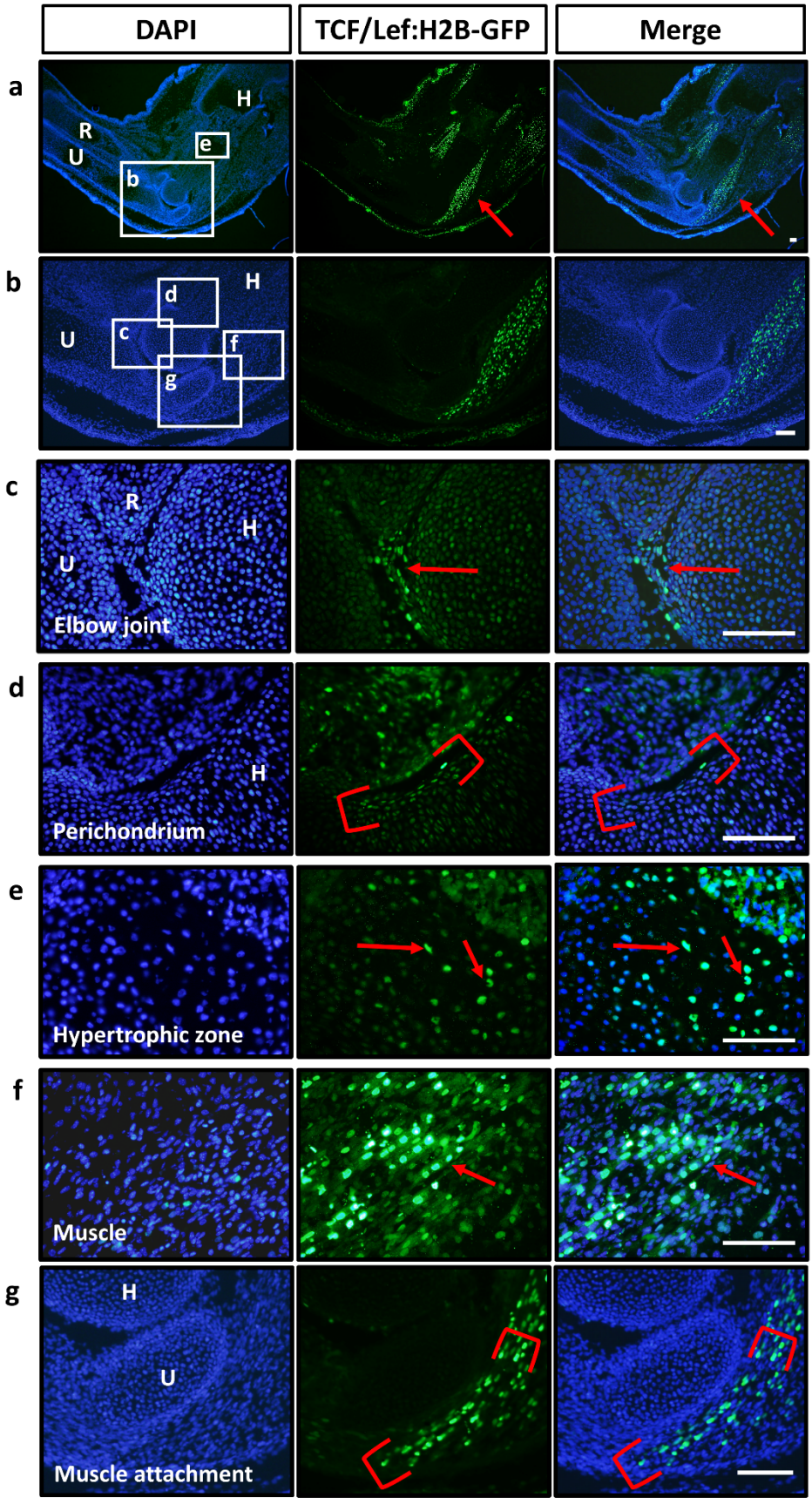
DAPI
TCF/Lef:H2B-GFP
Merge
a
H
R
U
e
b
b
H
d
U
c
f
g
c
R
H
U
Elbow joint
d
H
Perichondrium
e
Hypertrophic zone
f
Muscle
g
H
U
Muscle attachment

Canonical Wnt activity is also indicated by nuclear accumulation of β-catenin. Immunodetection of β-catenin showed enhanced staining at the joint line in the shoulder (Fig. 3.7a, a'; red arrow) and elbow (Fig. 3.7c, c'; red arrow) and in cells adjacent to the perichondrium (Fig. 3.7a, c; black arrows). To assess changes in β-catenin protein levels in the muscle-less mutant, *Pax3*$^{Spd/Spd}$ embryos showed no detectable β-catenin expression in either shoulder or elbow joint line (Fig. 3.7b, b', d, d'; red arrows). β-catenin levels were unaffected in the perichondrium of the rudiments, remaining detectable in the muscle-less *Spd* mutants (Fig. 3.7b', d'; black arrows).

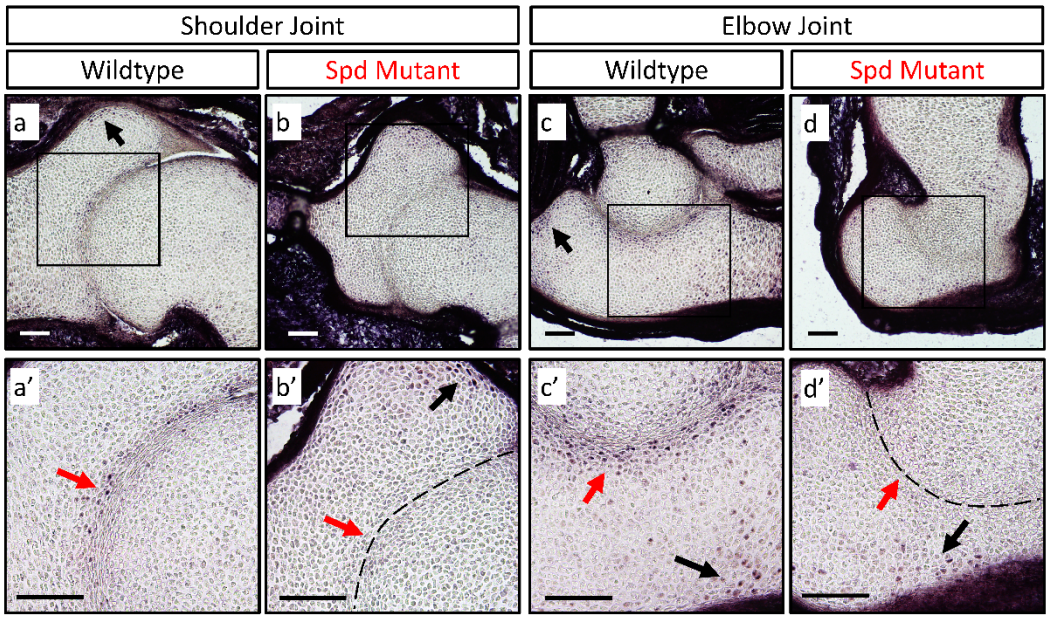

Fig. 3.7. Immunolocalisation of β-catenin in wildtype and Spd muscle-less tissue. Immunolocalisation was performed on paraffin sections (10 µm) which were developed colourimetrically with alkaline phosphatase. β-catenin protein levels were assessed in the wildtype and mutant shoulder (a-b') and elbow joints (c-d'). Images in (a' - d') are higher magnification images of the boxed areas in (a - d). Expression or lack thereof at the joint line is indicated by red arrows; black arrows indicate expression in the rudiment perichondrium. Dashed lines indicate joints. Scale bars are 100 µm.

3.2.1.5. Alteration of Wnt signalling during skeletal development: *ex ovo* electroporation and preliminary functional analysis

As demonstrated above, canonical Wnt activity is reduced in the developing joints of immobilised embryos, where tissues are mis-patterned and partial fusion of cartilage across the joint is observed (Fig. 3.5a-b' and Fig. 3.7). To test the functional

relationship between altered canonical Wnt activity and joint mis-specification, we sought to manipulate Wnt signalling specifically at the joint in order to examine if the phenotype resembles that of immobilisation. A chick *ex ovo* culture system was developed (Fig. 3.8A-C), in tandem with an electroporation protocol (described in Section 2.7) with the intention of targeting constructs to alter Wnt activity in the developing joint. Co-electroporation with a GFP-expressing construct showed successful delivery and expression of the constructs (Fig. 3.8D) but highlighted two difficulties with this approach. First, expression of the transgene was generally limited to a small number of cells Fig. 3.8D), limiting the magnitude of the transgene's effect in the tissue. Second, there was limited control of the site of delivery, which affected precise hypothesis testing and repeatability.

To attempt to locally alter Wnt signalling, chick forelimb buds were co-electroporated at E5 (approx. HH25-26) with constructs encoding GFP and either a constitutively active β-catenin-Tcf fusion protein or Sfrp3 (Frzb), a Wnt antagonist (c.f. Section 2.7.2). For sham controls, GFP and PBS were co-injected. Microinjection of the constructs was targeted as far as possible to the region of the developing elbow in the forelimb bud. Embryos were harvested 24 hr after electroporation, at E6 (approx. HH27-29) and assessed for any phenotypic effects, using GFP to indicate the extent and location of transgene expression. *In situ* hybridisation for *Col2aI* and subsequent OPT scanning and 3-D reconstruction was used to reveal any subtle changes in skeletal patterning in electroporated limbs (Fig. 3.9). A total of 379 embryos were electroporated over 26 experiments. From those embryos which survived 24 hours after electroporation to be harvested, and which displayed appropriate GFP expression, a total of 19 specimens were selected for staining, scanning, and analysis: five Sfrp3- and seven β-catenin electroporated specimens and seven Sham (PBS)-electroporated control specimens. Fig. 3.9 shows the analysis of 1 representative specimen for each of these groups. Visualisation of electroporated cells using GFP (Fig. 3.9a, d, g; yellow arrows) showed that a number of cells in these specimens had taken up and were expressing the constructs; construct expression was also confirmed by immunostaining for FLAG and HA epitopes which were incorporated into the β-catenin and Sfrp3 constructs, respectively (c.f. Section 2.7.2) (data not shown). The contra-lateral (generally left) forelimb ('Non-EP Limb') was used as a control for the electroporated (generally right) forelimb ('EP Limb'). At the stage of harvesting (E6, generally

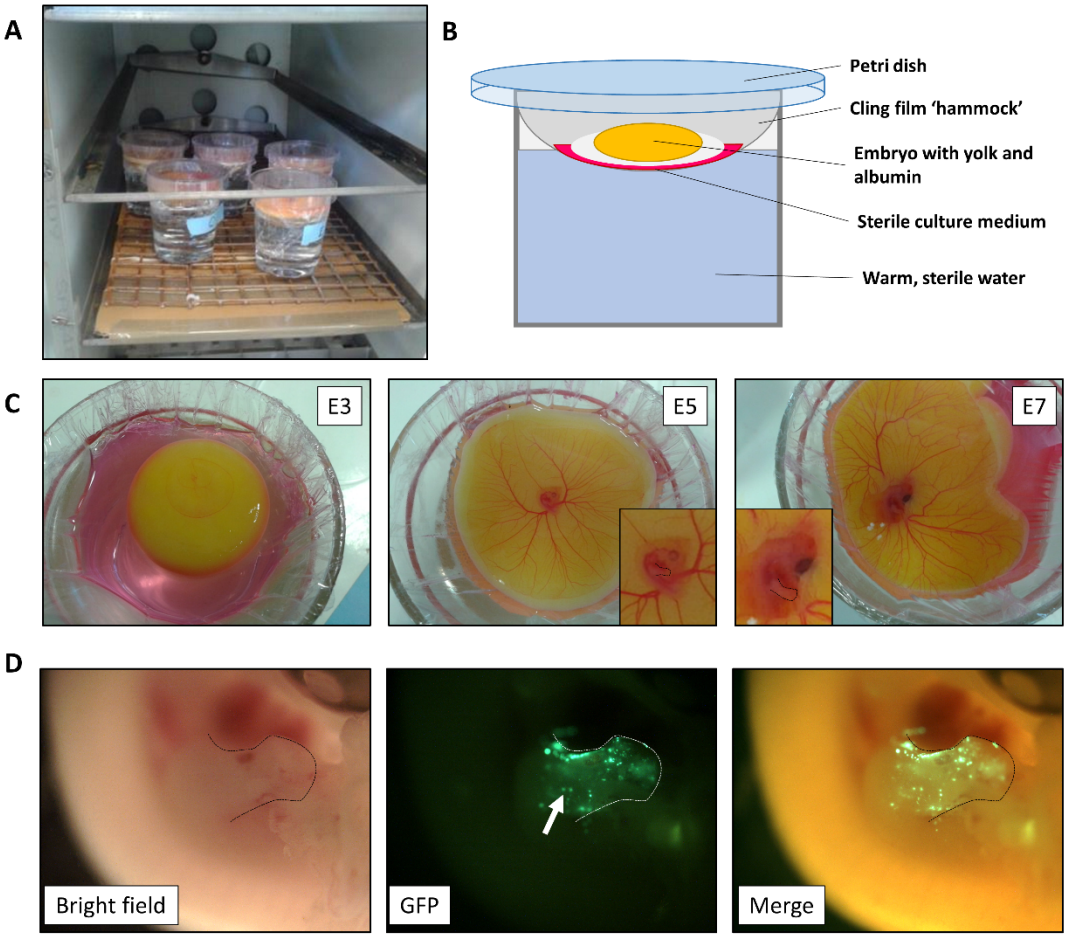

Fig. 3.8. Establishment of an e*x ovo* electroporation technique. An *ex ovo* technique of culturing chick embryos outside their shells was optimised (adapted after Schomann et al. (2013)). Chick embryos were cultured under normal conditions, *ex ovo*, in a humidified incubator at 37°C (A). A schematic explanation of the *ex ovo* culture system (B), in which embryos were cultured in cling film supports attached to drinking glasses. Embryos remained healthy and viable over the culture period (C): shown here are embryos at embryonic day (E) 3, E5, and E7. Inset images show healthy embryos with robust vasculature; forelimbs are outlined. Embryos cultured *ex ovo* displayed normal skeletal development at a rate comparable to embryos cultured *in ovo*. Electroporation of a GFP-encoding construct was used to assess electroporation efficiency (D). Shown here is an example embryo showing widespread take-up and expression of the GFP-encoding construct, one day after electroporation. Merging of GFP and bright field channels shows localisation of GFP expression to the forelimb; individual cells are visible (white arrow).

HH27-29), the scapula, humerus, radius, and ulna are formed and can be visualised by *in situ* hybridisation for *Col2aI*. In the Sfrp3-electroporated specimen shown, cells at the shoulder site took up the constructs (Fig. 3.9a, yellow arrow), and this corresponds to a reduction in the shoulder joint (Fig. 3.9b, b'; yellow arrows). In comparison, the

shoulder joint in the contra-lateral limb is distinct and rudiments are clearly separate (Fig. 3.9c, c'; yellow arrows). In the β-catenin electroporated specimen shown, cells in both the proximal and distal regions of the forelimb took up the constructs (Fig. 3.9d, yellow arrows). The elbow joint is slightly enlarged (Fig. 3.9e, e'; yellow arrows) compared to the control limb (Fig. 3.9f, f'; yellow arrows). As a control, Sham (PBS)-electroporated embryos were also assessed. Many cells throughout the limb took up the GFP construct (Fig. 3.9g). Electroporation itself did not have an obvious effect on forelimb rudiments; rudiments of the electroporated forelimb (Fig. 3.9h, h') appear to be at a similar stage of development as the rudiments of the non-electroporated limb (Fig. 3.9i, i'), with the ulna and humerus territories not yet separated but the humerus and radius distinct (Fig. 3.9h-i', yellow arrows).

These specimens were selected for the correspondence between GFP expression and observed phenotypic effects. Electroporation efficiency varied between specimens, and in some instances low numbers of cells and/or cells at a distance from the joint were successfully targeted and no effect was seen in electroporated limbs compared to non-electroporated contra-lateral limbs. Micro-injection into the forelimb was aimed to deliver the constructs to the developing joint region, yet this proved difficult and resulted in a range of electroporation domains across specimens. Typically, well-electroporated specimens displayed GFP in dozens of cells (see, for example Fig. 3.9g), but other specimens possessed only a few-GFP positive cells. In all cases, individual GFP-positive cells were visible, indicating that not all cells within a given territory had taken up the constructs, further reducing the effect of the constructs on skeletogenesis.

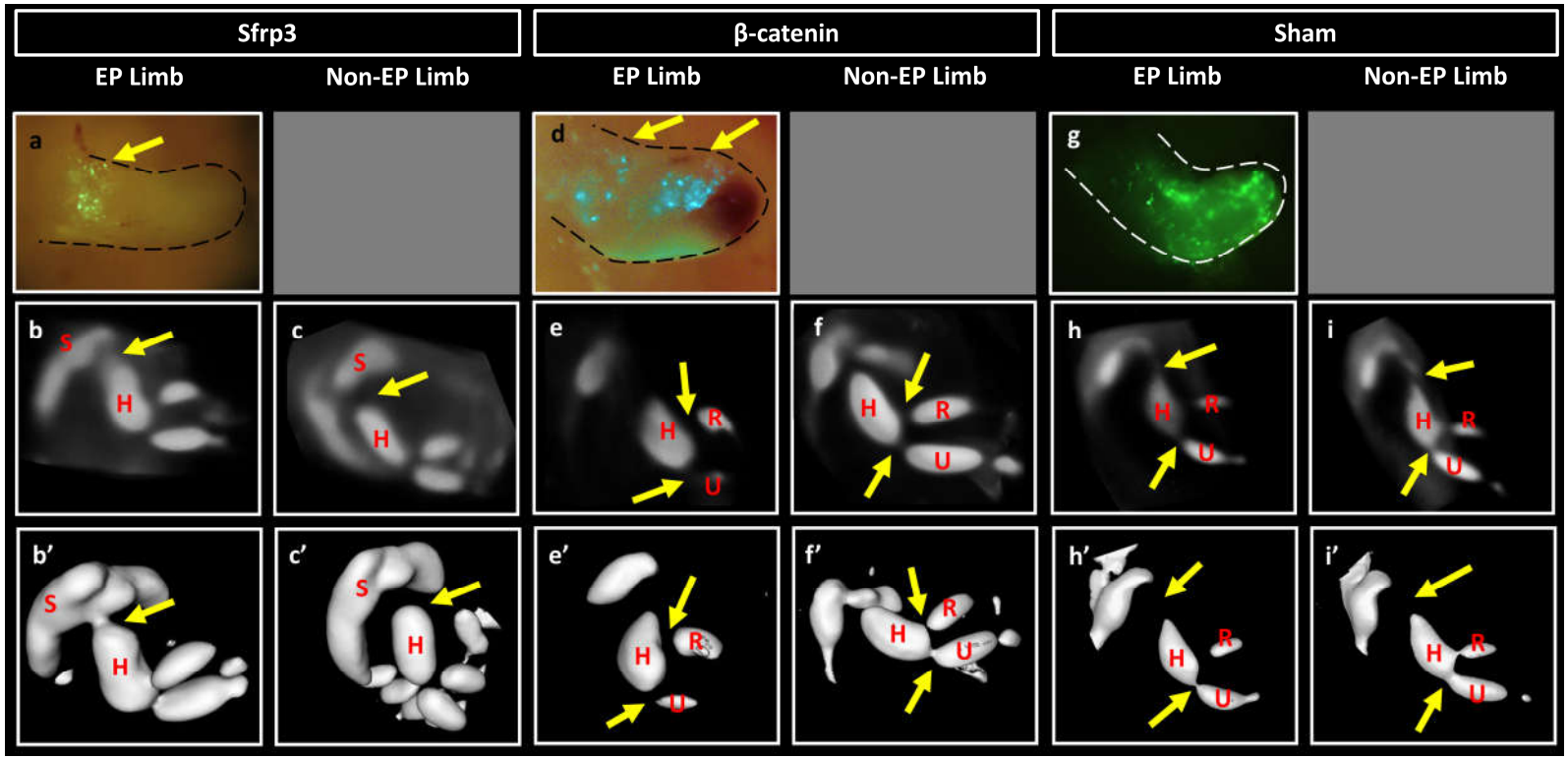

Fig. 3.9. Electroporation of chick forelimbs with constructs to alter Wnt pathway activity affected skeletogenesis. Forelimbs of chick embryos were electroporated at E5 with constructs encoding GFP and either Sfrp3 (a Wnt antagonist) (a-b') or constitutively active β-catenin (the canonical pathway effector) (d-e'). Sham controls were electroporated with GFP and PBS (g-h'). Generally, the right forelimb was electroporated ('EP Limb') and the left forelimb served as a contra-lateral, non-electroporated control ('Non-EP Limb') for the same specimen (c, c', f, f', i, i'). Wholemount fluorescent and brightfield merged images of visible GFP expression following harvest (a, d, g; yellow arrows; dashed lines indicate the forelimb boundaries). Embryos were subsequently *in situ* hybridised for *Col2aI*, embedded, OPT scanned, and reconstructed (Section 2.3.4). Presented here are volume renders of reconstructed 3-D scans (b-i) and surface renders of the same (b'-i'). Yellow arrows indicate joint sites. Abbreviations: humerus (H), radius (R), scapula (S), and ulna (U). Scale bar in (a) equal to 100 μm.

3.2.2 Identification of gene regulatory disturbances at the joint in mouse and chick immobilisation models

Analysis of Wnt pathway component gene expression highlighted the joint, particularly the joint line, chondrogenous layers and tissue adjacent to the joint site, as areas most sensitive to reduced movement in terms of impact on gene regulation. To further probe how altered mechanical stimulation affects tissue patterning at the developing joint, it would be valuable to examine how genes known to be specific to articular cartilage are affected under immobilisation. Therefore, a previously published transcriptomic dataset which identified genes enriched in the developing chick articular cartilage was utilised (Singh et al., 2016). This set of joint-specific genes was cross-referenced with the RNAseq transcriptomic data from the muscle-less mouse to identify genes in common which could be involved in the altered regulation of joint tissue patterning under reduced mechanical stimulation (Table 3.2). This transcriptomic comparison revealed six chick articular cartilage-specific genes which were significantly up-regulated in the muscle-less mouse and ten chick articular cartilage-specific genes which were significantly down-regulated in the muscle-less mouse. An additional 3 genes that were not significantly differentially regulated (using the criteria applied in Rolfe et al. (2014)) yet were articular specific were also included (BOC, Col26aI/Emid2, and Id1). In collaboration with Pratik Singh (PS) in the research group of Amitabha Bandypadhyay at the Indian Institute of Technology, Kanpur, we assessed the expression of these genes in control and immobilised embryos, with chick embryos immobilised in both Dublin and Kanpur being analysed in Kanpur. Selected chick expression data generated by PS are shown in Fig. A.1 and the results summarised in the right hand column of Table 3.2. This indicates that out of 13 genes analysed, 11 genes showed similar trends in altered expression (up or down) in both chick and mouse immobilised embryos. Genes which showed altered expression in joints of immobilised chick were assessed for read number and RNA *in situ* probe availability in the mouse and analysed by *in situ* hybridisation, in order to compare similarities in gene expression changes across the two systems.

Table 3.2. Overlap in genes differentially expressed in muscle-less mouse humeri and enriched in chick articular cartilage (as indicated). Genes more than 2-fold up- or down-regulated, with p<0.05, in the mutant mouse are indicated in bold. n-values in the right-hand column indicate number of specimens analysed. Selected expression data presented in Fig. A.1.

Gene symbol	RNAseq (Rolfe et al. 2014)				Microarray (Singh et al. 2016)	
	Read number		Fold-change	Adjusted P-value	Fold-change	Expression in immobilized chick hindlimb
	Wildtype	Mutant				
Upregulated in the muscle-less mouse						
BOC	4541	6140	1.35	0.0135	7.45	Upregulated in joint line (n=5)
Cadps2	134	317	2.37	1.80E-05	23	Not analysed
Col26a1 (Emid2)	4871	5651	1.16	0.3971	6.9463	Downregulated in joint (n=6)
Crabp1	1550	3707	2.39	4.80E-05	2.7816	Upregulated in joint line (n=3)
Epha5	275	624	2.27	8.29E-06	3.2243	Upregulated in infrapatellar fat pad Downregulated in joint line (n=3)
Foxc2	307	725	2.36	5.65E-07	8.625	Not analysed
Lrfn5	26	55	2.10	0.1039	3.3952	Not detected
Wnt4	135	273	2.03	0.0101	4.2055	Upregulated in joint line (n=7)
Downregulated in the muscle-less mouse						
Cd44	2273	1041	0.46	0.0007	2.3546	Downregulated in the joint line (previously reported, Roddy et al. 2011)
Chodl	1409	428	0.30	0.0006	4.3002	Upregulated in joint
Fabp3	447	119	0.27	0.3159	20.0519	Downregulated in joint line (n=3)
Glipr2	2473	968	0.39	1.42E-10	4.4755	Not analysed
Hspb1	1058	115	0.11	0.0309	4.6338	Downregulated in joint line (n=3)
Id1	1069	771	0.72	0.0837	20.05	Downregulated in joint line (n=3)
Sall1	85	34	0.40	0.1168	4.2299	Not detected
Scx	971	397	0.41	0.0480	5.6763	Downregulated in joint line (n=3)
Tmem100	511	189	0.37	9.49E-08	4.5363	Upregulated in infrapatellar fat pad
Tnmd	5445	1738	0.32	2.73E-10	2.9110	Not detected
Tppp3	1735	163	0.09	3.50E-08	87.375	Downregulated in joint line (n=3)

Comparative analysis revealed similar joint phenotypes following immobilisation in the chick and the mouse (Fig. 3.10). As highlighted by Safranin O staining, under reduced movement, tissue patterning at the joint line is altered, resulting in cartilage rudiments which are partially or fully fused at both the the mouse shoulder and elbow (Fig. 3.10a-b', black arrows) and at the chick knee (Fig. 3.10c, c'; black arrows). *In situ*

hybridisation of wildtype and muscle-less mouse forelimb sections correspondingly showed similar joint-specific gene expression patterns and similar alterations following immobilisation were observed at the joint across species. Biregional cell adhesion molecule-related/down-regulated by oncogenes binding protein (*Boc*) a co-receptor of Hedgehog ligands, was expressed in the chondrogenous layers of the rudiments at the mouse shoulder and elbow and chick knee joints, and this expression was increased at the joint line in muscle-less mouse (most striking in the elbow) and immobilised chick (Fig. 3.10d-f', black arrows). Expression in tissue adjacent to the joint was also observed in both wildtype mouse and control chick (Fig. 3.10d, e, f, red arrows), although most strikingly at the mouse elbow joint at this stage (Fig. 3.10e, red arrows). The expression around the joint was more extensive in the immobilised mouse (Fig. 3.10e', red arrows), although this was not as apparent in the chick (Fig. 3.10f', red arrows). Contrastingly, expression of Tubulin Polymerization Promoting Protein Family Member 3 (*Tppp3*), which plays a role in cytoskeleton assembly, was decreased under reduced mechanical stimulation, most strikingly in the mouse (Fig. 3.10g-i'). In the wildtype mouse, it is seen throughout the intermediate layer of the forming shoulder and elbow joint (Fig. 3.10g, h; black arrows), and in the control chick, light expression is observed at the intermediate layer of the knee (Fig. 3.10i, black arrow). In the muscle-less mouse, there was no detectable expression at the joints (Fig. 3.10g', h'; black arrows), and in immobilised chick there was diffuse staining in the intermediate layer (Fig. 3.10i', black arrow) which extended outside of the joint territory (Fig. 3.10i', red arrow). Collagen type 26 alpha I (*Col26aI*), an extra-cellular structural protein, also had decreased expression under immobilisation. In the mouse, expression was detected in the chondrogenous layer of the shoulder joint (Fig. 3.10j, k; black arrow) and in the perichondrium of both shoulder and elbow joints (Fig. 3.10j, k; red arrows). In the muscle-less mutant, expression at the chondrogenous layers was lost (Fig. 3.10j', k'; black arrows), although expression was maintained or increased adjacent to the shoulder and elbow joints in the perichondrium (Fig. 3.10j', k'; red arrows). Likewise, in chick, expression was observed in the chondrogenous layers at the knee joint (Fig. 3.10l, black arrow), and extended outside the joint zone (Fig. 3.10l, red arrow). Under immobilisation, this expression was lost within the forming joint (Fig. 3.10l', black arrow) but light expression was still observed at the perichondrium of the femur (Fig. 3.10l', red arrow).

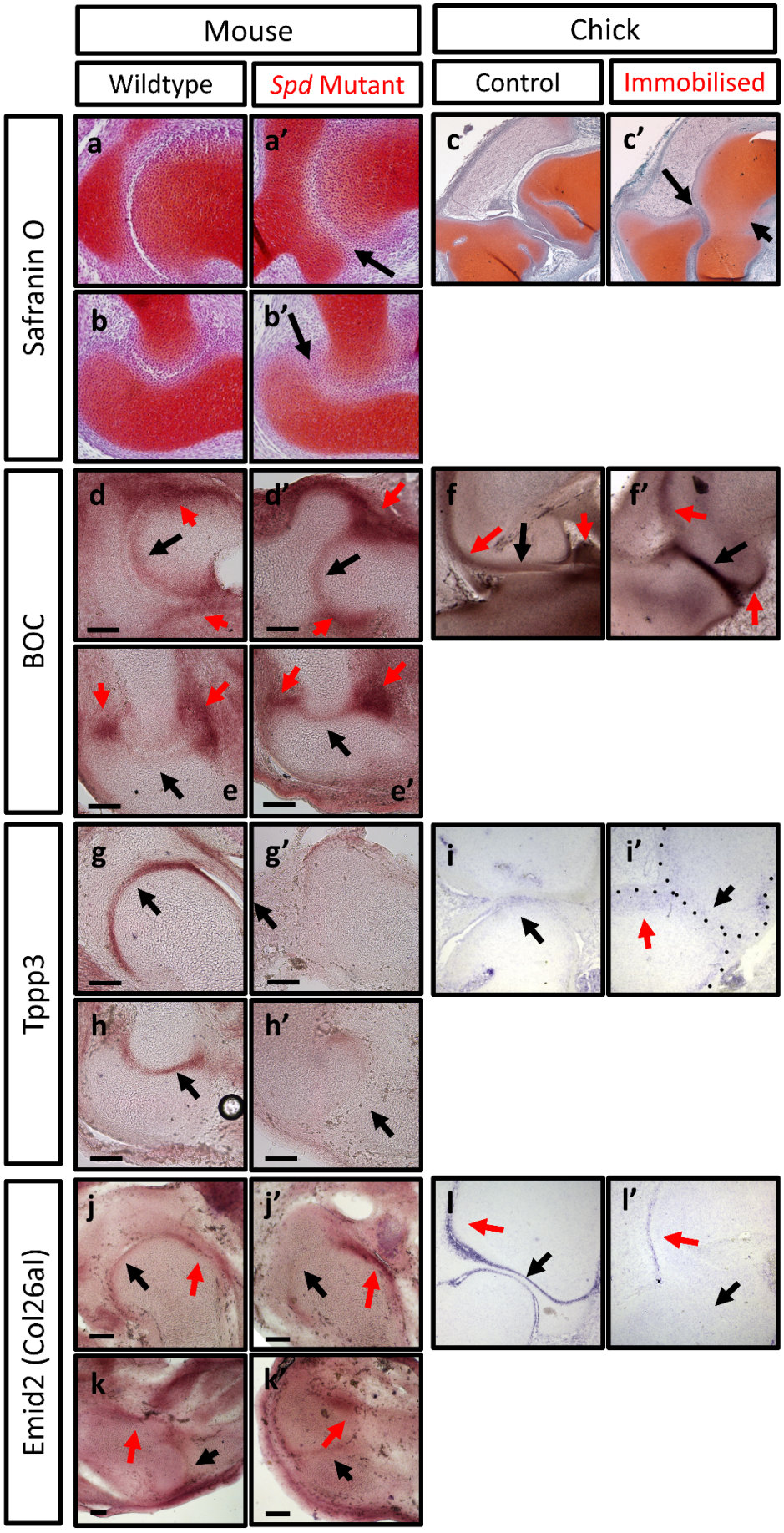
Mouse
Chick
Wildtype
Spd Mutant
Control
Immobilised
Safranin O
BOC
Tppp3
Emid2 (Col26al)
a
a'
b
b'
c
c'
d
d'
e
e'
f
f'
g
g'
h
h'
i
i'
j
j'
k
k'
l
l'

Fig. 3.10 (previous page). Gene expression of articular cartilage specific genes is similarly altered in immobilised mouse and chick joints. Comparison of expression patterns of selected genes in mouse and chick immobilisation models is presented: Safranin O staining (a-c') and *in situ* hybridisation for *BOC* (d-f'), *Tppp3* (g-i'), and *Emid2*/*Col26aI* (j-l') on sections of wildtype and muscle-less mouse shoulder (left column, top row of each gene) and elbow joints (left column, bottom row of each gene) and sections of control and immobilised chick knee joints (right column). Dashed lines in (g') indicates rudiments. Black arrows in (a', b', c') indicate joint fusion; black arrows in (d-l') indicate expression or absence thereof at the joint line; red arrows indicate expression or absence thereof adjacent to joint sites. Chick data from Pratik Singh; Safranin O mouse data from Rebecca Rolfe. Scale bars are 100 μm.

3.2.3 Characterization of BMP signalling pathway activity during altered embryonic movement

Activity of the BMP pathway in the joint region was analysed because differential expression of several pathway components was noted in the muscle-less mouse, indicating that the pathway may have altered activity in immobilised embryos (Rolfe et al., 2014). Additionally, the phenotype observed when the pathway inhibitor Noggin is removed is similar to the immobilisation phenotype (i.e. joint fusion) (Brunet et al., 1998, Ray et al., 2015). To assess BMP pathway activity at the joint, immunolocalisation of pSMAD1/5/8, the active form of the transcriptional activator of the BMP pathway, was performed (Fig. 3.11). Overall higher levels of pSMAD1/5/8 were detected in the muscle-less rudiments at the elbow joint, compared to wildtype (Fig. 3.11a-d). In the wildtype, pSMAD1/5/8 detection was restricted to the subchondral cartilage at a distance from the joint line; the presumptive articular region contained little to no detectable protein (Fig. 3.11a', c'). Contrastingly, pSMAD1/5/8 was detected at high levels, extending up through the articular region in the muscle-less mutant, as well as in the subchondral cartilage (Fig. 3.11b', d'). Interestingly, immunolocalization of Noggin revealed overall higher levels of protein in mutant rudiments compared to wildtype (Fig. 3.11e, f) with a similar expansion in the region of the joint.

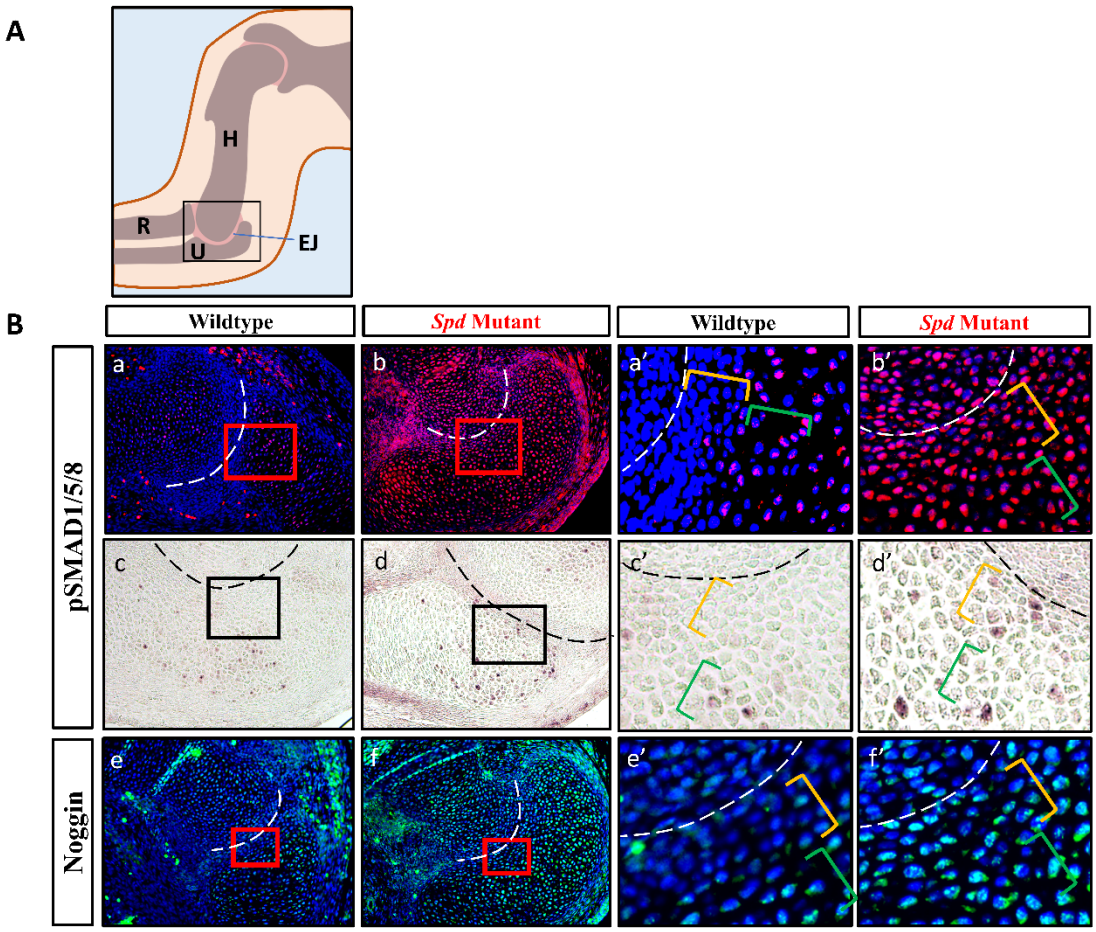

Fig. 3.11. Immunolocalisation of pSMAD1/5/8 and Noggin protein at the wildtype and muscle-less mutant elbow joint. Immunolocalisation of pSMAD1/5/8 and Noggin protein highlighted changes in protein localisation at the elbow joint. Images shown represent the elbow joint (EJ), as indicated by the boxed-in area in (A), specifically the joint formed by the humerus (H), and ulna (U), although comparable changes were also seen at the joint formed by the humerus and radius (R). Fluorescent and colourimetric (alkaline phosphatase) immunolocalisation (B) was carried out on paraffin sections (10 µm). Wildtype sections (a, a', c, c', e, e') were compared to corresponding *Pax3*$^{Spd/Spd}$ mutant sections (b, b', d, d', f, f'), for pSMAD1/5/8 and Noggin protein detection, as indicated. Red and black boxes in (a-f) indicate regions of higher magnification in (a'-f', respectively). Yellow brackets indicate presumptive articular cartilage; green brackets indicate sub-chondral cartilage.

3.3 Discussion

The work presented in this chapter sought to conduct a more comprehensive analysis of Wnt and BMP signalling in the developing mouse forelimb skeleton at a key stage of skeletogenesis which is sensitive to mechanoregulation from movement. Most strikingly, it showed that Wnt and BMP pathway activity is altered at the joint line in muscle-less mouse embryos, similarly to immobilised chick. While Wnt activity at the joint is lost under immobilisation, BMP activity is expanded to the joint line, indicating that misregulation of pathway activities could explain some of the phenotypic effects which are observed at the joint under reduced mechanical stimulation and a reciprocal relationship across the regulation of these two key pathways, co-ordinatedly regulated by movement.

Using analysis of transcriptomic data, this study identified potential genes for detailed spatial localisation analysis via *in situ* hybridisation. This revealed novel patterns of expression for several Wnt pathway components, including the ligands, receptors, and other key pathway proteins, expanding our knowledge of the molecular components involved. As a group, Wnt-encoding genes were expressed at relatively low levels, but showed more localised patterns of expression, while the Fzd-encoding genes had higher read counts but with the exception of *Fzd3* and *Fzd6* had no observable expression patterns. This could be due to more widespread expression of Fzd receptor-encoding genes in the developing rudiments and joints, which would result in overall higher read counts. Notably, the transcriptomic approach, which compared muscle-less ($Pax3^{Spd/Spd}$) humeri and associated joints to wildtype, identified pathway genes which were differentially regulated in the muscle-less mutant and therefore particularly interesting genes to examine by *in situ* hybridisation. This revealed that several key components of Wnt signalling, including the *Wnt4* ligand and *Sfrp*2 antagonist, were altered under reduced mechanical stimulation. A particularly striking finding was increased expression of several genes at the peripheral margins of the joint. Further investigation of this area showed an increase in size of this region in the muscle-less mutant, identifying the peripheral joint as a potentially important cellular region during skeletal differentiation. Examination of the β-catenin effector of the Wnt pathway also confirmed that the pathway is active in a restricted territory during skeletal development, and that this is altered under immobilisation.

Cross-comparison of transcriptomic data for mechanosensitive genes with articular-cartilage specific genes allowed for the identification of genes (*Boc*, *Col26aI*, and *Tppp3*) that are active at the joint and which are impacted by reduced mechanical stimulation. All three genes displayed reduced expression at the joint line itself, but both *Boc* and *Col26aI* showed increased expression at the peripheral joint, again emphasising the potential importance of this region to joint development. BOC is a cell-surface receptor which can bind all three mammalian Hedgehog ligands (Kavran et al., 2010) and is expressed in the early cartilage condensations of the limb buds, where it is thought to mediate cell-cell interactions essential for aggregation (Mulieri et al., 2002). Specific expression in the presumptive articular cartilage has previously been shown in horse and chick (Vanderman et al., 2011, Singh et al., 2016), but the expression presented here is the first description in mouse. More importantly this is the first description of *Boc* expression as mechanosensitive, and the peripheral expression of *Boc* is also novel. *Tppp3* encodes a tubulin-polymerising protein which whose expression was previously reported in the sheaths of developing tendons and transiently in the cavitating elbow joint, and was suggested to demarcate between anatomically distinct entities, such as articulating rudiments (Staverosky et al., 2009); it has not previously been identified as a mechanosensitive gene. *Emid2/Col26aI* encodes a little-studied member of the collagen family (Sato et al., 2002), that has not previously been localised to the articular cartilage, nor linked to mechanical regulation. These novel gene expression descriptions, and their identification as mechanosensitive, contributes new knowledge of articular cartilage composition, suggests how mechanical cues are essential to patterning of this tissue, and further emphasises the role of peripheral cells in the formation of joint tissues.

Activity of the BMP pathway was examined in the context of joint development and immobilisation, and, like Wnt, was revealed to be differentially active under immobilisation. However, conversely to Wnt signalling, the territory of active BMP signalling was expanded in this context. Altogether, these results offer a comprehensive and integrated view of Wnt and BMP signalling during a key stage of skeletal development, when the elbow and shoulder joints are forming and when ossification of the long bones commences. It also offers insight into how signalling is disturbed upon the loss of movement, and how this correlates to mis-patterning of tissues during skeletogenesis.

Wnt and BMP signalling at the joint is spatially localised and complimentary, and this localisation is sensitive to embryonic movement. This study characterised the localised activity of the Wnt and BMP signalling pathways around the developing joint. Specifically, during normal embryonic movement canonical Wnt/β-catenin signalling is active at the joint, while BMP signalling via its pSMAD1/5/8 effector, is reduced or absent at and near the joint and the presumptive articular cartilage but is active in adjacent transient cartilage (Fig. 3.12). This localised signalling activity has the potential to simultaneously coordinate the differentiation of joint tissues (articular cartilage and the synovial cavity) and of transient cartilage which forms endochondral bone. Under immobilisation, this balance is disturbed: canonical Wnt signalling is reduced while the territory of cells with detectable BMP signalling is expanded to the joint (Fig. 3.12). The altered expression of articular cartilage-specific genes under immobilisation revealed here (Section 3.2.2) further characterises the tissue mis-patterning effects seen under reduced mechanical stimulation. Furthermore, working in collaboration with the Bandyopadhyay lab, we showed that these changes are common to the mouse and chick models.

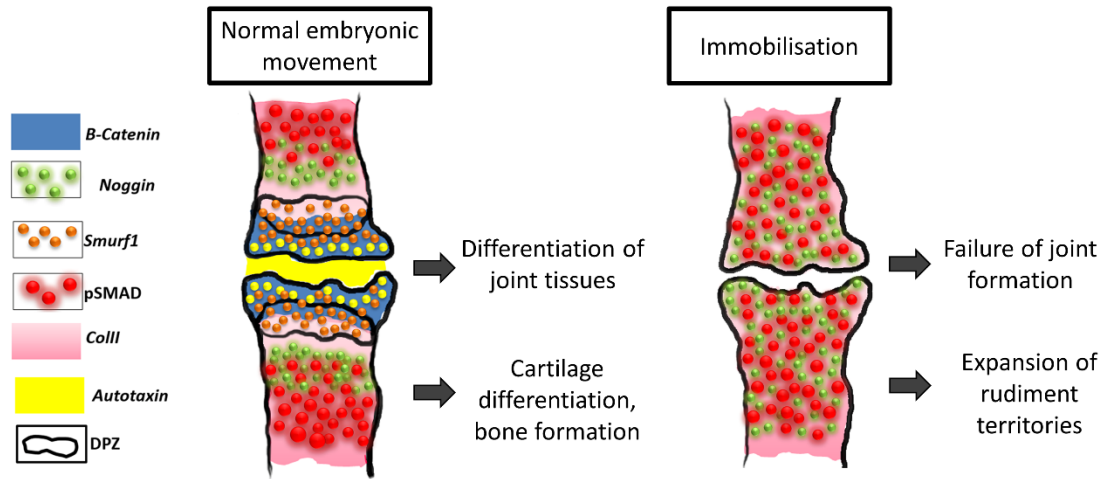

Fig. 3.12. Model for signalling pathway activity and regulation at the joint in normal and immobilised embryos. Normal differentiation of adjacent joint and bone tissues requires localised Wnt and BMP signals. During normal embryonic movement, canonical Wnt/β-catenin signalling (blue shading) is localised to the chondrogenous layers of the joint; this joint-specific expression is reduced or lost under immobilisation. Conversely, BMP activity via pSMAD1/5/8 (red dots) is confined to the transient cartilage, or future bone. Noggin (green dots) is also localised to the transient cartilage. Under immobilisation, both pSMAD and Noggin are detected at higher levels throughout the rudiments. In both wildtype and mutant, chondrocytes express *Col2aI* (pink shading); in the mutant, the failure of joint formation results in *Col2aI* territories

which are closer together. Failure of joint formation also results in the loss of other joint-specific markers such as Autotaxin (yellow shading). (Taken from Singh et al. (2018)).

A surprising finding was the concomitant increase of detectable pSMAD1/5/8 and Noggin protein under immobilisation. Noggin is a well-characterised inhibitor of BMP signalling (Zimmerman et al., 1996), and a reduction in Noggin activity at the joint was hypothesized as a mechanism for increased BMP signalling. However, Noggin expression can also be induced by BMP signalling (Sela-Donenfeld and Kalcheim, 2002) and so it follows that the observed increase in Noggin levels could be the result of increased pSMAD1/5/8 transcriptional activity. This indicates that upregulation of BMP activity at the immobilised joint is under the control of a mechanism distinct from Noggin antagonism. Smurf proteins, which directly regulate pSMAD activity, could constitute such a mechanism, and are discussed below.

Expression of Wnt pathway components in novel, previously unreported territories. Comprehensive assessment of Wnt and Fzd gene expression in skeletal rudiments at E14.5 revealed several novel regions of gene expression as well as confirmed known expression patterns. The combination of transcriptomic and *in situ* hybridisation data presented here was an unbiased approach which sought to examine previously undetected or under surveyed genes in the context of skeletal development. Detection of *Wnt2* and *Wnt2b* expression in humeral transcriptomics was a surprise. By *in situ* hybridisation, low level expression of *Wnt2* and *Wnt2b* were detected in the perichondrium, and this was corroborated by data retrieved from the EurExpress database. Low-level *Wnt2* expression in this study compared to very strong staining in the EurExpress data is surprising, and could be explained by extended development of the EurExpress sections which are part of a high-throughput survey and may contain high background staining. While *Wnt2* was detected by the transcriptomic analysis of *Spd* tissue, both mutant and wildtype, the read counts were not high in comparison to other genes and could explain the low detection in this study, despite the observation that both genes were significantly upregulated in the muscle-less mutant humerus. During postnatal skeletal development, *Wnt2* is expressed in adult osteoblasts (Zhong et al., 2012), so it is possible that the gene also has a role in formation of the embryonic skeleton, and reveals a novel potential role for *Wnt2* and *Wnt2b*.

Wnt9a was similarly detected in the perichondrium by *in situ* hybridisation and EurExpress data further corroborated this finding; previously, descriptions of *Wnt9a* expression were limited to the joints (Hartmann and Tabin, 2001, Spater et al., 2006). A surprising result of the survey of Frizzled ligands is that few Fzd genes had specific, or in some cases, even detectable, expression patterns. Given the high read counts for all Fzd family members (Fig. 3.2B), we expected more members to have specific expression in the developing skeleton. However, a high read count can be an indicator of general expression, which could be the case here. Although *Wnt4*, *Wnt9a*, and Wnt16 have well-characterised expression at the joint (Hartmann and Tabin, 2001, Guo et al., 2004, Spater et al., 2006, Witte et al., 2009), the Fzd receptors which mediate their activity have not been identified. The observed joint-specific expression of Fzd3 and Fzd6 which is presented here is therefore novel, and suggests that these two could be key regulators of Wnt signalling at the joint.

Cells peripheral to the joint express multiple Wnt pathway components: the significance of these cells in joint development. The screen of Wnt pathway components in the muscle-less vs. wildtype forelimb skeleton identified several regions of interest where expression of multiple pathway components was observed. One such region is the peripheral joint territory at both the shoulder and elbow (Fig. 3.5B). Expression of *Wnt4*, *Sfrp2*, *Fzd3*, and *Fzd6* was noted here, as well as *Boc*, *Tppp3*, and *Col26aI*. Histological staining of forelimb sections by Mallory's Trichrome did not reveal any obvious difference in tissue organisation present in wildtype and muscle-less mutant; however, the territory of peripheral cells appears enlarged in the mutant when compared to the wildtype (Fig. 3.5B). As described in Section 1.2, during joint development cells at the interzone are specified within the mesenchymal condensation which prefigures the rudiments; cells at the interzone subsequently differentiate into distinct joint tissues. However, cells from outside the joint territory have been shown to migrate into the joint after interzone specification to contribute to joint tissues. Hyde et al. (2008) observed *Col2aI*-negative cells originating from outside the interzone migrating into the territory of the knee meniscus by E14.5 and later expressing *Col2aI*. Likewise, Pacifici et al. (2006) used DiI to label cells adjacent to the joint and observed these cells within the articular cartilage and joint capsule at later stages. The same group noticed that in *Ihh*-null mutants, *Gdf5*-positive cells which are normally localised to the joint interzones were restricted to either side of continuous digit anlagen

(Koyama et al., 2007). They hypothesised that under normal *Ihh* signalling, the anlagen become discontinuous and *Gdf5*-positive cells migrate into the joint territory. The role of *Gdf5*-positive cells was further elaborated by Shwartz et al. (2016), who used a knock-in *Gdf5-CreER*^{T2} mouse and a range of tamoxifen pulse-chase timings to track the different lineage contributions of cells expressing *Gdf5* over time. They noted the presence of these cells outside the forming joint territory, and their subsequent contribution to the menisci, ligaments, and epiphyseal and articular cartilages.

It is possible that under reduced mechanical stimulation, these *Gdf5*-expressing cells fail to migrate to the joint territory and that this contributes to the failure of joint formation under immobilisation. In the *Spd* mutant mouse, expression of *Gdf5* is lost at the shoulder and elbow joints (R. Rolfe, unpublished data). This could be explained by a failure of *Gdf5*-expressing cells to migrate into the joint and differentiate to joint tissues, loss of *Gdf5* in cell populations contributing to the joint territory, or both. The observed increased expression of several Wnt and BMP-related genes in the peripheral cell territory (*Wnt4*, *Sfrp2*, and *Col26a1*) suggests that these signalling pathways may be active in peripheral cell migration; indeed, GDF5 is a TGF-β family member, closely related to BMP ligands (Storm and Kingsley, 1999).

Alteration of signalling activity tests the functionality of pathways *in vivo*. BMP pathway activity can be regulated at multiple levels: Noggin is a receptor-level antagonist, while Smurfs function further downstream in the BMP pathway. Smurf1 and Smurf2 are E3 ubiquitin-protein ligases which interact with BMP-specific SMADs, leading to their ubiquitinylation and degradation (Zhu et al., 1999, Lin et al., 2000). As part of a collaboration with the Bandyopadhyay laboratory examining immobilisation in chick joint development this group has shown that in chick, *Smurf1* is well-expressed in the rudiments and across the joint territory at the knee, and this expression is lost in immobilised chick (Fig. 3.13Ba-a'). *Smurf2* expression in the chick knee is localised to the articular cartilage; again, this expression is lost under immobilisation (Fig. 3.13C, b-b'). Although no specific expression pattern of *Smurf1* was observed in either wildtype or muscle-less mouse, *Smurf1* and *2* had high read counts in both wildtype and mutant tissue as detected by RNAseq (>1000 reads in all cases) and could be expressed in a more widespread pattern in the mouse. Neither gene was significantly differentially expressed in the muscle-less mutant transcriptome, although localised downregulation which is below the detection level of *in situ* hybridisation could explain

this. Alternatively, Smurf regulation of pSMAD activity could operate differently between the mouse and chick models, necessitating identification of an alternate mechanism for regulation of BMP activity in the mouse.

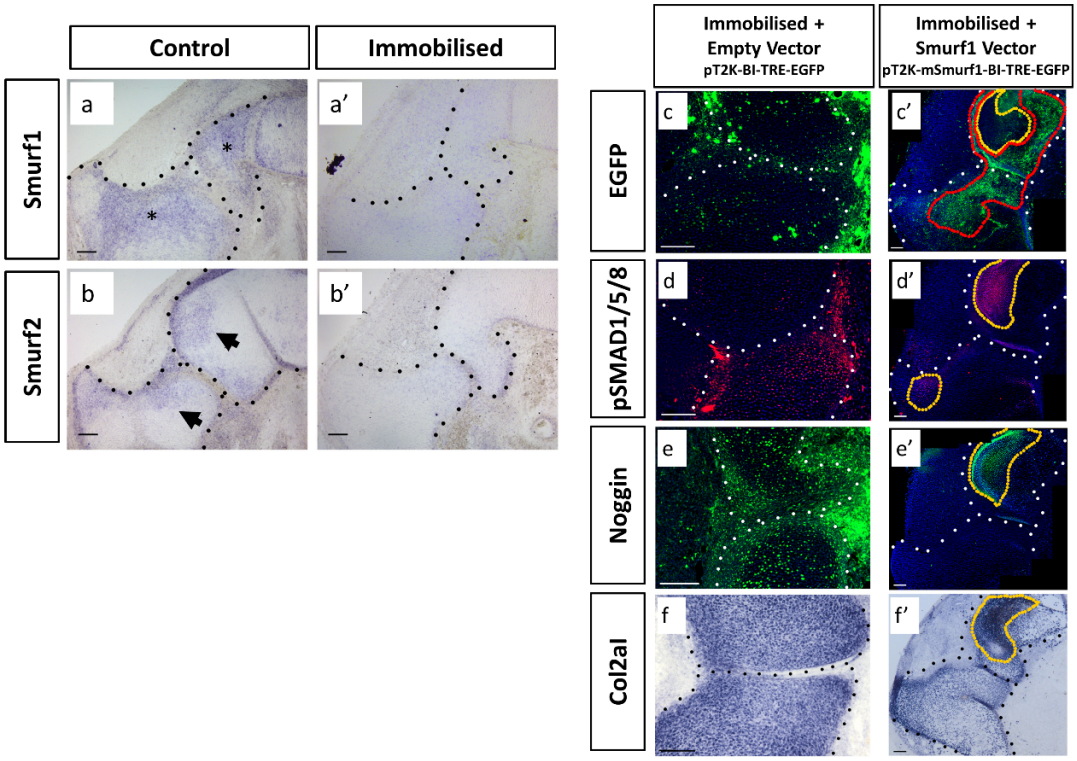

Fig. 3.13. Smurf expression and activity at the chick knee. In the chick knee, Smurf1 and Smurf2 are expressed in the presumptive articular cartilage and across the knee joint (a, b; asterisks and arrows). Under immobilisation, this expression is reduced or lost (a', b'). Immobilised control-electroporated chicks show the expected high levels of pSMAD1/5/8 and Noggin proteins, and *Col2aI* gene expression at the chick knee. Electroporation of immobilised chicks with an inducible Smurf1 vector (Fig. A.2) generated specific territories of Smurf1-positive cells which had reduced pSMAD1/5/8, Noggin, and *Col2aI* (area outlined in red, c') and Smurf1-negative cells which had high levels of pSMAD1/5/8, Noggin, and *Col2aI* (area outlined in yellow, c'-f'). (Adapted from Singh et al. (2018)).

To directly test the role of Smurf in pSMAD1/5/8 regulation in the chick joint, the Bandyopadhyay group has carried out electroporation of an inducible Smurf1 plasmid in the chick lateral plate mesoderm at E2, followed by immobilisation at E4.5-7.5, and doxycycline induction carried out at E7 when the joints begin to cavitate. These chicks were compared to immobilised chicks electroporated with an empty vector (both the empty and Smurf1 vectors were bi-directional and also encoded an EGFP protein as a

reporter) (Fig. A.2). As expected, immobilised controls had detectable pSMAD1/5/8 and Noggin protein as well as expression of *Col2aI* at the knee joint (c-f). In the immobilised experimental chicks, the territory electroporated with Smurf1 (as detected by EGFP; area outlined in red in Fig. 3.13c') was devoid of detectable pSMAD1/5/8 or Noggin and had lower levels of *Col2aI* expression (c'-f'). Conversely, the territory in which cells had not taken up the construct was enriched for pSMAD1/5/8, as well as *Col2aI* expression (area outlined in yellow, Fig. 3.13c'-f'). This demonstrates that Smurf1 can regulate pSMAD1/5/8 stability *in vivo*, in this tissue at a crucial stage of patterning, suggesting it as a possible mechanism for regulation of BMP signalling activity which is affected by reduced embryonic movement.

Separately, we sought to ectopically activate or inhibit Wnt signalling in a localised manner via *ex ovo* electroporation of chick forelimbs. However, despite a large number of embryos electroporated, those surviving until harvest and displaying appropriate GFP expression were limited, thereby reducing the number of specimens analysed and presented in this study. While a useful tool, this approach was limited by the difficulty of precisely microinjecting the plasmids into the desired tissue. This was likely due to the high cell density and complex extra cellular matrix in cartilage rudiments at the time of electroporation (E5, approx. HH25-26), which doesn't allow for introduction of a liquid solution the way that a cavity (such as the neural tube, a popular tissue for electroporation) does, without risk of damaging the embryo. Early electroporation into the entire limb field of the lateral plate mesoderm, coupled with the use of an inducible plasmid, such as the doxycycline-inducible plasmid utilised for Smurf1 electroporation (Fig. 3.13) (Singh et al., 2018), is an alternative which avoids this problem. In that approach, the plasmid is microinjected into the coelom underlying the lateral plate mesoderm, and an electrical current is passed through such that the plasmid is electroporated into cells at the site of the future fore- or hindlimb bud (Suzuki and Ogura, 2008). The transcription of the plasmid is induced at the desired time by treating the embryos with doxycycline (Sato et al., 2007). Despite the challenges inherent in our electroporation approach, and the very limited number of informative specimens in these experiments, the data presented here support our hypothesis for Wnt signalling activity during joint development. Here, selected specimens showed that ectopic Sfrp3 co-localised with observed fusion of rudiments, while a constitutively activated form of β-catenin electroporated territory corresponded to an enlargement of

the joint territory. As a control, sham-electroporated forelimbs did not display phenotypic effects. These data agree with the observation that rudiment fusion in the immobilised mouse corresponds to a loss of Wnt activity in this region. To further test this hypothesis, more localised control of either activation or inhibition of Wnt pathway activity, for example through use of early electroporation and inducible plasmids, would be needed. Alternately, the combination of Wnt reporter lines (such as the Tcf/LEF:H2B-GFP reporter utilised here) with immobilisation models could offer a direct method for assessment of Wnt activity in the context of reduced mechanical stimulation.

Conclusions. While Smurf proteins represent a possible mechanism for regulating BMP activity during joint development, it remains unclear why these genes have a differential expression pattern under immobilisation. There must be a component upstream to Smurf that differentially regulates expression of these genes to affect downstream BMP signalling. Likewise, although this study confirmed differential expression of a number of Wnt components and altered Wnt signalling activity under reduced movement, it does not identify a mechanotransductive mechanism. Still missing from our understanding of gene and protein regulatory changes under immobilisation is a means for mechanical stimuli to contribute to these changes. Such a mechanotransductive mechanism could potentially broadly regulate gene expression and protein stability, integrating morphogens with localised mechanical cues to regulate specific tissue differentiation events. Two such mechanotransductive mechanisms are investigated in the following chapters.

Chapter 4

Investigation of a candidate mechanism of mechanotransduction in the developing skeleton: The Hippo-YAP pathway

4.1 Introduction

The Hippo signalling pathway has been well-characterised in *Drosophila* as a regulator of organ size and cellular proliferation and has been implicated in responding to the physical environment of cells in a number of contexts (reviewed in Section 1.5.1). Its effector molecule, Yorkie (Yki) regulates the transcription of downstream target genes affecting cellular proliferation and differentiation, thereby balancing the growth and maturation of tissues. Upstream control of the Hippo pathway in *Drosophila* comes from the Fat (Ft) membrane receptor, which regulates the kinase cascade responsible for Yki activity (Fig. 4.1).

Homologs of many *Drosophila* Hippo pathway components have been identified in mammalian systems, including the Yki homologs YAP and TAZ (Huang et al., 2005). The pathway is active in regulating cellular proliferation and differentiation, similar to its activity in *Drosophila* (Zhao et al., 2010, Yu et al., 2015). At its core is a functional kinase cascade, composed of MST1/2 and LATS1/2, which regulates YAP and TAZ in a way homologous to the regulation of Yki by the *Drosophila* orthologues Hippo (Hpo) and Warts (Wts) (Fig. 4.1). Numerous other proteins are also involved in regulating YAP/TAZ phosphorylation in a complex manner (Fig. 4.1; reviewed in Yu et al. (2015)). In *Drosophila*, the cell membrane protocadherin Fat, which is involved in planar cell polarity, activates Hippo signalling (reviewed in Oh and Irvine (2010)). Although there are three other Fat orthologues in mouse (Fat1-4), only *Fat4* is considered to be homologous to *Drosophila* Fat; Fat1-3 are orthologues to *Drosophila* Fat-like, which differs from Fat in its intracellular domain, and is not involved in the

Hippo pathway (Rock et al., 2005). Although *Fat4* is the orthologue of *Drosophila* Fat, and despite the otherwise general conservation of pathway components, there are questions over the involvement of mammalian *Fat4* in the Hippo pathway because mutations in *Fat4* do not affect YAP or LATS1 protein levels in mouse (Mao et al., 2011). This relationship needs to be further explored.

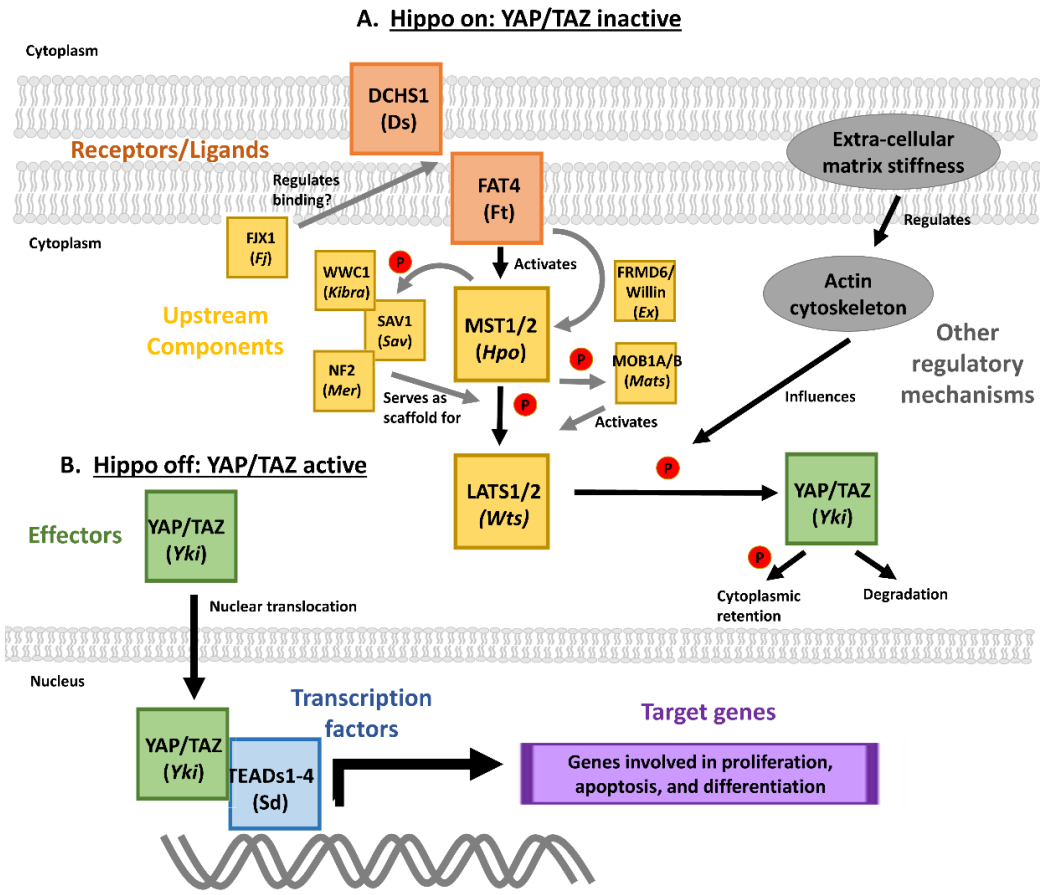

Fig. 4.1. Schematic representation of the canonical Hippo pathway, with alternative upstream regulatory mechanisms (grey). The core of the Hippo pathway consists of the kinase molecules MST1/2 (*Drosophila* Hippo) and LATS1/2 (Warts), and the target(s) YAP/TAZ (Yorkie), which can either be inactivated by phosphorylation (A) or, in the unphosphorylated form, can translocate to the nucleus to activate downstream target genes (B). The role of other regulatory proteins and pathway components are noted (with homologs in *Drosophila* indicated in brackets). Outside of this canonical kinase cascade, YAP/TAZ phosphorylation status can be regulated by the cytoskeleton, which is influenced by cell attachment and other extra-cellular environmental influences (shown in grey). Different levels of the pathway (receptors/ligands, upstream components, effector molecules, transcription factors, and target genes) are indicated, and are grouped and colour-coded according to a scheme that will be used throughout this work, as indicated on the figure (e.g. effectors in green). Based on literature reviewed in Zhao et al. 2012.

The extent to which YAP/TAZ are regulated through the core, "canonical" kinase cascade or may additionally be regulated by alternative mechanisms is also unclear, particularly in the context of a mechanical response. Other components of the mammalian pathway are regulated outside the core kinase cascade: for example, in MCF10A cells, LATS1/2 was shown to be phosphorylated independent of MST1/2 activity; LATS1/2 activity was instead dependent on cell detachment from an ECM substrate (Zhao et al., 2012). Here, the F-actin and microtubule cytoskeletons were implicated in phosphorylation, and therefore activity, of YAP. Several studies have likewise noted the role of the cytoskeleton in regulation of YAP/TAZ activity outside of, or in conjunction with, the canonical Hippo cascade (Dupont et al., 2011, Aragona et al., 2013, Rauskolb et al., 2014). In this work, the term (canonical) Hippo signalling is used to refer to the core kinase cascade of MST1/2 and LATS1/2 and their inhibition of YAP/TAZ signalling activity. In this work, therefore, the term YAP/TAZ signalling is used to indicate the activity of these components which may be regulated by mechanisms outside the canonical Hippo kinase cascade, or where upstream regulation is not clear.

In particular, mechanical forces have been demonstrated to regulate YAP/TAZ activity independent of the canonical pathway. Cytoskeletal tension is dependent on intra- and extracellular forces which are generated by the cellular environment. Indeed YAP/TAZ phosphorylation and subcellular localisation were shown to be regulated by the rigidity of the extra cellular matrix as well as cell shape (Hong et al., 2005, Dupont et al., 2011). Further, the level of YAP/TAZ activity contributed to the differentiation fate of mesenchymal stem cells: a rigid environment and more nuclear YAP/TAZ promoted osteogenesis, while softer matrices and cytoplasmic YAP/TAZ promoted adipogenesis (Engler et al., 2006, Halder et al., 2012). Therefore, YAP/TAZ have the potential to serve as a focal point for the transduction of mechanical signals to gene expression, and in this way to regulate cellular differentiation. In the developing skeleton, the observed phenotypic and genetic changes that occur under reduced mechanical stimulation could be the result of altered activity of this pathway. Therefore, the work reported in this chapter, examined aspects of the Hippo pathway in the embryonic forelimb at key stages of limb development, and investigated if aspects of the pathway(s) and their activities were changed in the *Pax3*$^{Spd/Spd}$ (muscle-less) mutant.

The implication of YAP/TAZ phosphorylation state and nuclear localisation in controlling the differentiation of mesenchymal stem cells suggests that these pathway effectors and their upstream regulation could play a similar role in the differentiation of progenitor cells during organogenesis. However, there are relatively few descriptions of components of these pathways in mammalian tissues. In early embryonic development, nuclear YAP/TAZ distinguishes cells of trophectoderm from those of the inner cell mass (which have cytoplasmic (inactive) YAP/TAZ) (Nishioka et al., 2009). The developing kidney requires the function of both YAP and TAZ, although the two effector molecules appear to operate differently here (YAP is active during nephron morphogenesis while TAZ inactivity causes polycystic kidney disease). YAP activity has been demonstrated in the developing heart, where it regulates cardiomyocyte proliferation (Von Gise et al. 2001). It is clear that YAP (and TAZ) have context dependent functions. For example, mutations in YAP/TAZ, as well as constitutively high levels of YAP/TAZ activity, have been linked to the misregulation of proliferation in certain types of cancers (Zanconato et al., 2015). This correlates with Yki's known role as a regulator of organ size and progenitor cell proliferation. However, although YAP/TAZ are frequently characterised as pro-proliferative, YAP has also been shown to be pro-apoptotic in human embryonic kidney cells (Oka et al., 2008). The subcellular localisation of YAP/TAZ in the early embryo, as mentioned above also implies that nuclear activity of these proteins can promote differentiation over pluripotency and proliferation. Such context-dependent functions underscore a need for careful characterisation of the pathway in different tissues and cell types. Indeed, the multiple upstream regulatory mechanisms of YAP/TAZ shows that signalling via these effector molecules is complex in mammalian systems and that different modes of YAP/TAZ signalling may be active in different cell types and tissues.

YAP and TAZ are paralogs and are frequently referred to as a functional unit. Although they have high structural similarity and conserved binding domains, there is evidence that they sometimes act opposingly (reviewed in Zhao et al., 2008a). YAP knockout mice are embryonic lethal at E8.5, and targeted deletion of YAP in cartilage cells results in longer bones and elevated hypertrophy (Morin-Kensicki et al., 2006, Deng et al., 2016). In contrast, TAZ knockout mice live to adulthood, albeit with slightly smaller skeletons and slightly reduced lifespans (Hossain et al., 2007). Double YAP/TAZ knockouts appear to be lethal prior to the morula stage (only one cross is

reported in the literature; heterozygote crosses generated no double mutants at the morula stage, where 6.25% was expected), confirming that these genes are not entirely redundant (Nishioka et al., 2009). The relatively normal adult skeletons of TAZ knockouts (Hossain et al., 2007) also suggests a limited role for TAZ in skeletogenesis compared to YAP. Because the work presented here focuses on YAP, the term Hippo-YAP signalling is used to refer to the pathway as it relates to the regulation of YAP transcriptional activity. Where upstream regulation of YAP is unclear or irrelevant, YAP activity is specifically referred to.

Only two partial descriptions of YAP expression and localisation in the developing skeleton exist in the literature to date, with apparent contradictory findings. Karystinou et al. (2015) described high levels of nuclear YAP in the perichondrium and high levels of phosphorylated, cytosolic YAP throughout the cartilage of E13.5 hindlimb phalanges. At a later stage (E16.5), they noted strong levels of nuclear YAP in pre-hypertrophic and hypertrophic chondrocytes, suggesting a role for YAP in driving chondrocyte maturation. Contrastingly, Deng et al. (2016) report higher levels of nuclear YAP in resting and proliferative chondrocytes compared to hypertrophic chondrocytes in E14.5 tibiae. They suggest that YAP inhibits hypertrophy by negatively regulating *Col10aI*. Both studies report decreasing YAP expression over time in high-density culture of adult human MSCs (Karystinou et al. 2015) or the chondroprogenitor cell line ATDC5 and embryonic limb bud cells (Deng et al. 2016). Similarly, both studies report that YAP inhibits chondrogenesis *in vitro*. While indicating that YAP regulation is important during skeletal development, these studies also emphasise the need for clarification of the roles of YAP and Hippo during chondrogenesis and subsequent cartilage maturation and hypertrophy. Another important gap in our knowledge is the possibility of a link between YAP activation and the mechanical impact on skeletal development from embryo movement.

4.1.1 Aims of this chapter

The work presented in Chapter 3 revealed that complex molecular signalling networks, linking Wnt and BMP signalling, are active during skeletal development and cell signalling changes occur under altered mechanical stimulation. The Hippo-YAP/TAZ pathway is a relatively recently characterised pathway and as such, much of its functionality remains unknown, particularly in the context of skeletal development.

Chapter 3 revealed in particular that the activity of Wnt and BMP signalling networks is mechanosensitive, and that misregulation of cellular signalling correlates with phenotypic anomalies that occur under reduced mechanical stimulation. A major gap in current knowledge is the relationship between mechanical stimuli and gene regulation. The work presented in this chapter therefore set out to test the hypothesis that the Hippo-YAP pathway plays a role in mechanoregulation of skeletal development by examining components of the pathway in the developing limb rudiments and by comparing selected components in wildtype and muscle-less (*Pax3*$^{Spd/Spd}$) embryos.

Specific aims were:

1) *To establish which components of the Hippo-YAP pathway are expressed in an E14.5 developing skeletal rudiment and associated joints.* This was conducted by analysing transcriptomic (RNAseq) data for wildtype and muscle-less mutants.
2) *To characterise the pattern of localisation of the main effector molecule of the pathway, YAP, during skeletal development.* The pattern of protein distribution of YAP, as well as its phosphorylated (inactive) form was examined in wildtype and compared to muscle-less mutant forelimb tissue.
3) *To analyse the expression patterns of known target genes of the pathway.* The expression of recognised YAP target genes in the developing rudiments of both wildtype and muscle-less mutant embryos was assayed by *in situ* hybridisation and qRT-PCR, as a means of assessing YAP activity.
4) *To analyse the expression of, and therefore potential role for, the Fat4 receptor in skeletal development.* The gene encoding the *Fat4* receptor was selected as a candidate gene of particular interest in this context because a) it is a potential upstream mediator of the pathway b) it was found to be upregulated in muscle-less humeri and c) no expression data are available for the developing skeleton.
5) *To assess the role of YAP during chondrogenesis by manipulating YAP activity* in vitro. To functionally test the role of YAP in chondrogenesis, two approaches were applied to primary embryonic limb bud cells in micromass culture: 1) the small molecule Verteporfin, was used to inhibit YAP binding to TEAD transcription factors, and 2) YAP silencing RNA was used to inhibit YAP translation.

4.2 Results

4.2.1 Major components of the Hippo pathway are expressed in the developing skeletal rudiments.

To examine if known components of the Hippo pathway are expressed in the developing forelimb skeleton at E14.5, expression levels of canonical pathway components and reported pathway target genes were extracted from existing transcriptomic data sets for wildtype and muscle-less humeri and associated joints at E14.5 (Rolfe et al., 2014). The list of pathway components and target genes examined were compiled from relevant literature as laid out in Table 4.1. The genes are divided into subgroups according to the level of the pathway at which they operate (colour coded as indicated in Table 4.1; Fig. 4.1- Fig. 4.3). This specific analysis revealed that all investigated components of the Hippo signalling pathway, as well as all pathway target genes examined here, are expressed in the rudiments at E14.5 (Table 4.1, Fig. 4.2). Comparison of wildtype and muscle-less mutant transcriptomic read counts revealed that four genes were differentially expressed in the muscle-less mutant: the receptor *Fat4* (upregulated), the transcription factor *Tead4* (downregulated), and the pathway targets *Anrkd1* (downregulated) and *Col8aI* (upregulated). Differential expression was defined as more than 2-fold up- or down-regulated, with an adjusted p-value of < 0.05. Adjusted p-values were calculated according to the Benjamini and Hochberg procedure (Benjamini and Hochberg, 1995), which controls for the false discovery rate (FDR) (i.e. reduces false positives).

Table 4.1. Transcription of Hippo pathway component genes in E14.5 humeri as detected by RNAseq. Genes more than 2-fold up- or down-regulated, with an adjusted p-value <0.05 are indicated in red or blue, respectively.

Gene Symbol (synonym)	Full Gene name (synonym)	Role in mammals (Reference)	Drosophila homolog (gene symbol)	Wildtype reads	Mutant reads	Fold Change	Adjusted P-value
RECEPTORS/LIGANDS							
Fat4	FAT atypical cadherin 4	Similar cytoplasmic domain to *Drosophila Fat* (Tanoue and Takeichi, 2005); involved in PCP pathway (Saburi et al., 2008); role in Hippo unclear	FAT tumor supressor (Ft)	**4,367**	**12,916**	2.95	<0.0001
Dchs1	Dachsous cadherin-related 1	Interacts with *Fat4* to regulate PCP (Mao et al., 2011, Kuta et al., 2016); no clear role in Hippo	Dachsous (Ds)	**6,349**	**7,478**	1.18	0.8101
UPSTREAM COMPONENTS							
Fjx1	Four jointed box 1	Possibly regulates *Fat4*/Dchs1 binding (Rock et al., 2005)	Four-jointed	**980**	**689**	0.70	0.2893
Nf2	Neurofibromatosis type 2	Tumour suppressor which complexes with Kibra and Sav1 to inactivate YAP (Zhang et al., 2010b)	Merlin	**2,814**	**3,132**	1.11	0.8939
Wwc1 (Kibra)	WW and C2-domain containing protein 1 (Kibra)	Stimulates phosphorylation of LATS1/2 (Xiao et al., 2011)	Kibra	**188**	**176**	0.94	0.9896
Frmd6 (Willin)	FERM-domain containing protein 6	Activates MST1/2 (Angus et al., 2012)	Expanded (Ex)	**2,030**	**2,501**	1.23	0.5679
Sav1	Salvador homolog 1	Associates with MST1/2, promotes LATS1/2 phosphorylation (Callus et al., 2006)	Salvador	**1,898**	**1,795**	0.95	0.9909
Mob1a (Mobkl1a)	MOB kinase activator 1A	Phosphorylation by MST1/2 allows for binding/activation of LATS1/2 (Praskova et al., 2008)	Mob as tumor suppressor (Mats)	**358**	**375**	1.05	1.0000
Mob1b (Mobkl1b)	MOB kinase activator 1B			**878**	**1289**	1.46	0.6650

Gene Symbol (synonym)	Full Gene name (synonym)	Role in mammals (Reference)	Drosophila homolog (gene symbol)	WT reads	Mut reads	Fold Change	Adjusted P-value
Mst1 (Stk4)	Mammalian sterile 20-like 1 (Serine/ threonine-protein kinase 4)	Phosphorylates LATS1/2, MOB1A/B, and SAV1 (Chan et al., 2005, Callus et al., 2006, Praskova et al., 2008)	Hippo (Hpo)	1,225	1,429	1.16	0.8174
Mst2 (Stk3)	Mammalian sterile 20-like 2 (Serine/ threonine-protein kinase 4)	Phosphorylates LATS1 (Chan et al., 2005, Oka et al., 2008) and LATS2 (Oka et al., 2008)		921	951	1.04	>0.9999
Lats1	Large tumor suppressor homolog 1	Phosphorylates YAP (Oka et al., 2008)	Warts (Wts)	2,099	2,883	1.38	0.4693
Lats2	Large tumor suppressor homolog 2			1,633	2,208	1.35	0.3197
CORE COMPONENTS							
Yap1	Yes-Associated Protein 1	Transcriptional co-activator/effector of the Hippo pathway (Yagi et al., 1999, Huang et al., 2005, Zhang et al., 2010b)	Yorkie (Yki)	4,857	5,121	1.06	>0.9999
Taz (Wwtr1)	Transcriptional activator with PDZ-binding motif (WW-domain containing transcription regulator 1)	Transcriptional co-activator/effector of the Hippo pathway (Lei et al., 2008)		4,107	4,081	0.99	0.783
TRANSCRIPTION FACTORS							
Tead1 (Tef1)	TEA-domain family member 1 (Transcriptional enhancer factor 1)	TEA-domain transcription factors bound by YAP/TAZ (Zhao et al., 2008b)	Scalloped (Sd)	2,966	2,919	0.99	0.9916
Tead2 (Tef4)	TEA-domain family member 2 (Transcriptional enhancer factor 1)		Scalloped (Sd)	3,800	2,819	0.74	0.5507
Tead3 (Tef5)	TEA-domain family member 3 (Transcriptional enhancer factor 1)			919	953	1.04	>0.9999
***Tead4* (Tef3)**	TEA-domain family member 4 (Transcriptional enhancer factor 3)			265	69	0.26	<0.0001

Gene Symbol (synonym)	Full Gene name (synonym)	Role in mammals (Reference)	Drosophila homolog (gene symbol)	WT reads	Mut reads	Fold Change	Adjusted P-value
Vgll4	Vestigial-like family member 4	Transcription factor which competes with TEADs to bind YAP/TAZ and inhibit transcriptional activity (Guo et al., 2013)	Scalloped-binding protein/Tondu domain-containing growth inhibitor (SdBP/Tgi)	531	913	1.72	0.0419
DOWNSTREAM TRANSCRIPTIONAL TARGETS							
Ankrd1	Ankyrin repeat domain-containing protein 1	Skeletal muscle component; target of YAP (Zanconato et al., 2015)		233	2	0.01	0.0001
Birc5	Baculoviral inhibitor of apoptosis repeat-containing 5 (Survivin)	Inhibitor of apoptosis; target of YAP (Dong et al., 2007)		1,775	1,223	0.69	0.6008
Ctgf (Ccn2)	Connective tissue growth factor (CCN family member 2)	Heparin-binding matricellular protein; target of YAP (Zhao et al., 2008b)		2,714	3,633	1.34	0.6374
Cyr61 (Ccn1)	Cystein-rich angiogenic inducer 61 (CCN family member 1)	Promotes endothelial cell adhesion; target of YAP (Zhang et al., 2008)		2,658	3,146	1.18	0.6374
Inha	Inhibin alpha	FSH secretion inhibitor; target of YAP (Piccolo et al., 2014)		197	123	0.62	0.4949
Axl	AXL receptor kinase	Tyrosine kinase; target of YAP (Zanconato et al., 2015)		5,409	6,671	1.23	<0.0001
Col8a1	Collagen VIII alpha I	Structural component of extra-cellular matrix; target of YAP (Zhang et al., 2008)		1,879	4,312	2.30	0.0001

Fat4 and *Dchs1* ligand/receptor cell-membrane components were both highly expressed (>4,000 reads) in wildtype rudiments; additionally, *Fat4* was 2.96-fold upregulated in the mutant. Other intra-cellular components, acting upstream of YAP/TAZ (here, collectively referred to as upstream components), were more moderately expressed, ranging from approx. 200-3,000 reads in the wildtype. The core components (effector molecules) *Yap1* and *Taz* were highly expressed (>4,000 reads) in both wildtype and mutant. Among the transcription factors, *Tead1* and *Tead2* were more highly expressed (approx. 3,000-4,000 reads in wildtype and mutant), while *Tead3* was more moderately expressed (approx. 1,000 reads in wildtype and mutant). *Tead4* was expressed at a lower level than the other family members (265 reads) and was indicated to be significantly differentially expressed (downregulated 3.84-fold in the mutant); however the low read count in the wildtype could result in a false positive for differential expression. The competing transcription factor *Vgll4* was also moderately expressed in both wildtype and mutant (between 500 and 1,000 reads).

Examination of target genes revealed that *Ankrd1* had relatively low expression in both the wildtype and mutant (233 and 2 read counts, respectively), compared to the other five target genes, which had high read counts in both wild-type and mutant (approx. 1,000-7,000). Among the examined target genes, *Ankrd1* was significantly downregulated in the mutant (116.5-fold), while there were slightly fewer *Birc5* transcripts in the mutant (not significant). *Col8aI* was significantly upregulated (2.29-fold) while there were elevated transcript numbers for *Ctgf*, *Cyr61*, and *Inha* yet not significantly upregulated by the criteria used.

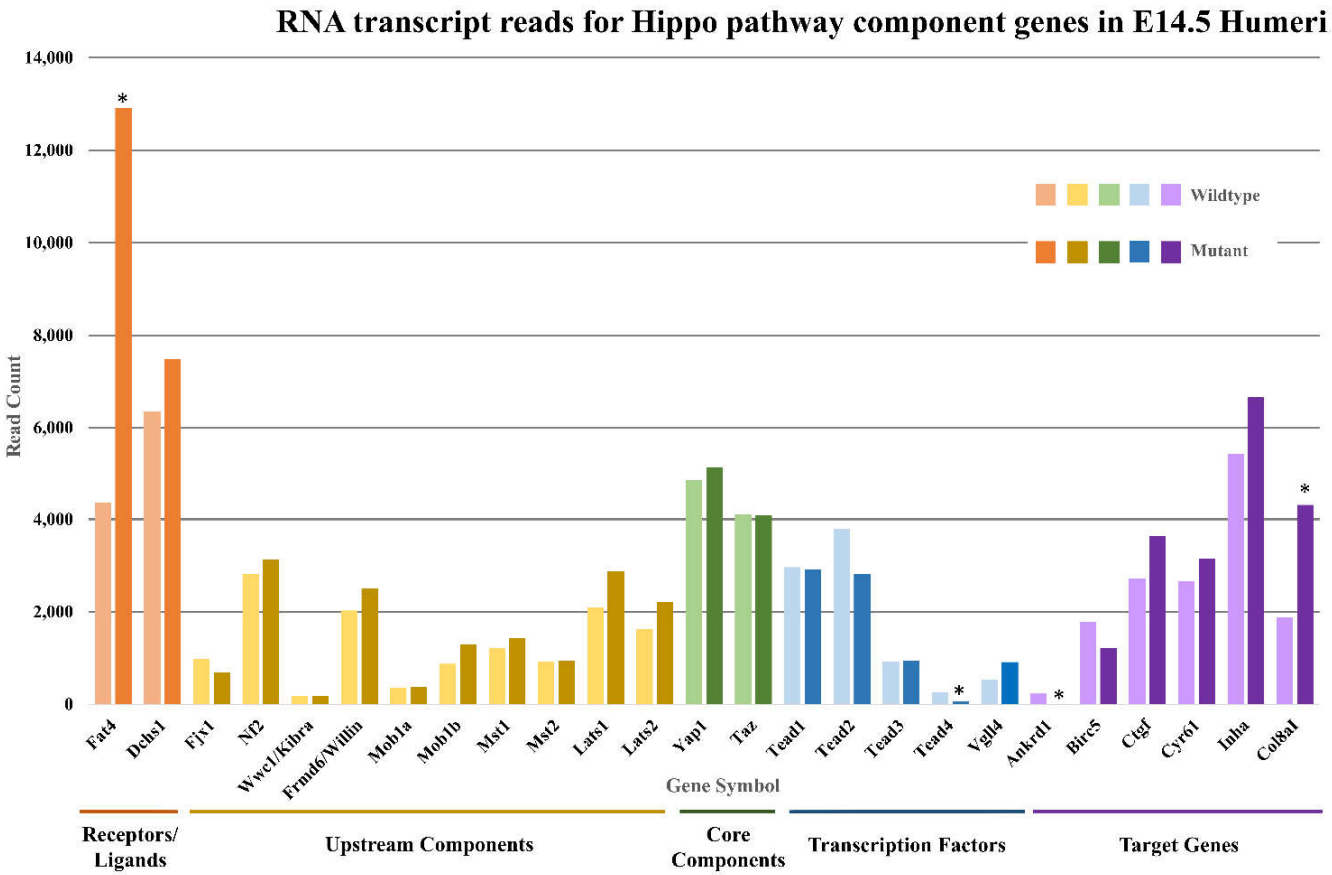

Fig. 4.2. Multiple components of the Hippo pathway are expressed in the E14.5 developing humerus and joints. Number of RNA transcript reads (y-axis) for Hippo pathway component genes (x-axis) in RNA extracted from E14.5 humeri, as detected by RNAseq. Genes are grouped according to the level within the pathway at which they operate. In each case the darker colour shows the read count in the muscle-less mutant tissue. Genes which were significantly (adjusted p-value < 0.05) differentially expressed more than 2-fold up or down in the mutant are indicated by asterisks.

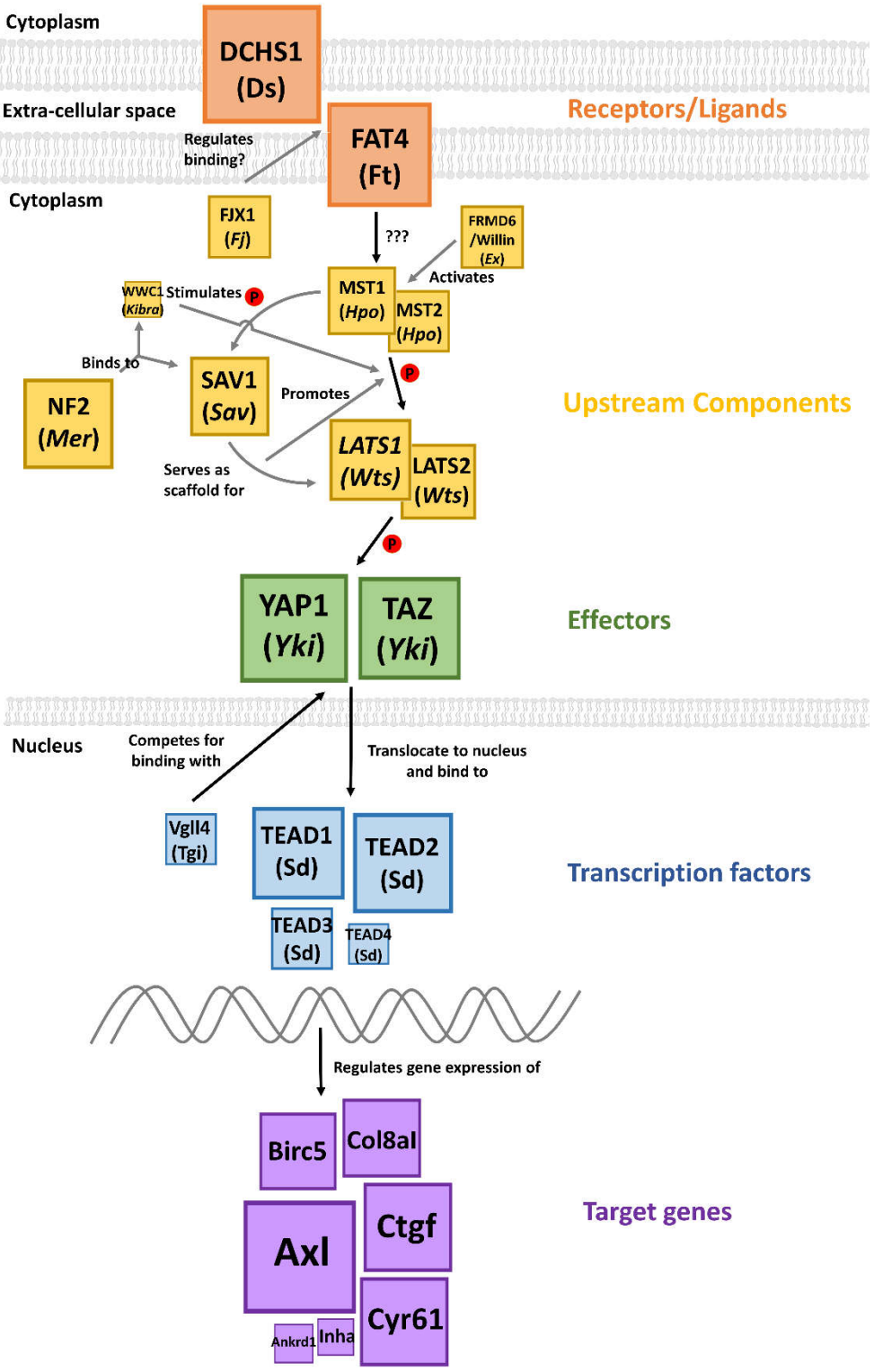

Fig. 4.3. Schematic representation of Hippo pathway components and their relative expression in the E14.5 humerus. Pathway elements are presented here as boxes proportional to their RNA read count in wildtype tissue (Fig. 4.2).

In general, Hippo component genes analysed here are relatively abundantly expressed in wildtype humeri and associated joints (Fig. 4.4) with 9/25 genes (36.0%) having read counts of 100-1,000, 14/25 genes (56.0%) with read counts between 1,000-5,000, and 2/25 genes (8.0%) with read counts above 5,000. Examination of all genes represented in the transcriptome showed that 4,301/15,214 genes (28.3%) have read counts between 1,000 and 5,000 compared to 56.0% of Hippo genes (Fig. 4.4). Similarly, while 3693/15,214 genes (24%) in the whole transcriptome were detected at 100 reads or fewer, all examined Hippo genes showed more than 100 reads, demonstrating relatively abundant transcription of these genes in wildtype humeri and associated joints at this stage.

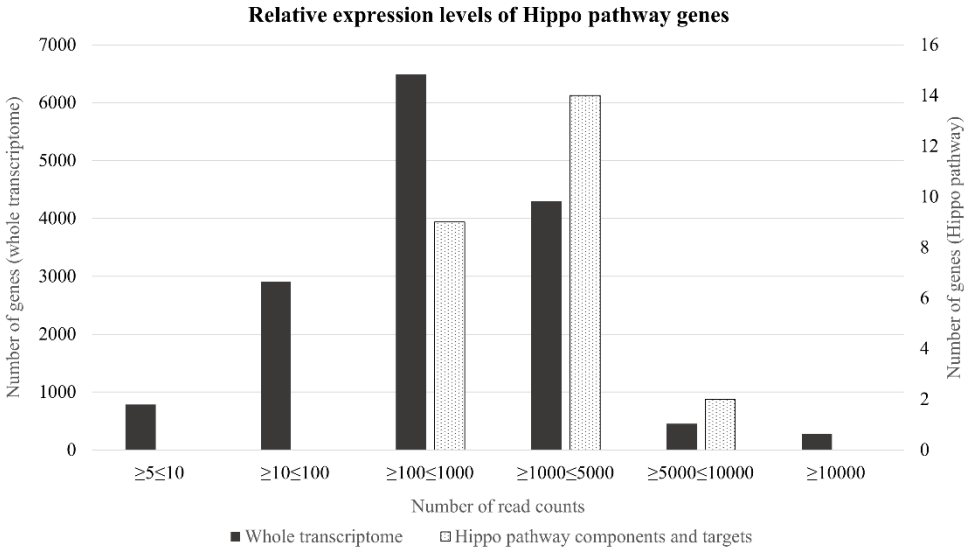

Fig. 4.4. Hippo pathway genes are relatively highly expressed in the E14.5 humerus. The number of genes (y axis) in each transcript abundance category (x-axis) for the entire transcriptome (dark bars; number of genes shown on the left) and for Hippo pathway genes (light bars; number of genes shown on the right). This shows that all Hippo pathway genes analysed are relatively abundantly expressed.

4.2.2 YAP protein localisation in the developing forelimb skeleton

4.2.2.1 YAP expression is highest in the hypertrophic zone and in morphological protrusions

As discussed in Section 4.1, YAP localisation has been reported during skeletal development, yet existing reports are somewhat contradictory (Karystinou et al., 2015, Deng et al., 2016). To examine broad patterns of YAP localisation in TS23 forelimbs, YAP protein was detected by means of a specific antibody (raised against an epitope which spans the primary phosphorylation site of YAP protein) and alkaline phosphatase colourimetric development. While alkaline phosphatase has endogenous activity in the developing skeleton, negative controls with no primary antibody were used to prevent misinterpretation of staining; some light background staining was seen in musculature but not within the rudiments (Fig 4.5f'', g''; black arrows). Additionally, alkaline phosphatase was found to be preferable to other colourimetric methods, such as horseradish peroxidase-mediated staining, which did not give a robust signal. Colourimetric staining revealed that the strongest levels of staining were in the hypertrophic zones of the humerus and deltoid tuberosity (Fig. 4.5a-c, arrows). With extended staining time, localised patterns of YAP were also detected within the olecranon process of the ulna (Fig. 4.5d-f', arrows) and the coracoid process of the scapula (Fig. 4.5g, g'; black arrow). Serial sections through the elbow joint revealed that elevated YAP levels were more apparent in the more lateral olecranon process (Fig. 4.5d-e'; arrows); while the more medial olecranon process still displayed elevated YAP levels in comparison to the rest of the ulna, although this was not as obvious (Fig. 4.5f, f'; arrows).

Fig. 4.5 (next page). Regions of elevated YAP protein are localised in the forelimb skeletal rudiments. Paraffin sections of TS23 forelimbs were immunostained for YAP and developed colourimetrically by alkaline phosphatase. YAP staining was detected in the hypertrophic zone and deltoid tuberosity (a-c), near the elbow (d-f) and shoulder (g) joints, and within the olecranon process (OP) (d', e', f') and coracoid process (CP) (g, g'). Serial sections at the elbow joint (d'-f'), from lateral (d, d') to medial (f, f'). Black and yellow arrows indicate localised YAP protein. Higher magnification views in (d'-g') are indicated by dashed boxes in (d-g). Comparable sections stained with alkaline phosphatase and no primary antibody as negative controls are shown for the elbow (f'') and shoulder (g''). Abbreviations: coracoid process (CP), humerus (H), olecranon process (OP), radius (R), ulna (U). Scale bars are 100 μm.

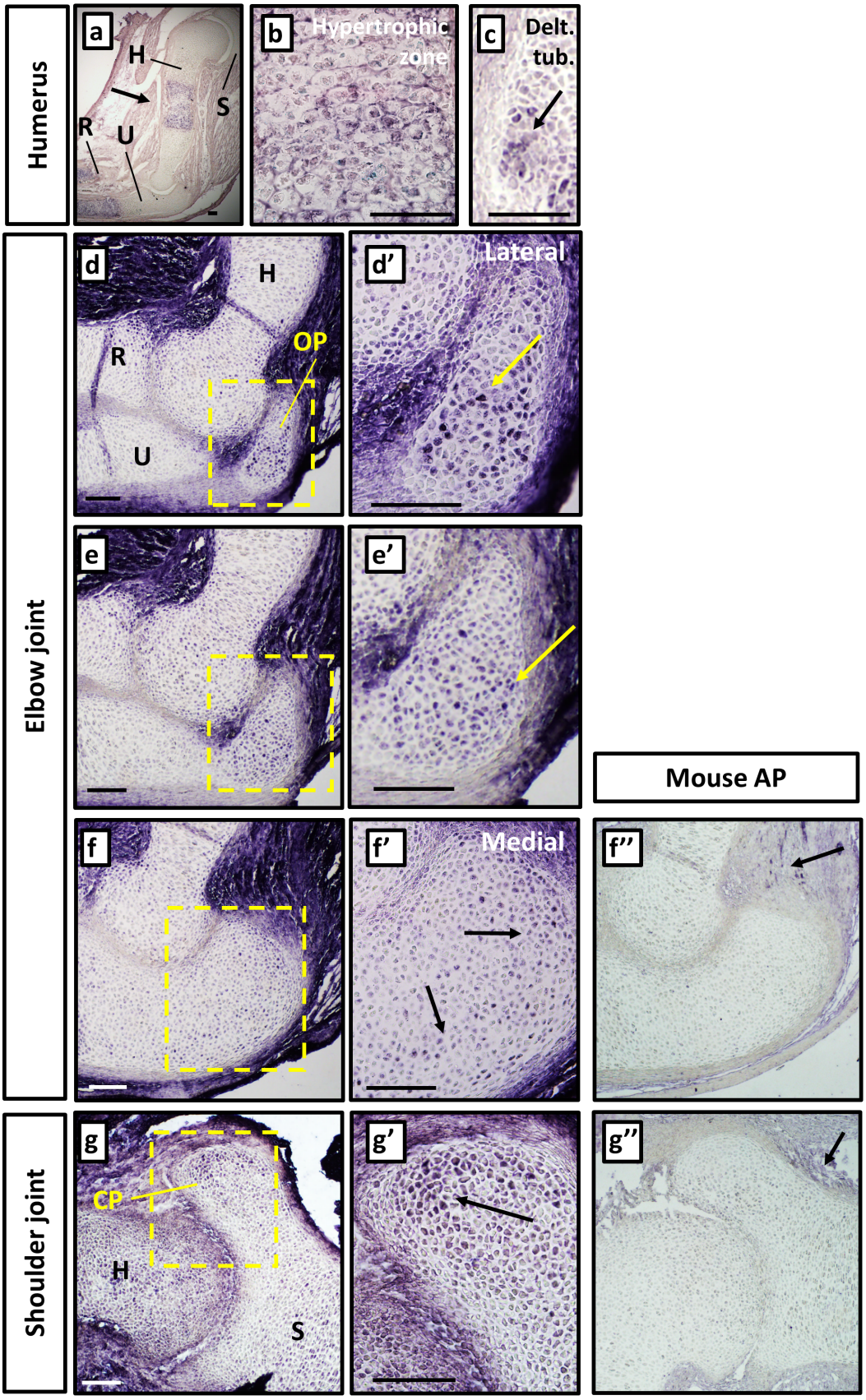
Humerus
a
H
R
U
S
b
Hypertrophic zone
c
Delt. tub.
Elbow joint
d
H
R
OP
U
d'
Lateral
e
e'
Mouse AP
f
f'
Medial
f''
Shoulder joint
g
CP
H
S
g'
g''

4.2.2.2 Phosphorylated YAP levels are more uniformly distributed throughout the rudiments

To further characterise YAP protein activity in the developing rudiments, the localisation of the phosphorylated, inactive form of YAP (pYAP) was assessed using a specific antibody (Fig. 4.6). The highest detectable level of pYAP was in the hypertrophic zone, but this was not as elevated compared to the rest of the rudiment as for YAP (Fig. 4.6a, black arrow; compare to Fig. 4.5a). In contrast to YAP, relatively higher levels of pYAP staining were detected throughout the rudiments, and no spatial localisation was observed (Fig. 4.6b-c', black arrows).

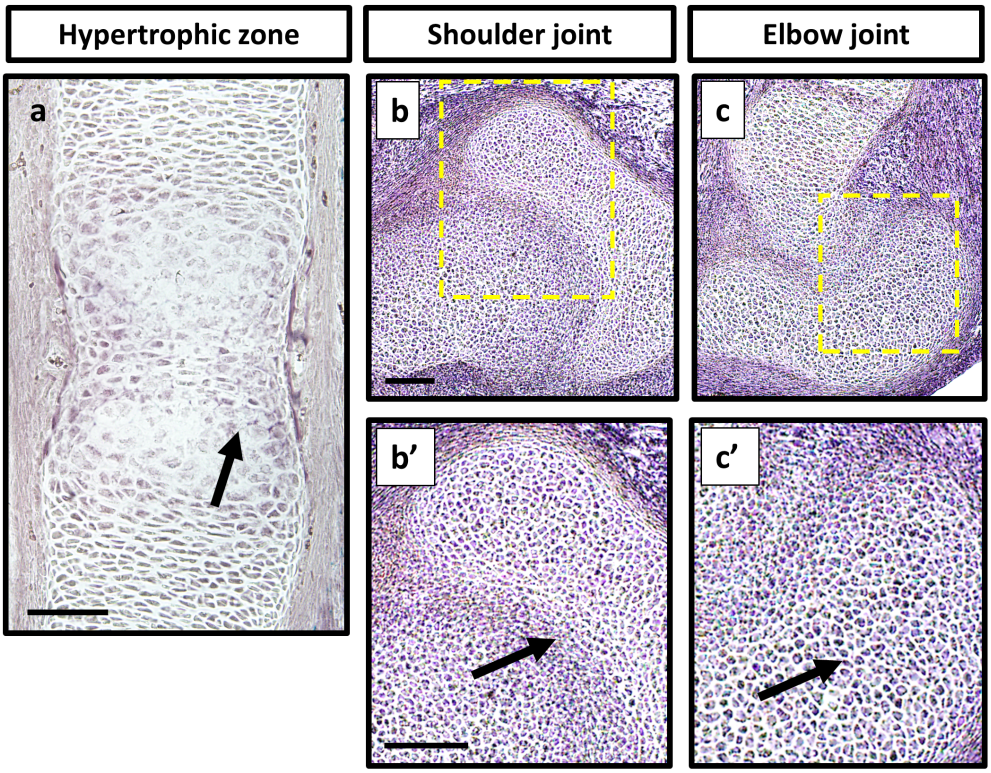

Fig. 4.6. Phosphorylated YAP protein is detected throughout the rudiment with slightly elevated levels in the hypertrophic zone. Phosphorylated YAP (pYAP) was immunostained and colourimetrically developed by alkaline phosphatase on TS23 forelimb paraffin sections. pYAP was detected in the hypertrophic zone (a, black arrow), and throughout the rudiments (b-c), including up to the shoulder (b, b') and elbow joints (c, c'); black arrows). (b', c') are larger magnification images of the boxes indicated in (b, c). Scale bars are equal to 100 µm.

4.2.2.3 Nuclear YAP is detected in sites of elevated YAP localisation.

To examine if YAP protein was active in the developing skeleton, its nuclear localisation in the chondrocytes of the rudiments was assessed. As above, YAP protein was detected using an antibody raised against an epitope spanning the primary phosphorylation site for YAP protein, and clear fluorescent detection followed tyramide amplification. This was compared to DAPI staining to determine nuclear localisation, which was taken as an indicator of transcriptional activity (Fig. 4.7). Confirming the colourimetric detection results, YAP protein overall was most distinct in the hypertrophic zone (Fig. 4.7a) but was also detectable in other parts of the rudiment, such as the olecranon process of the ulna (Fig. 4.7b) and the distal head of the humerus (Fig. 4.7c) and was clearly localised to the nucleus in these regions (Fig. 4.7a'-c'; white arrows). Not all detected YAP was nuclear: some YAP protein was also detected outside the nucleus (Fig. 4.7a'-c', yellow arrows). This indicates that both active and inactive forms of YAP are present in chondrocytes of the developing rudiments.

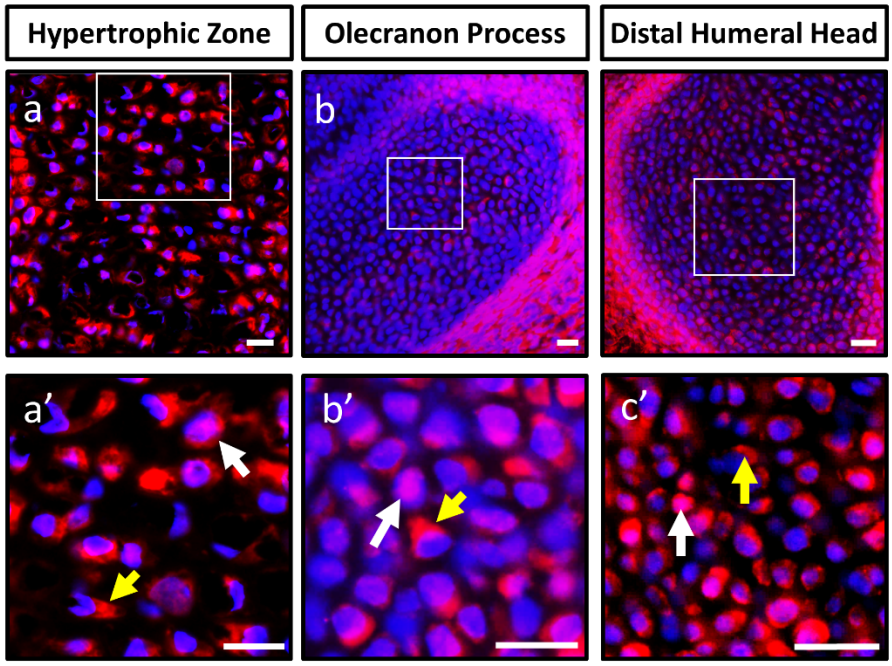

Fig. 4.7. YAP protein is localised to the nucleus in the developing skeleton. Fluorescent immunodetection of YAP in wildtype TS23 forelimb cryosections (10 μm), counterstained with DAPI. Shown here are the hypertrophic zone (a-a'), olecranon process (b-b'), and distal head of the humerus (c-c'). Images in (a'-c') are higher-magnification images of the white boxed regions in (a-c). White arrows in (a'-c') indicate nuclear YAP; yellow arrows in the same indicate cytoplasmic YAP protein. Scale bars are 25 μm.

4.2.2.4 Abundance and spatial localisation of YAP, but not pYAP, are altered in the muscle-less mutant

To assess pattern changes in YAP protein under reduced mechanical stimulation, YAP was assessed colourimetrically in the muscle-less mutant forelimb at TS23, and compared to wildtype tissue. In the muscle-less mutant, YAP protein was not spatially restricted, as in the wildtype (Fig. 4.8a', e'; black arrows), but was detected at high levels throughout the rudiments (Fig. 4.8b', f'; black arrows). Additionally, while YAP levels were reduced or absent at the joint line in the wildtype elbow and shoulder (Fig. 4.8c', e'; brackets), high levels of detectable YAP were observed across the joint line in muscle-less specimens (Fig. 4.8d', f'; black arrows).

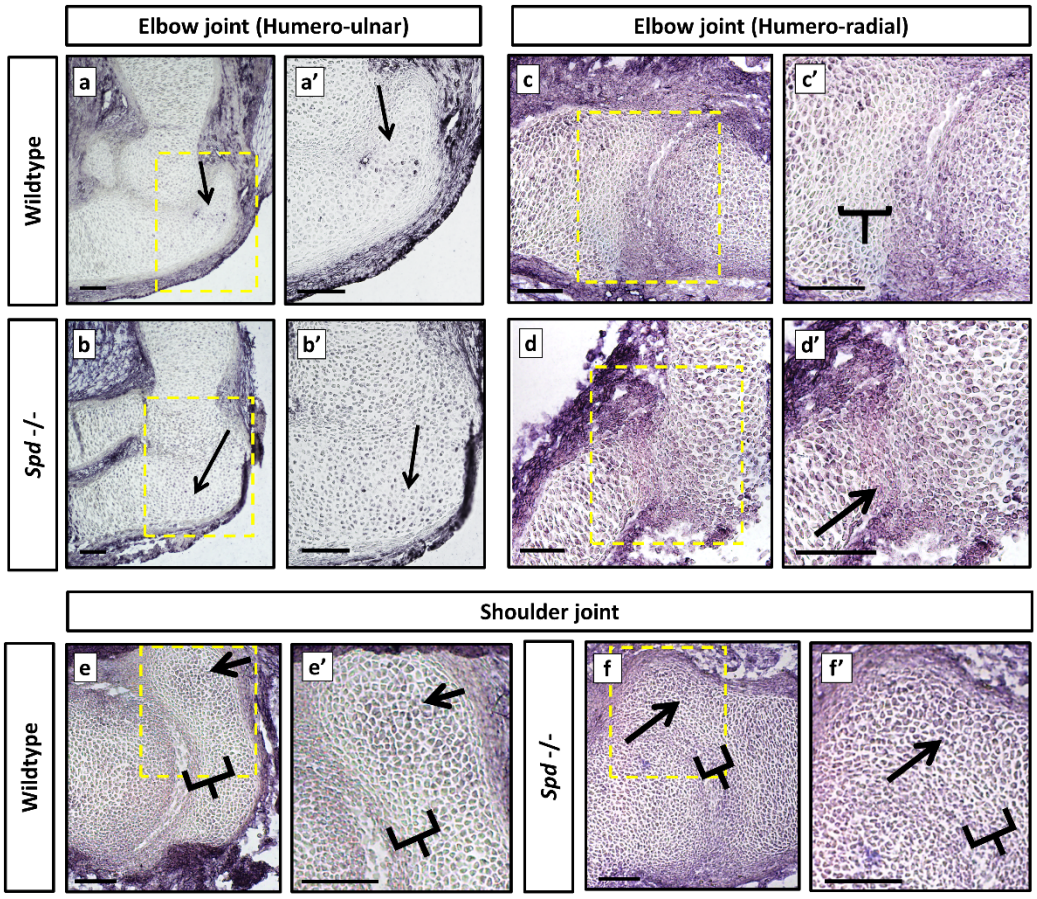

Fig. 4.8. YAP levels are elevated and more evenly distributed in the muscle-less mutant. YAP protein was detected colourimetrically using alkaline phosphatase in TS23 wildtype (a, c, e) and muscle-less (b, d, f) forelimb sections. YAP protein was detected in the region of the elbow (a-d') and shoulder joints (e-f'). The images in (a'-f') are higher magnification images of the yellow dashed boxes indicated in (a-f). Black arrows indicate observed expression; black brackets indicate expression or lack thereof in chondrogenous layers. Scale bars are equal to 100 µm.

Phosphorylated YAP was then assessed in the muscle-less mutant and compared to detection in wildtype forelimbs. Colourimetric detection of pYAP revealed no differences in detection levels in muscle-less rudiments compared to wildtype tissue sections (Fig. 4.9). Expression in both muscle-less and wildtype rudiments was slightly elevated in the hypertrophic zone (Fig. 4.9a, b; black brackets). In the regions of the shoulder and elbow joints, pYAP was detected up to the joint line in both muscle-less and wildtype tissue (Fig. 4.9c-f, black arrows), with no obvious protein localisation in the rudiments.

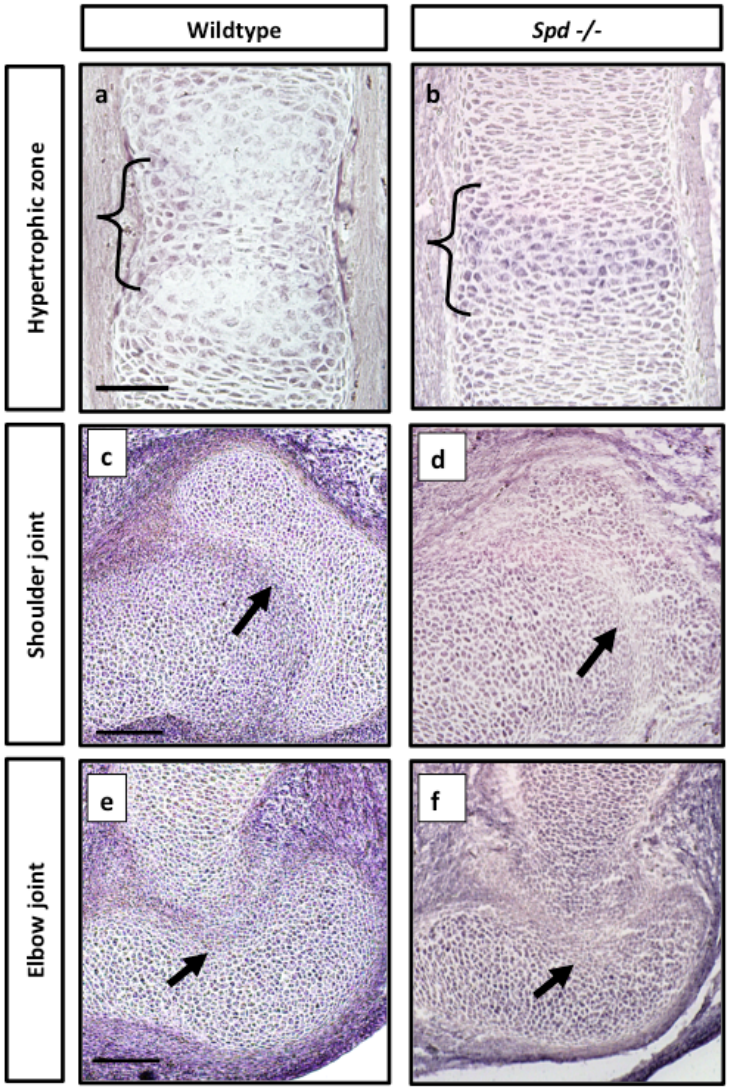

Fig. 4.9. Phosphorylated YAP is not visibly altered in the muscle-less mutant. Phosphorylated YAP (pYAP) was detected using immunostaining and colourimetric detection on TS23 cryosections. pYAP levels were compared in wildtype (a, c, e) and muscle-less (b, d, f) tissue, and pYAP was detectable in the hypertrophic zone (a, b), shoulder joint (c, d) and elbow joint (e, f). Black arrows and brackets indicate observable expression. Scale bars are 100 µm.

To assess if nuclear localisation of YAP protein is altered under reduced mechanical stimulation, forelimb sections of TS23 *Pax3*$^{Spd/Spd}$ (muscle-less) mutants were compared to wildtype. Fluorescent localisation revealed high levels of detectable YAP in muscle-less rudiments (Fig. 4.10a-d); as in wildtype, YAP protein was localised to the nucleus in the olecranon process and distal humeral head (Fig. 4.10a'-d', white arrows), while cytoplasmic YAP was also observed (Fig. 4.10a'-d', yellow arrows).

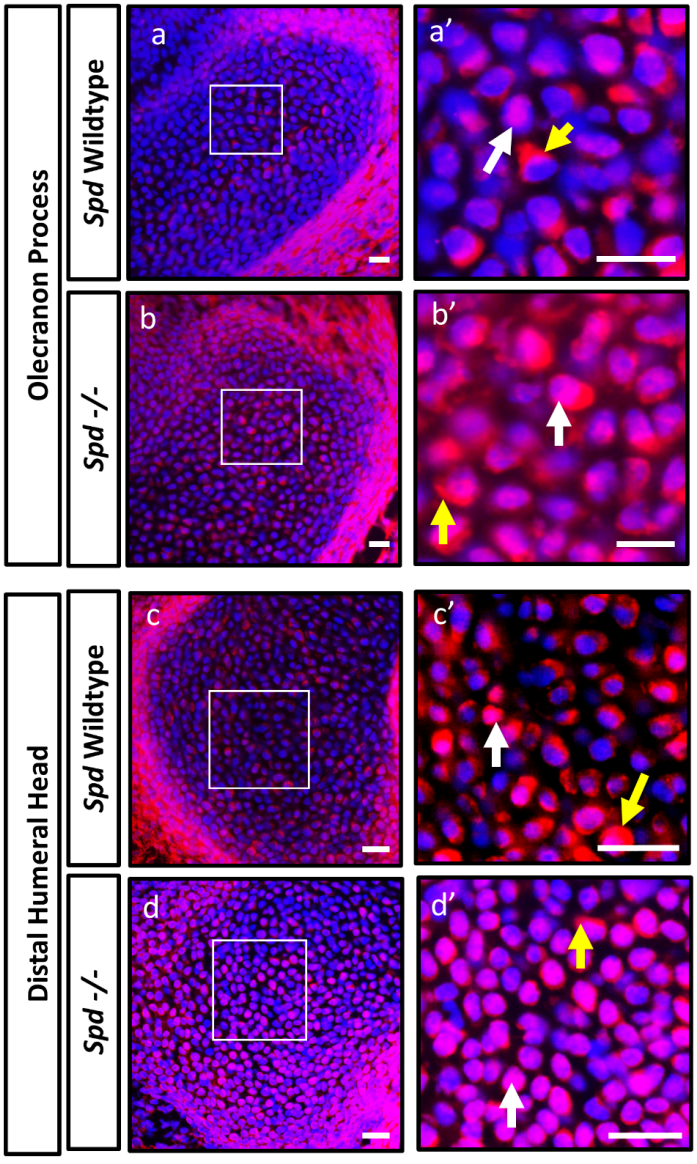

Fig. 4.10. YAP protein is more strongly detected in the muscle-less mutant, while being similarly localised to the nucleus. Cryosections of TS23 forelimbs fluorescently stained for YAP and counterstained with DAPI, for both wildtype (a, b) and muscle-less (c, d) tissue. Both nuclear and cytoplasmic YAP were observed (white and yellow arrows, respectively), at the olecranon process (a, b) and distal humeral head (c, d). The images in (a'-d') are higher-magnification images of the white boxed areas in a-d). Scale bars are 25 μm.

4.2.2.5 Localised expression of YAP target genes CTGF and *Cyr61* is altered in the muscle-less mutant

Five YAP target genes, *Ankrd1*, *Birc5*, *Ctgf*, *Col8aI*, and *Cyr61* (Table 4.1) were selected for expression analysis in wildtype and mutant forelimb rudiments as they are commonly used as indicators of YAP transcriptional activity. Differential regulation in muscle-less humeri indicated by RNA-seq (Table 4.1) was verified by quantitative reverse-transcription polymerase chain reaction (qRT-PCR) (Table 4.2). The expression changes as assessed by qRT-PCR were largely consistent with the RNA-Seq and microarray transcriptomic data. *Ankrd1* was highly downregulated (20-fold by qRT-PCR). *Birc5* was virtually unchanged and *Ctgf* and *Cyr61* were slightly upregulated by all three methods. This confirmed expression of these genes in the developing skeleton, warranting further investigation by *in situ* hybridisation in mutant rudiments.

Table 4.2. Expression level fold changes of selected YAP target genes in mutant vs. wildtype *Spd* humeri. For qRT-PCR, two replicates (for each of wildtype and mutant) of pooled, dissected humeri were averaged. For comparison, microarray and RNA-Seq data are shown (from Rolfe et al. 2014). Significant microarray or RNA-Seq values are indicated: P<0.05 (*).

Gene symbol	Gene name	Microarray Fold Change	RNA-Seq Fold Change	qRT-PCR Fold Difference Average
Ankrd1	Ankyrin repeat domain-containing protein 1	75.14 down*	97.74 down*	**19.86 down**
Birc5	Baculovirus IAP repeat containing 5	1.16 down	1.45 down	**1.06 up**
Ctgf	Cell transforming growth factor	1.34 up	1.34 up	**2.43 up**
Cyr61	Cysteine rich angiogenic inducer 61	1.39 up	1.18 up	**1.15 up**

In situ hybridisation of *Ctgf* and *Cyr61* revealed distinct, localised expression patterns, which were altered in the mutant. *Ctgf* expression was detected in the perichondrium (Fig. 4.11a, d; black arrows) and joint chondrogenous zones (Fig. 4.11b, black arrowhead), lightly outlining the rudiments (Fig. 4.11c, red arrow), and at a low level in the hypertrophic zone (Fig. 4.11a, red arrowhead). In the mutant, expression in the perichondrium is increased (Fig. 4.11a'-d', black arrows), as is expression within the hypertrophic zone (Fig. 4.11a', red arrowhead). In particular, the *Ctgf*-expressing territory in the chondrogenous layer at the shoulder and elbow joints, corresponding to the presumptive articular cartilage, is strongly increased and expanded in the mutant (Fig. 4.11b'-c', black arrowheads). Another striking expression change in the mutant is

at the edge of the olecranon process of the ulna, where staining at the perichondrium was again expanded and much more intense than in the wildtype (Fig. 4.11c', red arrow).

Cyr61 is similarly detected in the chondrogenous layer at the joint (Fig. 4.11f, black arrowheads) and in some regions of the perichondrium, such as at the hypertrophic zone and at the ulna (Fig. 4.11e, g; black and red arrows), but at even lower levels than *Ctgf*. Although it is not upregulated at the joint it is dramatically upregulated in the olecranon process, similar to *Ctgf*, yet unlike *Ctgf* it is also detected throughout the olecranon process in the mutant (Fig. 4.11g', red arrow). In addition, *Cyr61* was observed in the prehypertrophic chondrocytes of the wildtype humerus and scapula (Fig. 4.11e-f, red arrowheads), and in chondrocytes in the mutant resting zones and hypertrophic zone (Fig. 4.11e'-f', red arrowheads), where chondrocyte maturation is delayed compared to the wildtype.

Birc5 and *Col8aI* transcripts were detected by RNA-Seq at high levels (Table 4.1; 1,775 and 1,879 read counts, respectively, in the wildtype). *Birc5* showed high level expression throughout the skeletal rudiment with no localised pattern except for more intense staining in the chondrogenous layers at the joint, where cell density is typically higher (Fig. 4.11h, i, black arrows). There was no discernible change in expression in the mutant (Fig. 4.11 h', i'). *Col8aI* similarly was detected throughout the skeletal rudiments with no discernible pattern except for lighter staining at the joint territory in both wildtype and mutant rudiments (Fig. 4.11j-k', black arrows). It was also detected in the muscles of the wildtype forelimb (Fig. 4.11j, red arrow).

Ankrd1 was detected by RNA-Seq at a low level (Table 4.1; 233 reads in the wildtype). By *in situ* hybridisation, *Ankrd1* was expressed at a high level in adjacent muscle (Fig. 4.11l-m, yellow arrows). Some faint staining was observed in the chondrogenous layers at the joint, but this pattern was very weak (Fig. 4.11m-m', black arrows). Therefore, while *Ankrd1* was dramatically downregulated according to RNA-Seq analysis of microdissected tissue, this was most likely due to some contamination of muscle tissue in the wildtype specimen which would be absent in the muscle-less tissue.

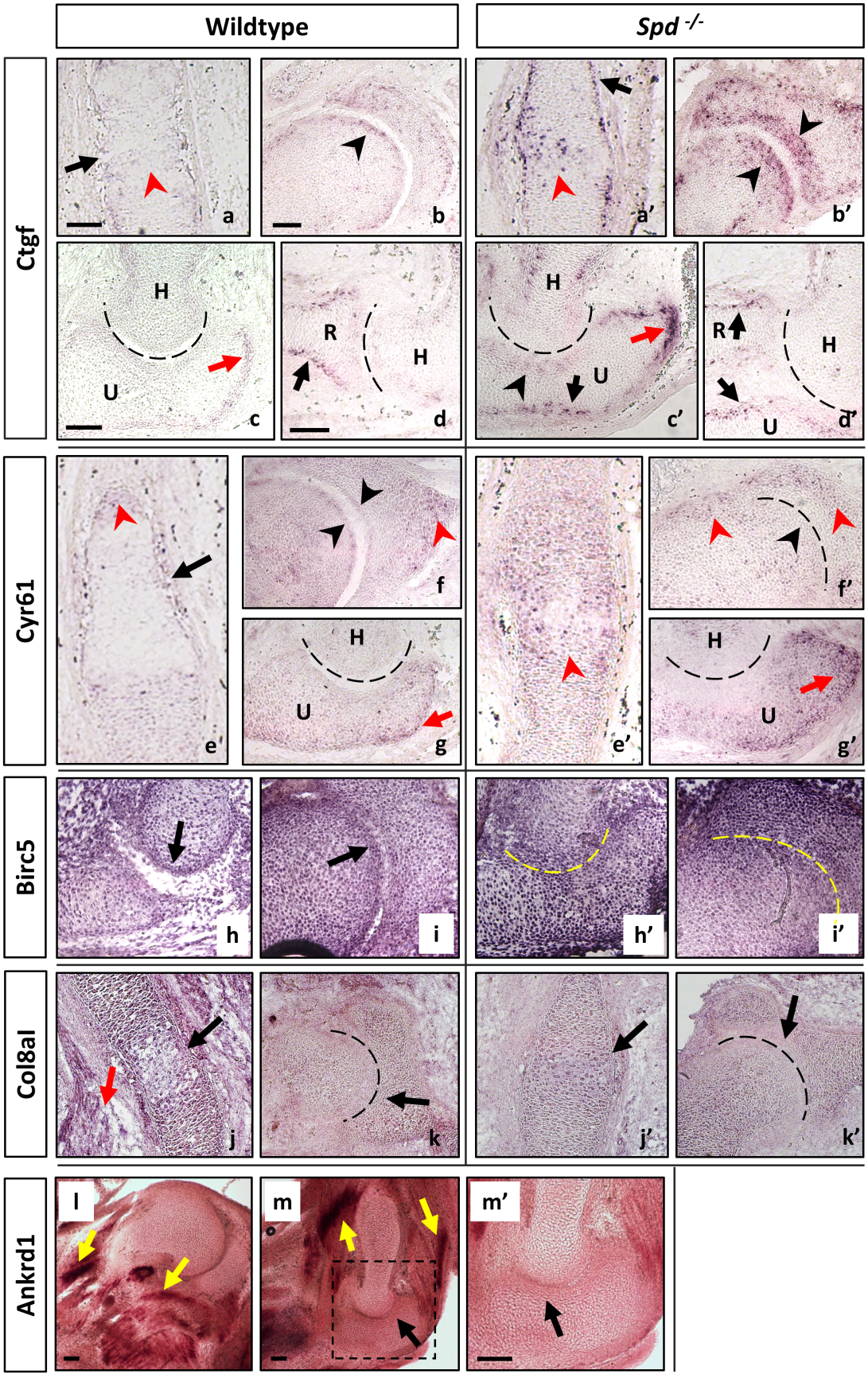
Wildtype
Spd -/-
Ctgf
Cyr61
Birc5
Col8a1
Ankrd1
a
b
a'
b'
H
U
c
R
H
d
H
U
c'
R
H
U
d'
e
f
e'
f'
H
U
g
H
U
g'
h
i
h'
i'
j
k
j'
k'
l
m
m'

Fig. 4.11 (previous page). YAP target genes *Ctgf* and *Cyr61* have localised expression in the skeletal rudiments which is altered in the muscle-less (*Spd*$^{-/-}$) mutant. Cryosections (10 μm) were *in situ* hybridised for YAP target genes *Ctgf*, *Cyr61*, *Birc5*, and *Col8aI*, comparing wildtype forelimb tissue (a-k) to muscle-less mutant tissue (a'-k'). Vibratome sections (60 μm) were *in situ* hybridised for *Anrkd1* (l-m). The image in (m') is a higher magnification of the dashed region indicated in (m). Black and red arrows and arrowheads indicate detectable expression. Dashed black or yellow lines indicate joint lines. Regions of notable expression included the humeral diaphysis midpoint (a, a', e, e', j, j'), the shoulder joint (b, b', f, f', i, i', k, k'), the humero-ulnar joint of the elbow (c, c', g, g', h, h'), and the humero-radial joint of the elbow (d, d'). Abbreviations: humerus (H), radius (R), ulna (U). Scale bars are 100 μm.

4.2.3 Manipulation of YAP activity *in vitro*

4.2.3.1 Inhibition of YAP by Verteporfin reduces nodule formation and chondrogenic gene expression in embryonic limb bud micromass culture

To manipulate the activity of YAP in culture, the small molecule verteporfin was utilised, which inhibits YAP binding to its TEAD transcription factors (Liu-Chittenden et al., 2012). Treatment of embryonic limb bud micromass cultures with 200 nM verteporfin resulted in reduced nodule formation compared to DMSO-treated controls, although nodules still formed in the verteporfin-treated micromasses (Fig. 4.12a, b). Overall, the number of nodules formed in verteporfin-treated micromasses was significantly reduced, while the size of individual nodules was unchanged (Fig. 4.12c and d). Gene expression was also affected upon addition of verteporfin: expression of marker genes of early chondrogenesis (*Sox9*, *Col2aI*) was significantly downregulated in verteporfin treated cultures compared to DMSO controls (Fig. 4.12e). Surprisingly, while expression of hypertrophy marker *Col10aI* was also significantly downregulated after addition of verteporfin, an earlier hypertrophy marker, *Ihh*, was not (Fig. 4.12e), but this may be related to the assay time point (6 days of culture) when *Ihh* expression has normally peaked and returned to low levels (Saha et al., 2016). Indicative of reduced YAP activity, expression of YAP target genes *Ctgf* and *Cyr61* were both downregulated in verteporfin-treated cultures, *Cyr61* significantly so; *Ctgf* was notably downregulated, just outside the significance threshold at p=0.058 (Fig. 4.12f).

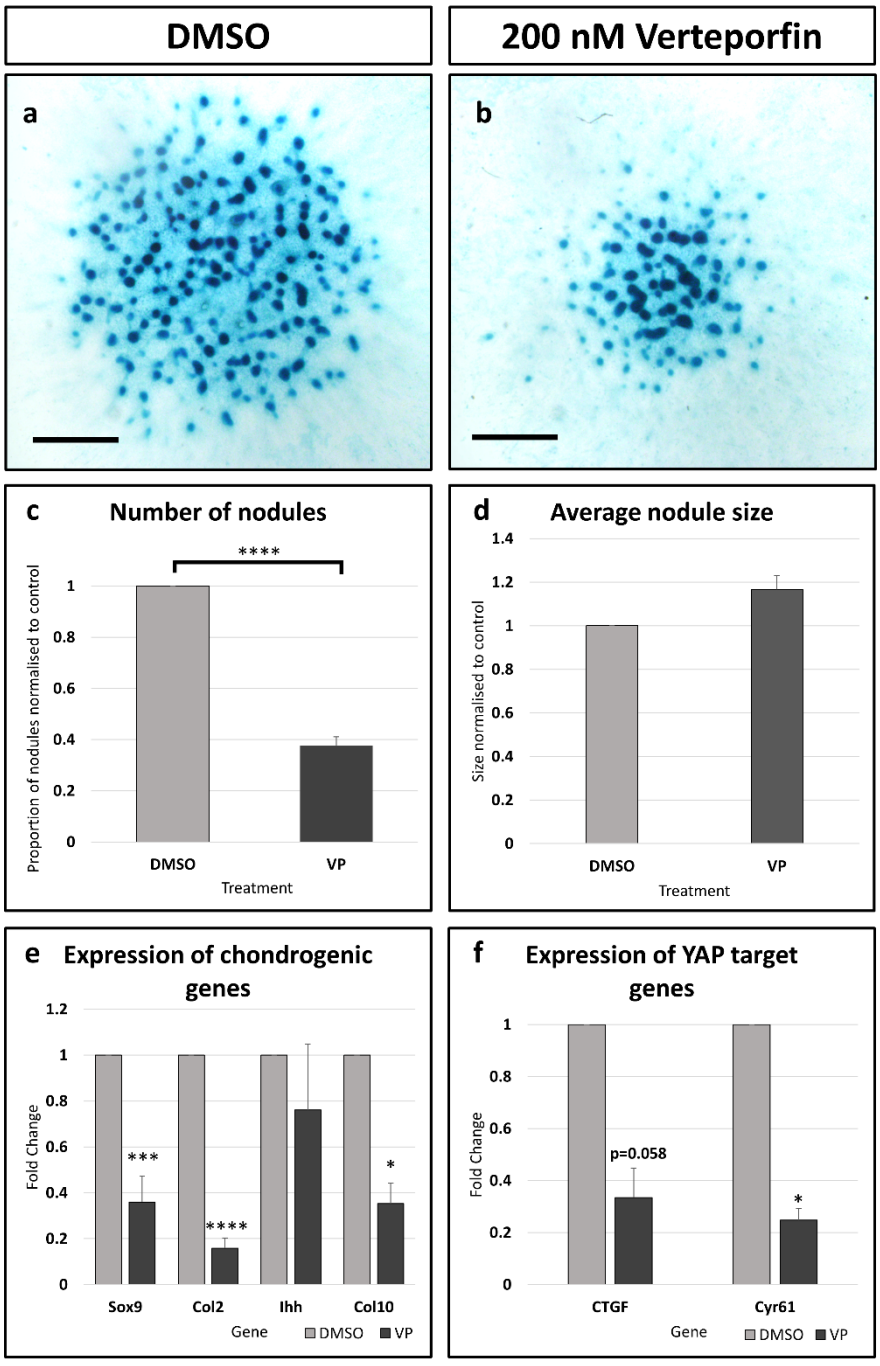

Fig. 4.12. Nodule formation is altered in the presence of Verteporfin. Micromass cultures were treated with DMSO (a) or with 200 nM Verteporfin in DMSO (b) for 6 days, fixed, and stained with Alcian Blue (representative images shown). Images of stained cultures were analysed for nodule number (c) and size (d), with measurements for Verteporfin-treatment normalised to DMSO-treatment in the same experiment. Day 6 micromasses were assessed by real time qRT-PCR, for expression of chondrogenic genes (e) and YAP-related genes (f); all gene expression levels were normalised to GAPDH expression. Scale bars in (a) and (b) are 1 mm. Significance: $p<0.05$ (*), $p<0.01$ (**), $p<0.005$(***) $p<0.0001$ (****). n=2 3 independent experiments.; 2 replicates/experiment.

4.2.4 Expression of the canonical Hippo pathway receptor *Fat4* during limb development

***Fat4* is expressed in multiple tissues, including limbs, between E10.5 and E13.5.** As described in Section 1.5.1, YAP/TAZ activity can be modulated by multiple upstream regulators. Therefore, expression of the canonical Hippo pathway receptor gene *Fat4* was investigated during key stages of limb development to assess if this canonical receptor is a potential regulator of YAP activity during skeletal development. Wholemount *in situ* hybridisation of wildtype (CD-1) mouse embryos was carried out from TS17/E10.5, when the limb bud begins to elongate from the trunk, to TS22/E13.5, just prior to ossification at the mid-point of the long bones. 3D scanning of whole mount embryos using Optical projection tomography (OPT) (Sharpe et al., 2002, Summerhurst et al., 2008), as described in Section 2.3.4, was used to generate digital representations of the data and analyse internal expression through virtual sections.

Since embryonic expression data on *Fat4* is limited (Rock et al., 2005, Zakaria et al., 2014, Kuta et al., 2016), expression across the whole embryo was analysed and sites outside the limb are noted. Distinct, restricted expression patterns of *Fat4* were observed in multiple tissues across E10.5-E13.5 (Fig. 4.13): in the forebrain (telencephalon) eye, branchial arches, neural tube, otic vesicle, the scleratome region of the somites which include precursor cells of the axial skeleton, and the developing limb buds as indicated (Fig. 4.13).

Focussing on the limbs, at E10.5, *Fat4* expression in the forelimb is strongest at the distal tip of the limb bud in the Apical Ectodermal Ridge (AER) (Fig. 4.13e, e'; red arrows), in mesenchyme underlying this territory (Fig. 4.13e, white dashed area), skewed toward posterior, and in a deep zone of mesenchyme at the dorsal base of the limb which is particularly extensive at the anterior aspect (Fig. 4.13e, e'; green arrows). Expression is also seen in the ventral ectoderm, continuous with the ventral body wall (Fig. 4.13e, e'; white arrows). In the hindlimb at E10.5, lower levels of expression are observed, although, as in the forelimb, there is a distinct region of expression in the anterior dorsal base (Fig. 4.13i', green arrow), as well as in the distal posterior mesenchyme (Fig. 4.13i, i'; white dashed areas) and in the ventral ectoderm (Fig. 4.13i, i'; white arrows).

At E11.5, expression persists at the base of the limb, still more extensive at the anterior aspect (Fig. 4.13f, f'; green arrows), and in the distal posterior mesenchyme (Fig. 4.13f,

f'; white arrows) while AER-associated expression is no longer detected in the distal ectoderm at the tip of the limb bud (Fig. 4.13f, f'). In the hindlimb, expression at the anterior base of the limb is lower compared to the forelimb, but still notable (Fig. 4.13j, j'; green arrows). Expression persists in the distal posterior mesenchyme (Fig. 4.13j, white arrow) and the distal tip of the limb bud (Fig. 4.13j, j'; red arrows) and is also observable in the region of the developing knee joint (kj) and margins of the condensing mesenchyme core (Fig. 4.13j').

At E12.5, expression at the base of the limb is reduced, and no longer extends onto the body trunk, but is limited to the anterior limb bud (Fig. 4.13g, g'; green arrows). Virtual sections reveal that within the limb bud, expression is localised to the margins of the forming rudiments (Fig. 4.13g', white arrows). It is now particularly strong in the tissue adjacent to the digit condensations (Fig. 4.13g, g'; yellow arrows). Expression at the base of the hindlimb is also much reduced (Fig. 4.13k', green arrow), and, as in the forelimb, staining is strongest in the tissue surrounding the rudiments (Fig. 4.13k, k'; white arrows), in the region of the developing knee joint (kj) (Fig. 4.13k') and in the tissue adjacent to the digit condensations (Fig. 4.13k, k'; yellow arrows).

At E13.5, expression is mostly restricted to the digital plate, although weak expression is detectable in the ectoderm along the length of the limb (Fig. 4.13h, h'; green arrows). Expression in the tissue surrounding the developing digits of the handplate (hp) is stronger and more clearly defined (Fig. 4.13h, h'; white arrows). Staining in the hindlimb is similar, localised to the ectoderm along the length of the limb (Fig. 4.13l, l'; green arrows) and the tissue outlining the forming digits of the footplate (fp) (Fig. 4.13l, l'; white arrows).

Fig. 4.13 (next page). *Fat4* is expressed in multiple tissue over key stages of limb development. Wholemount *in situ* hybridisation of wildtype (CD-1) mouse embryos (a-d) indicated expression of *Fat4* in the telencephalon (t), eye (e), branchial arches (ba), neural tube (nt), otic vesicle (ov), somites (s), and fore- (FL) and hindlimb (HL) buds. ***Fat4* expression patterns are distinct in the fore- and hindlimb buds.** Expression of *Fat4* in the developing limb buds was assessed in wholemount embryos (e-l), and virtual OPT sections (e'-l'). Sections show expression patterns within the limbs; arrows indicate specific expression as described in the text. Dashed regions in (f', h', l') indicate the boundaries of embryonic tissue. Blue outlines in (g', j') indicate developing rudiments. Abbreviations: knee joint (kj), shoulder joint (sj), elbow joint (ej), handplant (hp), footplate (fp). Scale bars in (e'-l') are 1 mm. Axes in (e'-l') are

anterior-posterior (a-po), dorsal-ventral (d-v), and proximal-distal (pr-d). n= 3 independent *in situ* hybridisation experiments; 3 embryos were stained per stage per experiment.

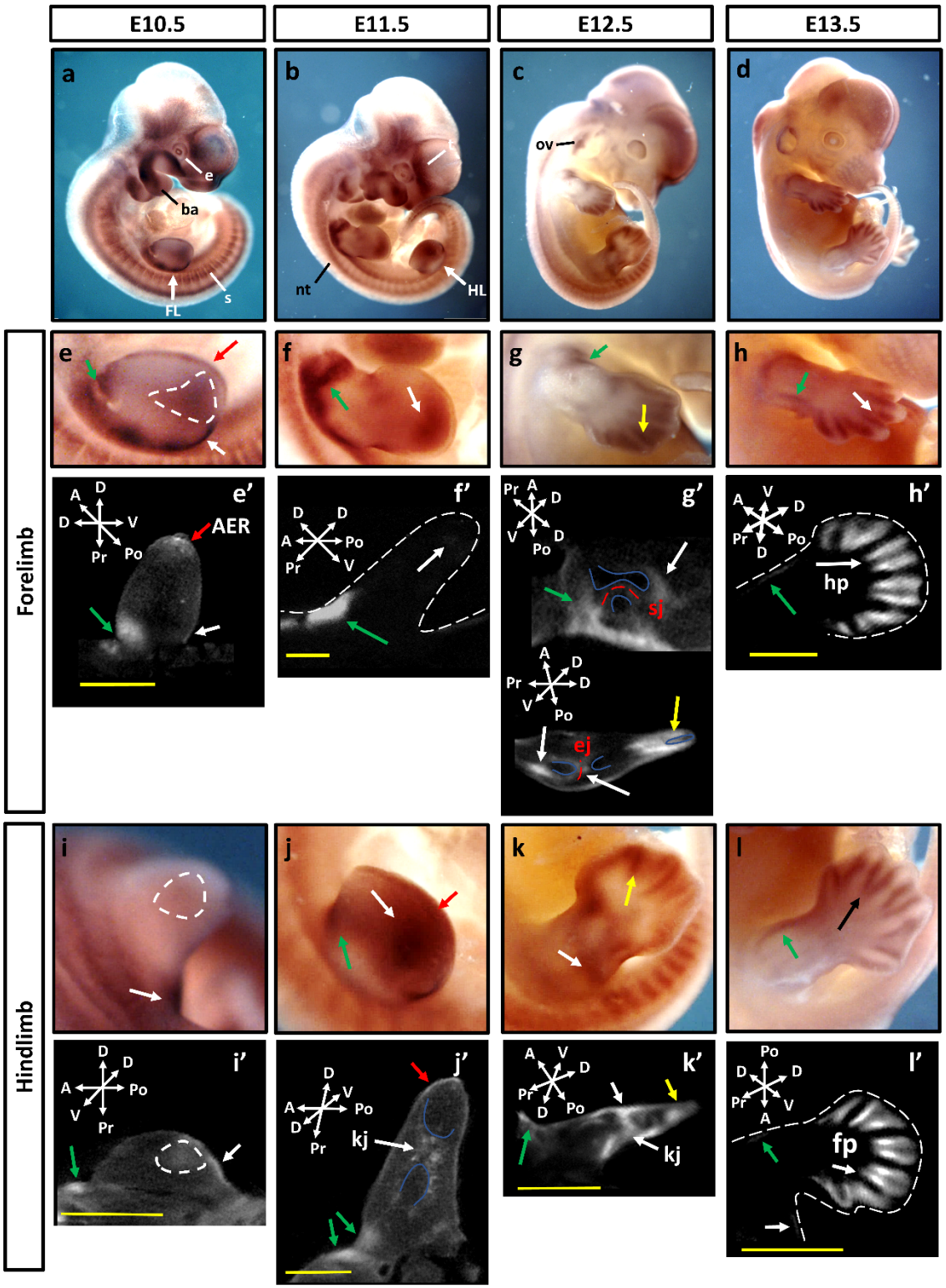

4.2.4.1 *Fat4* is expressed outside the limb

As noted above, there is limited expression data in the literature concerning *Fat4* expression, and wholemount *in situ* of embryos during key stages of limb development revealed notable patterns of expression in numerous other tissues. Although not of primary relevance in the current study, these are novel data, worthy of note. Patterns of *Fat4* in tissues outside the limb buds are displayed in Fig. 4.14 and are described in further detail in Table 4.3. Of particular interest was expression in the eye, which was consistently strong across E10.5-13.5, in multiple tissues including the developing lens and cornea (Fig. 4.14Ai-Di). Expression was also noted in other facial features including the facial ectoderm, branchial arches, and nasal cavities (Fig. 4.14). As had been previously reported, there was strong *Fat4* expression in the neural tube across stages, and weaker expression in other parts of the brain (Fig. 4.14Ai-Dii). Expression was also noted in the developing heart, lungs, and digestive system; of note is the relatively weak expression observed in the developing kidney, given the known functional relevance of *Fat4* expression in the kidney (Fig. 4.14Av-Div).

Fig. 4.14 (next page). Virtual sections of wholemount embryos *in situ* hybridised with *Fat4*. Virtual sections following digital OPT reconstruction of expression patterns for embryos at E10.5 (A) to E13.5 (D) are shown through specific developing structures. Notable expression patterns in the neural tube/hindbrain/eye (Ai-Di), forebrain/midbrain (Aii-Dii), branchial arches and other facial features (Aiii-Diiib), somites (Aiv-Civ) and heart, lungs, and other visceral organs (Av-Div) are indicated here. Sagittal virtual sections in the left column indicate the orientation of virtual sections displayed in Ai-Div; yellow dashed boxes indicate sagittal sections (the same plane as shown); blue dashed lines indicate the position of transverse sections. Orientation of sections for each feature are the same across stages, except where noted. Scale bars in A-D are equal to 1 mm. Images in the left column merge the gene expression staining pattern (pseudo-coloured in green) with autofluorescence signal for the whole embryo (pseudo-coloured in red). All other images show grey level data for the gene expression staining (white to grey). Abbreviations for orientation axes: anterior (A), posterior (P), dorsal (D), ventral (V). Abbreviations for anatomical features: branchial arches (ba), corneal ectoderm (ce), digestive tract (di), foregut (fg), frontonasal (fn), hindbrain (hb), heart (h), lens (ls), lens vesicle (lv), liver (li), lungs (lu), mandibular process, (mp), midbrain (mb), nasal cartilage (nc), nasal pit (np), nasal septum (ns), nerve root (nr), neural tube (nt), pinnae (pi), somite (s), telencephalon (te). n= 3 independent *in situ* hybridisation experiments; 3 embryos were stained per stage per experiment.

Neural tube/ hindbrain/eye
Forebrain/midbrain
Branchial arches/facial
Somites
Heart/lungs/ viscera
A
E10.5
B
E11.5
C
E12.5
D
E13.5
A
D
V
P
lv
nt
mb
hb
te
fn
1st ba
s
fg
ba
h
ce
fr
2nd ba
vw
di
ia
ib
iiia
iiib
nr
nc
ns
pi
mp
vi
ls
lu
li

Table 4.3. *Fat4* expression in developing structures and tissues, outside the limbs at E10.5-E13.5.

	Embryonic age (stage)			
Tissue	**E10.5 (TS17)**	**E11.5 (TS19)**	**E12.5 (TS21)**	**E13.5 (TS22)**
Neural tube/hindbrain	Ventricular layer of the neural tube (nt), lateral to ventral midline, starting just posterior to midbrain/hindbrain boundary and extending throughout neural tube; stronger more posteriorly.	Ventricular layer, again lateral to midline, extending from hindbrain to posterior neural tube.	As previously but further anteriorly reduced; persists from mid-trunk level and extends posteriorly. More dorsal at mid-trunk level than in the posterior neural tube. In nerve roots, extending ventrally at mid-trunk and hindlimb level.	Low level of expression in the neural tube; strong expression in the nerve roots throughout.
Midbrain/forebrain	Low level at dorsal/anterior midbrain (mb), just posterior to diencephalon. Ventricular layer of the telencephalic vesicles (te).	Low level persists in the midbrain and the ventricular layer of the telencephalic vesicles.	Dorsal and lateral ventricular layer in telencephalic vesicles; extends into lateral cortical hem.	Low level of expression in the ventricular layer of the telencephalic vesicles.
Frontonasal process and pinnae	Throughout the frontonasal region, except lining of nasal pits. Strongest at midline and lateral to nasal pits.	Persists, but more superficial; continuous with lateral head mesenchyme. Clearly ectodermal at midline of medial nasal processes but otherwise unclear.	Ectoderm covering forebrain, hindbrain; lateral midbrain. Elevations at vibrissae (vi). Mesenchyme surrounding the eye. Ectoderm and mesoderm of the primordial pinnae (pi). Precartilage primordia of nasal capsule (nc) and septum, and overlaying ectoderm.	Extensive in ectoderm covering forebrain; lower level of expression in ectoderm covering hindbrain and midbrain. Stronger now in precartilage primordia of nasal capsule (nc) and septum, and overlaying ectoderm. In ectoderm and mesoderm of the primordial pinnae and throughout this region.

	Embryonic age (stage)			
Tissue	**E10.5 (TS17)**	**E11.5 (TS19)**	**E12.5 (TS21)**	**E13.5 (TS22)**
Branchial arches (BA)	Anterior maxillary process. Mandibular process of 1st BA: expression throughout the surface, more extensive on medial aspect and deeper on lateral aspect. 2nd BA: superficial, skewed posterior at the ventral aspect.	Mandibular process: superficial on external posterior aspect continuing into the branchial pouch. Midline of the anterior and posterior aspects of the oro-pharyngeal cavity. 2nd BA: most intense on lateral aspect.	Core mesenchyme in the maxillary and mandibular processes of 1st BA, anterior to the 2nd BA.	Faint expression outlining the developing maxillary portion of the jaw.
Somites	Lateral aspect of the somites (s) in the region of the scleratome (future vertebrae).	Persists, in the superficial layer (scleratome) of the somites.	Persists, but more weakly stained, and only in somites posterior to the hindlimbs.	No observable expression
Kidney and liver	Very faint expression in the lining of the uteric buds of the kidney	No remarkable expression in kidney or liver.	No remarkable expression in kidney or liver.	Weak expression throughout the liver and its vasculature.
Lateral and ventral body wall/surface ectoderm	Ventral body wall at level of the heart, as well as the lateral body wall domain extending anterior and posteriorly from the forelimbs.	Throughout the ventral body wall (vw), around the heart but weaker than branchial region. Base of limb expression continues as stripe across the lateral body wall, between the fore- and hindlimbs.	Throughout the surface ectoderm in the dorsal region, most intense lateral to the neural tube.	No remarkable expression in the surface ectoderm of the trunk or lower body
Eye	Strong in the outer layer of the lens vesicle (lv), which is not yet fully closed.	Visible in corneal ectoderm (ce), except in central region; more extensive anterio-posteriorly than medio-laterally. Also visible in lens vesicle.	Now throughout the corneal ectoderm, and as a stripe on surface of the future eyelids, and in the mesenchyme surrounding the eye.	Persists in the corneal ectoderm and throughout the optic disc.

	Embryonic age (stage)			
Tissue	**E10.5 (TS17)**	**E11.5 (TS19)**	**E12.5 (TS21)**	**E13.5 (TS22)**
Foregut/digestive and respiratory systems	Visible in the trachea and lung buds; dorsal and ventral aspects of the upper foregut (fg)	Expression in the inner lining of the digestive tract (di)	Umbilical hernia and midgut.	Persists in the umbilical hernia and the midgut; strong expression throughout lungs.
Vasculature	Walls of the dorsal aorta and associated anterior vessels.	Weak expression in the dorsal aorta.	Possibly ersists in the walls of the dorsal aorta, which branches into axial (femoral) veins.	Potentially in the dorsal aorta.
Heart	Expression the ventricular wall of the heart (h)	Ventricular and atrial walls of the heart.	Strong in the ventricular wall of the heart, and in the atrial wall	Weak expression in the heart; possibly obscured by stronger expression in lungs.

4.2.4.2 *Fat4* expression at E14.5 in wildtype and muscle-less mutant forelimbs

At E14.5, embryonic tissues, especially in the skeleton, are too dense and complex to allow for effective wholemount *in situ* hybridisation, as RNA probes and/or staining components have limited penetration. To assess the expression pattern of *Fat4* at E14.5 (TS23), when the long bones begin to ossify and joints begin to cavitate, and the stage at which the phenotypic effect of immobilisation is first clearly evident, *in situ* hybridisation on vibratome sections was used. This showed expression patterns consistent with the whole mount approaches at earlier stages. Sections revealed distinct *Fat4* expression in the ectoderm and/or sub-ectodermal tissue of both wildtype and *Pax3*$^{Spd/Spd}$ muscle-less mutant forelimbs (Fig. 4.15a, a', black arrows). In the handplate, expression was detected in the tissue adjacent to the developing phalanges (Fig. 4.15b, b'; black arrows). Moderate expression was detected around the more proximal rudiments, in some places possibly in the perichondrium or muscle attachment points near the shoulder and elbow joints (Fig. 4.15c, c', d, d' black arrows). However, no detectable expression was observed at the core of the skeletal elements, either within the rudiments, or at the shoulder or elbow joint line. There was, however, some weak expression observed within the digit joints (Fig. 4.15b, b'; red arrows). Overall, there were no distinguishable differences between staining patterns in wildtype and *Pax3*$^{Spd/Spd}$ muscle-less mutant tissue.

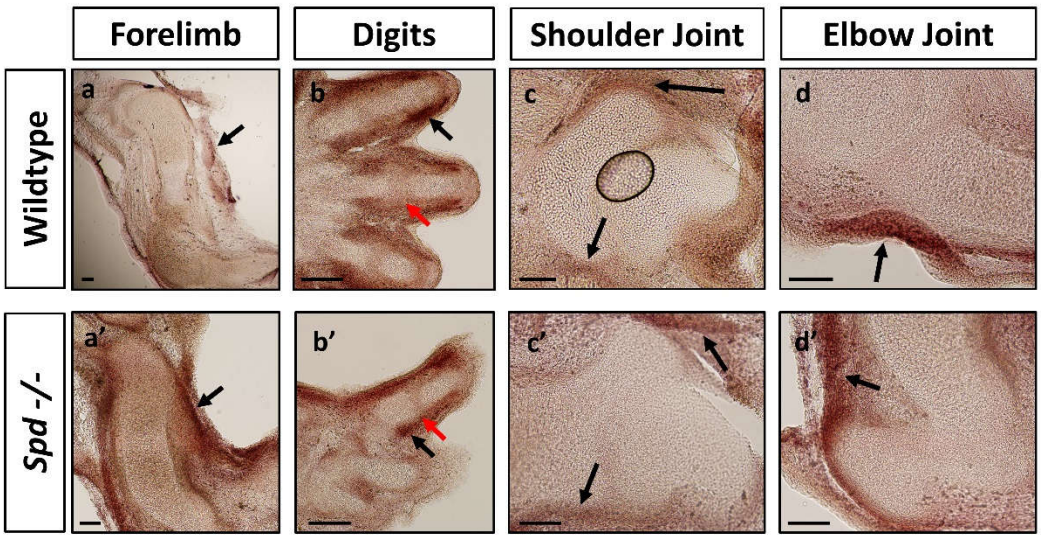

Fig. 4.15. *Fat4* is expressed in the forelimb ectoderm, perichondrium, and digit joints at E14.5. Vibratome sections (60µm) were *in situ* hybridised for *Fat4* in wildtype (a-d) and muscle-less mutant (a'-d') forelimb tissue. Arrows indicate observed expression, as described in the text. Scale bars are equal to 100 µm.

To further examine if *Fat4* is involved in skeletal development, *Fat4* null embryos (obtained from Dr. Helen McNeill (Toronto, Canada)) were examined by *in situ* hybridisation for collagen type IIaI (*Col2aI*) as a marker of the emerging cartilage rudiments, and compared to the phenotype of muscle-less ($Pax3^{Spd/Spd}$) null embryos (Fig. 4.16). *Col2aI* expression revealed no obvious abnormalities in joint formation in *Fat4* null mice, when compared to wildtype littermates or wildtype *Spd* mice: all three had clear separation of *Col2aI*-positive territories at the shoulder joint (Fig. 4.16a, a', b; black arrows) and the humero-ulnar (Fig. 4.16c, c', d; black arrows) and humero-radial (Fig. 4.16e', f) components of the elbow joint. This is in contrast to muscle-less embryos ($Spd^{-/-}$), where *Col2aI* expression is continuous at certain points in the shoulder and elbow joints (Fig. 4.16b', d' f', red arrows), indicating a reduced joint territory and partial fusion of skeletal rudiments. Ossification at the hypertrophic zone of *Fat4* null embryos also appeared relatively normal: when compared to *Fat4* wildtype littermates, this zone was similarly devoid of detectable *Col2aI* expression and was of normal size (Fig. 4.16g, g'; black bracket), and largely similar to the hypertrophic zone of *Spd* wildtype mouse (Fig. 4.16h, black bracket). This is in comparison to the muscle-less mutant, whose hypertrophic zone is reduced in size and lags in maturation, as indicated by reduced *Col2aI* staining in this region (Fig. 4.16h', red bracket).

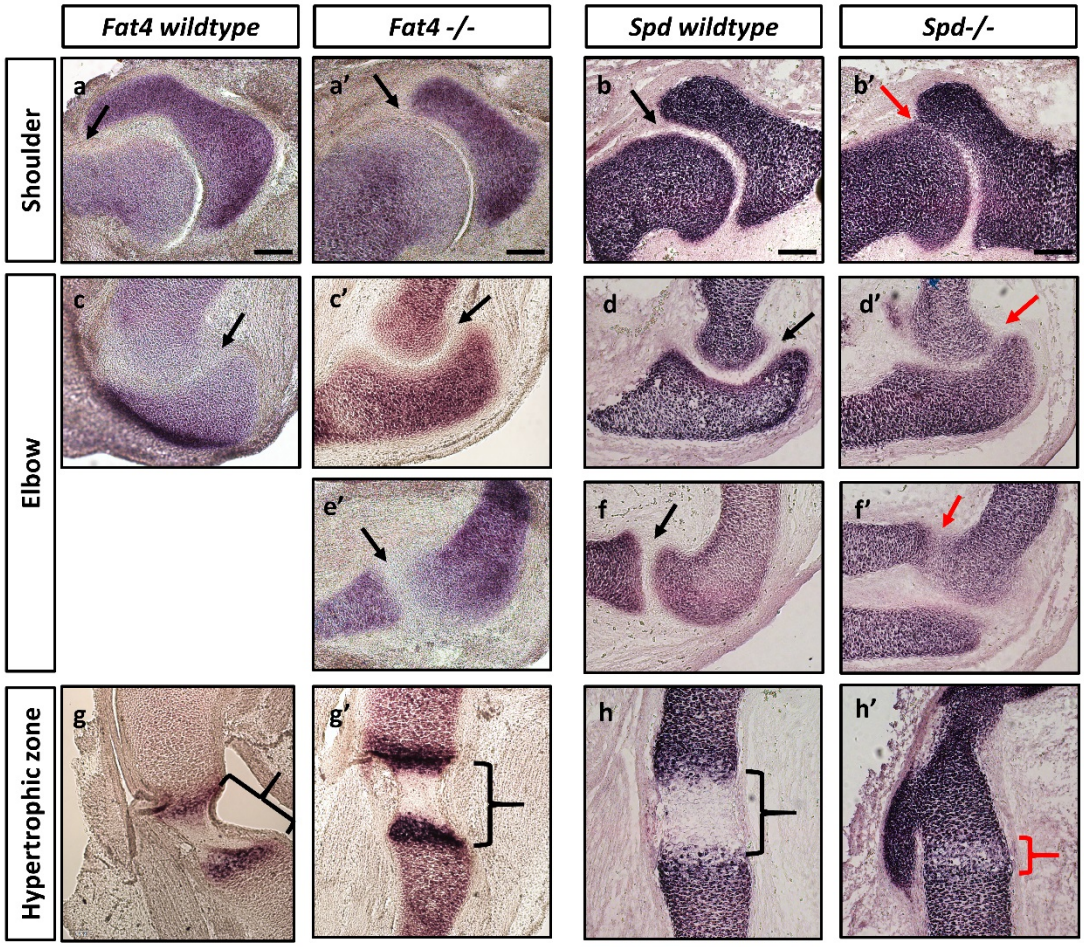

Fig. 4.16. Expression of *Col2aI* (to visualise the forming skeleton) in *Fat4* and *Spd* wildtype and mutant mouse forelimb skeleton. Paraffin sections of *Fat4* wildtype (a, c, g) and null mouse forelimbs (a', c', e', g'), as well as $Pax3^{Spd-/-}$ wildtype (b, d, f, h) and mutant (b', d', f', h') mouse forelimbs at TS23 (E14.5), underwent *in situ* hybridisation for collagen type 2aI to characterise skeletal formation at the shoulder (a-b') and elbow (c-f') joints and at the hypertrophic zone (g-h'). Black arrows and brackets indicate outwardly normal skeletal development, as described in the text, while red arrows and brackets indicate malformed skeletal elements, as described in the text. Scale bars equal 100 µm.

4.3 Discussion

The Hippo-YAP pathway is a relatively recently characterised signalling mechanism which has been implicated in mechanotransduction and cell differentiation. Its activity during development is not fully characterised, and the few descriptions of YAP activity in the developing skeleton are apparently conflicting. To address this, the work presented in this chapter sought to characterise the presence of pathway components in developing skeletal tissues, to form a basis for Hippo-YAP pathway involvement during normal skeletal development. This study revealed that YAP protein shows localised accumulation in key areas of the developing limb skeletal rudiments, and that this contrasts to the more uniform distribution of the inactive form of YAP, pYAP. It further showed that YAP protein levels are increased in the rudiments of the muscle-less mutant, which corresponds to expanded and increased expression of YAP pathway target genes, and indicates increased pathway activity under reduced mechanical stimulation. This study also demonstrated that blocking YAP pathway activity in micromass culture reduced chondrogenesis. Taken together this provides preliminary evidence that Hippo/YAP signalling is involved in regulating aspects of skeletogenesis and in particular mediating aspects of known mechnoresponsiveness.

Major components of the Hippo-YAP pathway — receptor/ligands, components upstream of the main effectors which modulate their activity, the main effectors YAP and TAZ, and YAP target genes — were determined to be expressed in mouse humeri and associated joints at E14.5. Compared to the expression levels of the whole transcriptome at this stage, Hippo-YAP genes are expressed at moderate to high levels. Another aim of this part of the work was to identify changes in Hippo-YAP pathway component expression or activity under reduced mechanical stimulation. Comparison of pathway component expression readout in wildtype and muscle-less tissue revealed that most genes maintained comparable levels of expression under reduced mechanical stimulation. Several genes, including the receptor *Fat4*, the transcription factor *Tead4*, and the target genes *Ankrd1* and *Col8aI*, were more than 2-fold up-or down-regulated. While *Tead4*, and *Ankrd1* were strongly down-regulated, genes with low read counts, particularly if expressed in adjacent muscle in the wildtype, are potentially more susceptible to inacuracy due to trace amounts of contaminating muscle tissue being included in the wildtype sample; this could result in a false positive of differential expression. Indeed, *Ankrd1*, which is known to be a major component of cardiac

muscle, was shown here to be highly expressed in muscle tissue and differential expression in skeletal rudiments was not supported by *in situ* hybridisation. *Fat4* and *Col8aI* were both significantly upregulated; however, neither showed localised increases in expression by *in situ* hybridisation. This could be explained by more widespread upregulation of these genes across tissues, which would not be observable by eye. Therefore the most striking differences in localisation of pathway components between wildtype and muscle-less embryos was in fact for YAP protein itself and two YAP target genes, *Ctgf* and *Cyr61*.

Current descriptions of YAP protein localisation during skeletal development in the literature are apparently conflicting. To attempt to resolve this, YAP protein localisation to skeletal tissues was assessed at E14.5, and the highest levels were observed in the hypertrophic zone. Lower, yet still distinct, protein levels were seen in morphological prominences such as the olecranon process of the ulna and the coronoid process of the scapula. These features allow for functional joint articulation and muscle attachment. Under immobilisation, rudiment morphology is affected, contributed to by reduced proliferation, and results in misshapen joints (Roddy et al., 2011b). In muscle-less rudiments, YAP levels are elevated throughout, and there is no distinct localisation of YAP protein to these morphological features. Further, YAP protein in the wildtype is reduced in the presumptive articular cartilage, while protein is detected up to the joint line in muscle-less tissue. This suggests more widespread Hippo-YAP signalling activity under reduced mechanical stimulation and loss of distinction between territories. In this study, YAP protein was detected in both the cytoplasmic and nuclear compartments of cells within the rudiments of wildtype and muscle-less specimens. Quantification of the proportion of cells with nuclear YAP, or the ratio between the staining intensity of cytoplasmic and nuclear YAP could be useful to assess overall levels of YAP transcriptional activity. Any differences in sub-cellular YAP localisation in muscle-less mouse could explain observed differences in YAP target gene expression, and would support a mechanosensory role for YAP in skeletal development. Conditional overexpression of YAP under the *Col2aI* promoter/enhancer was reported to show reduced hypertrophy and mineralisation, smaller growth plates, and overall shorter bones (Deng et al., 2016), similar to the phenotypic changes occurring under reduced mechanical stimulation. Although joint formation in YAP-overexpression mice were not obviously affected, epiphyseal subchondral bone was

reduced, and this would presumably affect joint morphology and functionality (Deng et al., 2016), which has not been specifically reported.

Increased Hippo-YAP signalling in the muscle-less mutant correlates with the observed changes in the expression patterns of YAP target genes *Ctgf* and *Cyr61*, both of which showed expanded detectable expression domains in muscle-less rudiments and joints. These genes encode extracellular matrix proteins which are structurally similar and belong to the same protein family, the CCN (*Cyr61*/Ccn1, *Ctgf*/Ccn2, and Nephroblastoma overexpressed/Ccn3) proteins (reviewed in Krupska et al., 2015). In early skeletal development, *Ctgf* is involved in the formation of mesenchymal cell condensations, but its expression is complementary to *Sox9*, and its downregulation is potentially required for subsequent cartilage differentiation (Song et al., 2007b). Later, *Ctgf* is expressed in the perichondrium and prehypertrophic/hypertrophic chondrocytes of the long bones, and *Ctgf*-null mice have expanded hypertrophic domains, which indicates that *Ctgf* inhibits chondrogenic maturation/hypertrophy (Friedrichsen et al., 2003, Ivkovic et al., 2003). Surprisingly, increased expression of *Ctgf* was observed in these domains in the muscle-less mouse, which contrasts with a reduction in other hypertrophic markers such as *Col10aI*. However, the reduced hypertrophic domain observed in the long bones of the muscle-less mouse could result in increased numbers of pre-hypertrophic cells which express *Ctgf*. The perichondrium matures ahead of the underlying cartilage, to which it sends molecular signals, and increased expression in the perichondrium of the olecranon process and other regions could indicate misregulation of the timing of cartilage maturation under reduced mechanical stimulation.

Increased intensity and an expanded domain of *Ctgf* expression in the presumptive articular cartilage at the joints of muscle-less mouse is particularly noticeable. Upregulation of *Ctgf* has been observed during skeletal repair and osteoarthritis (Nakata et al., 2002, Blaney Davidson et al., 2006, Nozawa et al., 2009), although it has conflictingly been suggested as a chondro-protective molecule during cartilage degeneration (Itoh et al., 2013). *Ctgf* is well-positioned for a role in the differentiation and maintenance of articular cartilage, as it binds with integrins to regulate cell-matrix interactions, which are crucial to cellular proliferation and differentiation (reviewed in Arnott et al., 2011). It can also influence the activity of matrix metallo-proteinases, which carry out extra-cellular matrix remodelling during skeletogenesis, and are

responsible for cartilage degradation during endochondral ossification (Vincenti and Brinckerhoff, 2002, Itoh et al., 2013).

Cyr61 is also well-expressed during skeletal development and contributes to chondrogenic differentiation (O'Brien and Lau, 1992, Wong et al., 1997), but in contrast to *Ctgf*, has been suggested to increase chondrocyte hypertrophy (Zhang et al., 2016). The reduction of expression in muscle-less rudiments at the hypertrophic zone fits with this role. Similar to *Ctgf*, it is upregulated in both fracture repair and osteoarthritis (Hadjiargyrou et al., 2000, Chijiiwa et al., 2015). In this study, *Cyr61* expression was increased in subchondral cartilage. The cartilage degradation that occurs during osteoarthritis does not necessarily correspond to the misregulation of articular cartilage differentiation that occurs under reduced mechanical stimulation, and so a reduction of *Cyr61* expression here could still be indicative of cartilage malformation. Mechanical stress has been demonstrated to regulate the expression of both *Ctgf* and *Cyr61* in numerous cell types, including chondrocytes (reviewed in Chaqour and Goppelt-Struebe, 2006), although the up- or down-regulation is dependent on cell type and context. Additionally, studies examining the effect of mechanical stimulation have been primarily in vitro, with little examination of gene expression in tissue.

Fat4 was examined as a potential regulator of Hippo signalling, as it is orthologous to *Fat*, the cell-surface receptor which mediates Hippo signalling in *Drosophila*. The role of *Fat4* in mammalian Hippo signalling is not well-defined, and other mechanoresponsive mechanisms which can regulate YAP transcriptional activity, such as cytoskeletal tension, have been identified. *Fat4* expression was noted in the developing limb over E10.5-E14.5, but this did not correspond with mesenchymal condensations. However, *Fat4* expression was observed at the periphery of the developing rudiments, which is potentially in the perichondrium. The perichondrium has a different genetic and developmental profile to underlying cartilage, and expression of *Fat4* here could indicate a role for canonical Hippo signalling in this tissue. Expression of *Fat4* was also noted across the territory of the developing knee and elbow joints at intermediate stages of joint development (E11.5-12.5), as well as in digit joints (E14.5). However, *Fat4*-null mice showed no obvious defects in joint formation, suggesting that *Fat4* is not required for normal joint patterning nor cavitation, despite its expression here. Therefore, while this study identified differential

patterns of protein localisation in the muscle-less mutant, it remains unclear how YAP protein localisation within the developing rudiments is regulated by mechanical stimulation.

A mechanism of YAP regulation which presents an alternative to *Fat4*-mediated control is the molecule Angiomotin (Amot) which, along with Angiomotin-like 1 and 2 (Amotl1/2), can bind YAP at cell junctions to interface with canonical Hippo proteins NF2/Mer, or can operate independently of Hippo signalling during development (Zhao et al., 2011, Leung and Zernicka-Goetz, 2013). As noted above, the lack of overlap between detected *Fat4* expression and YAP protein localisation in the developing skeleton suggests that a mode of YAP regulation that is independent from *Fat4*-mediated Hippo signalling is required during skeletal development. This signalling may additionally be independent from the canonical MST/LATS kinase cascade, and the cytoskeleton and Angiomotin and its associated proteins are mechanisms that could be investigated to further identify upstream regulators of YAP activity during skeletal development. Numerous cytoskeletal components were found to be differentially regulated in the muscle-less mouse humerus and associated joints (Rolfe et al., 2014), and so an alteration in the structure of the cytoskeleton under reduced mechanical stimulation has the potential to alter YAP activity. In the same transcriptomic data, *Amot* and *Amotl1/2* are all highly-expressed (>3,000 reads) in both wildtype and muscle-less mutant humeri and associated joints and therefore could be involved in YAP regulation, either independently or as part of the canonical Hippo signalling pathway.

Crosstalk between YAP and other signalling pathways has been reported in multiple contexts, and adds another layer to our understanding of YAP regulation and activity. Both non-canonical and Wnt/β-catenin signalling regulate YAP activity directly, meaning that Wnt signalling could regulate the expression of YAP target genes indirectly via YAP, or directly (Azzolin et al., 2014, Park et al., 2015). The same studies note that YAP is a required component of the β-catenin destruction complex, and that non-canonical *Wnt5a*/b are targets of YAP signalling, suggesting that YAP and Wnt engage in signalling feedback loops. Further, the expression of YAP target genes can also be regulated by Wnt signalling: *Ctgf* has binding sites for *Sox9* and TCF/LEF which can regulate *Ctgf* expression, independent of YAP involvement (Huang et al., 2010b), and *Cyr61* can also be upregulated by canonical Wnt signalling through β-

catenin (Morin-Kensicki et al., 2006, Zhang et al., 2016). Changes in YAP protein and target gene expression under reduced mechanical stimulation, as observed here, could therefore be related to observed Wnt signalling changes. A relationship between YAP and BMP signalling in the context of chondrogenesis and osteogenesis has also been reported in the literature: YAP overexpression in mesenchymal C3H10T1/2 cells downregulated pSMAD1/5/8 and BMP target gene expression in high-density chondrogenic culture (Karystinou et al., 2015), but the same caused upregulated BMP4 expression in endothelial cells and promoted intramembranous ossification (Uemura et al., 2016). An expansion of BMP activity was observed in the joints of immobilised mouse and chick (Chapter 3) and this could be caused by or related to increased YAP activity, as presented in this chapter. YAP has been implicated in the regulation of TGF-β signalling in renal and lung development, but not in the context of skeletogenesis (reviewed in Hansen et al., 2015).

To further define the role of YAP during chondrogenesis, micromass cultures were treated with the YAP-inhibitory molecule verteporfin. Embryonic limb bud cells cultured in high density micromass robustly undergo chondrogenic differentiation (Section 1.6; described in detail in Chapter 6). Inhibition of YAP by verteporfin reduced chondrogenesis, as indicated by Alcian Blue staining and expression of marker genes of chondrogenesis and hypertrophy. These results indicate that YAP has a pro-chondrogenic role in this system, and suggest that YAP could act in a similar manner during *in vivo* skeletogenesis. This agrees with other *in vitro* observations that stiffer substrates, which promote chondrogenesis and osteogenesis, induce higher levels of nuclear YAP in MSCs (Halder et al., 2012). To refine the role of YAP and its upstream regulation during skeletal development, conditional mutants or other *in vivo* functional studies are required. YAP conditional ectopic expression or deletion under the *Col2aI* promoter/enhancer was previously used to examine the role of YAP in chondrogenic differentiation and maturation (Deng et al., 2016). While this study examined changes in target genes by qRT-PCR, it would be useful to examine spatial changes in the expression of *Ctgf* and *Cyr61* to confirm their role as YAP targets in this tissue. YAP and TAZ, while structurally similar, can have distinct and sometimes opposing functions, and therefore could have very different functions during skeletal development. Although in this study the premise has been taken that YAP is predominantly implicated in skeletogenesis, it would be useful to conditionally delete

both genes and compare to single knockouts, or to examine if ectopic TAZ expression could compensate for loss of YAP in these tissues, to definitively distinguish between these two proteins. Conditional expression or deletion under *Col2aI* control is frequently used to examine the role of genes in cartilage maturation and hypertrophy; however, conditional mutants under the control of earlier markers of skeletal development, such as the *Sox9* transcription factor, would allow for assessment of YAP's role in other stages of skeletogenesis. Likewise, further restriction of YAP deletion, for example under the control of *Gdf5* to target the joint, could be used to explore the role of YAP in the differentiation of articular cartilage. The use of small molecules, such as verteporfin, is an alternative to genetic manipulation, and is another means to inhibit YAP activity in order to assess its function. This would be an attractive option in the context of mechanical stimulation, as such treatment could be combined with a neuromuscular inhibitor in the chick model. To date, there are very few studies of Hippo signalling or YAP activity in chick, and the pathway could operate differently than in the mouse. However, as the chick embryo is more accessible to manipulation during development, this could be a valuable means to simultaneously examine YAP and mechanical stimulation during skeletogenesis.

Chapter 5

Investigation of a candidate mechanism of mechanotransduction in the developing skeleton: The primary cilium

5.1 Introduction

The primary cilium is a specialised organelle present on diverse cell types in developing and mature tissues. Cilia have been studied during organogenesis of the kidneys, nervous system, heart, and skeleton (Gerdes et al., 2009, Fry et al., 2014). As reviewed in Section 1.5.2, the role of cilia in the development of each of these organs is characterised to a different extent, and varies between organs and cell types. However, in multiple contexts they have been shown to act as signalling centres for the Hedgehog, Wnt, and calcium signalling pathways, with components of these pathways localising to the cilium body (Goggolidou, 2014, Delling et al., 2016, Bangs and Anderson, 2017). Further, they have been implicated in mechanosensensation, suggesting that they could coordinate the regulation of signalling pathways and physical stimuli simultaneously during the differentiation of cell and tissue types.

As described in Section 1.5.2, cilia have been observed and described on chondrocytes in culture, on embryonic sternal cartilage, and in adult skeletal tissues. The ablation of cilia during skeletal development is detrimental to the formation of the rudiments, resulting in shortened long bones, disorganised growth plates, and polydactyly (reviewed in Haycraft and Serra, 2008) (Table 1.2). Conditional knockouts of Smad1/5, which have disorganised growth plates and altered hedgehog signalling displayed a loss of normal cilium orientation (parallel to the long axis of proliferative chondrocytes), suggesting that cilium orientation is essential to the columnar alignment

of proliferative chondrocytes (Ascenzi et al., 2011). This is further suggested by the loss of columnar organisation in growth plate cartilage of ciliary knockouts (Song et al., 2007a). Despite the proven necessity of functional cilia during skeletal development, a description or characterisation of the cilia in the developing rudiments and joints is lacking from the literature, making it difficult to identify instances of abnormal cilia in skeletal tissues. Such a description would also be an important basis to assessing the possible contribution of cilia to the mechanoregulation of skeletal development.

The location and structure of the cilium – on the exterior of the cell and extending outward – positions it ideally to respond to extra-cellular stimuli and mechanical forces. The main shaft of the cilium projects into the extra-cellular space, potentially interacting with components of the extra cellular matrix as well as with ligands or other diffusible molecules. This position also allows it to respond to mechanical forces such as fluid flow, tension, and compression, as has been shown in mesenchymal stem cells (MSCs), and cells of the mature endothelia, kidney, liver, and bone (reviewed in Hoey et al., 2012a, Spasic and Jacobs, 2017b). During development, the fluid flow mechanosensitivity of primary cilia is crucial to establishment of asymmetry at the embryonic node, as well as calcium signalling during kidney development; inhibition of these processes results in patterning defects and polycystic kidney disease (Nonaka et al., 2002, reviewed in Bisgrove and Yost, 2006).

The length of the cilium is dynamic, and varies between cell types (summarised in Dummer et al., 2016): chondrocytes have been reported to have short cilia (typically between 1-4 μm) (Poole et al., 2001, McGlashan et al., 2008, Ascenzi et al., 2011, Thompson et al., 2014, Martin et al., 2017), while cilia detected on neuronal cells are longer (approx. 10 μm) (Miyoshi et al., 2014, Hamamoto et al., 2016). The length of the cilium has implications for mechanosensitivity and cell signalling, as does the capacity of the cilium to be deflected with respect to the rest of the cell. Several studies have modelled the effect of cilium deflection on cell membrane strain under simulated fluid flow conditions, demonstrating that short (e.g. 0.5 or 3 μm) cilia could not effectively serve as mechanosensors, while longer (e.g. 4 or 10 μm) cilia were capable of greater membrane strain and cilium deflection (Khayyeri et al., 2015, Vaughan et al., 2015). However, few *in vitro* studies exist which directly examine the effect of cilium length on mechanosensation. Artificial elongation (a 26-46% increase from 3 μm to 3.5-5μm) or shortening (from 3.4 μm to 2.5 μm) of cilia on bone cells have

demonstrated that longer cilia are more mechanosensitive (Ehnert et al., 2017, Spasic and Jacobs, 2017a). Contrarily, idiopathic scoliosis osteocytes, which have lengthened cilia (a 30-40% increase from ~2 μm to ~3 μm), have impaired mechanosensitivity (Oliazadeh et al., 2017). Additionally, in response to compression or fluid flow, chondrocyte, tendon, and renal cilia are shortened (from 2.2 to 1.3 μm, from 3 to 1 μm, and from 2.6 to 2 μm, respectively) (Resnick and Hopfer, 2007, McGlashan et al., 2010, Gardner et al., 2011). Changes in cilia length have been shown to also alter cell signalling dynamics: elongated cilia increase the inflammatory signalling response while shortened cilia decrease Hedgehog signalling activity on articular chondrocytes (Wann and Knight, 2012, Thompson et al., 2014). Contrastingly, cilium length is inversely correlated to Wnt activity: elongated cilia on MSCs (from 2.5 μm to 3 μm) have decreased canonical Wnt activity, while shortened cilia (from 3 μm to 2 μm) have increased nuclear β-catenin (McMurray et al., 2013). These properties suggest that the cilium can sense and respond to the extra-cellular environment, and therefore could be a mechanotransductive mechanism for cells in the emerging skeletal tissues.

An important pre-requisite for identifying a role for cilia in specific cell types or regions of the developing limb skeleton is the presence of cilia on those cells. If cilia play an active role in the transduction of mechanical forces during skeletal development, then reduced mechanical stimulation during embryonic development could impact the differentiation of skeletal tissues by altering signalling activity at the cilium. The presence of cilia, and cilia characteristics such as length and orientation have also been related to cell activities such as proliferation, with cilia shortened or dismantled as chondrocytes divide (Thompson et al., 2017). Therefore, a description of cilium occurrence, length and orientation would be valuable for assessing their potential role. In addition, alteration of these properties in skeletal tissues under reduced mechanical stimulation would support a role for cilia in mechanotransduction in this context.

5.1.1 Aims of this chapter

1. *To characterize primary cilia in the developing skeletal rudiments and joints at E14.5.* Primary cilia have been observed and described on chondrocytes in culture and in adult skeletal tissues, and have been observed during skeletal development, however there is no thorough description or characterisation of cilia during development of the limb skeleton. This work sought to address this lack of knowledge by characterising the occurrence, length, orientation, and cellular location of cilia in different regions of the developing skeletal rudiments and joints. This was performed by immunofluorescent localisation of cilia in forelimb rudiments at TS23 (E14.5), followed by image analysis and quantification.
2. *To compare the characteristics of primary cilia in* $Pax3^{Spd/\ Spd}$ *(muscle-less) rudiments and joints to those in wildtype rudiments.* Cilia have been implicated in the sensation of physical forces, and in the regulation of intracellular signalling. Therefore, an alteration in cilia occurrence or structure under reduced mechanical stimulation could indicate a response to reduced stimulation and contribute to the observed phenotypic differences in the developing skeleton. For this reason, the characteristics of the primary cilia (occurrence, location, orientation, and length) were evaluated in muscle-less forelimb rudiments and joints at TS23 by immunofluorescent localisation and image analysis and quantification, and were compared to the wildtype. This identifed differences in cilia characteristics occurring under immobilisation.

5.2 Methods

5.2.1 Immunolocalisation of cilia and image collection

Cryosections (10 µm) of wildtype and mutant *Pax3*^{Spd} mouse forelimbs at TS23 were prepared as described in Section 2.1.3. A total of 4 wildtype and 3 mutant specimens were analysed, with images collected from 1-2 sections per specimen. Immunofluorescence was carried out as described in Section 2.4, using antibodies against two types of tubulin which localise to different parts of the primary cilium (acetylated α-tubulin to the cilium shaft and γ-tubulin to the cilium base (Table 2.3), and counterstained with DAPI to visualise nuclei (Fig. 5.1A). Images were collected using a fluorescent microscope with a 40x objective, or a confocal microscope with a 40x or 63x objective, capturing nine different regions of the developing rudiments and associated joints (Fig. 5.1B).

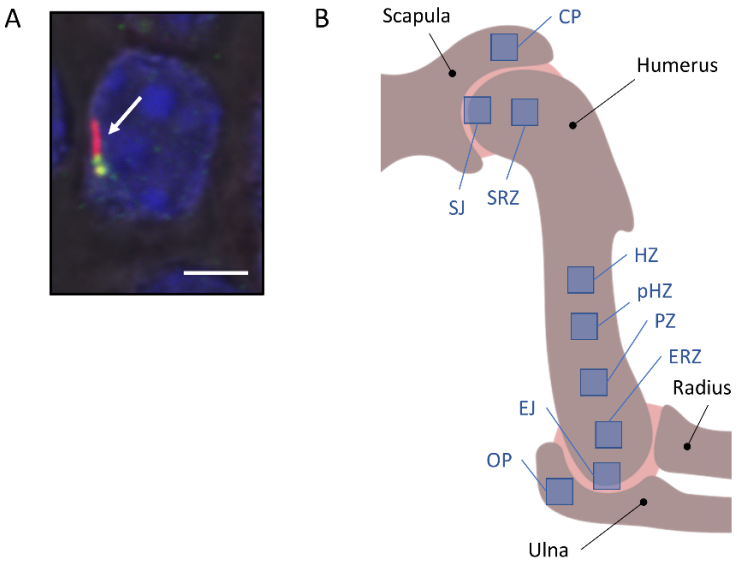

Fig. 5.1. Methodology for visualisation and imaging of primary cilia. (A) Representative image (confocal) of a primary cilium (white arrow) on a chondrocyte in the resting zone of the radius at TS23, immunostained with α-acetylated tubulin (red) and γ-tubulin (green); the nucleus is stained with DAPI (blue). Scale bar is 2 µm. (B) Schematic of the developing humerus and associated joints, with sampled territories indicated. Territories sampled in this study are indicated by blue boxes (100 x 100 µm): coracoid (CP) and olecranon (OP) processes of the scapula and ulna, respectively, elbow (EJ) and shoulder (SJ) joints, elbow and shoulder resting zones (ERZ and SRZ, respectively), hypertrophic zone (HZ), prehypertrophic zone (pHZ) and proliferative zone (PZ). Box sizes are approximately to scale, relative to forelimb structures.

5.2.2 Image processing

After image collection, images captured with different filters (different wavelength channels) were imported into ImageJ software (National Institutes of Health, Bethesda, MD, USA) and cropped to defined regions of interest (ROIs) (100 μm by 100 μm) (Fig. 5.2). The individual colour images were each processed with the Split Channels function, which splits images to their respective red, green, and blue colour components (Fig. 5.2d-f''). Depending on the exposure time, different channels gave the best signal-to-noise ratio (the channels selected for further analysis were kept consistent within an experiment, but could vary between experiments). In general, the blue or green channels were used for nuclei, the red or green channels were used for α-acetylated tubulin, and the green channel was used for γ-tubulin. Once the colour components were selected (Fig. 5.2d', e'', f; yellow boxes), these greyscale images were used for further processing (Fig. 5.3).

Fig. 5.2 (following page). Processing of colour images for cilia analysis. An example of image processing is shown here, for the resting zone of the proximal humerus. Cryosections (10 μm) were immunostained for DAPI (a-f), acetylated α-tubulin (b'-f'), and γ-tubulin (b''-f'''). (a) Low-magnfication (20x) image of the proximal humerus (outlined by yellow dashed line); regions of interest indicated by boxes. Images captured at 40x magnification (b-b'') were processed for cilia analysis by cropping to 100 x 100 μm regions of interest (c-c''; yellow boxes in (b-b'')). The cropped images were split into their component colour channels, which generated three greyscale panels for each image (d-f''). The channels which gave the strongest signal to noise ratio (d', e'', f; outlined in yellow) were saved as greyscale images and further processed. Scale bars are 200 μm.

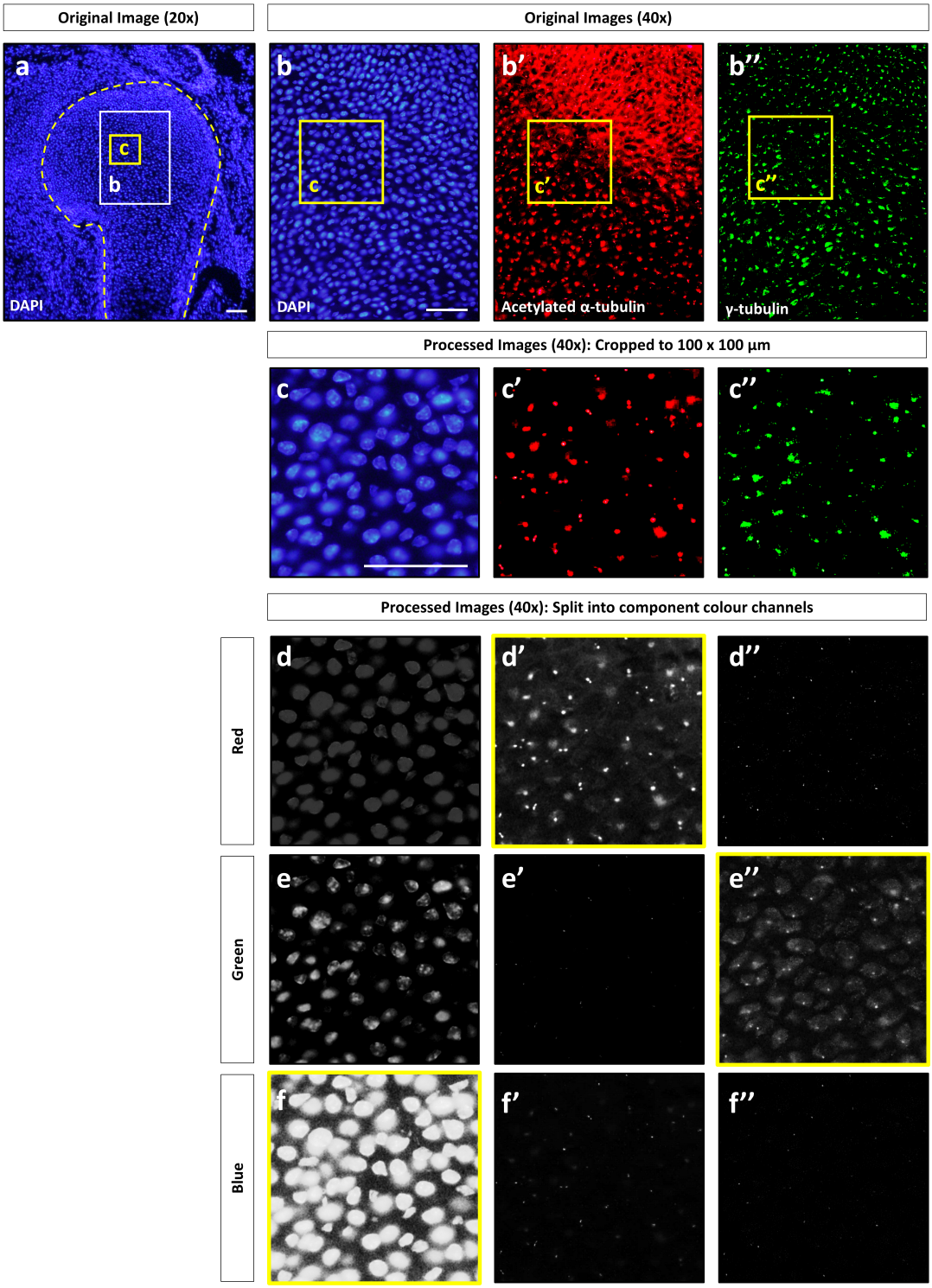
Original Image (20x)
Original Images (40x)
a
c
b
DAPI
b
c
DAPI
b'
c'
Acetylated α-tubulin
b''
c''
γ-tubulin
Processed Images (40x): Cropped to 100 x 100 µm
c
c'
c''
Processed Images (40x): Split into component colour channels
Red
Green
Blue
d
d'
d''
e
e'
e''
f
f'
f''

The greyscale DAPI image was further processed in order to count the number of cells (nuclei) within an ROI. This was done by applying a Gaussian Blur filter (typically with a sigma value of 3 pixels) (Fig. 5.3a). This is a smoothening function which improves subsequent detection of the nuclei. The greyscale image for DAPI was then converted to a black and white image using the Threshold function, which divides images into two classes of pixel (foreground and background) (Fig. 5.3c). The level of thresholding was determined by using the Auto Threshold level set by ImageJ as a guide, and subtracting 10 (a lower threshold value for bright objects on a black background, as for fluorescently-stained cells, indicates that more pixels were classed as foreground). Overall, thresholding was consistent across images collected from individual specimens, with applied thresholds varying only slightly. The Despeckle and Watershed functions were then applied to the black and white image (Fig. 5.3d). Despeckling eliminates salt-and-pepper noise from the images by replacing pixels with their median neighbourhood (3 x 3 pixels) value. Watershed segmentation separates detected objects (such as nuclei) that are touching or overlapping. The final thresholded nuclei image was compared by eye to the original, colour, nuclei image to ensure that all nuclei were separated. In some cases, Watershed did not detect merged nuclei as two distinct objects, and so a line was manually drawn (width = 2 pixels) between the nuclei using the Freehand tool. Finally, each thresholded, 'cleaned' image was processed with the Analyze Particles function which outlines and counts each detected 'particle' or object within an image. The minimum size for particle detection was set to 20 μm^2 for nuclei (to eliminate out-of-plane nuclei). For all analyses, objects on the edge of the image were not counted. Before running the Analyze Particles function, ImageJ was set to measure the X and Y coordinates of the centroid of each object, as well as the size. These data were saved as .csv files. Details of this process are included in Appendix B.

Simultaneously, the greyscale tubulin images were combined and processed, to identify cilia by the colocalization of detectable α- and γ- tubulin at the base of the cilium, which is specific to primary cilia. This was done using the Colocalization Plugin in ImageJ (https://imagej.nih.gov/ij/plugins/colocalization.html) (Fig. 5.3a'-b'), which merges two images together as red and green channels, while converting colocalised pixels to white (Fig. 5.3b'; inset, yellow arrow). Pixels are considered colocalised if they are above the respective threshold intensity of each channel, and if their ratio of

intensity is higher than a set percentage (50% by default; 10% was found to be optimal for processing images here). To determine the appropriate threshold intensity for the red and green channels, the threshold value given by ImageJ under the 'moments' method (in place of the 'default' method) was used, without adjustment. The Colocalization plugin also outputs a binary image with colocalised points in white, which was inverted to a white background with black points (Fig. 5.3c'; inset, red arrow). Despeckling was not useful here, as the points were typically small and would be misinterpreted as noise using this function; nor was watershedding useful, as the points were usually distinct. The image was then processed as above through Analyze Particles (a minimum size of 2 pixels to eliminate noise), to count the number of cilia (Fig. 5.3e') and generate a list of X and Y coordinates for each colocalised point. To verify the detected cilia, the colocalised points were compared to a merged colour image of nuclei and α- and γ-tubulin. In some instances, cilia were detected on cells which were at the edges of the ROI and therefore not included in the analysis, or on cells below the 20 μm size threshold; these were removed from the data set.

Fig. 5.3 (following page). Processing of greyscale images for cilia analysis. Greyscale component colour images, as described in (Fig. 5.2), were used for further processing and analysis. Nuclei were first processed (a-e). A Gaussian Blur (of sigma size 3.00) was applied to the DAPI image (a), to smooth nuclei shape (b). A threshold was then applied to generate a black-and-white (binary) image (c). Noise was removed using the Despeckle function (d). Merged nuclei were separated by applying the Watershed function (d). The resulting image was compared by eye to the original DAPI image to verify separation of all nuclei. Where automated Watershed processing had not separated nuclei, a white (background colour) line was drawn by hand (width = 2 pixels). Images were then processed with the Analyze Particles function, which outlined and numbered each detected particle above a set minimum size (20 μm^2) (e). At the same time, the tubulin images were processed (a'-e'). The Colocalization function was used to detect overlapping α- and γ-tubulin staining by merging the grayscale images together (a' and a''). The resulting overlay shows red and green channels with overlapping pixels (above a specified threshold) converted to white (b'; inset, yellow arrow). The "Colocalized points 8-bit" option in this function generates a binary image of colocalization, with overlapping pixels in white and all others in black; this can be inverted to generate black points on a white background (c'; inset, red arrow). Analyze Particles is run, with no minimum particle size (e').

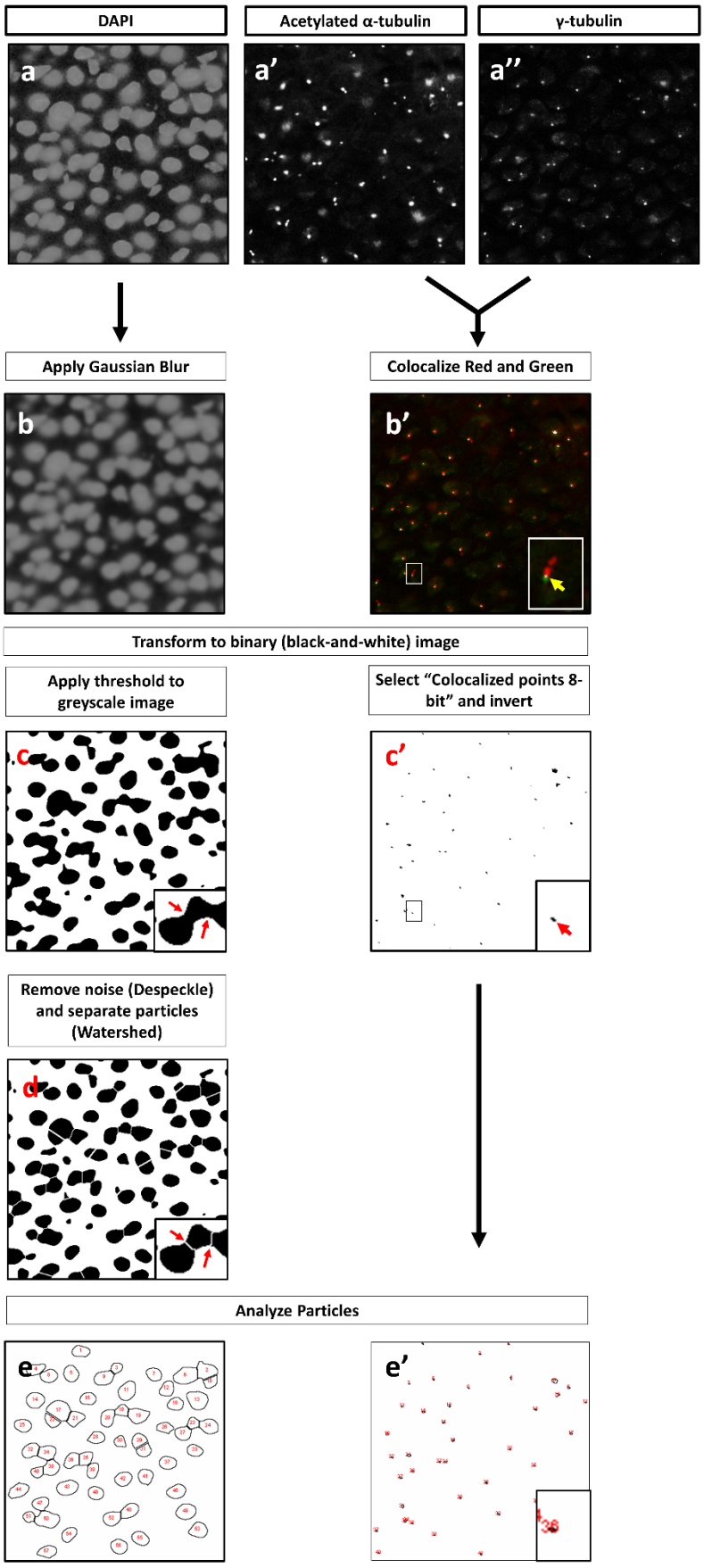
DAPI
Acetylated α-tubulin
γ-tubulin
a
a'
a''
Apply Gaussian Blur
Colocalize Red and Green
b
b'
Transform to binary (black-and-white) image
Apply threshold to greyscale image
Select "Colocalized points 8-bit" and invert
c
c'
Remove noise (Despeckle) and separate particles (Watershed)
d
Analyze Particles
e
e'

5.2.3 Quantification of cilia properties

Quantification of ciliated cells (cilia occurrence) and position of cilium on the cell. To determine the number of ciliated cells within a given region of interest, the results of the Analyze Particles processes for both nuclei and colocalised tubulin staining (cilia) were used. The proportion of ciliated cells (**cilia occurrence**) was simply calculated as the total number of cilia divided by the total number of detected cells, as indicated by DAPI-stained nuclei (Fig. 5.4A, black arrows). Nuclei below the 20 μm size threshold did not count toward the total cell count, as these cells are likely outside the plane of focus and could represent false negatives for cilia occurrence (Fig. 5.4A, orange arrow). The use of multiple antibodies to detect cilia eliminated the possibility of false positives that could result from use of a single antibody, due to the presence of α-tubulin at the mitotic spindle, or γ-tubulin in basal bodies during cell division (Fig. 5.4A, yellow arrow). Additionally, the mitotic spindle is easily recognisable, as it is structurally distinct from a cilium (Fig. 5.4A), and therefore this did not contribute to the cilium count.

A set of reference axes were fitted to the processed images, where 0°-180° is the proximal-distal long axis of the humerus and 90°-270° is perpendicular to this, as the anterior-posterior axis (Fig. 5.4B). As the shoulder joint is not perfectly aligned to this axis, and varies slightly according to the section examined, the reference axes for the shoulder joint were set so that the anterior-posterior axis (90-270°) was parallel to the joint line (Fig. 5.4B, inset). At the shoulder resting zone, the main reference axes (with 0°-180° aligned to the long axis of the humerus) were used, as the images analysed were sufficiently distant from the joint line. The reference axes were used for cilia position and orientation measurements.

The x- and y-coordinates of each detected cilium and each cell centre within the ROI were also generated from the Analyze Particles process, and these were used to calculate characteristics of the **cilium position** on the cell (Fig. 5.4C). The distance from the cell centre to the cilium was calculated by Pythagorean distance (distance = $\sqrt{(x_c-x_n)^2+(y_c-y_n)^2}$, where (x_c, y_c) are the coordinates of the cilium and (x_n, y_n) are the coordinates of the cell (nucleus) centre). From these coordinates, the angle of the line made from the cell centre to the cilium with respect to the reference axes could be calculated. To categorise cilium position with respect to forelimb orientation, four

quadrants were set: 45°-135° (Q1; anterior), 135°-225° (Q2; distal), 225°-315° (Q3; posterior) and 315°-360° and 0°-45° (Q4; proximal) (Fig. 5.4C).

Quantification of cilia orientation and length. Confocal images, collected on a Leica SP8 scanning confocal microscope, were used to quantify cilia orientation and length (Fig. 5.4D and E). Confocal z-stacks (stack size 4-5 μm; z-step 200 nm; xy resolution 120 or 240 nm) were merged into a single image using the Z-projection function in ImageJ, with maximum pixel intensity. To quantify **orientation of the cilium** shaft, the x- and y-coordinates of the base of the cilium as indicated by γ-tubulin staining (x_γ, y_γ), and of the centre of the shaft of the cilium as indicated by α-tubulin staining (x_α, y_α) were used (Fig. 5.4D). These coordinates were obtained by thresholding individual channels and using the Analyze Particles function, as described for the analysis of cilia occurrence and position (above). The angle (θ) formed by the Pythagorean line between these two and the reference axes was then calculated (Fig. 5.4D).

Cilium length was calculated using confocal z-stacks of images and applying the Skeletonize3D plugin in ImageJ (Fig. 5.4E). Image stacks were first converted to 8-bit by thresholding under the same parameters as used for measuring cilium orientation (above), and run through the Skeletonize3D plugin, which removes pixels from the edges of detected objects, effectively thinning them until a single-pixel centreline (skeleton) remains (Lee et al., 1994) (Fig. 5.4E, black curved line). Detected cilia were quantified by applying the Analyze Skeleton (2D/3D) function in ImageJ to skeletonized stacks, which reports the length of each detected element. To verify the accuracy of this method, automated length measurements of representative cilia were compared to a manual method of cilia length measurement. The manual method consisted of measuring the cilium length in x-y space using the line tool in ImageJ on maximum-intensity Z-projected images, and measuring cilium depth by noting the first and last z-slices in which the cilium was visible above the set threshold. From these measures, the length of the cilium could be calculated in Euclidean space, where length = $\sqrt{((\text{cilium xy length})^2+(\text{cilium z depth})^2)}$. The automated method of cilium measurement, using skeletons, was determined to be more representative of actual cilium length, as cilia are frequently curved in 3-D space and this curvature is not reflected in a simple Pythagorean calculation. In both the automated and manual methods, cilia appearing in the first or last z-slice were excluded from analysis.

Data plotting and statistical analysis. Directional data (cilium position, cilium orientation) were plotted as rose histograms using the R package Circular (Agostinelli and Lund, 2017). Statistical analyses were done using NCSS and GraphPad/Prism software for one-way ANOVA, chi-squared, and t-tests, and for further analysis of circular statistics. Goodness-of-fit tests for uniform distribution were conducted by Kuiper's and Watson's methods; tests of equal distribution and direction between wildtype and mutant were done using the Mardia-Watson-Wheeler uniform scores test (distribution) and the Watson-Williams F test (direction), using NCSS software.

Fig. 5.4 (following page). Aspects of cilia captured in this analysis.

A. Cilia occurrence was calculated as the total number of cilia (black arrows) divided by the total number of cells, as indicated by DAPI staining of nuclei (blue circles). DAPI signal smaller than 20 μm^2 (light blue circles) did not contribute to the cell count (orange arrows). Co-localisation of both α-tubulin (red) and γ-tubulin (green) ensured that false positives did not result from staining of the mitotic spindle or basal bodies during cell division (yellow arrow), structures which are easily identifiable and which did not contribute towards the cilium count.
B. Reference axes were drawn with respect to the orientation of the forelimb, with 0°-180° as the proximal-distal long axis of the humerus and 90°-270° (anterior-posterior) perpendicular to this. At the shoulder, the reference axes were shifted so that the axis from 90°-270° was parallel to the joint line (inset).
C. Cilium position on the cell was calculated using the x- and y- coordinates of the cilium and the cell centre; this generated both the distance of the cilium from the cell centre, as well as the angle (θ) which a line drawn from the centre of the cell to the cilium makes with the reference axes. Cilium position was scored as belonging to one of four quadrants on the cell, relating to the orientation of the humerus: 45°-135° (Q1; anterior), 135°-225° (Q2; distal), 225°-315° (Q3; posterior) and 315°-360° and 0°-45° (Q4; proximal).
D. Cilium orientation was determined using confocal stacks, where individual images were merged into a single image for analysis. The x- and y-coordinates of the base of the cilium (indicated by γ-tubulin staining, green circle) (x_γ, y_γ), and of the centre of the shaft of the cilium (indicated by α-tubulin staining, red line) (x_α, y_α) and calculating the angle (θ) formed by the Pythagorean line between these two and the reference axes (B).
E. Cilium length was calculated using unmerged confocal z-stacks which were skeletonized, resulting in traces (black curved line) of each cilium from base (x_1, y_1, z_1) (black dots) to the distal tip of the shaft (x_2, y_2, z_2) (black dots). The length of the skeleton in 3-D space (as represented by the dashed cuboid) was measured in ImageJ.

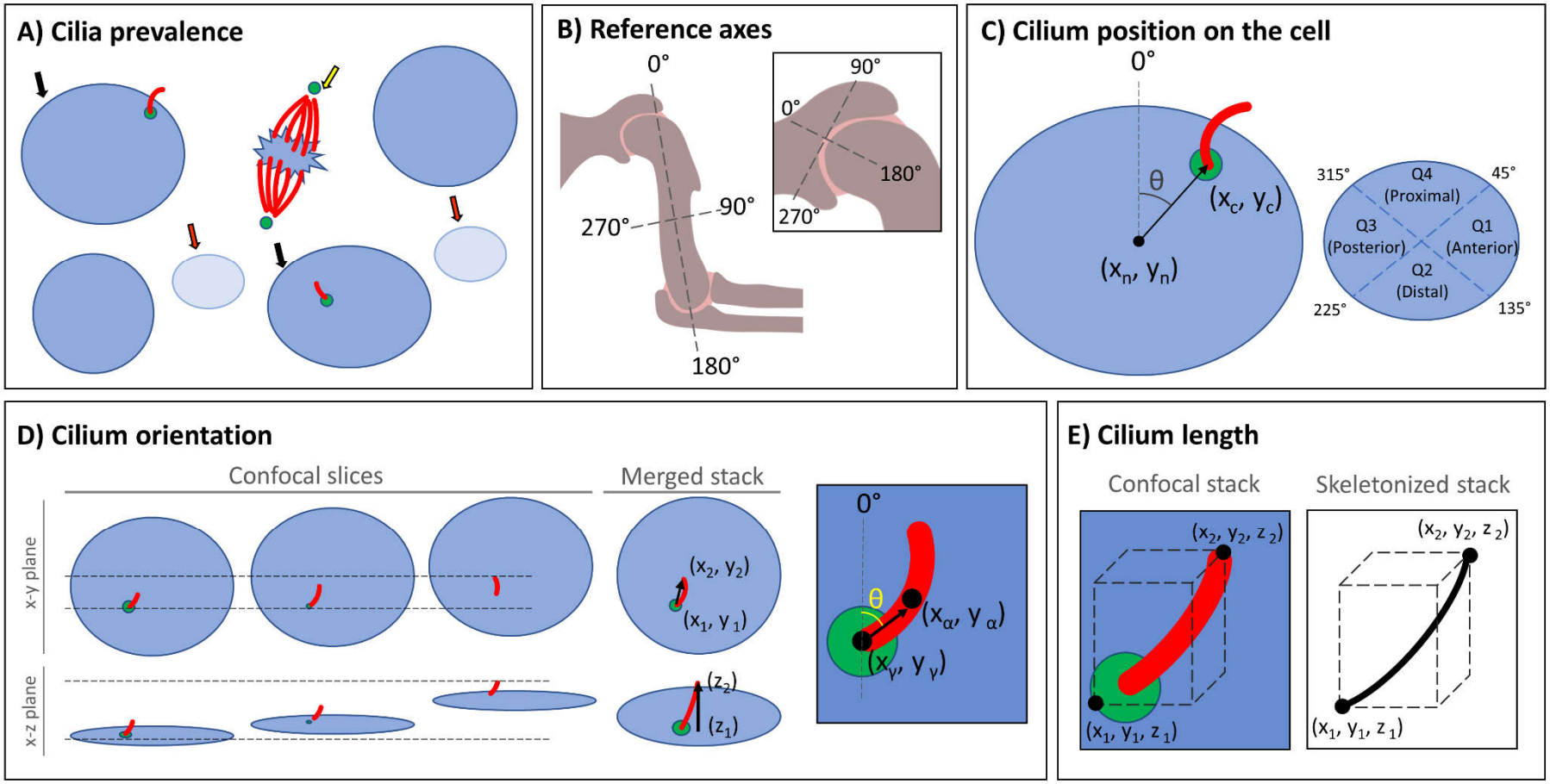
A) Cilia prevalence
B) Reference axes
0°
90°
270°
180°
C) Cilium position on the cell
θ
(x_c, y_c)
(x_n, y_n)
315°
45°
225°
135°
Q4 (Proximal)
Q3 (Posterior)
Q1 (Anterior)
Q2 (Distal)
D) Cilium orientation
Confocal slices
Merged stack
x-y plane
x-z plane
(x_2, y_2)
(x_1, y_1)
(z_2)
(z_1)
(x_α, y_α)
(x_γ, y_γ)
E) Cilium length
Confocal stack
Skeletonized stack
(x_2, y_2, z_2)
(x_1, y_1, z_1)

5.3 Results

5.3.1 Characterisation of primary cilia in the wildtype developing skeletal rudiments

Cilia occurrence. Immunolocalisation was used to detect cilia in the wildtype rudiments. Co-localisation of acetylated α-tubulin and γ-tubulin, which identify the shaft and the base of the cilium, respectively, was used as an indicator of a primary cilium (Fig. 5.5). Cilia were visible throughout the rudiments, on chondrocytes in the resting, proliferative, pre-hypertrophic and hypertrophic zones (Fig. 5.5A). They were also detectable on chondrocytes at the shoulder and elbow joints (Fig. 5.5B), and in morphological features such as the olecranon and coracoid processes (Fig. 5.5C). To assess the proportion of ciliated cells, 1-2 sections from 2-4 specimens were analysed for each zone (Fig. 5.6, B, Table 5.1). For elbow joint measurements, the humeral-ulnar aspect of the joint was analysed.

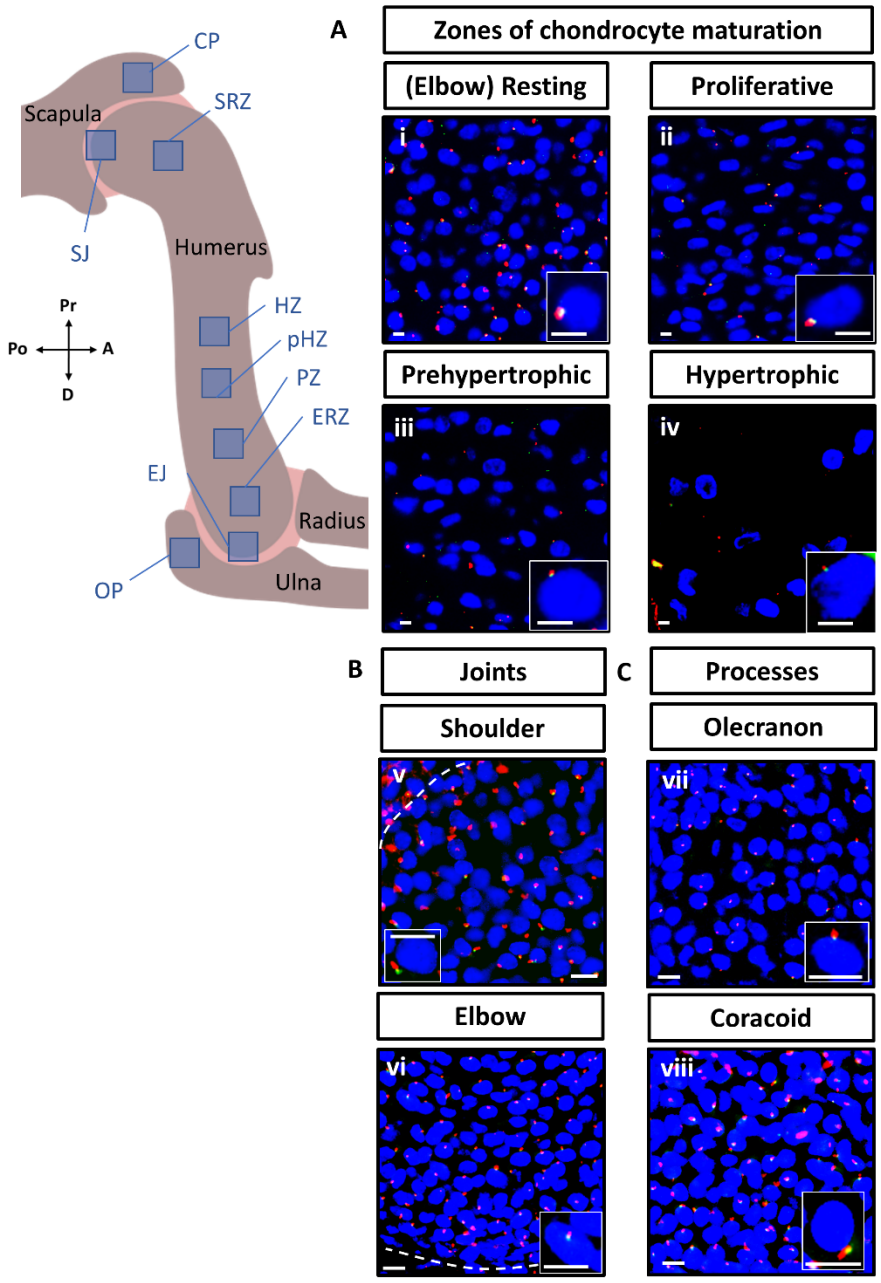

Fig. 5.5. Cilia are present on chondrocytes throughout the humerus and its associated joints. Immunolocalisation of α- (red) and γ-tubulin (green) on TS23 forelimb cryosections (10 μm) revealed detectable cilia on chondrocytes in regions of the developing humerus (A), its associated joints (B), and its morphological features (processes) (C), as indicated in the schematic on the left. Images are oriented as indicated by the axes (anterior-posterior (A-Po) and proximal-distal (Pr-D)), on the left. Cilia were detected in all regions (i-viii). The resting zones at the shoulder and elbow were largely similar; only the resting zone at the elbow is presented here (i). Dashed white lines indicate joint line; scale bars, 10 μm. Abbreviations: coracoid process (CP), elbow joint (EJ), elbow resting zone (ERZ), hypertrophic zone (HZ), olecranon process

(OP), prehypertrophic zone (pHZ), proliferative zone (PZ), shoulder joint (SJ), shoulder resting zone (SRZ).

In the wildtype rudiments, the proportion of ciliated cells varied from 0.15 to 0.88, with the observed mean proportion for each group between 0.33 (in the hypertrophic zone) and 0.70 (in the shoulder resting zone) (Table 5.1, Fig. 5.6). The hypertrophic region had a significantly lower proportion of ciliated cells than all other groups (mean 0.33 ± standard error (SE) 0.08), except the proliferative zone and the olecranon process (Table 5.1, Fig. 5.6) ($p<0.05$-0.01). Another significant difference was observed between the shoulder resting zone (mean 0.70 ± SE 0.06) and the proliferative zone (mean 0.42 ± SE 0.07), with a higher proportion of ciliated cells in the resting zone (Fig. 5.6) ($p<0.05$). The elbow resting zone (mean 0.63 ± SE 0.04) also had a higher mean proportion of ciliated cells than the proliferative zone, but this was not significant.

Table 5.1. Proportion of ciliated cells (cilia occurrence) in regions of the developing humerus. Occurrence is represented by mean proportion ± standard error. Total cilia/cells indicates total number of cilia counted/total number of cells counted. Number of samples and abbreviations for regions as detailed in Fig. 5.6.

Region	**CP**	**ERZ**	**SRZ**	**PZ**
Mean ± SE	0.68 ± 0.06	0.63 ± 0.04	0.70 ± 0.06	0.42 ± 0.07
Range	0.52-0.80	0.45-0.74	0.49-0.89	0.26-0.65
Total cilia/cells	189/302	184/306	216/301	108/248
Region	**OP**	**EJ**	**SJ**	**HZ**
Mean ± SE	0.55 ± 0.08	0.54 ± 0.05	0.54 ± 0.05	0.33 ± 0.08
Range	0.43-0.77	0.32-0.73	0.39-0.69	0.15-0.54
Total cilia/cells	149/260	170/315	159/342	17/64

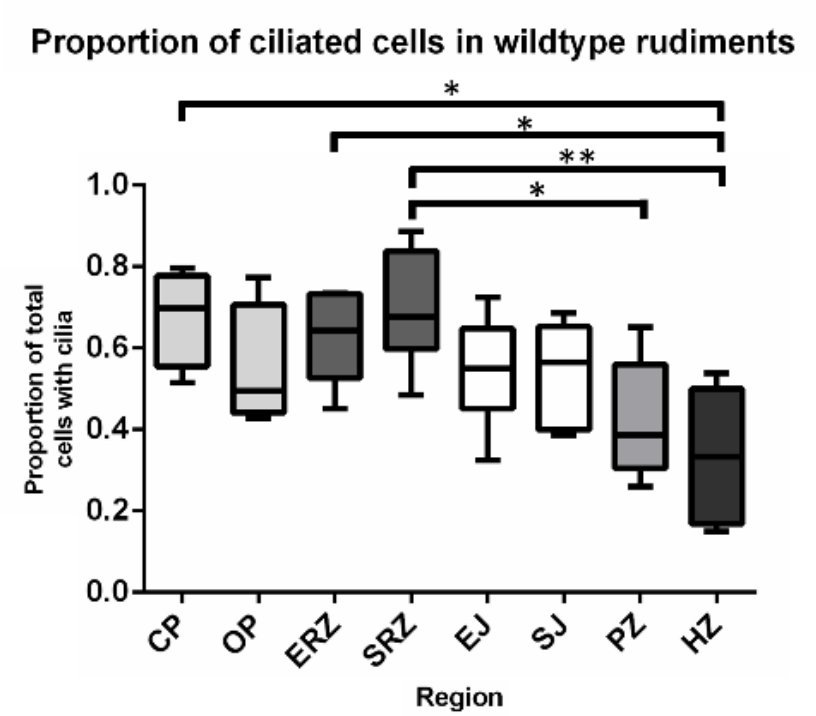

Fig. 5.6. Regions of the developing rudiment have differing proportions of ciliated cells. Box-plot of proportion of total cells which were ciliated in indicated regions of the skeletal rudiments and joints of the forelimb; bars represent the maximum and minimum of each group. Significance (determined by one-way ANOVA): $p<0.05$ (*), $p<0.01$ (**). Abbreviations: coracoid process (CP), olecranon process (OP), elbow resting zone (ERZ), shoulder resting zone (SRZ), elbow joint (EJ), shoulder joint (SJ), proliferative zone (PZ), hypertrophic zone (HZ). 1-2 sections from 2-4 independent replicates were analysed (n=4 for coracoid/olecranon processes; n=5 for proliferative and hypertrophic zones; n=6 for elbow/shoulder joints and resting zones).

Cilium length. Cilium length was assessed using confocal z-stacks (Table 5.2, Fig. 5.7). Across regions, measured lengths varied between 0.1 μm and 4.9 μm (Table 5.2), with the lowest mean observed in the elbow joint (1.27 μm ± 0.61), and the highest mean observed in the shoulder joint (1.86 μm ± 0.56).

Table 5.2. Cilium length in regions of the developing wildtype humerus. Length (in μm) is shown as mean ± standard error. Number of samples and abbreviations for regions as in Fig. 5.7.

Region	ERZ	EJ	SRZ	SJ	PZ
Mean ± SE	1.60 ± 0.65	1.27 ± 0.61	1.64 ± 0.68	1.86 ± 0.56	1.80 ± 0.58
Range	0.12-4.53	0.20-4.38	0.24-4.21	0.20-3.70	0.20-4.92

Cilia in the proliferative zone were significantly longer than those in the elbow joint region, while cilia in the resting zone(s) were not significantly different from either of those territories (Fig. 5.7) ($p<0.01$). Interestingly, cilia at the elbow joint were also significantly shorter than cilia measured at the shoulder joint (Fig. 5.7) ($p<0.005$). As noted above, few cilia were visible in the hypertrophic zone, and the few that were visible were very short (<0.2 μm), and so are not included in the data set presented below.

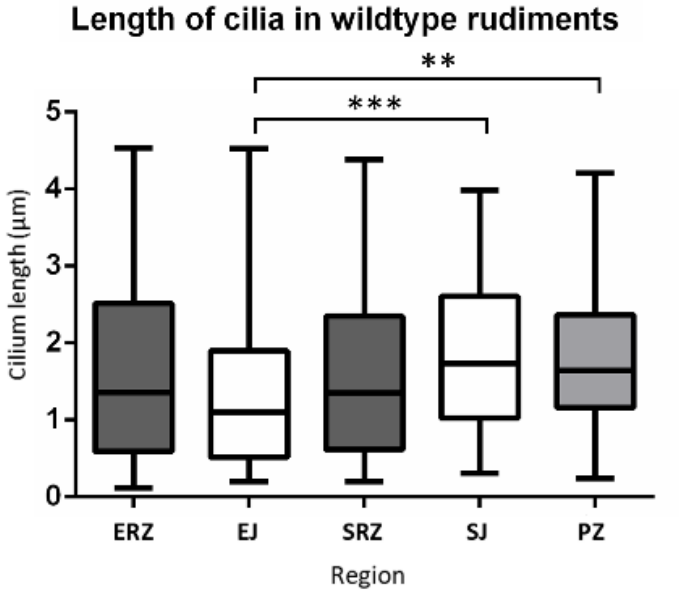

Fig. 5.7. Cilia are significantly shorter at the elbow joint than at the shoulder joint and proliferative zone. Boxplots of cilium length measurements in the different regions of wildtype forelimb skeleton, as indicated. Significance calculated from one-way ANOVA with post-hoc Tukey tests; $p<0.01$ (**), $p<0.005$ (***). Measurements represent n=3 independent specimens (1 section per region, per specimen; total number of cilia in each group 50-150).

Cilium distance from cell centre. The distance of the cilia from the centre of nuclei in the plane of view was also quantified (Fig. 5.8, A), as a high proportion of cilia positioned at larger distances from the centre of the nucleus could be indicative of preferential ciliary position and cellular polarisation, as is the case in migrating or intercalating cells (Veland et al., 2014). Cilium distance from the nucleus ranged from close to 0 μm to 11 μm. Within each region surveyed, there was a wide range of

distances observed (Fig. 5.8, A). Observed cilia were furthest from the cell centre in cells of the hypertrophic zone; this difference was significant when compared to the cilia distance in other regions (Fig. 5.8, A). Another significant difference was in the elbow joint, compared to the proliferative zone ($p < 0.01$), and compared to the shoulder joint ($p<0.05$) (Fig. 5.8, A). In both cases, cilia at the elbow joint were observed to be closer to the cell centre than in the shoulder joint or proliferative zone. These differences are further illustrated by comparing the proportion of cilia which belong to each distance category (Fig. 5.8, B). Stacked bar graphs representing different distances from the cell centre show that a larger proportion of cilia fall in the 1-3 μm distance range in the elbow joint than in other regions (Fig. 5.8, B). Similarly, the majority of cilia are more than 3 μm from the cell centre in the hypertrophic zone, while this is a minority in each of the other regions (Fig. 5.8, B). However, these observed differences may be explained by differences in cell size, density and shape in each of the regions (cells at the joint line tend to be flatter and more densely packed in comparison to enlarged hypertrophic cells or rounded resting zone cells).

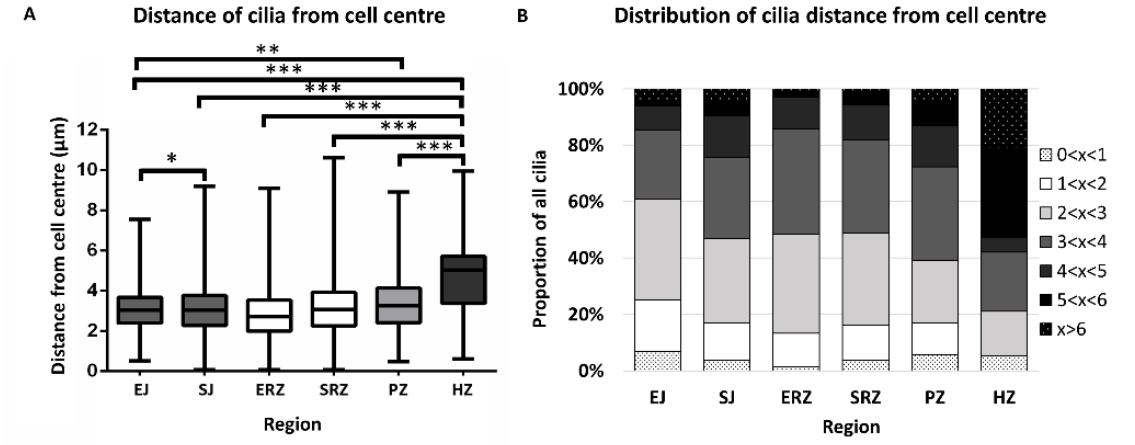

Fig. 5.8. Cilium distance from the cell centre varies between regions. (A) Boxplot of distance measurements for each cilium to its cell centre (taken to be the centre of the DAPI-stained nucleus), grouped by region as indicated. (B) Stacked column plot of the proportion of cilia at a given distance from the cell centre, as indicated in the legend. Significance: $p<0.05$ (*), $p<0.01$ (**), $p<0.005$ (***). Abbreviations: elbow joint (EJ), shoulder joint (SJ), elbow resting zone (ERZ), shoulder resting zone (SRZ), proliferative zone (PZ), hypertrophic zone (HZ). n=1-2 sections from 2-4 independent replicates (total n=4 for coracoid/olecranon processes; n=5 for proliferative and hypertrophic zones; n=6 for elbow/shoulder joints and resting zones).

Cilium position on the cell. The position of each cilium on the cell was scored in one of four quadrants, relative to major axes of the rudiment (Fig. 5.4B, C; Fig. 5.9A). This revealed that within several regions of the rudiment, there are preferred positions of the cilia. At both the shoulder and elbow joints, the largest proportion of cilia were located on the quadrant of the cell facing away from the joint line: at the elbow joint, this was the proximal quadrant (Q4; 42%, $p<0.001$) (Fig. 5.9Ai); at the shoulder joint, this was the distal quadrant (Q2; 58%, $p<0.001$) (Fig. 5.9Aii) (n=1-2 sections from 4 individual specimens; total n=6). This trend was also observed in the resting zones adjacent to each joint: the elbow resting zone had the highest proportion of its cilia in the proximal quadrant (Q4; 58%, $p<0.001$) (Fig. 5.9Ai) and the shoulder resting zone had the largest proportion in the distal quadrant (Q2; 38%, $p<0.001$) (Fig. 5.9Aii). Interestingly, cilia in the proliferative and hypertrophic zones were also unevenly distributed: in the proliferative zone, the smallest proportion of cilia were found in the distal quadrant (Q2; 4%), while the highest proportion of cilia were located in the posterior quadrant (Q3; 48%, $p<0.05$) (Fig. 5.9Aiii); in the adjacent hypertrophic zone, the largest proportion of cilia was also in the posterior quadrant (Q3; 37%, $p<0.05$) (Fig. 5.9Aiv).

Plotting the position of cilia in rose histograms confirmed the biased position in the elbow and shoulder regions (Fig. 5.9B). Again, the resting and joint lines showed similar trends at both the elbow and shoulder (Fig. 5.9Bi-ii'). The mean positional direction of cilia at the elbow resting zone and joint was 354º and 348º, respectively (Fig. 5.9Bi, i'), demonstrating that cilia in this region tend to be positioned on the proximal side of the cell. Likewise, at the shoulder resting zone and joint, the mean positional direction was 227º and 228º, respectively (Fig. 5.9Bii, ii'), demonstrating a distal-posterior bias. The proliferative zone had a mean positional direction of 242º, which is posterior, however the rose histogram suggests an anterior-posterior bimodal distribution, with most values clustered around 90º and 270º (Fig. 5.9iii). The hypertrophic zone had a mean positional direction of 289º, however the rose histogram showed a wide distribution of values (Fig. 5.9iv). These observations were supported by assessing the goodness-of-fit of each observed distribution to a hypothetical uniform distribution: all zones, except the hypertrophic zone, were significantly different

(p<0.001 for all shoulder and elbow regions and p<0.05 for the proliferative zone) from a hypothetical uniform distribution, confirming an uneven distribution of cilia in these zones.

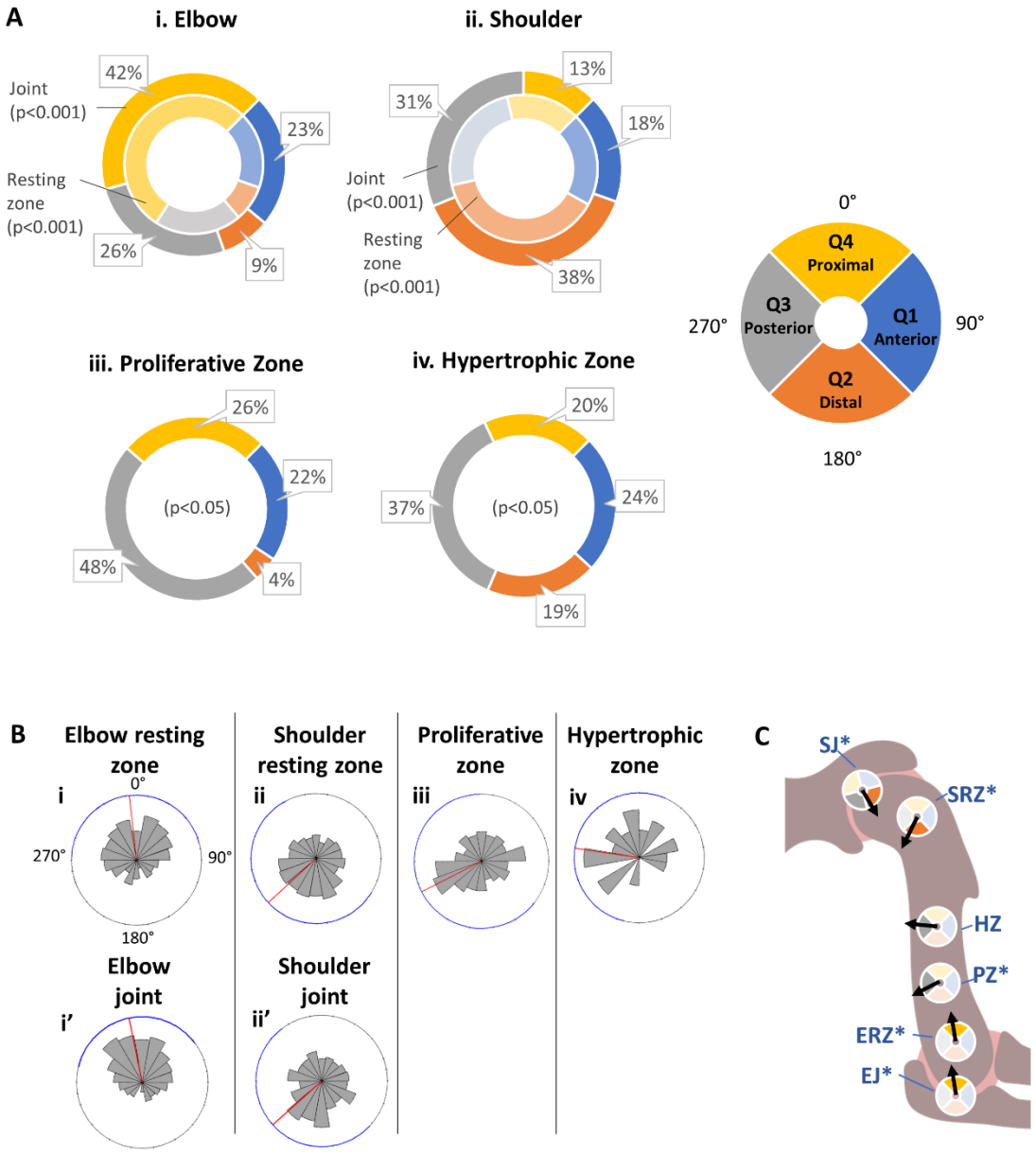

Fig. 5.9. The position of cilia on individual cells differs between regions of the developing skeleton. Position of the cilium relative to the cell centre was measured in the indicated territories of forelimb rudiments and joints of wildtype *Pax3*^{Spd} embryos at E14.5, as described in Fig. 5.4C. (A) Cilium position was scored in one of four quadrants of the cell: anterior (Q1; 45-135°), distal (Q2; 135-225°), posterior (Q3; 225-320°), and proximal (Q4; 320-45°) (illustrated in schematic on the right). The

proportion of cilia in each quadrant is represented for each region of the rudiments and joints. The resting zone and joint line for the elbow and joint, respectively, are combined in (i) and (ii), with the resting zone represented by lighter colours in the inner circle. P-values (indicated in parentheses) were determined by chi-squared tests comparing observed data to expected distributions of 25% in each quadrant. (B) Rose histograms of cilium position; bin width of 20°; mean positional direction indicated by red line and standard deviation indicated by blue arc. (C) Summary schematic of findings presented in (A) and (B). A representative humerus and the regions analysed are shown; quadrant(s) with the highest proportion of cilia in each region, as presented in (A), are coloured; arrows represent the mean positional direction of cilia in each region, as presented in (B), and asterisks indicate that observed distributions are significantly different to a uniform distribution. To eliminate error resulting from estimation of the cell centre, only cilia more than 2 μm from the centre of the cell are presented here. Reference axes are as defined in Fig. 5.4B. Data represent 1-2 sections each from 4 individual specimens (total n=5-6).

Cilium orientation. Next, the orientation of the cilium shaft with respect to the rudiment was assessed (Fig. 5.10). This revealed several trends in orientation of the cilium shaft. In the elbow resting zone, the cilium shaft tended to be oriented either toward or away from the joint line (Fig. 5.10i), while at the shoulder resting zone, cilia tended to be oriented away from the joint line (Fig. 5.10iii). At both the elbow and shoulder joints, there was an overall trend of cilium orientation away from the joint line (close to 0º, or proximal, at the elbow and close to 180º, or distal, at the shoulder) (Fig. 5.10ii and iv). In the proliferative zone, there was an apparently more even distribution of cilium orientation, with a posterior mean direction (Fig. 5.10v). Relatively few cilia were visible in the hypertrophic zone, and observed cilia appeared very short (<0.2 μm), this region was not included in analysis of cilium orientation. Goodness-of-fit tests of uniform distributions in each region revealed that the distribution of cilia orientation at both the elbow joint and elbow resting zone was statistically different from a uniform distribution ($p<0.005$ in both cases), indicating a strong directional trend at the elbow. Surprisingly, the proliferative zone was also significantly different from a uniform distribution ($p<0.05$). Neither the shoulder resting zone nor the joint had a significantly non-uniform distribution.

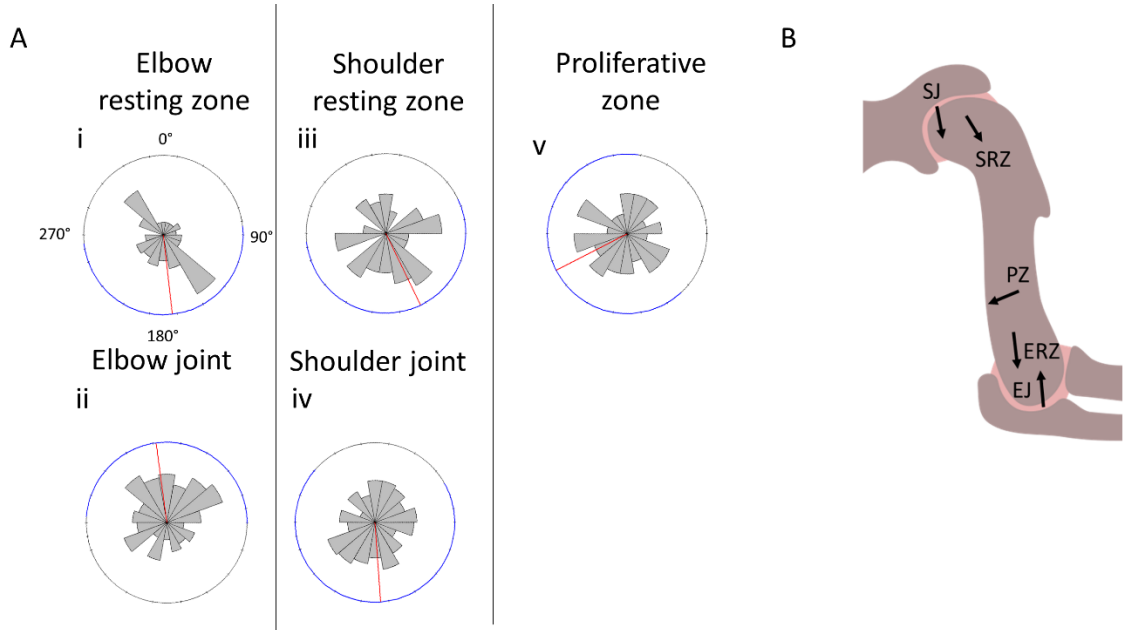

Fig. 5.10. Preferred cilium orientation by region in the wildtype forelimb rudiments and joints. (A) Rose histograms of the direction of the cilium shaft in the indicated territories of forelimb rudiments and joints of wildtype *Pax3*^{Spd} embryos at E14.5; bin width of 20°. Reference axes are as defined in Fig. 5.4B. Red lines indicate mean direction of each data set; blue arcs represent mean direction ± standard error. (B) Schematic summary of findings presented in (A); a representative humerus is shown with arrows in each region indicating the mean direction of cilia. Abbreviations: elbow joint (EJ), elbow resting zone (ERZ), proliferative zone (PZ), shoulder joint (SJ), shoulder resting zone (SRZ).

5.3.2 Characterisation of primary cilia in the mutant developing skeletal rudiments

Cilia occurrence. Compared to the wildtype forelimb skeleton, regions of the mutant forelimb skeleton showed similar proportions of ciliated cells, with no significant differences between wildtype and mutant in any of the zones observed, with similar mean values in each region and trends between regions (Fig. 5.11, Table 5.3). Comparing between regions of the developing mutant humerus, there were significantly fewer cilia in the proliferative zone compared to the elbow resting zone and the coracoid process of the scapula (Fig. 5.11), overall showing the same trend of fewer cilia in the proliferative and hypertrophic zones as in control rudiments.

Table 5.3. Proportion of ciliated cells (cilia occurrence) in regions of the developing wildtype and mutant humerus. Occurrence is represented by mean proportion ± standard error. Total cilia/cells indicates total number of cilia counted/total number of cells counted. Number of samples and abbreviations for regions as detailed in Fig. 5.11.

Region	**CP**		**OP**	
Phenotype	**WT**	**MUT**	**WT**	**MUT**
Mean ± SE	0.68 ± 0.06	0.73 ± 0.05	0.55 ± 0.08	0.62 ± 0.15
Range	0.52-0.80	0.57-0.92	0.43-0.77	0.51-0.86
Total cilia/cells	189/302	159/219	149/260	164/254
Region	**ERZ**		**SRZ**	
Phenotype	**WT**	**MUT**	**WT**	**MUT**
Mean ± SE	0.63 ± 0.04	0.71 ± 0.09	0.70 ± 0.06	0.56 ± 0.10
Range	0.45-0.74	0.53-1.0	0.49-0.89	0.50-0.64
Total cilia/cells	184/306	271/398	216/301	180/323
Region	**EJ**		**SJ**	
Phenotype	**WT**	**MUT**	**WT**	**MUT**
Mean ± SE	0.54 ± 0.05	0.60 ± 0.08	0.54 ± 0.05	0.55 ± 0.004
Range	0.32-0.73	0.49-0.72	0.39-0.69	0.40-0.68
Total cilia/cells	170/315	194/324	159/342	218/400
Region	**PZ**		**HZ**	
Phenotype	**WT**	**MUT**	**WT**	**MUT**
Mean ± SE	0.42 ± 0.07	0.37 ± 0.03	0.33 ± 0.08	0.45 ± 0.05
Range	0.26-0.65	0.26-0.47	0.15-0.54	0.32-0.54
Total cilia/cells	108/248	107/288	17/64	28/67

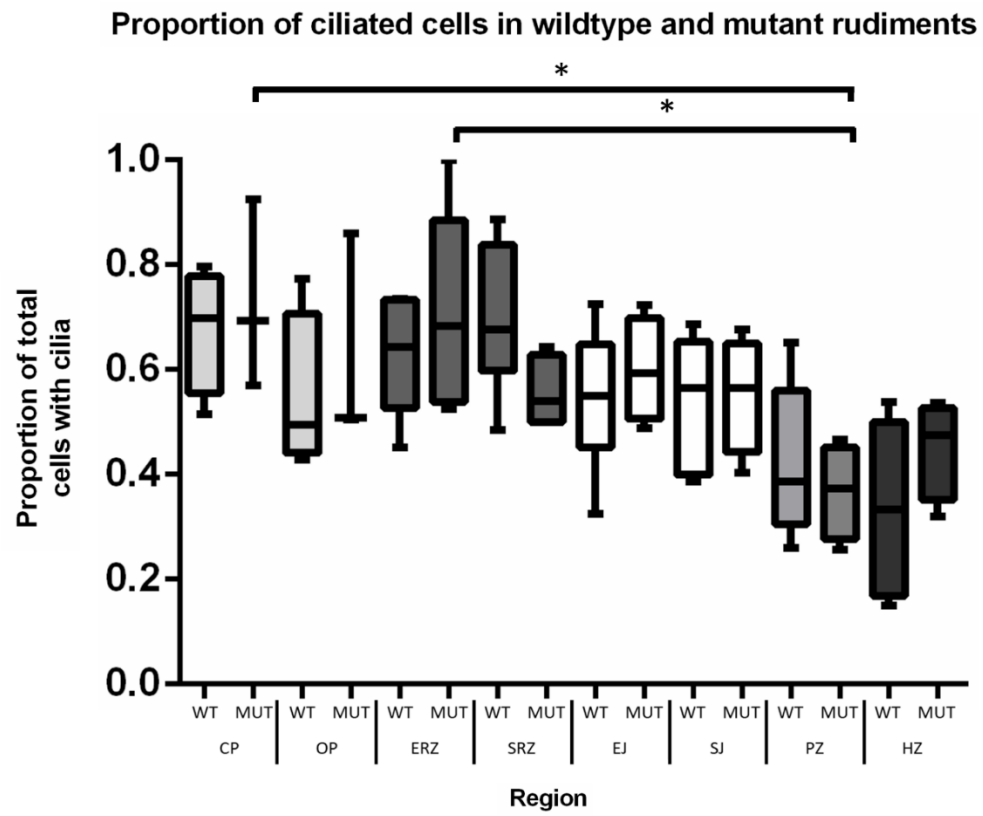

Fig. 5.11. Cilia in mutant rudiments display a similar trend to cilia in wildtype rudiments. Graph of proportion of total cells which were ciliated in indicated regions of the skeletal rudiments and joints of *Pax3*^{Spd} wildtype and mutant forelimbs. Abbreviations: coracoid process (CP), elbow joint (EJ), elbow resting zone (ERZ), hypertrophic zone (HZ), mutant (MUT), olecranon process (OP), proliferative zone (PZ), shoulder joint (SJ), shoulder resting zone (SRZ), wildtype (WT). Significance was calculated using t-tests; $p<0.05$ (*). Data represent n=1-2 sections from 2-4 independent replicates (total n=4-6).

Cilium length. Cilium length was measured in regions of the mutant forelimb skeleton (Table 5.4, Fig. 5.12). When these measurements were compared to wildtype, cilia in the mutant elbow resting zone (mean 1.02 ± SE 0.43 in mutant), were significantly shorter (mean 1.60 ± SE 0.65 in wildtype), as were cilia in the mutant shoulder joint (mean 1.35 ± SE 0.53 in mutant vs. mean 1.86 ± SE 0.56 in wildtype) (Table 5.4, Fig. 5.12). There was no significant difference between wildtype and mutant in other regions, although an overall trend of a shorter median cilium length was observed across all regions (Table 5.4). Cilia in the hypertrophic zone were excluded from analyses because of their short length.

Table 5.4. Cilium length in regions of the developing wildtype and mutant humerus. Length (in μm) is presented as median ± standard error. Number of samples and abbreviations for regions as detailed in Fig. 5.12.

Region	**ERZ**		**EJ**	
Phenotype	**WT**	**MUT**	**WT**	**MUT**
Mean ± SE	1.60 ± 0.65	1.02 ± 0.43	1.27 ± 0.61	1.37 ± 0.56
Range	0.12-4.53	0.2-2.79	0.20-4.38	0.2-3.70
Median	1.36	0.78	1.10	1.06
Region	**SRZ**		**SJ**	
Phenotype	**WT**	**MUT**	**WT**	**MUT**
Mean ± SE	1.64 ± 0.68	1.27 ± 0.45	1.86 ± 0.56	1.35 ± 0.53
Range	0.24-4.21	0.20-2.97	0.20-3.70	0.20-4.92
Median	1.36	1.08	1.73	1.09
Region	**PZ**			
Phenotype	**WT**	**MUT**		
Mean ± SE	1.80 ± 0.58	1.55 ± 0.69		
Range	0.20-4.92	0.20-4.76		
Median	1.64	1.52		

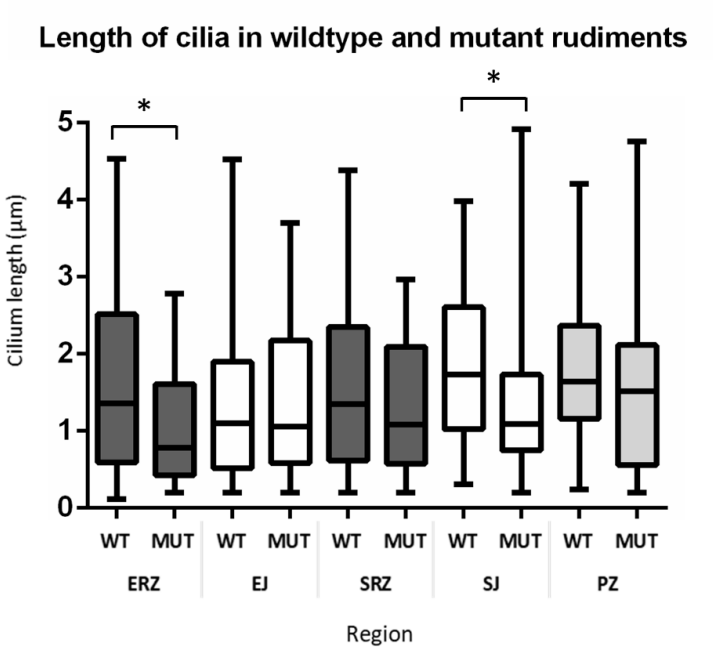

Fig. 5.12. Cilium length is shorter in the mutant forelimb skeleton. Boxplots of cilium length measurements in the different regions of the *Pax3*^{Spd} wildtype and mutant forelimb skeleton, as indicated. Abbreviations: elbow joint (EJ), elbow resting zone (ERZ), mutant (MUT), proliferative zone (PZ), shoulder resting zone (SRZ), shoulder joint (SJ), wildtype (WT). Significance was determined by t-tests; $p<0.05$ (*). Measurements represent n=3 independent specimens for wildtype and n=2 independent specimens for mutant (total number of cilia in each group 25-150).

Cilium distance from cell centre. The distance of cilia from the cell centre was similar on chondrocytes from mutant embryos in corresponding regions of the wildtype forelimb skeleton: in all regions, cilia were significantly further from the cell centre in the hypertrophic zone compared to other zones (Fig. 5.13A). Interestingly, at the mutant shoulder joint, cilia were significantly closer to the cell centre than in the wildtype (this trend was also observed at the elbow joint, however here it was not significant) (Fig. 5.13A). Contrastingly, at the elbow resting zone, cilia were significantly further away from the cell centres in the mutant compared to the wildtype (Fig. 5.13A). These differences are also apparent in examining the proportion of cilia belonging to each distance group in the regions assessed: a larger portion of the observed cilia belong to the 2-3 µm group in the shoulder joint of the mutant than in the wildtype (Fig. 5.13B).

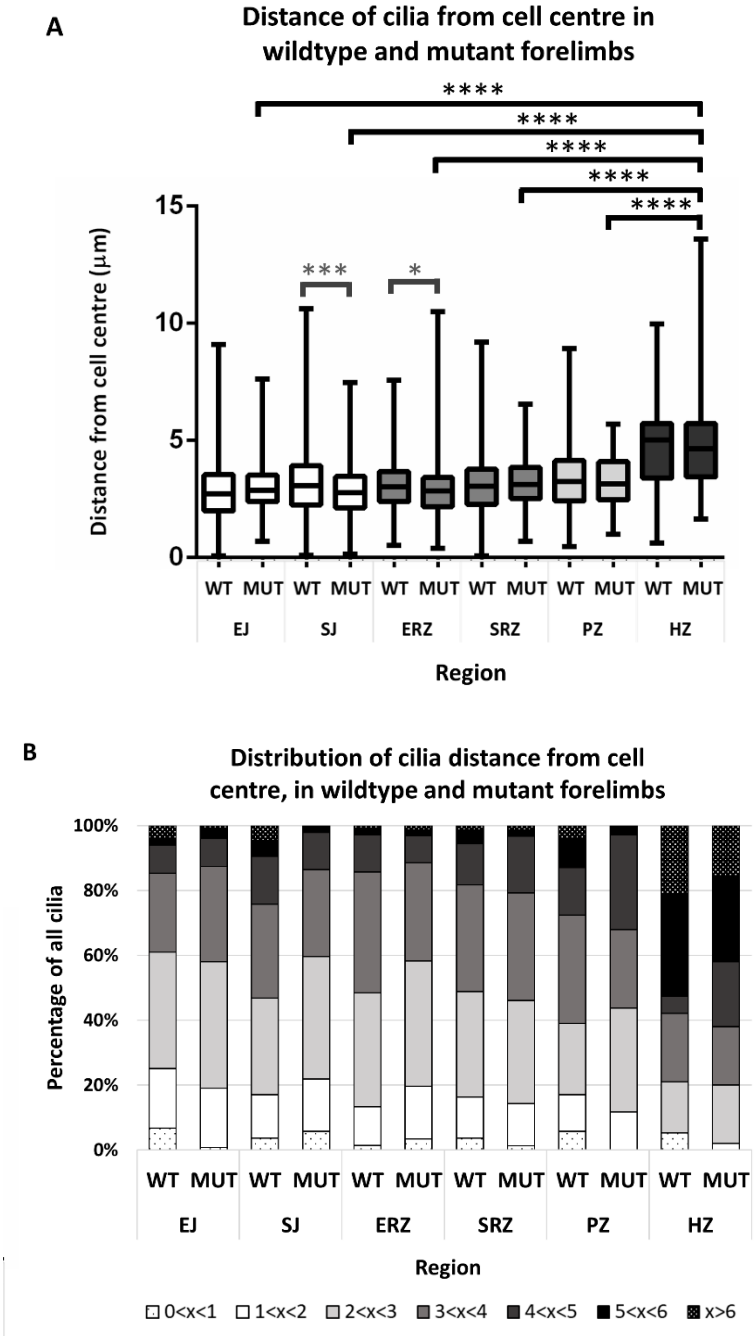

Fig. 5.13. Cilium distance from the cell centre varies between regions in mutant rudiments and joints, and between wildtype and mutant at the shoulder joint and elbow resting zone. (Left) Boxplot of distance measurements for each cilium to the cell centre, grouped by genotype and region as indicated. (Right) Stacked column plot of the proportion of cilia at a given distance from the cell centre, as indicated in the legend. Significance: $p<0.05$ (*), $p<0.01$ (**), $p<0.005$ (***). Abbreviations: proliferative zone (PZ), hypertrophic zone (HZ), resting zone (RZ), coracoid process & olecranon process (CP/OP), elbow joint (EJ), shoulder joint (SJ).

Cilium position. Comparison of the position of cilia on cells in mutant forelimb skeleton revealed trends similar to the wildtype, as well as some notable differences (Fig. 5.14). At both the elbow joint and resting zone, the highest proportion of cilia was in the proximal quadrant (Q4; 47% and 64%, respectively) ($p<0.001$) (Fig. 5.14I, ii). Likewise, at the shoulder joint and resting zone, the highest proportion was in the distal quadrant (Q2; 33% ($p<0.001$) and 40% ($p<0.05$), respectively) (Fig. 5.14iii, iv). As noted above, in the wildtype proliferative zone the largest proportion of cilia was in the posterior quadrant (Fig. 5.9); this trend was also observed in the mutant, with an even larger proportion of cilia in this quadrant (53% compared to 48% in the wildtype) (Fig. 5.14v). In the mutant hypertrophic zone, although more cilia were observed in the distal and posterior quadrants than in the wildtype, the distribution of cilia here was not significantly different to a normal distribution (Fig. 5.14vi).

Comparison of the angle of the cilium base relative to the cell centre (cilium positional direction) showed that, near the elbow and shoulder, cilium position is similar in the wildtype compared to the mutant, with the exception of the shoulder resting zone (Fig. 5.14B). At the elbow joint and resting zone, cilia are positioned close to 0º (proximal) (Fig. 5.14i',ii'), while at the shoulder joint cilia are clustered around 210º (distal) (Fig. 5.14 iv'). There was no significant difference between wildtype and mutant when examining the positional direction or distribution of cilia at either the shoulder or elbow joint, or in the elbow resting zone. However in the shoulder resting zone, both the distribution and the positional direction were significantly different between the wildtype and mutant specimens ($p<0.01$). In the wildtype shoulder resting zone, the mean positional direction is distal and slightly posterior (201º), while in the mutant, it is distal and slightly anterior (132º), with a wider distribution (Fig. 5.14iii, iii').

At the mutant proliferative zone, the positional direction of cilia was significantly posterior, similar to what was observed in the wildtype (Fig. 5.14v, v'). However, the bi-modal distribution observed in the wildtype proliferative zone was absent, and the mutant positional distribution and direction was significantly different to the wildtype (Fig. 5.14vi'). In the mutant hypertrophic zone, there was again a posterior bias of positional direction (although this was not a significant trend), and the positional direction was significantly different to the wildtype (Fig. 5.14vi').

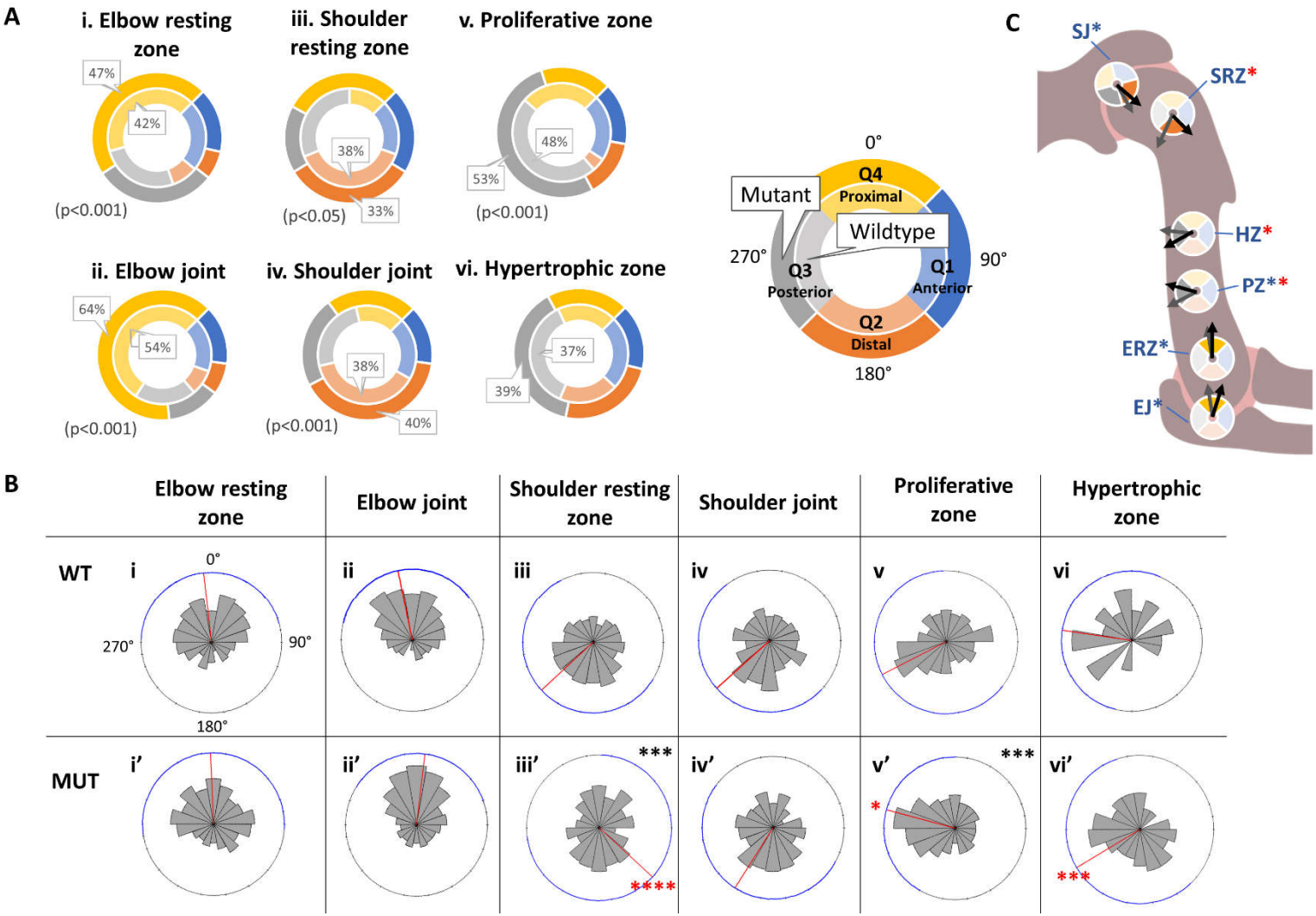
A
i. Elbow resting zone
47%
42%
(p<0.001)
iii. Shoulder resting zone
38%
33%
(p<0.05)
v. Proliferative zone
48%
53%
(p<0.001)
ii. Elbow joint
64%
54%
(p<0.001)
iv. Shoulder joint
38%
40%
(p<0.001)
vi. Hypertrophic zone
37%
39%
0°
Q4
Proximal
Mutant
Wildtype
270°
Q3
Posterior
Q1
Anterior
90°
Q2
Distal
180°
C
SJ*
SRZ*
HZ*
PZ**
ERZ*
EJ*
B
Elbow resting zone
Elbow joint
Shoulder resting zone
Shoulder joint
Proliferative zone
Hypertrophic zone
WT
MUT
i
ii
iii
iv
v
vi
i'
ii'
iii'
iv'
v'
vi'
0°
270°
90°
180°
***
****
*
***

Fig. 5.14 (previous page). The position of cilia on individual cells differs between regions of the developing skeleton in mutant forelimbs. Position of the cilium relative to the cell centre was measured in the indicated territories of forelimb rudiments and joints of wildtype and mutant *Pax3*^{Spd} embryos at TS23, as described in Fig. 5.4C. (A) Cilium position was scored in one of four quadrants of the cell as illustrated in schematic on the right. The proportion of cilia in each quadrant is represented for wildtype and mutant. P-values for mutant distributions are shown. (B) Rose histograms of cilium positional direction; bin width of 20°; mean positional direction indicated by red line and standard deviation indicated by blue arc. Red asterisks indicate positional direction which is significantly different to the wildtype; black asterisks indicate positional distribution which is significantly different to the wildtype. Significance values: $p<0.05$(*), $p<0.01$(**), $p<0.005$(***), $p<0.001$(****). (C) Summary schematic of findings presented in (A) and (B). A representative humerus and the regions analysed are shown; quadrant(s) with the highest proportion of cilia are coloured. Grey and black arrows represent mean positional direction of cilia for wildtype and mutant, respectively. Blue asterisks indicate that significantly non-uniform observed distributions for the mutant; red asterisks indicate a significant difference in positional distribution or direction between wildtype and mutant. Reference axes are as defined in Fig. 5.4B. Data represent 1-2 sections each from 4 individual specimens (total n=5-6) for wildtype, and 1-2 sections each from 2-3 individual specimens (total n=4-5) for mutant. Total numbers of cilia were, respectively for wildtype and mutant: 19 and 50 (hypertrophic zone), 123 and 91 (proliferative zone) and approx. 250-300 and approx. 150-250 (elbow/shoulder joint/resting zone).

Orientation of the cilium shaft was also assessed in mutant rudiments (Fig. 5.15). In the proliferative zones, cilia were similarly oriented in the wildtype and mutant, with a mean posterior direction (Fig. 5.15i, i'). At the mutant elbow resting zone, there was a mean orientation away from the joint (close to 0º, proximal), which contrasted with the roughly bi-modal distribution in the wildtype (Fig. 5.15ii, ii'). Contrastingly, in the elbow and shoulder joints, and at the shoulder resting zone, the mean cilium direction in the mutant reflected similar trends of cilium orientation away from the joint line (close to 0º, proximal, at the elbow and close to 180º, distal, at the shoulder) which were observed in the mutant (Fig. 5.15iii-v'). Despite similarities in the mean direction observed, only the mutant elbow joint had a distribution of cilium orientations which was significantly different from a uniform distribution ($p<0.05$). Comparing cilium

orientation in comparable regions revealed that only the elbow resting zone was significantly different ($p<0.0001$) between wildtype and mutant specimens.

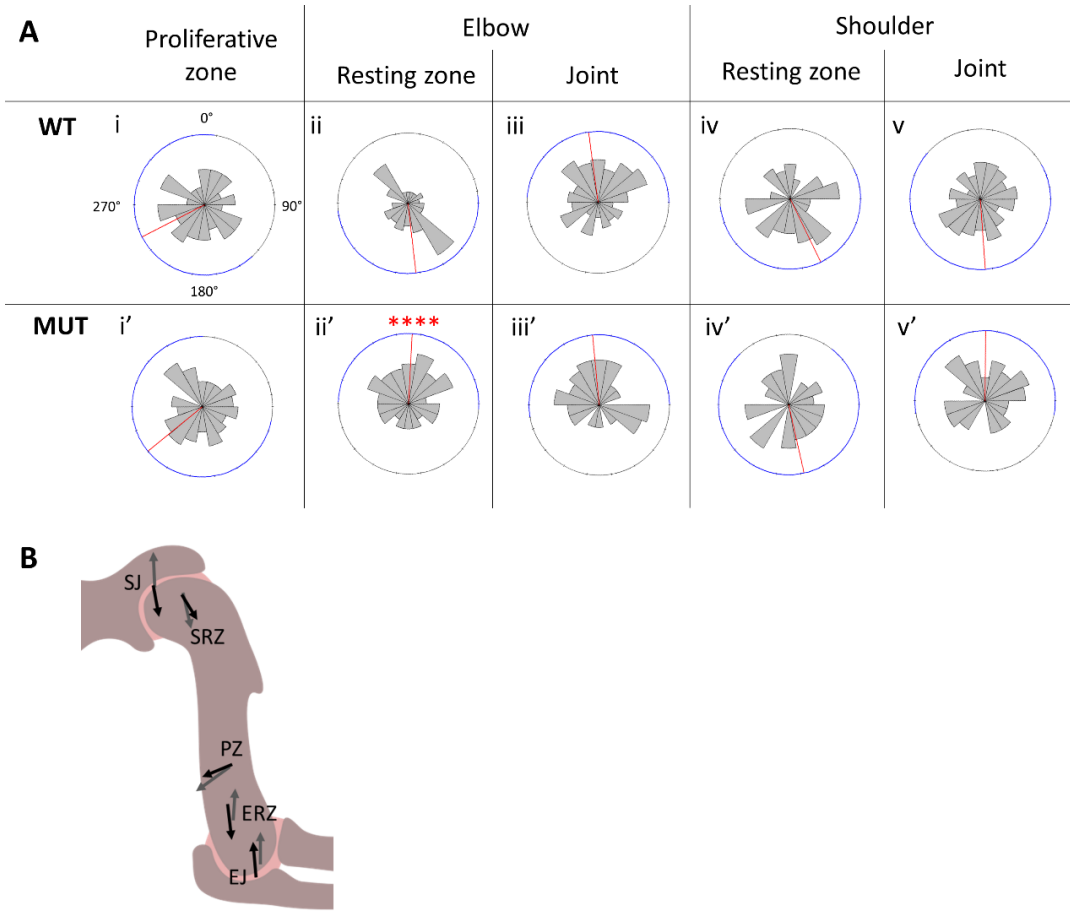

Fig. 5.15. Cilium orientation is most distinct at the elbow joint, and varies between regions in the mutant forelimb rudiments and joints. (A) Rose histograms of cilium direction in the indicated territories of forelimb rudiments and joints of wildtype (i-v) and mutant (i'-v') *Pax3*^{Spd} embryos at E14.5; bin width of 20°. Reference axes are as defined in Fig. 5.4B. n=2-4 for each group. Red lines indicate mean direction; blue arcs indicate standard mean ± standard error. Red asterisks indicate significant difference from wildtype; $p<0.0001$ (*****). (B) Summary schematic of mean cilium orientation for each region; grey arrows indicate wildtype mean orientation while black arrows indicate that of the mutant. Abbreviations: elbow joint (EJ), elbow resting zone (ERZ), proliferative zone (PZ), shoulder joint (SJ), shoulder resting zone (SRZ).

5.4 Discussion

This study reveals previously unknown trends in ciliary occurrence, length, position, and orientation in developing skeletal rudiments. It highlights several interesting differences, and surprising similarities, between wildtype and muscle-less mutant rudiments. Strikingly, this study showed that joint regions tend to have cilia positioned and oriented away from the joint, while there was a less obvious, but still notable, preferred position and orientation in the proliferative and hypertrophic zones. It was also shown that regions of the developing rudiments have characteristic proportions of ciliated cells, with more cilia in the resting and joint zones compared to the proliferative and hypertrophic zones. Comparing wildtype to mutant, cilia at the mutant joints surprisingly maintained a position and orientation away from the joint line. Notably, while cilium occurrence was not significantly altered in the mutant, there was an overall trend of shorter cilia in the mutant rudiments. These findings are summarised in Fig. 5.16.

Cilia occurrence in the wildtype varied between regions, ranging from a mean of 0.33 in the hypertrophic zone to 0.70 in the shoulder resting zone (Fig. 5.16i). In the mutant, a similar range was observed, from 0.37 in the elbow joint to 0.73 in the coracoid process (Fig. 5.16i'). In both wildtype and mutant, cilia occurrence roughly correlated to chondrocyte maturity: more immature chondrocytes (resting zone) exhibited a higher proportion of cilia, followed by proliferative and hypertrophic chondrocytes, which are more mature. In general, the mutant joint regions had a higher proportion of ciliated cells than in the wildtype, although this was not significant for any individual region.

Examination of cilia length revealed that the cilia were shortest at the elbow joint, and surprisingly longer in the proliferative zone. This is contrary to studies of cells in culture where shorter cilia are observed in proliferating populations (Thompson et al., 2017), due to active deconstruction and reconstruction during cell division. However, rates of proliferation *in vivo* may be very different to cells in culture. There was also a trend of shorter cilia in the mutant, indicating a possible response to stimulation in the control or changes in regulation of cilia construction in the mutant (Fig. 5.16ii, ii'). Interestingly, correspondence between cilium length and density was observed in both wildtype and mutant specimens, with shorter cilia in regions of high occurrence (e.g.

resting zones) and longer cilia in regions of low occurrence (e.g. proliferative zone) (Fig. 5.16i-ii').

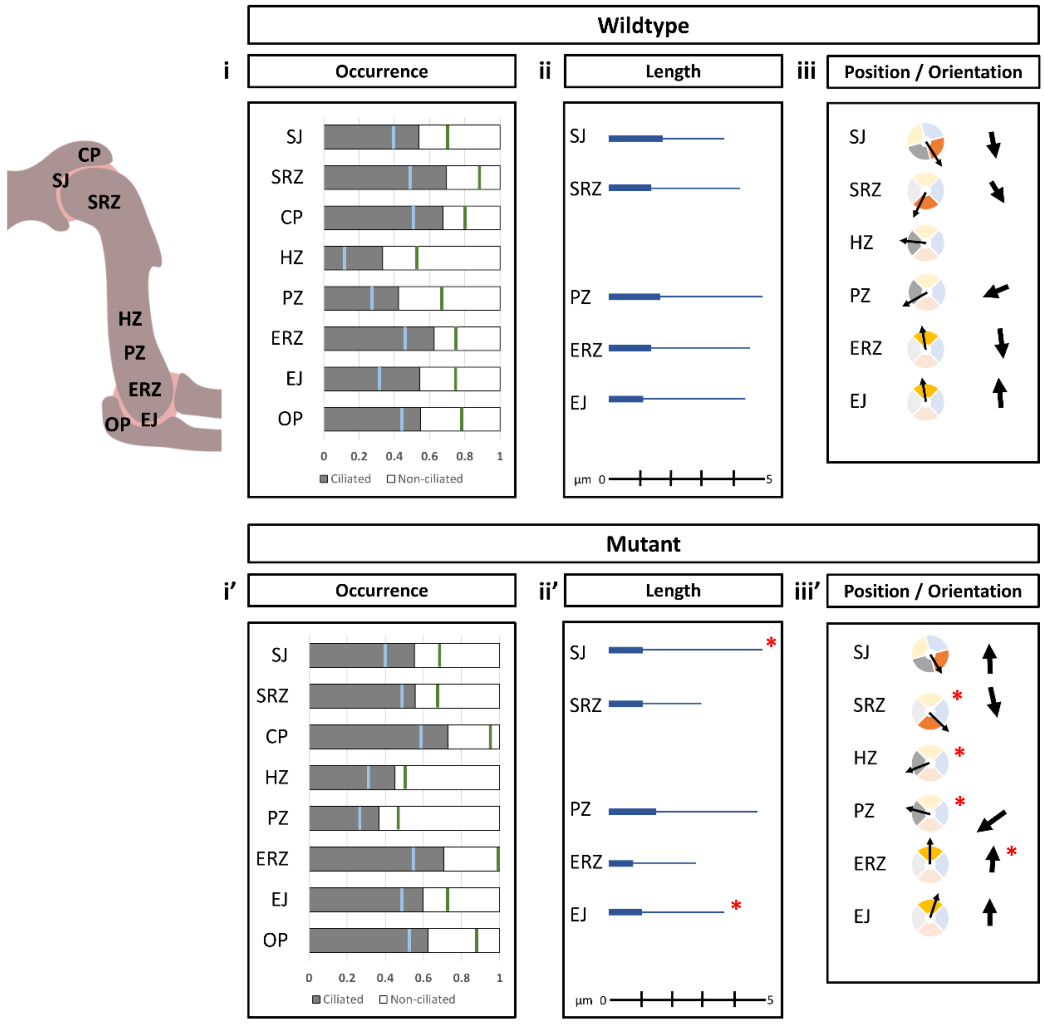

Fig. 5.16. Summary of cilia characteristics measured in this work. Ciliary occurrence, length, position, and orientation, as reported here, are schematically represented for indicated regions (as denoted in the schematic on the left). Occurrence (proportion of total cells with cilia) is indicated by dark grey bars; blue and green lines indicate minimum and maximum values, respectively (i). Median length in each zone is represented by thick blue bars; thin blue bars represent maximum observed length in each zone (ii). Cilium position is indicated by darker shading of the dominant quadrant (as in Fig. 5.9); small black arrows represent mean positional direction of cilia, while large black arrows represent mean direction of cilium orientation (iii). Comparative data for mutant specimens is similarly represented (i'-iii'). Red asterisks indicate significant differences between wildtype and mutant. Abbreviations: coracoid process (CP), elbow joint (EJ), elbow resting zone (ERZ), hypertrophic zone (HZ), olecranon process (OP), proliferative zone (PZ), shoulder joint (SJ), shoulder resting zone (SRZ).

While other organs whose development relies on ciliary function were not examined in this study, these tissues could be useful for comparison purposes. For example, development of the neural tube relies on *Pax3* and Splotch delayed mutants frequently display spina bifida (Vogan et al., 1993); however, neural tube development is unaffected in other models of reduced mechanical stimulation. Although *Pax3* has no known ciliary role, examination of neural tube cilia in the muscle-less mutant would help delinate between changes in ciliary characteristics resulting from immobilisation and those due to the *Pax3* mutation itself.

In the mutant, chondrocyte maturation and hypertrophy are delayed (Nowlan et al., 2010a), which corresponds to decreased numbers of cilia observed in the mutant proliferative zone, and an increased number observed in the mutant hypertrophic zone. These changes suggest that differences in cilium occurrence could be responsible for changes in the skeletal phenotype observed in the mutant. In both wildtype and mutant resting zones, relatively high proportions (up to 80%) of chondrocytes exhibited visible cilia, and this could be indicative of a mechanotransductive role for cilia here. Another notable trend was the high occurrence of cilia in the morphological processes (olecranon and coracoid) which were comparable to those found in the resting zones; this was consistent between wildtype and mutant (Fig. 5.16i, i'). Morphology has been shown to be altered under reduced mechanical stimulation (Roddy et al., 2011b), and the large number of cilia observed in these regions corresponds to a role for cilia in mechanotransduction here.

A notable trend which was observed in this study was the position of cilia at the joint lines and adjacent resting zones (Fig. 5.16iii, iii'). At both the elbow and shoulder, cilia were disproportionately positioned on the side of the cells facing away from the joint line (at the shoulder, the distal edge of the cell, and at the elbow, the proximal edge). While chondrocytes are 3D and rounded *in vivo*, analysis of 2D images collected on an epifluorescent microscope was taken to be an accurate representation of ciliary position for several reasons. Chondrocytes in the developing rudiment are tightly packed together with the nucleus located roughly at the centre and taking up most of the cell volume, meaning that DAPI staining is an accurate means for identifying the position of individual cells. In this study, longitudinal sections of the humerus were analysed,

and while analysis of 2D images does not allow for measurement of cilium position of along the dorso-ventral aspect of the cell, this was not of interest to this study, as predicted mechanical stimuli in the humerus vary along the antero-posterior and proximo-distal axes, but not dorso-ventrally (Nowlan et al., 2012). Further, data were generated by quantifying only nuclei which were in the focal plane of imaging, and by excluding nuclei under a threshold size, thereby eliminating noise. Finally, cilia located closer than 2 μm from the centre of the nucleus were also excluded, to remove noise due to imprecision. It has previously been reported that cilia in adult articular cartilage point away from the joint line (McGlashan et al., 2008, Farnum and Wilsman, 2011). There have been several proposed explanations for the orientation of cilia away from the joint, including enabling cells to migrate away from the joint (Farnum and Wilsman, 2011). Interestingly, orientation and position overall were not significantly altered in the mutant joints (with the exception of a more anterior position at the shoulder resting zone, and a less proximal orientation at the shoulder joint), suggesting that if cilia are ideally positioned for the sensation of physical forces in the developing rudiments, cilia near joints not undergoing movement could be involved in the observed alteration of signalling pathways which occurs here. Although the position of cilia was largely not affected at the mutant joint, there were significant differences seen in the proliferative and hypertrophic zones. In the mutant proliferative zone, cilia were positioned more in the posterior quadrant; this contrasted with the wildtype, which had a more bimodal anterior-posterior distribution. It is possible that cilium positioning is carefully regulated in the posterior zone; indeed, the observed bimodal distribution in the wildtype recalls the orientation of cell division in this zone (Li and Dudley, 2009), and could be reflective of this process. Ascenzi et al. (2011) previously noted that misregulation of proliferative chondrocyte maturation and intercalation corresponded to changes in cilium orientation. In the mutant, regulation of cilium position could be disturbed by reduced mechanical stimulation, potentially resulting in mis-regulation of cilium construction and a skewed distribution of cilia on cells which could ultimately be detrimental to skeletal development. In the hypertrophic zone, the positional trend was less clear: although the position of cilia was significantly different between the wildtype and mutant, both showed an overall posterior trend. The relatively small number of cilia in the hypertrophic zone, particularly in the wildtype, makes it difficult

to conclusively identify a positional trend in this zone, but suggests that cilia in this zone are similar to those in the proliferative zone.

The purpose of this study was to characterise primary cilia in the developing forelimb skeleton to identify structural changes which occurring under reduced mechanical stimulation. It identified several key differences in occurrence, position, and length between regions of the wildtype rudiment, and highlighted changes which occur in the mutant rudiments. Despite these subtle differences between cilia in wildtype and mutant forelimb skeletons, cilia are largely similar in appearance. This underlines the fact that changes in cilia-mediated signalling which may occur under reduced mechanical stimulation would not be visible by the means utilised here. However, identification of subtle changes in ciliary structural properties will enable better understanding of how signalling pathways mediated by cilia can be affected under reduced mechanical stimulation, and how cilia function as potential mechanosensors during normal skeletal development. While this study used the midpoint of the cilium shaft as an indicator of cilium orientation, higher-resolution imaging could be used in future to additionally quantify cilium shape. Cilia are deflected by fluid flow (Downs et al., 2014), and quantification of cilium curvature could be of interest in the context of mechanical stimulation.

Fewer muscle-less mutant specimens (n=3 individuals) were analysed in this study, compared to wildtype specimens (n=4 individuals). In some instances, such as length measurements, only 2 mutant specimens were available for analysis. Further, due to the large number of rudiment regions (nine) characterised here, it was not feasible for all four ciliary characteristics to be examined in all regions for both wildtype and mutant. However, this study has highlighted several differences across regions and between wildtype and mutant specimens, and can be further verified by the analysis of additional replicates for regions of particular interest. An increase in *n* numbers could also result in statistical significance for trends which were observed here but which were not statistically significant across regions, such as the reduction in cilium length in the muscle-less mutant.

Ciliary ablation during skeletal development can result in severe deformation, but the precise mechanism of this action is not entirely understood. Additionally, while some

effects of reduced mechanical stimulation occur when cilia are absent (e.g. hypomineralisation, chondrocyte disorganisation), others do not (e.g. joint contractures) (Section 1.5.2). The strong orientation and position of cilia at the developing joints points to a role for cilia in the differentiation of tissues here, which could be examined using targeted ablation of cilia in joint tissues. Wnt pathway activity is crucial for joint formation, and cilia-mediated Wnt signalling could also be examined in this region. The data presented in this chapter, therefore, represent an assessment of ciliary characteristics under normal and immobilised conditions, to add context to the role of cilia during skeletal development, and to inform future examination of the role of cilia in specific processes of skeletal development.

Chapter 6

Establishment of *in vitro* methods to test chondrogenesis[1]

6.1 Introduction

Manipulation of the cellular environment *in vivo* is a powerful means for understanding cellular differentiation and tissue patterning, but its complexity can hamper efforts to elucidate signalling networks or the effects of mechanical stimulation during organogenesis. Further, manipulation of signalling *in vivo* can have unintended secondary effects and can also be limited by the difficulty of targeting specific tissues or cell types. Studies of mechanical forces *in vivo* are difficult to conduct as it is not currently feasible to directly measure the forces experienced by cells in complex tissues, although modelling of physical forces experienced by the developing embryo does offer a way to examine patterns, if not magnitudes, of mechanical forces (e.g., Nowlan et al., 2008a, Roddy et al., 2011a). Additionally, mechanical manipulation of developing tissues *in vivo* is limited by the accessibility of the embryo during development, especially mammalian embryos. Therefore, systems of *in vitro* chondrogenesis are required to test environmental factors which affect cartilage formation.

Certain types of both adult- and embryo-derived cells have chondrogenic potential, and have had widespread use in chondrogenic assays. Multiple adult-derived cell types

[1] Work on micromass pattern and signalling molecule treatment was carried out in collaboration with Dr. Rebecca Rolfe, with contribution from intern student Dermott McMorrough under my supervision (micromass pattern and signalling molecule treatment).

have been utilised for assessment of chondrogenesis in culture: bone marrow-derived mesenchymal stem cells are widely-used (Scharstuhl et al., 2007), as are adult-derived cell lines such as C-28/I2 (immortalised human articular chondrocytes) (Goldring, 2004, Greco et al., 2011). High-density cultures of these cells are regularly performed as an assessment of chondrogenic potential, whether in 2-D (microdrop) or 3-D (pellet) cultures (Zhang et al., 2010a).

Embryonic cartilage is derived from mesodermal progenitor cells, and limb bud cells harvested from the embryo just prior to chondrogenic differentiation can easily be induced towards cartilage formation in culture. Micromass culture, where cells are plated in microdroplets at high density, is a simple, robust method for achieving chondrogenesis in culture (Mello and Tuan, 1999). In this system, embryonic mesenchymal cells from the early limb buds (approx. TS19), spontaneously undergo chondrogenesis. A notable aspect of this system is the generation of self-organised patterns of chondrogenic condensations, or nodules. Other embryonically derived cells, such as the ATDC5 cells line (derived from mouse embryonic teratocarnioma) (Atsumi et al., 1990) are commonly used to assay chondrogenesis and have been demonstrated to form characteristic nodules in micromass culture (Seemann et al., 2005, Lin et al., 2014). Interestingly, the cell line C3H10T1/2 (derived from mouse embryonic sarcoma) has an embryonic origin but fails to form nodules in micromass culture (Takacs et al., 2013). However, when compared to limb bud-derived micromasses, C3H10T1/2 micromasses express comparable levels of chondrogenic marker genes (Takacs et al., 2013). Despite their embryonic origin, and chondrogenic capability, these cells appear to have lost the ability to form nodules. High density cultures of adult cells also fail to form a characteristic pattern of nodules, instead showing diffuse Alcian Blue staining throughout cultures (e.g., Greco et al., 2011). Chondrogenic potential of micromasses is typically assessed by overall histological staining (e.g. Alcian Blue) or by quantitative assessment of chondrogenic gene expression. However, the findings above demonstrate that different cell types have variable potential for nodule formation and therefore differing capabilities to form spatially-organised patterns, which is an innate property of limb-bud derived cells.

Another hallmark of embryonic micromass culture is the cells' capacity to undergo chondrogenesis; crucially, cells must be at high density, but in general no additional signalling molecules are required for robust cartilage formation. In comparison, adult-derived cells require high density as well as certain growth factors (such as TGF-β) to stimulate chondrogenesis, further underscoring the limitations of adult-derived cells for chondrogenesis. Embryonically-derived C3H10T1/2 cells have been reported to form cartilage in high-density culture only after treatment with BMP-2 (Denker et al., 1999, Takacs et al., 2013), suggesting that the capability to self-organise could be linked to the ability to spontaneously differentiate without the addition of signalling molecules.

Linear morphogen gradients are not sufficient to describe certain complex patterns of tissue differentiation which occur in the developing embryo. Instead, Turing mechanisms can be used to explain the emergence of patterns consisting of discrete, repeated units such as the lung buds or the intestinal villi (Menshykau et al., 2014, Walton et al., 2016). In the developing limb bud, Turing mechanisms involving BMP, Wnt, and *Sox9* signals have been proposed to regulate the formation of digits, which cannot be explained by linear morphogen gradients (Badugu et al., 2012, Raspopovic et al., 2014). The apparently regular spacing of nodule formation events in micromass culture recalls the spacing of digits in developing hand- and footplates, and could be the result of such a Turing mechanism with different parameters. The characteristic pattern of nodule spacing is determined by a self-organising population of cells, as demonstrated by Raspopovic et al. (2014), who showed that *Sox9*-positive (pre-cartilage) and -negative (non-cartilage) cells derived from embryonic limb buds are both capable of establishing nodule patterns in micromass culture. This demonstrates that the formation of cellular condensations is based on whole-culture dynamics, potentially via diffuse signalling molecules and/or mechanical contacts between cells. A robust method to quantitatively describe and assess nodule formation in micromass culture therefore represents a way to examine and then manipulate proposed Turing mechanisms *in vitro*, in an effort to elucidate the phenomenal ability of these cells to self-organise spatially.

In addition to molecular signals, cellular differentiation is influenced by mechanical stimuli, which can be manipulated to engineer desired cell or tissue types for

therapeutic purposes. Adult-derived mesenchymal stem cells (MSCs), such as those derived from bone marrow stroma, are useful for tissue regeneration efforts as they can be manipulated to differentiate to multiple cell types (Owen and Friedenstein, 1988, Caplan, 1991, reviewed in García-Castro et al., 2008). The relative ease of obtaining large numbers of cells also makes them an attractive cell source. Mesenchymal stem cells are multi-potent, being able to differentiate to adipocytes (fat cells), osteocytes (bone cells) and chondrocytes (cartilage cells), among other cell types (reviewed in Oreffo et al., 2005). They can be induced to follow a particular differentiation pathway by the addition of signalling molecules and as noted in Section 4.1, by manipulation of the mechanical environment, where smaller, rounder cells on soft matrices tend towards adipogenesis while more spread cells on stiffer matrices tend towards osteogenesis, and intermediate environments give a range of cellular differentiation outcomes (Engler et al., 2006, Hadden and Choi, 2016) (Fig. 6.1). Despite their potential for chondrogenesis, the engineering of stable, articular cartilage *in vitro* is hampered by the propensity of cartilage to progress towards hypertrophy and form bone (Tang et al., 2015). This necessitates the identification of factors, both molecular and mechanical, which can be used to maintain stable differentiated cartilage *in vitro*.

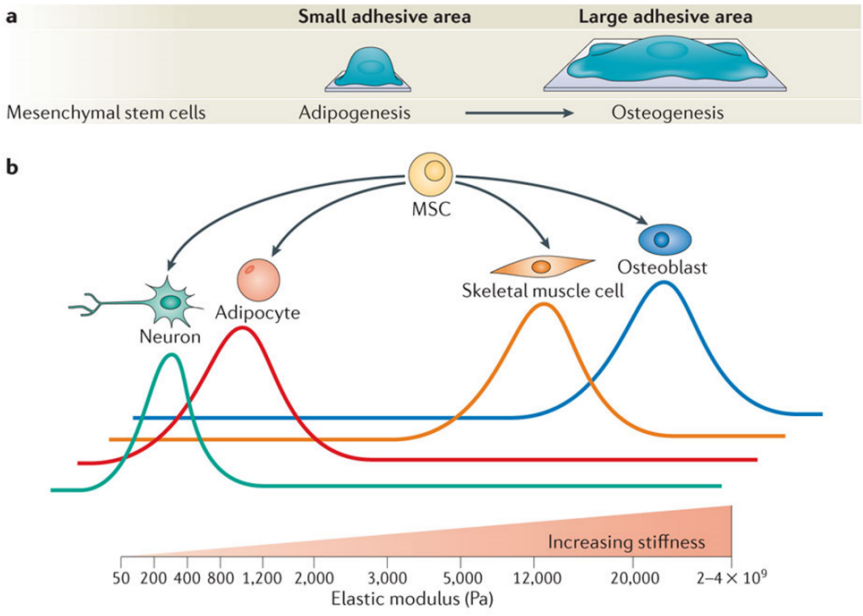

Fig. 6.1. Mechanical forces influence differentiation of MSCs. Cell shape and spreading (a) as well as stiffness of the extracellular environment (b) influence the differentiation of mesenchymal stem cells (MSCs) toward neurons, adipocytes, muscle cells, and osteoblasts. Adapted from Halder et al. (2012).

As elaborated in Section 1.6, cells in developing embryonic tissues experience dynamic mechanical stimulation, in the form of tension, compression, shear, and other physical forces. The gene regulatory changes occurring in cells under reduced mechanical stimulation, as presented in this work and by others (described in Section 1.6), further demonstrate a role for mechanical forces in the differentiation of cells and tissues during embryonic skeletal development. Likewise, mechanical forces have been shown to be involved in the differentiation of cells, both embryonic and adult-derived, *in vitro* (reviewed in Kelly and Jacobs, 2010, Delaine-Smith and Reilly, 2012). This is particularly relevant to chondrogenic differentiation, where mechanical stimuli have repeatedly been shown to be integral to the engineering of cartilage tissue *in vitro* (reviewed in Schumann et al., 2006, Grad et al., 2011). Several important features of this mechanoregulation occur: physical stimuli have the potential to increase cartilage stability (i.e. inhibit chondrocyte hypertrophy) in chondrogenic cultures; and physical stimuli are most effective when dynamic, allowing cells to recover from mechanical stress and to experience a range of physical forces. For example, previous work from this group reported a reduction in hypertrophy of MSCs and of embryonic micromass cultures subjected to daily cycles of hydrostatic pressure (Saha et al., 2016). However, there is a lack of knowledge concerning how patterns of physical stimuli correspond to patterns of cellular differentiation within 3-D tissues, and if tissue patterning *in vitro* can be spatially manipulated by regulating the mechanical forces experienced by cells. Understanding of such a relationship would add power and nuance to our current capability to engineer complex tissues *in vitro* and requires a method of exposing cells to known gradients of mechanical stimuli in order to assess resultant cellular differentiation.

6.1.1 Aims of this chapter

The objective of this part of the work was to examine models for studying patterns of chondrogenesis *in vitro*. It set out to characterise pattern alteration by manipulation of different signalling pathways and of mechanical stimuli. The specific aims were:

1) *To establish an approach to analyse spatial patterns of chondrogenesis using limb bud micromass culture.* Limb bud micromass culture generates a pattern

of chondrogenic condensations (nodules) which were characterised in a robust, quantitative manner (Fig. 6.2).

2) *To assess changes in pattern that occur under treatment with signalling molecules.* To investigate a role for different cell signalling pathways in the establishment of nodule pattern, signalling molecules were applied to micromass cultures and the effect on pattern formation was examined.

3) *To identify the timing of chondrogenic pattern formation under treatment with signalling molecules.* Expression of chondrogenic marker genes was used to follow chondrogenesis in micromass cultures, and to assess the impact of signalling molecule treatment on the timing and magnitude of gene expression.

4) *In a parallel work, to assess if dynamic mechanical stimulation could alter the spatial pattern of chondrogenesis of adult derived MSCs.* Mechanical stimulation is crucial to the regulation of chondrogenesis and chondrocyte maturation, as demonstrated *in vivo* in chick and mouse models. To mimic the dynamic nature of physical forces which cells in the developing skeleton experience *in vivo*, a custom-designed bioreactor which would subject differentiating cells in culture to 4-point bending was utilised. Chondrogenesis was assessed in cells subjected to dynamic bending compared to free swelling controls, to directly examine the effect of mechanical stimulation *in vitro.*

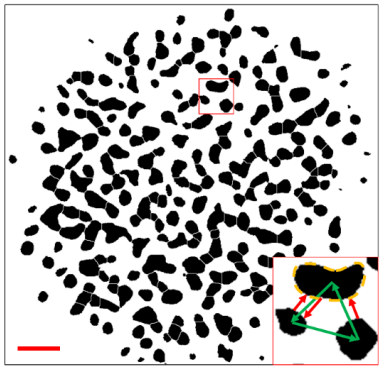

Fig. 6.2. Quantification of nodule characteristics and pattern. A representative processed image of a micromass culture is shown, where nodules are black objects (image processing described in Section 6.2.1). Nodule number, area and shape (inset, orange dashed outline) were used to quantitatively describe pattern, nodule spacing (distance between nodule centres; inset, green arrows) and nodule proximity (distance between nodule edges; inset, red arrows) were measured. Scale bar = 0.5 mm.

6.2 Methods

6.2.1 Micromass Image Analysis

Images of Alcian Blue-stained micromasses were processed using ImageJ (Fig. 6.3). Original TIFF (.tif) files were cropped to a circle of 5 mm diameter which was centred over the micromass by eye (Fig. 6.3b). Images were 'cleaned' by encircling debris with the Freehand tool, and filling the enclosed space with white colour to match the background (Fig. 6.3c). Cleaned images were split into component colour 'channels' (Fig. 6.3d); the green channel was determined to have the best signal-to-noise ratio and so was used for further analysis (Fig. 6.3d'). Images were converted to an 8-bit black and white image by setting a minimum threshold, using the auto-threshold function as a guideline (Fig. 6.3e). This converted every pixel above the threshold in the greyscale green channel image to black, and every pixel below the threshold to white. Treatment groups within an experiment were thresholded at the same value, but the appropriate threshold values were determined independently by eye for each experiment, due to unavoidable variability in staining contrast or intensity, and in image capture. Noise was removed and converged nodules were separated using the Despeckle and Watershed functions, respectively (Fig. 6.3f; compare inset images in (Fig. 6.3e and f). To avoid edge effects, images were further cropped to a circular region of interest with a 2-mm diameter, centred within the larger 5 mm region of interest. Both 5 mm and 2 mm images were used for analysis.

Nodules were counted and measured using the Analyze Particles function, with a minimum particle size of 0.005 μm^2. The total number of detected nodules was taken from the count of particles detected in the 5-mm region of interest. Other parameters, including the size of each detected nodule (in μm^2) and shape descriptors such as circularity and solidity (described in Fig. 6.4) were based on the 2-mm region of interest. Nodules touching the edge of the circular frame were excluded to prevent inaccurate size measurements (as these nodules are partially outside the frame of measurement). Exclusion of nodules at the edges could affect the measurements of nodule spacing and proximity slightly, but this difference was determined to not be significant. The details of each tool and command used, as well as the text of macros

used are included in Appendix B. Each step of the procedure outlined above, and detailed in Appendix B was independently optimised. Manual counts of nodule number were compared to automated counts, to ensure accuracy of the method; manual and automated counts were found to be similar, with some slight differences. At earlier time points (e.g. day 2), nodules are very faint in appearance, even after staining, and automated processing ensures that nodules are counted accurately by setting a threshold level. Automated watershedding separates detected objects which overlap. When counting by eye, these individual nodules were sometimes not easily distinguishable, especially at later time points (e.g. day 6), when nodules had grown and their edges appeared merged. Therefore, watershedding effectively separated nodules in an unbiased manner.

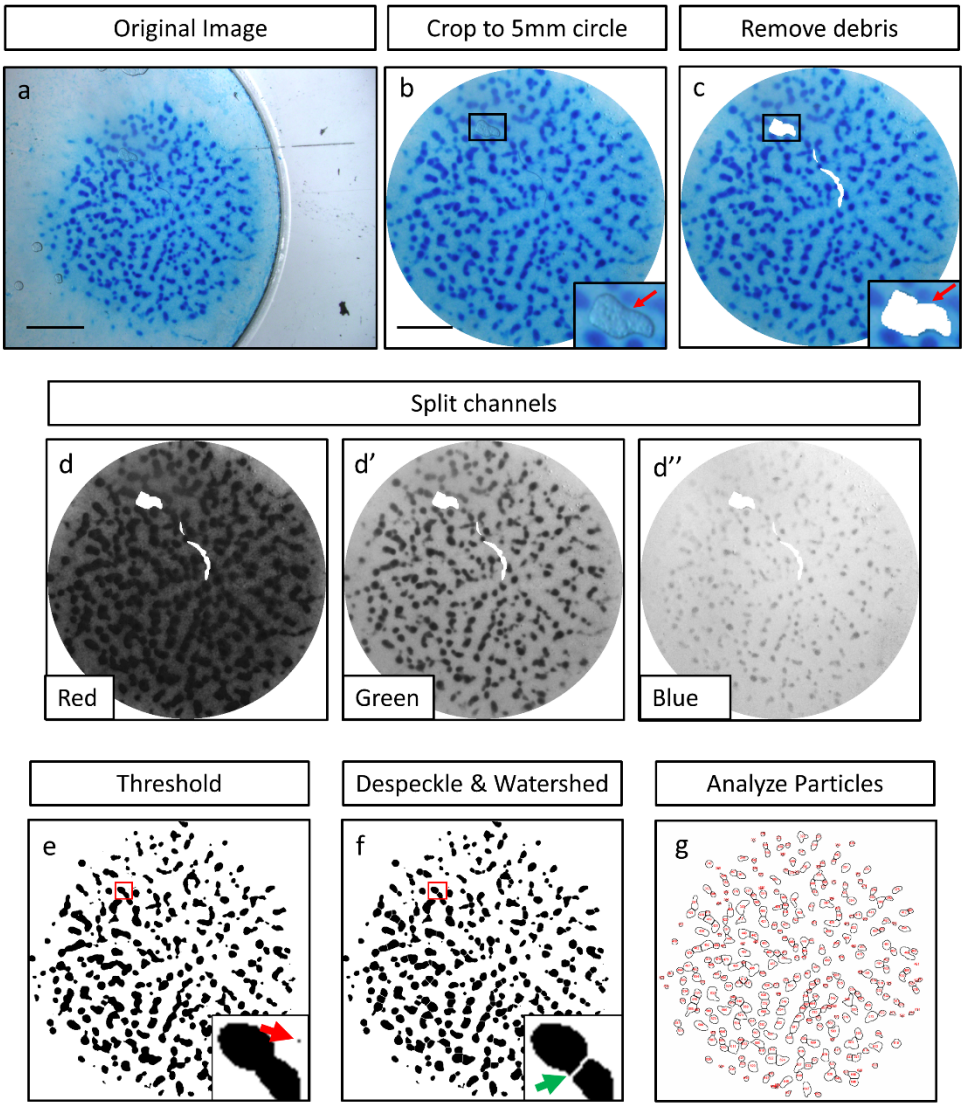

Fig. 6.3. Methodology for micromass image processing using ImageJ. Shown here is a representative Alcian Blue-stained micromass (a). Original images (a) were cropped to a circle 5 mm in diameter (b) then cleaned by covering debris and bubbles with white background (b and c, inset and red arrows). Images were converted to grayscale by splitting them into their component colour channels (d-d''), and the green channel was used for further processing (d'). A minimum threshold detection level was set and the image was converted to black-and-white (e). Noise was removed and converged nodules were separated using the Despeckle and Watershed functions (f). The Despeckle function removes small particles which are not visible as debris during the cleaning step (c), but are much smaller than nodules (inset in e, red arrow; compare to inset in f). The Watershed function separates converged nodules by placing a white (background) line between detected objects (inset in f, green arrows; compare to inset in e). The images were then processed using the Analyze Particles tool (g). Scale bars in (a) and (b) = 1 mm.

The Analyze Particles function generated measures of circularity and solidity for each detected nodule. The concepts of circularity and solidity are described in Fig. 6.4. Circularity is the measure of how close to a perfect circle a given shape is, as calculated by 4π times the shape area divided by the shape perimeter squared (Fig. 6.4A). A perfect circle has a circularity value of 1.0; as the shape becomes more elongated (ellipsoid), its circularity value decreases. Solidity is an indicator of the convexity, or "smoothness", of an object, as calculated by shape area divided by the convex hull area (Fig. 6.4B). The convex area is the area of the smallest ellipse that can be drawn around the object, completely enclosing it. A circle or ellipse has a solidity value of 1.0; as the shape becomes more concave, or "rougher", the solidity value decreases.

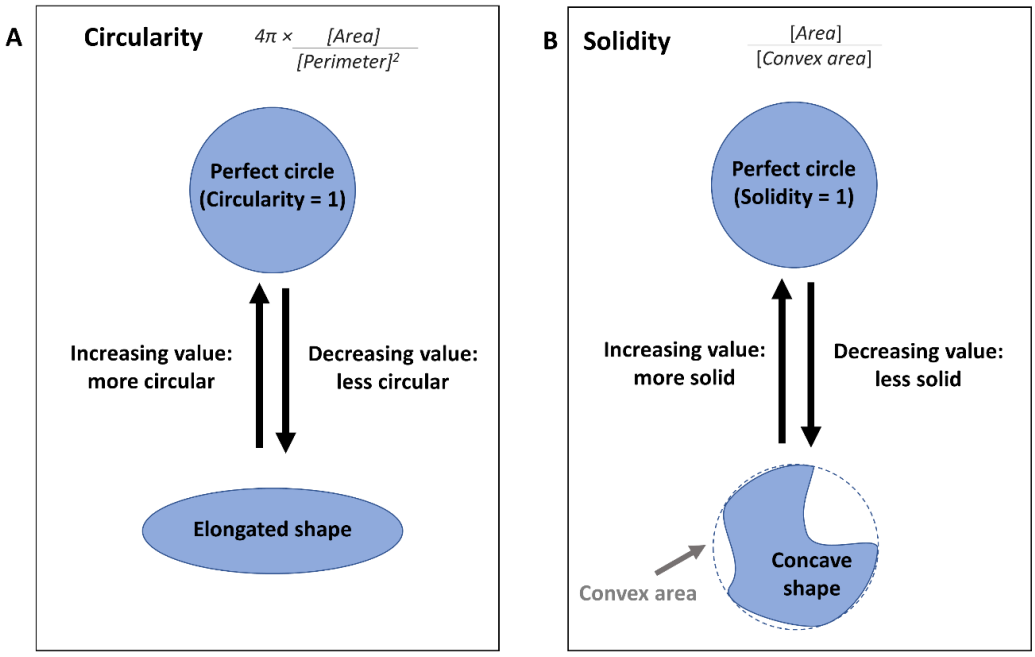

Fig. 6.4. Schematic explanation of the shape descriptors circularity and solidity. ImageJ was used to measure the circularity and solidity of nodules over time. The concepts of circularity (A) and solidity (B) were calculated according to the indicated equations. An example of convex area used to calculate solidity is indicated by the dashed line in (B). A perfect circle has circularity and solidity values of 1.0. A decreasing circularity value indicates a more elongated shape (A); a decreasing solidity value indicates a "rougher" or more concave shape (B).

Nodule spacing and proximity. To quantify nodule pattern, the spacing and proximity of nodules were calculated (Fig. 6.5). The Analyze Particles data generated above (Fig. 6.3) included the x and y coordinates of the centre point of each detected nodule as part of the .csv file output. These data were analysed using the SpatStat package in R, to measure spacing, or the distance of each nodule centre point to the nearest centre point of another nodule (Fig. 6.5A; details of R commands given in Appendix C). Because SpatStat is restricted to point patterns (i.e. shapes cannot be ascribed to the points), ArcGIS and a Python script were used to analyse the processed TIFF files used for the Analyze Particles analysis (Fig. 6.3f), to calculate nodule proximity, or the distance from a given nodule to its nearest neighbour as determined by nodule edges (Fig. 6.5b; details of Python script and procedure given in Appendix C). Calculation of both types of nearest neighbour distance allowed for a more nuanced analysis of nodule pattern than simply relying on one measurement.

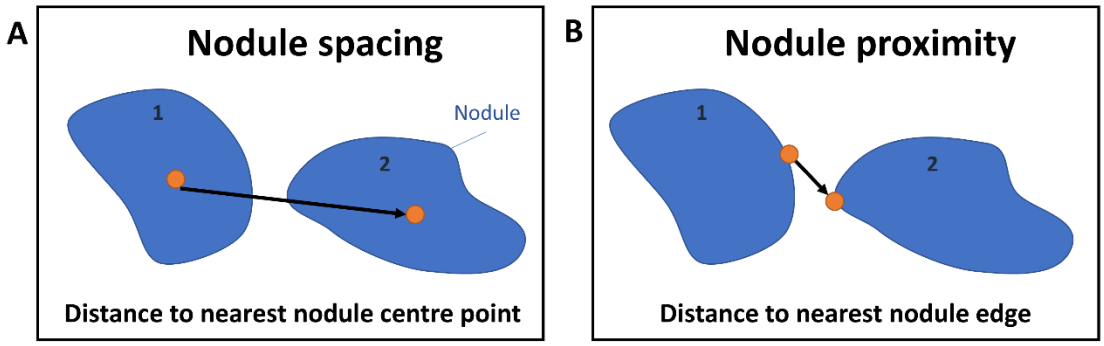

Fig. 6.5. Quantification of nodule pattern: spacing and proximity. A schematic representation of two aspects of nodule pattern quantified here is shown. The first aspect considered was nodule spacing, or the distance of a given nodule to the nearest centre point of another nodule (A). The second aspect considered was the nodule proximity, or the distance from the perimeter of a given nodule to the nearest edge point of another nodule (B). Measured distances are indicated by black arrows; orange circles represent nodule centre points (A) or points on nodule edges (B).

Statistical Analysis. In total, 6 independent experiments were analysed with 2-4 replicates in each group, per experiment, yielding a total of 85 micromasses processed for Alcian Blue staining and pattern analysis (Table 6.1). Prism software (GraphPad, v.6.01) was used for statistical analysis. In order to assess significance over time, one-way ANOVA was performed, followed by Tukey's post hoc test with a 95%

confidence interval. To assess significant differences between treatment groups at each time point, student's t-tests were performed, with a 95% confidence interval. P values of ≤ 0.05 were considered significant.

Table 6.1. Number of micromass cultures analysed. Note: this table includes only micromasses which were harvested and fixed for Alcian Blue staining and pattern analysis; micromasses harvested for qRT-PCR are not included here. Abbreviations: growth medium (GM), bone morphogenetic protein 2 (BMP-2), day (D).

Treatment	Day of harvest	Number of experiments performed	Total number of micromasses analysed
GM	D2	3	5
GM	D4	5	10
GM	D6	6	13
BMP-2	D2	1	2
BMP-2	D4	3	7
BMP-2	D6	4	8
NOG	D2	3	6
NOG	D4	3	6
NOG	D6	5	10
WNT-3A	D2	3	6
WNT-3A	D4	2	4
WNT-3A	D6	4	8

6.2.2 Mechanical Stimulation of Cell-Seeded 3-D Agarose Constructs

To mechanically stimulate cells in 3-D culture in a way that mimics a bending limb, a bending bioreactor was purpose designed for this work with Prof. Danny Kelly and Dr. Simon Carroll, at the Trinity Centre for Bioengineering (TCBE) (Fig. 6.6). The bioreactor uses a geared stepper motor coupled to a shaft which turns in both directions. This shaft joins to a dish where the 3-D constructs are cultured. Rectangular constructs (16 mm x 3 mm x 3 mm) (Fig. 6.6a) were moulded as described below, secured into the grips of the centre of the bioreactor dish (Fig. 6.6b) and flooded with medium (Fig. 6.6c). Constructs were held in place in the dish at one end by the dish centre piece and at the other end were fitted between a pair of fixed stainless-steel pins (Fig. 6.6d). Turning of the shaft simultaneously turns the coupled dish, resulting in bending of the constructs 2.1° to each side (Fig. 6.6d).

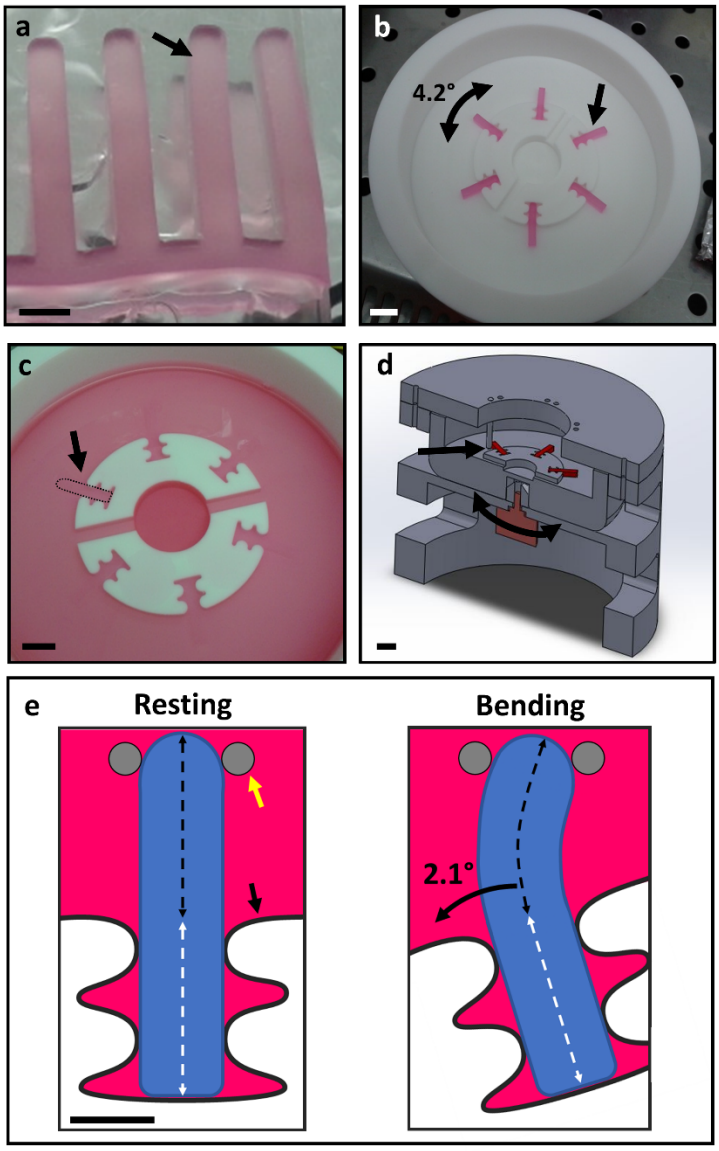

Fig. 6.6. Experimental setup of a bending bioreactor. A bending bioreactor was designed to mechanically stimulate cells seeded in 3-D constructs. Cells were mixed with agarose and injected into a mould to form constructs 16 mm x 3 mm x 3 mm (a, black arrow). Constructs were fitted into grips at the centre of the bioreactor dish (b, black arrow) and flooded with medium (c). To mechanically stimulate constructs, a geared stepper motor with a rotating shaft was coupled to the dish, allowing the centrepiece holding the constructs to be moved in each direction (b and d, double-headed arrows). At their outer end, constructs were constrained by stainless steel pins (d, black arrow; e, yellow arrow). Rotation of the central shaft moved constructs from a resting position to a bending position (e). The 2.1° movement in either direction, would bend the constructs along their outward half (e, dashed black arrow) while the halves fixed into the grips remained straight (e, dashed white arrow). Scale bars in (a) and (e) equal to 3 mm; scale bars in (b), (c), (d) equal to 10 mm.

Porcine bone-marrow derived mesenchymal stem cells had been previously harvested (as described in Lennon and Caplan (2006)) and stored in liquid nitrogen, before being thawed and plated. 1 x 10^6 cells were plated at 5000 cells/cm^2, and were cultured in 5% CO_2 at 37°C in expansion medium (10% FBS and 100 units/mL Penicillin-Streptomycin in DMEM, high glucose, GlutaMax (Gibco 61965)) and passaged at confluence. At the second passage, cells were mixed with an equal amount of 4% low melting point type VII agarose, yielding a final composition of 2% agarose with 15 x 10^6 cells/mL. This mixture was injected into a mould to form constructs 16 mm x 3 mm x 3 mm. Constructs were secured into the bioreactor with 2% agarose and cultured under free-swelling conditions for 7 days before commencing mechanical stimulation. During free-swelling and bending, cells in constructs were fed with Chondrogenic Differentiation Medium (CDM), containing sodium pyruvate, L-proline, bovine serum albumin, 100 units/mL Penicillin-Streptomycin, 1X insulin-transferrin-sodium supplement (Sigma-Aldrich, St. Louis MO), 10 ng/mL TGF-β3, dexamethasone, 50 μg/mL ascorbic acid, and linoleic acid in DMEM. Medium was changed every 2-3 days.

Dynamic bending was carried out for 2 hr/day for 21 days, following 7 days of free-swelling. Free-swelling controls were cultured for 28 days under matching conditions (e.g. constructs were positioned into an identical dish without bending). After 28 days of culture, constructs were harvested and fixed overnight in 4% PFA in PBS for paraffin embedding, sectioning and staining (Section 2.1.4, Section 2.2), or processed for qRT-PCR (Section 2.6).

6.3 Results

6.3.1 Analysis and manipulation of chondrogenic differentiation patterns in limb bud micromass culture

6.3.1.1 Characterisation of nodule formation in limb bud micromass culture over time

High-density micromass cultures of limb bud cells formed cellular condensations which were faintly visible after 1 day in culture and appeared more distinct and optically dense when monitored over time in live cultures (Fig. 6.7a-f; red arrows). Staining of fixed cultures revealed that these condensations become Alcian Blue positive chondrogenic nodules, faintly stained at day 2 and becoming more distinct and strongly stained at days 4 and 6 (Fig. 6.7g-i, black arrows).

Nodule number, size, and shape were quantified at days 2, 4, and 6 as described in Section 2.8.1 (Fig. 6.7j-m). The average number of nodules detected increased significantly between day 2 and day 4, but not between day 4 and day 6 (Fig. 6.7j). Contrastingly, average nodule size increased significantly between day 2 and day 4 as well as between day 4 and day 6 (Fig. 6.7k). Similarly, the percentage area covered by nodules increased significantly between day 2 and day 4, and between day 4 and day 6 (Fig. 6.7l). Shape was described by quantifying circularity and solidity of detected nodules. The average nodule circularity tended to decrease between day 4 and day 6, with a significance level just under the 95% confidence limit ($p=0.0518$) (Fig. 6.7m), indicating an elongation of nodules as they mature and enlarge between day 4 and day 6. Nodule solidity did not significantly change between day 4 and day 6 (Fig. 6.7m). Day 2 nodules were excluded from analyses of circularity and solidity because of their small size (Fig. 6.7k), which could lead to inaccuracy and skew shape measurements.

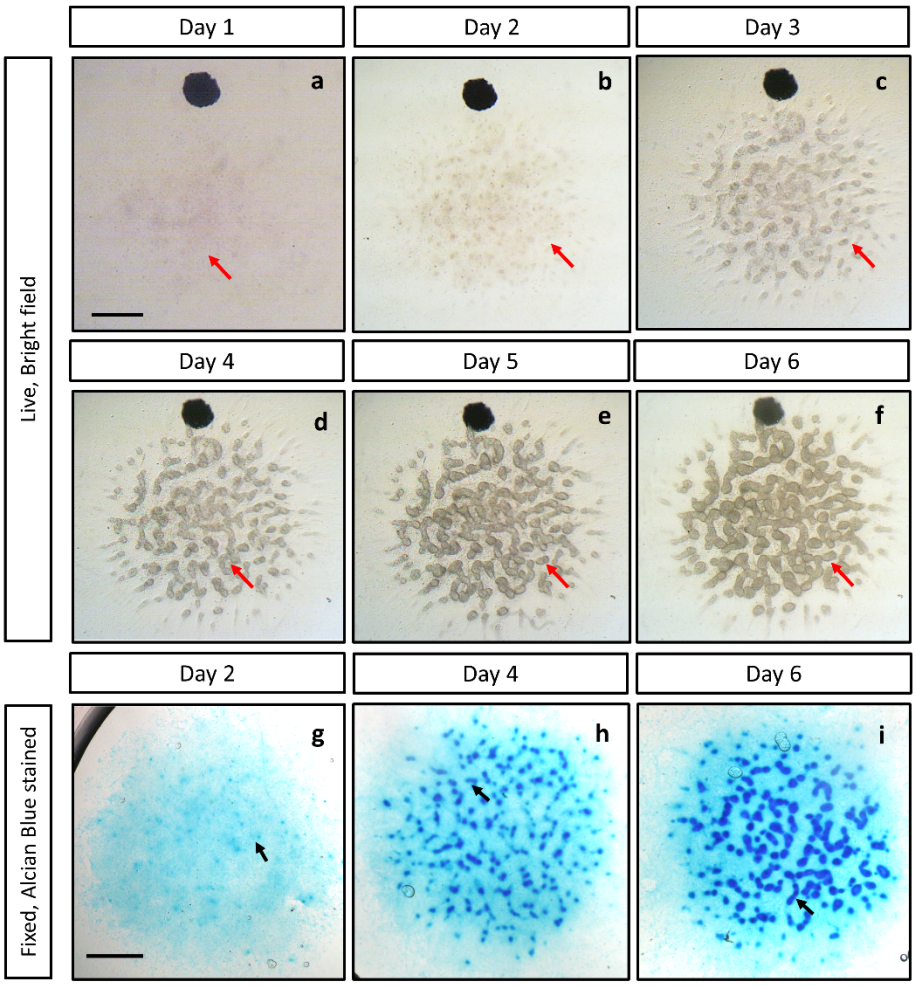
Day 1
Day 2
Day 3
Live, Bright field
a
b
c
Day 4
Day 5
Day 6
d
e
f
Day 2
Day 4
Day 6
Fixed, Alcian Blue stained
g
h
i

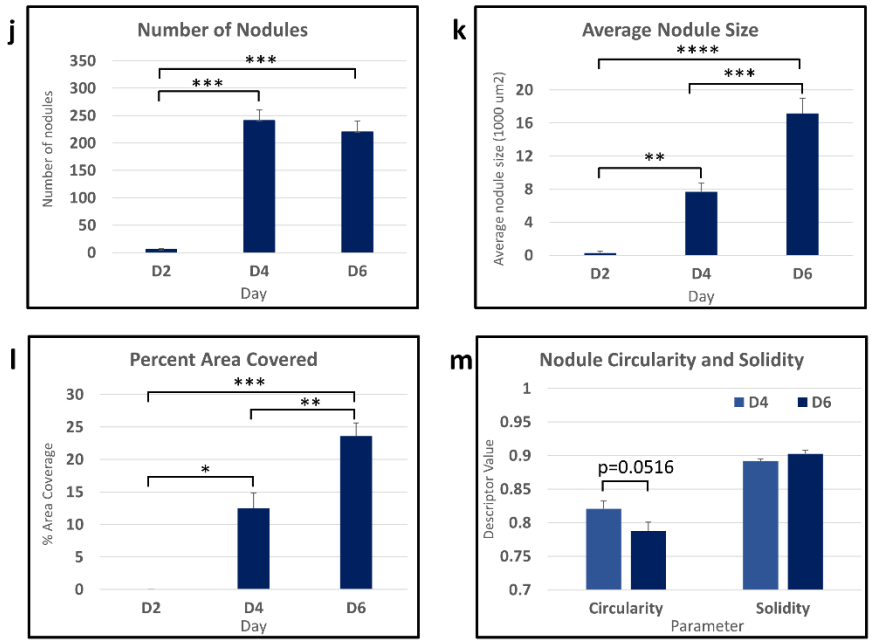
j
Number of Nodules
Number of nodules
350
300
250
200
150
100
50
0
***
***
D2
D4
D6
Day
k
Average Nodule Size
Average nodule size (1000 um2)
20
16
12
8
4
0
****
***
**
D2
D4
D6
Day
l
Percent Area Covered
% Area Coverage
30
25
20
15
10
5
0
***
**
*
D2
D4
D6
Day
m
Nodule Circularity and Solidity
Descriptor Value
1
0.95
0.9
0.85
0.8
0.75
0.7
D4
D6
p=0.0516
Circularity
Solidity
Parameter

Fig. 6.7 (previous page). Cartilage nodules forming in micromass culture change in number, size, and shape over time. Example images of whole micromass cultures (a-i): live, bright field images of the same micromass cultures captured at days 1-6 of culture (black mark used for image orientation) with cellular condensations visible as optically dense spots (a-f, red arrows indicate a single condensation over time). Multiple micromass cultures from an individual experiment, harvested and fixed at indicated timepoints, stained with Alcian Blue to visualise cartilage (g-i; black arrows indicate nodules). Scale bars in (a), (g) equal 1 mm and are representative of all images. Nodules were quantified in ImageJ, based on circular regions of interest; either 5-mm diameter (for total number of nodules) or 2-mm diameter (for all other parameters). Total number of nodules (j), average nodule size (k), total percentage of the analysed area covered by nodules (l), and average nodule circularity and solidity (m) were assessed (n=5, 10, and 13, for days 2, 4, and 6, respectively). Error bars represent standard error. Significance was determined by one-way ANOVA or Student's t-tests where appropriate; $p \leq 0.05$(*), $p \leq 0.01$(**), $p \leq 0.005$(***).

To quantitively describe nodule pattern, the spacing and proximity of nodules were measured using neighbour distances (Fig. 6.5, Fig. 6.8). To measure spacing, the distance between a given nodule's centre point and the nearest centre point of another nodule was calculated for each nodule in each micromass (Fig. 6.5A). To measure proximity, the distance between a point on the perimeter of a given nodule and a point on the perimeter of the closest distinct nodule was calculated (Fig. 6.5B). For each method, the mean distance was subsequently calculated for each micromass and the results grouped by day (Fig. 6.8). Both spacing and proximity returned values for day 2 which were significantly higher than those for either day 4 or day 6 (Fig. 6.8a and b), indicating that detectable nodules at day 2 are far apart compared to later time points. When comparing later time points, spacing was not significantly different between day 4 and day 6 (Fig. 6.8a), but the proximity of nodules was significantly lower at day 6 compared to day 4 (Fig. 6.8b). This indicates that the nodules remain spaced apart at day 6 similarly to day 4, but that their edges come closer together over time. Further, the relatively large error bars for both nodule spacing and proximity at day 2 compared to the relatively small error bars at days 4 and 6 (Fig. 6.8) indicate that at later time points, nodule spacing and proximity across cultures is more regular, with little variation in the distance between nodule centre points or edges.

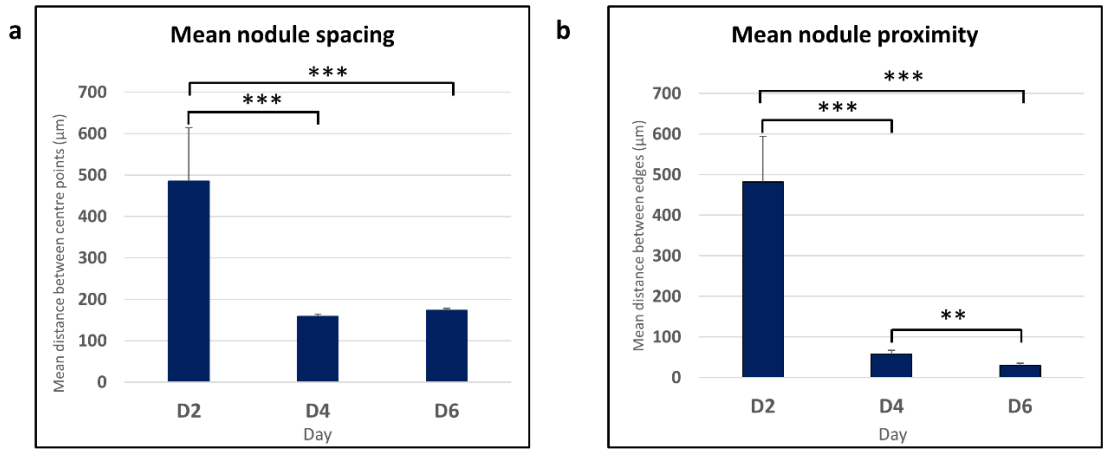

Fig. 6.8. Nodule spacing changes over time. The nearest neighbour distance was calculated using nodule centre points (a) and or nodule edges (b). The nearest neighbour for each nodule in a given micromass was calculated, and values were averaged together for individual micromasses (n=5, 10, and 13, respectively, for days 2, 4, and 6). The results are presented here, grouped by day. Error bars are expressed as the standard error. Significance was determined by student's t-tests; $p \leq 0.01$(**), $p \leq 0.005$(***).

6.3.1.2 Nodule pattern changes following treatment with signalling molecules

The formation of a regular pattern of nodules within a population of limb-bud derived cells (Fig. 6.8) could be hypothesised to be the result of a Turing mechanism. Further, a Turing-type mechanism involving BMP and Wnt signalling activity was suggested to generate *in vivo* patterns of digit formation (Raspopovic et al., 2014). To test if BMP and Wnt signalling are involved in generating the pattern of chondrogenic nodules in micromass culture, aspects of pattern following treatment with Wnt and BMP pathway ligands (BMP-2 and WNT-3A) and a BMP pathway inhibitor (Noggin) were examined. Cultures were treated with growth medium with or without 100 ng/mL of either BMP-2 or Noggin, or with 50 ng/mL of mouse WNT-3A or 200 ng/mL of human WNT-3A protein (Section 2.8.1.1). Fixed cultures were stained with Alcian Blue to visualise, quantify, and characterise nodule formation (Fig. 6.9) (n numbers for control and BMP treated cultures listed in Table 6.1). Staining revealed that nodules were first visible at day 2 in growth medium cultures, and in cultures treated with BMP-2 and Noggin (Fig. 6.9a-c, red arrows) but not in cultures treated with 200 ng/mL human WNT-3A (Fig.

6.9d) (n=2 for BMP-2 and n=6 for Noggin and WNT-3A respectively). At day 4, numerous nodules were easily visible in growth medium and BMP-2 cultures (Fig. 6.9a' and b', red arrows), but remained scarce and faint, or absent, in Noggin and WNT-3A cultures (Fig. 6.9c' and d'). At day 6, nodules remained strongly visible in growth medium and BMP-2 cultures (Fig. 6.9a'' and b''). In general, while some nodules were visible in Noggin cultures, there were dramatically fewer than in growth medium or BMP-2 cultures at the same time point (Fig. 6.9c''). In WNT-3A cultures at day 6, nodules were either faint, or not detectable (Fig. 6.9d''). Images of Noggin or WNT-3A micromasses at day 6 (n=7 and n=8, respectively) were processed in the same manner as control or BMP-2 treated micromasses to assess nodule number: nodule counts ranged from 0-10, and so are excluded from the analysis presented in Fig. 6.9. Bright field imaging of live micromasses corresponded with Alcian Blue staining, with condensation number and density in Noggin- and WNT-3A treated micromasses dramatically reduced (data not shown).

To quantitatively describe changes in nodule pattern upon signalling molecule treatment, the quantification approach outlined above was applied to BMP-2 treated cultures and compared to control cultures (Fig. 6.9). There is no difference in average nodule number at day 2; by day 4 the average nodule number in BMP-2 treated cultures is higher, but not significantly; and at day 6 of culture, there are significantly more nodules in BMP-2 micromasses (Fig. 6.9e). Contrastingly, although there is no significant difference in nodule size with BMP2 treatment there is a trend toward smaller average size at day 6 (Fig. 6.9f). As in growth medium cultures, average nodule size significantly increased in BMP treated cultures from day 4 to day 6 (Fig. 6.9f). There was no significant difference between growth medium and BMP-2 cultures for the percent area covered by nodules at day 4 or day 6, despite more nodules in BMP-2 micromasses, which further indicates a reduction in nodule size (Fig. 6.9g). For nodule shape, the circularity index decreased and solidity index increased in BMP-2 cultures between days 4 and 6 (Fig. 6.9h and Fig. 6.9i), indicating that nodules in BMP-2 cultures become less circular but smoother from day 4 to day 6. This is similar to growth medium cultures, where nodules become less circular from day 4 to day 6, but with no significant change in solidity (Fig. 6.7m). When comparing BMP-2 and

growth medium cultures at each time point, there are no significant differences between the groups (Fig. 6.9h and Fig. 6.9i).

Fig. 6.9 (next page). More nodules form in BMP-2 treated cultures, while Noggin and WNT-3A treatment severely impact nodule formation. Micromasses were fed with normal growth medium or treated with signalling molecules (100 ng/mL BMP-2 or Noggin, or 200 ng/mL human WNT-3A), as indicated, from the time of plating. Representative images of treated micromasses are shown in a-d''; red arrows indicate visible nodules. Alcian Blue stained micromasses were processed for analysis and quantification as described in Section 2.8.1.1, revealing changes in nodule number (e), percentage area covered by nodules (f), nodule size (g), and shape descriptors circularity (h) and solidity (i); (n numbers as listed in Table 6.1). Scale bar = 1 mm. Error bars represent standard error. Significance was determined by one-way ANOVA or Student's t-test; $p \leq 0.01$(**), $p \leq 0.005$(***).

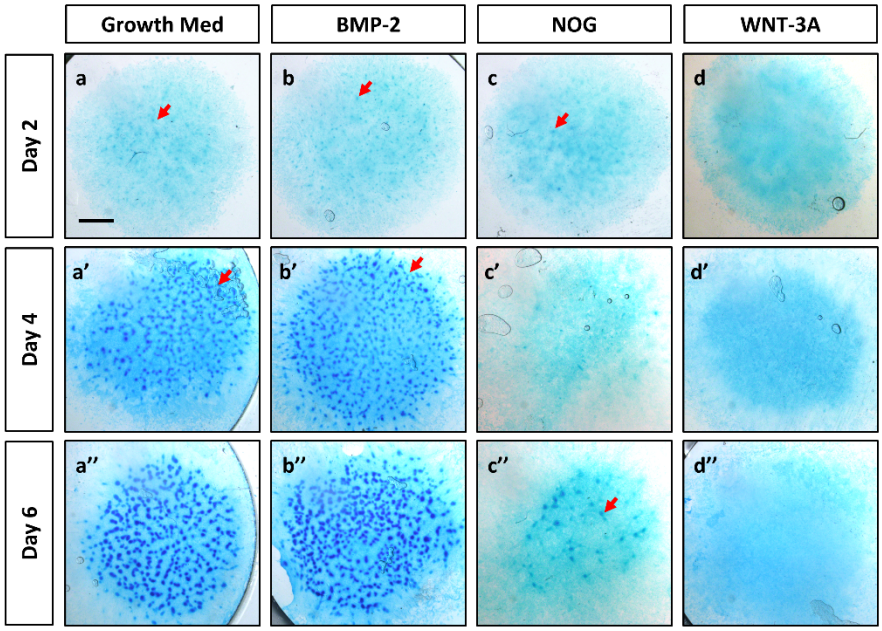
Growth Med
BMP-2
NOG
WNT-3A
Day 2
Day 4
Day 6
a
b
c
d
a'
b'
c'
d'
a''
b''
c''
d''

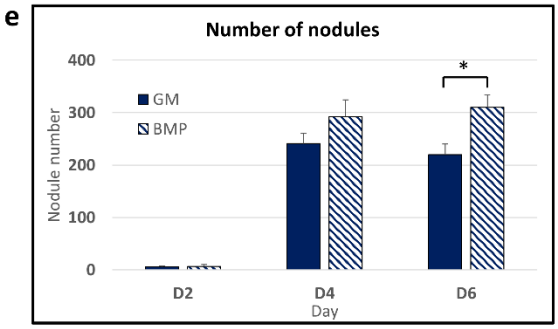
e
Number of nodules
Nodule number
400
300
200
100
0
GM
BMP
*
D2
D4
D6
Day

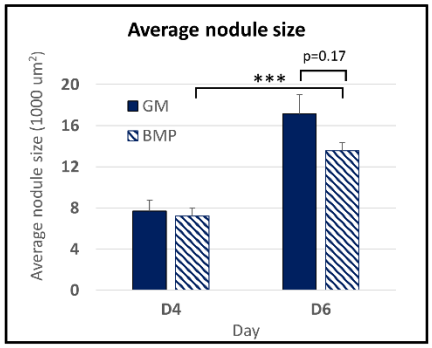
f
Average nodule size
Average nodule size (1000 um²)
20
16
12
8
4
0
p=0.17
***
GM
BMP
D4
D6
Day

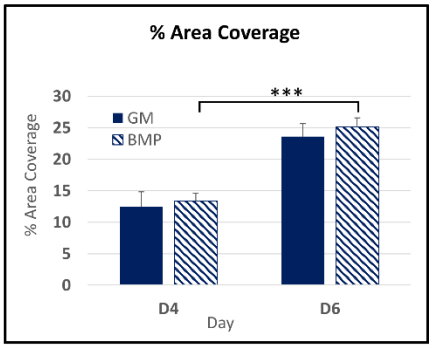
g
% Area Coverage
% Area Coverage
30
25
20
15
10
5
0
***
GM
BMP
D4
D6
Day

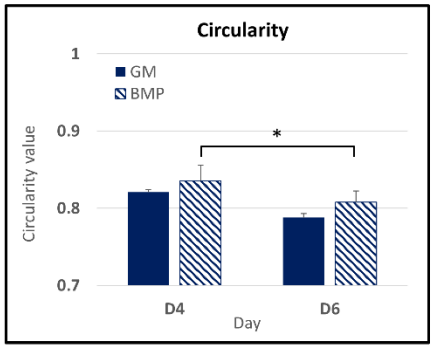
h
Circularity
Circularity value
1
0.9
0.8
0.7
GM
BMP
*
D4
D6
Day

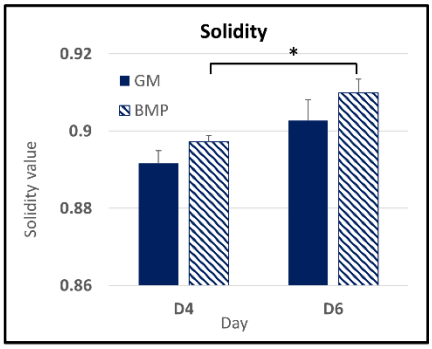
i
Solidity
Solidity value
0.92
0.9
0.88
0.86
GM
BMP
*
D4
D6
Day

To assess the effect of BMP-2 on nodule pattern, nodule spacing and proximity were measured as described in Section 6.2.1. Analysis of nodule spacing using nodule centre point distance measurements revealed that at day 6, nodule centre points were significantly closer together in BMP-2 cultures compared to growth medium cultures (Fig. 6.10a). Interestingly, there was no significant difference in nodule spacing between the groups at day 4, or between day 4 and day 6 for BMP-2 cultures, but there is a significant reduction in nodule spacing on day 6 in the presence of BMP-2 (Fig. 6.10a). Assessment of nodule proximity indicated no significant difference in the distance between nodule edges between BMP-2 and growth medium cultures at either day 4 or day 6 (Fig. 6.10b). As for growth medium cultures (Fig. 6.8b), there was a significant decrease in the distance between nodule edges for BMP-2 cultures between day 4 and day 6, indicating that nodules in both control and treated cultures grow closer together over time but despite a significant increase in nodule number the proximity of neighbouring nodules tends to be maintained in BMP-2 treated cultures.

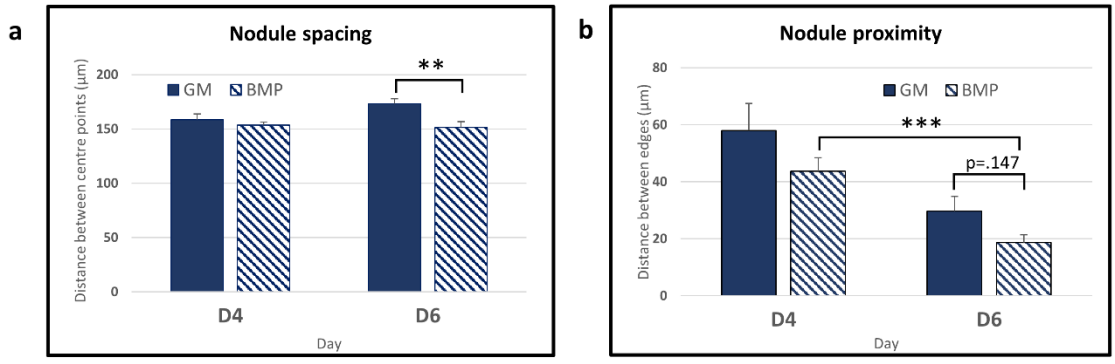

Fig. 6.10. Nodules in BMP treated micromasses are spaced closer together than in control micromasses, but the distance between nodule edges does not change significantly. Nodule spacing and proximity were assessed by measuring the distance between nearest nodule centre points (a) and nearest nodule edges (b), respectively, for BMP-2 treated micromasses and GM micromasses at day 4 and day 6. Error bars are expressed as standard error. n values given in Table 6.1. Significance was determined by Student's t-tests; $p \leq 0.01$(**), $p \leq 0.005$(***).

6.3.2 Timing of chondrogenesis in micromass culture is altered on addition of BMP and Wnt pathway signalling molecules

To examine the time profile of chondrogenesis and progression of hypertrophy occurring in micromass cultures treated with signalling molecules, qRT-PCR was used to measure the expression levels of genes associated with these processes, starting at 12 hr post-plating (Fig. 6.11). Gene expression levels were normalised to GAPDH expression and are expressed as fold changes relative to day 0 cells (c.f. Section 2.6.2). Saha et al. (2016) previously established that *Sox9* and Col2a1 chondrogenic markers were already upregulated after 1 day in culture, as was the cartilage maturation marker *Ihh*, while the hypertrophic marker *Col10aI* was upregulated by day 3.

Although time points later than day 2 (day 4 and day 6) are presented here for WNT3A-treated micromasses, they are represented by a single replicate of 2 pooled cultures, and so no statistical analysis could be performed. *Sox9* expression decreases at 24 hr in growth medium cultures, while it continues to increase in BMP-2 treatment (Fig. 6.11a). Levels of *Sox9* expression are increased until day 4 of culture; expression then decreases in both growth medium and BMP-2 cultures by day 6. Contrastingly, Noggin (NOG) and WNT-3A treatment resulted in reduced expression of *Sox9* by 12 hr, with a significant decrease by day 2 in WNT-3A treated cultures, and by day 6 in Noggin treated cultures (Fig. 6.11a).

Col2aI expression showed a similar pattern between growth medium and BMP-2 treated cultures, with significant increases in *Col2aI* occurring between day 2 and day 4 of culture (Fig. 6.11b). However there were no significant differences in Col2a1 levels between GM and BMP2 treated cultures. Noggin treated cultures had reduced levels of *Col2aI* expression: at days 4 and 6, there was significantly less *Col2aI* than in GM and BMP-2 treated cultures at the same time points (Fig. 6.11b). WNT-3A treated cultures also showed reduced levels of *Col2aI* expression, and at all time points but 36 hr and day 2 had levels of *Col2aI* lower than those in day 0 cells (Fig. 6.11b). There was significantly less *Col2aI* expressed in WNT-3A cultures than in growth medium cultures at 12 hr, 36 hr, and day 2 (Fig. 6.11b).

The hypertrophy markers *Ihh* and *Col10aI*, surprisingly both showed a trend of up-regulation from the earliest time points (Fig. 6.11c and d). Both *Ihh* and *Col10aI* levels in BMP-2 treated cultures showed strong increase from 12 hr but while *Ihh* levels dropped after day 2, Col10a1 remained high (Fig. 6.11c and d). In growth medium cultures, *Ihh* had an early increase in expression at hr 12-36, before decreasing by day 6 (Fig. 6.11c). BMP-2 cultures had higher levels of *Ihh* and *Col10aI* expression at all time points in comparison to growth medium cultures, with a significant difference at day 2 (Fig. 6.11c and d). Noggin cultures, in comparison, had decreased levels of *Ihh* at days 2, 4, and 6, compared to day 0 cells (Fig. 6.11c). WNT-3A cultures had a dramatic early increase in *Ihh* expression, followed by a dramatic decrease at days 2, 4, and 6 (Fig. 6.11c).

Noggin and WNT-3A appeared to have a stronger repressive effect on *Ihh* than on Col10a1, and Col10a1 levels appeared less repressed by WNT-3A treatment than did other genes examined here (Fig. 6.11). Noggin cultures surprisingly did not have a significant reduction in the expression of *Col10aI* at days 4 and 6, and although there was a reduction in Col10I expression at day 2 relative to day 0 cells and GM and BMP-2 cultures at day 2, this was not significant (Fig. 6.11d). WNT-3A cultures showed a pattern of early *Col10aI* expression which was similar to that of BMP-2 cultures, with increases in expression relative to day 0 at 12 and 36 hr, with a subsequent dramatic reduction in expression (Fig. 6.11d).

Overall, BMP-2 treatment increased both chondrogenesis and progression to hypertrophy, as shown by increased early expression of *Sox9* and an earlier peak of *Ihh* and *Col10aI* expression (Fig. 6.11a, c and d). Contrastingly, Noggin treatment decreased chondrogenesis, indicated by reduced *Sox9* expression and a delayed peak of *Col2aI* expression (Fig. 6.11a and b); interestingly, Noggin treatment negatively impacted *Ihh* expression but not *Col10aI* expression, indicating a mixed effect on progression and hypertrophy of cultures (Fig. 6.11c and d). Wnt treatment inhibited expression of all marker genes by day 4 or 6, with expression levels of all these genes lower than those of day 0 cells (Fig. 6.11a-d), indicating strong inhibition of chondrogenesis and progression towards hypertrophy, but again there is a less dramatic effect on Col10a1 than on *Ihh*. Surprisingly, early expression of *Ihh* and *Col10aI* was

not repressed in WNT-3A cultures; these genes were well expressed prior to day 2, with expression comparable to growth medium cultures.

Fig. 6.11 (next page). BMP-2 treatment increases amount and onset of chondrogenesis and hypertrophy, while Noggin and WNT-3A suppress these processes. Expression of early chondrogenic marker genes *Sox9* (a) and collagen type 2aI (Col2) (b) as well as markers of cartilage maturation and hypertrophy Indian hedgehog *Ihh* (c) and collagen type 10aI (Col10) (d) was assessed by qRT-PCR. Gene expression was measured in control micromasses grown in un-supplemented medium (GM), or in medium treated with 100 ng/mL BMP-2 or Noggin (NOG), or 50ng/mL mouse WNT-3A or 200 ng/mL human WNT-3A. Micromasses for qRT-PCR were harvested at the indicated time points (12, 24, and 36 hr, and days 2, 4, and 6). For all timepoints (except WNT-3A at days 4 and 6), 1-3 individual replicates from 2-6 individual experiments were analysed. Gene expression was normalised to GAPDH for each sample and is expressed as fold changes relative to day 0 cells which were harvested at the time of plating (note the different scales for each gene). Error bars represent standard error. Significance was determined by one-way ANOVA or student's t-tests, where appropriate; $p \leq 0.05$(*), $p \leq 0.01$(**), $p \leq 0.005$(***), $p \leq 0.001$(****).

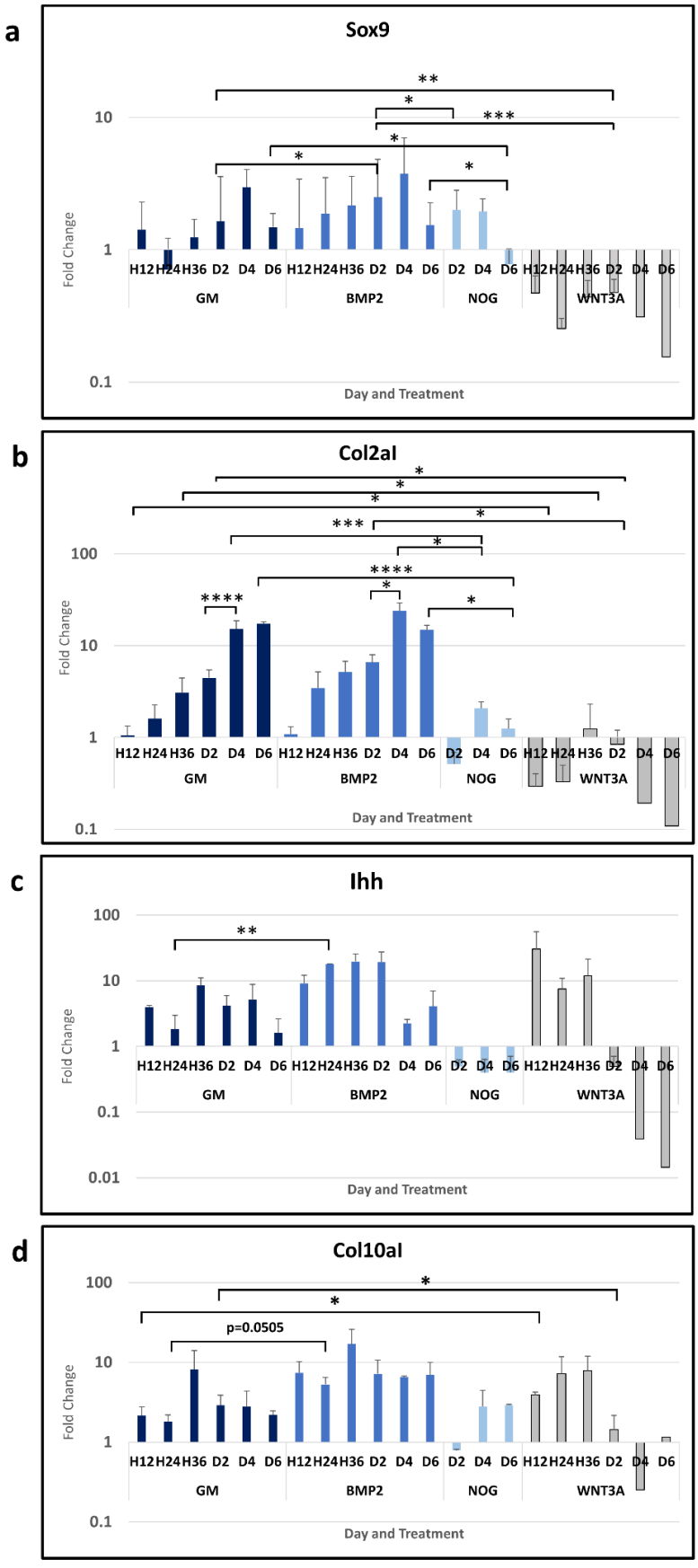
a
Sox9
Fold Change
10
1
0.1
H12 H24 H36 D2 D4 D6 H12 H24 H36 D2 D4 D6 D2 D4 D6 H12 H24 H36 D2 D4 D6
GM
BMP2
NOG
WNT3A
Day and Treatment
b
Col2a1
Fold Change
100
10
1
0.1
H12 H24 H36 D2 D4 D6 H12 H24 H36 D2 D4 D6 D2 D4 D6 H12 H24 H36 D2 D4 D6
GM
BMP2
NOG
WNT3A
Day and Treatment
c
Ihh
Fold Change
100
10
1
0.1
0.01
H12 H24 H36 D2 D4 D6 H12 H24 H36 D2 D4 D6 D2 D4 D6 H12 H24 H36 D2 D4 D6
GM
BMP2
NOG
WNT3A
Day and Treatment
d
Col10a1
Fold Change
100
10
1
0.1
p=0.0505
H12 H24 H36 D2 D4 D6 H12 H24 H36 D2 D4 D6 D2 D4 D6 H12 H24 H36 D2 D4 D6
GM
BMP2
NOG
WNT3A
Day and Treatment

6.3.3 Mechanical stimulation (3-point bending) of seeded 3D-hydrogel constructs

To establish a 3-D culture system which could assess the impact of mechanical stimuli on chondrogenic differentiation, a bending bioreactor was designed to subject cells to dynamic forces during differentiation. In long-term culture this was particularly used to assess the effect on progression to hypertrophy and mineralisation. Adult porcine mesenchymal stem cells in agarose constructs were subjected to two hr of bending per day for 21 days, following 7 days of free-swelling (Section 6.2.2). After the 28-day culture period, the bending constructs had extensive visible signs of mineralisation in comparison to free-swelling control constructs as judged by regions of high opacity (white coloration) within the constructs (Fig. 6.12). While mineralisation was also visible in free-swelling constructs, it was only observed as small white regions on two constructs (Fig. 6.12A, red arrows). In comparison, all six bending constructs each had multiple areas of mineralisation (Fig. 6.12B). While mineralisation patterns varied between bending constructs, several trends emerged: mineralisation was observed at the mid-point of the long axis of the constructs, (Fig. 6.12vii-xii, red arrows) and also at the longitudinal edges of the constructs (Fig. 6.12vii-xii, blue arrows). Mineralisation was not homogenous, but appeared as multiple distinct regions within individual constructs (Fig. 6.12xi, asterisks).

Fig. 6.12 (next page). Dynamic bending resulted in increased visible mineralisation in constructs. Agarose constructs seeded with adult mesenchymal stem cells at high density were fitted into custom-designed dishes, flooded with medium, and cultured under either free swelling (A) or bending conditions (B) for 21 days, after an initial 7-day free swelling period. Superficial views immediately following the culture period show obvious signs of mineralisation (i-xii). Mineralisation was visible in some free swelling constructs (i, ii; red arrows) and in all bending constructs (vii-xii, red and blue arrows). In bending constructs, mineralisation tended to occur at the longitudinal mid-point of constructs (vii-xii, red arrows) and the longitudinal edges (vii-xii, blue arrows). Mineralisation was not homogenous across constructs, but appeared as distinct foci (xi, black asterisks). FE modelling of the mechanical forces generated in such a construct on bending predicted patterns of tension and compression under bending conditions in one direction (C). Maximum force for both tension and compression was predicted at the longitudinal mid-point of the constructs (C, black arrows). Blue lines in (i-vi) indicate construct edges. FE modelling was done by Simon Carroll, TCBE. n=1 experimental replicate.

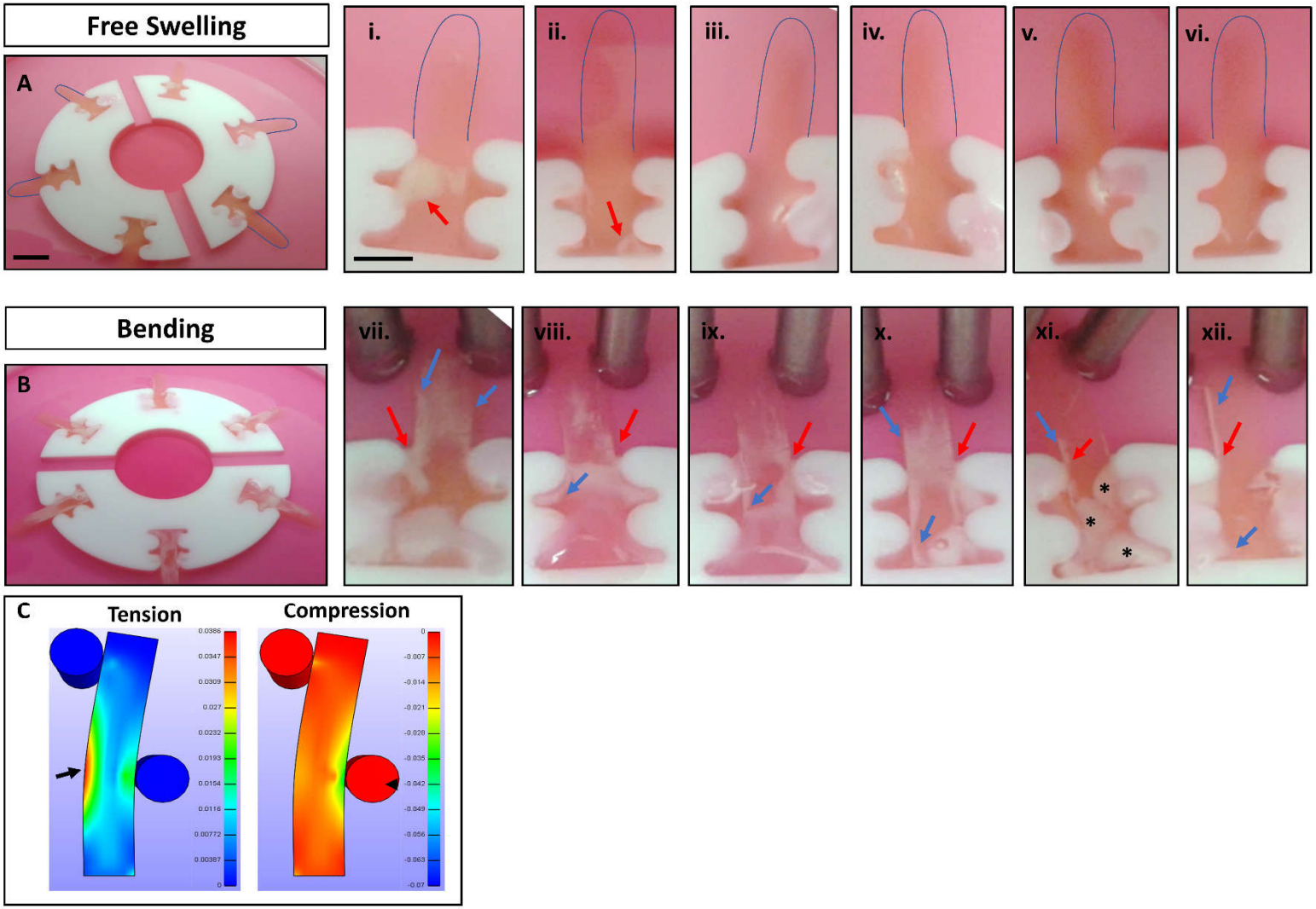
Free Swelling
A
i.
ii.
iii.
iv.
v.
vi.
Bending
B
vii.
viii.
ix.
x.
xi.
xii.
C
Tension
Compression

To assess the extent of mineralisation and cartilage formation, constructs were wax embedded, sectioned longitudinally, and stained for Alizarin Red and Safranin O (Fig. 6.13). Safranin O staining revealed that cartilage formation in the free swelling construct was localised to the fixed, "dish" end of the construct (Fig. 6.13a and b, black bracket), compared to extensive cartilage formation in the bending construct (Fig. 6.13c, black bracket). Although cartilaginous matrix was detected throughout the length of the bending construct, in the "dish" end of the construct which was fixed into the bioreactor dish, Safranin O staining extends to the edges of the construct (Fig. 6.13c, double-headed arrow) while at the "tail" end of the construct which was fitted between the steel pins, Safranin O staining was limited to the interior of the construct and was not detected at the edges (Fig. 6.13c, black arrows). Alizarin Red staining revealed overall higher levels of mineralisation throughout the bending construct (Fig. 6.13e, e') compared to the free swelling construct (Fig. 6.13d, d'). There were no observed differences in Alizarin staining between the dish and tail ends of constructs.

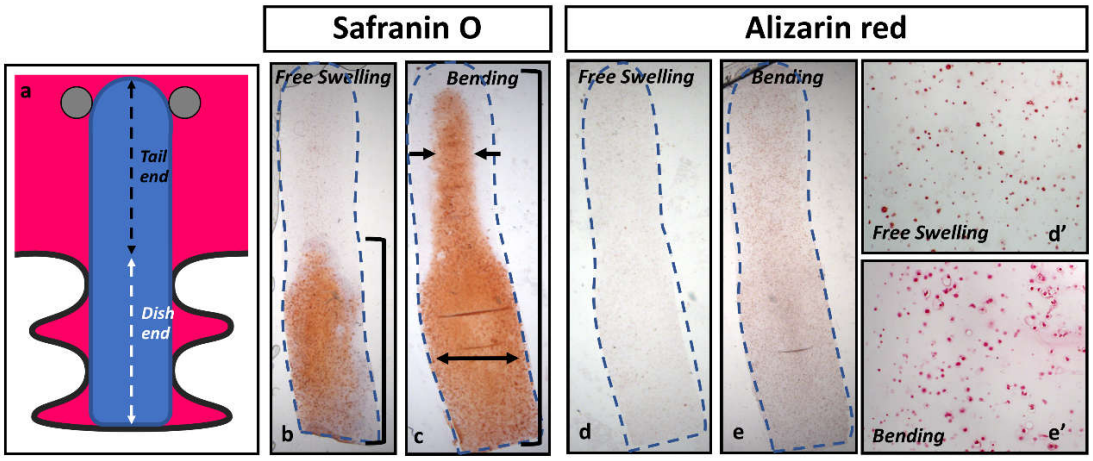

Fig. 6.13. Bending constructs show greater cartilage formation and mineralisation in a spatially localised manner. Constructs were sectioned (10 μm paraffin) and stained to detect mineralisation and cartilage formation. Images in (b)-(e) are oriented as in (a). Safranin O staining revealed localised cartilage formation in the free swelling construct, restricted to the end of the construct that was fixed within the dish (b). Contrastingly, Safranin O staining was detected throughout the bending construct, in both the fixed (dish) and free (tail) ends (c). Alizarin red staining for mineralisation revealed greater overall levels of stain in bending constructs compared to free swelling (compare (e) to (d) and (e') to (d')). (d') and (e') are higher magnification views of (d) and (e). Blue dashed lines indicate construct edges.

To quantify changes in gene expression caused by mechanical stimulation, qRT-PCR was performed on both whole constructs (Fig. 6.14A) and construct halves (Fig. 6.14B and C); gene expression was normalised to GAPDH. Indicators of cartilage formation collagen type 2aI (*Col2aI*) and aggrecan (*Acan*), and of chondrocyte maturation and hypertrophy collagen type 10aI (*Col10aI*) and Indian Hedgehog (*Ihh*) were assessed. Expression levels of all four genes were dramatically upregulated in the bending construct relative to the free swelling construct (Fig. 6.14A), consistent with visual and histological observations of increased mineralisation in the bending group (Fig. 6.12, Fig. 6.13). *Col10aI* and *Ihh* had the highest fold changes (56.8-fold and 24.3-fold increases, respectively), while *Col2aI* and *Acan* (5.1-fold) had more moderate fold changes (12.7-fold and 5.1-fold, respectively), indicating that mechanical stimulation increased both chondrogenic differentiation and hypertrophy in the population of cells as a whole; data represent a comparison of individual constructs, and so it was not possible to calculate significance.

Three constructs from each group were halved at their longitudinal midpoint and gene expression was compared between the tail and dish ends of the same construct (Fig. 6.14B). For both free swelling and bending constructs, the tail ends expressed lower levels of each of the four genes assessed (Fig. 6.14B). However, the magnitude of the difference between halves was lower in bending constructs compared to free swelling constructs for each of the genes assessed, and this was significant for *Ihh* (Fig. 6.14B).

Comparison of bending to free swelling dish ends revealed comparable levels of *Col2aI* in the dish ends of the bending and free swelling groups (Fig. 6.14C, light grey arrow), with significantly higher levels of expression of *Acan*, and *Col10aI* in the dish end of bending constructs compared to free swelling constructs. When comparing bending to free swelling tail ends, there was higher expression of *Acan*, *Col10aI*, and *Ihh* in the bending group (Fig. 6.14C, dark grey arrow). The magnitude of the differences in gene expression between the bending and free swelling halves (Fig. 6.14C, bracket) was significantly greater for tail ends than the dish ends for *Col10aI* and *Ihh*. This indicated that the dish ends of free-swelling and bending constructs are more similar than are the tail ends of the two groups. This corresponds to observed histological staining for Safranin O (Fig. 6.13), where the dish ends of free-swelling and bending constructs appeared more similar than the tail ends. It further showed that mechanical stimuli generated by bending had a greater impact on gene expression of cells in the "tail" end.

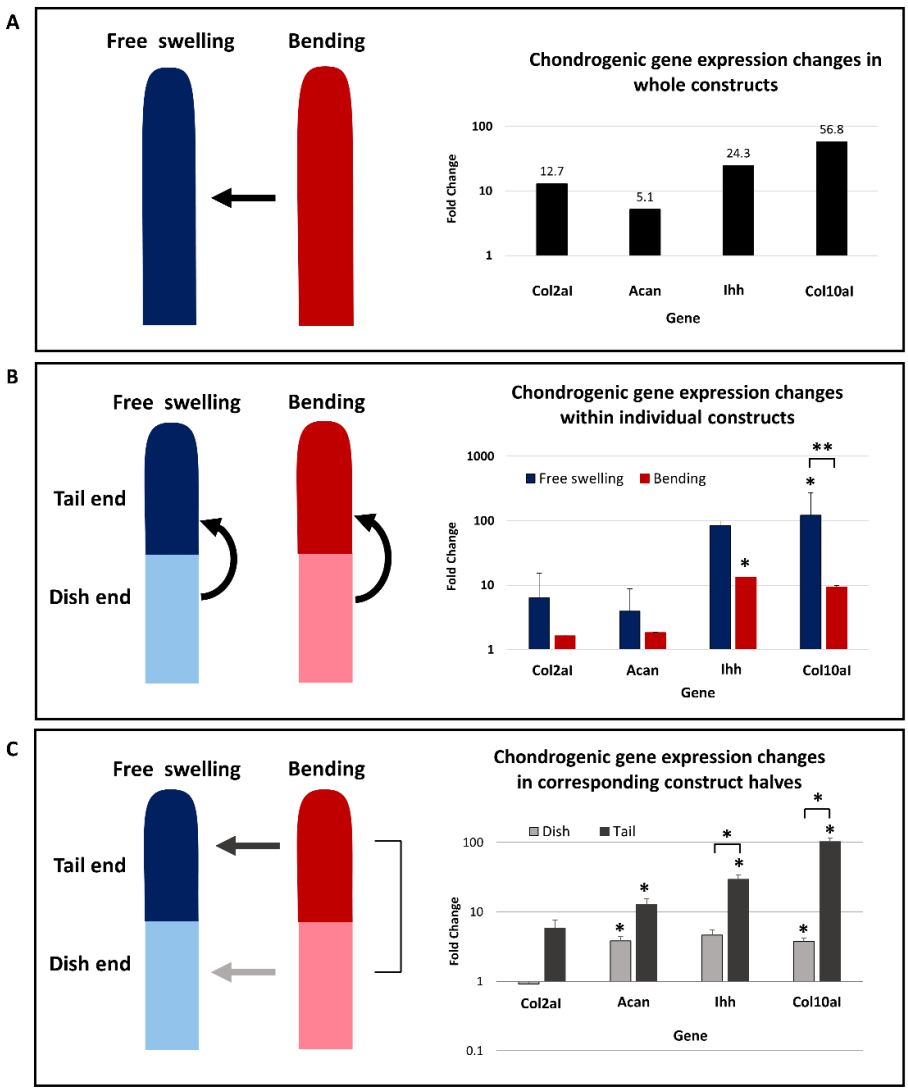

Fig. 6.14. Bending constructs expressed higher levels of chondrogenic genes, and bending constructs were more heterogenous. Graphs of gene expression levels in construct, assessed by qRT-PCR. Expression levels of chondrogenic marker genes was assessed in whole constructs (A) and in half constructs (B and C). Gene expression was assessed for collagen 2aI (*Col2aI*) and collagen 10aI (*Col10aI*), aggrecan (*Acan*), and Indian hedgehog (*Ihh*). Gene expression for each sample was normalised to GAPDH expression, and is shown as fold change of a bending sample relative to a free swelling sample (A), of dish ends relative to tail ends for individual constructs (B), or of bending dish or tail ends relative to free swelling dish or tail ends (C). For (A), n=1; for (B) and (C), n=3 in each of the four groups. In (B), construct halves were compared for each individual construct, and gene expression is presented as the average of each group (n=3). One-way ANOVA was then performed on the bending vs. free swelling values. In (C), each bending construct half was compared to each free swelling corresponding half and these were averaged for n=3 values which were then statistically assessed using one-way ANOVA. Significance: $p \leq 0.05$(*), $p \leq 0.01$(**).

6.4 Discussion

The aim of this part of the work was to establish *in vitro* assays to examine specific aspects of pattern formation during chondrogenesis, which was accomplished by micromass culture and the use of a bending bioreactor in two very different scenarios. These assays allowed for controlled examination and manipulation of patterns of chondrogenesis. First, micromass culture of embryonic limb bud cells was used to explore self-organising patterns of chondrogenesis. These patterns were quantified and manipulated by the addition of signalling molecules in order to investigate the involvement of a proposed BMP-Wnt Turing mechanism in the establishment of chondrogenic condensations (nodules). Second, the use of a bending bioreactor revealed that patterns of cellular differentiation relate to predicted patterns of tension and compression, suggesting that spatial patterns of mechanical force contribute to non-homogenous tissue differentiation. Establishment of these two systems will enable further examination of patterns of *in vitro* differentiation in future.

The role of Turing mechanisms in the formation of self-organising nodule patterns. Patterns of nodule formation in micromass culture are potentially the result of a Turing-like mechanism, similar to the network involving BMP, Wnt, and *Sox9* signals which was proposed to regulate the formation of digits in the developing digital plate (Raspopovic et al., 2014). To quantitatively assess this pattern as it emerges and progresses over time, descriptors of nodule number, size, shape, spacing and proximity were established. This characterisation then allowed for a precise description of how the pattern is changed after treatment with signalling molecules related to the BMP and canonical Wnt pathways. Measurement of nodule number and size across time revealed that nodule number is established early and does not change significantly between later time points, although the size of the nodules continues to grow, at least up to day 6. Similarly, the distance between the centres of nodules does not change significantly between later time points, but the distance between the edges of nodules decreases. Taken together, these data indicate that nodules are established a certain distance apart, and grow closer together by increasing in size. In some cases, nodules merge together after several days in culture, although Alcian Blue-deficient territories are maintained even after 12 days in culture (data not shown) so a certain distance appears to be maintained. Treatment of cultures with BMP-2 increased the number of nodules formed, and tended to decrease the average size, so that the area covered by

nodules remained constant. This generated a pattern of nodules whose centres were spaced closer together, but whose edges were similarly far apart as in control cultures. In this way, despite the stimulation of chondrogenesis by BMP-2, the proximity of nodules (the distance between their edges) was maintained, by tending to reduce the size of nodules. A key feature of Turing mechanisms is their ability to self-regulate or modulate the patterns they generate based on integrated signals (reviewed in Kondo and Miura, 2010). The adaptability of the nodule pattern in the presence of BMP-2, where overall chondrogenesis increases (as indicated by gene expression) but the spatial relationship between nodules is maintained, supports the operation of a Turing reaction-diffusion mechanism. This could be further explored by altering the concentration of BMP-2, and assessing the resulting effects on nodule pattern, using the methodology established here.

Conversely, the nodule patterns in cultures treated with WNT-3A to stimulate canonical Wnt signalling, or Noggin to inhibit BMP signalling, were dramatically decreased. The concentrations of these ligands which were applied to cultures in this study were sufficiently high to observe that they have a nodule inhibitory role. Nodule patterns are characterised as much by the presence of nodules as by the presence of non-nodule cells in between them; chondrogenic cultures of some cell types stain diffusely with Alcian Blue, indicating a more generalised chondrogenic differentiation without the spatially organised pattern. Therefore, generation of nodule patterns requires spatially-regulated chondrogenic differentiation as well as simultaneous inhibition of this process in between nodules. The differentiation of less-dense, non-chondrogenic cells adjacent to nodule cells requires the local regulation and integration of chondrogenic promoters (such as BMP-2) and inhibitors (such as WNT-3A and Noggin). A Turing mechanism would be sufficiently capable of integrating such signals to generate the observed nodule pattern. As noted, the concentrations of WNT-3A and Noggin reported here effectively eliminated nodule formation and prevented the description of pattern alteration following treatment with these signalling molecules. However, titration of the molecules to lower concentrations has been promising, with a visible reduction in nodule number that is still sufficiently robust as to be analysed following the methodology presented here (data not shown). The role of each of these signals in nodule formation can therefore be further quantitatively explored in the assay system established here.

This system could potentially be used in future to assess the effects of changing the mechanical environment on patterns of chondrogenesis. Previous work in this group showed that the addition of dynamic hydrostatic pressure did not obviously affect nodule pattern, but did influence chondrogenic stability and reduced hypertrophy (Saha et al., 2016). In future, this system could be used in conjunction with manipulation of the mechanical environment experienced by cells, by plating cells on different substrates or by physically manipulating substrates (e.g. by stretching). The system could also be used to assess the effects of experimentally altering mechanisms capable of integrating molecular and biophysical cues, such as specific cytoskeletal components, to explore the role of such mechanisms in cellular behaviour and pattern formation.

The quantitative pattern description established in this work can also be integrated with expression data for chondrogenic marker genes to consider the time course of nodule pattern formation. Chondrogenic nodules, as ascertained by Alcian Blue staining, are faintly visible by 2 days of culture. However, expression data for the early marker *Sox9* and the cartilage component *Col2aI* indicate that expression of these genes is elevated as early as 12 hr after plating; this refines the timescale previously reported, that after 1 day in culture these genes are elevated (Saha et al., 2016). Treatment with BMP-2 hastened the onset of chondrogenic gene expression, which may be related to the differences in nodule pattern observed, if timing and pattern are closely linked. Both Noggin and WNT-3A treatment reduced overall gene expression but with very different dynamics indicating that they affect the system in different ways. Interestingly, levels of chondrogenic gene expression in Noggin treated cultures by days 2-6 were close to levels expressed in limb bud cells harvested at the time of plating, while levels in WNT-3A treated cultures were substantially lower than these base levels. This suggests that inhibition of BMP signalling may block chondrogenic gene expression in such a way that cells do not undergo chondrogenesis, but still maintain progenitor cell-like levels of gene expression. Contrarily, Wnt signalling appears to negatively regulate chondrogenic gene expression such that the chondrogenic potential of these cells could be much less than that of the mesenchymal progenitor cells. One way to test this would be the addition of BMP-2 following treatment with either Noggin or WNT-3A, to observe the capacity of cells to undergo chondrogenic differentiation or form nodules following inhibition of these processes. Conversely, treatment with Noggin or

WNT-3A after BMP-2 or no treatment could be used to explore stabilisation of cartilage in culture. After approx. 5 days in culture, nodules tend towards hypertrophy and mineralisation as ascertained by Alizarin Red staining (data not shown and (Saha et al., 2016)). Chondrogenic differentiation followed by treatment with Noggin or Wnt-3A to suppress progression towards hypertrophy could be explored with the methodology established here. This would correspond to *in vivo* suppression of hypertrophy which occurs within the articular cartilage of the joints, where the canonical Wnt pathway is active. A major impediment to engineering stable cartilage *in vitro* is the tendency of cartilage towards hypertrophy, and the establishment of combinations of signalling molecules to stabilise cartilage *in vitro* would be beneficial to tissue engineering efforts.

A future direction of this work will be to examine a balance of BMP and Wnt signalling *in vitro* by combining these molecules – either temporally or spatially—in micromass culture. As presented in Chapter 3, spatial restriction of these signalling activities is required for the adjacent differentiation of transient and permanent cartilage. Localisation of these signalling molecules, for example in beads placed in different positions relative to the cultures, could be used to further manipulate nodule pattern, thereby verifying and refining our understanding of potential Turing mechanisms in this system. This could also improve regimes for simultaneous engineering of bone and cartilage tissues, which have the challenge of integrating multiple differentiation regimes in a coordinated manner (reviewed in Dormer et al., 2010). It could inform the combinations and placement of combined signals to be tested in tissue constructs, examining effects on transient and stable cartilage differentiation in the same construct.

The relationship between patterns of mechanical stimulation and cellular differentiation. The second assay presented here was used to address the effect of stresses and strains generated by movement on the differentiation and progression of adult derived MSCs with the use of a bending bioreactor for *in vitro* mechanical stimulation of differentiating cells. This bioreactor was custom-designed to partially mimic the effect of limb bending movements by subjecting 3-D constructs densely seeded with mesenchymal stem cells to gradients of tension and compression for a short period each day, separated by lengthy recovery periods. The extensive mineralisation exhibited by bending constructs after four weeks of culture, which was observable both superficially and in histological sections, demonstrated the pro-chondrogenic and pro-

osteogenic role of dynamic mechanical force on these stem cells. Visible mineralisation occurred in all constructs at the longitudinal edges, and especially at the longitudinal mid-point, which corresponded to FE predictions of maximal tensile and compressive forces, and suggests a relationship between the magnitude of dynamic mechanical stimulation and the extent of apparent mineralisation. It also suggests that patterns of strains and stress could spatially control chondrogenesis and mineralisation within populations of cells.

An interesting trend which emerged was the differential pattern of Safranin O staining within constructs, and between bending and free-swelling constructs. The Safranin O pattern was more uniform across the length of the bending constructs, suggesting that chondrogenesis in bending constructs was more homogenous than in static constructs. Additionally, at the end of the construct which was subject to mechanical stimulation, the Safranin O staining pattern indicated that chondrogenesis was limited to cells at the core. These patterns were supported by qRT-PCR, which showed increased chondrogenic gene expression in bending constructs, and differences in gene expression between construct halves. Notably, the halves which were fixed into the dishes in both the free-swelling and bending groups had greater levels of chondrogenic gene expression than the ends which extended out from the centre of the dish, but this may be explained by other factors, explored below. Taken together, histological and gene expression data indicate that dynamic mechanical stimulation increases chondrogenesis and mineralisation.

The pattern of chondrogenesis as indicated by Safranin O was not homogenous across the length of either bending or free-swelling constructs, and this could be partially explained by factors such as oxygenation or fluid exchange. The ends of the constructs which were fixed into the dish were enclosed on three sides. This would greatly reduce their available surface area for oxygen or nutrient exchange in the medium. Hypoxia, or reduced oxygen in the environment, has been previously demonstrated to increase chondrogenesis (Shang et al., 2014), and this could be occurring here. Similarly, if cells within the construct which are undergoing chondrogenesis are releasing soluble molecules, these molecular signals could be effectively trapped and maintained at high levels in the dish end of the construct. Contrastingly, molecular signals could diffuse from the tail end of the constructs into the surrounding medium, and be diluted, thereby reducing local chondrogenesis. It was also noted that levels of chondrogenesis and

mineralisation were less homogenous along the longitudinal axis of the free swelling constructs compared to bending constructs. Physically bending the construct could have increased nutrient exchange between construct halves (Panadero et al., 2016), making a more homogenous environment for cellular differentiation.

A future direction for the work with this bioreactor will be to compare the chondrogenic potential of embryonic cells to that of adult-derived cells and to identify potential differences in their response to a spatial pattern of stresses and strains generated by movement. This will allow for refinement of the relationship between patterns of mechanical stimuli and cellular differentiation. Embryonic and adult-derived cells have differing potentials with respect to overall levels of chondrogenesis, and also to chondrogenic pattern formation. An interesting question to consider would be if dynamic bending could overcome the limitations, or alter the potential of adult-derived cells to form chondrogenic patterns. As presented in Chapter 3, and as noted above, the capability to simultaneously regulate the differentiation of distinct tissues is dependent on restricted BMP and Wnt signalling activity. This capability may also rely on patterns of physical forces, with maxima colocalising to the future sites of particular tissue types. To explore this scenario, the bioreactor could potentially be coupled with spatially localised signalling molecules to regulate cellular differentiation patterns. The use of engineered scaffolds which couple biomaterials such as alginate and hydroxyapatite with signalling molecules is a current effort in bioengineering, with promise shown by using scaffolds coupled with BMP-2 to repair bone fractures in animal models (reviewed in Mitchell et al., 2016). Such an approach could be taken to create a gradient of signalling molecules in a 3-D scaffold, in conjunction with mechanical manipulation. In addition to BMP and Wnt signalling pathways, the role of the mechanosensitive Hippo-YAP pathway could also be explored in a 3-D mechanical context. This pathway has a demonstrated role in the differentiation of mesenchymal stem cells *in vitro*, and this relationship could be tested and explored in the bioreactor assay.

The work presented in this chapter sought to establish and evaluate methods for assaying patterns of chondrogenesis *in vitro*. While more extensive analysis is necessary, in particular for the bending bioreactor, these assays are useful tools for studying how patterns of cellular differentiation can be manipulated by altering signalling molecules and mechanical stimulation.

Chapter 7

Discussion

7.1 Significance of key findings

Findings in both mouse and chick models of immobilisation, by this group and others, have demonstrated that differentiation of skeletal tissues is altered under reduced mechanical stimulation, and that this corresponds to changes in the expression of genetic markers of chondrogenesis and ossification (Nowlan et al., 2008b, Nowlan et al., 2010a, Roddy et al., 2011b, reviewed in Rolfe et al., 2013). Transcriptomic analysis has further revealed that expression of numerous genes involved in diverse cellular processes, including intracellular signalling, is affected by reduced mechanical stimulation, indicating widespread mechanoregulation of gene expression (Rolfe et al., 2014). The work presented here investigated molecular mechanisms underlying the role of embryo-generated mechanical stimulation in limb skeletal development, meeting the specific aims outlined in Section 1.7.

7.1.1 Localised, complimentary Wnt and BMP signalling activity and mechanosensitive gene expression at the developing joint

The Wnt and BMP signalling pathways are crucial to rudiment and joint formation and patterning (reviewed in Section 1.3). However, the activity of these major signalling pathways during specific processes of skeletal development, such as the formation of articular cartilage at the joint, is currently not well-defined; additionally, previous work by this group revealed that expression of pathways components was altered under reduced mechanical stimulation (Rolfe et al., 2014). This warranted closer examination of potential involvement of these pathways in the regulation of tissue differentiation under normal mechanical stimulation. To explore such a role for Wnt, the expression patterns of key components of the Wnt signalling pathway were examined, which

revealed novel expression patterns of several ligands and receptors where the canonical Wnt pathway is active. In the wild-type embryo this expanded current knowledge of where components are localised and where the pathway is active at a time when mechanical stimuli impact the system. In the immobilised embryo, this analysis showed where the system is disturbed, with the loss of canonical signalling at the joint line. Examination of the expression of candidate articular cartilage-specific genes demonstrated several with joint-specific expression, altered under reduced mechanical stimulation, consistent in both mouse and chick models of immobilisation. Activity of BMP, in addition to Wnt, was examined at the developing joint, and it was established that these pathways have spatially restricted, complimentary activities which are disturbed under reduced mechanical stimulation.

This study highlighted expression of the ligand *Wnt4*, the antagonist *Sfrp*2, and the receptors Fzd3 and Fzd6, which were localised to the peripheral joint territory. These genes (and others) were found to be specifically expressed in the cells flanking the elbow and shoulder joints (Fig. 3.4 and Fig. 3.5). Cells comprising the mature joint originate from multiple populations, including from outside the mesenchymal condensations that preFig. the skeletal rudiments (Hyde et al., 2008, Koyama et al., 2008). Indeed, this territory adjacent to the developing joint has previously been suggested to be a source of progenitor cells during joint differentiation, contributing to the articular cartilages and other joint structures, and even capable of joint regeneration in the case of excision (Ozpolat et al., 2012, Li et al., 2013, Shwartz et al., 2016). The finding in this study, that Wnt pathway component expression is localised to this region and increases upon immobilisation, together with an enlargement of the territory of cells, is therefore intriguing as it suggests that these cells are particularly affected under reduced mechanical stimulation and that their characteristics may well be altered. In particular, increased expression of *Wnt4* and Sfpr2 in the muscle-less mutant ($Pax3^{Spd/Spd}$), as well as histological observations of a larger territory of peripheral cells suggests that defects in joint formation under reduced mechanical stimulation could be due to decreased migration of progenitor cells into the developing joint territory. This study therefore highlighted this region as an area of interest for continued study.

As noted earlier, ligands of the BMP and Wnt pathways have been implicated in skeletal development, but their activities had not been clearly defined at the joint line during the time of greatest sensitivity to mechanical stimulation. To address this, a

number of approaches were taken: immunolocalisation of pSMAD1/5/8 to reveal BMP activity, and use of a reporter mouse (GFP under the control of canonical Wnt responsive regulatory elements (Ferrer-Vaquer et al., 2010)) and immunolocalisation of β-catenin to reveal Wnt activity. This revealed that BMP activity is spatially restricted to the transient cartilage of the rudiments, at a distance from the joint line, while Wnt activity is localised to the developing articular cartilage and joint region at this stage, with a few scattered cells in the sub-articular region. Under immobilisation, these activities were altered, with detectable pSMAD1/5/8 spread up to and across the joint territory, while β-catenin protein was lost at the presumptive articular cartilage. As BMP activity is typical of transient cartilage and Wnt is characteristic of joint differentiation, this further informs the observed changes in joint development which occur under reduced mechanical stimulation, namely, the reduction or absence of articular chondrogenous zones and the spread of transient cartilage markers across the joint, resulting in partial joint fusion (Roddy et al., 2011b). This work has led to a proposed model which integrates BMP and Wnt signalling with mechanical stimuli in joint territory patterning. The model fits with available data and will be an important basis for further investigation of the dynamics between major regulatory components: Wnt, BMP, and mechanical stimuli.

The current work went a step further to functionally test one aspect of this model, that canonical Wnt activity at the joint line is required for the normal patterning of joint territories. *Ex ovo* electroporation of a plasmid encoding the Wnt antagonist Sfrp3 reduced joint territories in a manner reminiscent of joint formation under immobilisation; likewise, electroporation of a constitutively active form of β-catenin to upregulate Wnt activity corresponded to an enlargement of the developing joints. While these data are limited by the difficulty of targeting misexpression precisely using this approach, taken together, they indicate that spatially-localised activity of Wnt and BMP signalling pathways is co-ordinated and essential to simultaneous differentiation of permanent and transient cartilages at the joint. Furthermore, they confirm that mechanical stimulation is required for the correct co-ordination of spatial territories of BMP and Wnt signalling activities at the joint which, when lost, leads to misspecification of tissue differentiation.

Complimentary to the examination of BMP and Wnt pathway, this work defined a set of 19 articular cartilage-specific genes which are affected under immobilisation by

cross-referencing previously-generated transcriptomic data sets (Rolfe et al., 2014, Singh et al., 2016). The mechanosensitive characterisation of these genes which is presented in this work highlights the lack of knowledge concerning the composition of articular cartilage, which is structurally complex. Identification of mechanosensitive genes in this tissue broadens current knowledge of articular cartilage differentiation by highlighting genes which are essential to its patterning and offering clues as to how mechanical stimuli could be involved in regulation of articular cartilage differentiation.

7.1.2 The Hippo-YAP pathway as a mechanotransductor during skeletal development

While changes in gene expression under altered mechanical stimulation suggest widespread mechanoregulation of gene expression, the mechanotransduction of biophysical cues to gene regulation has remained unidentified in the context of skeletal development. This work therefore examined a potential role for the mechanotransductive Hippo-YAP pathway in skeletal development. Analysis of RNA-Seq transcriptomic data of wildtype humeri and associated joints at TS23 revealed that all major components of the Hippo-YAP pathway are expressed at this stage of skeletal development, at relatively high levels, indicated that Hippo-YAP signalling is likely involved in this stage of skeletogenesis Comparison of transcriptomic data of muscle-less mutant humeri and associated joints showed that overall most components were similarly expressed, with a few significantly differentially regulated genes, including the potential receptor *Fat4* and several target genes. Again, this indicated that the Hippo-YAP pathway is well-positioned to play a role in skeletal development at this stage and potentially placing the pathway upstream rather than downstream of mechanical input.

Immunolocalisation of the Hippo pathway effector YAP revealed that while YAP was localised to the nucleus throughout the developing rudiments, protein levels are highest in the hypertrophic zone and in regions of emerging morphology such as the olecranon process and the coracoid process of the scapula. Comparison of YAP immunolocalisation in the muscle-less mutant forelimb showed that YAP protein was again localised to the nucleus, but was overall detected at higher levels throughout the developing rudiments. Notably, YAP protein was expressed at high levels across the presumptive joint territory, unlike in the wildtype where there were low protein levels

at the joint. This change in detectable YAP is particularly intriguing, as joint development is severely affected by reduced mechanical stimulation, and could potentially be affected by differential gene expression mediated by YAP. These findings support Hippo-YAP pathway activity in the developing skeleton, and suggest that it plays a role in the processes of cartilage maturation and rudiment morphogenesis. The wildtype data agree with a previously published description of high levels of YAP in the hypertrophic zone of E16.5 hindlimb phalanges (Karystinou et al., 2015), but disagree with another description of YAP *in vivo*, which showed the highest levels of detectable YAP in the immature chondrocytes of E14.5 tibia, with comparatively little YAP detected in hypertrophic chondrocytes (Deng et al., 2016). Nevertheless, Deng et al. (2016) do show nuclear YAP in all chondrocyte zones, and this might be taken as a more reliable indicator of YAP activity than overall staining intensity. In this respect, the finding presented here of nuclear YAP throughout the rudiments, agrees with their data. Significantly, this work revealed that there are regions of elevated YAP protein accumulation in the emerging condylar processes, which are undergoing expansion and morphogenesis at these stages. This indicates that spatial regulation of YAP activity is lost under immobilisation, concomitant with a key phenotypic outcome: altered morphology and dysfunctional shape emergence at joints (Roddy et al., 2009, Roddy et al., 2011b).

Nuclear localisation of YAP in cells of both wildtype and mutant rudiments indicated YAP transcriptional activity. To assess this, expression of YAP target genes was examined by *in situ* hybridisation, revealing strong, localised expression of *Ctgf* and *Cyr61* in the joint region and the perichondrium, which was increased in the muscle-less mutant. These changes in target gene expression correspond to observed changes in protein levels of YAP – adjacent to the joint and in regions of morphological expansion – suggesting that they are targets of YAP transcriptional regulation during skeletal development. While *Ctgf* was previously implicated in normal skeletal development (Arnott et al., 2011, Huang et al., 2010b), its role is not clear, and its overexpression could be detrimental to normal skeletal tissue function (Blaney Davidson et al., 2006, Itoh et al., 2013). The role of *Cyr61* during skeletogenesis, and the significance of its increased expression in the muscle-less mutant is also not clear, although it was previously implicated in both chondrogenesis and hypertrophy (Wong et al., 1997, Chijiiwa et al., 2015). However, both genes have been demonstrated as

mechanosensitive, albeit primarily *in vitro* (Chaqour and Goppelt-Struebe, 2006), and so expression changes in the muscle-less mutant which were observed here could indicate a mechanosensitive role in normal skeletogenesis, further supporting the Hippo-YAP pathway as a key player in the mechanoregulation of skeletal development.

To further define the role of YAP activity during cellular differentiation, high-density micromass was used as an *in vitro* chondrogenesis assay. Application of the small molecule verteporfin, which inhibits YAP transcriptional activity (Liu-Chittenden et al., 2012), decreased chondrogenic nodule formation in micromass culture and increased nodule size; it also significantly decreased the expression of markers of chondrogenesis, but not hypertrophy. This indicates that YAP promotes early chondrogenesis, but perhaps not later chondrogenic maturation, which both agrees with and differs slightly from previously published reports concerning the role of YAP during *in vitro* cartilage formation. Deng et al. (2016) demonstrated that YAP is involved in progenitor cell proliferation and early chondrogenesis. They also show that YAP expression decreases over time in high density cultures, and implicate YAP as a negative regulator of chondrocyte maturation. Contrastingly, Karystinou et al. (2015) demonstrated that YAP inhibits early chondrogenesis and its downregulation is required for the initial stages of chondrogenic differentiation. These differences could be partially explained by the use of different cell types: Karystinou et al. (2015) used C3H10T1/2 cells, which are embryonic in origin but behave more similarly to adult mesenchymal stem cells, while Deng et al. (2016) examined E12.5 limb bud-derived cells, which have been determined by this group to have reduced chondrogenic potential compared to earlier embryonically-derived cells (data unpublished). Indeed, the data presented in this study, which are based on E11.5 limb-bud derived cells, are more in agreement with the findings of Deng et al. (2016), further supporting a role for YAP during early chondrogenesis *in vitro*.

Phosphorylation state, and therefore transcriptional activity, of YAP is known to be regulated by multiple mechanisms, including the canonical Hippo pathway kinase cascade and the cytoskeleton (reviewed in Yu et al., 2015). To examine upstream control of YAP activity, expression of *Fat4*, the mammalian orthologue of the *Drosophila* Hippo pathway receptor, and a potential regulator of mammalian Hippo signalling (Rock et al., 2005), was assessed. This revealed several interesting expression patterns in the limb bud across key stages of limb development. One

notable region of expression was the anterior aspect of limb buds at E10.5-11.5, where the limb bud joins the body trunk. This location does not correspond to a defined anatomical structure, and suggests a previously un-reported centre for cellular signalling. Interestingly, it corresponds to a region of Wnt pathway activity identified in parallel work in this research group (unpublished). Expression of *Fat4* was also detected in mesenchyme adjacent to the forming rudiments at various stages of limb development, and in the perichondrium of both wildtype and muscle-less mutant forelimb sections at TS23. However, at no stage of limb development was there obvious expression of *Fat4* at the core of the developing rudiments. Further, within the skeletal rudiments at TS23, there was no detectable expression of *Fat4* where the highest levels of YAP protein were detected – namely, in the hypertrophic zone and in regions of morphological expansion. Therefore, while *Fat4* may be involved in intracellular signalling at the periphery of the developing skeletal elements, these data strongly suggest that YAP is regulated by other mechanisms at the core of the skeletal rudiments. *Fat4* signalling was previously shown to regulate vertebral skeletal development, but this was determined to be independent of YAP or TAZ activity (Kuta et al., 2016). Therefore, in mammals *Fat4* may have a discrete mechanism for regulating cellular differentiation independent of the Hippo pathway, which should be considered when examining *Fat4* expression in the developing limb and in other tissues.

7.1.3 Characteristic cilium properties in the developing rudiments: the potential of the primary cilium as a mechanotransductor

Another mechanotransductive mechanism, the primary cilium, was characterised, with occurrence, length, position, and orientation quantified. The primary cilium can sense physical stimuli and is a site of intracellular signalling (reviewed in Fry et al., 2014, Spasic and Jacobs, 2017b), and is therefore a potential bridge between mechanical stimulation and genetic regulation. In the developing skeleton, cilia are known to be important, as their ablation results in severe skeletal defects such as bone shortening and polydactyly (reviewed in Haycraft and Serra, 2008), but they have not been fully characterised in the developing skeletal rudiments. In this work, the characterisation of cilia occurrence, length, position, and orientation, highlighted the capacity of cilia to direct skeletal development, and identified that different regions of the developing

skeleton display characteristic cilium traits. Cilia were present on a large proportion of chondrocytes in different regions throughout the skeletal rudiments, but varied considerably between regions, indicating that they could easily contribute to the differentiation of skeletal tissues. While a range of cilium lengths were measured, the average in each territory was approximately 1.5 μm, which is consistent with previous reports of chondrocyte cilia (McGlashan et al., 2010, Chang et al., 2012, Dummer et al., 2016). A notable trend revealed by this study was that different regions of the rudiments have characteristic ciliary positions and orientations. This was particularly evident at the joint line and the adjacent resting territories of both the shoulder and elbow joint, where cilia were disproportionately located on the side of the cell opposite the joint line (the distal side of the cell for the shoulder, and the proximal side of the cell for the elbow) and pointing away from the joint line (with the exception of the elbow resting zone, where cilia were observed to be oriented either towards or away from the joint). Although position has not been previously examined the observations of orientation presented here are consistent with previous reports on mature articular chondrocytes which noted cilia frequently oriented towards or away from the joint line (McGlashan et al., 2007, Chang et al., 2012, Ruhlen and Marberry, 2014). In tendon, another load-bearing tissue, ciliary orientation was observed to be tightly correlated with the arrangement of the extracellular matrix, with cilia aligned to the primary loading direction of the tendon (Donnelly et al., 2010); ECM structure has also been suggested as possible reason for the observed orientation of chondrocyte cilia (McGlashan et al., 2008).

Characterisation of cilia within muscle-less mutant rudiments revealed that while there were no significant changes in cilia occurrence under reduced mechanical stimulation, there were intriguing differences in length. Overall, cilia were shortened in all regions analysed. Several studies have demonstrated that cilia with a longer axoneme are more mechanosensitive, while shorter cilia have an impaired signalling capacity (Ehnert et al., 2017, Spasic and Jacobs, 2017a), suggesting that the shorter cilia observed in the mutant rudiments could significantly alter the capability of chondrocytes in the developing rudiments to respond appropriately to mechanical signals; it also suggests that length, and possibly capacity to respond is itself mechanosensitive. Interestingly, the tendencies of cilium position which were observed in the wildtype rudiments were exaggerated in the mutant, and orientation of cilia at the elbow resting zone was also

significantly altered, with a greater proportion of cilia oriented towards the joint. If cilia in wildtype rudiments are optimally positioned to interpret mechanical stimuli at the joint, then cilia in mutant rudiments would also seem to be ideally positioned, and would therefore perhaps be capable of transmitting a lack of mechanical stimulation, such as occurs under immobilisation, to the chondrocytes of the rudiments.

7.1.4 Contributory regulatory signals to pattern formation during *in vitro* chondrogenesis

This work established methods for *in vitro* chondrogenesis to assess the input of molecular and mechanical signals into cellular differentiation. High density micromass culture is a well-established technique for assessing the chondrogenic capacity of cells, but patterns of chondrogenic condensation (nodule) formation within such cultures have previously received little attention. Therefore, this work presents a quantitative assessment of nodule pattern formation over time, revealing that nodule formation is established early in micromass culture, with genetic markers indicative of chondrogenesis increasing at early time points. It was also shown that self-generated patterns of nodules emerge with set spacing but with proximity which changed over time. Nodules also change shape over time, becoming less circular, but smoother. The methodology presented here represents a simple, quantitative method for description of nodule patterns. While several studies have previously measured shape and size of individual nodules (Duke et al., 1998, Butterfield et al., 2017), the spatial relationships between nodules have not been examined. This work therefore represents a novel method for quantifying spatial patterns *in vitro*. Upon application of signalling molecules (BMP-2, Noggin, and WNT-3A), nodule formation was significantly altered, as was the timing and magnitude of marker gene expression. However, in the case of BMP-2 treatment, while nodule formation was significantly impacted, the spacing between nodules was not, indicating a robust self-regulatory mechanism in this system.

The establishment of nodule patterns has been proposed to be regulated by a Turing mechanism involving BMP, Wnt, and So9 (Raspopovic et al., 2014), so the involvement of BMP and Wnt in the establishment of this pattern was of particular interest. The addition of BMP-2 suggests that increased BMP signals alters the Turing pattern by causing more nodule establishment events to occur, but the mechanism adjusts appropriately to maintain the proximity of nodule edges. This emphasises the

robust nature of Turing mechanisms, and their capacity to regulate the development of discrete, repetitive units from an initially uniform population. Both WNT-3A and Noggin severely impacted nodule formation, with few to no nodules formed after six days of culture. However, differences in the effects of Noggin and Wnt3a indicate the very different ways in which Wnt and BMP signalling impact chondrogenic potential, suggesting that increasing Wnt signalling not only blocks BMP induced chondrogenesis but changes the potential of the cells to respond.

The second *in vitro* chondrogenesis system, a bending bioreactor, was used to examine the application of gradients of mechanical stimulation on cellular differentiation. This custom-designed apparatus applied dynamic tension and compression to 3-D agarose scaffolds seeded with adult-derived mesenchymal stem cells, resulting in observable increased mineralisation in bending constructs compared to free-swelling controls. Additionally, spatial patterns of chondrogenesis were observed, with more homogenous chondrogenesis occurring throughout the bending constructs compared to free-swelling. An externally visible increase in mineralisation in the bending group corresponded with histological examination of sections, which showed increases in Safranin O and Alizarin red staining in bending constructs compared to free-swelling. Further, there was increased chondrogenesis and hypertrophy in the dish end of the constructs, compared to the free (tail) end, indicating that chondrogenesis and hypertrophy are promoted by dynamic mechanical stimulation, which agrees with previous *in vitro* findings. However, this study is novel in that it differentially applies mechanical force to constructs, and specifically examines spatial patterns of chondrogenesis and hypertrophy. The heterogeneity of cellular differentiation observed here is promising for applications where complex, non-homogenous tissues are desired, such as osteochondral implants for joint replacement.

7.2 Future directions and implications of this work

7.2.1 Integration of signalling pathways

This work addressed the activity of discrete signalling pathways – primarily Wnt, BMP, Hippo-YAP, and Hedgehog – while raising questions about the relationship between these pathways and potential crosstalk between pathway activities. The work presented in Chapter 3 described the complimentary spatial localisation of Wnt and BMP activity

at the joint, and the disturbance of this balance under immobilisation. There is considerable crosstalk between Hippo-YAP signalling and Wnt or BMP signalling. For example, YAP/TAZ has been shown to be integrated into the β-catenin construction complex, while non-canonical Wnt signalling can regulate YAP/TAZ activity (Azzolin et al., 2014, Park et al., 2015). Similarly, several YAP target genes, *Ctgf* and *Cyr61*, can also be regulated by Wnt signalling, suggesting that activity of the Hippo pathway is not solely reliant on YAP/TAZ activity. Additionally, both TGF-β and BMP signalling are influenced by and can influence YAP/TAZ activity (Grannas et al., 2015, Karystinou et al., 2015). This introduces intriguing possibilities for YAP regulation of Wnt and BMP signalling during skeletal development, which could help to explain changes in these pathways observed under reduced mechanical stimulation.

Wnt and Hh signalling are integrated at the primary cilium (Liu et al., 2014), making this structure particularly important to the regulation of these signalling pathways. Primary cilia are well-characterised as regulators of Hh activity, and promote Hh signalling and downstream transcriptional activity; the role of primary cilia in Wnt signalling is less well-characterised, although it is thought that cilia could act as a switch between canonical and non-canonical pathways (Goetz and Anderson, 2010b). Here, cilia on proliferative chondrocytes were shown to be abundant, with strong trends in position and orientation. This reinforces a role for cilia in mediating Hedgehog signalling, as ablation of cilia in skeletal tissues is known to impact long bones and to impede Indian hedgehog (*Ihh*) expression (Haycraft et al., 2007a). Altered Wnt signalling activity after ciliary ablation has not been examined, however, and this could be another means by which the long bones are affected in the absence of cilia. Cilia have been implicated in non-canonical Wnt/PCP signalling, which is responsible for convergent extension of proliferating chondrocytes as the rudiments and developed bones grow in length (Goetz and Anderson, 2010b). Previously, convergent extension was shown to be impeded under immobilisation, which could be an effect of altered non-canonical Wnt signalling, mediated by cilia which sense and transmit reduced mechanical stimuli.

7.2.2 Localised alteration of signalling activity

Techniques such as electroporation allow for expression of protein constructs in a localised manner in a tissue of interest (Momose et al., 1999). In this work, Wnt

signalling was locally activated or inhibited in developing chick forelimbs. The stage of interest, approx. HH25-26, when ossification of the long bones and cavitation of the elbow and shoulder commence, occurs around E5.5, when the chick is rapidly developing and is quite heavy, causing the embryo to sink into the underlying yolk, and impeding access. This issue was addressed by utilising the *ex ovo* electroporation technique, where chick embryos are cultivated in glasses (Cloney and Franz-Odendaal, 2015). This allowed for much greater ease of access to the embryo, alleviating the issue of angling the microcapillary for injection into the forelimb bud. However, precision was still difficult to achieve, with variable amounts of plasmid delivered into the forelimb bud, and variation in the location of injection. In practice, injection into the developing elbow region was difficult to achieve, and the injection site ranged from the developing shoulder joint to the digits, compromising the number of informative replicates achieved in this study. Accordingly, this made skeletal abnormalities resulting from the microinjection difficult to interpret and compare across groups, as each specimen was unique. Despite these limitations, in specimens where injection was in or around the developing joints, the size of the resulting joints corresponded to the model proposing here, where restricted Wnt signalling at the joint is crucial to patterning. To more precisely localise ectopic Wnt activation or inhibition, the use of a doxycycline-activated plasmid (Das et al., 2016), combined with early microinjection into the lateral plate mesoderm, as was used in a collaborative study (Singh et al., under revision), could be used in future. Use of a doxycycline-activated plasmid allows for early introduction of the plasmid in the whole limb field and delayed activation of the plasmid at a desired time-point, such as when the presumptive joints are forming, thereby allowing for wider introduction of the transgene and timed control of ectopic expression in the limb bud. Integration of a tissue-specific promotor or enhancer, such as *Gdf5* for the joint, could allow for further specification of plasmid expression in tissues of interest. Other gene technologies, such as the CRISPR-Cas9 system (Dow et al., 2015), could also allow for more readily generated and more sophisticated approaches to specific alteration of signalling pathways, and should be explored in future. More efficient approaches will not only reduce the number of specimens required, but would potentially allow for concomitant ectopic activation and inhibition of multiple signalling pathways (such as activation of BMP signalling and inhibition of Wnt signalling at the joint), allowing for precise testing of the complimentary signalling

model proposed in this work. In addition, a less invasive approach could allow combined immobilisation and altered pathway activity to explore the interplay between influences.

7.2.3 The cytoskeleton and other mechanisms of mechanotransduction

This work examined two mechanisms for mechanotransduction of physical stimuli to intracellular signalling, the Hippo-YAP pathway and the primary cilia. The results presented here point to a role for both YAP activity and cilia-mediated signalling in the maturation of rudiments and the development of articular cartilage. Further exploration of the mechanotransductive capacities of these mechanisms is required to fully understand how physical stimuli regulate gene expression during skeletogenesis and the cytoskeleton provides a potential point of interaction of these influences. In particular, transcriptomic analysis of mouse humeri and associated joints at TS23 had previously revealed that in the muscle-less mutant, expression of genes involved in cytoskeletal architecture was significantly affected under reduced mechanical stimulation (Rolfe et al., 2014). This suggests that disturbances in cytoskeletal dynamics could alter cell signalling in mutant chondrocytes, as the cytoskeleton is responsible for giving cells shape and rigidity, as well as for mediating cellular interactions with the extracellular matrix and modulating intracellular vesicular trafficking (Woods et al., 2007, Docheva et al., 2014, Gao et al., 2014). Additionally, mechanical signals interpreted by the cytoskeleton can control differentiation of MSCs (reviewed in Steward and Kelly, 2015, Pongkitwitoon et al., 2016), suggesting a potential role for the cytoskeleton in skeletal development. In this work, *Fat4*, the putative receptor of the Hippo pathway, was shown to be an unlikely candidate for upstream control of YAP activity, implying that other cellular mechanisms must be actively controlling YAP. Indeed, the cytoskeleton has previously been shown to regulate YAP activity *in vitro* (Dupont et al., 2011), and this could be the mechanism of YAP control during skeletal development. Cytoskeletal dynamics are also critical to the primary cilium, whose internal skeleton is primarily composed of tubulin (Pedersen et al., 2012). In this study, one cytoskeletal-linked gene, the tubulin-polymerisation protein Tppp3, was demonstrated to have decreased expression at the joint line of the muscle-less mutant, which could be indicative of significant changes in the expression patterns of other genes related to cytoskeletal architecture, as is supported by previously-reported

transcriptomic data. Characterisation of normal cytoskeletal gene expression, as well as normal cytoskeletal architecture during skeletal development could be a first step to understanding precisely how the cytoskeleton is altered under reduced mechanical stimulation. Multiple approaches exist to alter the cytoskeleton (e.g. pharmacological interference); however, using such approaches during *in vivo* skeletal development is challenging and an *in vitro* approach, such as high-density micromass, or 3-D construct culture, may be more appropriate. This would allow for precise examination of how the cytoskeleton contributes to chondrogenic differentiation, and exemplifies the value of the *in vitro* work reported in Chapter 6. Both micromass culture and the bending bioreactor would be suitable here, to explore how the cytoskeleton is involved in patterning and in the transmission of mechanical stimuli. This would also allow for investigation of how the cytoskeleton may interface with both the Hippo-YAP pathway and the primary cilium to regulate cellular differentiation, by directly altering these components in *in vitro* systems.

7.2.4 Application of mechanical and molecular stimuli *in vitro*

Elucidation of the process of skeletal development has evident biomedical implications, as knowledge of the molecular and mechanical regulators of tissue differentiation can advance the development of novel therapeutics for age- or injury-related degeneration of skeletal tissues. For example, osteoarthritis and osteoporosis can lead to debilitating injuries, and affect millions of people worldwide (Ballane et al., 2017, Nelson, 2017). Effective cell-based therapeutic treatments for such conditions, where damaged tissues could be replaced, would therefore be highly societally and economically beneficial.

In particular, the work in this thesis which confirms mechanical stimulation as an integral component of articular cartilage differentiation has relevance to the generation of articular cartilage from stem cells for joint replacement purposes. Current efforts to generate stable cartilage *in vitro* are hampered by the tendency of adult-derived stem cells to hypertrophy, making them unsuitable for replacement of cartilage which has been degraded by osteo- or rheumatoid arthritis, or otherwise injured (Tang et al., 2015). This has necessitated prosthetic replacement of the joint using metal and polymer prostheses, which can degrade over time, producing an inflammatory response in patients and requiring replacement (Man et al., 2017). However, efforts to utilise biomaterial scaffolds to develop cell-seeded prostheses are improving and becoming

more clinically feasible, but still demonstrate a need for biomechanical stimuli during *in vitro* culture prior to implantation (Huang et al., 2016). Better understanding of how dynamic mechanical stimuli can regulate the formation of stable articular cartilage during embryonic skeletogenesis therefore has great potential benefit for the design of tissue engineering regimes to control stem cell differentiation. Notably, the finding in this thesis, that patterns of dynamic tension and compression correspond to patterns of cellular differentiation, suggest that graded biomechanical stimuli could be utilised to generate heterogenous, complex tissues, such as those required for joint replacement.

This work utilised both embryonic and adult cells to examine pattern formation *in vitro*, while considering molecular and mechanical stimuli. Embryonic and adult-derived cells have differing capacities to differentiate to skeletal tissues. Currently, cartilage engineering efforts are focused on adult-derived cell sources, as these cells are more accessible and are available in the large numbers required for *de novo* tissue engineering. Consideration of the different potentials of various cell types is therefore important; for example, the propensity of embryonic cells to form nodule patterns *in vitro* is indicative of self-organising mechanisms that are lacking in adult cells. Comparison of embryonic and adult cells must therefore consider these differences when applying mechanical regimes to *in vitro* cell culture efforts, and can also take advantage of these differences, by exploring how adult-derived stem cells could be influenced to more closely resemble developmentally plastic embryonically-derived cells.

7.2.5 Potential therapeutic applications for *in utero* skeletal developmental defects

Restriction of movement during embryonic skeletal development has a severe impact on human babies. Hypomineralised bones and joint contractures (arthrogryposis) can affect the long-term quality of life of affected individuals if left untreated, and current surgical, therapeutic, or nutritional intervention is in many cases not sufficient to regain full skeletal function (Fassier et al., 2009, Ahmad et al., 2010). Better understanding of the processes occurring during skeletal development has the potential to contribute to the development of therapeutic strategies to treat individuals impacted by restricted foetal movement. Specifically, identification of the type and magnitude of mechanical

stimuli required for normal skeletogenesis would inform the design of appropriate physical therapy regimes to substitute or compensate for embryo-generated movement.

Pre-term human infants (born before 37 weeks' gestation) experience decreased bone mineral density, because of reduced time for mineral accretion and movement *in utero* (Dokos et al., 2013); therefore, approaches for treating the skeletal effects of prematurity will be instructive developing treatments for pre- or full-term infants affected by limited foetal movement. Post-natal nutrient-supplemented diets have been recommended to alleviate the effects of prematurity, including low bone density (osteopenia), but are not sufficient to restore bone mineral density to normal levels (Weiler et al., 2006). However, physical therapy consisting of gentle movements of the limbs can alleviate the effect of osteopenia, increasing bone thickness and strength compared to unexercised infants (Moyer-Mileur et al., 1995, Eliakim and Nemet, 2005, Vignochi et al., 2008, Stalnaker and Poskey, 2016, Litmanovitz et al., 2016). Crucially, such a physical therapy regime is capable of being administered by parents or caregivers at home, making it a simple, low-cost solution (McQueen et al., 2013). Current treatments for joint contractures also point to physical therapy as an effective approach. In the case of neuromuscular disorders, gentle physical therapy can help reduce the severity of joint contractures in affected individuals (Skalsky and McDonald, 2012). Surgical intervention for severe joint contractures is in some instances recommended, but can be enhanced by the addition of physical therapy starting as early as infancy, thereby reducing the number and severity of surgeries (Lampasi et al., 2012, Binkiewicz-Glinska et al., 2013). Further understanding of the types and magnitudes of stimuli experienced by the developing foetus to promote skeletal tissue development will therefore improve the success of physical therapy efforts, and could potentially even be used to lessen the effects of limited movement pre-natally by developing novel *in utero* physical therapy treatments for affected foetuses.

In addition to physical therapy, low-intensity pulsed ultrasound is a potential method for delivering physical loads to developing bones. This method is suggested to deform treated tissues, thereby mimicking the effects of mechanical loading on bone formation (Veronick et al., 2017). Animal studies *in vivo* have demonstrated that ultrasound application can increase bone formation to an extent comparable to mechanical loading (Perry et al., 2009) and can also improve fracture healing (reviewed in Martinez de

Albornoz et al., 2011). Human studies have been relatively limited, and have focused on fracture repair in adults, indicating that ultrasound can increase the rate of fracture repair (Bashardoust Tajali et al., 2012). Most promising are studies of *ex vivo* cultivation of rudiments and *in vitro* differentiation of progenitor cells subjected to ultrasound. *Ex vivo* cultivation of E16-E17 mouse metatarsals showed that low-intensity pulsed ultrasound increased the number of proliferative cells, ossification, and overall rudiment length (Wiltink et al., 1995, Nolte et al., 2001). *In vitro* application of ultrasound to MSCs has been demonstrated to increase both chondrogenic and osteogenic differentiation (Aliabouzar et al., 2017, Costa et al., 2018), while application to cartilage explants increased proteoglycan content (Uddin and Qin, 2013). These studies suggest that low-intensity pulsed ultrasound could stimulate cartilage or bone development *in vivo*, although extensive further testing and refinement of parameters is required to develop a treatment for humans. However, the non-invasive nature of ultrasound makes this approach particularly promising, as it could potentially be easily used to treat infants *in utero* who are affected by reduced mechanical stimulation. Again, characterisation of foetal mechanical stimuli, as well as a better understanding of the forces delivered by ultrasound, would be required for such an approach to be effective.

Biophysical cues generated by movement are also crucial to the maintenance and remodelling of mature skeletal tissues (Vanwanseele et al., 2002, Spencer et al., 2010). However, skeletal tissues are thought to become less responsive to loading with age, as muscle strength decreases and tissues experience reduced mechanical stimulation (Frost, 1997, Novotny et al., 2015). This coincides with increased rates of osteoporosis and arthritis in older populations. Currently, hormone replacement treatment is suggested to alleviate these conditions, as changes in the hormonal environment experienced by the skeleton plays a role in the reduced response of skeletal tissues and in the onset of osteoporosis (Callewaert et al., 2010, Zaman et al., 2010, reviewed in Khosla, 2013). This approach has had limited results, and in future could be augmented by identifying the mechanical stimulation required to abrogate bone resorption and increase mineral deposition, as in younger adults, thereby improving skeletal function (Rubin et al., 2006).

In order to design effective therapeutic regimens for individuals affected by skeletal deformation or degradation, better understanding of the molecular and mechanical

regulation of skeletal development and maintenance is required. Additionally, comprehension of the relationship between these types of cues, as this thesis has investigated, is essential. Mouse and chick are currently useful for investigating the effects of mechanical stimulation on skeletal patterning, as well as in elucidating the signalling and cellular events which contribute to mature skeletal tissues. Findings in these systems could potentially be applied to therapeutic efforts to treat humans for developmental and age-related disorders. Although there is still much remaining to be revealed about how cells integrate molecular and biophysical cues to form temporally and spatially appropriate tissue types during development, and how this knowledge can be effectively translated to a clinical setting, this area of research holds great promise for practical applications in both regenerative and obstetric/neonatal medicine.

References

ADAMS, M. A. 2006. The mechanical environment of chondrocytes in articular cartilage. *Biorheology,* 43**,** 537-45.

ADAMS, S. L., COHEN, A. J. & LASSOVA, L. 2007. Integration of signaling pathways regulating chondrocyte differentiation during endochondral bone formation. *J Cell Physiol,* 213**,** 635-41.

AGOSTINELLI, C. & LUND, U. 2017. R package 'circular': Circular Statistics. 0.4-93 ed.

AHMAD, I., NEMET, D., ELIAKIM, A., KOEPPEL, R., GROCHOW, D., COUSSENS, M., GALLITTO, S., RICH, J., PONTELLO, A., LEU, S. Y., COOPER, D. M. & WAFFARN, F. 2010. Body composition and its components in preterm and term newborns: A cross-sectional, multimodal investigation. *Am J Hum Biol,* 22**,** 69-75.

AHRENS, M. J. & DUDLEY, A. T. 2011. Chemical Pretreatment of Growth Plate Cartilage Increases Immunofluorescence Sensitivity. *Journal of Histochemistry and Cytochemistry,* 59**,** 408-418.

AKIYAMA, T. & KAWASAKI, Y. 2006. Wnt signalling and the actin cytoskeleton. *Oncogene,* 25**,** 7538-44.

ALBERS, J., SCHULZE, J., BEIL, F. T., GEBAUER, M., BARANOWSKY, A., KELLER, J., MARSHALL, R. P., WINTGES, K., FRIEDRICH, F. W., PRIEMEL, M., SCHILLING, A. F., RUEGER, J. M., CORNILS, K., FEHSE, B., STREICHERT, T., SAUTER, G., JAKOB, F., INSOGNA, K. L., POBER, B., KNOBELOCH, K.-P., FRANCKE, U., AMLING, M. & SCHINKE, T. 2011. Control of bone formation by the serpentine receptor Frizzled-9. *The Journal of Cell Biology,* 192**,** 1057-1072.

ALIABOUZAR, M., LEE, S. J., ZHOU, X., ZHANG, G. L. & SARKAR, K. 2017. Effects of scaffold microstructure and low intensity pulsed ultrasound on chondrogenic differentiation of human mesenchymal stem cells. *Biotechnol Bioeng*.

ALVAREZ, J., HORTON, J., SOHN, P. & SERRA, R. 2001. The perichondrium plays an important role in mediating the effects of TGF-beta1 on endochondral bone formation. *Dev Dyn,* 221**,** 311-21.

ANGUS, L., MOLEIRINHO, S., HERRON, L., SINHA, A., ZHANG, X., NIESTRATA, M., DHOLAKIA, K., PRYSTOWSKY, M. B., HARVEY, K. F., REYNOLDS, P. A. & GUNN-MOORE, F. J. 2012. Willin/FRMD6 expression activates the Hippo signaling pathway kinases in mammals and antagonizes oncogenic YAP. *Oncogene,* 31**,** 238-50.

ARAGONA, M., PANCIERA, T., MANFRIN, A., GIULITTI, S., MICHIELIN, F., ELVASSORE, N., DUPONT, S. & PICCOLO, S. 2013. A mechanical checkpoint controls multicellular growth through YAP/TAZ regulation by actin-processing factors. *Cell,* 154**,** 1047-59.

ARCHER, C. W., WILLIAMS, R., NELSON, L. & KHAN, I. M. 2012. Articular Cartilage-Derived Stem Cells: Identification, Characterisation and their Role in Spontaneous Repair. *Rheumatol Curr Res,* S3**,** 005.

ARNOTT, J. A., LAMBI, A. G., MUNDY, C., HENDESI, H., PIXLEY, R. A., OWEN, T. A., SAFADI, F. F. & POPOFF, S. N. 2011. The role of connective tissue growth factor (CTGF/CCN2) in skeletogenesis. *Crit Rev Eukaryot Gene Expr,* 21**,** 43-69.

ARNSDORF, E. J., TUMMALA, P. & JACOBS, C. R. 2009. Non-canonical Wnt signaling and N-cadherin related beta-catenin signaling play a role in mechanically induced osteogenic cell fate. *PLoS One,* 4**,** e5388.

ARONSSON, D. D., GOLDBERG, M. J., KLING, T. F., JR. & ROY, D. R. 1994. Developmental dysplasia of the hip. *Pediatrics,* 94**,** 201-8.

ASCENZI, M.-G., BLANCO, C., DRAYER, I., KIM, H., WILSON, R., RETTING, K. N., LYONS, K. M. & MOHLER, G. 2011. Effect of localization, length and orientation of chondrocytic primary cilium on murine growth plate organization. *Journal of theoretical biology,* 285**,** 147-155.

ASHE, A., BUTTERFIELD, N. C., TOWN, L., COURTNEY, A. D., COOPER, A. N., FERGUSON, C., BARRY, R., OLSSON, F., LIEM, K. F., JR., PARTON, R. G., WAINWRIGHT, B. J., ANDERSON, K. V., WHITELAW, E. & WICKING, C. 2012. Mutations in mouse Ift144 model the craniofacial, limb and rib defects in skeletal ciliopathies. *Hum Mol Genet,* 21**,** 1808-23.

ATSUMI, T., IKAWA, Y., MIWA, Y. & KIMATA, K. 1990. A chondrogenic cell line derived from a differentiating culture of AT805 teratocarcinoma cells. *Cell Differentiation and Development,* 30**,** 109-116.

AUGELLO, A. & DE BARI, C. 2010. The regulation of differentiation in mesenchymal stem cells. *Hum Gene Ther,* 21**,** 1226-38.

AZZOLIN, L., PANCIERA, T., SOLIGO, S., ENZO, E., BICCIATO, S., DUPONT, S., BRESOLIN, S., FRASSON, C., BASSO, G., GUZZARDO, V., FASSINA, A., CORDENONSI, M. & PICCOLO, S. 2014. YAP/TAZ incorporation in the beta-catenin destruction complex orchestrates the Wnt response. *Cell,* 158**,** 157-70.

BADDELEY, A., RUBAK, E. & TURNER, R. 2015. Spatial Point Patterns: Methodology and Applications with R. London: Chapman and Hall/CRC Press.

BADUGU, A., KRAEMER, C., GERMANN, P., MENSHYKAU, D. & IBER, D. 2012. Digit patterning during limb development as a result of the BMP-receptor interaction. *Sci Rep,* 2**,** 991.

BALDOCK, R., BARD, J., BRUNE, R., HILL, B., KAUFMAN, M., OPSTAD, K., SMITH, D., STARK, M., WATERHOUSE, A., YANG, Y. & DAVIDSON, D. 2001. The Edinburgh Mouse Atlas: Using the CD. *Briefings in Bioinformatics,* 2**,** 159-169.

BALL, P. 2015. Forging patterns and making waves from biology to geology: a commentary on Turing (1952) 'The chemical basis of morphogenesis'. *Philosophical Transactions of the Royal Society B: Biological Sciences,* 370**,** 20140218.

BALLANE, G., CAULEY, J. A., LUCKEY, M. M. & EL-HAJJ FULEIHAN, G. 2017. Worldwide prevalence and incidence of osteoporotic vertebral fractures. *Osteoporos Int,* 28**,** 1531-1542.

BANCROFT, G. N., SIKAVITSAS, V. I., VAN DEN DOLDER, J., SHEFFIELD, T. L., AMBROSE, C. G., JANSEN, J. A. & MIKOS, A. G. 2002. Fluid flow increases mineralized matrix deposition in 3D perfusion culture of marrow stromal osteoblasts in a dose-dependent manner. *Proc Natl Acad Sci U S A,* 99**,** 12600-5.

BANGS, F. & ANDERSON, K. V. 2017. Primary Cilia and Mammalian Hedgehog Signaling. *Cold Spring Harb Perspect Biol,* 9.

BASHARDOUST TAJALI, S., HOUGHTON, P., MACDERMID, J. C. & GREWAL, R. 2012. Effects of low-intensity pulsed ultrasound therapy on fracture healing: a systematic review and meta-analysis. *Am J Phys Med Rehabil,* 91**,** 349-67.

BEALES, P. L., BLAND, E., TOBIN, J. L., BACCHELLI, C., TUYSUZ, B., HILL, J., RIX, S., PEARSON, C. G., KAI, M., HARTLEY, J., JOHNSON, C., IRVING, M., ELCIOGLU, N., WINEY, M., TADA, M. & SCAMBLER, P. J. 2007. IFT80, which encodes a conserved intraflagellar transport protein, is mutated in Jeune asphyxiating thoracic dystrophy. *Nat Genet,* 39**,** 727-9.

BELL, D. M., LEUNG, K. K., WHEATLEY, S. C., NG, L. J., ZHOU, S., LING, K. W., SHAM, M. H., KOOPMAN, P., TAM, P. P. & CHEAH, K. S. 1997. SOX9 directly regulates the type-II collagen gene. *Nat Genet,* 16**,** 174-8.

BENJAMINI, Y. & HOCHBERG, Y. 1995. Controlling the False Discovery Rate: A Practical and Powerful Approach to Multiple Testing. *Journal of the Royal Statistical Society. Series B (Methodological),* 57**,** 289-300.

BHATTACHARJEE, M., COBURN, J., CENTOLA, M., MURAB, S., BARBERO, A., KAPLAN, D. L., MARTIN, I. & GHOSH, S. 2015. Tissue engineering strategies to study cartilage development, degeneration and regeneration. *Adv Drug Deliv Rev,* 84**,** 107-22.

BI, W., DENG, J. M., ZHANG, Z., BEHRINGER, R. R. & DE CROMBRUGGHE, B. 1999. Sox9 is required for cartilage formation. *Nat Genet,* 22**,** 85-9.

BIAN, L., ZHAI, D. Y., ZHANG, E. C., MAUCK, R. L. & BURDICK, J. A. 2012. Dynamic compressive loading enhances cartilage matrix synthesis and distribution and suppresses hypertrophy in hMSC-laden hyaluronic acid hydrogels. *Tissue Eng Part A,* 18**,** 715-24.

BIKKAVILLI, R. K., FEIGIN, M. E. & MALBON, C. C. 2008. G alpha o mediates WNT-JNK signaling through dishevelled 1 and 3, RhoA family members, and MEKK 1 and 4 in mammalian cells. *J Cell Sci,* 121**,** 234-45.

BINKIEWICZ-GLINSKA, A., SOBIERAJSKA-REK, A., BAKULA, S., WIERZBA, J., DREWEK, K., KOWALSKI, I. M. & ZABOROWSKA-SAPETA, K. 2013. Arthrogryposis in infancy, multidisciplinary approach: case report. *BMC Pediatr,* 13**,** 184.

BISGROVE, B. W. & YOST, H. J. 2006. The roles of cilia in developmental disorders and disease. *Development,* 133**,** 4131.

BLANEY DAVIDSON, E. N., VITTERS, E. L., MOOREN, F. M., OLIVER, N., BERG, W. B. & VAN DER KRAAN, P. M. 2006. Connective tissue growth factor/CCN2 overexpression in mouse synovial lining results in transient fibrosis and cartilage damage. *Arthritis Rheum,* 54**,** 1653-61.

BLITZ, E., VIUKOV, S., SHARIR, A., SHWARTZ, Y., GALLOWAY, J. L., PRYCE, B. A., JOHNSON, R. L., TABIN, C. J., SCHWEITZER, R. & ZELZER, E. 2009. Bone ridge patterning during musculoskeletal assembly is mediated through SCX regulation of Bmp4 at the tendon-skeleton junction. *Dev Cell,* 17**,** 861-73.

BOULTER, C., MULROY, S., WEBB, S., FLEMING, S., BRINDLE, K. & SANDFORD, R. 2001. Cardiovascular, skeletal, and renal defects in mice with a targeted disruption of the Pkd1 gene. *Proc Natl Acad Sci U S A,* 98.

BRUNET, L. J., MCMAHON, J. A., MCMAHON, A. P. & HARLAND, R. M. 1998. Noggin, cartilage morphogenesis, and joint formation in the mammalian skeleton. *Science,* 280**,** 1455-7.

BRUNT, L. H., BEGG, K., KAGUE, E., CROSS, S. & HAMMOND, C. L. 2017. Wnt signalling controls the response to mechanical loading during zebrafish joint development. *Development,* 144**,** 2798-2809.

BRUNT, L. H., NORTON, J. L., BRIGHT, J. A., RAYFIELD, E. J. & HAMMOND, C. L. 2015. Finite element modelling predicts changes in joint shape and cell behaviour due to loss of muscle strain in jaw development. *J Biomech,* 48**,** 3112-22.

BUTTERFIELD, N. C., QIAN, C. & LOGAN, M. P. O. 2017. Pitx1 determines characteristic hindlimb morphologies in cartilage micromass culture. *PLOS ONE,* 12**,** e0180453.

CALLEWAERT, F., BOONEN, S. & VANDERSCHUEREN, D. 2010. Sex steroids and the male skeleton: a tale of two hormones. *Trends Endocrinol Metab,* 21**,** 89-95.

CALLUS, B. A., VERHAGEN, A. M. & VAUX, D. L. 2006. Association of mammalian sterile twenty kinases, Mst1 and Mst2, with hSalvador via C-terminal coiled-coil domains, leads to its stabilization and phosphorylation. *Febs j,* 273**,** 4264-76.

CAPLAN, A. I. 1991. Mesenchymal stem cells. *J Orthop Res,* 9**,** 641-50.

CARROLL, S. F., BUCKLEY, C. T. & KELLY, D. J. 2014. Cyclic hydrostatic pressure promotes a stable cartilage phenotype and enhances the functional development of cartilaginous grafts engineered using multipotent stromal cells isolated from bone marrow and infrapatellar fat pad. *J Biomech,* 47**,** 2115-21.

CASE, N., MA, M., SEN, B., XIE, Z., GROSS, T. S. & RUBIN, J. 2008. Beta-catenin levels influence rapid mechanical responses in osteoblasts. *J Biol Chem,* 283**,** 29196-205.

CAVERZASIO, J. & MANEN, D. 2007. Essential role of Wnt3a-mediated activation of mitogen-activated protein kinase p38 for the stimulation of alkaline phosphatase activity and matrix mineralization in C3H10T1/2 mesenchymal cells. *Endocrinology,* 148**,** 5323-30.

CHAN, E. H., NOUSIAINEN, M., CHALAMALASETTY, R. B., SCHAFER, A., NIGG, E. A. & SILLJE, H. H. 2005. The Ste20-like kinase Mst2 activates the human large tumor suppressor kinase Lats1. *Oncogene,* 24**,** 2076-86.

CHANG, C.-F., RAMASWAMY, G. & SERRA, R. 2012. Depletion of primary cilia in articular chondrocytes results in reduced Gli3 repressor to activator ratio, increased Hedgehog signaling, and symptoms of early osteoarthritis. *Osteoarthritis and Cartilage,* 20**,** 152-161.

CHAQOUR, B. & GOPPELT-STRUEBE, M. 2006. Mechanical regulation of the Cyr61/CCN1 and CTGF/CCN2 proteins. *Febs j,* 273**,** 3639-49.

CHEN, J. H., LIU, C., YOU, L. & SIMMONS, C. A. 2010. Boning up on Wolff's Law: mechanical regulation of the cells that make and maintain bone. *J Biomech,* 43**,** 108-18.

CHIJIIWA, M., MOCHIZUKI, S., KIMURA, T., ABE, H., TANAKA, Y., FUJII, Y., SHIMIZU, H., ENOMOTO, H., TOYAMA, Y. & OKADA, Y. 2015. CCN1 (Cyr61) Is Overexpressed in Human Osteoarthritic Cartilage and Inhibits ADAMTS-4 (Aggrecanase 1) Activity. *Arthritis Rheumatol,* 67**,** 1557-67.

CHIMAL-MONROY, J., RODRIGUEZ-LEON, J., MONTERO, J. A., GAÑAN, Y., MACIAS, D., MERINO, R. & HURLE, J. M. 2003. Analysis of the molecular cascade responsible for mesodermal limb chondrogenesis: sox genes and BMP signaling. *Developmental Biology,* 257**,** 292-301.

CHO, E. & IRVINE, K. D. 2004. Action of fat, four-jointed, dachsous and dachs in distal-to-proximal wing signaling. *Development,* 131**,** 4489-500.

CHOWDHURY, T. T., SALTER, D. M., BADER, D. L. & LEE, D. A. 2004. Integrin-mediated mechanotransduction processes in TGFbeta-stimulated monolayer-expanded chondrocytes. *Biochem Biophys Res Commun,* 318**,** 873-81.

CHRISTENSEN, S. T., CLEMENT, C. A., SATIR, P. & PEDERSEN, L. B. 2012. Primary cilia and coordination of receptor tyrosine kinase (RTK) signalling. *J Pathol,* 226.

CHUNG, U. I., SCHIPANI, E., MCMAHON, A. P. & KRONENBERG, H. M. 2001. Indian hedgehog couples chondrogenesis to osteogenesis in endochondral bone development. *J Clin Invest,* 107**,** 295-304.

CHURCH, V., NOHNO, T., LINKER, C., MARCELLE, C. & FRANCIS-WEST, P. 2002. Wnt regulation of chondrocyte differentiation. *J Cell Sci,* 115**,** 4809-18.

CLEMENT, C. A., AJBRO, K. D., KOEFOED, K., VESTERGAARD, M. L., VELAND, I. R., HENRIQUES DE JESUS, M. P. R., PEDERSEN, L. B., ANDERSEN, A., LARSEN, C. Y. & CHRISTENSEN, S. T. 2013. TGF-β signaling is associated with endocytosis at the pocket region of the primary cilium. *Cell Rep,* 3.

CLONEY, K. & FRANZ-ODENDAAL, T. A. 2015. Optimized ex-ovo culturing of chick embryos to advanced stages of development. *J Vis Exp***,** 52129.

COLNOT, C., LU, C., HU, D. & HELMS, J. A. 2004. Distinguishing the contributions of the perichondrium, cartilage, and vascular endothelium to skeletal development. *Dev Biol,* 269**,** 55-69.

CORBIT, K. C., SHYER, A. E., DOWDLE, W. E., GAULDEN, J., SINGLA, V., CHEN, M. H., CHUANG, P. T. & REITER, J. F. 2008. Kif3a constrains beta-catenin-dependent Wnt signalling through dual ciliary and non-ciliary mechanisms. *Nat Cell Biol,* 10**,** 70-6.

COSTA, V., CARINA, V., FONTANA, S., DE LUCA, A., MONTELEONE, F., PAGANI, S., SARTORI, M., SETTI, S., FALDINI, C., ALESSANDRO, R., FINI, M. & GIAVARESI, G. 2018. Osteogenic commitment and differentiation of human mesenchymal stem cells by low-intensity pulsed ultrasound stimulation. *J Cell Physiol,* 233**,** 1558-1573.

DALY, A. C., FREEMAN, F. E., GONZALEZ-FERNANDEZ, T., CRITCHLEY, S. E., NULTY, J. & KELLY, D. J. 2017. 3D Bioprinting for Cartilage and Osteochondral Tissue Engineering. *Adv Healthc Mater,* 6.

DAS, A. T., TENENBAUM, L. & BERKHOUT, B. 2016. Tet-On Systems For Doxycycline-inducible Gene Expression. *Curr Gene Ther,* 16**,** 156-67.

DATTA, N., PHAM, Q. P., SHARMA, U., SIKAVITSAS, V. I., JANSEN, J. A. & MIKOS, A. G. 2006. In vitro generated extracellular matrix and fluid shear stress synergistically enhance 3D osteoblastic differentiation. *Proc Natl Acad Sci U S A,* 103**,** 2488-93.

DAY, T. F., GUO, X., GARRETT-BEAL, L. & YANG, Y. 2005. Wnt/beta-catenin signaling in mesenchymal progenitors controls osteoblast and chondrocyte differentiation during vertebrate skeletogenesis. *Dev Cell,* 8**,** 739-50.

DE VRIES, J. I. & FONG, B. F. 2006. Normal fetal motility: an overview. *Ultrasound Obstet Gynecol,* 27**,** 701-11.

DELAINE-SMITH, R. M. & REILLY, G. C. 2012. Mesenchymal stem cell responses to mechanical stimuli. *Muscles Ligaments Tendons J,* 2**,** 169-80.

DELGADO, I. & TORRES, M. 2016. Gradients, waves and timers, an overview of limb patterning models. *Semin Cell Dev Biol,* 49**,** 109-15.

DELLING, M., INDZHYKULIAN, A. A., LIU, X., LI, Y., XIE, T., COREY, D. P. & CLAPHAM, D. E. 2016. Primary cilia are not calcium-responsive mechanosensors. *Nature,* 531**,** 656-60.

DENG, Y., WU, A., LI, P., LI, G., QIN, L., SONG, H. & MAK, K. K. 2016. Yap1 Regulates Multiple Steps of Chondrocyte Differentiation during Skeletal Development and Bone Repair. *Cell Rep,* 14**,** 2224-37.

DENKER, A. E., HAAS, A. R., NICOLL, S. B. & TUAN, R. S. 1999. Chondrogenic differentiation of murine C3H10T1/2 multipotential mesenchymal cells: I. Stimulation by bone morphogenetic protein-2 in high-density micromass cultures. *Differentiation,* 64**,** 67-76.

DIEZ-ROUX, G., BANFI, S., SULTAN, M., GEFFERS, L., ANAND, S., ROZADO, D., MAGEN, A., CANIDIO, E., PAGANI, M., PELUSO, I., LIN-MARQ, N., KOCH, M., BILIO, M., CANTIELLO, I., VERDE, R., DE MASI, C., BIANCHI, S. A., CICCHINI, J., PERROUD, E., MEHMETI, S., DAGAND, E., SCHRINNER, S., NURNBERGER, A., SCHMIDT, K., METZ, K., ZWINGMANN, C., BRIESKE, N., SPRINGER, C., HERNANDEZ, A. M., HERZOG, S., GRABBE, F., SIEVERDING, C., FISCHER, B., SCHRADER, K., BROCKMEYER, M., DETTMER, S., HELBIG, C., ALUNNI, V., BATTAINI, M. A., MURA, C., HENRICHSEN, C. N., GARCIA-LOPEZ, R., ECHEVARRIA, D., PUELLES, E., GARCIA-CALERO, E., KRUSE, S., UHR, M., KAUCK, C., FENG, G., MILYAEV, N., ONG, C. K., KUMAR, L., LAM, M., SEMPLE, C. A., GYENESEI, A., MUNDLOS, S., RADELOF, U.,

LEHRACH, H., SARMIENTOS, P., REYMOND, A., DAVIDSON, D. R., DOLLE, P., ANTONARAKIS, S. E., YASPO, M. L., MARTINEZ, S., BALDOCK, R. A., EICHELE, G. & BALLABIO, A. 2011. A high-resolution anatomical atlas of the transcriptome in the mouse embryo. *PLoS Biol,* 9**,** e1000582.

DOCHEVA, D., POPOV, C., ALBERTON, P. & ASZODI, A. 2014. Integrin signaling in skeletal development and function. *Birth Defects Res C Embryo Today,* 102**,** 13-36.

DOKOS, C., TSAKALIDIS, C., TRAGIANNIDIS, A. & RALLIS, D. 2013. Inside the "fragile" infant: pathophysiology, molecular background, risk factors and investigation of neonatal osteopenia. *Clin Cases Miner Bone Metab,* 10**,** 86-90.

DONG, J., FELDMANN, G., HUANG, J., WU, S., ZHANG, N., COMERFORD, S. A., GAYYED, M. F., ANDERS, R. A., MAITRA, A. & PAN, D. 2007. Elucidation of a Universal Size-Control Mechanism in Drosophila and Mammals. *Cell,* 130**,** 1120-1133.

DONNELLY, E., ASCENZI, M.-G. & FARNUM, C. 2010. Primary cilia are highly oriented with respect to collagen direction and long axis of extensor tendon. *Journal of orthopaedic research : official publication of the Orthopaedic Research Society,* 28**,** 77-82.

DORMER, N. H., BERKLAND, C. J. & DETAMORE, M. S. 2010. Emerging techniques in stratified designs and continuous gradients for tissue engineering of interfaces. *Ann Biomed Eng,* 38**,** 2121-41.

DOW, L. E., FISHER, J., O'ROURKE, K. P., MULEY, A., KASTENHUBER, E. R., LIVSHITS, G., TSCHAHARGANEH, D. F., SOCCI, N. D. & LOWE, S. W. 2015. Inducible in vivo genome editing with CRISPR-Cas9. *Nat Biotechnol,* 33**,** 390-394.

DOWNS, M. E., NGUYEN, A. M., HERZOG, F. A., HOEY, D. A. & JACOBS, C. R. 2014. An experimental and computational analysis of primary cilia deflection under fluid flow. *Comput Methods Biomech Biomed Engin,* 17**,** 2-10.

DOWTHWAITE, G. P., FLANNERY, C. R., FLANNELLY, J., LEWTHWAITE, J. C., ARCHER, C. W. & PITSILLIDES, A. A. 2003. A mechanism underlying the movement requirement for synovial joint cavitation. *Matrix Biol,* 22**,** 311-22.

DRACHMAN, D. B. & SOKOLOFF, L. 1966. The role of movement in embryonic joint development. *Developmental Biology,* 14**,** 401-420.

DU, J., ZU, Y., LI, J., DU, S., XU, Y., ZHANG, L., JIANG, L., WANG, Z., CHIEN, S. & YANG, C. 2016. Extracellular matrix stiffness dictates Wnt expression through integrin pathway. *Sci Rep,* 6**,** 20395.

DUKE, P. J., MONTUFAR-SOLIS, D., HAMAZAKI, T. & SATO, A. 1998. Clinorotation reduces number, but not size, of cartilaginous nodules formed in micromass cultures of mouse limbbud cells. *Adv Space Res,* 21**,** 1065-72.

DUMMER, A., POELMA, C., DERUITER, M. C., GOUMANS, M.-J. T. H. & HIERCK, B. P. 2016. Measuring the primary cilium length: improved method for unbiased high-throughput analysis. *Cilia,* 5**,** 7.

DUPONT, S., MORSUT, L., ARAGONA, M., ENZO, E., GIULITTI, S., CORDENONSI, M., ZANCONATO, F., LE DIGABEL, J., FORCATO, M., BICCIATO, S., ELVASSORE, N. & PICCOLO, S. 2011. Role of YAP/TAZ in mechanotransduction. *Nature,* 474**,** 179-83.

DUPREZ, D., BELL, E. J., RICHARDSON, M. K., ARCHER, C. W., WOLPERT, L., BRICKELL, P. M. & FRANCIS-WEST, P. H. 1996. Overexpression of BMP-2 and BMP-4 alters the size and shape of developing skeletal elements in the chick limb. *Mech Dev,* 57**,** 145-57.

EAMES, B. F., DE LA FUENTE, L. & HELMS, J. A. 2003. Molecular ontogeny of the skeleton. *Birth Defects Res C Embryo Today,* 69**,** 93-101.

EDLUND, S., LANDSTROM, M., HELDIN, C. H. & ASPENSTROM, P. 2002. Transforming growth factor-beta-induced mobilization of actin cytoskeleton requires signaling by small GTPases Cdc42 and RhoA. *Mol Biol Cell,* 13**,** 902-14.

EDWARDS, J., WILKINSON, L., JONES, H., SOOTHILL, P., HENDERSON, K., WORRALL, J. & PITSILLIDES, A. A. 1994. Formation of human synovial joint cavities: a possible role for hyaluronan and CD44 in altered interzone cohesion. *Journal of Anatomy,* 185**,** 355-367.

EHNERT, S., SREEKUMAR, V., ASPERA-WERZ, R. H., SAJADIAN, S. O., WINTERMEYER, E., SANDMANN, G. H., BAHRS, C., HENGSTLER, J. G., GODOY, P. & NUSSLER, A. K. 2017. TGF-beta1 impairs mechanosensation of human osteoblasts via HDAC6-mediated shortening and distortion of primary cilia. *J Mol Med (Berl),* 95**,** 653-663.

ELDER, S. H., KIMURA, J. H., SOSLOWSKY, L. J., LAVAGNINO, M. & GOLDSTEIN, S. A. 2000. Effect of compressive loading on chondrocyte differentiation in agarose cultures of chick limb-bud cells. *J Orthop Res,* 18**,** 78-86.

ELIAKIM, A. & NEMET, D. 2005. Osteopenia of prematurity - the role of exercise in prevention and treatment. *Pediatr Endocrinol Rev,* 2**,** 675-82.

ENGLER, A. J., SEN, S., SWEENEY, H. L. & DISCHER, D. E. 2006. Matrix elasticity directs stem cell lineage specification. *Cell,* 126**,** 677-89.

ENOMOTO-IWAMOTO, M., KITAGAKI, J., KOYAMA, E., TAMAMURA, Y., WU, C., KANATANI, N., KOIKE, T., OKADA, H., KOMORI, T., YONEDA, T., CHURCH, V., FRANCIS-WEST, P. H., KURISU, K., NOHNO, T., PACIFICI, M. & IWAMOTO, M. 2002. The Wnt antagonist Frzb-1 regulates chondrocyte maturation and long bone development during limb skeletogenesis. *Dev Biol,* 251**,** 142-56.

EVANS, N. D., MINELLI, C., GENTLEMAN, E., LAPOINTE, V., PATANKAR, S. N., KALLIVRETAKI, M., CHEN, X., ROBERTS, C. J. & STEVENS, M. M. 2009. Substrate stiffness affects early differentiation events in embryonic stem cells. *Eur Cell Mater,* 18**,** 1-13; discussion 13-4.

FAGET, L. & HNASKO, T. S. 2015. Tyramide Signal Amplification for Immunofluorescent Enhancement. *Methods Mol Biol,* 1318**,** 161-72.

FAHY, N., ALINI, M. & STODDART, M. J. 2017. Mechanical stimulation of mesenchymal stem cells: Implications for cartilage tissue engineering. *J Orthop Res*.

FARNUM, C. E. & WILSMAN, N. J. 2011. Orientation of Primary Cilia of Articular Chondrocytes in Three-Dimensional Space. *The Anatomical Record: Advances in Integrative Anatomy and Evolutionary Biology,* 294**,** 533-549.

FASSIER, A., WICART, P., DUBOUSSET, J. & SERINGE, R. 2009. Arthrogryposis multiplex congenita. Long-term follow-up from birth until skeletal maturity. *J Child Orthop,* 3**,** 383-90.

FELL, H. B. & CANTI, R. G. 1934. Experiments on the development in vitro of the avian knee joint. *Proc R Soc B,* 116**,** 316-351.

FERRER-VAQUER, A., PILISZEK, A., TIAN, G., AHO, R. J., DUFORT, D. & HADJANTONAKIS, A. K. 2010. A sensitive and bright single-cell resolution live imaging reporter of Wnt/ss-catenin signaling in the mouse. *BMC Dev Biol,* 10**,** 121.

FIELD, J., NIKAWA, J., BROEK, D., MACDONALD, B., RODGERS, L., WILSON, I. A., LERNER, R. A. & WIGLER, M. 1988. Purification of a RAS-responsive adenylyl cyclase complex from Saccharomyces cerevisiae by use of an epitope addition method. *Mol Cell Biol,* 8**,** 2159-65.

FRANZ, T., KOTHARY, R., SURANI, M. A., HALATA, Z. & GRIM, M. 1993. The Splotch mutation interferes with muscle development in the limbs. *Anat Embryol (Berl),* 187**,** 153-60.

FRIEDLAND-LITTLE, J. M., HOFFMANN, A. D., OCBINA, P. J., PETERSON, M. A., BOSMAN, J. D., CHEN, Y., CHENG, S. Y., ANDERSON, K. V. & MOSKOWITZ, I. P. 2011. A novel murine allele of Intraflagellar Transport Protein 172 causes a syndrome including VACTERL-like features with hydrocephalus. *Hum Mol Genet,* 20**,** 3725-37.

FRIEDRICHSEN, S., HEUER, H., CHRIST, S., WINCKLER, M., BRAUER, D., BAUER, K. & RAIVICH, G. 2003. CTGF expression during mouse embryonic development. *Cell Tissue Res,* 312**,** 175-88.

FROST, H. M. 1994. Wolff's Law and bone's structural adaptations to mechanical usage: an overview for clinicians. *Angle Orthod,* 64**,** 175-88.

FROST, H. M. 1997. On our age-related bone loss: insights from a new paradigm. *J Bone Miner Res,* 12**,** 1539-46.

FROST, H. M. 2001. From Wolff's law to the Utah paradigm: insights about bone physiology and its clinical applications. *Anat Rec,* 262**,** 398-419.

FRY, A. M., LEAPER, M. J. & BAYLISS, R. 2014. The primary cilium: guardian of organ development and homeostasis. *Organogenesis,* 10**,** 62-8.

FU, S. L., ZHAO, W. Y., ZHANG, W. J., SONG, H., JI, H. B. & TANG, N. 2017. Hippo signaling pathway in lung development, regeneration, and diseases. *Yi Chuan,* 39**,** 597-606.

GAO, L., MCBEATH, R. & CHEN, C. S. 2010. Stem cell shape regulates a chondrogenic versus myogenic fate through Rac1 and N-cadherin. *Stem Cells,* 28**,** 564-72.

GAO, Y., LIU, S., HUANG, J., GUO, W., CHEN, J., ZHANG, L., ZHAO, B., PENG, J., WANG, A., WANG, Y., XU, W., LU, S., YUAN, M. & GUO, Q. 2014. The ECM-Cell Interaction of Cartilage Extracellular Matrix on Chondrocytes. *BioMed Research International,* 2014**,** 648459.

GARCÍA-CASTRO, J., TRIGUEROS, C., MADRENAS, J., PÉREZ-SIMÓN, J. A., RODRIGUEZ, R. & MENENDEZ, P. 2008. Mesenchymal stem cells and their use as cell replacement therapy and disease modelling tool. *Journal of Cellular and Molecular Medicine,* 12**,** 2552-2565.

GARDNER, K., ARNOCZKY, S. P. & LAVAGNINO, M. 2011. Effect of in vitro stress-deprivation and cyclic loading on the length of tendon cell cilia in situ. *J Orthop Res,* 29**,** 582-7.

GERDES, J. M., DAVIS, E. E. & KATSANIS, N. 2009. The Vertebrate Primary Cilium in Development, Homeostasis, and Disease. *Cell,* 137**,** 32-45.

GERHARDT, C., LIER, J. M., BURMUHL, S., STRUCHTRUP, A., DEUTSCHMANN, K., VETTER, M., LEU, T., REEG, S., GRUNE, T. & RUTHER, U. 2015. The transition zone protein Rpgrip1l regulates proteasomal activity at the primary cilium. *J Cell Biol,* 210**,** 115-33.

GERMILLER, J. A. & GOLDSTEIN, S. A. 1997. Structure and Function of Embryonic Growth Plate in the Absence of Functioning Skeletal Muscle. *Journal of Orthopaedic Research,* 15**,** 362-370.

GOETZ, S. C. & ANDERSON, K. V. 2010a. The Primary Cilium: A Signaling Center During Vertebrate Development. *Nature reviews. Genetics,* 11**,** 331-344.

GOETZ, S. C. & ANDERSON, K. V. 2010b. The primary cilium: a signalling centre during vertebrate development. *Nat Rev Genet,* 11**,** 331-44.

GOGGOLIDOU, P. 2014. Wnt and planar cell polarity signaling in cystic renal disease. *Organogenesis,* 10**,** 86-95.

GOLDRING, M. B. 2004. Immortalization of human articular chondrocytes for generation of stable, differentiated cell lines. *Methods Mol Med,* 100**,** 23-36.

GOMEZ, C., DAVID, V., PEET, N. M., VICO, L., CHENU, C., MALAVAL, L. & SKERRY, T. M. 2007. Absence of mechanical loading in utero influences bone mass and architecture but not innervation in Myod-Myf5-deficient mice. *J Anat,* 210**,** 259-71.

GRAD, S., EGLIN, D., ALINI, M. & STODDART, M. J. 2011. Physical stimulation of chondrogenic cells in vitro: a review. *Clin Orthop Relat Res,* 469**,** 2764-72.

GRANNAS, K., ARNGARDEN, L., LONN, P., MAZURKIEWICZ, M., BLOKZIJL, A., ZIEBA, A. & SODERBERG, O. 2015. Crosstalk between Hippo and TGFbeta: Subcellular Localization of YAP/TAZ/Smad Complexes. *J Mol Biol,* 427**,** 3407-15.

GRECO, K. V., IQBAL, A. J., RATTAZZI, L., NALESSO, G., MORADI-BIDHENDI, N., MOORE, A. R., GOLDRING, M. B., DELL'ACCIO, F. & PERRETTI, M. 2011. High density micromass cultures of a human chondrocyte cell line: A reliable assay system to reveal the modulatory functions of pharmacological agents. *Biochemical pharmacology,* 82**,** 1919-1929.

GUO, J., JIN, J. & COOPER, L. F. 2008. Dissection of sets of genes that control the character of wnt5a-deficient mouse calvarial cells. *Bone,* 43**,** 961-71.

GUO, T., LU, Y., LI, P., YIN, M.-X., LV, D., ZHANG, W., WANG, H., ZHOU, Z., JI, H., ZHAO, Y. & ZHANG, L. 2013. A novel partner of Scalloped regulates Hippo signaling via antagonizing Scalloped-Yorkie activity. *Cell Research,* 23**,** 1201-1214.

GUO, X., DAY, T. F., JIANG, X., GARRETT-BEAL, L., TOPOL, L. & YANG, Y. 2004. Wnt/beta-catenin signaling is sufficient and necessary for synovial joint formation. *Genes Dev,* 18**,** 2404-17.

GUO, X., MAK, K. K., TAKETO, M. M. & YANG, Y. 2009. The Wnt/beta-catenin pathway interacts differentially with PTHrP signaling to control chondrocyte hypertrophy and final maturation. *PLoS One,* 4**,** e6067.

HADDEN, W. J. & CHOI, Y. S. 2016. The extracellular microscape governs mesenchymal stem cell fate. *J Biol Eng,* 10**,** 16.

HADJIARGYROU, M., AHRENS, W. & RUBIN, C. T. 2000. Temporal expression of the chondrogenic and angiogenic growth factor CYR61 during fracture repair. *J Bone Miner Res,* 15**,** 1014-23.

HALDER, G., DUPONT, S. & PICCOLO, S. 2012. Transduction of mechanical and cytoskeletal cues by YAP and TAZ. *Nat Rev Mol Cell Biol,* 13**,** 591-600.

HALL, B. K. & HERRING, S. 1999. Altered skeletal growth of paralyzed chick. *Journal of Morphology,* 206**,** 45-56.

HALL, B. K. & HERRING, S. W. 1990. Paralysis and growth of the musculoskeletal system in the embryonic chick. *J Morphol,* 206**,** 45-56.

HALL, B. K. & MIYAKE, T. 2000. All for one and one for all -- condensations and the initiation of skeletal development. *BioEssays,* 22**,** 138-147.

HALL, J. G. 1986. Analysis of Pena Shokeir phenotype. *Am J Med Genet,* 25**,** 99-117.

HALL, J. G. 2009. Pena-Shokeir phenotype (fetal akinesia deformation sequence) revisited. *Birth Defects Res A Clin Mol Teratol,* 85**,** 677-94.

HALL, J. G., ALDINGER, K. A. & TANAKA, K. I. 2014. Amyoplasia revisited. *Am J Med Genet A,* 164a**,** 700-30.

HALL, J. G., REED, S. D., MCGILLIVRAY, B. C., HERRMANN, J., PARTINGTON, M. W., SCHINZEL, A., SHAPIRO, J. & WEAVER, D. D. 1983. Part II. Amyoplasia: twinning in amyoplasia--a specific type of arthrogryposis with an apparent excess of discordantly affected identical twins. *Am J Med Genet,* 15**,** 591-9.

HAMAMOTO, A., YAMATO, S., KATOH, Y., NAKAYAMA, K., YOSHIMURA, K., TAKEDA, S., KOBAYASHI, Y. & SAITO, Y. 2016. Modulation of primary cilia length by melanin-concentrating hormone receptor 1. *Cell Signal,* 28**,** 572-84.

HAMBURGER, V. & BALABAN, M. 1963. Observations and experiments on spontaneous rhythmical behavior in the chick embryo. *Developmental Biology,* 7**,** 533-545.

HAMBURGER, V. & HAMILTON, H. L. 1951. A series of normal stages in the development of the chick embryo. *J Morphol,* 88**,** 49-92.

HAMBURGER, V. & WAUGH, M. 1940. The primary development of the skeleton in nerveless and poorly innervated limb transplants of chick embryos. *Physiological Zoology,* 13**,** 367-380.

HANDLER, M., YURCHENCO, P. D. & IOZZO, R. V. 1997. Developmental expression of perlecan during murine embryogenesis. *Dev Dyn,* 210**,** 130-45.

HANSEN, C. G., MOROISHI, T. & GUAN, K.-L. 2015. YAP and TAZ: a nexus for Hippo signaling and beyond. *Trends in cell biology,* 25**,** 499-513.

HAO, Y., CHUN, A., CHEUNG, K., RASHIDI, B. & YANG, X. 2008. Tumor suppressor LATS1 is a negative regulator of oncogene YAP. *J Biol Chem,* 283**,** 5496-509.

HART, E. K., JINNIN, M., HOU, B., FUKAI, N. & OLSEN, B. R. 2007. Kinesin-2 Controls Development and Patterning of the Vertebrate Skeleton by Hedgehog- and Gli3-Dependent Mechanisms. *Developmental biology,* 309**,** 273-284.

HARTMANN, C. & TABIN, C. J. 2000. Dual roles of Wnt signaling during chondrogenesis in the chicken limb. *Development,* 127**,** 3141-59.

HARTMANN, C. & TABIN, C. J. 2001. Wnt-14 plays a pivotal role in inducing synovial joint formation in the developing appendicular skeleton. *Cell,* 104**,** 341-351.

HAUDENSCHILD, A. K., HSIEH, A. H., KAPILA, S. & LOTZ, J. C. 2009. Pressure and distortion regulate human mesenchymal stem cell gene expression. *Ann Biomed Eng,* 37**,** 492-502.

HAVIS, E., BONNIN, M. A., ESTEVES DE LIMA, J., CHARVET, B., MILET, C. & DUPREZ, D. 2016. TGFbeta and FGF promote tendon progenitor fate and act downstream of muscle contraction to regulate tendon differentiation during chick limb development. *Development,* 143**,** 3839-3851.

HAYCRAFT, C. J. & SERRA, R. 2008. Cilia involvement in patterning and maintenance of the skeleton. *Curr Top Dev Biol,* 85**,** 303-32.

HAYCRAFT, C. J., ZHANG, Q., SONG, B., JACKSON, W. S., DETLOFF, P. J., SERRA, R. & YODER, B. K. 2007a. Intraflagellar transport is essential for endochondral bone formation. *Development,* 134**,** 307-16.

HAYCRAFT, C. J., ZHANG, Q., SONG, B., JACKSON, W. S., DETLOFF, P. J., SERRA, R. & YODER, B. K. 2007b. Intraflagellar transport is essential for endochondral bone formation. *Development,* 134.

HE, X. 2008. Cilia put a brake on Wnt signalling. *Nat Cell Biol,* 10**,** 11-3.

HENS, J. R., WILSON, K. M., DANN, P., CHEN, X., HOROWITZ, M. C. & WYSOLMERSKI, J. J. 2005. TOPGAL mice show that the canonical Wnt signaling pathway is active during bone development and growth and is activated by mechanical loading in vitro. *J Bone Miner Res,* 20**,** 1103-13.

HENSTOCK, J. R., ROTHERHAM, M., ROSE, J. B. & EL HAJ, A. J. 2013. Cyclic hydrostatic pressure stimulates enhanced bone development in the foetal chick femur in vitro. *Bone,* 53**,** 468-77.

HEYWOOD, J. L., MCENTEE, G. M. & STICKLAND, N. C. 2005. In ovo neuromuscular stimulation alters the skeletal muscle phenotype of the chick. *J Muscle Res Cell Motil,* 26**,** 49-56.

HINITS, Y., WILLIAMS, V. C., SWEETMAN, D., DONN, T. M., MA, T. P., MOENS, C. B. & HUGHES, S. M. 2011. Defective cranial skeletal development, larval lethality and haploinsufficiency in Myod mutant zebrafish. *Dev Biol,* 358**,** 102-12.

HOEY, D. A., DOWNS, M. E. & JACOBS, C. R. 2012a. The mechanics of the primary cilium: an intricate structure with complex function. *J Biomech,* 45**,** 17-26.

HOEY, D. A., TORMEY, S., RAMCHARAN, S., O'BRIEN, F. J. & JACOBS, C. R. 2012b. Primary cilia-mediated mechanotransduction in human mesenchymal stem cells. *Stem Cells,* 30**,** 2561-70.

HOGG, D. A. & HOSSEINI, A. 1992. The effects of paralysis on skeletal development in the chick embryo. *Comp Biochem Physiol Comp Physiol,* 103**,** 25-8.

HOLDER, N. 1977. An experimental investigation into the early development of the chick elbow joint. *J Embryol Exp Morphol,* 39**,** 115-27.

HONG, J. H., HWANG, E. S., MCMANUS, M. T., AMSTERDAM, A., TIAN, Y., KALMUKOVA, R., MUELLER, E., BENJAMIN, T., SPIEGELMAN, B. M., SHARP, P. A., HOPKINS, N. & YAFFE, M. B. 2005. TAZ, a transcriptional modulator of mesenchymal stem cell differentiation. *Science,* 309**,** 1074-8.

HOPP, T. P., PRICKETT, K. S., PRICE, V. L., LIBBY, R. T., MARCH, C. J., PAT CERRETTI, D., URDAL, D. L. & CONLON, P. J. 1988. A Short Polypeptide Marker Sequence Useful for Recombinant Protein Identification and Purification. *Nat Biotech,* 6**,** 1204-1210.

HOSSAIN, Z., ALI, S. M., KO, H. L., XU, J., NG, C. P., GUO, K., QI, Z., PONNIAH, S., HONG, W. & HUNZIKER, W. 2007. Glomerulocystic kidney disease in mice with a targeted inactivation of Wwtr1. *Proceedings of the National Academy of Sciences of the United States of America,* 104**,** 1631-1636.

HOSSEINI, A. & HOGG, D. A. 1991a. The effects of paralysis on skeletal development in the chick embryo. I. General effects. *J Anat,* 177**,** 159-68.

HOSSEINI, A. & HOGG, D. A. 1991b. The effects of paralysis on skeletal development in the chick embryo. II. Effects on histogenesis of the tibia. *J Anat,* 177**,** 169-78.

HOWARD, P. W., HOWARD, T. L. & MAURER, R. A. 2010. Generation of mice with a conditional allele for Ift172. *Transgenic Res,* 19**,** 121-6.

HU, K. & OLSEN, B. R. 2017. Vascular endothelial growth factor control mechanisms in skeletal growth and repair. *Dev Dyn,* 246**,** 227-234.

HUANG, A. H. 2017. Coordinated development of the limb musculoskeletal system: Tendon and muscle patterning and integration with the skeleton. *Dev Biol,* 429**,** 420-428.

HUANG, A. H., FARRELL, M. J., KIM, M. & MAUCK, R. L. 2010a. Long-term dynamic loading improves the mechanical properties of chondrogenic mesenchymal stem cell-laden hydrogel. *Eur Cell Mater,* 19**,** 72-85.

HUANG, B. J., HU, J. C. & ATHANASIOU, K. A. 2016. Cell-based tissue engineering strategies used in the clinical repair of articular cartilage. *Biomaterials,* 98**,** 1-22.

HUANG, B. L., BRUGGER, S. M. & LYONS, K. M. 2010b. Stage-specific control of connective tissue growth factor (CTGF/CCN2) expression in chondrocytes by Sox9 and beta-catenin. *J Biol Chem,* 285**,** 27702-12.

HUANG, C. Y., HAGAR, K. L., FROST, L. E., SUN, Y. & CHEUNG, H. S. 2004. Effects of cyclic compressive loading on chondrogenesis of rabbit bone-marrow derived mesenchymal stem cells. *Stem Cells,* 22**,** 313-23.

HUANG, J., WU, S., BARRERA, J., MATTHEWS, K. & PAN, D. 2005. The Hippo Signaling Pathway Coordinately Regulates Cell Proliferation and Apoptosis by Inactivating Yorkie, the Drosophila Homolog of YAP. *Cell,* 122**,** 421-434.

HUANGFU, D. & ANDERSON, K. V. 2005. Cilia and Hedgehog responsiveness in the mouse. *Proceedings of the National Academy of Sciences of the United States of America,* 102**,** 11325-11330.

HUEBSCH, N., LIPPENS, E., LEE, K., MEHTA, M., KOSHY, S. T., DARNELL, M. C., DESAI, R. M., MADL, C. M., XU, M., ZHAO, X., CHAUDHURI, O., VERBEKE, C., KIM, W. S., ALIM, K., MAMMOTO, A., INGBER, D. E., DUDA, G. N. & MOONEY, D. J. 2015. Matrix elasticity of void-forming hydrogels controls transplanted-stem-cell-mediated bone formation. *Nat Mater,* 14**,** 1269-77.

HUEY, D. J., HU, J. C. & ATHANASIOU, K. A. 2012. Unlike Bone, Cartilage Regeneration Remains Elusive. *Science (New York, N.Y.),* 338**,** 917-921.

HYDE, G., BOOT-HANDFORD, R. P. & WALLIS, G. A. 2008. Col2a1 lineage tracing reveals that the meniscus of the knee joint has a complex cellular origin. *J Anat,* 213**,** 531-8.

HYDE, G., DOVER, S., ASZODI, A., WALLIS, G. A. & BOOT-HANDFORD, R. P. 2007. Lineage tracing using matrilin-1 gene expression reveals that articular chondrocytes exist as the joint interzone forms. *Dev Biol,* 304**,** 825-33.

ISAAC, A., RODRIGUEZ-ESTEBAN, C., RYAN, A., ALTABEF, M., TSUKUI, T., PATEL, K., TICKLE, C. & IZPISUA-BELMONTE, J. C. 1998. Tbx genes and limb identity in chick embryo development. *Development,* 125**,** 1867-75.

ITOH, S., HATTORI, T., TOMITA, N., AOYAMA, E., YUTANI, Y., YAMASHIRO, T. & TAKIGAWA, M. 2013. CCN family member 2/connective tissue growth factor (CCN2/CTGF) has anti-aging effects that protect articular cartilage from age-related degenerative changes. *PLoS One,* 8**,** e71156.

ITOU, J., KAWAKAMI, H., QUACH, T., OSTERWALDER, M., EVANS, S. M., ZELLER, R. & KAWAKAMI, Y. 2012. Islet1 regulates establishment of the posterior hindlimb field upstream of the Hand2-Shh morphoregulatory gene network in mouse embryos. *Development,* 139**,** 1620-9.

IVKOVIC, S., YOON, B. S., POPOFF, S. N., SAFADI, F. F., LIBUDA, D. E., STEPHENSON, R. C., DALUISKI, A. & LYONS, K. M. 2003. Connective tissue growth factor coordinates chondrogenesis and angiogenesis during skeletal development. *Development (Cambridge, England),* 130**,** 2779-2791.

JENSEN, C. G., POOLE, C. A., MCGLASHAN, S. R., MARKO, M., ISSA, Z. I., VUJCICH, K. V. & BOWSER, S. S. 2004. Ultrastructural, tomographic and confocal imaging of the chondrocyte primary cilium in situ. *Cell Biol Int,* 28**,** 101-10.

JENSEN, V. L. & LEROUX, M. R. 2017. Gates for soluble and membrane proteins, and two trafficking systems (IFT and LIFT), establish a dynamic ciliary signaling compartment. *Curr Opin Cell Biol,* 47**,** 83-91.

JIANG, S., CHEN, G., FENG, L., JIANG, Z., YU, M., BAO, J. & TIAN, W. 2016. Disruption of kif3a results in defective osteoblastic differentiation in dental mesenchymal stem/precursor cells via the Wnt signaling pathway. *Mol Med Rep,* 14**,** 1891-900.

JUHASZ, T., MATTA, C., SOMOGYI, C., KATONA, E., TAKACS, R., SOHA, R. F., SZABO, I. A., CSERHATI, C., SZODY, R., KARACSONYI, Z., BAKO, E., GERGELY, P. & ZAKANY, R. 2014. Mechanical loading stimulates chondrogenesis via the PKA/CREB-Sox9 and PP2A pathways in chicken micromass cultures. *Cell Signal,* 26**,** 468-82.

KAAN, H. Y. K., CHAN, S. W., TAN, S. K. J., GUO, F., LIM, C. J., HONG, W. & SONG, H. 2017. Crystal structure of TAZ-TEAD complex reveals a distinct interaction mode from that of YAP-TEAD complex. *Scientific Reports,* 7**,** 2035.

KAHN, J., SHWARTZ, Y., BLITZ, E., KRIEF, S., SHARIR, A., BREITEL, D. A., RATTENBACH, R., RELAIX, F., MAIRE, P., ROUNTREE, R. B., KINGSLEY, D. M. & ZELZER, E. 2009. Muscle contraction is necessary to maintain joint progenitor cell fate. *Dev Cell,* 16**,** 734-43.

KAN, A., IKEDA, T., FUKAI, A., NAKAGAWA, T., NAKAMURA, K., CHUNG, U.-I., KAWAGUCHI, H. & TABIN, C. J. 2013. SOX11 contributes to the regulation of GDF5 in joint maintenance. *BMC Developmental Biology,* 13**,** 4.

KARAMBOULAS, K., DRANSE, H. J. & UNDERHILL, T. M. 2010. Regulation of BMP-dependent chondrogenesis in early limb mesenchyme by TGFbeta signals. *J Cell Sci,* 123**,** 2068-76.

KARAPLIS, A. C., LUZ, A., GLOWACKI, J., BRONSON, R. T., TYBULEWICZ, V. L., KRONENBERG, H. M. & MULLIGAN, R. C. 1994. Lethal skeletal dysplasia from targeted disruption of the parathyroid hormone-related peptide gene. *Genes Dev,* 8**,** 277-89.

KARP, S. J., SCHIPANI, E., ST-JACQUES1, B., HUNZELMAN, J., KRONENBERG, H. & MCMAHON, A. P. 2000. *Indian Hedgehog* coordinates endochondral bone growth and morphogenesis via *Parathyroid hormone related-Protein*-dependent and -independent pathways. *Development,* 127**,** 543-548.

KARYSTINOU, A., ROELOFS, A. J., NEVE, A., CANTATORE, F. P., WACKERHAGE, H. & DE BARI, C. 2015. Yes-associated protein (YAP) is a negative regulator of chondrogenesis in mesenchymal stem cells. *Arthritis Res Ther,* 17**,** 147.

KATO, K., BHATTARAM, P., PENZO-MÉNDEZ, A., GADI, A. & LEFEBVRE, V. 2015. SOXC Transcription Factors Induce Cartilage Growth Plate Formation in Mouse Embryos by Promoting Noncanonical WNT Signaling. *Journal of Bone and Mineral Research,* 30**,** 1560-1571.

KAVANAGH, E., CHURCH, V. L., OSBORNE, A. C., LAMB, K. J., ARCHER, C. W., FRANCIS-WEST, P. H. & PITSILLIDES, A. A. 2006. Differential regulation of GDF-5 and FGF-2/4 by immobilisation in ovo exposes distinct roles in joint formation. *Dev Dyn,* 235**,** 826-34.

KAVRAN, J. M., WARD, M. D., OLADOSU, O. O., MULEPATI, S. & LEAHY, D. J. 2010. All mammalian Hedgehog proteins interact with cell adhesion molecule, down-regulated by oncogenes (CDO) and brother of CDO (BOC) in a conserved manner. *J Biol Chem,* 285**,** 24584-90.

KELLER, B., YANG, T., CHEN, Y., MUNIVEZ, E., BERTIN, T., ZABEL, B. & LEE, B. 2011. Interaction of TGFbeta and BMP signaling pathways during chondrogenesis. *PLoS One,* 6**,** e16421.

KELLER-PECK, C. R. & MULLEN, R. J. 1997. Altered cell proliferation in the spinal cord of mouse neural tube mutants curly tail and Pax3 splotch-delayed. *Brain Res Dev Brain Res,* 102**,** 177-88.

KELLY, D. J. & JACOBS, C. R. 2010. The role of mechanical signals in regulating chondrogenesis and osteogenesis of mesenchymal stem cells. *Birth Defects Res C Embryo Today,* 90**,** 75-85.

KERKHOFS, J., ROBERTS, S. J., LUYTEN, F. P., VAN OOSTERWYCK, H. & GERIS, L. 2012. Relating the chondrocyte gene network to growth plate morphology: from genes to phenotype. *PLoS One,* 7**,** e34729.

KHAYYERI, H., BARRETO, S. & LACROIX, D. 2015. Primary cilia mechanics affects cell mechanosensation: A computational study. *J Theor Biol,* 379**,** 38-46.

KHOSLA, S. 2013. Pathogenesis of age-related bone loss in humans. *J Gerontol A Biol Sci Med Sci,* 68**,** 1226-35.

KIM, H. D., AMIRTHALINGAM, S., KIM, S. L., LEE, S. S., RANGASAMY, J. & HWANG, N. S. 2017. Biomimetic Materials and Fabrication Approaches for Bone Tissue Engineering. *Adv Healthc Mater*.

KIM, J., JO, H., HONG, H., KIM, M. H., KIM, J. M., LEE, J. K., HEO, W. D. & KIM, J. 2015. Actin remodelling factors control ciliogenesis by regulating YAP/TAZ activity and vesicle trafficking. *Nat Commun,* 6**,** 6781.

KIM, M. & JHO, E.-H. 2014. Cross-talk between Wnt/β-catenin and Hippo signaling pathways: a brief review. *BMB Reports,* 47**,** 540-545.

KISIDAY, J. D., FRISBIE, D. D., MCILWRAITH, C. W. & GRODZINSKY, A. J. 2009. Dynamic compression stimulates proteoglycan synthesis by mesenchymal stem cells in the absence of chondrogenic cytokines. *Tissue Eng Part A,* 15**,** 2817-24.

KOBAYASHI, T., LYONS, K. M., MCMAHON, A. P. & KRONENBERG, H. M. 2005. BMP signaling stimulates cellular differentiation at multiple steps during cartilage development. *Proc Natl Acad Sci U S A,* 102**,** 18023-7.

KONDO, S. & MIURA, T. 2010. Reaction-Diffusion Model as a Framework for Understanding Biological Pattern Formation. *Science,* 329**,** 1616.

KOSHER, R. A., KULYK, W. M. & GAY, S. W. 1986. Collagen gene expression during limb cartilage differentiation. *J Cell Biol,* 102**,** 1151-6.

KOSHIMIZU, T., KAWAI, M., KONDOU, H., TACHIKAWA, K., SAKAI, N., OZONO, K. & MICHIGAMI, T. 2012. Vinculin functions as regulator of chondrogenesis. *J Biol Chem,* 287**,** 15760-75.

KOYAMA, E., OCHIAI, T., ROUNTREE, R. B., KINGSLEY, D. M., ENOMOTO-IWAMOTO, M., IWAMOTO, M. & PACIFICI, M. 2007. Synovial joint formation during mouse limb skeletogenesis: roles of Indian hedgehog signaling. *Ann N Y Acad Sci,* 1116**,** 100-12.

KOYAMA, E., SHIBUKAWA, Y., NAGAYAMA, M., SUGITO, H., YOUNG, B., YUASA, T., OKABE, T., OCHIAI, T., KAMIYA, N., ROUNTREE, R. B., KINGSLEY, D. M., IWAMOTO, M., ENOMOTO-IWAMOTO, M. & PACIFICI, M. 2008. A distinct cohort of progenitor cells participates in synovial joint and articular cartilage formation during mouse limb skeletogenesis. *Dev Biol,* 316**,** 62-73.

KRUPSKA, I., BRUFORD, E. A. & CHAQOUR, B. 2015. Eyeing the Cyr61/CTGF/NOV (CCN) group of genes in development and diseases: highlights of their structural likenesses and functional dissimilarities. *Human Genomics,* 9**,** 24.

KUSUMBE, A. P., RAMASAMY, S. K. & ADAMS, R. H. 2014. Coupling of angiogenesis and osteogenesis by a specific vessel subtype in bone. *Nature,* 507**,** 323-328.

KUTA, A., MAO, Y., MARTIN, T., FERREIRA DE SOUSA, C., WHITING, D., ZAKARIA, S., CRESPO-ENRIQUEZ, I., EVANS, P., BALCZERSKI, B., MANKOO, B., IRVINE, K. D. & FRANCIS-WEST, P. H. 2016. Fat4-Dchs1 signalling controls cell proliferation in developing vertebrae. *Development,* 143**,** 2367-75.

KWAKWA, K. A., VANDERBURGH, J. P., GUELCHER, S. A. & STERLING, J. A. 2017. Engineering 3D Models of Tumors and Bone to Understand Tumor-Induced Bone Disease and Improve Treatments. *Curr Osteoporos Rep,* 15**,** 247-254.

LAMB, K. J., LEWTHWAITE, J. C., LIN, J. P., SIMON, D., KAVANAGH, E., WHEELER-JONES, C. P. & PITSILLIDES, A. A. 2003. Diverse range of fixed positional deformities and bone growth restraint provoked by flaccid paralysis in embryonic chicks. *Int J Exp Pathol,* 84**,** 191-9.

LAMPASI, M., ANTONIOLI, D. & DONZELLI, O. 2012. Management of knee deformities in children with arthrogryposis. *Musculoskelet Surg,* 96**,** 161-9.

LANCASTER, M. A. & GLEESON, J. G. 2010. Cystic Kidney Disease: the Role of Wnt Signaling. *Trends in molecular medicine,* 16**,** 349-360.

LANSKE, B., KARAPLIS, A. C., LEE, K., LUZ, A., VORTKAMP, A., PIRRO, A., KARPERIEN, M., DEFIZE, L. H., HO, C., MULLIGAN, R. C., ABOU-SAMRA, A. B., JUPPNER, H., SEGRE, G. V. & KRONENBERG, H. M. 1996. PTH/PTHrP receptor in early development and Indian hedgehog-regulated bone growth. *Science,* 273**,** 663-6.

LAURIN, M., FRADET, N., BLANGY, A., HALL, A., VUORI, K. & COTE, J. F. 2008. The atypical Rac activator Dock180 (Dock1) regulates myoblast fusion in vivo. *Proc Natl Acad Sci U S A,* 105**,** 15446-51.

LAZJUK, G. I., CHERSTVOY, E. D., LURIE, I. W. & NEDZVED, M. K. 1978. Pulmonary hypoplasia, multiple ankyloses, and camptodactyly: one syndrome or some related forms? *Helv Paediatr Acta,* 33**,** 73-9.

LEE, R. T. H., ZHAO, Z. & INGHAM, P. W. 2016. Hedgehog signalling. *Development,* 143**,** 367.

LEE, T. C., KASHYAP, R. L. & CHU, C. N. 1994. Building Skeleton Models via 3-D Medial Surface Axis Thinning Algorithms. *CVGIP: Graphical Models and Image Processing,* 56**,** 462-478.

LEFEBVRE, V., HUANG, W., HARLEY, V. R., GOODFELLOW, P. N. & DE CROMBRUGGHE, B. 1997. SOX9 is a potent activator of the chondrocyte-specific enhancer of the pro alpha1(II) collagen gene. *Mol Cell Biol,* 17**,** 2336-46.

LEI, Q. Y., ZHANG, H., ZHAO, B., ZHA, Z. Y., BAI, F., PEI, X. H., ZHAO, S., XIONG, Y. & GUAN, K. L. 2008. TAZ promotes cell proliferation and epithelial-mesenchymal transition and is inhibited by the hippo pathway. *Mol Cell Biol,* 28**,** 2426-36.

LELKES, G. 1958. Experiments in vitro on the role of movement in the development of joints. *J Embryol Exp Morphol,* 6**,** 183-6.

LENNON, D. P. & CAPLAN, A. I. 2006. Isolation of human marrow-derived mesenchymal stem cells. *Exp Hematol,* 34**,** 1604-5.

LEUNG, C. Y. & ZERNICKA-GOETZ, M. 2013. Angiomotin prevents pluripotent lineage differentiation in mouse embryos via Hippo pathway-dependent and -independent mechanisms. *Nat Commun,* 4**,** 2251.

LI, T., LONGOBARDI, L., MYERS, T. J., TEMPLE, J. D., CHANDLER, R. L., OZKAN, H., CONTALDO, C. & SPAGNOLI, A. 2013. Joint TGF-beta type II receptor-expressing cells: ontogeny and characterization as joint progenitors. *Stem Cells Dev,* 22**,** 1342-59.

LI, Y. & DUDLEY, A. T. 2009. Noncanonical frizzled signaling regulates cell polarity of growth plate chondrocytes. *Development,* 136**,** 1083-92.

LI, Y. J., BATRA, N. N., YOU, L., MEIER, S. C., COE, I. A., YELLOWLEY, C. E. & JACOBS, C. R. 2004. Oscillatory fluid flow affects human marrow stromal cell proliferation and differentiation. *J Orthop Res,* 22**,** 1283-9.

LI, Z., KUPCSIK, L., YAO, S. J., ALINI, M. & STODDART, M. J. 2010a. Mechanical load modulates chondrogenesis of human mesenchymal stem cells through the TGF-beta pathway. *J Cell Mol Med,* 14**,** 1338-46.

LI, Z., YAO, S. J., ALINI, M. & STODDART, M. J. 2010b. Chondrogenesis of human bone marrow mesenchymal stem cells in fibrin-polyurethane composites is modulated by frequency and amplitude of dynamic compression and shear stress. *Tissue Eng Part A,* 16**,** 575-84.

LIANG, W., LI, Z., WANG, Z., ZHOU, J., SONG, H., XU, S., CUI, W., WANG, Q., CHEN, Z., LIU, F. & FAN, W. 2017. Periodic Mechanical Stress INDUCES Chondrocyte Proliferation and Matrix Synthesis via CaMKII-Mediated Pyk2 Signaling. *Cell Physiol Biochem,* 42**,** 383-396.

LIEM, K. F., JR., ASHE, A., HE, M., SATIR, P., MORAN, J., BEIER, D., WICKING, C. & ANDERSON, K. V. 2012. The IFT-A complex regulates Shh signaling through cilia structure and membrane protein trafficking. *J Cell Biol,* 197**,** 789-800.

LIN, S. S., TZENG, B. H., LEE, K. R., SMITH, R. J., CAMPBELL, K. P. & CHEN, C. C. 2014. Cav3.2 T-type calcium channel is required for the NFAT-dependent Sox9 expression in tracheal cartilage. *Proc Natl Acad Sci U S A,* 111**,** E1990-8.

LIN, X., LIANG, M. & FENG, X. H. 2000. Smurf2 is a ubiquitin E3 ligase mediating proteasome-dependent degradation of Smad2 in transforming growth factor-beta signaling. *J Biol Chem,* 275**,** 36818-22.

LITMANOVITZ, I., EREZ, H., ELIAKIM, A., BAUER-RUSEK, S., ARNON, S., REGEV, R. H., SIROTA, G. & NEMET, D. 2016. The Effect of Assisted Exercise Frequency on Bone Strength in Very Low Birth Weight Preterm Infants: A Randomized Control Trial. *Calcif Tissue Int,* 99**,** 237-42.

LIU, B., CHEN, S., CHENG, D., JING, W. & HELMS, J. A. 2014. Primary cilia integrate hedgehog and Wnt signaling during tooth development. *J Dent Res,* 93**,** 475-82.

LIU, J., LI, Q., KUEHN, M. R., LITINGTUNG, Y., VOKES, S. A. & CHIANG, C. 2013. Sonic hedgehog signaling directly targets Hyaluronic Acid Synthase 2, an essential regulator of phalangeal joint patterning. *Dev Biol,* 375**,** 160-71.

LIU-CHITTENDEN, Y., HUANG, B., SHIM, J. S., CHEN, Q., LEE, S.-J., ANDERS, R. A., LIU, J. O. & PAN, D. 2012. Genetic and pharmacological disruption of the TEAD–YAP complex suppresses the oncogenic activity of YAP. *Genes & Development,* 26**,** 1300-1305.

LOGAN, M., SIMON, H. G. & TABIN, C. 1998. Differential regulation of T-box and homeobox transcription factors suggests roles in controlling chick limb-type identity. *Development,* 125**,** 2825-35.

LOGAN, M. & TABIN, C. J. 1999. Role of Pitx1 upstream of Tbx4 in specification of hindlimb identity. *Science,* 283**,** 1736-9.

LONG, F. & LINSENMAYER, T. F. 1998. Regulation of growth region cartilage proliferation and differentiation by perichondrium. *Development,* 125**,** 1067-1073.

LORDA-DIEZ, C. I., MONTERO, J. A., CHOE, S., GARCIA-PORRERO, J. A. & HURLE, J. M. 2014. Ligand- and stage-dependent divergent functions of BMP signaling in the differentiation of embryonic skeletogenic progenitors in vitro. *J Bone Miner Res,* 29**,** 735-48.

LU, W., SHEN, X., PAVLOVA, A., LAKKIS, M., WARD, C. J., PRITCHARD, L., HARRIS, P. C., GENEST, D. R., PEREZ-ATAYDE, A. R. & ZHOU, J. 2001. Comparison of Pkd1-targeted mutants reveals that loss of polycystin-1 causes cystogenesis and bone defects. *Hum Mol Genet,* 10**,** 2385-96.

LUO, K. 2017. Signaling Cross Talk between TGF-beta/Smad and Other Signaling Pathways. *Cold Spring Harb Perspect Biol,* 9.

LYONS, K. M., HOGAN, B. L. & ROBERTSON, E. J. 1995. Colocalization of BMP 7 and BMP 2 RNAs suggests that these factors cooperatively mediate tissue interactions during murine development. *Mech Dev,* 50**,** 71-83.

MA, M., GALLAGHER, A. R. & SOMLO, S. 2017. Ciliary Mechanisms of Cyst Formation in Polycystic Kidney Disease. *Cold Spring Harb Perspect Biol*.

MACKIE, E. J., AHMED, Y. A., TATARCZUCH, L., CHEN, K. S. & MIRAMS, M. 2008. Endochondral ossification: how cartilage is converted into bone in the developing skeleton. *Int J Biochem Cell Biol,* 40**,** 46-62.

MACKIE, E. J., TATARCZUCH, L. & MIRAMS, M. 2011. The skeleton: a multi-functional complex organ: the growth plate chondrocyte and endochondral ossification. *J Endocrinol,* 211**,** 109-21.

MAILHOT, G., YANG, M., MASON-SAVAS, A., MACKAY, C. A., LEAV, I. & ODGREN, P. R. 2008. BMP-5 expression increases during chondrocyte differentiation in vivo and in vitro and promotes proliferation and cartilage matrix synthesis in primary chondrocyte cultures. *J Cell Physiol,* 214**,** 56-64.

MALESKI, M. P. & KNUDSON, C. B. 1996. Hyaluronan-mediated aggregation of limb bud mesenchyme and mesenchymal condensation during chondrogenesis. *Exp Cell Res,* 225**,** 55-66.

MALONE, A. M., ANDERSON, C. T., TUMMALA, P., KWON, R. Y., JOHNSTON, T. R., STEARNS, T. & JACOBS, C. R. 2007. Primary cilia mediate mechanosensing in bone cells by a calcium-independent mechanism. *Proc Natl Acad Sci U S A,* 104**,** 13325-30.

MAMMOTO, T., MAMMOTO, A., TORISAWA, Y. S., TAT, T., GIBBS, A., DERDA, R., MANNIX, R., DE BRUIJN, M., YUNG, C. W., HUH, D. & INGBER, D. E. 2011. Mechanochemical control of mesenchymal condensation and embryonic tooth organ formation. *Dev Cell,* 21**,** 758-69.

MAN, K., JIANG, L. H., FOSTER, R. & YANG, X. B. 2017. Immunological Responses to Total Hip Arthroplasty. *J Funct Biomater,* 8.

MAO, Y., MULVANEY, J., ZAKARIA, S., YU, T., MORGAN, K. M., ALLEN, S., BASSON, M. A., FRANCIS-WEST, P. & IRVINE, K. D. 2011. Characterization of a Dchs1 mutant mouse reveals requirements for Dchs1-Fat4 signaling during mammalian development. *Development,* 138**,** 947-57.

MARINI, J. C. & BLISSETT, A. R. 2013. New genes in bone development: what's new in osteogenesis imperfecta. *J Clin Endocrinol Metab,* 98**,** 3095-103.

MARTIN, L., KACI, N., ESTIBALS, V., GOUDIN, N., GARFA-TRAORE, M., BENOIST-LASSELIN, C., DAMBROISE, E. & LEGEAI-MALLET, L. 2017. Constitutively-active FGFR3 disrupts primary cilium length and IFT20 trafficking in various chondrocyte models of achondroplasia. *Hum Mol Genet*.

MARTINEZ DE ALBORNOZ, P., KHANNA, A., LONGO, U. G., FORRIOL, F. & MAFFULLI, N. 2011. The evidence of low-intensity pulsed ultrasound for in vitro, animal and human fracture healing. *Br Med Bull,* 100**,** 39-57.

MARTURANO, J. E., ARENA, J. D., SCHILLER, Z. A., GEORGAKOUDI, I. & KUO, C. K. 2013. Characterization of mechanical and biochemical properties of

developing embryonic tendon. *Proceedings of the National Academy of Sciences,* 110**,** 6370-6375.

MATSUMOTO, S., FUMOTO, K., OKAMOTO, T., KAIBUCHI, K. & KIKUCHI, A. 2010. Binding of APC and dishevelled mediates Wnt5a-regulated focal adhesion dynamics in migrating cells. *Embo j,* 29**,** 1192-204.

MAUCK, R. L., SOLTZ, M. A., WANG, C. C., WONG, D. D., CHAO, P. H., VALHMU, W. B., HUNG, C. T. & ATESHIAN, G. A. 2000. Functional tissue engineering of articular cartilage through dynamic loading of chondrocyte-seeded agarose gels. *J Biomech Eng,* 122**,** 252-60.

MAUPIN, K. A., DROSCHA, C. J. & WILLIAMS, B. O. 2013. A Comprehensive Overview of Skeletal Phenotypes Associated with Alterations in Wnt/β-catenin Signaling in Humans and Mice. *Bone Research,* 1**,** 27-71.

MCBEATH, R., PIRONE, D. M., NELSON, C. M., BHADRIRAJU, K. & CHEN, C. S. 2004. Cell shape, cytoskeletal tension, and RhoA regulate stem cell lineage commitment. *Dev Cell,* 6**,** 483-95.

MCCLANAHAN, B. S., HARMON-CLAYTON, K., WARD, K. D., KLESGES, R. C., VUKADINOVICH, C. M. & CANTLER, E. D. 2002. Side-to-side comparisons of bone mineral density in upper and lower limbs of collegiate athletes. *J Strength Cond Res,* 16**,** 586-90.

MCGLASHAN, S. R., CLUETT, E. C., JENSEN, C. G. & POOLE, C. 2008. Primary cilia in osteoarthritic chondrocytes: from chondrons to clusters. *Dev Dyn,* 237.

MCGLASHAN, S. R., HAYCRAFT, C. J., JENSEN, C. G., YODER, B. K. & POOLE, C. A. 2007. Articular cartilage and growth plate defects are associated with chondrocyte cytoskeletal abnormalities in Tg737orpk mice lacking the primary cilia protein polaris. *Matrix Biology,* 26**,** 234-246.

MCGLASHAN, S. R., KNIGHT, M. M., CHOWDHURY, T. T., JOSHI, P., JENSEN, C. G., KENNEDY, S. & POOLE, C. A. 2010. Mechanical loading modulates chondrocyte primary cilia incidence and length. *Cell Biol Int,* 34**,** 441-6.

MCMAHON, L. A., CAMPBELL, V. A. & PRENDERGAST, P. J. 2008. Involvement of stretch-activated ion channels in strain-regulated glycosaminoglycan synthesis in mesenchymal stem cell-seeded 3D scaffolds. *J Biomech,* 41**,** 2055-9.

MCMURRAY, R. J., WANN, A. K., THOMPSON, C. L., CONNELLY, J. T. & KNIGHT, M. M. 2013. Surface topography regulates wnt signaling through control of primary cilia structure in mesenchymal stem cells. *Sci Rep,* 3**,** 3545.

MCQUEEN, D., LAKES, K., RICH, J., VAUGHAN, J., HAYES, G., COOPER, D. & OLSHANSKY, E. 2013. Feasibility of a caregiver-assisted exercise program for preterm infants. *J Perinat Neonatal Nurs,* 27**,** 184-92.

MEASE, A. D., YEATMAN, G. W., PETTETT, G. & MERENSTEIN, G. B. 1976. A syndrome of ankylosis, facial anomalies and pulmonary hypoplasia secondary to fetal neuromuscular dysfunction. *Birth Defects Orig Artic Ser,* 12**,** 193-200.

MELLO, M. A. & TUAN, R. S. 1999. High density micromass cultures of embryonic limb bud mesenchymal cells: an in vitro model of endochondral skeletal development. *In Vitro Cell Dev Biol Anim,* 35**,** 262-9.

MELROSE, J., SHU, C., WHITELOCK, J. M. & LORD, M. S. 2016. The cartilage extracellular matrix as a transient developmental scaffold for growth plate maturation. *Matrix Biol,* 52-54**,** 363-383.

MENG, Z., MOROISHI, T., MOTTIER-PAVIE, V., PLOUFFE, S. W., HANSEN, C. G., HONG, A. W., PARK, H. W., MO, J. S., LU, W., LU, S., FLORES, F., YU, F. X., HALDER, G. & GUAN, K. L. 2015. MAP4K family kinases act in parallel to MST1/2 to activate LATS1/2 in the Hippo pathway. *Nat Commun,* 6**,** 8357.

MENSHYKAU, D., BLANC, P., UNAL, E., SAPIN, V. & IBER, D. 2014. An interplay of geometry and signaling enables robust lung branching morphogenesis. *Development,* 141**,** 4526-36.

MIKIC, B., WONG, M., CHIQUET, M. & HUNZIKER, E. B. 2000. Mechanical modulation of tenascin-C and collagen-XII expression during avian synovial joint formation. *J Orthop Res,* 18**,** 406-15.

MILLER, M. E. 2003. The lesson of temporary brittle bone disease: all bones are not created equal. *Bone,* 33**,** 466-474.

MILLER, M. E. & HANGARTNER, T. N. 1999. Temporary brittle bone disease: association with decreased fetal movement and osteopenia. *Calcif Tissue Int,* 64**,** 137-43.

MINGUILLON, C., DEL BUONO, J. & LOGAN, M. P. 2005. Tbx5 and Tbx4 are not sufficient to determine limb-specific morphologies but have common roles in initiating limb outgrowth. *Dev Cell,* 8**,** 75-84.

MININA, E., KRESCHEL, C., NASKI, M. C., ORNITZ, D. M. & VORTKAMP, A. 2002. Interaction of FGF, Ihh/Pthlh, and BMP signaling integrates chondrocyte proliferation and hypertrophic differentiation. *Dev Cell,* 3**,** 439-49.

MININA, E., WENZEL, H. M., KRESCHEL, C., KARP, S. J., GAFFIELD, W., MCMAHON, A. P. & VORTKAMP, A. 2001. BMP and Ihh/PTHrP signaling interact to coordinate chondrocyte proliferation and differentiation. *Development,* 128**,** 4523-4534.

MITCHELL, A. C., BRIQUEZ, P. S., HUBBELL, J. A. & COCHRAN, J. R. 2016. Engineering growth factors for regenerative medicine applications. *Acta Biomater,* 30**,** 1-12.

MITROVIC, D. 1978. Development of the diarthrodial joints in the rat embryo. *Am J Anat,* 151**,** 475-85.

MITROVIC, D. 1982. Development of the articular cavity in paralyzed chick embryos and in chick embryo limb buds cultured on chorioallantoic membranes. *Acta Anat (Basel),* 113**,** 313-24.

MITSOU, I., MULTHAUPT, H. A. B. & COUCHMAN, J. R. 2017. Proteoglycans, ion channels and cell-matrix adhesion. *Biochem J,* 474**,** 1965-1979.

MIYOSHI, K., KASAHARA, K., MURAKAMI, S., TAKESHIMA, M., KUMAMOTO, N., SATO, A., MIYAZAKI, I., MATSUZAKI, S., SASAOKA, T., KATAYAMA, T. & ASANUMA, M. 2014. Lack of dopaminergic inputs elongates the primary cilia of striatal neurons. *PLoS ONE,* 9.

MOESSINGER, A. C. 1983. Fetal Akinesia Deformation Sequence - An Animal Model. *Pediatrics,* 72**,** 857-863.

MOMOSE, T., TONEGAWA, A., TAKEUCHI, J., OGAWA, H., UMESONO, K. & YASUDA, K. 1999. Efficient targeting of gene expression in chick embryos by microelectroporation. *Dev Growth Differ,* 41**,** 335-44.

MORIN-KENSICKI, E. M., BOONE, B. N., HOWELL, M., STONEBRAKER, J. R., TEED, J., ALB, J. G., MAGNUSON, T. R., O'NEAL, W. & MILGRAM, S. L. 2006. Defects in yolk sac vasculogenesis, chorioallantoic fusion, and embryonic axis elongation in mice with targeted disruption of Yap65. *Mol Cell Biol,* 26**,** 77-87.

MOUW, J. K., CONNELLY, J. T., WILSON, C. G., MICHAEL, K. E. & LEVENSTON, M. E. 2007. Dynamic compression regulates the expression and synthesis of chondrocyte-specific matrix molecules in bone marrow stromal cells. *Stem Cells,* 25**,** 655-63.

MOYER-MILEUR, L., LUETKEMEIER, M., BOOMER, L. & CHAN, G. M. 1995. Effect of physical activity on bone mineralization in premature infants. *J Pediatr,* 127**,** 620-5.

MULIERI, P. J., KANG, J. S., SASSOON, D. A. & KRAUSS, R. S. 2002. Expression of the boc gene during murine embryogenesis. *Dev Dyn,* 223**,** 379-88.

MURRAY, P. D. & DRACHMAN, D. B. 1969. The role of movement in the development of joints and related structures: the head and neck in the chick embryo. *J Embryol Exp Morphol,* 22**,** 349-71.

NAKASHIMA, K., ZHOU, X., KUNKEL, G., ZHANG, Z., DENG, J. M., BEHRINGER, R. R. & DE CROMBRUGGHE, B. 2002. The novel zinc finger-containing transcription factor osterix is required for osteoblast differentiation and bone formation. *Cell,* 108**,** 17-29.

NAKATA, E., NAKANISHI, T., KAWAI, A., ASAUMI, K., YAMAAI, T., ASANO, M., NISHIDA, T., MITANI, S., INOUE, H. & TAKIGAWA, M. 2002. Expression of connective tissue growth factor/hypertrophic chondrocyte-specific gene product 24 (CTGF/Hcs24) during fracture healing. *Bone,* 31**,** 441-7.

NELSON, A. E. 2017. Osteoarthritis year in review 2017: clinical. *Osteoarthritis Cartilage*.

NGUYEN, A. M. & JACOBS, C. R. 2013. Emerging role of primary cilia as mechanosensors in osteocytes. *Bone,* 54**,** 196-204.

NISHIMOTO, S. & LOGAN, M. P. 2016. Subdivision of the lateral plate mesoderm and specification of the forelimb and hindlimb forming domains. *Semin Cell Dev Biol,* 49**,** 102-8.

NISHIOKA, N., INOUE, K., ADACHI, K., KIYONARI, H., OTA, M., RALSTON, A., YABUTA, N., HIRAHARA, S., STEPHENSON, R. O., OGONUKI, N., MAKITA, R., KURIHARA, H., MORIN-KENSICKI, E. M., NOJIMA, H., ROSSANT, J., NAKAO, K., NIWA, H. & SASAKI, H. 2009. The Hippo signaling pathway components Lats and Yap pattern Tead4 activity to distinguish mouse trophectoderm from inner cell mass. *Dev Cell,* 16**,** 398-410.

NOHNO, T., KAWAKAMI, Y., WADA, N., KOMAGUCHI, C. & NISHIMATSU, S. 1999. Differential expression of the frizzled family involved in Wnt signaling during chick limb development. *Cell Mol Biol (Noisy-le-grand),* 45**,** 653-9.

NOLTE, P. A., KLEIN-NULEND, J., ALBERS, G. H., MARTI, R. K., SEMEINS, C. M., GOEI, S. W. & BURGER, E. H. 2001. Low-intensity ultrasound stimulates endochondral ossification in vitro. *J Orthop Res,* 19**,** 301-7.

NONAKA, S., SHIRATORI, H., SAIJOH, Y. & HAMADA, H. 2002. Determination of left-right patterning of the mouse embryo by artificial nodal flow. *Nature,* 418**,** 96-99.

NONAKA, S., TANAKA, Y., OKADA, Y., TAKEDA, S., HARADA, A., KANAI, Y., KIDO, M. & HIROKAWA, N. 1998. Randomization of left-right asymmetry due to loss of nodal cilia generating leftward flow of extraembryonic fluid in mice lacking KIF3B motor protein. *Cell,* 95.

NOVOTNY, S. A., WARREN, G. L. & HAMRICK, M. W. 2015. Aging and the muscle-bone relationship. *Physiology (Bethesda),* 30**,** 8-16.

NOWLAN, N. C., BOURDON, C., DUMAS, G., TAJBAKHSH, S., PRENDERGAST, P. J. & MURPHY, P. 2010a. Developing bones are differentially affected by compromised skeletal muscle formation. *Bone,* 46**,** 1275-1285.

NOWLAN, N. C., DUMAS, G., TAJBAKHSH, S., PRENDERGAST, P. J. & MURPHY, P. 2012. Biophysical stimuli induced by passive movements compensate for lack of skeletal muscle during embryonic skeletogenesis. *Biomech Model Mechanobiol,* 11**,** 207-19.

NOWLAN, N. C., MURPHY, P. & PRENDERGAST, P. J. 2008a. A dynamic pattern of mechanical stimulation promotes ossification in avian embryonic long bones. *J Biomech,* 41**,** 249-58.

NOWLAN, N. C., PRENDERGAST, P. J. & MURPHY, P. 2008b. Identification of mechanosensitive genes during embryonic bone formation. *PLoS Comput Biol,* 4**,** e1000250.

NOWLAN, N. C. & SHARPE, J. 2014. Joint shape morphogenesis precedes cavitation of the developing hip joint. *J Anat,* 224**,** 482-9.

NOWLAN, N. C., SHARPE, J., RODDY, K. A., PRENDERGAST, P. J. & MURPHY, P. 2010b. Mechanobiology of embryonic skeletal development: Insights from animal models. *Birth Defects Res C Embryo Today,* 90**,** 203-13.

NOZAWA, K., FUJISHIRO, M., KAWASAKI, M., KANEKO, H., IWABUCHI, K., YANAGIDA, M., SUZUKI, F., MIYAZAWA, K., TAKASAKI, Y., OGAWA, H., TAKAMORI, K. & SEKIGAWA, I. 2009. Connective tissue growth factor promotes articular damage by increased osteoclastogenesis in patients with rheumatoid arthritis. *Arthritis Res Ther,* 11**,** R174.

O'BRIEN, T. P. & LAU, L. F. 1992. Expression of the growth factor-inducible immediate early gene cyr61 correlates with chondrogenesis during mouse embryonic development. *Cell Growth Differ,* 3**,** 645-54.

O'RAHILLY, R. & MULLER, F. 2010. Developmental stages in human embryos: revised and new measurements. *Cells Tissues Organs,* 192**,** 73-84.

OBERLENDER, S. A. & TUAN, R. S. 1994. Expression and functional involvement of N-cadherin in embryonic limb chondrogenesis. *Development,* 120**,** 177-187.

OCBINA, P. J., TUSON, M. & ANDERSON, K. V. 2009. Primary cilia are not required for normal canonical Wnt signaling in the mouse embryo. *PLoS One,* 4**,** e6839.

OH, H. & IRVINE, K. D. 2008. In vivo regulation of Yorkie phosphorylation and localization. *Development,* 135**,** 1081-8.

OH, H. & IRVINE, K. D. 2010. Yorkie: the final destination of Hippo signaling. *Trends in cell biology,* 20**,** 410-417.

OHASHI, K., FUJIWARA, S. & MIZUNO, K. 2017. Roles of the cytoskeleton, cell adhesion and rho signalling in mechanosensing and mechanotransduction. *J Biochem,* 161**,** 245-254.

OHUCHI, H., NAKAGAWA, T., YAMAMOTO, A., ARAGA, A., OHATA, T., ISHIMARU, Y., YOSHIOKA, H., KUWANA, T., NOHNO, T., YAMASAKI, M., ITOH, N. & NOJI, S. 1997. The mesenchymal factor, FGF10, initiates and maintains the outgrowth of the chick limb bud through interaction with FGF8, an apical ectodermal factor. *Development,* 124**,** 2235-44.

OKA, T., MAZACK, V. & SUDOL, M. 2008. Mst2 and Lats kinases regulate apoptotic function of Yes kinase-associated protein (YAP). *J Biol Chem,* 283**,** 27534-46.

OLIAZADEH, N., GORMAN, K. F., EVELEIGH, R., BOURQUE, G. & MOREAU, A. 2017. Identification of Elongated Primary Cilia with Impaired Mechanotransduction in Idiopathic Scoliosis Patients. *Sci Rep,* 7**,** 44260.

OREFFO, R. O., COOPER, C., MASON, C. & CLEMENTS, M. 2005. Mesenchymal stem cells: lineage, plasticity, and skeletal therapeutic potential. *Stem Cell Rev,* 1**,** 169-78.

ORTEGA, N., BEHONICK, D. J. & WERB, Z. 2004. Matrix remodeling during endochondral ossification. *Trends in cell biology,* 14**,** 86-93.

ORWOLL, E. S., ADLER, R. A., AMIN, S., BINKLEY, N., LEWIECKI, E. M., PETAK, S. M., SHAPSES, S. A., SINAKI, M., WATTS, N. B. & SIBONGA, J. D. 2013. Skeletal health in long-duration astronauts: nature, assessment, and management recommendations from the NASA Bone Summit. *J Bone Miner Res,* 28**,** 1243-55.

OSBORNE, A. C., LAMB, K. J., LEWTHWAITE, J. C., DOWTHWAITE, G. P. & PITSILLIDES, A. A. 2002. Short-term rigid and flaccid paralyses diminish growth of embryonic chick limbs and abrogate joint cavity formation but differentially preserve pre-cavitated joints. *J Musculoskelet Neuronal Interact,* 2**,** 448-56.

OWEN, M. & FRIEDENSTEIN, A. J. 1988. Stromal stem cells: marrow-derived osteogenic precursors. *Ciba Found Symp,* 136**,** 42-60.

OZPOLAT, B. D., ZAPATA, M., DANIEL FRUGE, J., COOTE, J., LEE, J., MUNEOKA, K. & ANDERSON, R. 2012. Regeneration of the elbow joint in the developing chick embryo recapitulates development. *Dev Biol,* 372**,** 229-38.

PACIFICI, M., KOYAMA, E., SHIBUKAWA, Y., WU, C., TAMAMURA, Y., ENOMOTO-IWAMOTO, M. & IWAMOTO, M. 2006. Cellular and molecular

mechanisms of synovial joint and articular cartilage formation. *Ann N Y Acad Sci,* 1068**,** 74-86.

PAI, A. C. 1965. Developmental genetics of a lethal mutation, muscular dysgenesis (mdg), in the mouse: II. Developmental analysis. *Developmental Biology,* 11**,** 93-109.

PAIVA, K. B. & GRANJEIRO, J. M. 2014. Bone tissue remodeling and development: focus on matrix metalloproteinase functions. *Arch Biochem Biophys,* 561**,** 74-87.

PANADERO, J. A., LANCEROS-MENDEZ, S. & RIBELLES, J. L. 2016. Differentiation of mesenchymal stem cells for cartilage tissue engineering: Individual and synergetic effects of three-dimensional environment and mechanical loading. *Acta Biomater,* 33**,** 1-12.

PARK, H. W., KIM, Y. C., YU, B., MOROISHI, T., MO, J. S., PLOUFFE, S. W., MENG, Z., LIN, K. C., YU, F. X., ALEXANDER, C. M., WANG, C. Y. & GUAN, K. L. 2015. Alternative Wnt Signaling Activates YAP/TAZ. *Cell,* 162**,** 780-94.

PATERSON, C. R., BURNS, J. & MCALLION, S. J. 1993. Osteogenesis imperfecta: the distinction from child abuse and the recognition of a variant form. *Am J Med Genet,* 45**,** 187-92.

PATERSON, C. R. & MONK, E. A. 2011. Temporary brittle bone disease: relationship between clinical findings and judicial outcome. *Pediatr Rep,* 3**,** e24.

PAZOUR, G. J., DICKERT, B. L., VUCICA, Y., SEELEY, E. S., ROSENBAUM, J. L., WITMAN, G. B. & COLE, D. G. 2000. Chlamydomonas IFT88 and Its Mouse Homologue, Polycystic Kidney Disease Gene Tg737, Are Required for Assembly of Cilia and Flagella. *The Journal of Cell Biology,* 151**,** 709.

PEDERSEN, L. B., SCHRODER, J. M., SATIR, P. & CHRISTENSEN, S. T. 2012. The ciliary cytoskeleton. *Compr Physiol,* 2**,** 779-803.

PELTON, R. W., SAXENA, B., JONES, M., MOSES, H. L. & GOLD, L. I. 1991. Immunohistochemical localization of TGF beta 1, TGF beta 2, and TGF beta 3 in the mouse embryo: expression patterns suggest multiple roles during embryonic development. *J Cell Biol,* 115**,** 1091-105.

PELTTARI, K., WINTER, A., STECK, E., GOETZKE, K., HENNIG, T., OCHS, B. G., AIGNER, T. & RICHTER, W. 2006. Premature induction of hypertrophy during in vitro chondrogenesis of human mesenchymal stem cells correlates with calcification and vascular invasion after ectopic transplantation in SCID mice. *Arthritis Rheum,* 54**,** 3254-66.

PENA, S. D. & SHOKEIR, M. H. 1976. Syndrome of camptodactyly, multiple ankyloses, facial anomalies and pulmonary hypoplasia--further delineation and evidence for autosomal recessive inheritance. *Birth Defects Orig Artic Ser,* 12**,** 201-8.

PERRY, M. J., PARRY, L. K., BURTON, V. J., GHEDUZZI, S., BERESFORD, J. N., HUMPHREY, V. F. & SKERRY, T. M. 2009. Ultrasound mimics the effect of mechanical loading on bone formation in vivo on rat ulnae. *Med Eng Phys,* 31**,** 42-7.

PERSSON, M. 1983. The role of movements in the development of sutural and diarthrodial joints tested by long-term paralysis of chick embryos. *J Anat,* 137 (Pt 3)**,** 591-9.

PICCOLO, S., DUPONT, S. & CORDENONSI, M. 2014. The biology of YAP/TAZ: hippo signaling and beyond. *Physiol Rev,* 94**,** 1287-312.

PITSILLIDES, A. A. & ASHHURST, D. E. 2008. A critical evaluation of specific aspects of joint development. *Dev Dyn,* 237**,** 2284-94.

PITTENGER, M. F., MACKAY, A. M., BECK, S. C., JAISWAL, R. K., DOUGLAS, R., MOSCA, J. D., MOORMAN, M. A., SIMONETTI, D. W., CRAIG, S. & MARSHAK, D. R. 1999. Multilineage potential of adult human mesenchymal stem cells. *Science,* 284**,** 143-7.

PIZETTE, S. & NISWANDER, L. 2000. BMPs are required at two steps of limb chondrogenesis: formation of prechondrogenic condensations and their differentiation into chondrocytes. *Dev Biol,* 219**,** 237-49.

PONGKITWITOON, S., UZER, G., RUBIN, J. & JUDEX, S. 2016. Cytoskeletal Configuration Modulates Mechanically Induced Changes in Mesenchymal Stem Cell Osteogenesis, Morphology, and Stiffness. *Sci Rep,* 6**,** 34791.

POOLE, C. A., ZHANG, Z.-J. & ROSS, J. M. 2001. The differential distribution of acetylated and detyrosinated alpha-tubulin in the microtubular cytoskeleton and primary cilia of hyaline cartilage chondrocytes. *Journal of Anatomy,* 199**,** 393-405.

POSFAI, E., PETROPOULOS, S., DE BARROS, F. R., SCHELL, J. P., JURISICA, I., SANDBERG, R., LANNER, F. & ROSSANT, J. 2017. Position- and Hippo signaling-dependent plasticity during lineage segregation in the early mouse embryo. *Elife,* 6.

POULET, B. 2017. Models to define the stages of articular cartilage degradation in osteoarthritis development. *Int J Exp Pathol,* 98**,** 120-126.

PRASKOVA, M., XIA, F. & AVRUCH, J. 2008. MOBKL1A/MOBKL1B phosphorylation by MST1 and MST2 inhibits cell proliferation. *Curr Biol,* 18**,** 311-21.

PROVENZANO, P. P. & KEELY, P. J. 2011. Mechanical signaling through the cytoskeleton regulates cell proliferation by coordinated focal adhesion and Rho GTPase signaling. *J Cell Sci,* 124**,** 1195-205.

PUNNETT, H. H., KISTENMACHER, M. L., VALDES-DAPENA, M. & ELLISON, R. T., JR. 1974. Syndrome of ankylosis, facial anomalies, and pulmonary hypoplasia. *J Pediatr,* 85**,** 375-7.

R CORE TEAM 2017. R: A language and environment for statistical computing. R Foundation for Statistical Computing. Vienna, Austria.

RAI, V., DILISIO, M. F., DIETZ, N. E. & AGRAWAL, D. K. 2017. Recent strategies in cartilage repair: A systemic review of the scaffold development and tissue engineering. *J Biomed Mater Res A,* 105**,** 2343-2354.

RASPOPOVIC, J., MARCON, L., RUSSO, L. & SHARPE, J. 2014. Digit patterning is controlled by a Bmp-Sox9-Wnt Turing network modulated by morphogen gradients. *Science,* 345**,** 566-570.

RAUSKOLB, C., SUN, S., SUN, G., PAN, Y. & IRVINE, KENNETH D. 2014. Cytoskeletal Tension Inhibits Hippo Signaling through an Ajuba-Warts Complex. *Cell,* 158**,** 143-156.

RAY, A., SINGH, P. N., SOHASKEY, M. L., HARLAND, R. M. & BANDYOPADHYAY, A. 2015. Precise spatial restriction of BMP signaling is essential for articular cartilage differentiation. *Development,* 142**,** 1169-79.

REGINENSI, A., SCOTT, R. P., GREGORIEFF, A., BAGHERIE-LACHIDAN, M., CHUNG, C., LIM, D. S., PAWSON, T., WRANA, J. & MCNEILL, H. 2013. Yap- and Cdc42-dependent nephrogenesis and morphogenesis during mouse kidney development. *PLoS Genet,* 9**,** e1003380.

RESNICK, A. & HOPFER, U. 2007. Force-response considerations in ciliary mechanosensation. *Biophys J,* 93.

RIDDLE, R. C., TAYLOR, A. F., GENETOS, D. C. & DONAHUE, H. J. 2006. MAP kinase and calcium signaling mediate fluid flow-induced human mesenchymal stem cell proliferation. *Am J Physiol Cell Physiol,* 290**,** C776-84.

RIX, S., CALMONT, A., SCAMBLER, P. J. & BEALES, P. L. 2011. An Ift80 mouse model of short rib polydactyly syndromes shows defects in hedgehog signalling without loss or malformation of cilia. *Human Molecular Genetics,* 20**,** 1306-1314.

ROBINSON, J. A., CHATTERJEE-KISHORE, M., YAWORSKY, P. J., CULLEN, D. M., ZHAO, W., LI, C., KHARODE, Y., SAUTER, L., BABIJ, P., BROWN, E. L., HILL, A. A., AKHTER, M. P., JOHNSON, M. L., RECKER, R. R., KOMM, B. S. & BEX, F. J. 2006. Wnt/beta-catenin signaling is a normal physiological response to mechanical loading in bone. *J Biol Chem,* 281**,** 31720-8.

ROCK, R., SCHRAUTH, S. & GESSLER, M. 2005. Expression of mouse dchs1, fjx1, and fat-j suggests conservation of the planar cell polarity pathway identified in Drosophila. *Dev Dyn,* 234**,** 747-55.

RODDY, K. A., KELLY, G. M., VAN ES, M. H., MURPHY, P. & PRENDERGAST, P. J. 2011a. Dynamic patterns of mechanical stimulation co-localise with growth and cell proliferation during morphogenesis in the avian embryonic knee joint. *J Biomech,* 44**,** 143-9.

RODDY, K. A., NOWLAN, N. C., PRENDERGAST, P. J. & MURPHY, P. 2009. 3D representation of the developing chick knee joint: a novel approach integrating multiple components. *J Anat,* 214**,** 374-87.

RODDY, K. A., PRENDERGAST, P. J. & MURPHY, P. 2011b. Mechanical influences on morphogenesis of the knee joint revealed through morphological, molecular and computational analysis of immobilised embryos. *PLoS One,* 6**,** e17526:1-14.

RODRIGUEZ, J. I., GARCIA-ALIX, A., PALACIOS, J. & PANIAGUA, R. 1988a. Changes in the long bones due to fetal immobility caused by neuromuscular disease. A radiographic and histological study. *J Bone Joint Surg Am,* 70**,** 1052-60.

RODRIGUEZ, J. I., PALACIOS, J., GARCIA-ALIX, A., PASTOR, I. & PANIAGUA, R. 1988b. Effects of immobilization on fetal bone development. A

morphometric study in newborns with congenital neuromuscular diseases with intrauterine onset. *Calcif Tissue Int,* 43**,** 335-9.

RODRIGUEZ, J. I., PALACIOS, J., RUIZ, A., SANCHEZ, M., ALVAREZ, I. & DEMIGUEL, E. 1992. Morphological changes in long bone development in fetal akinesia deformation sequence: an experimental study in curarized rat fetuses. *Teratology,* 45**,** 213-21.

RODRIGUEZ-ESTEBAN, C., TSUKUI, T., YONEI, S., MAGALLON, J., TAMURA, K. & IZPISUA BELMONTE, J. C. 1999. The T-box genes Tbx4 and Tbx5 regulate limb outgrowth and identity. *Nature,* 398**,** 814-8.

ROHATGI, R., MILENKOVIC, L., CORCORAN, R. B. & SCOTT, M. P. 2009. Hedgehog signal transduction by Smoothened: Pharmacologic evidence for a 2-step activation process. *Proceedings of the National Academy of Sciences,* 106**,** 3196-3201.

ROHATGI, R., MILENKOVIC, L. & SCOTT, M. P. 2007. Patched1 regulates hedgehog signaling at the primary cilium. *Science,* 317.

ROHATGI, R. & SNELL, W. J. 2010. The Ciliary Membrane. *Current opinion in cell biology,* 22**,** 541-546.

ROLFE, R., RODDY, K. & MURPHY, P. 2013. Mechanical regulation of skeletal development. *Curr Osteoporos Rep,* 11**,** 107-16.

ROLFE, R. A., BEZER, J. H., KIM, T., ZAIDON, A. Z., OYEN, M. L., IATRIDIS, J. C. & NOWLAN, N. C. 2017. Abnormal fetal muscle forces result in defects in spinal curvature and alterations in vertebral segmentation and shape. *J Orthop Res,* 35**,** 2135-2144.

ROLFE, R. A., NOWLAN, N. C., KENNY, E. M., CORMICAN, P., MORRIS, D. W., PRENDERGAST, P. J., KELLY, D. & MURPHY, P. 2014. Identification of mechanosensitive genes during skeletal development: alteration of genes associated with cytoskeletal rearrangement and cell signalling pathways. *BMC Genomics,* 15**,** 48.

ROSS, T. D., COON, B. G., YUN, S., BAEYENS, N., TANAKA, K., OUYANG, M. & SCHWARTZ, M. A. 2013. Integrins in mechanotransduction. *Curr Opin Cell Biol,* 25**,** 613-8.

ROT-NIKCEVIC, I., REDDY, T., DOWNING, K. J., BELLIVEAU, A. C., HALLGRIMSSON, B., HALL, B. K. & KABLAR, B. 2006. Myf5-/- :MyoD-/- amyogenic fetuses reveal the importance of early contraction and static loading by striated muscle in mouse skeletogenesis. *Dev Genes Evol,* 216**,** 1-9.

RUANO-GIL, D., NARDI-VILARDAGA, J. & TEIXIDOR-JOHE, A. 1985. Embryonal hypermobility and articular development. *Acta Anat (Basel),* 123**,** 90-2.

RUANO-GIL, D., NARDI-VILARDAGA, J. & TEJEDO-MATEU, A. 1978. Influence of extrinsic factors on the development of the articular system. *Acta Anat (Basel),* 101**,** 36-44.

RUBIN, C., JUDEX, S. & QIN, Y. X. 2006. Low-level mechanical signals and their potential as a non-pharmacological intervention for osteoporosis. *Age Ageing,* 35 Suppl 2**,** ii32-ii36.

RUDNICKI, J. A. & BROWN, A. M. 1997. Inhibition of chondrogenesis by Wnt gene expression in vivo and in vitro. *Dev Biol,* 185**,** 104-18.

RUDNICKI, M. A., SCHNEGELSBERG, P. N., STEAD, R. H., BRAUN, T., ARNOLD, H. H. & JAENISCH, R. 1993. MyoD or Myf-5 is required for the formation of skeletal muscle. *Cell,* 75**,** 1351-9.

RUHLEN, R. & MARBERRY, K. 2014. The chondrocyte primary cilium. *Osteoarthritis Cartilage,* 22**,** 1071-6.

RUIZ-PEREZ, V. L., BLAIR, H. J., RODRIGUEZ-ANDRES, M. E., BLANCO, M. J., WILSON, A., LIU, Y.-N., MILES, C., PETERS, H. & GOODSHIP, J. A. 2007. Evc is a positive mediator of Ihh-regulated bone growth that localises at the base of chondrocyte cilia. *Development,* 134**,** 2903.

RUIZ-PEREZ, V. L. & GOODSHIP, J. A. 2009. Ellis-van Creveld syndrome and Weyers acrodental dysostosis are caused by cilia-mediated diminished response to hedgehog ligands. *Am J Med Genet C Semin Med Genet,* 151c**,** 341-51.

RYAN, J. A., EISNER, E. A., DURAINE, G., YOU, Z. & REDDI, A. H. 2009. Mechanical compression of articular cartilage induces chondrocyte proliferation and inhibits proteoglycan synthesis by activation of the ERK pathway: implications for tissue engineering and regenerative medicine. *J Tissue Eng Regen Med,* 3**,** 107-16.

RYU, J. H. 2002. Regulation of the chondrocyte phenotype by beta-catenin. *Development,* 129**,** 5541-5550.

SAAL, H. M., PROWS, C. A., GUERREIRO, I., DONLIN, M., KNUDSON, L., SUND, K. L., CHANG, C.-F., BRUGMANN, S. A. & STOTTMANN, R. W. 2015. A mutation in FRIZZLED2 impairs Wnt signaling and causes autosomal dominant omodysplasia. *Human Molecular Genetics,* 24**,** 3399-3409.

SABURI, S., HESTER, I., FISCHER, E., PONTOGLIO, M., EREMINA, V., GESSLER, M., QUAGGIN, S. E., HARRISON, R., MOUNT, R. & MCNEILL, H. 2008. Loss of Fat4 disrupts PCP signaling and oriented cell division and leads to cystic kidney disease. *Nat Genet,* 40**,** 1010-5.

SAHA, A., ROLFE, R., CARROLL, S., KELLY, D. J. & MURPHY, P. 2016. Chondrogenesis of embryonic limb bud cells in micromass culture progresses rapidly to hypertrophy and is modulated by hydrostatic pressure. *Cell Tissue Res*.

SALVA, J. E. & MERRILL, A. E. 2017. Signaling networks in joint development. *Dev Dyn,* 246**,** 262-274.

SARMA, S., KERWIN, J., PUELLES, L., SCOTT, M., STRACHAN, T., FENG, G., SHARPE, J., DAVIDSON, D., BALDOCK, R. & LINDSAY, S. 2005. 3D modelling, gene expression mapping and post-mapping image analysis in the developing human brain. *Brain Research Bulletin,* 66**,** 449-453.

SATO, K., YOMOGIDA, K., WADA, T., YORIHUZI, T., NISHIMUNE, Y., HOSOKAWA, N. & NAGATA, K. 2002. Type XXVI collagen, a new member of the collagen family, is specifically expressed in the testis and ovary. *J Biol Chem,* 277**,** 37678-84.

SATO, Y., KASAI, T., NAKAGAWA, S., TANABE, K., WATANABE, T., KAWAKAMI, K. & TAKAHASHI, Y. 2007. Stable integration and conditional expression of electroporated transgenes in chicken embryos. *Developmental Biology,* 305**,** 616-624.

SAY, B., BARBER, N. D. & LEICHTMAN, L. G. 1979. Ankylosis, facial anomalies, and pulmonary hypoplasia syndrome. *Am J Dis Child,* 133**,** 1196-7.

SCHARSTUHL, A., SCHEWE, B., BENZ, K., GAISSMAIER, C., BUHRING, H. J. & STOOP, R. 2007. Chondrogenic potential of human adult mesenchymal stem cells is independent of age or osteoarthritis etiology. *Stem Cells,* 25**,** 3244-51.

SCHINDELIN, J., ARGANDA-CARRERAS, I., FRISE, E., KAYNIG, V., LONGAIR, M., PIETZSCH, T., PREIBISCH, S., RUEDEN, C., SAALFELD, S., SCHMID, B., TINEVEZ, J. Y., WHITE, D. J., HARTENSTEIN, V., ELICEIRI, K., TOMANCAK, P. & CARDONA, A. 2012. Fiji: an open-source platform for biological-image analysis. *Nat Methods,* 9**,** 676-82.

SCHMID, T. M. & LINSENMAYER, T. F. 1985. Immunohistochemical localization of short chain cartilage collagen (type X) in avian tissues. *J Cell Biol,* 100**,** 598-605.

SCHNEIDER, C. A., RASBAND, W. S. & ELICEIRI, K. W. 2012. NIH Image to ImageJ: 25 years of image analysis. *Nat Methods,* 9**,** 671-5.

SCHOMANN, T., QUNNEIS, F., WIDERA, D., KALTSCHMIDT, C. & KALTSCHMIDT, B. 2013. Improved method for ex ovo-cultivation of developing chicken embryos for human stem cell xenografts. *Stem Cells Int,* 2013**,** 960958.

SCHUMANN, D., KUJAT, R., NERLICH, M. & ANGELE, P. 2006. Mechanobiological conditioning of stem cells for cartilage tissue engineering. *Bio-Medical Materials and Engineering,* 16**,** S37-S52.

SCHUURMAN, W., KLEIN, T. J., DHERT, W. J., VAN WEEREN, P. R., HUTMACHER, D. W. & MALDA, J. 2015. Cartilage regeneration using zonal chondrocyte subpopulations: a promising approach or an overcomplicated strategy? *J Tissue Eng Regen Med,* 9**,** 669-78.

SCOTTI, C., WIRZ, D., WOLF, F., SCHAEFER, D. J., BURGIN, V., DANIELS, A. U., VALDERRABANO, V., CANDRIAN, C., JAKOB, M., MARTIN, I. & BARBERO, A. 2010. Engineering human cell-based, functionally integrated osteochondral grafts by biological bonding of engineered cartilage tissues to bony scaffolds. *Biomaterials,* 31**,** 2252-9.

SEEMANN, P., SCHWAPPACHER, R., KJAER, K. W., KRAKOW, D., LEHMANN, K., DAWSON, K., STRICKER, S., POHL, J., PLOGER, F., STAUB, E., NICKEL, J., SEBALD, W., KNAUS, P. & MUNDLOS, S. 2005. Activating and deactivating mutations in the receptor interaction site of GDF5 cause symphalangism or brachydactyly type A2. *J Clin Invest,* 115**,** 2373-81.

SEKIYA, I., TSUJI, K., KOOPMAN, P., WATANABE, H., YAMADA, Y., SHINOMIYA, K., NIFUJI, A. & NODA, M. 2000. SOX9 enhances aggrecan gene promoter/enhancer activity and is up-regulated by retinoic acid in a cartilage-derived cell line, TC6. *J Biol Chem,* 275**,** 10738-44.

SELA-DONENFELD, D. & KALCHEIM, C. 2002. Localized BMP4-noggin interactions generate the dynamic patterning of noggin expression in somites. *Dev Biol,* 246**,** 311-28.

SEN, M., LAUTERBACH, K., EL-GABALAWY, H., FIRESTEIN, G. S., CORR, M. & CARSON, D. A. 2000. Expression and function of wingless and frizzled homologs in rheumatoid arthritis. *Proc Natl Acad Sci U S A,* 97**,** 2791-6.

SERRA, R., JOHNSON, M., FILVAROFF, E. H., LABORDE, J., SHEEHAN, D. M., DERYNCK, R. & MOSES, H. L. 1997. Expression of a truncated, kinase-defective TGF-beta type II receptor in mouse skeletal tissue promotes terminal chondrocyte differentiation and osteoarthritis. *J Cell Biol,* 139**,** 541-52.

SHANG, J., LIU, H., LI, J. & ZHOU, Y. 2014. Roles of hypoxia during the chondrogenic differentiation of mesenchymal stem cells. *Curr Stem Cell Res Ther,* 9**,** 141-7.

SHARIR, A., STERN, T., ROT, C., SHAHAR, R. & ZELZER, E. 2011. Muscle force regulates bone shaping for optimal load-bearing capacity during embryogenesis. *Development,* 138**,** 3247-59.

SHARPE, J., AHLGREN, U., PERRY, P., HILL, B., ROSS, A., HECKSHER-SØRENSEN, J., BALDOCK, R. & DAVIDSON, D. 2002. Optical Projection Tomography as a Tool for 3D Microscopy and Gene Expression Studies. *Science,* 296**,** 541.

SHEA, C. A., ROLFE, R. A. & MURPHY, P. 2015. The importance of foetal movement for co-ordinated cartilage and bone development in utero : clinical consequences and potential for therapy. *Bone Joint Res,* 4**,** 105-16.

SHIH, Y. R., TSENG, K. F., LAI, H. Y., LIN, C. H. & LEE, O. K. 2011. Matrix stiffness regulation of integrin-mediated mechanotransduction during osteogenic differentiation of human mesenchymal stem cells. *J Bone Miner Res,* 26**,** 730-8.

SHINOHARA, H., NAORA, H., HASHIMOTO, R., HATTA, T. & TANAKA, O. 1990. Development of the innervation pattern in the upper limb of staged human embryos. *Acta Anat (Basel),* 138**,** 265-9.

SHU, Z. & DENG, W. M. 2017. Differential Regulation of Cyclin E by Yorkie-Scalloped Signaling in Organ Development. *G3 (Bethesda),* 7**,** 1049-1060.

SHWARTZ, Y., FARKAS, Z., STERN, T., ASZODI, A. & ZELZER, E. 2012. Muscle contraction controls skeletal morphogenesis through regulation of chondrocyte convergent extension. *Dev Biol,* 370**,** 154-63.

SHWARTZ, Y., VIUKOV, S., KRIEF, S. & ZELZER, E. 2016. Joint Development Involves a Continuous Influx of Gdf5-Positive Cells. *Cell Reports,* 15**,** 2577-2587.

SINGH, P. N., RAY, A., AZAD, K. & BANDYOPADHYAY, A. 2016. A comprehensive mRNA expression analysis of developing chicken articular cartilage. *Gene Expr Patterns,* 20**,** 22-31.

SINGH, P. N. P., SHEA, C., SONKER, S. K., ROLFE, R., RAY, A., KUMAR, S., GUPTA, P., MURPHY, P. & BANDYOPADHYAY, A. 2018. Precise spatial

restriction of BMP signaling in developing joints is perturbed upon loss of embryo movement. *Development*.

SINGLA, V. & REITER, J. F. 2006. The primary cilium as the cell's antenna: signaling at a sensory organelle. *Science,* 313**,** 629-33.

SKALSKY, A. J. & MCDONALD, C. M. 2012. Prevention and Management of Limb Contractures in Neuromuscular Diseases. *Physical medicine and rehabilitation clinics of North America,* 23**,** 675-687.

SOEDA, T., DENG, J. M., DE CROMBRUGGHE, B., BEHRINGER, R. R., NAKAMURA, T. & AKIYAMA, H. 2010. Sox9-expressing precursors are the cellular origin of the cruciate ligament of the knee joint and the limb tendons. *Genesis,* 48**,** 635-44.

SONG, B., HAYCRAFT, C. J., SEO, H.-S., YODER, B. K. & SERRA, R. 2007a. Development of the post-natal growth plate requires intraflagellar transport proteins. *Developmental biology,* 305**,** 202-216.

SONG, J. J., ASWAD, R., KANAAN, R. A., RICO, M. C., OWEN, T. A., BARBE, M. F., SAFADI, F. F. & POPOFF, S. N. 2007b. Connective tissue growth factor (CTGF) acts as a downstream mediator of TGF-beta1 to induce mesenchymal cell condensation. *J Cell Physiol,* 210**,** 398-410.

SPASIC, M. & JACOBS, C. R. 2017a. Lengthening primary cilia enhances cellular mechanosensitivity. *Eur Cell Mater,* 33**,** 158-168.

SPASIC, M. & JACOBS, C. R. 2017b. Primary cilia: Cell and molecular mechanosensors directing whole tissue function. *Semin Cell Dev Biol*.

SPATER, D., HILL, T. P., O'SULLIVAN R, J., GRUBER, M., CONNER, D. A. & HARTMANN, C. 2006. Wnt9a signaling is required for joint integrity and regulation of Ihh during chondrogenesis. *Development,* 133**,** 3039-49.

SPENCER, H. T., BOWEN, R. E., CAPUTO, K., GREEN, T. A. & LAWRENCE, J. F. 2010. Bone mineral density and functional measures in patients with arthrogryposis. *J Pediatr Orthop,* 30**,** 514-8.

SPYROPOULOU, A., KARAMESINIS, K. & BASDRA, E. K. 2015. Mechanotransduction pathways in bone pathobiology. *Biochim Biophys Acta,* 1852**,** 1700-8.

ST-JACQUES, B., HAMMERSCHMIDT, M. & MCMAHON, A. P. 1999. Indian hedgehog signaling regulates proliferation and differentiation of chondrocytes and is essential for bone formation. *Genes Dev,* 13**,** 2072-86.

STALNAKER, K. A. & POSKEY, G. A. 2016. Osteopenia of Prematurity: Does Physical Activity Improve Bone Mineralization in Preterm Infants? *Neonatal Netw,* 35**,** 95-104.

STAVENSCHI, E., LABOUR, M. N. & HOEY, D. A. 2017. Oscillatory fluid flow induces the osteogenic lineage commitment of mesenchymal stem cells: The effect of shear stress magnitude, frequency, and duration. *J Biomech,* 55**,** 99-106.

STAVEROSKY, J. A., PRYCE, B. A., WATSON, S. S. & SCHWEITZER, R. 2009. Tubulin polymerization-promoting protein family member 3, Tppp3, is a

specific marker of the differentiating tendon sheath and synovial joints. *Dev Dyn,* 238**,** 685-92.

STEWARD, A. J. & KELLY, D. J. 2015. Mechanical regulation of mesenchymal stem cell differentiation. *J Anat,* 227**,** 717-31.

STEWARD, A. J., WAGNER, D. R. & KELLY, D. J. 2014. Exploring the roles of integrin binding and cytoskeletal reorganization during mesenchymal stem cell mechanotransduction in soft and stiff hydrogels subjected to dynamic compression. *J Mech Behav Biomed Mater,* 38**,** 174-82.

STODDART, M. J., ETTINGER, L. & HAUSELMANN, H. J. 2006. Enhanced matrix synthesis in de novo, scaffold free cartilage-like tissue subjected to compression and shear. *Biotechnol Bioeng,* 95**,** 1043-51.

STORM, E. E. & KINGSLEY, D. M. 1999. GDF5 coordinates bone and joint formation during digit development. *Developmental Biology,* 209**,** 11-27.

SUMANASINGHE, R. D., BERNACKI, S. H. & LOBOA, E. G. 2006. Osteogenic differentiation of human mesenchymal stem cells in collagen matrices: effect of uniaxial cyclic tensile strain on bone morphogenetic protein (BMP-2) mRNA expression. *Tissue Eng,* 12**,** 3459-65.

SUMMERHURST, K., STARK, M., SHARPE, J., DAVIDSON, D. & MURPHY, P. 2008. 3D representation of Wnt and Frizzled gene expression patterns in the mouse embryo at embryonic day 11.5 (Ts19). *Gene Expr Patterns,* 8**,** 331-48.

SUN, C., DE MELLO, V., MOHAMED, A., ORTUSTE QUIROGA, H. P., GARCIA-MUNOZ, A., AL BLOSHI, A., TREMBLAY, A. M., VON KRIEGSHEIM, A., COLLIE-DUGUID, E., VARGESSON, N., MATALLANAS, D., WACKERHAGE, H. & ZAMMIT, P. S. 2017. Common and Distinctive Functions of the Hippo Effectors Taz and Yap in Skeletal Muscle Stem Cell Function. *Stem Cells (Dayton, Ohio),* 35**,** 1958-1972.

SUN, X., LEWANDOSKI, M., MEYERS, E. N., LIU, Y. H., MAXSON, R. E., JR. & MARTIN, G. R. 2000. Conditional inactivation of Fgf4 reveals complexity of signalling during limb bud development. *Nat Genet,* 25**,** 83-6.

SUZUE, T. & SHINODA, Y. 1999. Highly reproducible spatiotemporal patterns of mammalian embryonic movements at the developmental stage. *European Journal of Neuroscience,* 11**,** 2697-2710.

SUZUKI, T. & OGURA, T. 2008. Congenic method in the chick limb buds by electroporation. *Dev Growth Differ,* 50**,** 459-65.

TAKACS, R., MATTA, C., SOMOGYI, C., JUHASZ, T. & ZAKANY, R. 2013. Comparative analysis of osteogenic/chondrogenic differentiation potential in primary limb bud-derived and C3H10T1/2 cell line-based mouse micromass cultures. *Int J Mol Sci,* 14**,** 16141-67.

TAKAHASHI, I., NUCKOLLS, G. H., TAKAHASHI, K., TANAKA, O., SEMBA, I., DASHNER, R., SHUM, L. & SLAVKIN, H. C. 1998. Compressive force promotes sox9, type II collagen and aggrecan and inhibits IL-1beta expression resulting in chondrogenesis in mouse embryonic limb bud mesenchymal cells. *J Cell Sci,* 111 (Pt 14)**,** 2067-76.

TANG, X., FAN, L., PEI, M., ZENG, L. & GE, Z. 2015. Evolving concepts of chondrogenic differentiation: history, state-of-the-art and future perspectives. *Eur Cell Mater,* 30**,** 12-27.

TANOUE, T. & TAKEICHI, M. 2005. New insights into Fat cadherins. *Journal of Cell Science,* 118**,** 2347.

THEILER, K. 1989. *The House Mouse: Atlas of Embryonic Development,* New York, Springer-Verlag.

THOMPSON, B. J. & COHEN, S. M. 2006. The Hippo pathway regulates the bantam microRNA to control cell proliferation and apoptosis in Drosophila. *Cell,* 126**,** 767-74.

THOMPSON, C. L., CHAPPLE, J. P. & KNIGHT, M. M. 2014. Primary cilia disassembly down-regulates mechanosensitive hedgehog signalling: a feedback mechanism controlling ADAMTS-5 expression in chondrocytes. *Osteoarthritis Cartilage,* 22**,** 490-8.

THOMPSON, C. L., PLANT, J. C., WANN, A. K., BISHOP, C. L., NOVAK, P., MITCHISON, H. M., BEALES, P. L., CHAPPLE, J. P. & KNIGHT, M. M. 2017. Chondrocyte expansion is associated with loss of primary cilia and disrupted hedgehog signalling. *Eur Cell Mater,* 34**,** 128-141.

THORPE, S. D., BUCKLEY, C. T., VINARDELL, T., O'BRIEN, F. J., CAMPBELL, V. A. & KELLY, D. J. 2008. Dynamic compression can inhibit chondrogenesis of mesenchymal stem cells. *Biochem Biophys Res Commun,* 377**,** 458-62.

TICKLE, C. 2015. How the embryo makes a limb: determination, polarity and identity. *J Anat,* 227**,** 418-30.

TOOLE, B. P., JACKSON, G. & GROSS, J. 1972. Hyaluronate in morphogenesis: inhibition of chondrogenesis in vitro. *Proc Natl Acad Sci U S A,* 69**,** 1384-6.

TSUMAKI, N., NAKASE, T., MIYAJI, T., KAKIUCHI, M., KIMURA, T., OCHI, T. & YOSHIKAWA, H. 2002. Bone morphogenetic protein signals are required for cartilage formation and differently regulate joint development during skeletogenesis. *J Bone Miner Res,* 17**,** 898-906.

TUMMALA, P., ARNSDORF, E. J. & JACOBS, C. R. 2010. The Role of Primary Cilia in Mesenchymal Stem Cell Differentiation: A Pivotal Switch in Guiding Lineage Commitment. *Cell Mol Bioeng,* 3**,** 207-212.

TURING, A. M. 1990. The chemical basis of morphogenesis. 1953. *Bull Math Biol,* 52**,** 153-97; discussion 119-52.

UDDIN, S. M. & QIN, Y. X. 2013. Enhancement of osteogenic differentiation and proliferation in human mesenchymal stem cells by a modified low intensity ultrasound stimulation under simulated microgravity. *PLoS One,* 8**,** e73914.

UEMURA, M., NAGASAWA, A. & TERAI, K. 2016. Yap/Taz transcriptional activity in endothelial cells promotes intramembranous ossification via the BMP pathway. *Sci Rep,* 6**,** 27473.

VAN AMERONGEN, R., FUERER, C., MIZUTANI, M. & NUSSE, R. 2012. Wnt5a can both activate and repress Wnt/beta-catenin signaling during mouse embryonic development. *Dev Biol,* 369**,** 101-14.

VAN DER MEULEN, T., SCHIPPER, H., VAN LEEUWEN, J. L. & KRANENBARG, S. 2005. Effects of decreased muscle activity on developing axial musculature in nicb107 mutant zebrafish (Danio rerio). *J Exp Biol,* 208**,** 3675-87.

VAN GIJLSWIJK, R. P., ZIJLMANS, H. J., WIEGANT, J., BOBROW, M. N., ERICKSON, T. J., ADLER, K. E., TANKE, H. J. & RAAP, A. K. 1997. Fluorochrome-labeled tyramides: use in immunocytochemistry and fluorescence in situ hybridization. *J Histochem Cytochem,* 45**,** 375-82.

VANDERMAN, K. S., TREMBLAY, M., ZHU, W., SHIMOJO, M., MIENALTOWSKI, M. J., COLEMAN, S. J. & MACLEOD, J. N. 2011. Brother of CDO (BOC) expression in equine articular cartilage. *Osteoarthritis and Cartilage,* 19**,** 435-438.

VANWANSEELE, B., LUCCHINETTI, E. & STUSSI, E. 2002. The effects of immobilization on the characteristics of articular cartilage: current concepts and future directions. *Osteoarthritis Cartilage,* 10**,** 408-19.

VARELAS, X. 2014. The Hippo pathway effectors TAZ and YAP in development, homeostasis and disease. *Development,* 141**,** 1614-26.

VAUGHAN, T. J., MULLEN, C. A., VERBRUGGEN, S. W. & MCNAMARA, L. M. 2015. Bone cell mechanosensation of fluid flow stimulation: a fluid-structure interaction model characterising the role integrin attachments and primary cilia. *Biomech Model Mechanobiol,* 14**,** 703-18.

VELAND, I. R., LINDBAEK, L. & CHRISTENSEN, S. T. 2014. Linking the Primary Cilium to Cell Migration in Tissue Repair and Brain Development. *Bioscience,* 64**,** 1115-1125.

VERONICK, J. A., ASSANAH, F., PISCOPO, N., KUTES, Y., VYAS, V., NAIR, L. S., HUEY, B. D. & KHAN, Y. 2017. Mechanically Loading Cell/Hydrogel Constructs with Low-Intensity Pulsed Ultrasound for Bone Repair. *Tissue Eng Part A*.

VIEIRA, O. V., GAUS, K., VERKADE, P., FULLEKRUG, J., VAZ, W. L. & SIMONS, K. 2006. FAPP2, cilium formation, and compartmentalization of the apical membrane in polarized Madin-Darby canine kidney (MDCK) cells. *Proc Natl Acad Sci U S A,* 103**,** 18556-61.

VIERKOTTEN, J., DILDROP, R., PETERS, T., WANG, B. & RUTHER, U. 2007. Ftm is a novel basal body protein of cilia involved in Shh signalling. *Development,* 134**,** 2569-77.

VIGNOCHI, C. M., MIURA, E. & CANANI, L. H. 2008. Effects of motor physical therapy on bone mineralization in premature infants: a randomized controlled study. *J Perinatol,* 28**,** 624-631.

VINARDELL, T., ROLFE, R. A., BUCKLEY, C. T., MEYER, E. G., AHEARNE, M., MURPHY, P. & KELLY, D. J. 2012. Hydrostatic pressure acts to stabilise a chondrogenic phenotype in porcine joint tissue derived stem cells. *European Cells and Materials,* 23**,** 121-134.

VINCENTI, M. P. & BRINCKERHOFF, C. E. 2002. Transcriptional regulation of collagenase (MMP-1, MMP-13) genes in arthritis: integration of complex

signaling pathways for the recruitment of gene-specific transcription factors. *Arthritis Res,* 4**,** 157-64.

VOGAN, K. J., EPSTEIN, D. J., TRASLER, D. G. & GROS, P. 1993. The splotch-delayed (Spd) mouse mutant carries a point mutation within the paired box of the Pax-3 gene. *Genomics,* 17**,** 364-9.

VORTKAMP, A., LEE, K., LANSKE, B., SEGRE, G. V., KRONENBERG, H. M. & TABIN, C. J. 1996. Regulation of rate of cartilage differentiation by Indian hedgehog and PTH-related protein. *Science,* 273**,** 613-22.

VU, T. H., SHIPLEY, J. M., BERGERS, G., BERGER, J. E., HELMS, J. A., HANAHAN, D., SHAPIRO, S. D., SENIOR, R. M. & WERB, Z. 1998. MMP-9/gelatinase B is a key regulator of growth plate angiogenesis and apoptosis of hypertrophic chondrocytes. *Cell,* 93**,** 411-22.

WALTON, K. D., WHIDDEN, M., KOLTERUD, A., SHOFFNER, S. K., CZERWINSKI, M. J., KUSHWAHA, J., PARMAR, N., CHANDHRASEKHAR, D., FREDDO, A. M., SCHNELL, S. & GUMUCIO, D. L. 2016. Villification in the mouse: Bmp signals control intestinal villus patterning. *Development,* 143**,** 427-36.

WANG, J. & MARTIN, J. F. 2017. Hippo Pathway: An Emerging Regulator of Craniofacial and Dental Development. *J Dent Res,* 96**,** 1229-1237.

WANG, X., FREIRE VALLS, A., SCHERMANN, G., SHEN, Y., MOYA, I. M., CASTRO, L., URBAN, S., SOLECKI, G. M., WINKLER, F., RIEDEMANN, L., JAIN, R. K., MAZZONE, M., SCHMIDT, T., FISCHER, T., HALDER, G. & RUIZ DE ALMODOVAR, C. 2017. YAP/TAZ Orchestrate VEGF Signaling during Developmental Angiogenesis. *Dev Cell,* 42**,** 462-478.e7.

WANG, Y., MACKE, J. P., ABELLA, B. S., ANDREASSON, K., WORLEY, P., GILBERT, D. J., COPELAND, N. G., JENKINS, N. A. & NATHANS, J. 1996. A large family of putative transmembrane receptors homologous to the product of the Drosophila tissue polarity gene frizzled. *J Biol Chem,* 271**,** 4468-76.

WANG, Y.-K., SPÖRLE, R., PAPERNA, T., SCHUGHART, K. & FRANCKE, U. 1999. Characterization and Expression Pattern of thefrizzledGeneFzd9,the Mouse Homolog ofFZD9Which Is Deleted in Williams–Beuren Syndrome. *Genomics,* 57**,** 235-248.

WANG, Y. K., YU, X., COHEN, D. M., WOZNIAK, M. A., YANG, M. T., GAO, L., EYCKMANS, J. & CHEN, C. S. 2012. Bone morphogenetic protein-2-induced signaling and osteogenesis is regulated by cell shape, RhoA/ROCK, and cytoskeletal tension. *Stem Cells Dev,* 21**,** 1176-86.

WANN, K. T. & KNIGHT, M. M. 2012. Primary cilia elongation in response to interleukin-1 mediates the inflammatory response. *Cell Mol Life Sci,* 69.

WARD, D. F., JR., SALASZNYK, R. M., KLEES, R. F., BACKIEL, J., AGIUS, P., BENNETT, K., BOSKEY, A. & PLOPPER, G. E. 2007. Mechanical strain enhances extracellular matrix-induced gene focusing and promotes osteogenic differentiation of human mesenchymal stem cells through an extracellular-related kinase-dependent pathway. *Stem Cells Dev,* 16**,** 467-80.

WATANABE, H., YAMADA, Y. & KIMATA, K. 1998. Roles of aggrecan, a large chondroitin sulfate proteoglycan, in cartilage structure and function. *J Biochem,* 124**,** 687-93.

WEILER, H. A., FITZPATRICK-WONG, S. C., SCHELLENBERG, J. M., FAIR, D. E., MCCLOY, U. R., VEITCH, R. R., KOVACS, H. R. & SESHIA, M. M. 2006. Minimal enteral feeding within 3 d of birth in prematurely born infants with birth weight < or = 1200 g improves bone mass by term age. *Am J Clin Nutr,* 83**,** 155-62.

WIDELITZ, R. 2005. Wnt signaling through canonical and non-canonical pathways: recent progress. *Growth Factors,* 23**,** 111-6.

WILLECKE, M., HAMARATOGLU, F., KANGO-SINGH, M., UDAN, R., CHEN, C. L., TAO, C., ZHANG, X. & HALDER, G. 2006. The fat cadherin acts through the hippo tumor-suppressor pathway to regulate tissue size. *Curr Biol,* 16**,** 2090-100.

WILTINK, A., NIJWEIDE, P. J., OOSTERBAAN, W. A., HEKKENBERG, R. T. & HELDERS, P. J. 1995. Effect of therapeutic ultrasound on endochondral ossification. *Ultrasound Med Biol,* 21**,** 121-7.

WITTE, F., DOKAS, J., NEUENDORF, F., MUNDLOS, S. & STRICKER, S. 2009. Comprehensive expression analysis of all Wnt genes and their major secreted antagonists during mouse limb development and cartilage differentiation. *Gene Expr Patterns,* 9**,** 215-23.

WONG, M., KIREEVA, M. L., KOLESNIKOVA, T. V. & LAU, L. F. 1997. Cyr61, product of a growth factor-inducible immediate-early gene, regulates chondrogenesis in mouse limb bud mesenchymal cells. *Dev Biol,* 192**,** 492-508.

WONG, S. Y. & REITER, J. F. 2008. The primary cilium at the crossroads of mammalian hedgehog signaling. *Curr Top Dev Biol,* 85**,** 225-60.

WOODS, A., WANG, G. & BEIER, F. 2005. RhoA/ROCK signaling regulates Sox9 expression and actin organization during chondrogenesis. *J Biol Chem,* 280**,** 11626-34.

WOODS, A., WANG, G. & BEIER, F. 2007. Regulation of chondrocyte differentiation by the actin cytoskeleton and adhesive interactions. *J Cell Physiol,* 213**,** 1-8.

WU, D., MALDA, J., CRAWFORD, R. & XIAO, Y. 2007. Effects of hyperbaric oxygen on proliferation and differentiation of osteoblasts from human alveolar bone. *Connect Tissue Res,* 48**,** 206-13.

WU, M. Y. & HILL, C. S. 2009. Tgf-beta superfamily signaling in embryonic development and homeostasis. *Dev Cell,* 16**,** 329-43.

WU, Q. Q. & CHEN, Q. 2000. Mechanoregulation of chondrocyte proliferation, maturation, and hypertrophy: ion-channel dependent transduction of matrix deformation signals. *Exp Cell Res,* 256**,** 383-91.

WU, S., LIU, Y., ZHENG, Y., DONG, J. & PAN, D. 2008. The TEAD/TEF family protein Scalloped mediates transcriptional output of the Hippo growth-regulatory pathway. *Dev Cell,* 14**,** 388-98.

XIAO, L., CHEN, Y., JI, M. & DONG, J. 2011. KIBRA regulates the Hippo signaling activity via interactions with Lats kinases. *Journal of Biological Chemistry*.

XIAO, Z., ZHANG, S., MAHLIOS, J., ZHOU, G., MAGENHEIMER, B. S., GUO, D., DALLAS, S. L., MASER, R., CALVET, J. P., BONEWALD, L. & QUARLES, L. D. 2006. Cilia-like structures and polycystin-1 in osteoblasts/osteocytes and associated abnormalities in skeletogenesis and Runx2 expression. *J Biol Chem,* 281**,** 30884-95.

XU, X., WEINSTEIN, M., LI, C., NASKI, M., COHEN, R. I., ORNITZ, D. M., LEDER, P. & DENG, C. 1998. Fibroblast growth factor receptor 2 (FGFR2)-mediated reciprocal regulation loop between FGF8 and FGF10 is essential for limb induction. *Development,* 125**,** 753-65.

YAGI, R., CHEN, L. F., SHIGESADA, K., MURAKAMI, Y. & ITO, Y. 1999. A WW domain-containing yes-associated protein (YAP) is a novel transcriptional co-activator. *Embo j,* 18**,** 2551-62.

YAMAGUCHI, T. P., BRADLEY, A., MCMAHON, A. P. & JONES, S. 1999. A Wnt5a pathway underlies outgrowth of multiple structures in the vertebrate embryo. *Development,* 126**,** 1211-23.

YANG, X., CHEN, L., XU, X., LI, C., HUANG, C. & DENG, C. X. 2001. TGF-beta/Smad3 signals repress chondrocyte hypertrophic differentiation and are required for maintaining articular cartilage. *J Cell Biol,* 153**,** 35-46.

YANG, Y., TOPOL, L., LEE, H. & WU, J. 2003. Wnt5a and Wnt5b exhibit distinct activities in coordinating chondrocyte proliferation and differentiation. *Development,* 130**,** 1003-1015.

YIN, M. & PACIFICI, M. 2001. Vascular regression is required for mesenchymal condensation and chondrogenesis in the developing limb. *Dev Dyn,* 222**,** 522-33.

YOON, B. S. & LYONS, K. M. 2004. Multiple functions of BMPs in chondrogenesis. *J Cell Biochem,* 93**,** 93-103.

YOSHIDA, C. A., YAMAMOTO, H., FUJITA, T., FURUICHI, T., ITO, K., INOUE, K., YAMANA, K., ZANMA, A., TAKADA, K., ITO, Y. & KOMORI, T. 2004. Runx2 and Runx3 are essential for chondrocyte maturation, and Runx2 regulates limb growth through induction of Indian hedgehog. *Genes Dev,* 18**,** 952-63.

YU, F. X. & GUAN, K. L. 2013. The Hippo pathway: regulators and regulations. *Genes Dev,* 27**,** 355-71.

YU, F. X., ZHAO, B. & GUAN, K. L. 2015. Hippo Pathway in Organ Size Control, Tissue Homeostasis, and Cancer. *Cell,* 163**,** 811-28.

YU, H., LUI, Y. S., XIONG, S., LEONG, W. S., WEN, F., NURKAHFIANTO, H., RANA, S., LEONG, D. T., NG, K. W. & TAN, L. P. 2013a. Insights into the role of focal adhesion modulation in myogenic differentiation of human mesenchymal stem cells. *Stem Cells Dev,* 22**,** 136-47.

YU, H., SMALLWOOD, P. M., WANG, Y., VIDALTAMAYO, R., REED, R. & NATHANS, J. 2010. Frizzled 1 and frizzled 2 genes function in palate, ventricular septum and neural tube closure: general implications for tissue fusion processes. *Development,* 137**,** 3707-17.

YU, S., YERGES-ARMSTRONG, L. M., CHU, Y., ZMUDA, J. M. & ZHANG, Y. 2013b. E2F1 effects on osteoblast differentiation and mineralization are mediated through up-regulation of frizzled-1. *Bone,* 56**,** 234-41.

YUAN, X., SERRA, R. A. & YANG, S. 2015. Function and regulation of primary cilia and intraflagellar transport proteins in the skeleton. *Ann N Y Acad Sci,* 1335**,** 78-99.

YUAN, X. & YANG, S. 2015. Deletion of IFT80 Impairs Epiphyseal and Articular Cartilage Formation Due to Disruption of Chondrocyte Differentiation. *PLoS ONE,* 10**,** e0130618.

ZAKARIA, S., MAO, Y., KUTA, A., FERREIRA DE SOUSA, C., GAUFO, GARY O., MCNEILL, H., HINDGES, R., GUTHRIE, S., IRVINE, KENNETH D. & FRANCIS-WEST, PHILIPPA H. 2014. Regulation of Neuronal Migration by Dchs1-Fat4 Planar Cell Polarity. *Current Biology,* 24**,** 1620-1627.

ZAMAN, G., SAXON, L. K., SUNTERS, A., HILTON, H., UNDERHILL, P., WILLIAMS, D., PRICE, J. S. & LANYON, L. E. 2010. Loading-related regulation of gene expression in bone in the contexts of estrogen deficiency, lack of estrogen receptor alpha and disuse. *Bone,* 46**,** 628-42.

ZANCONATO, F., FORCATO, M., BATTILANA, G., AZZOLIN, L., QUARANTA, E., BODEGA, B., ROSATO, A., BICCIATO, S., CORDENONSI, M. & PICCOLO, S. 2015. Genome-wide association between YAP/TAZ/TEAD and AP-1 at enhancers drives oncogenic growth. *Nat Cell Biol,* 17**,** 1218-1227.

ZELLER, R., LOPEZ-RIOS, J. & ZUNIGA, A. 2009. Vertebrate limb bud development: moving towards integrative analysis of organogenesis. *Nat Rev Genet,* 10**,** 845-58.

ZHANG, H., LIU, C. Y., ZHA, Z. Y., ZHAO, B., YAO, J., ZHAO, S., XIONG, Y., LEI, Q. Y. & GUAN, K. L. 2009. TEAD transcription factors mediate the function of TAZ in cell growth and epithelial-mesenchymal transition. *J Biol Chem,* 284**,** 13355-62.

ZHANG, J., SMOLEN, G. A. & HABER, D. A. 2008. Negative regulation of YAP by LATS1 underscores evolutionary conservation of the Drosophila Hippo pathway. *Cancer Res,* 68**,** 2789-94.

ZHANG, L., SU, P., XU, C., YANG, J., YU, W. & HUANG, D. 2010a. Chondrogenic differentiation of human mesenchymal stem cells: a comparison between micromass and pellet culture systems. *Biotechnol Lett,* 32**,** 1339-46.

ZHANG, N., BAI, H., DAVID, K. K., DONG, J., ZHENG, Y., CAI, J., GIOVANNINI, M., LIU, P., ANDERS, R. A. & PAN, D. 2010b. The Merlin/NF2 Tumor Suppressor Functions through the YAP Oncoprotein to Regulate Tissue Homeostasis in Mammals. *Developmental Cell,* 19**,** 27-38.

ZHANG, Q., MURCIA, N. S., CHITTENDEN, L. R., RICHARDS, W. G., MICHAUD, E. J., WOYCHIK, R. P. & YODER, B. K. 2003. Loss of the Tg737 protein results in skeletal patterning defects. *Dev Dyn,* 227**,** 78-90.

ZHANG, T., WEN, F., WU, Y., GOH, G. S., GE, Z., TAN, L. P., HUI, J. H. & YANG, Z. 2015. Cross-talk between TGF-beta/SMAD and integrin signaling pathways

in regulating hypertrophy of mesenchymal stem cell chondrogenesis under deferral dynamic compression. *Biomaterials,* 38**,** 72-85.

ZHANG, W., GAO, Y., LI, P., SHI, Z., GUO, T., LI, F., HAN, X., FENG, Y., ZHENG, C., WANG, Z., LI, F., CHEN, H., ZHOU, Z., ZHANG, L. & JI, H. 2014. VGLL4 functions as a new tumor suppressor in lung cancer by negatively regulating the YAP-TEAD transcriptional complex. *Cell Res,* 24**,** 331-43.

ZHANG, Y., SHEU, T.-J., HOAK, D., SHEN, J., HILTON, M. J., ZUSCIK, M. J., JONASON, J. H. & O'KEEFE, R. J. 2016. CCN1 Regulates Chondrocyte Maturation and Cartilage Development. *Journal of bone and mineral research : the official journal of the American Society for Bone and Mineral Research,* 31**,** 549-559.

ZHAO, B., LEI, Q.-Y. & GUAN, K.-L. 2008a. The Hippo-YAP pathway: new connections between regulation of organ size and cancer. *Current Opinion in Cell Biology,* 20**,** 638-646.

ZHAO, B., LI, L., LEI, Q. & GUAN, K. L. 2010. The Hippo-YAP pathway in organ size control and tumorigenesis: an updated version. *Genes Dev,* 24**,** 862-74.

ZHAO, B., LI, L., LU, Q., WANG, L. H., LIU, C. Y., LEI, Q. & GUAN, K. L. 2011. Angiomotin is a novel Hippo pathway component that inhibits YAP oncoprotein. *Genes Dev,* 25**,** 51-63.

ZHAO, B., LI, L., WANG, L., WANG, C. Y., YU, J. & GUAN, K. L. 2012. Cell detachment activates the Hippo pathway via cytoskeleton reorganization to induce anoikis. *Genes Dev,* 26**,** 54-68.

ZHAO, B., WEI, X., LI, W., UDAN, R. S., YANG, Q., KIM, J., XIE, J., IKENOUE, T., YU, J., LI, L., ZHENG, P., YE, K., CHINNAIYAN, A., HALDER, G., LAI, Z. C. & GUAN, K. L. 2007. Inactivation of YAP oncoprotein by the Hippo pathway is involved in cell contact inhibition and tissue growth control. *Genes Dev,* 21**,** 2747-61.

ZHAO, B., YE, X., YU, J., LI, L., LI, W., LI, S., YU, J., LIN, J. D., WANG, C. Y., CHINNAIYAN, A. M., LAI, Z. C. & GUAN, K. L. 2008b. TEAD mediates YAP-dependent gene induction and growth control. *Genes Dev,* 22**,** 1962-71.

ZHONG, Z., ZYLSTRA-DIEGEL, C. R., SCHUMACHER, C. A., BAKER, J. J., CARPENTER, A. C., RAO, S., YAO, W., GUAN, M., HELMS, J. A., LANE, N. E., LANG, R. A. & WILLIAMS, B. O. 2012. Wntless functions in mature osteoblasts to regulate bone mass. *Proc Natl Acad Sci U S A,* 109**,** E2197-204.

ZHOU, D., CONRAD, C., XIA, F., PARK, J. S., PAYER, B., YIN, Y., LAUWERS, G. Y., THASLER, W., LEE, J. T., AVRUCH, J. & BARDEESY, N. 2009. Mst1 and Mst2 maintain hepatocyte quiescence and suppress hepatocellular carcinoma development through inactivation of the Yap1 oncogene. *Cancer Cell,* 16**,** 425-38.

ZHOU, Q., LI, L., ZHAO, B. & GUAN, K. L. 2015. The hippo pathway in heart development, regeneration, and diseases. *Circ Res,* 116**,** 1431-47.

ZHU, H., KAVSAK, P., ABDOLLAH, S., WRANA, J. L. & THOMSEN, G. H. 1999. A SMAD ubiquitin ligase targets the BMP pathway and affects embryonic pattern formation. *Nature,* 400**,** 687-93.

ZIMMERMAN, L. B., DE JESUS-ESCOBAR, J. M. & HARLAND, R. M. 1996. The Spemann organizer signal noggin binds and inactivates bone morphogenetic protein 4. *Cell,* 86**,** 599-606.

ZOU, H., WIESER, R., MASSAGUE, J. & NISWANDER, L. 1997. Distinct roles of type I bone morphogenetic protein receptors in the formation and differentiation of cartilage. *Genes Dev,* 11**,** 2191-203.

Appendix A. Supplementary gene expression data and plasmid maps.

Appendix Table A.1. RNA-Seq and microarray readout of Wnt ligands in TS23 wildtype vs. Spd mutant humeri and associated joints. Genes meeting both criteria of differential regulation and significance as defined are indicated in bold. Wnt16 was detected by multiple probes in the microarray; values from each probe are presented. NA: Not Applicable; ND: Not Detected.

Gene	RNA-Seq				Microarray			
	Read number		Fold	Adjusted	Normalized signal		Fold	Corrected
	Control	Mutant	Change	P-value	Control	Mutant	Change	P-value
Wnt1	2	1	0.3209	0.9700	8.6477	8.2186	-1.35	0.4964
Wnt2	42	167	3.9449	0.0036	1.8611	3.2205	2.57	0.3723
Wnt2b	53	184	3.5064	1.24E-06	1.5999	2.9715	2.59	0.2702
Wnt3	2	0	0.1989	0.9882	2.2532	1.9684	-1.22	0.8835
Wnt3a	0	0	NA	NA	ND	ND	NA	NA
Wnt4	135	273	2.0279	0.0101	7.6092	8.4185	1.75	0.2902
Wnt5a	1,873	3,650	1.9453	2.92E-05	10.5497	11.4779	1.90	0.1817
Wnt5b	454	514	1.1329	0.8914	11.8642	12.0195	1.11	0.7831
Wnt6	43	44	1.0210	1	6.7914	6.7086	-1.06	0.8851
Wnt7a	2	1	0.4293	1	2.0763	2.0039	-1.05	0.9716
Wnt7b	8	16	2	0.5703	3.8666	3.8229	-1.03	0.9723
Wnt8a	0	0	NA	NA	ND	ND	NA	NA
Wnt8b	1	1	0.7170	1	ND	ND	NA	NA
Wnt9a	475	535	1.1251	0.9911	9.2592	9.6881	1.35	0.4924
Wnt9b	1	0	0.2073	1	3.1384	3.4842	1.27	0.9030
Wnt10a	1	1	2.0420	1	4.1481	2.9984	-2.22	0.6668
Wnt10b	40	23	0.5743	0.4385	5.2173	4.6629	-1.47	0.5093
Wnt11	357	505	1.4142	0.4005	8.6816	9.2333	1.47	0.0233
Wnt16	19	59	3.0738	0.0162	3.4619	4.6988	2.36	0.6015
					4.3593	4.7530	1.31	0.4948

Appendix Table A.2. Table 3.3. RNA-Seq and microarray readout of Fzd receptors in TS23 wildtype vs. Spd mutant humeri and associated joints. Several genes (Fzd2, 5, 7) were detected by multiple probes in the microarray; values from each probe are presented.

Gene	RNA-Seq				Microarray			
	Read number		Fold Change	Adjusted P-value	Normalized signal		Fold Change	Corrected P-value
	Control	Mutant			Control	Mutant		
Fzd1	1276	2165	1.696	0.0034	10.4105	11.1266	1.6428	0.1453
Fzd2	3785	4771	1.2604	0.3315	12.7809	13.2564	1.3904	0.5093
					8.4446	9.1157	1.5901	0.1329
Fzd3	1012	1203	1.1888	0.7214	7.8829	7.8097	-1.0520	0.8892
Fzd4	783	1026	1.3111	0.7226	10.9466	10.6618	-1.1367	0.7599
Fzd5	537	449	0.8353	0.5749	6.1443	6.2109	1.0472	0.9463
					5.2258	5.1257	-1.0719	0.9678
Fzd6	454	561	1.2357	0.6316	6.6942	7.2139	1.4336	0.5564
Fzd7	2140	2877	1.3441	0.2393	8.7803	9.4067	1.5437	0.4224
					7.6324	8.2507	1.5351	0.5440
Fzd8	2448	2113	0.8630	0.7177	9.4843	9.6549	1.1255	0.8367
Fzd9	1123	1358	1.2094	0.4829	12.3317	12.5246	1.1431	0.6826
Fzd10	94	26	0.2795	0.2021	6.6345	5.3970	-2.3579	0.0643

Appendix Table A.3. Differentially regulated Wnt target genes. Wnt target genes more than 2-fold up- or down-regulated, with $p<0.05$ are listed. Abbreviations: co-activator (Co-act), potential target (PT), known target (T), transcription factor-activator (TF-act).

Gene symbol	Gene name	WT reads	Mut reads	Log2FC	P-value	
DOWN-REGULATED						
Fgf4	Fibroblast growth factor 4	56	0	N/A	0.02	T
Snai3	Snail homolog 3	32	0	N/A	0.02	PT
Cacng1	Calcium channel, voltage-dependent, gamma subunit 1	252	3	-6.51	0.00	T
Pitx3	Paired-like homeodomain transcription factor 3	206	5	-5.42	0.00	PT
Ccnb3	Cyclin B3	23	1	-4.88	0.00	PT
Rxrg	Retinoid X receptor gamma	455	37	-3.62	0.00	PT
Islr2	Immunoglobulin superfamily containing leucine-rich repeat 2	270	45	-2.57	0.00	PT
Pitx2	Paired-like homeodomain transcription factor 2	320	66	-2.29	0.02	T
Dll1	Delta-like 1	262	83	-1.66	0.00	T
Prg4	Lubricin	130	43	-1.61	0.00	T
Lrrn1	Leucine rich repeat protein 1, neuronal	2234	794	-1.49	0.05	T
Sall1	Sal-like 1	85	34	-1.33	0.12	PT
Tnik	TRAF2 and NCK interacting kinase	560	227	-1.30	0.00	TF-act
Tcf15	Transcription factor 15	94	40	-1.22	0.02	T
Met	Met proto-oncogene	437	189	-1.21	0.00	T
Jag2	Jagged2	458	219	-1.06	0.04	PT
UP-REGULATED						
Grem2	Gremlin 2	117	509	2.12	0.00	T
Kcnd2	Potassium voltage-gated channel,	224	638	1.51	0.00	T
Cldn1	Claudin-1	394	1076	1.45	0.00	T
Epha4	Eph receptor A4	1545	3657	1.24	0.00	T
Elavl2	ELAV (embryonic lethal, abnormal vision, Drosophila)-like 2	40	84	1.08	0.06	T
Cpz	Carboxypeptidase Z	157	331	1.07	0.15	Co-act

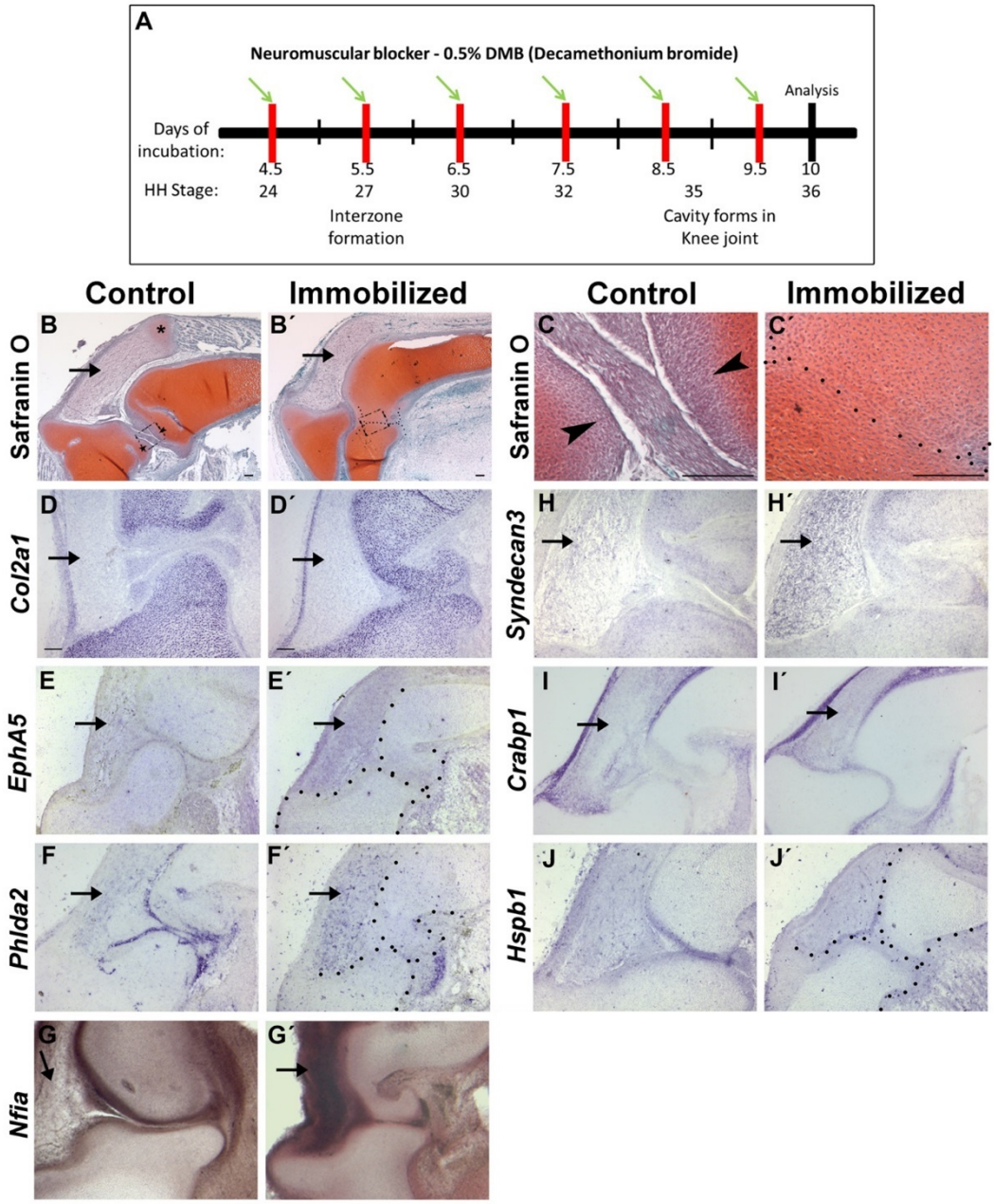

Fig. A.1. Articular cartilage-specific, mechanosensitive genes have altered expression at the immobilised chick knee. Chicks were immobilised using decamethonium bromide (DMB) as per the scheme in (A); controls were treated with PBS on the same schedule. Longitudinal paraffin or vibratome sections underwent staining for Safranin O (B-C') or *in situ* hybridisation for the indicated genes (D-J'). Immobilised chick sections (B'-J') were compared to PBS-treated controls (B-J). Black arrows in (B, B') indicate the fat pat. Black arrowheads in (C) indicate the articular cartilage forming at the chick knee. Black arrows in (D-J') indicate changes in gene expression under immobilisation. Dashed lines outline rudiments.

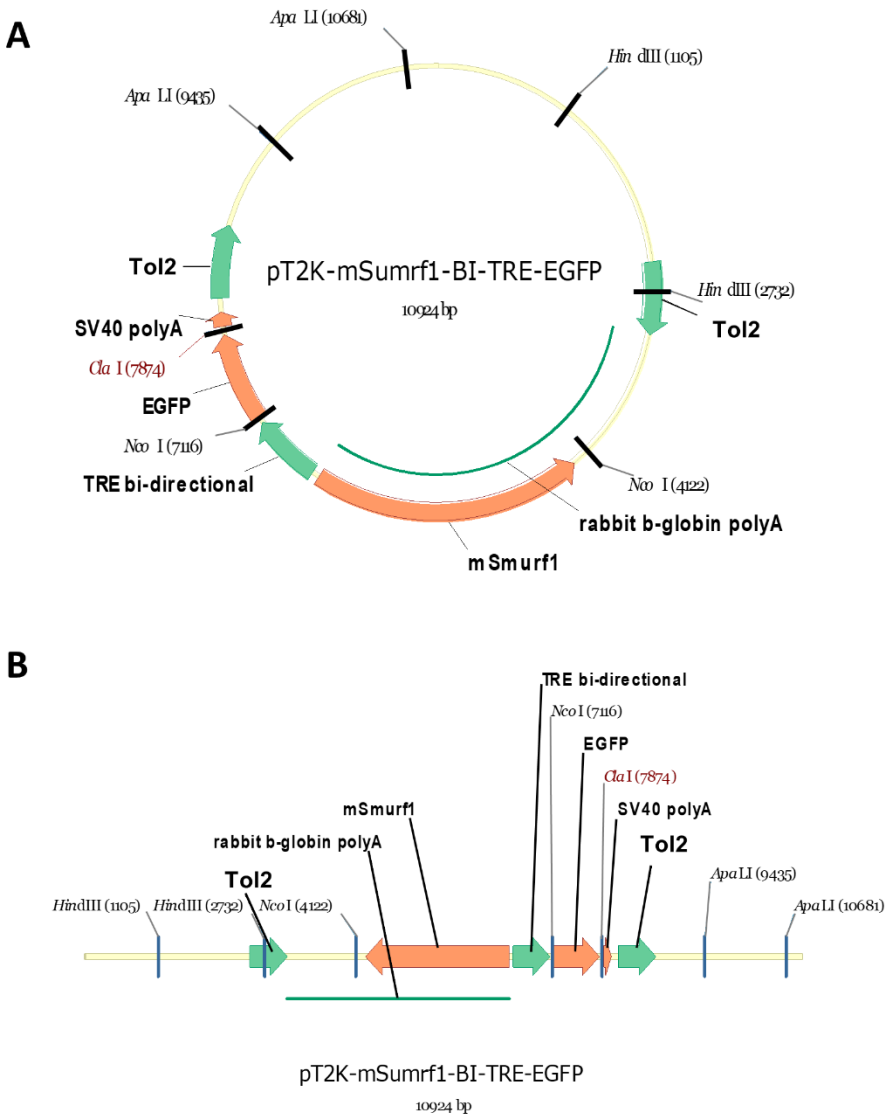

Fig. A.2. Smurf1 electroporation construct. Map of plasmid containing Smurf1 sequence which was electroporated into chick embryos (A). Map of element encoded by the Smurf1 plasmid (B). Maps from Pratik Singh.

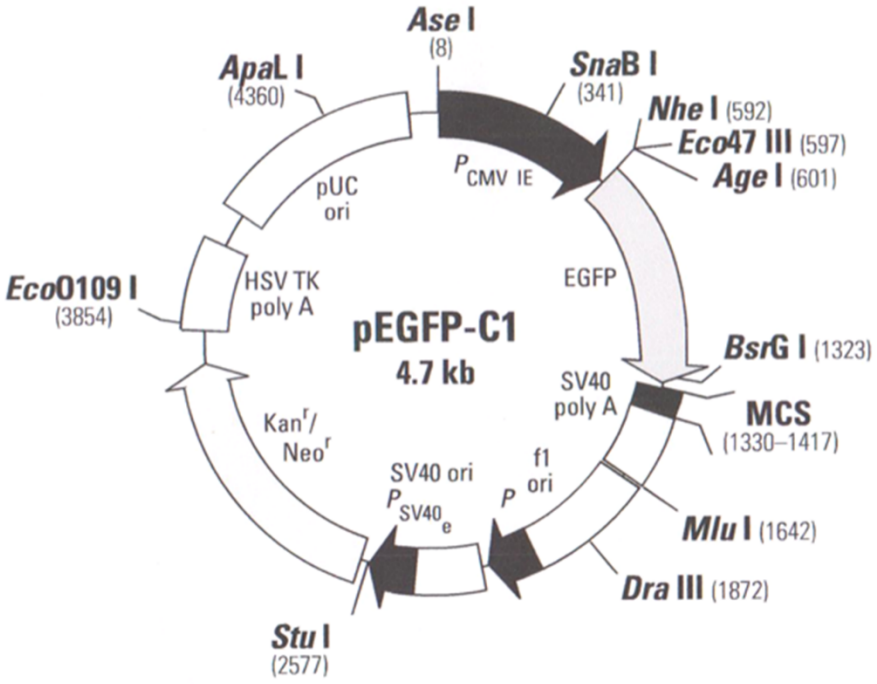

Fig. A.3. Map of GFP-encoding construct. Details of construct encoding an enhanced green fluorescent protein (EGFP), for electroporation into chick forelimb buds and mouse limb bud cells. Fig. from BD Clontech product information (Cat no. 6084-1; GenBank Accession no. U55763).

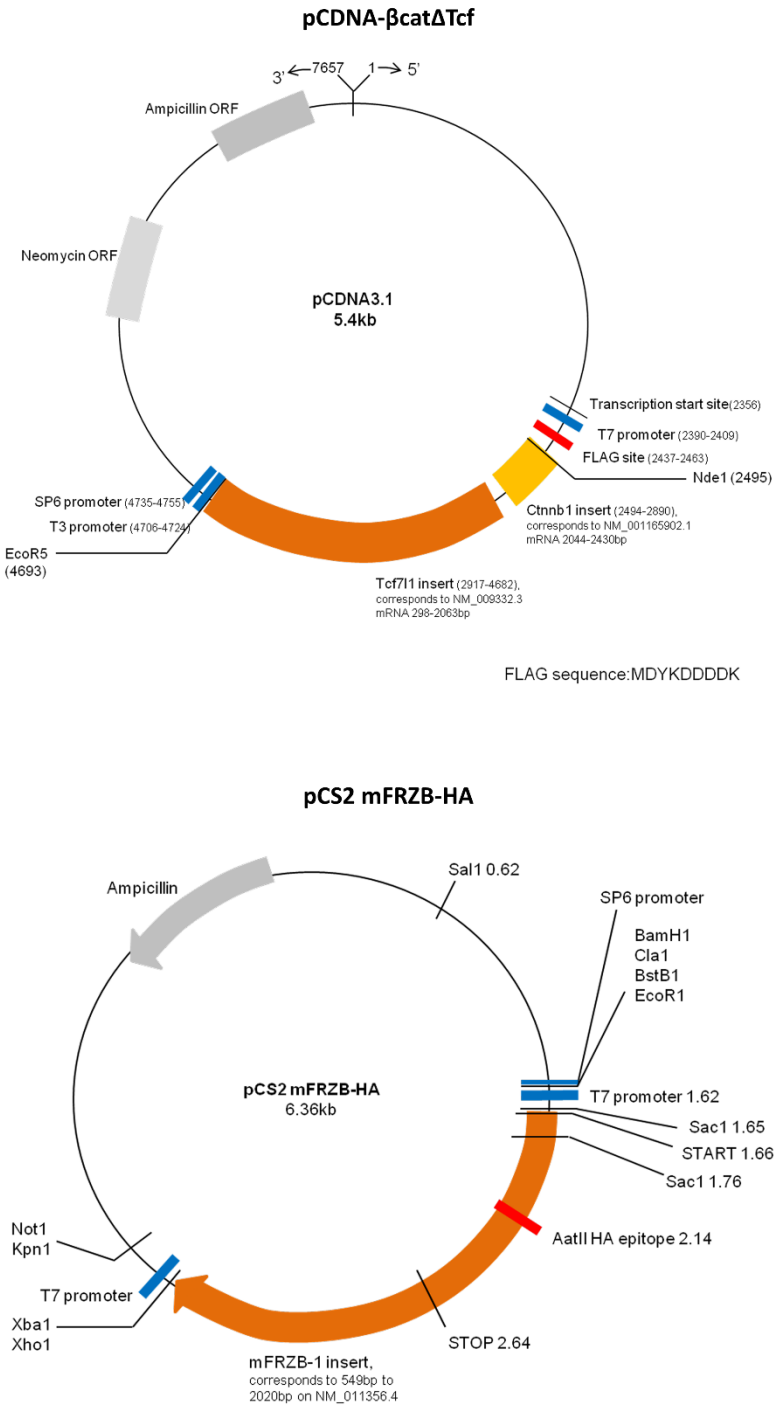

Fig. A.4. Maps of Wnt pathway constructs for chick limb bud electroporation. Details of constructs which were electroporated into chick forelimb buds to ectopically activate or inhibit Wnt pathway activity are given. The β-catenin construct was produced in collaboration with Margaret Buckingham and Frederic Relaix (Pasteur Institute, France) (GenBank Accession number KM189193) and the Frzb construct was the gift of Giulio Cossu (Milan, Italy). Figures from Rebecca Rolfe.

Appendix B. Procedure for analysis of micromasses in ImageJ.

ImageJ is free, public-domain image analysis software created and maintained by the National Institutes of Health (Bethesda, MD, USA) (Schindelin et al., 2012, Schneider et al., 2012). This software was utilised to systematically analyse multiple aspects of micromasses, including nodule number, size, area coverage, and centre points. Detailed below are the specific commands and tools used in ImageJ for this analysis, as outlined in Section 6.2.1.

1. Images of Alcian Blue-stained micromasses were captured on an Olympus dissecting microscope using either IPLab or CellSens software and saved in TIFF (.tif or .tiff) format. All images for a given experiment were captured in one session, to ensure comparable lighting conditions and other settings across replicates and different treatment groups.
2. Original images were opened in ImageJ software.
   > File > Open
3. The image scale was set. Because the dissecting microscope has a continuous-scale magnification objective, the magnification at which images were captured varied slightly between experiments. To ensure accuracy, an image of a ruler with mm markings was captured at the same time as micromasses were imaged. This ruler image was later opened in ImageJ at the same time as the micromass images, and the distance of 1mm was measured in pixels by drawing a line.
   > Analyze > Set Scale
   Distance in pixels: (as measured)
   Known distance: 1
   Unit: mm
4. The image was cropped to a circle with a diameter of 5 mm by specifying a circle which fits in a 5 x 5 mm box and using the cursor to centre the circle over the micromass (as determined by eye). The image was then cropped to this 5 x 5 mm box. The specified circle remains visible and is applied in the next step.
   > **Edit > Selection > Specify**
   Width: 5000
   Height: 5000
   Oval: yes
   Constrain square/circle: yes
   Scaled units (mm): yes
   OK
   > Image > Crop
5. The background area was set to white, and the area outside the circle was cleared (put in the background/filled with white).
   > Image > Color > Color Picker
   Black rectangle in foreground; white rectangle in background **(use ←→ to toggle)**
   > Edit > Clear Outside

Steps 4-5 can be automated by running Macro Circle Clear 5mm (below).

6. Bubbles, debris, and other artefacts were removed from the image by encircling the area to be removed with the freehand selection tool, and filling the shape with white (background).
   Select 'Freehand tool' and draw around the bubble or debris
   > Edit > Clear
7. Split image into three colour channels (red, green, and blue).
   > Image > Color > Split Channels
   Close the red and blue channels and proceed with the green channel window for analysis.
   > File > Close
8. Set the threshold limit for the image.
   > Image > Adjust > Threshold
   Set to manually enter the threshold limit, or use the sliders to adjust.
   Apply to apply the chosen threshold limit to the image.
   Dark background should be de-selected.
9. Remove small particles and noise from the image.
   > Process > Noise > Despeckle
10. Split merged nodules into individuals.
    > Process > Binary > Watershed
11. The desired parameters for analysis were selected.
    > Analyze > Set Measurements
    Area: yes
    Center of mass: yes
    Shape descriptors: yes
    Display label: yes
    Add to overlay: yes
    Decimal places: 3
    OK
12. If not already specified, the area to be analysed was encircled (a yellow circle 5mm in diameter should be visible in the image window). This is to ensure that the analysis is done on the area within the 5 mm circle, not within the 5 x 5 mm window, which would affect final calculations of area. It also ensures that nodules on the edge of the cropped circular area are excluded from the analysis, as they are not fully visible within the area to be analysed and therefore would skew the calculations of nodule size, shape, etc.
    > **Edit > Selection > Specify**
    Width: 5000
    Height: 5000
    Oval: yes
    Constrain square/circle: yes
    Scaled units (mm): yes
    OK

13. The Analyze Particles function is run to generate a list of all objects in the image and their parameters. A summary of object properties is also generated.
> Analyze > Analyze Particles
Size (µm^2): 0.005-Infinity
Pixel units: no
Circularity: 0.00-1.00
Show: Outlines
Display results: yes
Summarize: yes
Exclude on edges: yes
OK
Steps 9-13 can be automated by running Macro Circle Analysis (below).

14. The generated data can be saved as .csv files.
In the results window, select **> File > Save as** ***and name the file, or*** **> Edit > Copy** ***and paste the data into an Excel spreadsheet.***
In the summary window, select **> File > Save as** ***and name the file, or*** **> Edit > Copy** ***and paste the data into an Excel spreadsheet.***
The drawing window, showing outlined objects and their associated count number can be saved by selecting **File > Save as > Tiff** ***in the main toolbar.***

15. At any point in the above process, the intermediary images can be saved as Tiff files for future reference.
> File > Save as > Tiff

16. To create a smaller circle (2 mm in diameter).
> **Edit > Selection > Specify**
Width: 2000
Height: 2000
X coordinate: 2500
Y coordinate: 2500
Oval: yes
Constrain square/circle: yes
Centered: yes
Scaled units (mm): yes
OK

17. Crop image to the box surrounding the 2-mm circle, to create a 2 x 2mm image.
> Image > Crop

18. Clear outside the circle.
> Edit > Clear Outside

Macros are text (.txt) files containing strings of commands that can be run through ImageJ to automate image processing. The details of several macros used in this analysis are presented below. To run the macro, the image(s) to be analysed were opened and the following done:

> Plugins > Macros > Run…

Select the .txt file and click* Open.** ***The commands will be executed and output displayed, to be saved or manipulated by the user.

Macro Circle Clear 5mm

```
run("Specify...", "width=5000 height=5000 x=1 y=1 oval constrain scaled");
setBackgroundColor(255, 255, 255);
run("Clear Outside");
```

Macro Circle Clear 2mm

```
run("Specify...", "width=2000 height=2000 x=2500 y=2500 oval constrain centered scaled");
run("Crop");
setBackgroundColor(255, 255, 255);
run("Clear Outside");
makeLine(289, 29, 289, 29);
```

Macro Circle Analysis 5mm Circle

```
run("Despeckle");
run("Watershed");
run("Set Measurements...", "area centroid perimeter shape feret's redirect=None decimal=3");
run("Specify...", "width=5000 height=5000 x=0 y=0 oval constrain scaled");
run("Analyze Particles...", "size=0.0005-Infinity show=Outlines display exclude summarize");
```

Appendix C. Nearest Neighbour Distance Calculations.

I. Nodule spacing: Nearest Neighbour Distance (centre points), calculated in R.

R is computer language and tool for statistical calculation and analysis that is open-source and free (https://cran.r-project.org/) (R Core Team, 2017). "Packages", which are bundles of code, data, and documentation, are available for download for specific purposes. The package SpatStat is specific to the spatial analysis of 2-D point patterns (Baddeley et al., 2015). This package was used to calculate the nearest neighbour distance of nodule centre points as described in (Section #). The specific steps in R for this analysis are as follows ("#" indicates an explanatory note; ">" indicates an example line of script for R to execute):

The SpatStat package must be installed and opened in the current R session.
> install.packages("spatstat")
> library(spatstat)
The working directory (e.g. folder) must be specified; all .csv files for analysis should be in # the working directory folder
> setwd("Folder/Folder")
The .csv file is read into R as an 'object' (a data structure; in this case a 'data frame' which # is essentially a table)
> object <- read.csv("Data.csv")
The object is converted to a planar point pattern ('ppp'), an object type specific to SpatStat, # by specifying x- and y- coordinates from the above object. [,x] refers to the column
number within the original .csv file that contains the point x-coordinates, while [,y] refers to # the column number that contains the point y-coordinates. c(0,range) specifies the range of # values for x- or y-coordinates.
> pattern <- ppp(Example[,x], Object[,y], c(0.0,xrange), c(0.0,yrange))
The process of importing x- and y- centre point coordinates can be verified by plotting the
pattern. This should generate an image file that resembles the pattern of nodules within the # micromass.
> plot(pattern)
The nearest neighbour distance for each individual nodule (as represented by a centre point) # is calculated. For n number of nodules, this command will generate a list of n values.
> nndist(pattern)
The mean of all nearest neighbour distances in the data set is calculated.
> mean(nndist(pattern))
The standard deviation of the nearest neighbour distances in the data set is calculated.

> sd(nndist(pattern))
The list of n nearest neighbour distances is written to a .csv file in the working directory.
> write.csv(nndist(pattern), "filename")

An example of commands entered into R to calculate the nearest neighbour distances for a specific micromass are detailed below. (">" indicates a line of script for R to execute; "[1]" indicates an example line of output. Some executed steps have no visible output (e.g. naming objects), and others are not visible in the R workspace but are apparent elsewhere (e.g. writing a .csv file will not show any output in the workspace but the .csv file will appear in the directory folder).

Example
> Example <- read.csv("Example.csv")
> Pattern <-ppp(Example[,3], Example[,4], c(0.0,5000.0), c(0.0,5000.0))
> nndist(Pattern)
[1] 263.97817 220.87467 127.14567 127.14567 30.23123 30.23123 188.09638….
> mean(nndist(Pattern))
[1] 148.0279
> sd(nndist(Pattern))
[1] 58.58948
> write.csv(nndist(Pattern), "NNdistPattern.csv")

II. Nodule proximity: Nearest Neighbour Distance (edges), calculated with ArcGIS and Python.

ArcGIS is a software program for manipulating and analysing geographic information systems (GIS). While it is typically used to analyse landscape maps or similar information, we manipulated it to analyse 'maps' (images) of our micromasses. A script written in the Python programming language was used to process raw TIFF files through ArcGIS, calculating the nearest neighbour edge distance and creating a .csv file with the nearest neighbour distance recorded for each detected object (nodule). The average value was then calculated for each micromass. The code to calculate and list the nearest neighbour distances (NearestTable.py) and to rename the files (Rename_files.py) were both written by Dermott McMorrough with assistance from Jesko Zimmerman at TCD. The files NearestTable.py and Rename_files.py (which can be viewed and modified in a text editor) must be in the same folder as the TIFF files to be analysed. Running the NearestTable.py will automatically retrieve all TIFF files in the same folder, process them, and write a .csv file as explained above.

NearestTable.py

```
import os, arcpy, shutil, sys
abspath = os.path.abspath(__file__)
dname = os.path.dirname(abspath)
os.chdir(dname)
inFolder = dname
arcpy.env.workspace = inFolder
RasterList = arcpy.ListFiles("*.tif")
for inRaster in RasterList:
        outFC = arcpy.RasterToPolygon_conversion(inRaster,
os.path.basename(inRaster).replace('.tif', '.shp'))
        uCursor = arcpy.da.UpdateCursor(outFC, 'gridcode')
        for uRow in uCursor:
                if uRow[0] == 255:
                        uCursor.deleteRow()
        del uCursor
        arcpy.GenerateNearTable_analysis (outFC, outFC,
os.path.basename(inRaster).replace('.tif', '.csv'))
        arcpy.Delete_management(outFC)
```

Rename_files.py

```
import os, fnmatch, shutil, sys
abspath = os.path.abspath(__file__)
dname = os.path.dirname(abspath)
os.chdir(dname)
#for filename in os.listdir(abspath):
for filename in inFolder:
        if fnmatch.fnmatch(filename, [.tif (green).tif]):
                print filename
                #os.rename(filename, filename.replace('.tif (green).tif', '////////////.tif')
```